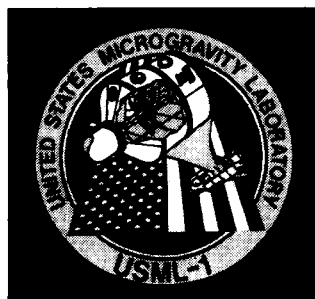


NASA Conference Publication 3272

Volume I

Joint Launch + One Year Science Review of USML-1 and USMP-1 with the Microgravity Measurement Group

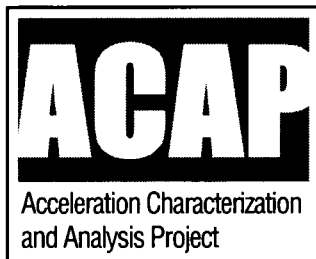
Edited by
N. Ramachandran, D.O. Frazier,
S.L. Lehoczky, and C.R. Baugher



(NASA-CP-3272-Vol-1) JOINT LAUNCH
+ ONE YEAR SCIENCE REVIEW OF USML-1
AND USMP-1 WITH THE MICROGRAVITY
MEASUREMENT GROUP (NASA. Marshall
Space Flight Center) 521 p

N95-14207
--THRU--
N95-14228
Uncclas

H1/88 0017011



Proceedings of a conference
held at Huntsville, Alabama
September 22-24, 1993

May 1994

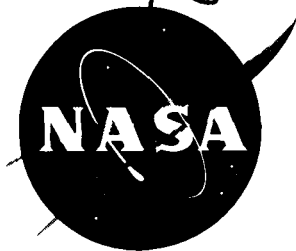
10 pg

324042

1995107793

NASA Conference Publication 3272

Volume I



Joint Launch + One Year Science Review of USML-1 and USMP-1 with the Microgravity Measurement Group

Edited by

N. Ramachandran

Universities Space Research Association

Huntsville, Alabama

D.O. Frazier, S.L. Lehoczky, and C.R. Baugher

NASA, Marshall Space Flight Center

Marshall Space Flight Center, Alabama

Proceedings of a conference
held at Huntsville, Alabama
September 22-24, 1993

National Aeronautics and Space Administration

Marshall Space Flight Center • Marshall Space Flight Center, Alabama 35812

May 1994

Foreword

On September 22-24, 1993, investigators from the First United States Microgravity Laboratory (USML-1) and the First United States Microgravity Payload (USMP-1) Missions met with the Microgravity Measurement Group (MGMG) in Huntsville, Alabama, to discuss science results and the microgravity environments from the respective missions. USML-1 was launched June 1992, and USMP-1 was launched October 1992. It was also the intent of the meeting to summarize, from the various investigations, the comprehensive results and highlights which have hitherto been available only on a piecemeal basis. This information dissemination was directed not only toward the scientific community but also for general public awareness and education. These two missions presented outstanding research opportunities and as Robert Rhome of NASA Headquarters put it, represented the threshold of the microgravity program contribution to the technological and competitive front of the United States. They ushered in a new era of microgravity research and we look forward to several more successful missions in the future.

The USML-1 mission was the first totally U.S.-sponsored mission dedicated to microgravity research and included 31 investigations in fluid dynamics, crystal growth, combustion, biotechnology, and technology demonstrations supported by 11 facilities. This mission was a cooperative effort between government, industry, and academia and boasted the longest shuttle flight to date (MET 13 days, 19 hours, 31 minutes), setting the stage for longer stays in orbit. Three new facilities, Crystal Growth Furnace, Surface Tension-Driven Convection Experiment, and Drop Physics Module, made their space flight debut on USML-1. A European Space Agency facility, Glovebox, also made its debut and provided an opportunity for scientists/astronauts to perform experiments much like they would in an Earth-bound laboratory.

Among the mission highlights, the Protein Crystal Growth Experiment yielded crystals of Malic Enzyme (a protein important in the development of anti-parasitic drugs) that showed a dramatic improvement in diffraction resolution over Earth-grown crystals. This success follows 2 years, and several hundred ground-based crystallization trials, during which researchers were unable to produce any crystals of high enough quality to allow determination of this protein's structure. The Crystal Growth Furnace completed 286 hours of processing time with no anomalies. At least two space-grown crystals of cadmium-zinc-telluride (used in devices for infrared energy detection) have dramatically demonstrated the benefits of removing gravity's influence during crystal formation. The crystals benefited from a thousand-fold

decrease, compared to Earth-grown counterparts, in the occurrence of dislocation defects, and showed infrared radiation-transmission levels approaching the theoretical maximum. The Surface Tension-Driven Convection Experiment was the first United States thermocapillary flow experiment conducted in the microgravity environment of Spacelab. Steady thermocapillary flows at large Marangoni numbers and with large curved free surfaces were quantitatively described over a wide range of conditions in a configuration not previously considered and with two different modes of imposing the thermal driving forces.

Both the MEPHISTO and the Lambda Point experiments, flown on the highly successful first United States Microgravity Payload (USMP-1) mission on STS-52, exceeded by over 100% their planned science objectives. For the first time the acceleration data provided by the Space Acceleration Measurement System (SAMS) were down-linked and analyzed in real-time by the Acceleration Characterization and Analysis Project (ACAP). Changes in the liquid/solid interface temperature as deduced from the *in situ* Seebeck data of the MEPHISTO Experiment clearly showed the strong influence of microgravity disturbances on the solidification process. The *in situ* measurements were also able to identify and quantify the evolution of the solidification front from planar to cellular to highly dendritic as a function of solidification speed. Such data are vital for a test of the range of validity of current theories pertaining to binary alloy solidification processes. The Lambda Point Experiment involved the best measurement of the heat capacity of liquid helium as it changes phase from the superfluid to the normal fluid phase to within 10^{-9} K of the transition temperature. The objective of the experiment was to rigorously test the range of validity of Wilson's Nobel Prize renormalization group theory as it pertains to critical phase transitions. Hydrostatic pressure effects, caused by gravity, result in increased "smearing" of the data as the critical point is approached. During flight, in the absence of hydrostatic pressure effects, over a ten-fold improvement in resolution could be achieved. Overall, the preliminary analysis of the results show the potential for yielding, by far, the most definitive test of renormalization group theory that has ever been performed.

The meeting, which concentrated on flight results, brought low-gravity investigators, accelerometer designers, and acceleration data analysis experts together. This format facilitated a tremendous amount of information exchange between these varied groups that will foster a better understanding of the complex issues that affect experiments onboard a spacecraft. Several of the experimenters showed results, some for the very first time, of the effects of residual accelerations experienced in Spacelab on their experiment. These types of correlations are a first step in understanding the secondary effects of g-jitter on experiments that can lead to better planning and execution in future efforts.

The meeting was held over 3 days with a good dispersion of the talks from the different disciplines. A press briefing was held on the second day and a poster session was also organized where 12 exhibitors participated. The contents of this document are closely based on the meeting agenda. Some of the Principal Investigator reports also include results from a separate Glovebox experiment by the same PI.

The untiring efforts and dedication of the STS-50 and STS-52 payload crew, the Mission and Program Managers, and the mission operations personnel were, of course, critical to the completion of these missions' objectives and are sincerely appreciated. The editors thank the Office of Life and Microgravity Sciences Applications (NASA Code U) and the Office of Advanced Concepts and Technology (NASA Code C) for support in organizing the conference. The editors also thank the MSFC Audio Visual department for audio and video coverage of the entire meeting, and all the participants for contributing to its success.

*Donald O. Frazier
Mission Scientist, USML-1, NASA MSFC*

*N. Ramachandran
USRA*

*Sandor L. Lehoczky
Mission Scientist, USMP-1, NASA MSFC*

*Roger Crouch
Program Scientist, USML-1
NASA Headquarters*

*Charles R. Baugher
ACAP Project Scientist, NASA MSFC*

*Stephen Davison
Program Scientist, USMP-1
The Bionetics Corp.*

| *Contents*

<i>Title/Principal Author</i>	<i>Page</i>
VOLUME I	
Opening Remarks — Robert Rhome / NASA HQ	1
<i>USMP-1 Investigations and STS Acceleration Environment</i>	
Heat Capacity and Thermal Relaxation of Bulk Helium Very Near the Lambda Point — John Lipa / Stanford University.....	5
Mass Transport Phenomena in Microgravity – Preliminary Results of the First MEPHISTO Flight Experiment — Jean Jacques Favier / CEREM.....	27
Basic Features of the STS/Spacelab Vibration Environment — Charles Baugher / NASA MSFC	45
Review of European Microgravity Measurements — Hans Hamacher / DLR	65
<i>USML-1 Investigations and Mission Quasi-Steady Acceleration Environment</i>	
The Solid Surface Combustion Experiment Aboard the USML-1 Mission — Robert Altenkirch / Mississippi State University	83
Preliminary OARE Absolute Acceleration Measurements on STS-50 — Robert Blanchard / NASA LaRC	103
Orbital Processing of High Quality CdTe Compound Semiconductors — David Larson / Grumman Aerospace Corp.	129
Crystal Growth of Selected II-VI Semiconducting Alloys by Directional Solidification — Sandor Lehoczky / NASA MSFC	163
The Study of Dopant Segregation Behavior During the Growth of GaAs in Microgravity — David Matthiesen / Case Western Reserve University....	223
Vapor Transport Crystal Growth of Mercury - Cadmium - Telluride in Microgravity — Heribert Wiedemeier / Rensselaer Polytechnic Institute	263
<i>USML-1 Investigations</i>	
Surface Tension Driven Convection Experiment (STDCE) — Simon Ostrach / Case Western Reserve University.....	271
Core-Centering of Compound Drops in Capillary Oscillations: Observations on USML-1 Experiments in Space — Taylor Wang / Vanderbilt University	301

Contents continued.

<i>Title/Principal Author</i>	<i>Page</i>
Bifurcation of Rotating Liquid Drops: Results From USML-1 Experiments in Space — Taylor Wang / Vanderbilt University	321 - 13
Surface Characterization Through Shape Oscillations of Drops in Microgravity and 1-g — Robert Apfel / Yale University	339 - 14
Measurement of Interfacial Tension of Immiscible Liquid Pairs in Microgravity — Michael Weinberg / University of Arizona.....	361 - 15
Extended Duration Orbiter Medical Project Microbial Air Sampler – (STS-50/USML-1) — Duane Pierson / NASA JSC	375 - 16
Extended Duration Orbiter Medical Project Variability of Blood Pressure and Heart Rate – (STS-50/USML-1) — Janice Fritsch-Yelle / NASA JSC	383 - 17
Extended Duration Orbiter Medical Project Countermeasure to Reduce Post Space Flight Orthostatic Intolerance (LBNP) (STS-50/USML-1) — John Charles / NASA JSC	391 - 18
Protein Crystal Growth Results From the United States Microgravity Laboratory-1 Mission — Lawrence DeLucas / University of Alabama at Birmingham	409 - 19
The Growth of Zeolites A, X, and Mordenite in Space — Albert Sacco / Worcester Polytechnic Institute	447 - 20
Commercial Investigation Results for the Generic Bioprocessing Apparatus Flown on United States Microgravity Laboratory-1 — Louis Stodieck / University of Colorado	473 - 21
The Astroculture™-1 Experiment on the USML-1 Mission — Theodore Tibbitts / University of Wisconsin - Madison	509 - 22

VOLUME II

USML-1 Glovebox Investigations

Interface Configuration Experiment: Preliminary Results — Paul Concus / University of California - Berkeley.....	525
Candle Flames in Microgravity: USML-1 Results - 1 Year Later — Howard Ross / NASA LeRc	541
Passive Accelerometer System: Measurements on STS-50 (USML-1) — Iwan Alexander / University of Alabama in Huntsville	569
Solid Surface Wetting and the Deployment of Drops in Microgravity — Eugene Trinh / NASA JPL	583
Marangoni Convection in Closed Containers (MCCC) — Robert Naumann / University of Alabama in Huntsville	601

Contents continued.

<i>Title/Principal Author</i>	<i>Page</i>
Microgravity Smoldering Combustion on the USML-1 Space Shuttle Mission — Carlos Fernandez-Pello / University of California - Berkeley	609
Wire Insulation Flammability Experiment: USML-1 One Year Post Mission Summary — Paul Greenberg / NASA LeRC.....	631
Fiber Pulling in Microgravity (FPM) — Robert Naumann / University of Alabama in Huntsville	657
Nucleation of Crystals From Solution in Microgravity (USML-1 Glovebox (GBX) Investigation) — Roger Kroes / NASA MSFC	663
Oscillatory Dynamics of Single Bubbles and Agglomeration in a Sound Field in Microgravity — Philip Marston / Washington State University	673
Double Float Zone (DFZ) — Robert Naumann / University of Alabama in Huntsville	691
Oscillatory Thermocapillary Flow Experiment (OTFE) — Simon Ostrach / Case Western Reserve University	701
Particle Dispersion Experiment (PDE): Preliminary Results From the USML-1 Glovebox — John Marshall / NASA ARC	717
<i>Microgravity Sensors, Measurements, and Analysis</i>	
ESA Activities on Microgravity and Microdynamics — Hendrik Stark ./ ESA-ESTEC	733
Microgravity Data Analysis and the MIR Environment — Jean-Pierre Granier / CNES	761
Orbital Acceleration Research Experiment Instrument Performance on STS-50 — Patrick McNally / Canopus Systems Inc.	771
Positive Energy Growth Effects on USML-1 — Brian Matisak / Teledyne Brown Engineering	785
Summary Status of the Space Acceleration Measurement System (SAMS) — Richard DeLombard / NASA LeRC	797
NASA Ultra-Sensitive Miniature Accelerometer — Frank Hartley / NASA JPL.....	813
Further Enhancements in Nano-g Accelerometry: The Cube MESA — Patrick McNally / Canopus Systems Inc.	827
Microgravity Measurement Assembly (MMA) – A Centralized On-Board Measurement Facility — Ingo Gerhard / DASA-ERNO Raumfahrttechnik.....	839

Contents continued.

<i>Title/Principal Author</i>	<i>Page</i>
QSAM – An Approach to Detect Low Frequency Acceleration in Spacelab — Hans Hamacher / DLR	857
EURECA Microgravity Environment – Preliminary Flight Data — D. Eilers / ERNO Raumfahrttechnik	869
Correlation of Accelerometer Data on STS-50 (USML-1) — Melissa Rogers / University of Alabama in Huntsville	893

Papers From the Poster Session

Design Considerations for a Microgravity Isolation System to Fly on Space Shuttle — Donald Edberg / McDonnell Douglas Aerospace	909
Preliminary Calibration Report of an Apparatus to Measure Vibration Characteristics of Low Frequency Disturbance Source Devices — James Russell / Lockheed Engineering and Sciences Co.....	921

Appendix

A. Keynote Address — Bonnie Dunbar / NASA JSC	935
B. The International Flight Accelerometer Data Base	939
C. Meeting Attendee List	947

Contents concluded.

OPENING REMARKS

Robert C. Rhome
Microgravity Science and Applications Division
NASA Headquarters, Washington, D.C.

This meeting has special significance to the entire microgravity community. We have the opportunity to listen first hand to the investigators as they review their scientific results from the First United States Microgravity Laboratory (USML-1) that flew in June 1992. The experiments covered a wide gamut of disciplines of scientific interest from protein crystal growth, fluid physics, and materials processing to areas in bio-medical technology that is vital for future long-duration flights and the space station. The meeting will also feature presentations from the principal investigators from the first United States Microgravity Payload (USMP-1) mission that flew in October 1992. The microgravity experimenters are joined here by experts from the acceleration measurement and analysis community with their presentations in providing a unique forum for the mutual exchange of scientific information. This effort should prove beneficial in the design and implementation of microgravity experiments in the future.

The sessions start with presentations from the two USMP-1 investigators this morning. The Lambda Point Experiment was unique in the development and use of a control system capable of being commanded from the ground by the Principal Investigator, in real time, to control the temperature with an accuracy approximating 1 billionth of a Kelvin; this was a hundred times better than possible on Earth. The microgravity science program, with the help of our Principal Investigator, John Lipa, defined it, designed it, developed it, shipped it, and it worked. I think that is an important part of the kind of things we are doing in a multi-disciplinary activity in supporting scientific research. As important, is the development of technology that not only enhances and enables but can be in fact transferred on to other activities, and I think we should never miss this link in our discussion about the science activities. The Lambda Point Experiment operated flawlessly; close to 100 high resolution heat capacity measurements were performed across the helium lambda point. This experiment also demonstrated the utility of the investigators on the ground being able to directly interact with flight instruments and the use of telescience as an important element that we are going to take advantage of in the future. Through the use of telescience, more than 5,000 commands were successfully sent up to that flight experiment. Telescience techniques were used to operate other experiments on USMP-1 and provided what Joel Kearns, NASA's solidification research program manager, described very succinctly for both USMP-1 and USML-1 when he said that when you look at telescience capabilities, you are really looking at a

window to the future for early space station operations. On the other hand, the commanding of the French-built MEPHISTO Experiment (Matériel pour l'Etude des PHénomènes Intéressant la Solidification sur Terre et en Orbite), again in real time, allowed the French-led investigator team on USMP-1 to successfully use the MEPHISTO instrument to collect data on solidification of a tin-based alloy system. Telescience and tele-operations are central to our plans for exploiting the capabilities of the spacecraft in our program and the space station in the future. I think we dramatically and successfully demonstrated that not only on USMP-1 but also on USML-1. The USML-1 mission has served as a space station precursor flight in low-Earth orbit in demonstrating the operating concept of the Space Station Furnace Facility. We remember the picture where our payload commander had one of the cartridges from the Crystal Growth Furnace (CGF) in her hands, and I think that demonstrating enabling capabilities is as important as the science we wanted to do.

As you will hear further this afternoon on our schedule, the CGF Furnace, also developed by MSFC in Huntsville, demonstrated three firsts to our particular program:

- 1) the use of up-link software commands directed by the investigators in response to the down-link data in order to control the experiments;
- 2) the automatic exchange of samples that the CGF offered to us as part of the integrated furnace experiment assembly, and
- 3) the demonstration of the manual exchange of the samples by the crew in order to improve the output of the facility using a flexible Glovebox designed specifically for that purpose by the user.

This provided, as I have indicated to you, proof of concept 5 years before space station is going to be available to us, that this particular kind of activity could in fact be done in low-Earth orbit and could be done to the advantage, not only of our particular use in the community, but to the larger international community.

Tomorrow we will hear more about the much applauded USML-1 mission and the program that represents the synthesis of program science and program management skills resulting in new approaches to meet the challenges of USML-1 launch commitment made to Congress in 1988. The first two flight experiments we will discuss tomorrow use major flight hardware that were developed and delivered at KSC only 3 years after payload confirmation and, once again, proved perfect that the user community can in fact, define, design, develop, test, and ship user hardware for our particular program. The first two flight experiments we will discuss tomorrow will be the Surface Tension-Driven Convection Experiment (developed by Lewis Research Center) that was used to conduct studies in fluid mechanics and heat transfer in low gravity, and the Drop Physics Module which was developed by the Jet Propulsion Laboratory which used sound waves to position and manipulate samples for three investigations and for physical and chemical properties and dynamics of liquid drops. The morning

session tomorrow will conclude with a discussion of the Extended Duration Orbiter Medical Program activities that were conducted aboard USML-1, a critical related program that builds a data base which will allow us to enable the extension of Spacelab and other crew flights to a 16-day duration. As you know for USML-2 in 1995, it is our hope through the use of the EDOMP program we will be able to fly a full 16-day mission with its very valuable science and is currently being developed by the user community and to aid the onboard crew that will begin undergoing training here in the not-too-distant future. Tomorrow afternoon we will review the acceleration measurement activities on USML-1 as related to evaluating thruster firing and crew exercise activities onboard missions involving hands-on, low-gravity research. We will review the results of protein crystal growth experiments jointly funded by the Microgravity Science and Applications Division and the Office of Advanced Concepts and Technology, through their Center for Macromolecular Crystallography, as part of their effort for the commercial development of space.

We will also look at the results from three other experiments that were sponsored by the Office of Advanced Concepts and Technology and from the Centers for the Commercial Development of Space. Specifically, we will review the activities of the Zeolite Crystal Growth conducted by the PI team from Battelle headed by Al Sacco, we will look at the Generic Bioprocessing Apparatus and the evaluation of a water delivery system to support the growth of the plants in microgravity which was called the Astroculture Experiment. We will close tomorrow with a plenary session with a first look at Glovebox investigations and I will discuss that briefly in just a second. Tomorrow night we have an opportunity to hear at the dinner a presentation by the payload commander on USML-1 to add her insight to the processes and experiences that were very critical to ensure success on that mission. I, along with you all, look forward to the opportunity to hear Dr. Bonnie Dunbar, and then we will adjourn and go to an IMAX film I understand that lets you see some of the things that have been going on, not only in this particular program, but in the space program as a whole.

In the continuing spirit of international cooperation, the European Space Agency provided the Spacelab Glovebox to us on USML-1 as part of a quid pro quo that we had developed as part of our ongoing collaboration program with all of our international partners in a broad range of activities. This particular quid pro quo allowed 24 NASA investigators to perform 16 different experiments on USML-1, and on Friday, we will be able to review the results of the remainder of those activities. The Glovebox offered us an additional capability to test and develop science and technology procedures in microgravity. It enabled crew members to handle, transfer, and otherwise manipulate samples of materials in ways that probably would not have been possible in the open environment of the Spacelab. It was, in fact, an enhancement to our onboard activities and certainly was enabling in many areas. You will hear on Friday, as we certainly heard around the Payload Operations Control Center during and

since the flight in June-July of last year, the investigative report that the Glovebox was an invaluable resource for us to perform microgravity experiments in a manner similar to those performed in a terrestrial laboratory. Microgravity sciences and the technology related activity thereto are hands-on activities so we hope to be able to do those things in space as closely as we have been doing them on Earth, in an interactive process involving a multi-disciplinary type activity. Based upon the results that you will hear on Friday, I think it is easy to see why the Space Station Microgravity Glovebox holds the highest priority for early development and deployment to Station of all the facilities under design and development for the international Space Station by NASA's Microgravity Science and Applications Division. As you know, we have participated as a program office, with our science advisory group and Principal Investigators currently in our program, to work with the Station in defining the capabilities for that particular piece of general lab support facility. We feel very comfortable with the process that we have used in collaboration with space station in defining those specifications and are now looking forward to ensure the development of that particular critical piece of equipment proceeds on schedule.

Last year was an exciting one for researchers both ground-based and those using the on-orbit facilities offered by USML-1 and USMP-1. The ground-based program is, in fact, the intellectual underpinning of our flight program, and many of you have spent years working on these programs refining and defining the activity that needs to be done to ensure that the parameter that you needed was, in fact, gravity. You demonstrated to yourself and to your peers that you had thought out the process to an extent that would allow you to test the hypothesis and that the hypothesis had meaning on the carrier to which it was assigned. For those of you involved in USMP and USML-1, the carrier choice was, in fact, Spacelab hardware and the Mission Peculiar Support Structure that was developed here at MSFC. For those of you who have been participating in our Spacelab program, you know that speed is not necessarily one of the things that we are well noted for, but as you listen to the results today and more on Friday, you will realize that the efforts to ensure that we have the right people at the right place with the right hardware at the right time is critical to the kinds of growth in the science program that we are looking at. We do look forward to building upon the results that you hear this week to develop and sustain a preeminent microgravity science program both in science research and applications as it relates to our activities.

22 pg

1995-107794

N95-14208

324046

17012

HEAT CAPACITY AND THERMAL RELAXATION OF BULK HELIUM P 21 VERY NEAR THE LAMBDA POINT

J. A. Lipa*, D. R. Swanson*, J. A. Nissen*, and T. C. P. Chui[†]

*Department of Physics, Stanford University, Stanford, CA.

[†]Jet Propulsion Laboratory, California Institute of Technology, Pasadena, CA.

ABSTRACT

In October 1992 a low temperature experiment was flown on the Space Shuttle in low Earth orbit. The objective of the mission was to measure the heat capacity and thermal conductivity of helium very close to the lambda point with the smearing effect of gravity removed. We report preliminary results from the experiment, and compare them with related measurements performed on the ground. The sample was a sphere of helium 3.5 cm in diameter contained within a copper calorimeter of very high thermal conductivity. The calorimeter was attached to a pair of high resolution paramagnetic salt thermometers with noise levels in the $10^{-10} K$ range and suspended from a high stability thermal isolation system. During the mission we found that the resolution of the thermometers was degraded somewhat due to the impact of charged particles. This effect limited the useful resolution of the measurements to about two nanokelvins from the lambda point. The results reported here are limited to about ten nanokelvins from the transition.

INTRODUCTION

Since the first high resolution measurements of the heat capacity singularity at the lambda point, this transition has become the most important testing ground for theories of second order phase transitions. The transition is very sharp because of the strain-free nature of the fluid and its relatively low compressibility. With sample heights of the order of millimeters, values of t as small as 10^{-7} can be reached on Earth before intrinsic distortion is encountered. Here $t = |1-T/T_\lambda|$ is a dimensionless temperature parameter, and T_λ is the transition temperature. The ultimate limit in ground based measurements is usually encountered when finite size effects¹ become appreciable, generally near $t \approx 5 \times 10^{-8}$. In space, the lambda transition may be sharp to $t \sim 10^{-12}$ or so², in optimal conditions. Since the early 70's the aim of most high resolution experiments in this region has been to test the renormalization group (RG) formalism developed by Wilson³ to predict the singular thermodynamic behavior observed in

many systems. In particular, this formalism led to numerical predictions for many 'universal' parameters, that is, system independent quantities, such as the exponents governing the divergence of various thermodynamic variables.

Over the past 18 years we have developed the technology to perform a high resolution heat capacity experiment near the lambda point on the Space Shuttle. High resolution thermometry with a resolution of $\sim 3 \times 10^{-10}$ K was developed, along with a thermal control system with a stability of about 10^{-8} K. The calorimeter was optimized for a residual acceleration level of 2×10^{-4} g, and a corresponding resolution at the lambda point of $t \sim 4 \times 10^{-10}$. The acceleration level was chosen as a compromise between the lower dc acceleration normally encountered on the Shuttle, and the somewhat higher ac level. The experiment design allows about two orders of magnitude higher resolution than is possible on Earth, leading to a substantially improved measurement of the heat capacity curve and a better estimate of the exponent α characterizing its divergence at the transition temperature. The thermal conductivity of the helium above the transition can also be derived from the relaxation data associated with the heat capacity measurements.

In this paper we briefly describe the technology that was developed to make the measurements, and discuss preliminary results from the mission, which was flown in October 1992. We also compare the results with extrapolations derived from ground-based data.

I. APPARATUS

The basic design of the apparatus is similar to that used for earlier heat capacity measurements⁴ on helium samples with small vertical height performed at Stanford. A number of structural changes were made to improve its ability to survive launch into space. In this and the following sections we briefly describe the flight design with emphasis on those features most critical for high resolution work.

The most significant problems one is faced with when designing a high resolution heat capacity experiment are temperature resolution and thermal control. Conventional thermometry, e.g. germanium resistance thermometry, allows a resolution approaching 10^{-7} near T_λ with low power dissipation. Higher resolution would require increasing the power input, which rapidly leads to unacceptable thermal gradients. Since the goal of our experiment was to achieve a resolution of 4×10^{-10} , we were immediately faced with the development of a new high resolution thermometer (HRT). The device we developed makes use of superconducting technology to achieve a resolution of about 3×10^{-10} K in a 1 Hz bandwidth with negligible power dissipation, and is briefly described below.

To make the heat capacity measurements with the desired resolution it is necessary to meter energy into the sample in units as small as $10^{-9}C$ Joules, where C is the heat capacity of the sample. In our case, for a heater that operates for a few seconds, this corresponds to powers of the order of 10^{-8} W.

In addition, during the period used to measure the corresponding temperature rise, the variability of the background power input must be less than $\sim 10^{-10}$ W. This means that very careful thermal control of the sample environment is necessary. To achieve this, we built a four stage thermal control system which used a HRT on the inner stage as a fine control sensor. This control system was the major portion of the low temperature apparatus which comprised the flight instrument. It is also described below. A third item of great importance is a helium dewar capable of operating in space. We made use of the previously flown JPL low temperature facility which has the capability of easily operating near 2 K in zero gravity. The performance of this system is described elsewhere⁵.

II. THERMOMETRY

The construction of the HRTs has been described in some detail elsewhere⁶. Briefly, they consist of a superconducting tube surrounding a crystal of paramagnetic salt which is thermally coupled to the experiment. The tube applies a fixed magnetic field to the salt. As the temperature of the experiment changes, so does the magnetization of the salt, due to its Curie law susceptibility. A superconducting pickup loop is wound on the salt and couples the changes in magnetization to an rf SQUID magnetometer for readout. A schematic view of the device is shown in figure 1. The HRTs were designed to be mechanically very rugged, and all critical wiring was bonded as firmly as possible. The salt pill and pickup coil assembly were heavily coated with a vacuum grease/kerosene mixture which froze early in the cool-down cycle. The holder of this assembly was in turn locked into the flux tube by differential contraction.

To reduce the effect of the varying orientation of the HRTs with respect to the Earth's magnetic field, three layers of shielding were used. The HRT flux tube itself has an extremely high theoretical shielding factor at the location of the pickup loop, but tests showed⁷ that this could be compromised by flux creep through the walls. The maximum safe shielding factor from this tube was estimated to be about 5×10^9 . A second superconducting shield was added around the instrument vacuum can with a theoretical shielding factor of about 200. Also, a layer of moly-permalloy was placed around the outside of the dewar to gain another factor of 100. Tests of the complete assembly showed no detectable signal for fields of the order of 1 G applied externally.

For a field of 100 G trapped in the flux tube, the sensitivity of a HRT is typically in the range 3 - 4 $\Phi_0/\mu\text{K}$, where Φ_0 is the quantum of magnetic flux. Since the SQUID noise level is at least as low as $10^{-4} \Phi_0/\sqrt{\text{Hz}}$, a resolution of $\sim 3 \times 10^{-11}$ deg is possible in principle. In general, a much larger noise level is seen. The noise characteristics of a HRT can be studied by attaching it to a large thermal reservoir and reducing the heating rate to below 10^{-12} K/sec by careful thermal control. A typical noise spectrum obtained this way is shown in figure 2. The noise data agrees well with the prediction of the fluctuation-

dissipation theorem applied to temperature fluctuations⁸. This is shown by the solid line in the figure, with no adjustable parameters. The HRT noise per unit bandwidth in the low frequency region is normally about $3 \times 10^{-10} \text{ K}/\sqrt{\text{Hz}}$. The absolute drift rate of the HRTs has been found to be $\sim 10^{-14} \text{ K/sec}$ by observing the apparent location of the lambda transition as a function of time in various high resolution experiments.

III. THERMAL CONTROL SYSTEM

The thermal control system used in the flight experiment consisted of a multi-stage thermal platform located in the helium dewar, and an electronics assembly that housed the servos for the various levels of thermal control, along with the readout electronics for the HRTs. It has been described in some detail elsewhere⁹. The platform (shown in figure 3) consists of a vacuum shell about 20 cm in diameter and 60 cm long surrounding four thermal control stages in series and the calorimeter. A set of four HRTs are housed in the lower part of the assembly and are surrounded by a thermal shield attached to the innermost stage of the control system. A solenoid is mounted on the outside of the lower portion of the vacuum can to allow the application of a magnetic field to the HRTs during initial cool-down. A cylindrical superconducting shield open at one end surrounds the assembly to minimize the effects of external fields on the HRTs.

A tripod structure with legs of stainless steel tubing hangs from the lid of the vacuum shell. Three OFHC copper rings intersect the legs of the tripod at intervals of about 3 cm. These rings form the first three stages of the isolation system and also serve to stiffen the tripod. Each stage has a germanium resistance thermometer (GRT) and heater for temperature readout and servo control. The thermal isolation of these stages is sufficient to reduce the thermal inhomogeneities to the point where they are dominated by the dissipation in the heater on stage 3. This effect is then limited by reducing the offset between the operating temperatures of stages 2 and 3 to the minimum possible value. Stage 4 was equipped with two HRTs, GRTs and heaters. Thermal control of this stage had two modes: a coarse mode with the GRT as sensor, and a fine mode with the HRT as sensor. Gradients in this stage were again minimized by reducing the temperature offset to stage 3.

The calorimeter assembly, stage 5, consisted of a spherical sample container, a superfluid tight valve, and pairs of HRTs, GRTs and heaters. The configuration was designed to minimize temperature offsets between the HRTs and the sample container. This was done by providing large area contacts between the HRTs and the container, thermally separated from the tripod attach point. Thermal gradient control was improved by deactivating the GRTs during high resolution measurements and using the heater only when step temperature changes were desired. In operation, temperature stability of stage 5 was obtained by fine adjustment of the temperature set point of stage 4. The limiting factor on thermal

control of stage 5 appeared to be variations in stray power pickup in the circuits attached to it, and charged particle dissipation in the structure. The sample container was a copper sphere of 3.5 cm internal diameter and 2 mm minimum wall thickness. The copper¹⁰ had a residual resistance ratio of over 4000. The sample container fill valve was held closed by a spring and opened by applying ~ 450 psi to a bellows system attached to the stem. The valve seal was formed between a beryllium-copper knife edge and a gold-plated copper flat. By locating the valve on the calorimeter it was possible to evacuate the fill line, eliminating the superfluid heat leak below the lambda point. The heaters and GRTs were attached to the spherical wall of the calorimeter via sapphire posts which minimized stray a.c. power due to capacitive ground loops.

The internal dimensions of the calorimeter set the inner limits at which distortion of the heat capacity curve due to residual acceleration and finite size phenomena reach a given value. For a 3.5 cm sample and a dc acceleration level of 2×10^{-4} g, easily attained on the Shuttle, the resolution at which the pressure gradient distortion of the heat capacity reaches 1% is $\sim 3 \times 10^{-10}$. The corresponding resolution for finite size distortion is $\sim 2 \times 10^{-11}$, based on the recent renormalization group model of this effect¹¹. Since the magnitude of the finite size effect is somewhat uncertain, it was decided to keep the calorimeter as large as possible consistent with mechanical constraints.

A charcoal adsorption pump assembly was attached to the top plate of the vacuum can to maintain a high vacuum inside the thermal control system. This pump was equipped with a heater and thermometer to allow regeneration after the experiment had reached earth orbit. During the launch phase the vacuum can was filled with ³He exchange gas to maintain a thermal short between the instrument and the bath. This procedure was needed to reduce the effect of vibration heating on the HRTs. The pump-down time was on the order of a day, dependent on the vacuum can wall temperature. Residual gas in the vacuum can formed an additional thermal link between the calorimeter and its surroundings, giving rise to small thermal gradients and offsets in the calorimeter assembly. For the pressures encountered during the mission, the gradients were estimated to be less than 10^{-10} K/cm in stage 5.

IV. FLIGHT EXPERIMENT

The instrument was maintained at 4 K or colder for 18 months before launch. In this period extensive tests were performed to verify its performance under various conditions. A number of preflight calibrations and heat capacity measurements were also completed. This data was very useful for deciding the details of the flight measurement sequence and for studying the general behavior of the system. Shortly before launch the helium in the dewar and the instrument were cooled to about 1.7 K, and the instrument vacuum space was filled with ³He exchange gas at a pressure of about 5 mm. About two hours into the flight, the experiment was activated and the exchange gas pump-out procedure was

started. This consisted of first venting to space until a pressure of 0.5 torr was reached, and then sealing off the instrument and using the internal cryopump. The dewar was also raised to its maximum safe operating temperature in space, close to 2.05 K, to aid in releasing adsorbed helium from the vacuum can walls.

When the pressure approached the 10^{-9} torr range the main measurement sequence was started. The first event of significance in the experiment was the generation of a small bubble in the calorimeter, used to establish a thermodynamic path close to constant pressure for the heat capacity measurements. This event occurred as the calorimeter warmed through 2.079 K and was detected by observing the small sudden cooling generated by the first order phase transition. The output from one of the GRTs on the calorimeter during this phase is shown in figure 4. The data are plotted as deviations from a best fit straight line to the temperature vs time signal. The size and polarity of the step are consistent with the known thermodynamic parameters of helium, and the temperature of the step is similar to that seen before the flight in ground testing.

Before the system could be used for high resolution work, the various stages needed to be brought to their normal operating temperatures. These temperatures were kept as close as practical to that of the calorimeter. A typical temperature profile of the thermal control system consisted of stage 5 at a given operating temperature and stage 4 in equilibrium with it, and stages 1, 2 and 3 servoed at 30, 10 and 1 mK below stage 4. The initial thermal alignment was performed with the calorimeter at the starting temperature for the HRT calibration sequence. Up to this point stage 4 was operated in the coarse mode, but after the thermal transients had settled, and the fine mode was activated. The final step was to reduce the drift rate of the calorimeter temperature to an acceptable value. It was found possible to reduce the drift rate of stage 5 to $\sim 10^{-12}$ K/s with little difficulty.

The HRTs were then calibrated against the GRTs. This procedure consisted of a set of 1 mK heating steps separated by 45 seconds of equilibration. The data was analyzed on the ground and verified to be within about 0.1% of the preflight results. The second phase of instrument calibration was to measure the change in the stray power dissipated in the heater circuit when it was switched on. This was done by measuring the heat capacity of the sample as a function of power dissipated in the heater at a preselected temperature well below the lambda point. Any power change that is unaccounted for in the measuring process causes an error in the calculated heat capacity. It is easy to show that this error adds a term to the heat capacity that is inversely proportional to the power. From measurements over the range 10^{-3} to 10^{-8} W, the stray power was estimated to be less than 10^{-10} W. After the calibration was completed, heat capacity measurements using the pulse technique were commenced and continued for the rest of the flight. The quantity of energy to be dissipated in the heater for each pulse was determined from a look-up table based on the distance from the lambda point. After an initial trial pulse, this distance

was determined from each heat capacity measurement by comparing it with a model of the singularity. After the lambda point had been reached the first time, this method was terminated and the apparatus was operated manually by ground command. Figure 5 shows the preliminary heat capacity values from the initial period on a semi-logarithmic scale. For comparison the broken line shows the expected values from a model based on ground results.

When measurements at the highest resolution were attempted, excess noise was found on the outputs of the HRTs. This was traced to the heat dissipation due to cosmic rays and other particles passing through the sensitive element of the thermometers. A comparison of the HRT output on the ground and in space is shown in figure 6. A slow variation in the drift rate of the calorimeter was also detected under nominally steady conditions. This was found to be due to charged particles dissipating energy in the copper calorimeter. To obtain accurate heat capacity results it is necessary to correct the raw data for the particle heating effects. Heating of the calorimeter by charged particles was anticipated, so the experiment carried a charged particle monitor for use as an indicator of periods of severe heating. The variation of the charged particle counting rate over a 24 hr. period is shown in figure 7. The four channels of data correspond to different energy thresholds for the particles. The background level of from 2 to 5 counts per second corresponds to the cosmic ray flux and the higher peaks are due to the particles trapped in the radiation belts. Models are being developed to correct the high resolution results for the heating effects. It is expected that a resolution of about 2 nanodegrees will be possible with good accuracy. Additional heat capacity data can be extracted from the cooling curves obtained when the calorimeter temperature is reset below the lambda point. However it is apparent that for this case careful modeling of thermal relaxation effects close to the transition will be needed. Some preliminary results in the high resolution region are shown in figure 8. While it is too early to draw any conclusions of theoretical interest from the data, it can be seen that the transition appears to be sharp on the scale of nanodegrees, as expected. An examination of selected measurements puts a limit of no more than 2 nanodegrees on the transition width. The correlation length at this resolution is expected to be about 150 microns. For comparison, very high resolution ground measurements on a helium sample 0.4 mm high are shown in figure 9. It can be seen that in this case the results are significantly perturbed by gravity and other effects over a range of about 200 nanodegrees.

Above the transition the calorimeter temperature initially overshoots its equilibrium value when a heat pulse is applied due to the finite thermal conductivity of the helium. From the resulting relaxation data an estimate of the thermal conductivity can be obtained. A typical response curve to a five second heat pulse is shown in figure 10. Also shown is a simple exponential fit to the relaxation data. The analysis of this data is less well developed than that for heat capacity, but some of the relaxation data has been converted into the equivalent solid body thermal conductivity. A comparison with expected

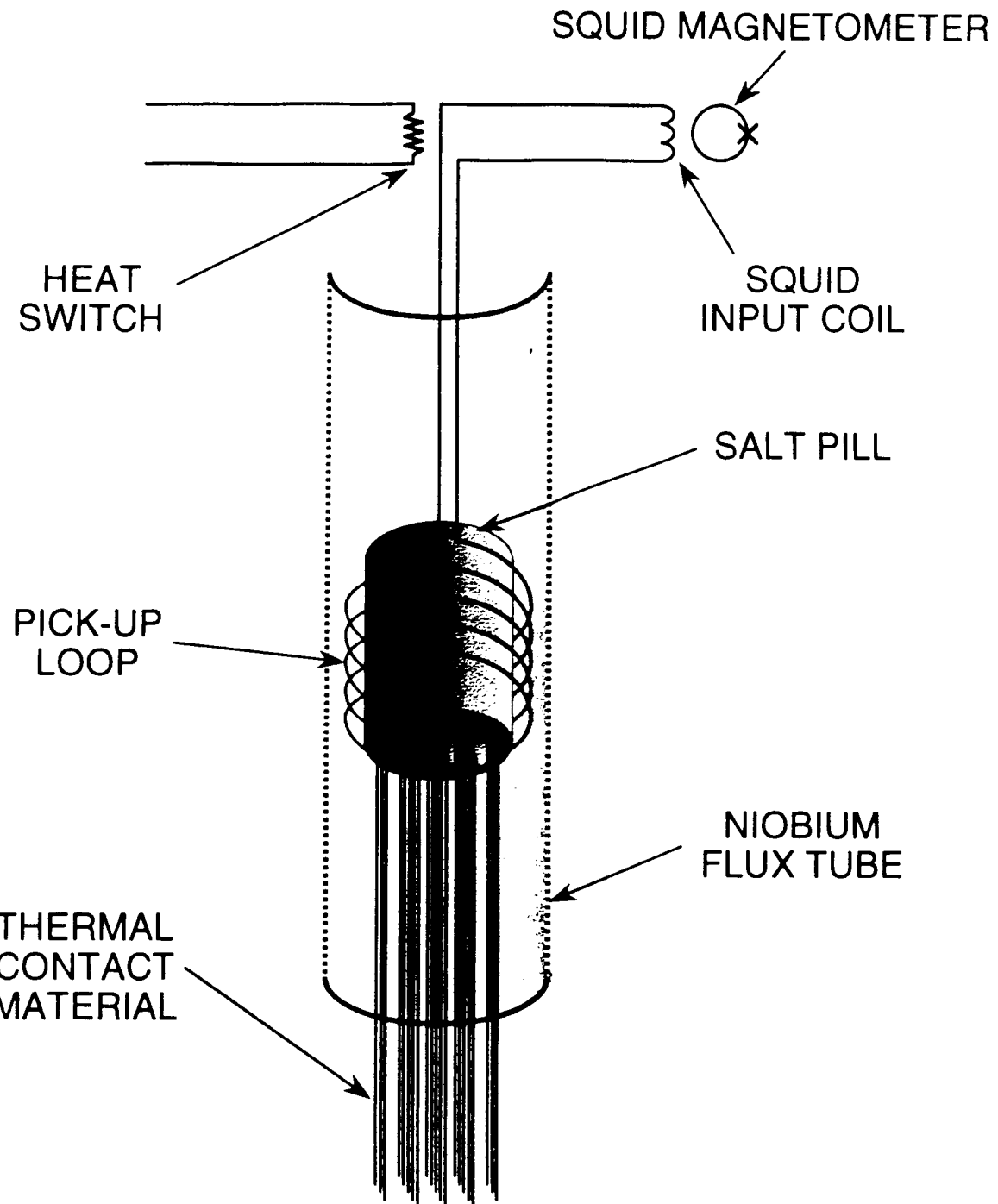
values based on extrapolation of ground results is shown in figure 11. When fully analyzed we expect the measurements to give thermal conductivity data for helium in the normal phase to within about ten nanodegrees of the transition.

ACKNOWLEDGMENTS

We wish to thank the Microgravity office of NASA for its support with contract JPL-957448, and the members of the LPE program at Stanford and JPL for their many contributions to the program, and Ball Aerospace for construction of major portions of the flight instrument.

REFERENCES

1. F. M. Gasparini and I. Rhee, *Progr. Low Temp. Phys.*, **13**, 1 (1992).
2. J. A. Lipa, *75th Jubilee Conference on Helium-4*, ed. J. G. M. Armitage (World Scientific, Singapore, 1983), p. 208.
3. K. G. Wilson, *Phys. Rev. B* **4**, 3174 (1971).
4. J. A. Lipa and T. C. P. Chui, *Phys. Rev. Lett.*, **51**, 2291 (1983).
5. D. Petrac, U. Israelsson and T. Luchik, *Cryogenics*, (1993), to be published.
6. J. A. Lipa, B. C. Leslie and T. C. Wallstrom, *Physica*, **107 B**, 331 (1981); T. C. P. Chui and J. A. Lipa, *Proc. 17th Internat. Conf. on Low Temp. Phys.* (Karlsruhe, 1984), p.931; M. J. Adriaans, T. C. P. Chui, M. Ndesandjo, D. R. Swanson and J. A. Lipa, *Physica*, **B 169**, 455 (1991); and T. C. P. Chui, D. R. Swanson, M. J. Adriaans, J. A. Nissen, and J. A. Lipa, *Temperature, its Measurement and Control in Science and Industry*, **6**, 1213 (1992).
7. D. Marek, *Jap. Journal App. Phys.*, **26**, Suppl. 26-3, p. BO08 (1987).
8. T. C. P. Chui, D. Swanson, M. J. Adriaans, J. A. Nissen, and J. A. Lipa, *Phys. Rev. Lett.*, **69**, 3005 (1992).
9. J. A. Lipa, T. C. P. Chui, J. A. Nissen and D. R. Swanson, *Temperature, its Measurement and Control in Science and Industry*, **6**, 949 (1992).
10. Nippon Mining Co., Japan, grade 6N (99.9999% pure).
11. R. Schmolke, A. Wacker, V. Dohm, and D. Frank, *Physica*, **B 165 &166**, 575, (1990).



PARAMAGNETIC SALT THERMOMETER

Figure 1 Schematic diagram of the high resolution thermometers.

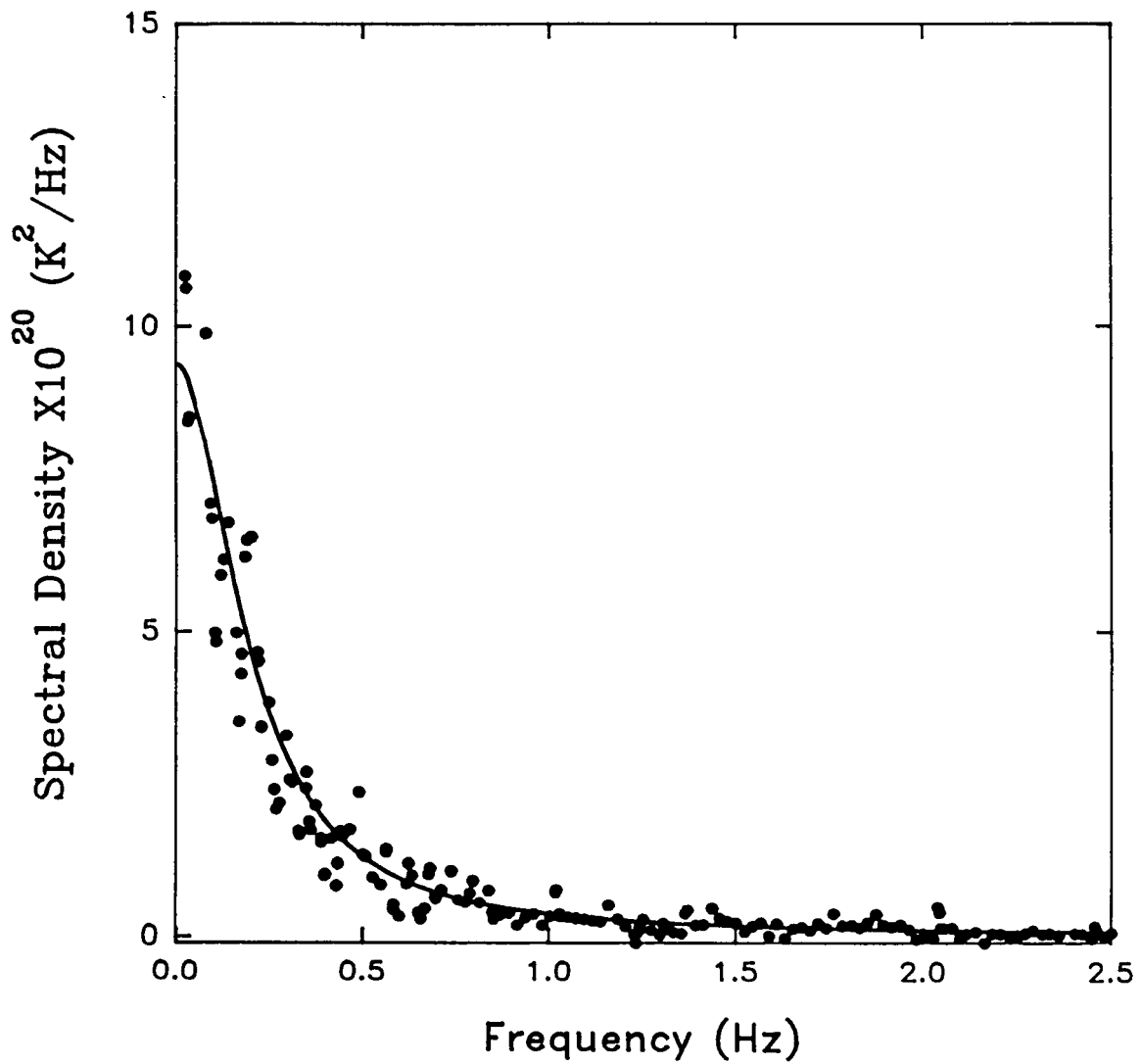


Figure 2 The noise spectrum of a high resolution thermometer. The solid line is the prediction of the fluctuation-dissipation theorem with no adjustable parameters.

LAMBDA-POINT EXPERIMENT FLIGHT INSTRUMENT

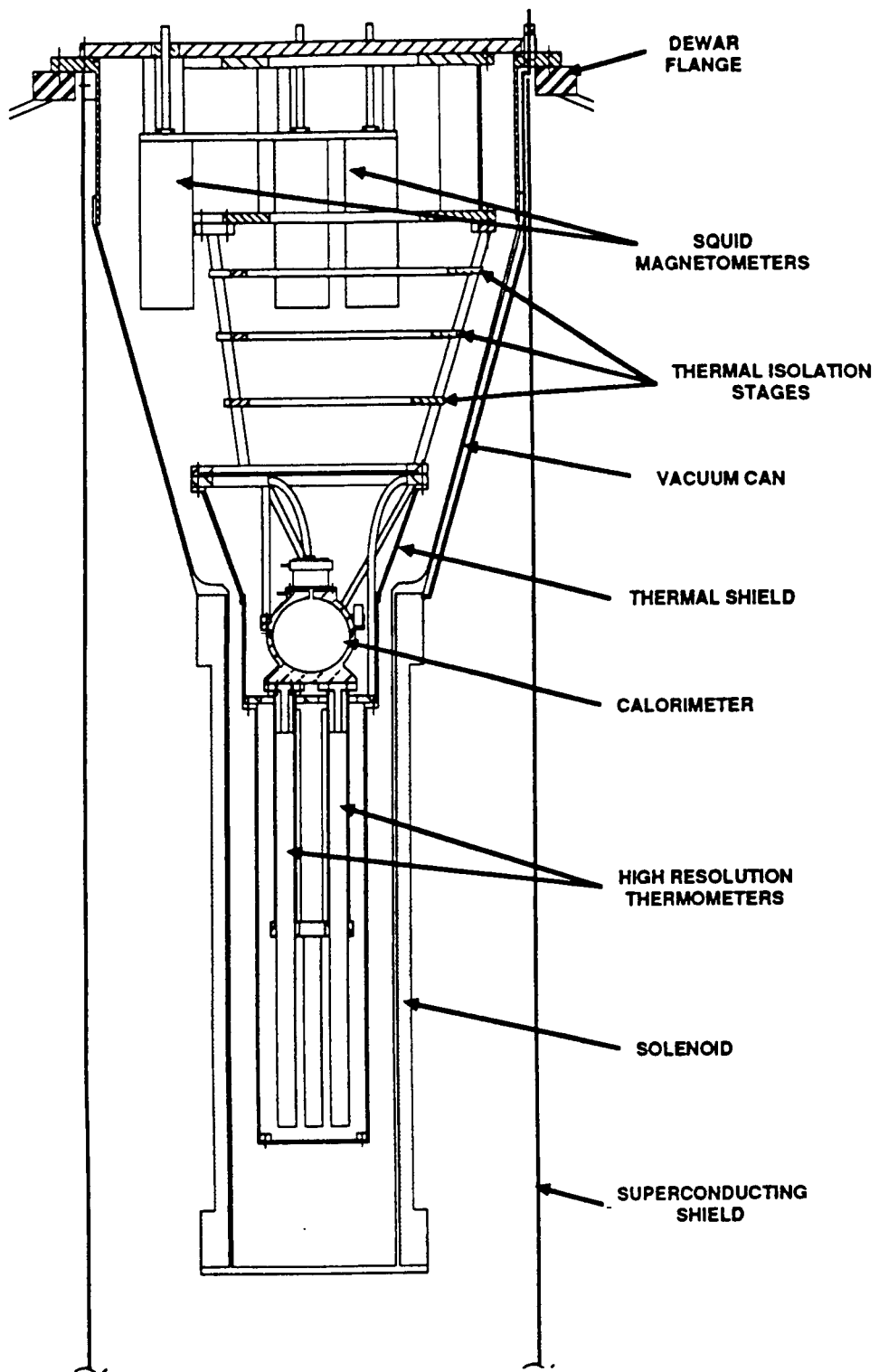


Figure 3 Schematic view of the thermal control system and calorimeter.

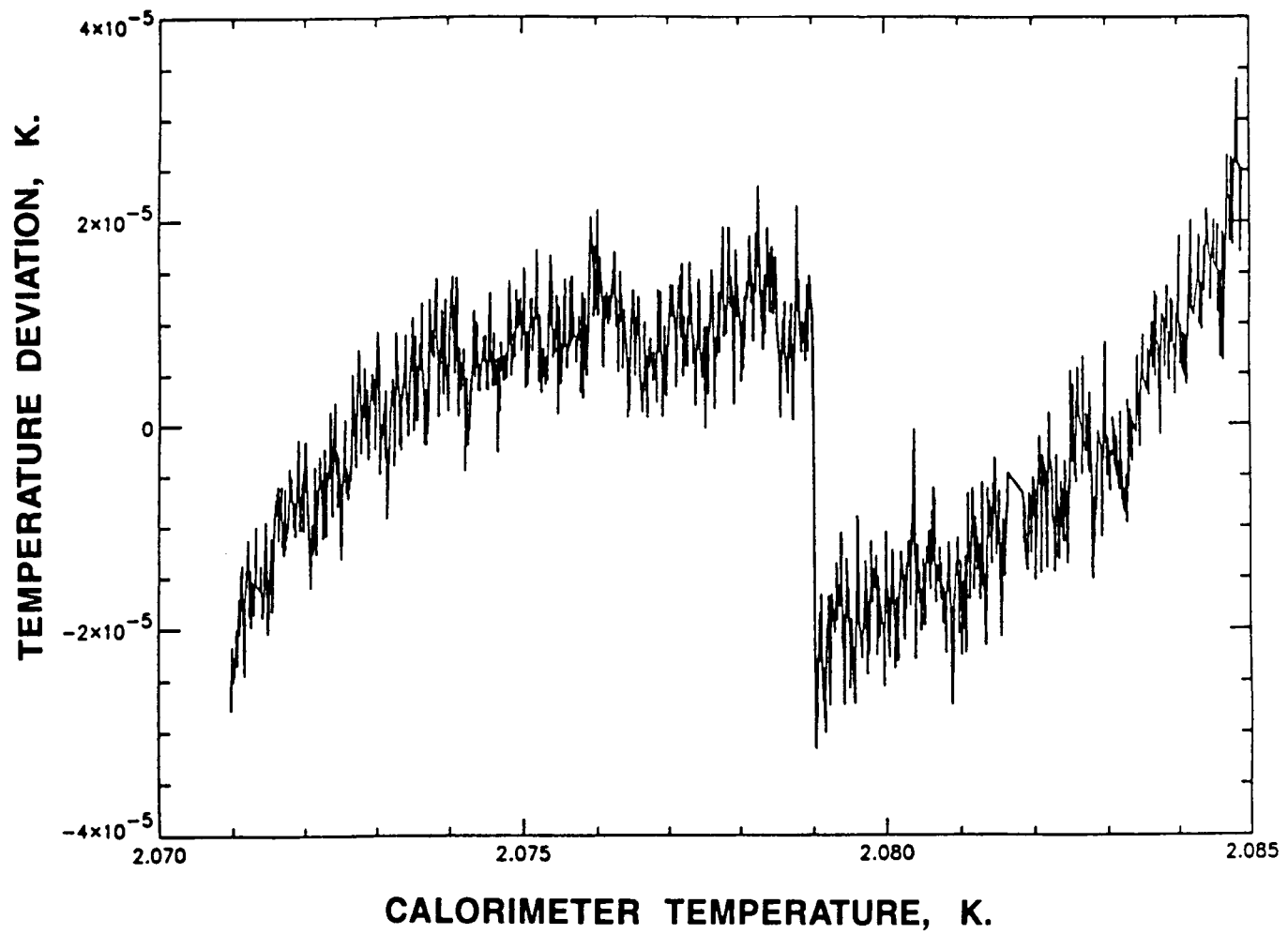


Figure 4 Output of calorimeter GRT showing bubble generation event near 2.079 K. Data is plotted as deviations from a best fit straight line to the raw signal.

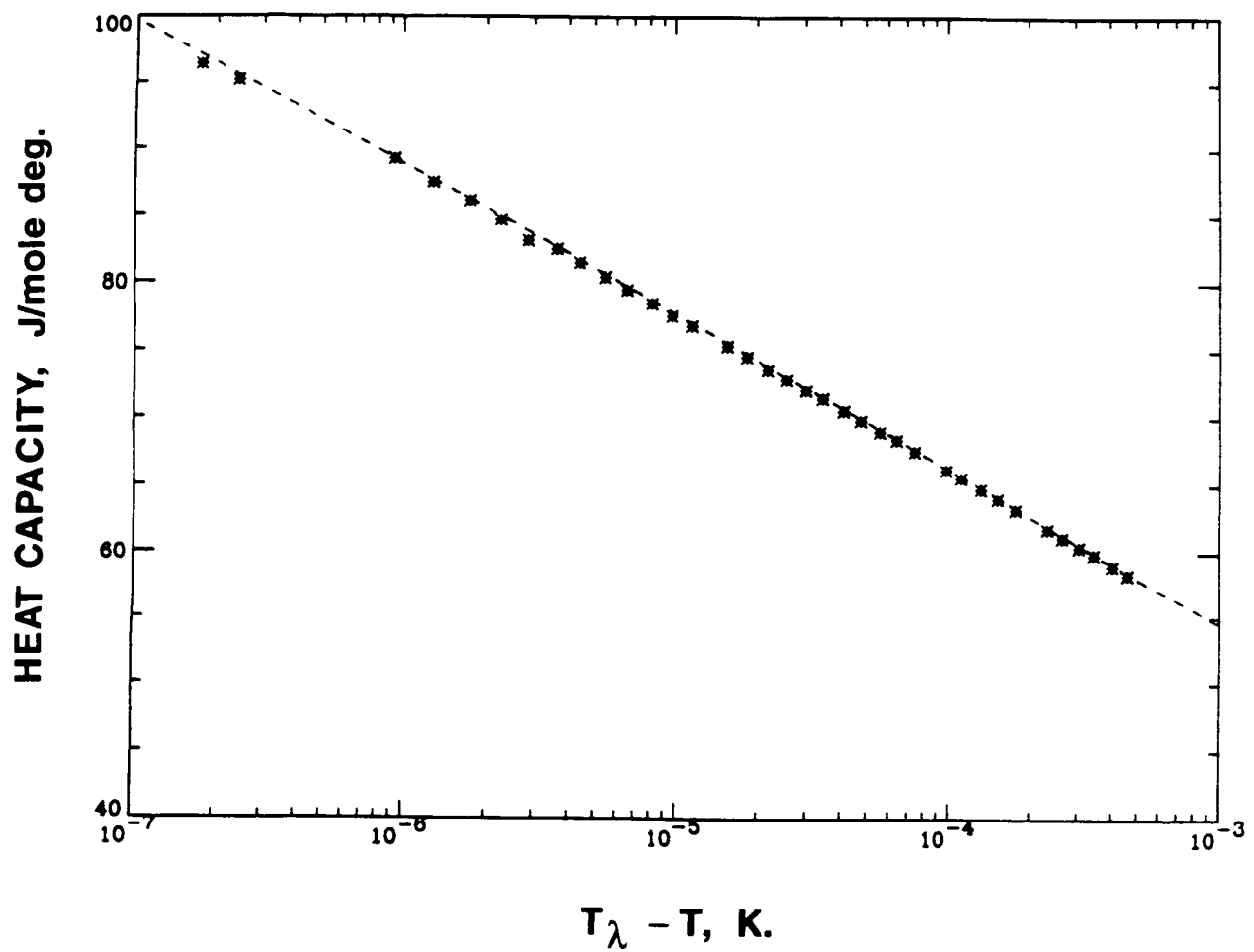


Figure 5 Wide range heat capacity data obtained early in the mission. Broken curve shows expected results based on earlier ground measurements.

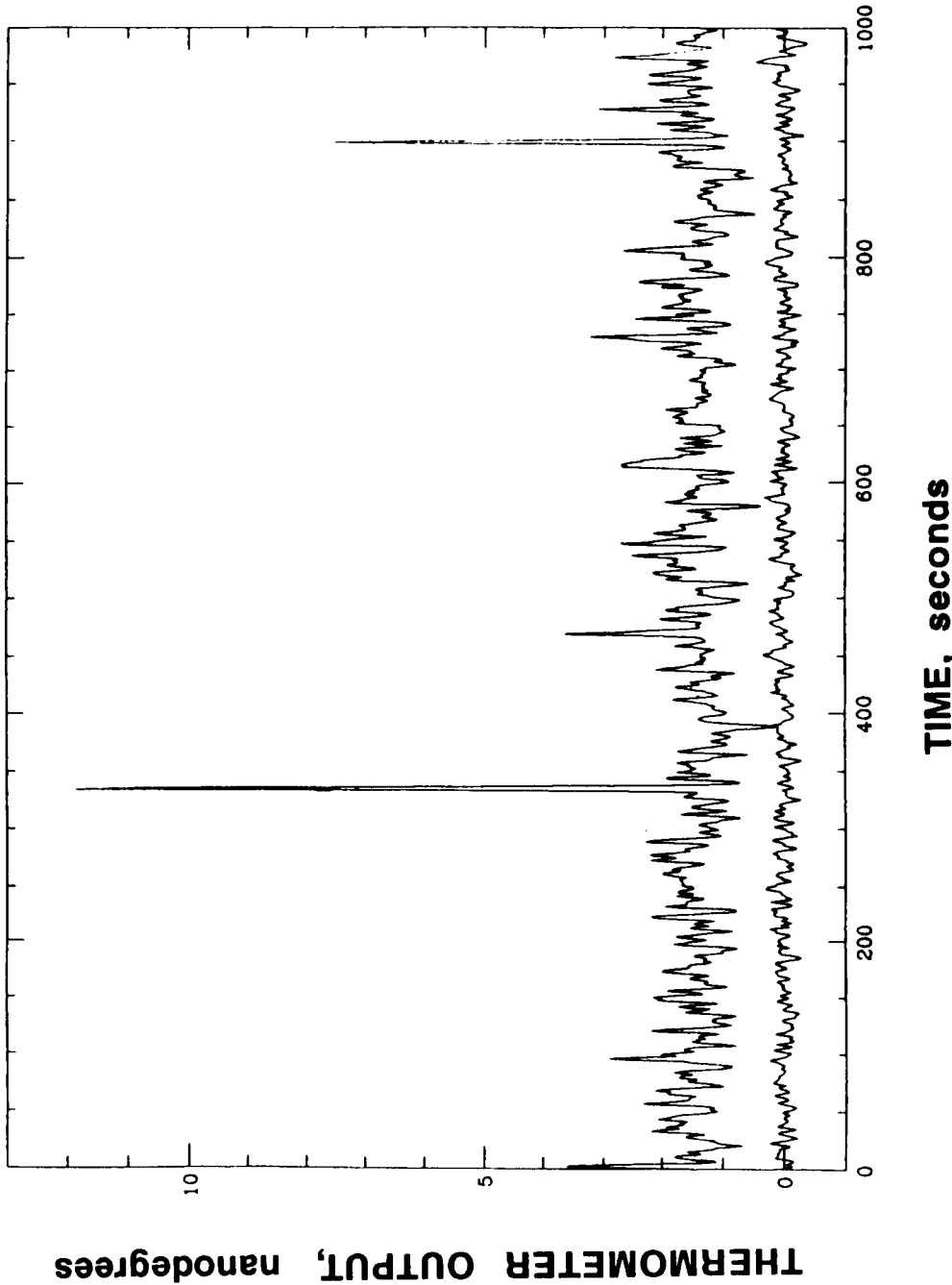


Figure 6 Comparison of HRT noise on the ground (lower curve) and in orbit. The excess noise in the flight data appears to be due to the proton and alpha particle flux, and the spikes to high-Z cosmic rays.

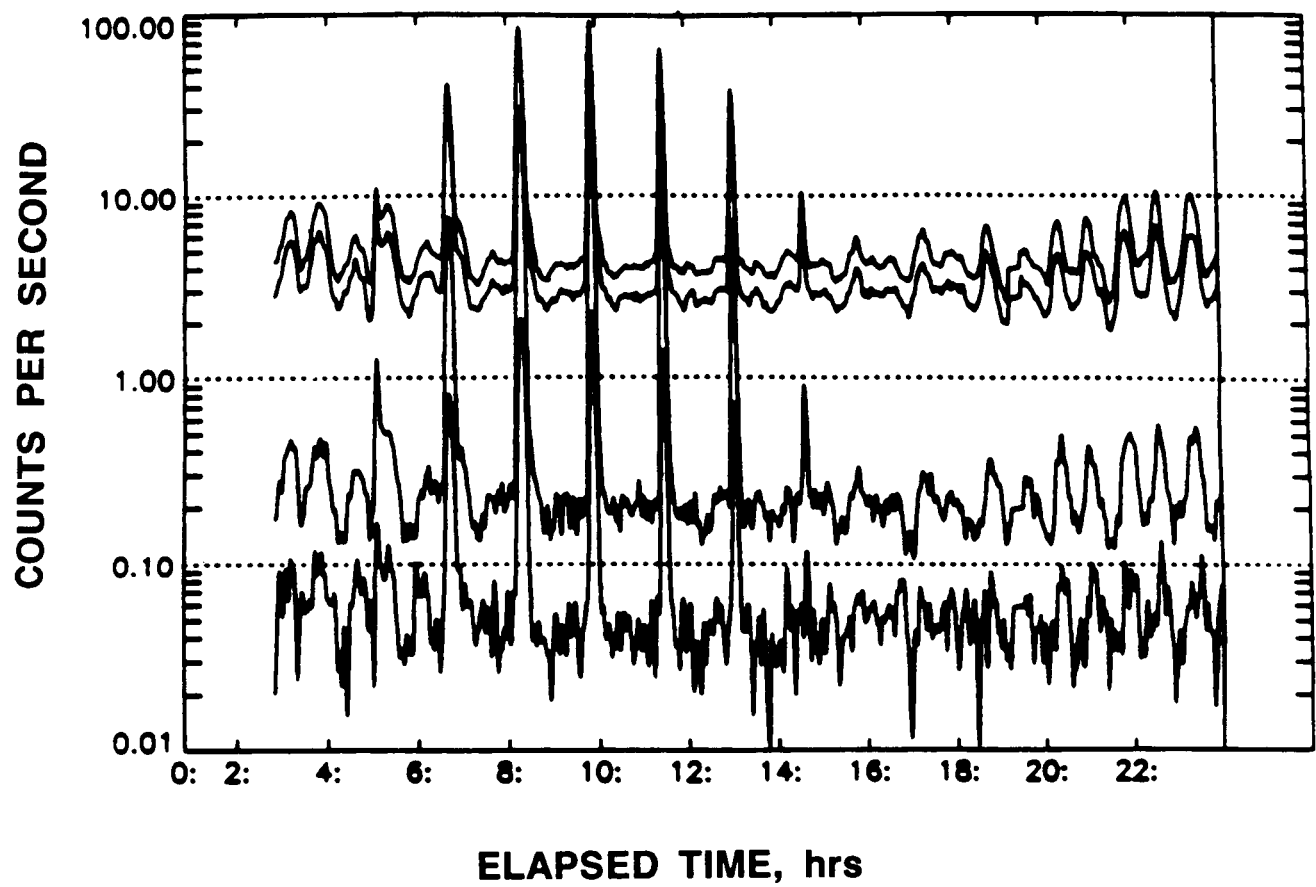


Figure 7 Variation of charged particle count rate over a 24 hr. period. Four channels correspond to different energy ranges.

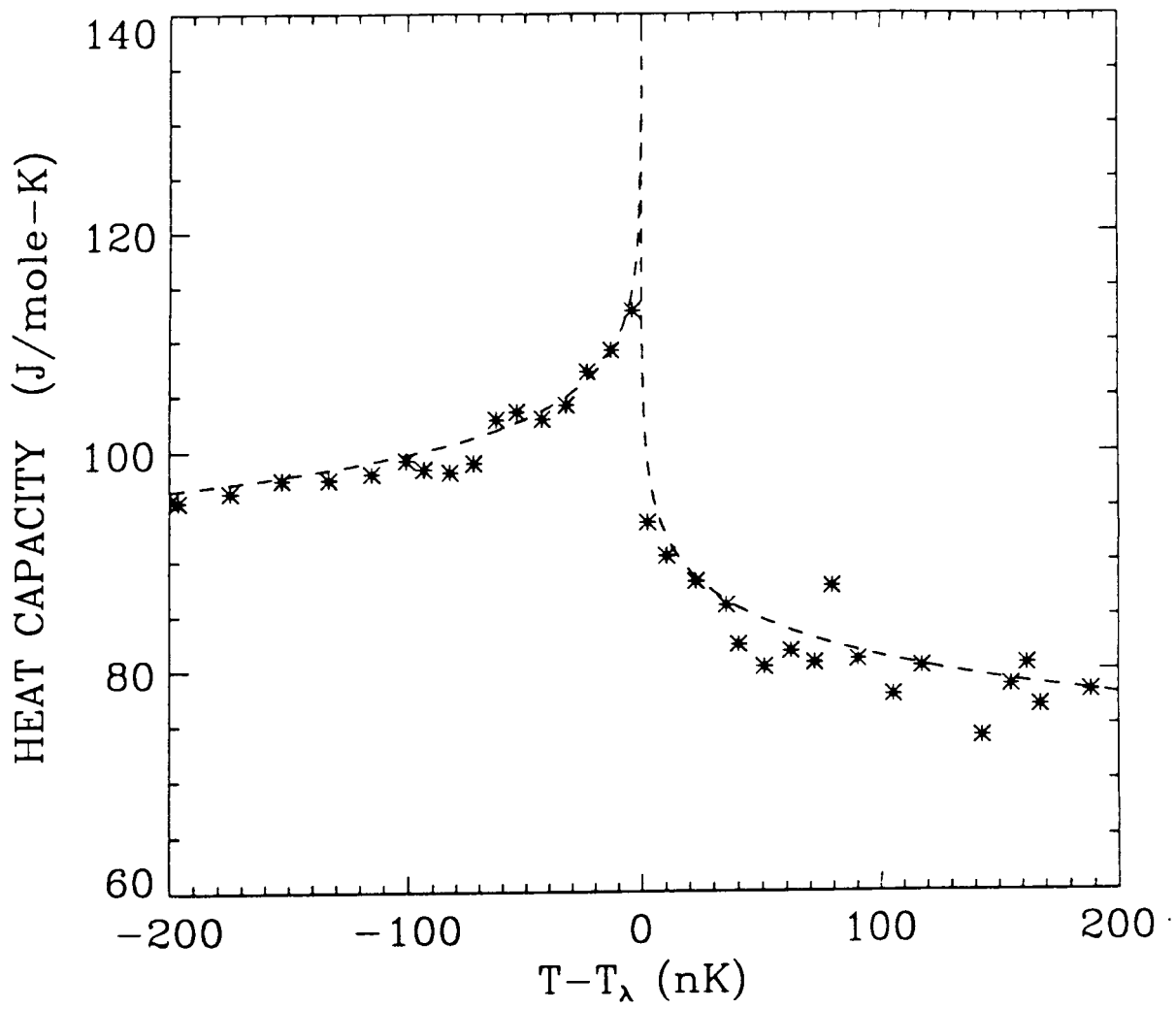


Figure 8 Preliminary high resolution heat capacity results in the region near the transition.

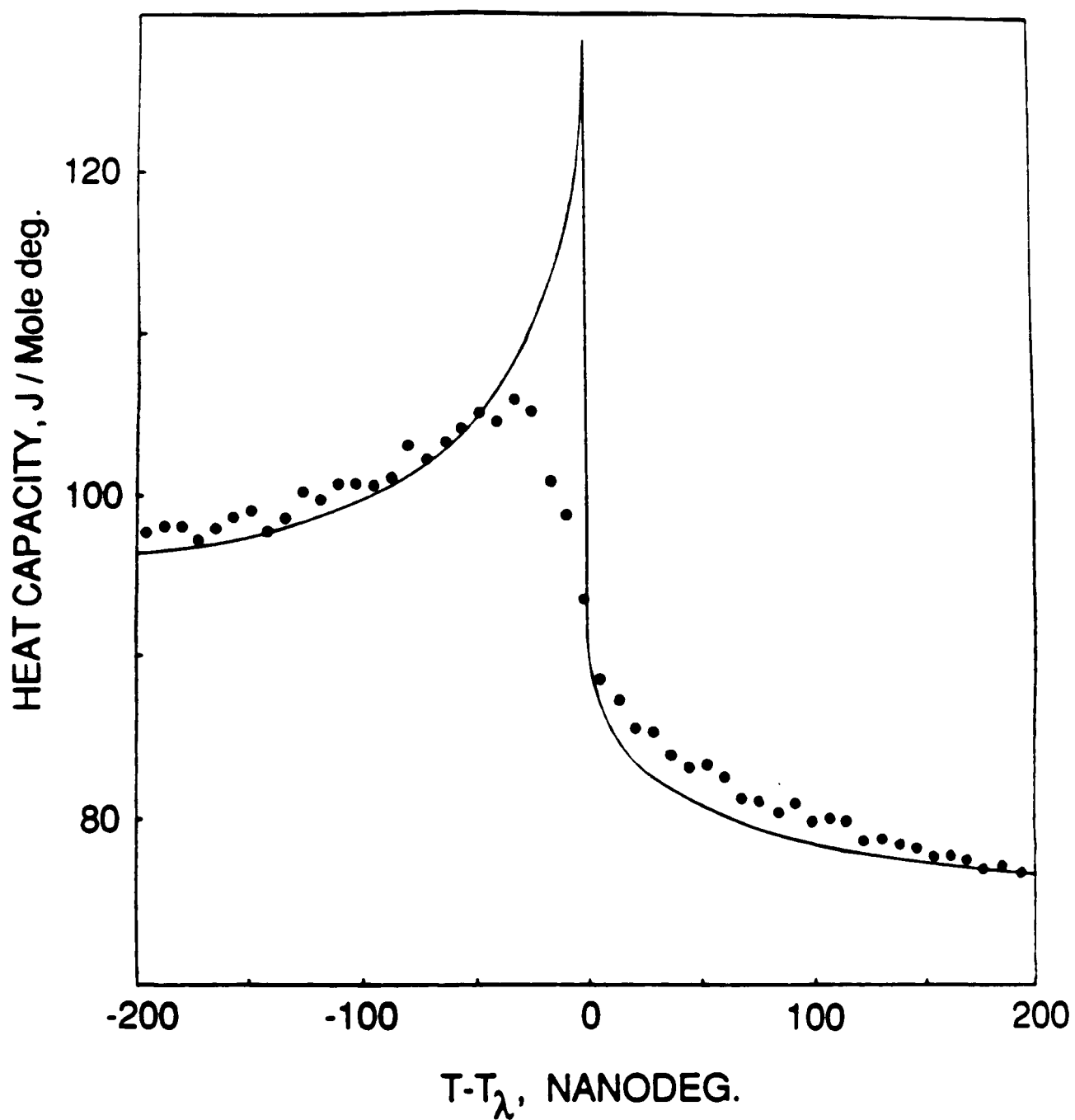


Figure 9 High resolution heat capacity measurements obtained on the ground showing the effects of gravitational and finite size distortion. Solid curve schematically shows expected curve from flight results.

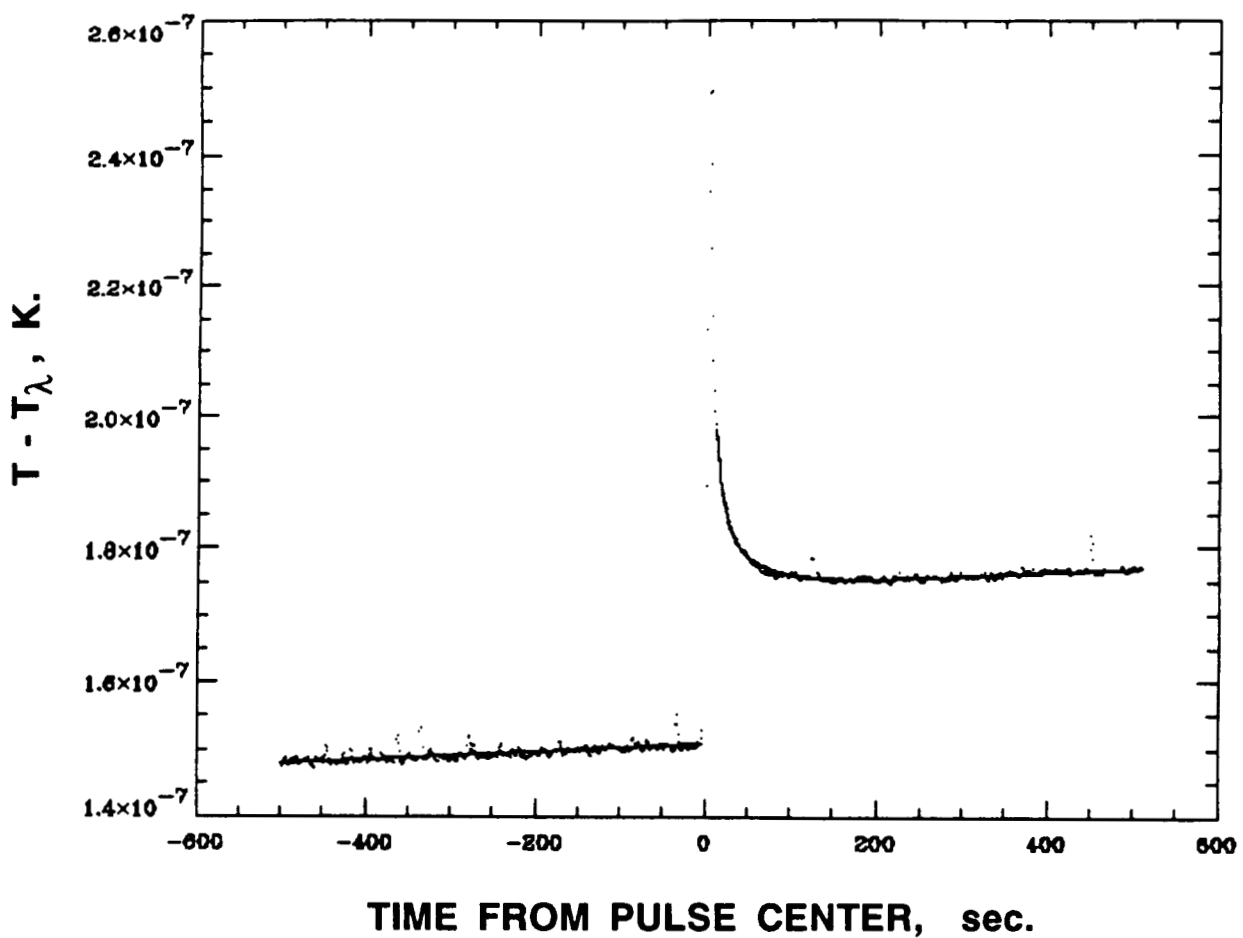


Figure 10 Temperature vs time data from a single heat pulse above the transition. Overshoot is due to the presence of normal helium in the calorimeter. Solid line is a simple exponential fitted to the high temperature data.

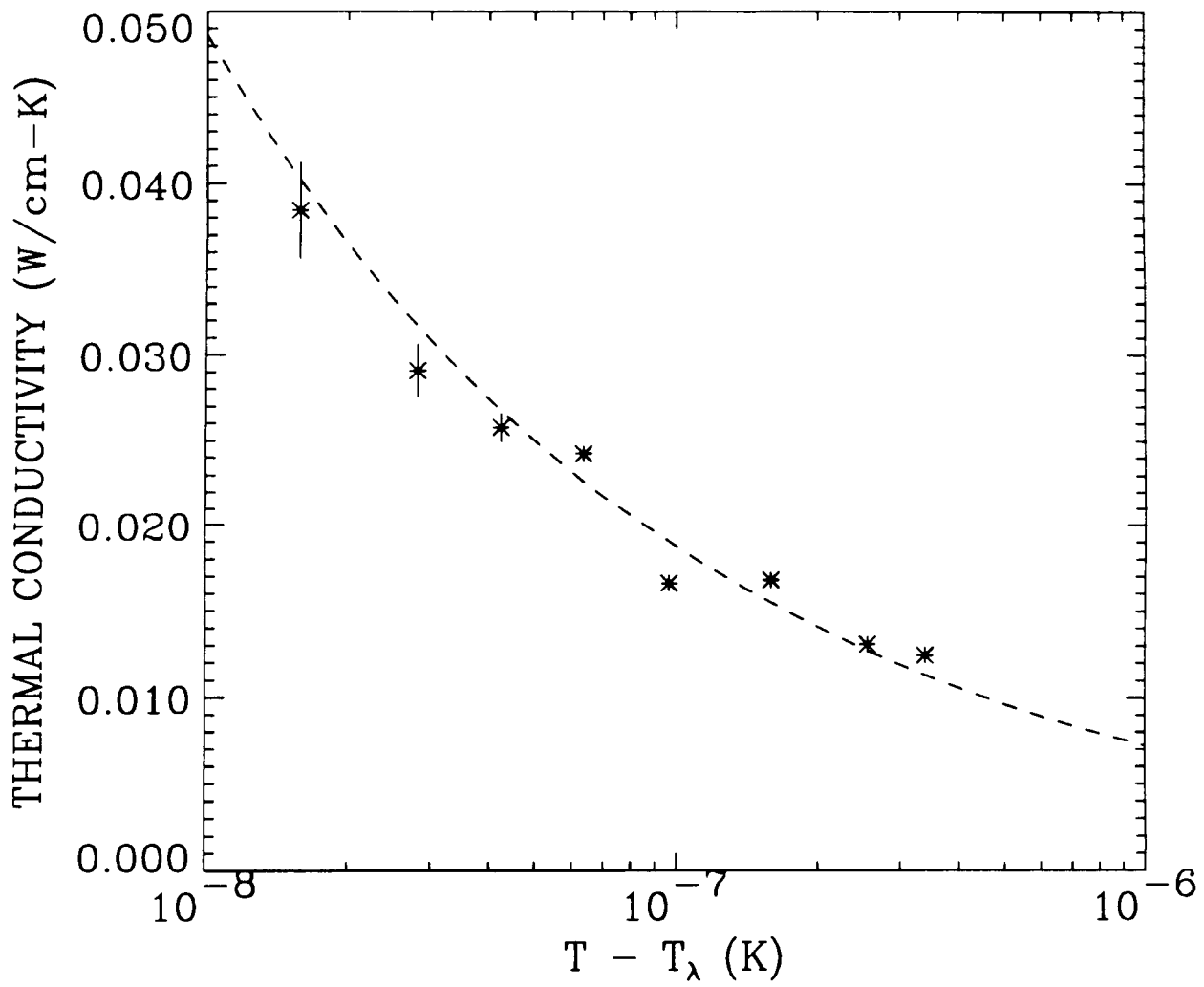


Figure 11 Preliminary comparison of expected (solid curve) and observed thermal conductivity in the region just above the transition.

Discussion

Question: Could you comment on the effects of radiation interactions (in terms of heating the fluid) on the experiment ?

Answer: There are two effects; one is heating of the fluid which is pretty negligible because the cross section for absorption of cosmic rays of the fluid is fairly low. The calorimeter that the helium is contained in has a relatively high cross section and most of the actual heating as a function of time occurs in the calorimeter. However there are also the particles that go through the salt of the thermometer itself and they do very local heating in the salt and they give you a burst of spike-like energy which you see in your output. They make noise but the total amount of heating in the salt in absolute terms is relatively small compared to the calorimeter.

Question: Following up on the last question, do you see any correlations of this effect ?

Answer: Yes. You can. You see correlations in the output about 20% of the time. That corresponds approximately to the solid angle that is subtended by the other one in its field of view. There is also some indication that the particles are not just the prime reason; they are more of a shower effect, you get a few more events than you would expect than just from the solid angle argument. But a lot of the noise is uncorrelated.

Question: In your opinion, do you think that the ground based (Lambda point) data will or will not be altered by the microgravity data in terms of the disparity between the experimental and the theoretical exponent ?

Answer: Well just from what I have seen over the years I would expect the flight data will be better by the time the analysis is completed than just the ground based measurement alone, but I think we will also probably have to take into account the ground based measurements and do analysis which sort of folds the two together to some extent. That is because in the outer regions far from the transition there are terms which go to zero but don't go to zero very quickly. These have to be considered and these are best determined from ground based measurements. I would think the issue of whether the discrepancy is as serious or not will depend on a couple of things. One is the uncertainties in the various experiments right now. Statistical uncertainty is very common in experimental work but the true underlying uncertainties are somewhat larger. Also the uncertainties in theoretical models are not negligible. It turns out, fortunately, that there has been a bit of a breakthrough in the last couple of years in the area of numerical modeling of phase transitions using Monte Carlo techniques and we are expecting there will be better estimates to come out quite soon on the experiments from the theoretical side. So it is a bit hard to say at this point what the final situation is going to be. I think it is still in a bit of a flux.

18 PG

MEPHISTO
324941

N95-14209

1103

P-18

MASS TRANSPORT PHENOMENA IN MICROGRAVITY

PRELIMINARY RESULTS OF THE FIRST MEPHISTO FLIGHT EXPERIMENT

J. J. Favier, J. P. Garandet, A. Rouzaud and D. Camel

Commissariat à l'Energie Atomique
DTA/CEREM/DEM/SESC
Centre d'Etudes Nucléaires de Grenoble, 85X 38041 Grenoble Cedex

ABSTRACT

The MEPHISTO space program is the result of a cooperative effort that involves the French nuclear and space agencies (Commissariat à l'énergie atomique, CEA - Centre National d'Etudes Spatiales, CNES) and the American National Aeronautics and Space Administration (NASA). The scientific studies and apparatus development were funded in the frame of the GRAMME agreement between CEA and CNES, the flight costs being taken in charge by NASA. Six flight opportunities are scheduled, with alternating French and American principal investigators. It is the purpose of this paper to briefly present MEPHISTO (more details can be found in refs. [1,2]) along with the preliminary results obtained during its first flight on USMP-1 in October 1992.

INTRODUCTION

The MEPHISTO space program is the result of a cooperative effort that involves the French nuclear and space agencies (Commissariat à l'énergie atomique, CEA - Centre National d'Etudes Spatiales, CNES) and the American National Aeronautics and Space Administration (NASA). MEPHISTO is basically a directional solidification furnace, where three samples are simultaneously processed. An original point is that there are in fact two heating/cooling subsystems (see fig. 1); one of them is maintained at a fixed position to provide a reference interface, whereas the other is allowed to move for solidification and melting of the samples. Only low melting point materials can be used in the furnace, its maximum temperature being presently 1000°C. The first flight featured bismuth doped tin alloys (Sn : 0.5% at. Bi), the second, scheduled for April 1994 with Prof. Abbaschian of the University of Florida as principal investigator, will focus on the other side of the phase diagram, i.e. tin doped bismuth alloys.

Sample #1 is dedicated to a measure of the Seebeck voltage between the two ends; we shall later come back in detail on the interpretation of the signal. At this point, we shall only state that the system acts as its own thermocouple, with a "cold" and a "hot" reference junction (respectively the

moving and fixed interfaces). The Seebeck voltage is then a measure of the undercooling at the growth front, a key feature being that the signal is obtained in real time. It is thus possible to run many experimental cycles on the same sample, which in turn allows to check the reproducibility of the process and to ensure a better accuracy of the results.

On sample #2, the position and the velocity of the moving interface are obtained from an on line resistance measurement. At the end of the experimental cycle, a quench freezes the structure of the solid-liquid front. Peltier pulse marking performed on sample #3 allow the determination of the shape of the interface at given time intervals. Moreover, thermocouples present in the liquid phase for both samples #2 and #3 are used to determine the temperature gradient and possible thermal fluctuations.

During the first flight, experiments were carried out both below and above the morphological stability threshold. As for the contents of this paper, sections I and II are respectively dedicated to the presentation of the planar and cellular front results. Since the metallographic analyses are not completed yet, we shall focus on the analysis of the Seebeck signals that were shown to correlate well with *a posteriori* concentration measurements in the solid phase [1].

I. PLANAR FRONT GROWTH

Undercooling with respect to the equilibrium temperature is a necessary driving force for solidification; it depends on a variety of process parameters, e.g. growth rate, convection level in the melt, partition ratio. Let us now see how it can be related to the Seebeck voltage; to do so, we have to consider the local thermoelectricity equation:

$$\mathbf{E} = \mathbf{j} / \sigma + \eta \nabla T \quad (1)$$

that relates electric field and current (\mathbf{E}, \mathbf{j}), electrical conductivity (σ), thermoelectric power (η) and temperature gradient (∇T). The MEPHISTO loop is schematized in fig. 2, the two solid parts being connected by a liquid bridge. No net current is allowed across a given section, that is:

$$\int_S \mathbf{j} \cdot d\mathbf{S} = 0 \quad (2)$$

Assuming that both interfaces are planar and that the thermoelectric powers of the liquid and the solid remain constant around the melting temperature, integration all over the sample leads to (see for instance [1,2]):

$$E_s = (\eta_s - \eta_L)(T_l - T_{eq}) \quad (3)$$

The observed Seebeck voltage is thus proportional to the difference between the temperatures of the moving and fixed -equilibrium- interfaces. We shall see later on, when we deal with cellular interfaces,

that the integration of eq. (1) is much more complicated. At this point however, the reader should keep in mind that the thermoelectric powers of liquid and solid tin near the melting temperature are very close, $\eta_s - \eta_L \approx 1.6 \mu V / K$. We thus have to deal with very low signals, ranging typically from 0.1 to 5 μV .

Shown in fig. 3 are two typical Seebeck results of the flight experiment obtained at solidification velocities of 5.2 and 2 $\mu m/s$. After an initial transient - longer for the lower growth rate - the curves reach a plateau and the undercooling falls back to zero when the pulling is stopped. Since both plateau appear to be at the same level, it may be thought that mass transfer during solidification was principally diffusive. It is indeed well known that convection in the melt is greatly reduced in microgravity experiments; however it may still have a significant influence on solute transport, specially at low growth velocities.

To check this important point, we relied on a scaling analysis approach. We shall not dwell on the theoretical basis of the method, the interested reader being here referred to Lin and Segel [3]. Briefly stated, the purpose of such an analysis is to identify the relevant non dimensional parameters of a given problem and to obtain order of magnitude relationships between them. This method was applied to the study of solute repartition in crystal growth configurations [4], and the agreement with existing numerical data was found to be very good [5,6].

The problem was seen to depend on the value of the Peclet number, $Pe = HV_l / D$, H being the inner diameter of the crucible, V_l the growth rate and D the diffusion coefficient. Also of importance is the product of the Grashof (Gr) and Schmidt (Sc) numbers, defined as:

$$Gr = \beta_T g G_L H^4 / v^2 \quad Sc = v / D$$

In the above expression, β_T is the thermal expansion coefficient, g the intensity of gravity, G_L the temperature gradient normal to g and v the kinematic viscosity of the fluid.

Moreover, an experimental validation was obtained from ground based studies in the frame of the MEPHISTO program. In fig. 4, the variation of the nondimensional parameter Δ , that measures the relative influence of diffusion and convection on mass transfer (see for instance [7]), is plotted versus Pe . For ground based experiments in bismuth and lead doped tin alloys, we had $Gr = 5.7 \times 10^4$ and $Sc = 144$. A good agreement was observed for both convective (low Pe , $\Delta \approx 0$) and diffusive (high Pe , $\Delta \approx 1$) mass transfer conditions.

Having gained confidence in the validity of the scaling analysis, we proceeded to apply it to the flight configuration. Considering the average "steady" background accelerations to be of the order of $10^5 g_0$, we found:

$V_l = 2 \mu m/s$	$\Delta = 0.98$
$V_l = 5.2 \mu m/s$	$\Delta = 1$

These high values of Δ are characteristic of very weak convective solute transport. A further confirmation was obtained applying the numerical method developed by Rouzaud [8] to solve the coupled heat/mass transfer Stefan problem. Taking the diffusion coefficient of Bi as a free parameter, the best fit was observed for the published value, $D = 1.8 \times 10^{-9} \text{ m}^2/\text{s}$ (see fig. 5).

It can thus be confidently stated that solute transport was indeed diffusive during the MEPHISTO flight experiment. However, one should keep in mind that convection may play a significant role even in microgravity. Indeed, for a pulling velocity of $0.5 \mu\text{m/s}$, the scaling analysis predicts a value of $\Delta = 0.71$, quite far away from unity. Moreover, transient effects (g-jitters) can also disrupt the diffusive regime.

Shown in fig. 6 is the response of the Seebeck signal to a major gravity perturbation (OMS burn) that occurred during the initial part of the USMP-1 mission. A significant variation of undercooling is observed, and the return to the steady regime is very slow. The numerical studies of Alexander et al. [9,10] indeed predicted important decay periods, but more work is certainly necessary to quantify the effect of g jitters during solidification.

II. CELLULAR GROWTH

As the pulling velocity is increased, the planar front becomes unstable; this is the well known morphological stability problem, first treated by Rutter and Chalmers [11]. Their approach was later refined by Mullins and Sekerka [12], and a lot of papers on the topic have been published in the past 30 years (see for instance [13,14]). Briefly stated, the thermal gradient at the solid liquid front G and the growth rate V are the key variables of the problem.

The critical interface velocity can be experimentally estimated following the Seebeck voltage on MEPHISTO. Indeed, we just saw that for planar front, diffusive conditions, the undercooling did not depend on the pulling rate. We shall soon come back on the interpretation of the Seebeck signal in cellular growth, but at this point we can assume that any departure from the plateau value will be characteristic of the morphological instability.

Shown in fig. 7 is the variation of the undercooling as a function of growth rate measured during the USMP-1 mission. A clear rupture is observed around $V_I^C = 21 \pm 2 \text{ mm/hr}^{-1}$. Let us now apply Mullins and Sekerka standard analysis,

$$\frac{\bar{G}}{V_I^c} = \frac{m_L}{D} \frac{1-k}{k} C_0 S(A) \quad (4)$$

where \bar{G} is the average temperature gradient at the solid-liquid front, V_I is the growth rate, m_L is the slope of the liquidus, k the partition coefficient and C_0 the nominal Bi concentration of the alloy. $S(A)$ is a correction factor accounting for capillarity phenomena. Using the growth parameters listed in table 1, we find: $V_I^C = 23.8 \text{ mm/hr}^{-1}$. V thus derived is slightly higher than the experimental value. However,

some of the variables of the problem (e.g. C_0 and G_L) will have to be accurately measured before a definite conclusion can be drawn.

When the pulling velocity is further increased, the narrow cells formed at the onset of morphological instability will elongate and finally turn into dendrites at high growth rates. In that case, the interpretation of the observed Seebeck voltage becomes more difficult; since we here propose a first tentative explanation, we shall proceed quite slowly. As done for the planar front case, integration of eq. (1) along a line parallel to the sample axis and over the cross section yields:

$$\frac{1}{S_s} \int_L \int E \cdot dL \cdot dS = E_s \quad (5)$$

Again, considering the second term in eq. (1), a contribution to the signal similar to that of planar front conditions is obtained:

$$\frac{1}{S_s} \int_L \int \eta \nabla T \cdot dl \cdot dS = (\eta_s - \eta_L) \left(\frac{1}{S_s} \int L T_1(x, y) dS - T_{eq} \right) \quad (6)$$

The first term in the bracket on the right hand side of eq. 6) simply represents the average temperature of the moving interface.

The main difference with the planar front case is that local thermoelectric currents (first term in eq. (1), see fig. 8a) may contribute significantly to the signal. In order to gain some insight into this problem, we considered an idealized, rectangular wave interface, the temperatures at the top and the bottom of the structure -of thickness z_B - being respectively T_T and T_B (see fig. 8b). Such a model can be used to describe qualitatively a cellular growth front, the main restriction being that the liquid surface fraction f_L is not allowed to vary along the cells.

Following the approach initially proposed by Albuessiere et al. [15], let us consider a local current loop in fig. 8b. If the model cells are sufficiently long for j to follow the sample axis, the integration of the $1/\sigma j \cdot dl$ term along the loop becomes straightforward:

$$\int \frac{1}{\sigma} j \cdot dl = z_B \left(\frac{j_s}{\sigma_s} - \frac{j_L}{\sigma_L} \right) = -\eta_s (T_T - T_B) - \eta_L (T_B - T_T) \quad (7)$$

If we further assume the current density to be uniform both within the liquid and the solid, we get from eq. (2):

$$f_L j_L + f_s j_s = 0 \quad (8)$$

Eqs. (7) and (8) determine the current densities in the liquid and the solid; integration over the cross section and along the structure then yields:

$$\frac{1}{S} \int_S \int_L \frac{1}{\sigma} j \cdot dl dS = -(\eta_s - \eta_L) f_L f_s (\sigma_L - \sigma_s) \left(\frac{1}{f_L \sigma_L + f_s \sigma_s} \right) (T_T - T_B) \quad (9)$$

Using the same rectangular wave growth front in the temperature term (eq. (6)), we find :

$$\frac{1}{S} \int_S \int_L \eta \nabla T \cdot dl dS = (\eta_s - \eta_L) [f_s (T_T - T_{eq}) + f_L (T_B - T_{eq})] \quad (10)$$

Combining eqs. (9) and (10), we finally get for the Seebeck voltage across the sample :

$$E_s = (\eta_s - \eta_L) \left[(T_T - T_{eq}) + \frac{f_L \sigma_L}{f_L \sigma_L + f_s \sigma_s} (T_B - T_T) \right] \quad (11)$$

Using this very idealized solidification interface, we were able to derive a relation between the Seebeck signal and some important characteristics of the cellular structure. However, to build the connection with the experimental data, a more realistic cell model would be necessary.

The contribution of the tip temperature ($T_T - T_{eq}$) can be easily determined solving the diffusion equation along with the boundary condition defining the solute gradient at the interface as \bar{G}/m_L . The tip undercooling is thus found to decrease with interface velocity as $D\bar{G}/V_I$. An estimation of the other term on the right hand side of eq. (11) is more difficult: indeed, both the temperature difference along the structure and the equivalent liquid fraction depend on the characteristics of the cellular growth model.

At this preliminary stage of the analysis, we tried to fit the experimental data obtained during the USMP-1 mission using a simple $D\bar{G}/V_I$ power law. The result, presented in fig. 9, clearly show that the tip undercooling alone can not account for the observed signal. The structure dependent contribution in eq. 11) is thus seen to play a significant role, and more work on this point is now necessary to estimate its value.

CONCLUDING REMARKS

All the results presented in this paper are based on the analysis of the undercooling signal. Since the correlation between the Seebeck and a posteriori concentration measurements in the solid phase was seen to be good in ground based experiments [1], we are confident that these preliminary conclusions are valid. Of course, the metallographic processing of our space samples - currently under way - will also provide additional valuable information.

Concerning the planar front solidification, it can be safely said that mass transport in the fluid phase was mainly diffusive during the flight. However, transient g jitters effects were observed; after

such perturbations, the return to the steady state was seen to be very slow. Along with the analysis of the correlation between accelerometric and undercooling data, an important modeling effort is necessary to understand the relevant transport mechanisms involved.

A tentative interpretation of the Seebeck signal in cellular growth, based on the approximate integration of the local thermoelectricity equation in the vicinity of a squared waved interface, was also proposed. Further work on the topic will feature an estimation of the structure dependent contribution using more realistic cellular models. Finally, the morphological stability threshold will be precise thanks to the experimental data.

ACKNOWLEDGMENTS

The present work was conducted within the frame of the GRAMME agreement between the CNES and the CEA. This paper would not have been possible without the outstanding work of the MEPHISTO technical team (B. Angelier, J. Comera, P. Contamin, F. Herbillon). The support of our CNES colleagues, and more specially G. Cambon, is also gratefully acknowledged.

REFERENCES

1. A. Rouzaud, J. Comera, P. Contamin, B. Angelier, F. Herbillon and J.J. Favier, *J. Crystal Growth*, 129 (1993) 173.
2. A. Rouzaud, J.J. Favier and D. Thevenard, *Adv. Space Res.*, 8 (1988) 49.
3. C.C. Lin and L.A. Segel, *Mathematics Applied to Deterministic problems in the Material Sciences*, Macmillan (1974).
4. J. P. Garandet, T. Duffar and J.J. Favier, *J. Crystal Growth*, 106 (1990) 437.
5. J. P. Garandet, A. Rouzaud, T. Duffar and D. Camel, *J. Crystal Growth*, 113 (1991) 587.
6. S. Kaddeche, H. Ben Hadid and D. Henry, submitted to *J. Crystal Growth*.
7. J. P. Garandet, J.J. Favier and D. Camel, *J. Crystal Growth*, 130 (1993) 122.
8. A. Rouzaud, *J. Crystal Growth*.
9. J. I. D. Alexander, J. Ouazzani and F. Rosenberger, *J. Crystal Growth*, 97 (1989) 285.
10. J. I. D. Alexander, S. Amroudine, J. Ouazzani and F. Rosenberger, *J. Crystal Growth*, 113 (1991) 21.
11. J. W. Rutter and B. Chalmers, *Can. J. Phys.*, 31 (1953) 15.
12. W.W. Mullins and R.F. Sekerka, *J. Appl. Phys.*, 34 (1963) 323.
13. S. R. Coriell, D.T.J. Hurle and R.F. Sekerka, *J. Crystal Growth*, 32 (1976) 1.

14. J. J. Favier and A. Rouzaud, J. Crystal Growth, 64 (1983) 367.
 15. T. Alboussiere, R. Moreau and D. Camel, C.R. Acad. Sci. Paris, 313 II, (1991) 749.

Table 1
Physicochemical Parameters and Nominal Growth Conditions during the
USMP-1 mission

Thermal expansion coefficient :	$\beta_T = 10^{-4} \text{ K}$
Kinematic viscosity :	$\nu = 2.6 \times 10^{-7} \text{ m}^2 \text{ s}^{-1}$
Bi diffusion coefficient :	$D = 1.8 \times 10^{-9} \text{ m}^2 \text{ s}^{-1}$
Partition coefficient :	$k = 0.29$
Liquidus slope :	$m_L = -2.2 \text{ K(at\% Bi)}^{-1}$
Electrical conductivity :	
liquid :	$\sigma_L = 2.15 \times 10^6 \Omega^{-1} \text{ m}^{-1}$
solid :	$\sigma_S = 4.3 \times 10^6 \Omega^{-1} \text{ m}^{-1}$
Global thermoelectric power :	$\eta_S - \eta_L = 1.6 \times 10^{-6} \text{ V K}^{-1}$
Nominal concentration :	$C_0 = 0.5 \text{ at\% Bi}$
Sample diameter :	$H = 6 \times 10^{-3} \text{ m}$
Thermal gradient :	
liquid :	$G_L = 13.5 \times 10^3 \text{ Km}^{-1}$
solid :	$G_S = 6.75 \times 10^3 \text{ Km}^{-1}$
Growth velocity :	$V_I = 2 \rightarrow 27 \times 10^{-6} \text{ ms}^{-1}$

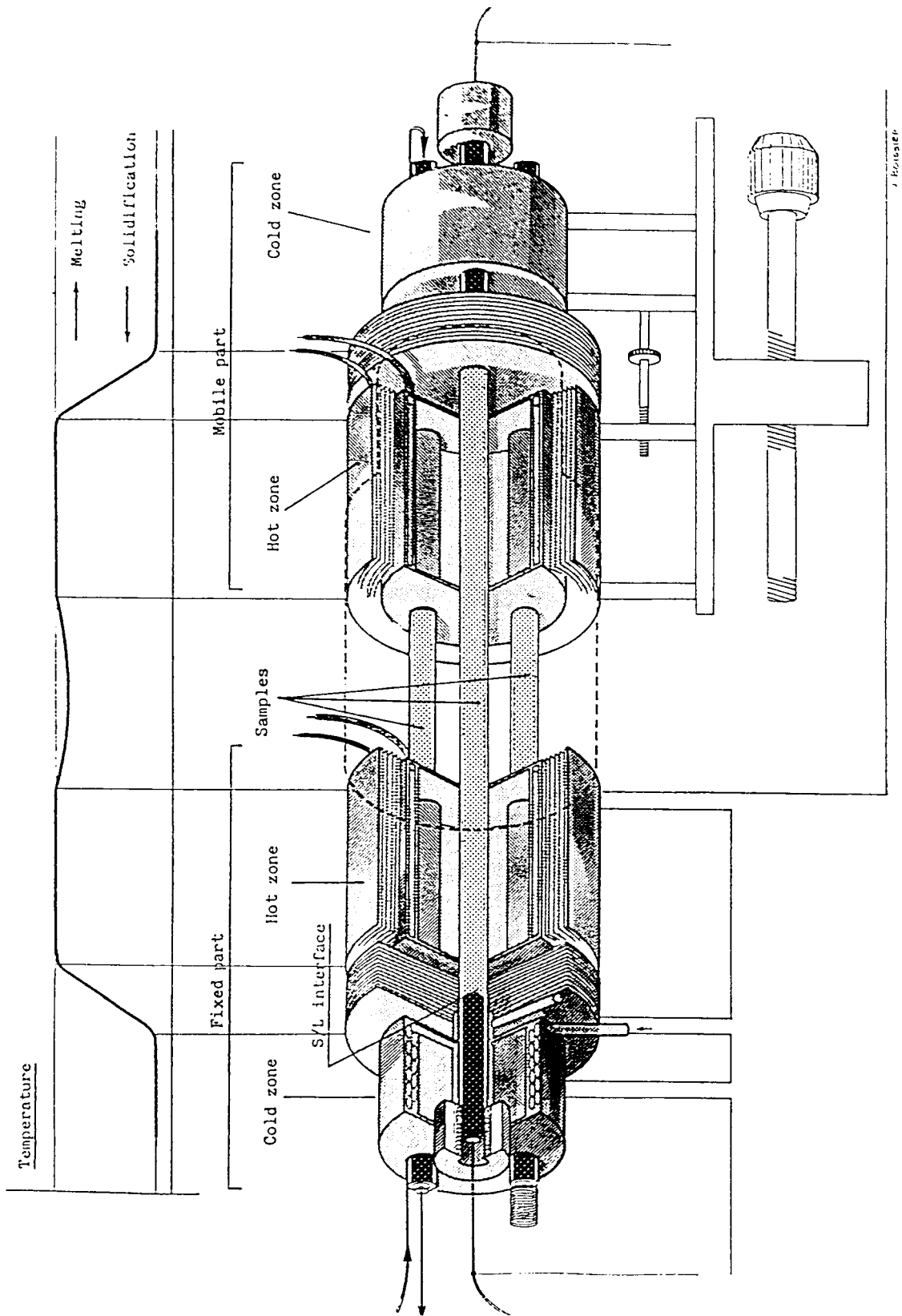


Figure 1 Schematic of MEPHISTO.

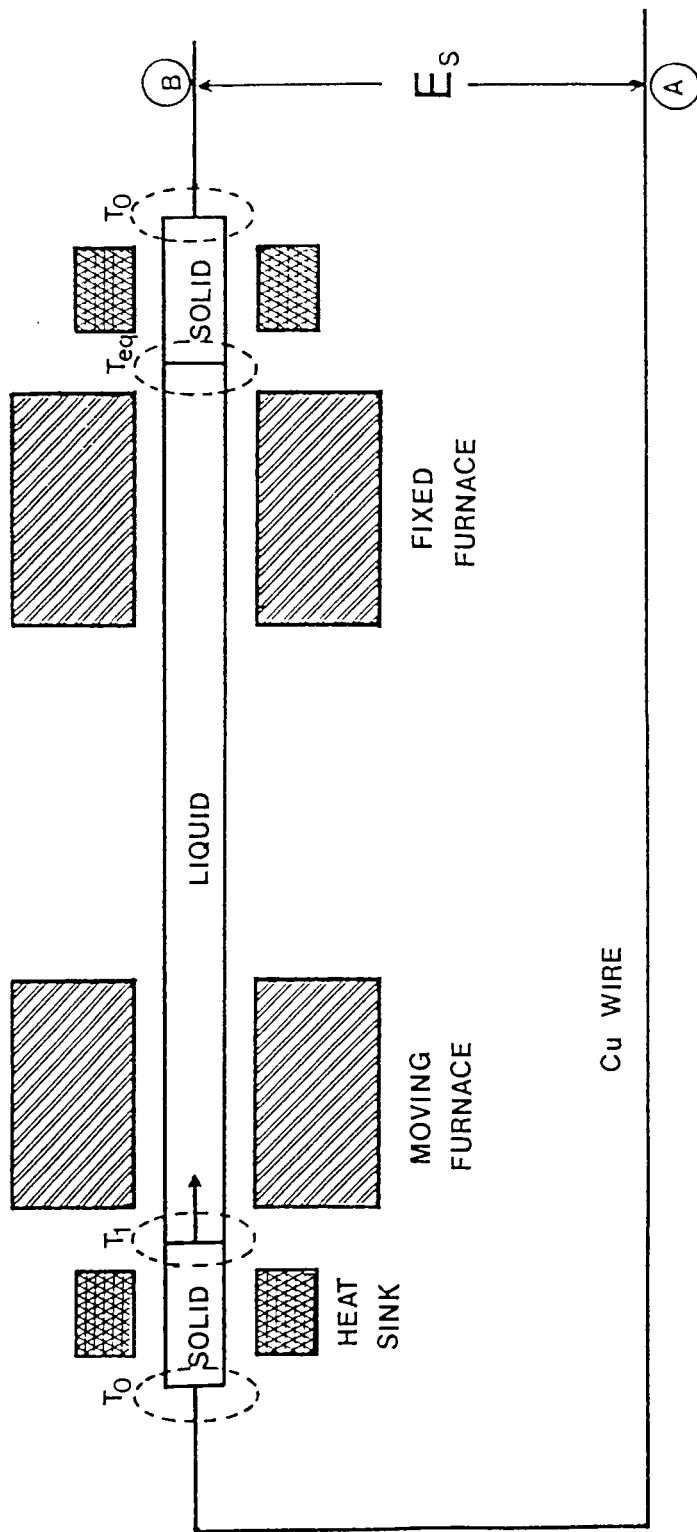


Figure 2 Seebeck thermoelectric loop featuring the two solid-liquid interfaces.

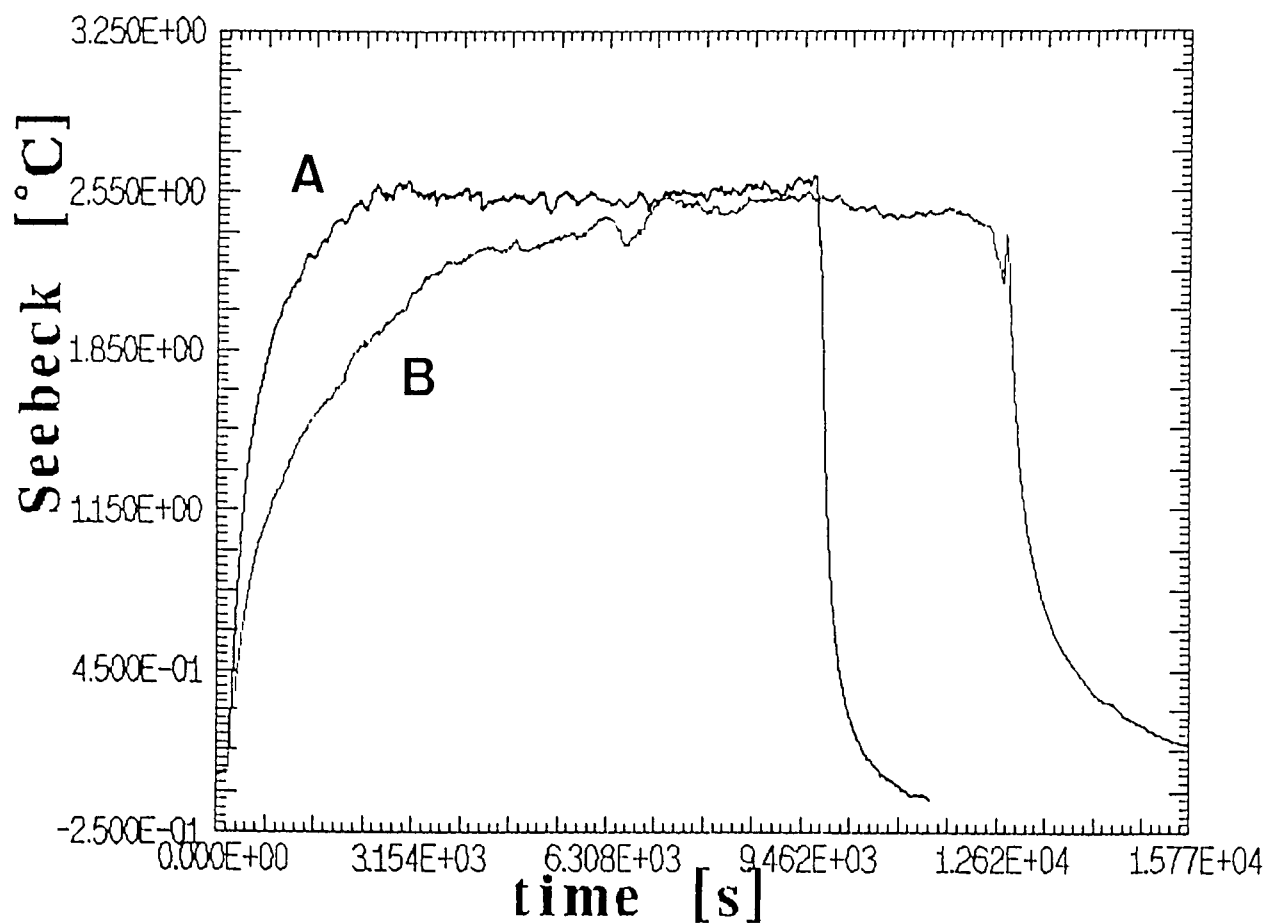


Figure 3 Typical planar front solidification Seebeck signals with interface velocities of 5.2 $\mu\text{m/s}$ (A) and 2 $\mu\text{m/s}$ (B).

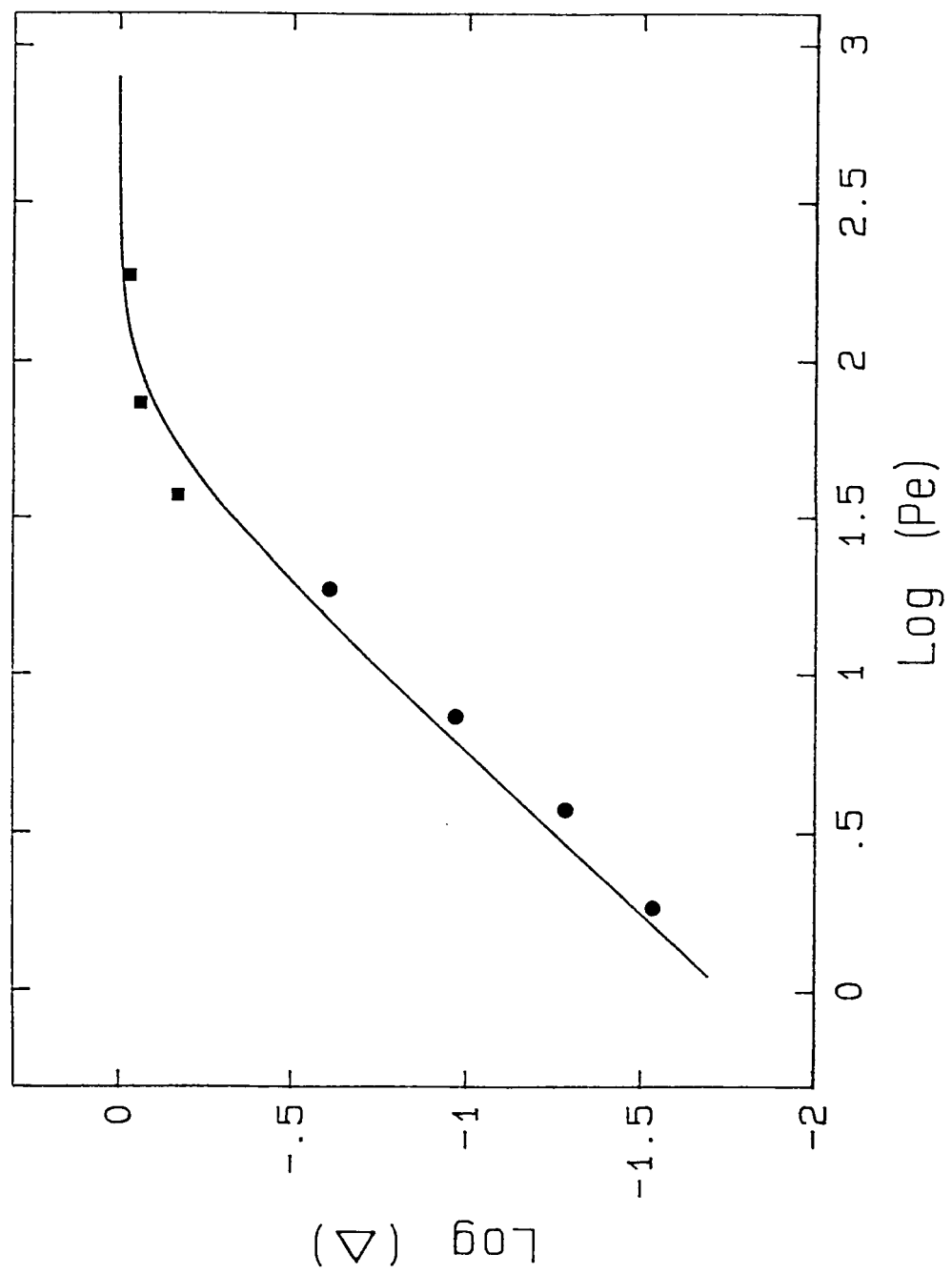


Figure 4 Variation of the experimental (symbols) and calculated (curve) values of the convecto-diffusive parameter Δ with the Peclet number.

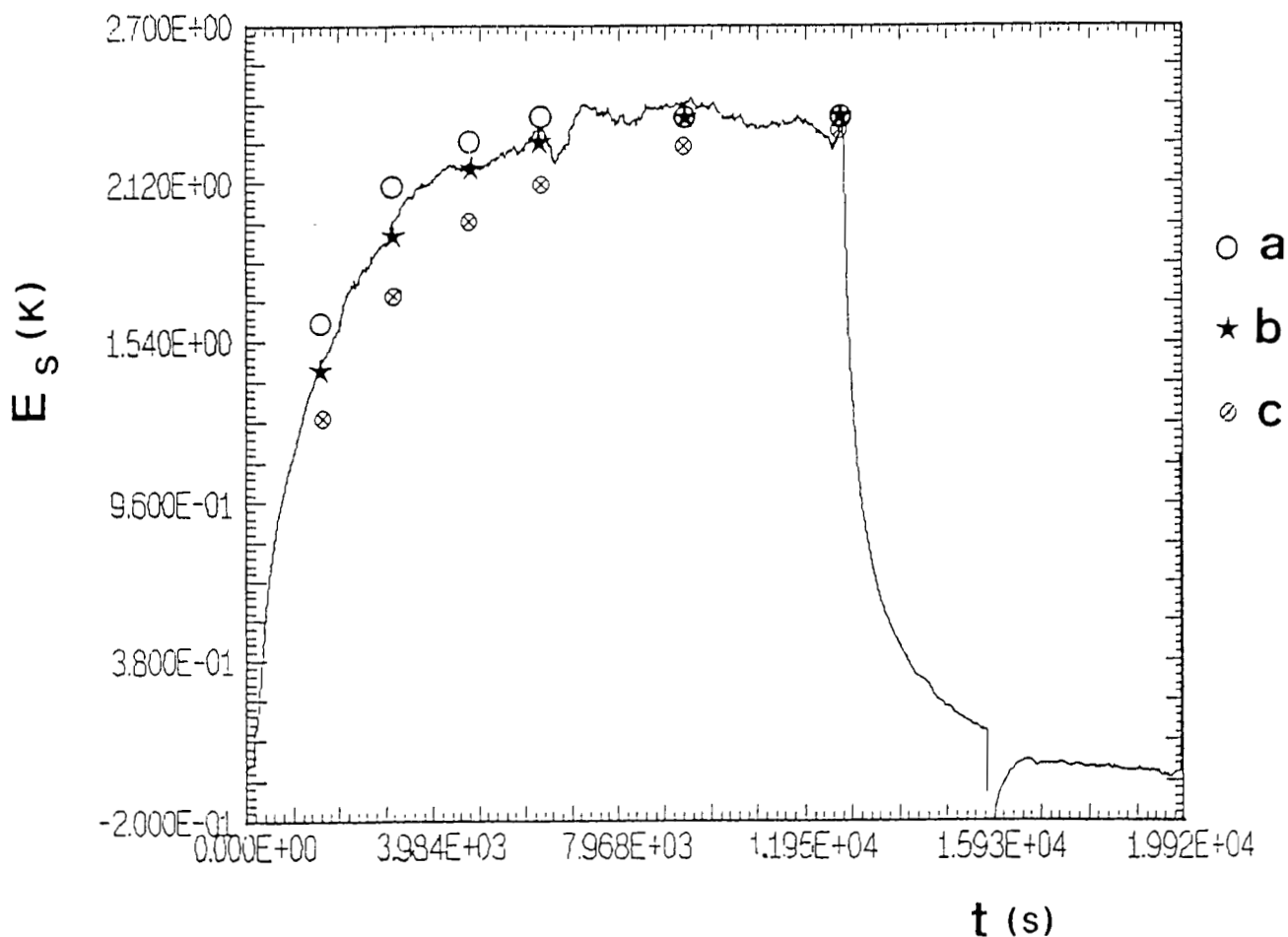


Figure 5 Fit of the observed Seebeck signal assuming negligible mass transport, with diffusion coefficients of $1.2 \times 10^{-9} \text{ m}^2\text{s}^{-1}$ (a), $1.8 \times 10^{-9} \text{ m}^2\text{s}^{-1}$ (b) and $2.5 \times 10^{-9} \text{ m}^2\text{s}^{-1}$ (c).

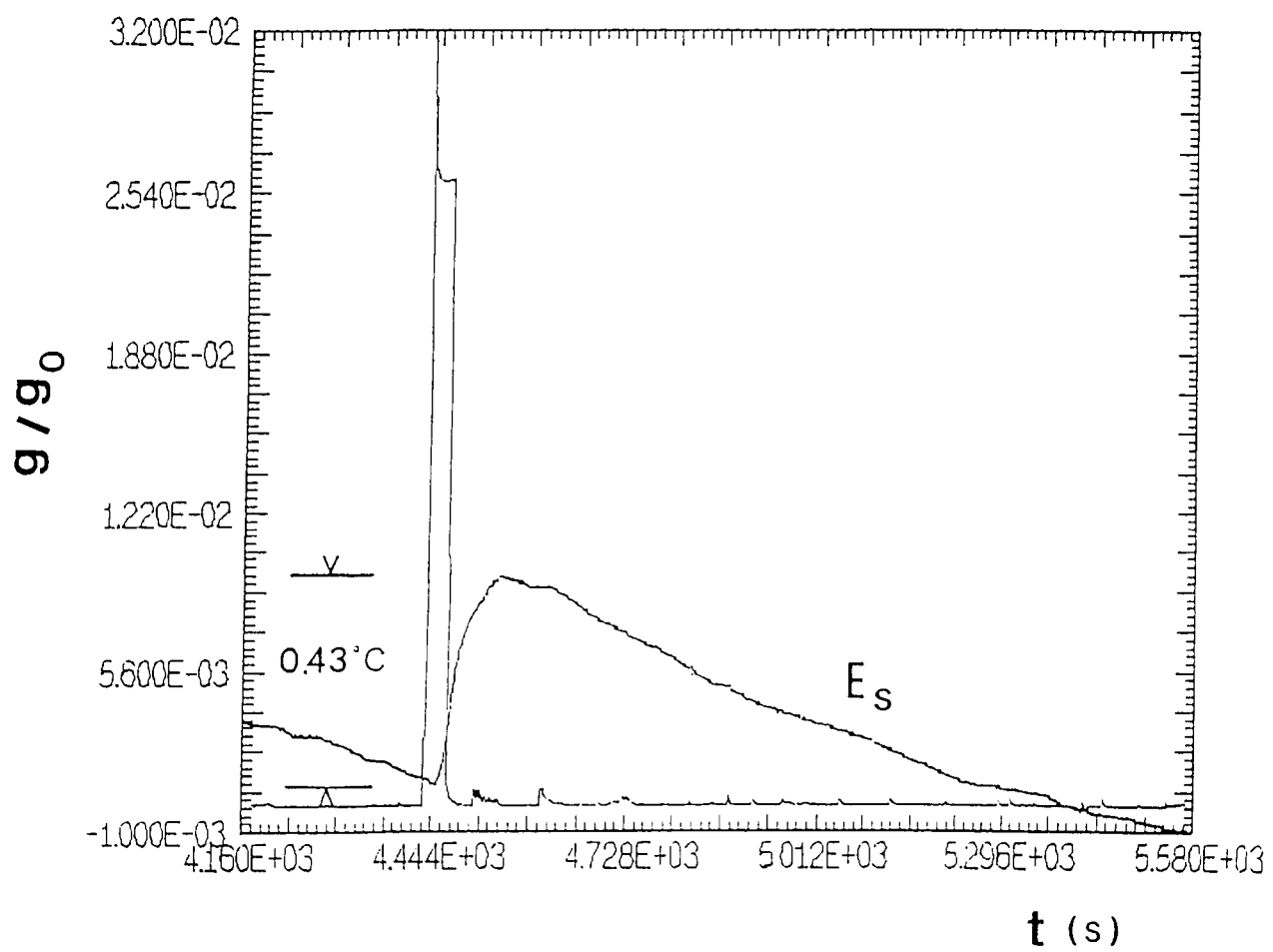


Figure 6 Effect of a major gravity perturbation (OMS burn) on the Seebeck signal E_S .

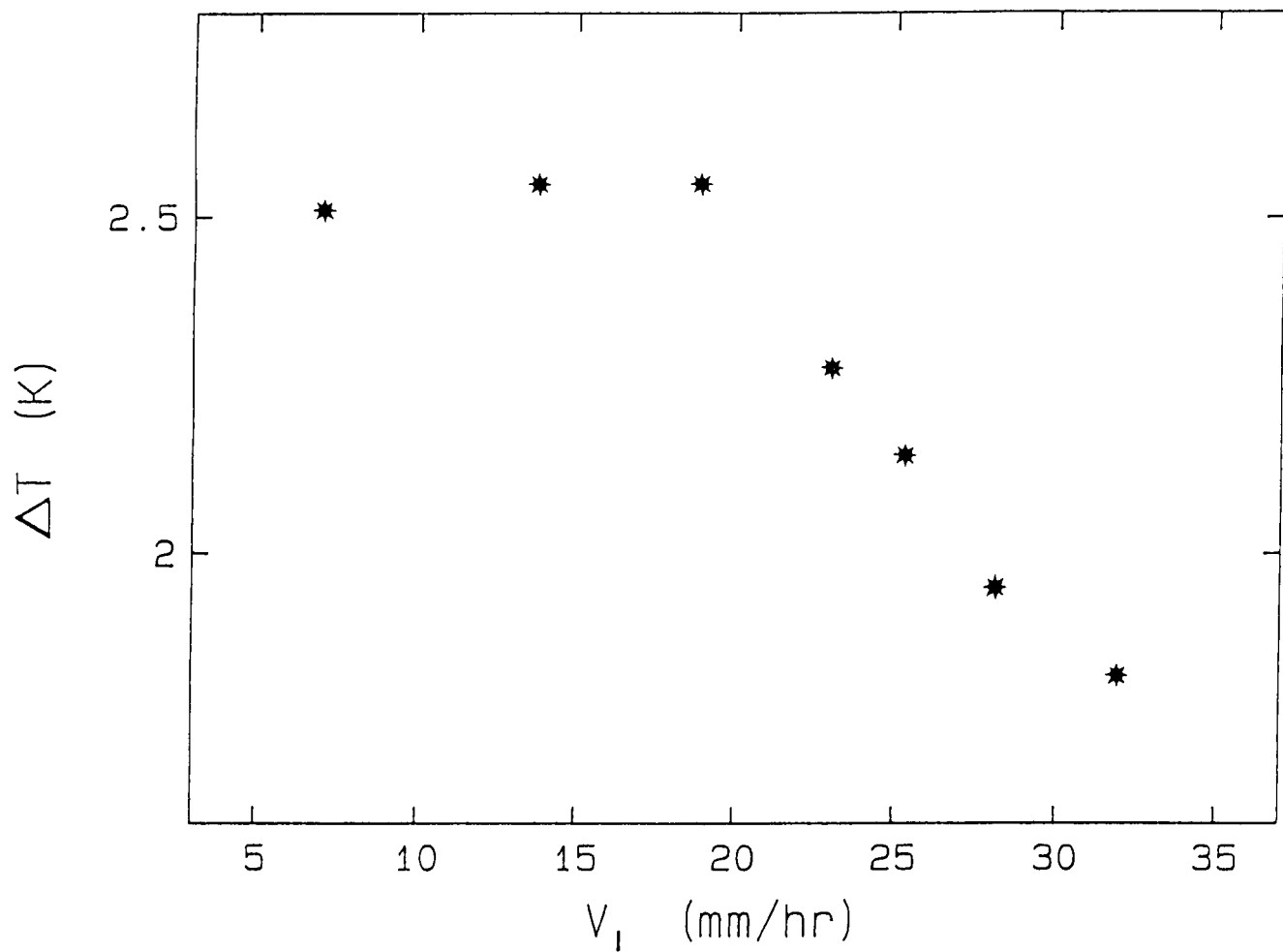


Figure 7 Variation of the experimentally observed undercooling around the morphological stability threshold.

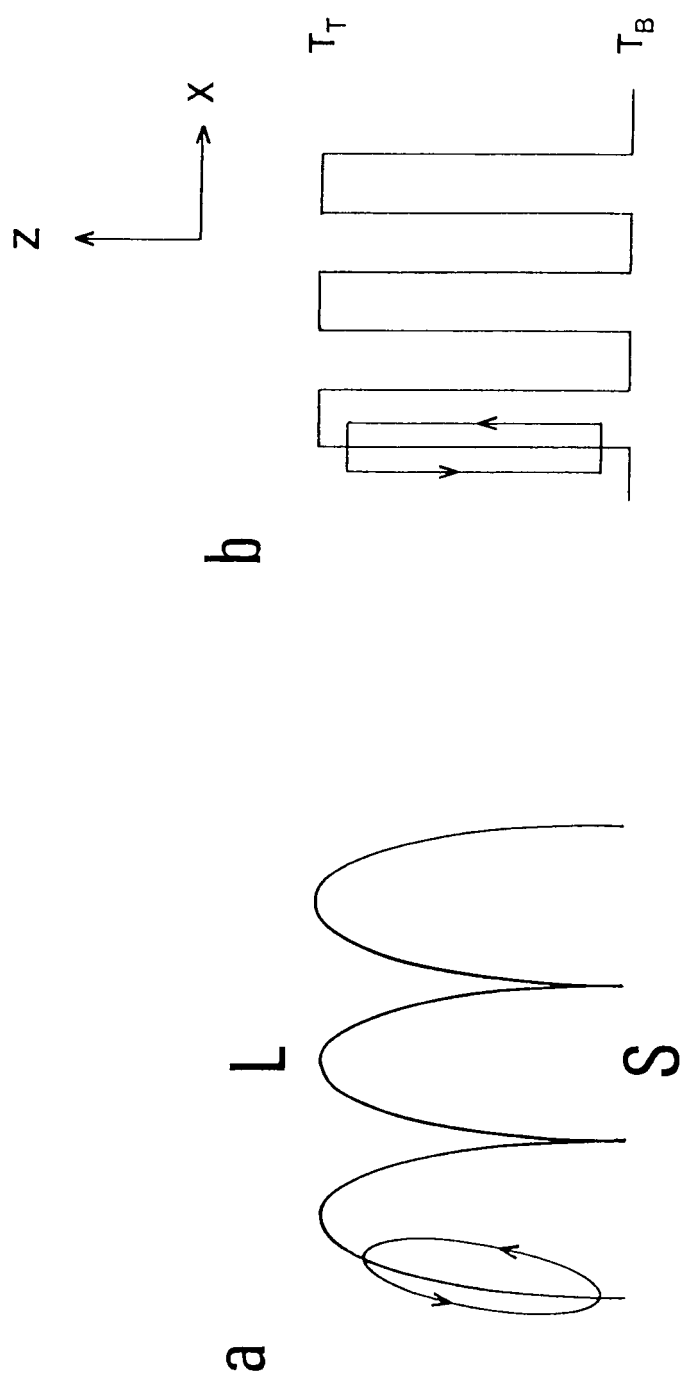


Figure 8 Actual (a) and model (b) cellular interfaces.

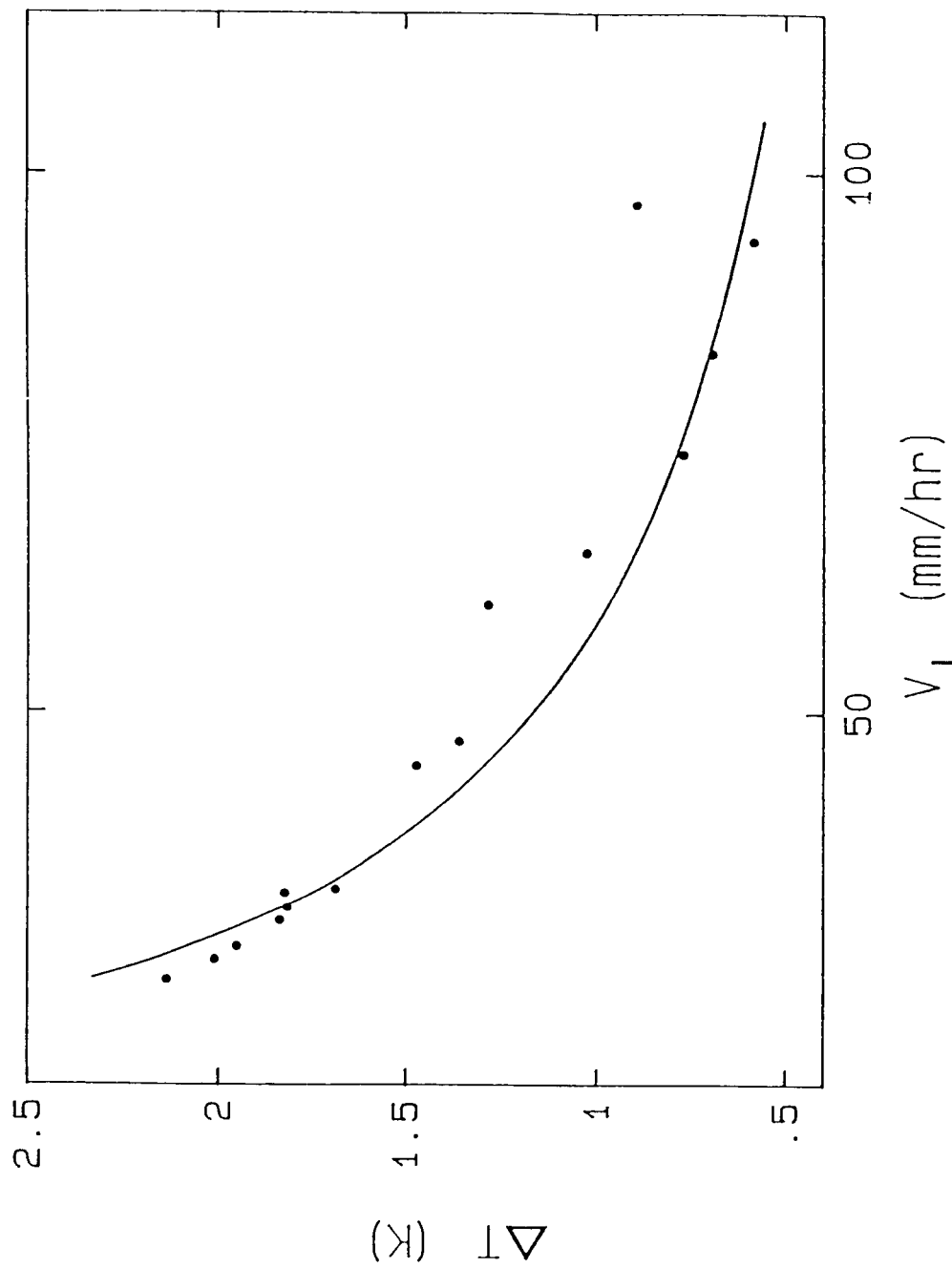


Figure 9 Variation of the experimental (symbols) and calculated (curve) undercoolings as a function of the growth velocity for cellular interfaces.

Discussion

Question: *In one of your charts, it appears as though higher velocities are present in some regions of the wall. Is that just an illusion or is that real?*

Answer: Our samples were put in quartz crucibles, and in order to get wetting of the crucible by the samples we design a specific roughness in the inner part of the wall. This ensures a contact between the liquid at any time and the quartz crucible. Again just sufficient contact with the wall only because afterwards we should be able to pull out the sample from the crucible. Maybe this is the illusion you got from the pictures of some of the morphologies.

Question: *Following up, then you are saying that the samples remained of constant diameter ?*

Answer: Yes. Except in the middle part of the sample between the two furnaces. We had two furnaces, so at the very end of the solidification we just shut down the furnaces and the middle part was just solidified without directional solidification. In that part we got some variation of the diameter of the sample.

Question: *It has been known for a long time that the morphological instabilities in these dilute alloys for these rough interface materials is a sub critical bifurcation; so this is induced by grain boundaries or the edges of the sample. Is the sub critical nature of these bifurcations taken into account?*

Answer: Yes. In this slide, you can see that the perturbation occurs in a specific region here and here which are in fact the regions where we had the grain boundaries in the cross sections.

Question: *Right. I am just asking, you compared it to what you called theory, does that theory take into account the presence of an initial grain boundary groove?*

Answer: No. It does not.

20 Pg

1995107796
324063

N95- 14210

NASA

BASIC FEATURES OF THE STS/SPACELAB VIBRATION ENVIRONMENT P- 92

C. R. Baugher* and N. Ramachandran[†]

*NASA Marshall Space Flight Center, Huntsville, Alabama

[†]Universities Space Research Association, Huntsville, Alabama

ABSTRACT

The Space Shuttle acceleration environment is characterized. The acceleration environment is composed of a residual or quasi-steady component and higher frequency components induced by vehicle structural modes and the operation of onboard machinery. Quasi-steady accelerations are generally due to atmospheric drag, gravity gradient effects, and rotational forces. These accelerations tend to vary with the orbital frequency ($\sim 10^{-4}$ Hz) and have magnitudes $\leq 10^{-6}g_0$ (where $1 g_0$ is terrestrial gravity). Higher frequency g-jitter is characterized by oscillatory disturbances in the 1-100 Hz range and transient components. Oscillatory accelerations are related to the response of large flexible structures like antennae, the Spacelab module, and the Orbiter itself and to the operation of rotating machinery. The Orbiter structural modes in the 1-10 Hz range, are excited by oscillatory and transient disturbances and tend to dominate the energy spectrum of the acceleration environment. A comparison of the acceleration measurements from different Space shuttle missions reveals the characteristic signature of the structural modes of the Orbiter overlaid with mission specific hardware induced disturbances and their harmonics. Transient accelerations are usually attributed to crew activity and Orbiter thruster operations. During crew sleep periods, the acceleration levels are typically on the order of $10^{-6}g_0$ (1 micro-g). Crew work and exercise tends to raise the accelerations to the $10^{-3}g_0$ (1 milli-g) level. Vernier reaction control system firings tend to cause accelerations of $10^{-4}g_0$, while primary reaction control system and Orbiter maneuvering system firings cause accelerations as large as $10^{-2}g_0$. The use of vibration isolation techniques (both active and passive systems) during crew exercise have shown to significantly reduce the acceleration magnitudes.

INTRODUCTION

The acceleration environment encountered in low Earth orbit is generally composed of three components: quasi-steady, oscillatory, and transient accelerations¹⁻². The low-gravity environment on board the NASA Space Shuttle Orbiters has been measured with a variety of instruments since the

Joint "L+1" Science Review for USML-1 and USMP-1 with the Microgravity Measurement Group, September 22-24, 1993, Huntsville, Alabama, USA.

inception of the Shuttle Program. Understanding the Orbiter acceleration environment is the first step not only in the conception and design of a microgravity experiment, but also in the post flight analysis of the results from the experiment. The underpinning of this acceleration measurement and characterization effort is to provide continuity and a concentrated focus for the analysis, interpretation, and dissemination of these observations on space missions. This approach allows the results of a variety of measurements to be organized into a technical investigation which evolves from discovery, to analysis, to synthesis. An overview of the shuttle acceleration environment is provided in this paper. The reader is referred to [3-6 and the references cited therein] for detailed information about specific issues. In section 2, the shuttle coordinate system and mission flight attitudes are introduced. In section 3 we describe the different acceleration classifications and summarize acceleration measurements made to date. In this section, we also focus on crew exercise activity as measured and recorded by the NASA Space Acceleration Measurement System (SAMS). The use of vibration isolation systems in reducing the impact to the acceleration environment is also discussed.

I. SPACE SHUTTLE COORDINATE AXIS AND FLIGHT ATTITUDES

The Orbiter coordinate axes and flight attitudes or orientations are first explained. The Orbiter Structural coordinate system shown in Fig. 1, is Orbiter-fixed with the origin in the Orbiter plane of symmetry, 400 inches below the center line of the Orbiter cargo bay. The most forward Y-Z plane of the cargo bay is at $X = 582$ inches. The X_0 axis is in the Orbiter plane of symmetry, parallel to and 400 inches below the centerline of the cargo bay. Positive sense is from the nose toward the tail. The Z_0 axis is in the Orbiter plane of symmetry and perpendicular to the X_0 axis. The positive sense for this axis is upward in the landing attitude as shown in the figure. The Y_0 axis completes the right hand, orthogonal coordinate system.

A schematic representation of the two most frequently used attitudes or orientations for flying microgravity missions is shown in Fig. 2. In the *Z-local vertical* attitude, the vehicle's z-axis (out of the cargo bay) is oriented along the radius vector to the center of the Earth. This attitude has somewhat lower drag, but requires more thruster firings to maintain the attitude. The second is the *gravity-gradient* attitude. In this case, the vehicle's center line (x axis) is along the radius vector. This attitude is inherently stable and minimizes the thruster firings at the expense of more drag³. During the flight of the first US Microgravity Laboratory (USML-1) in June 1992, the shuttle was flown in the *gravity-gradient* attitude during the use of the Crystal Growth Furnace (CGF) for the growth of several semiconductor crystals.

II. ORBITER ACCELERATION ENVIRONMENT

The accelerations experienced in a manned orbiting space laboratory are loosely classified as quasi-steady, oscillatory, and transient. The quasi-steady classification, by convention, is assigned to accelerations with frequency below about 0.01 Hz. This encompasses accelerations due to atmospheric drag, gravity gradient effects, and rotational forces. Using atmospheric models, the contribution from atmospheric drag on the Shuttle Orbiter is estimated to be on the order of $10^{-6}g_0$ ². This contribution varies with the orbital frequency of about 10^{-4} Hz.

Gravity gradient accelerations are related to the physical displacement of an experiment from the center of mass of the orbiting laboratory. The effect arises from the force imparted by the structure of the vehicle on the experiment, as the vehicle drags the experiment in the vehicle's orbit. Without the structure, the experiment would diverge into a slightly different orbit because of its displacement from the Orbiter center of mass. The magnitude of the force is dependent on the amount of displacement between the experiment and the vehicle's center of mass; the magnitude also differs depending on whether displacement is in the orbit plane, or perpendicular to it³. In general, the gravity gradient effect is on the order of $10^{-7}g_0$ per meter from the Orbiter center of mass. Rotational effects are on the order of $10^{-8}g_0$. Overall, depending on location, atmospheric drag or gravity gradient effects dominate the quasi-steady regime on the Shuttle Orbiter contributing to a total magnitude on the order of $10^{-6}g_0$ with frequency about 10^{-4} Hz.

Higher frequency accelerations experienced in low Earth orbit are generally referred to as g-jitter. In the 1 to 100 Hz range, measured accelerations on the Shuttle are usually related to the excitation of structural modes by oscillatory and transient sources. Vehicle maintenance and communications, experiment pumps, fans, and motors are all common oscillatory sources on an Earth orbiting laboratory. Common transient sources are nominal crew activity and exercise, and Orbiter thruster firings for attitude control and maneuvering. Acceleration levels on the Shuttle Orbiters related to such sources vary from $10^{-4} g_0$ (oscillatory, light crew activity, Vernier Reaction Control System (VRCS) firings) to $10^{-2} g_0$ (Primary Reaction Control System (PRCS) firings and Orbiter Maneuvering System (OMS) burns). Reports of acceleration measurements from various systems are available in the literature [see for instance, the references cited in 7].

A. Quasi-steady measurements - Orbital Acceleration Research Experiment (OARE)

The OARE is a state-of-the-art accelerometer system which is used for obtaining highly sensitive, low frequency measurements of the flight acceleration environment in combination with in situ calibration. The measurement system includes a very sensitive three-axis accelerometer, a full in-flight

calibration station, and a control microprocessor which can provide custom in-flight data processing and storage. The measurement system is built around a Bell Textron Miniature Electro-Static Accelerometer (MESA). The associated calibration station is a two-axis rate table which allows the instrument to be rotated at fixed rates to verify instrument performance parameters. The rotation serves the dual function of imposing a known centripetal acceleration on the accelerometer and allowing the individual axes to be inverted to separate fixed instrument biases from actual acceleration effects of the ambient environment. The OARE is designed for characterizing the Orbiter's aerodynamic acceleration along its principal axes at orbital altitudes and in the transition regime during re-entry. Therefore, the instrument has been optimized for measurements in a very low frequency regime and for amplitudes of a micro-g and less. The NASA Microgravity Science and Applications Division (MSAD) sponsors the OARE flights, which to date has flown on four missions in the Shuttle cargo bay. Table 1 identifies the OARE missions flown to date.

OARE flew on its second flight on STS-50 (USML-1), which was a mission dedicated to science, particularly to the study of the effects of reduced gravity on a variety of fundamental physical processes. The basic Shuttle/Spacelab flight configuration for the flight was the long Spacelab module with mission related experiments in both the Spacelab and the middeck area. A major goal of the mission's scientific investigations was the study of the sensitivity of the growth of semiconductor crystals to the effects of low-level, quasi-steady residuals. Pre-flight mathematical modeling of experiments in the Crystal Growth Furnace (CGF) facility indicated possible adverse responses of the experiments to long-period accelerations as low as a few tenths of a micro-g, if those forces were perpendicular to the longitudinal axis of the crystal. To avoid such forces during the experiment intervals, the CGF was located within two meters of the vehicle center of mass to minimize gravity gradient forces, and the vehicle was flown in a special attitude during experiment runs to direct drag forces parallel to the crystal axis.

The most important finding by the OARE instrument during the flight was the apparent presence of an anomalous force along the vehicle x-axis. A short section of the analyzed data from Ref. 8 is shown in Fig. 3. The gravity gradient mode for the flight had been carefully engineered to minimize the forces in this direction and pre-flight predictions had been for this component to average near zero. This section of data indicates a residual force of the order of 0.5 micro-g's was present for extended portions of the mission. The conclusion from analysis was that the Orbiter was creating the observed environment. The acceleration in the y-axis is slightly negative (\approx 0.2 micro-g) mostly due to aerodynamics and out-of-plane effects. The z-axis acceleration shows the day/night atmospheric effect, about 0.6 micro-gs. The OARE measurements on USML-1 clearly demonstrated the need for in-flight measurements due to two reasons: 1) to monitor and record the residual g level for subsequent

comparison to predicted theoretical models and 2) to correlate departures (in the residual g level) from predictions and experiment requirements, to observed experiment results.

B. Oscillatory and transient disturbance measurements - Space Acceleration Measurement System (SAMS)

SAMS was developed at the NASA Lewis Research Center for MSAD to serve as a standard accelerometer system for all MSAD-sponsored Orbiter microgravity missions. SAMS consists of three remote triaxial sensor heads, connecting cables, and a controlling data acquisition unit with a digital data recording system using optical disks with 200 megabyte storage capacity per side. With the availability of crew access to change the disks, data storage capacity is essentially unlimited. SAMS can be configured to fly in the Orbiter mid-deck, in the Spacelab module, and in the Orbiter cargo bay. To date, SAMS has flown on ten missions and has flown in all three configurations. We present here some results from the first Spacelab Life Sciences mission (SLS-1) which flew on Columbia in June 1991 on STS-40, USML-1 which flew on Columbia in June 1992 on STS-50, and the first United States Microgravity Payload (USMP-1) which flew on Columbia in October 1992 on STS-52. SAMS missions to date are identified in table 2. The individual SAMS heads are usually configured for different frequency ranges and located at areas of specific interest. For example, on STS-50, SAMS heads were located at 3 different locations in the Spacelab module; on rack 10 of Spacelab on the bottom of the Glovebox facility with a low pass cut-off frequency of 25 Hz, on rack 5 on the Surface Tension Driven Convection Experiment with a 5 Hz cut-off frequency, and on rack 9 on the Crystal Growth Furnace with a cut-off frequency of 2.5 Hz to monitor low frequency accelerations. Data sampling is typically done at five times the cut-off frequency. Data from these and other missions and from other accelerometer systems suggest that the low-gravity environment is fairly consistent between missions even with different payloads, configurations, and Orbiters⁴.

The SAMS data analysis comprises of 3 distinct steps: 1) Initial data recording and processing. This step involves in-flight data recording along with measurements of sensor temperature, gain setting, ancillary engineering data and a time record, 2) Post flight processing that involves corrections if any for temperature sensitivity, physical misalignments, electronic bias and filtering, etc., and 3) Final data presentation and analysis using time and frequency domain plots. Steps 2 and 3 mentioned above are usually carried out together as a combined analysis procedure. Error analysis indicates that SAMS measurements are typically accurate to the order of 10% when the data is completely within the dynamic range for the selected gain of each accelerometer. Measurement errors stem from both the accelerometer and the data system and is the result of numerous factors, including calibration error, random drift, noise and rectification error.

The algorithms and data presentations designed for the analysis mentioned in step 3 above, were formulated to summarize a very large volume of data on long term (2 hour) plots to discriminate periods of significant and reduced activity. To this end, the data is presented across the mission period in a time domain analysis, and expanded in depth by frequency domain analysis over selected intervals. The time domain analysis consists of parallel plots of the acceleration mean and the Root Mean Square (RMS), these forms being analogous to the dc and rms signals used in electrical measurements. The approach was established to separate an approximate indication of the low frequency environment (estimated by the mean) and contrast it with the time varying portion (estimated by the RMS).

The acceleration mean is calculated as the vector magnitude of the arithmetic mean of the acceleration on each axis typically over a 10 second period. To eliminate inaccurate data points attributed to gain change stability transients, transient points are discarded following each gain change⁹ and compensated for in subsequent calculations. Estimated instrument bias based on on-orbit values is removed and temperature compensation of bias, is performed before the acceleration mean is calculated. The RMS is similarly calculated as a vector of all 3 axes for each triaxial-sensor head. The mean is very useful to flag a condition in which the accelerometer senses a net acceleration component that is persistent for intervals of the order of ten seconds or more. Therefore, events such as thruster firings that provide a net thrust to the vehicle will be evident, while events internal to the vehicle (such as crew induced impacts) will tend to average out to zero. Fig. 4 shows an example of this processing for a complicated event from STS-40.

In the frequency domain, SAMS data is reported in two formats: 1) as magnitude spectrum color contour charts and 2) as Power Spectral Density (PSD) charts. The accelerometer data is first processed by a Fast Fourier Transform (FFT) algorithm. Each FFT is converted to a magnitude spectrum by calculating the vector sum of the real and imaginary parts of the transform at each point and represented as color charts with colors corresponding to the acceleration magnitude. The PSD representation is used to represent the average power, as opposed to the peak acceleration represented by the magnitude spectrum. During the FFT processing, no special windowing functions are implemented to suppress side lobes created by a finite sample interval. The bandwidth associated with the spectrums is noted on each chart to provide a record of the sample size used in the processing. More detail on the data acquisition and reduction procedures can be obtained from the mission summary reports.

Typical low frequency Orbiter structural modes are shown in Fig. 5 from data taken on STS-47. This plot represents the environment during nominal crew activity and is characterized by distinct frequency peaks in the 1-10 Hz range. The term nominal crew activity is used to indicate a time period when no significant acceleration sources such as vehicle maneuvers, water dumps, satellite launches and crew exercise were present. The measured acceleration magnitudes are generally found to vary with

the level of crew activity. Fig. 6 shows an example of the difference in levels during periods of crew sleep, nominal crew activity, and crew exercise on a bicycle ergometer taken on the STS-40 mission¹⁰.

The data in each plot is a PSD calculation performed on 50 seconds of raw SAMS data and presented in units of Micro-g/Hz^{1/2}. The RMS value for the data on each chart is shown in the upper right. Acceleration levels in time vary from 10^{-4} to $10^{-3}g_0$. The SAMS sensor, located in rack 5 in the Spacelab module, recorded data at 25 samples/sec with a 5 Hz low pass filter. An important characteristic of the g-jitter environment is that the oscillatory and transient sources tend to excite Orbiter and payload structural modes. Because of this, the effects of a high magnitude transient source may be felt by an experiment in the form of damped ringing for some time after the initial event occurred. The 3.5, 4.7 and 5.5 Hz components are all related to the excitation of structural modes by exercise activity and occasional thruster firings. Note the change of scales in the graphs.

Even during the sleep period, the observation is dominated by the vehicle structural modes, but the general level has decreased by an order of magnitude. An example of the excitation of structural modes by an oscillatory source is the 17 Hz signal (not shown in Fig. 5). The KU-band communications antennae on the Orbiters dithers at ~17 Hz to prevent stiction of the gimbal. This dither frequency tends to excite a 17 Hz Orbiter mode. During USMP-1, the SAMS recorded not only the 17 Hz signal, but also first through fourth harmonics at 34, 51, 68, and 85 Hz. The most interesting feature of this signal is the extreme variability of its signature. Acceleration levels while the antenna was operating varied by an order of magnitude. The source of the variability is presently unknown, but it seems likely that it is related to the pointing angles of the system. Further studies are in progress to evaluate the variability.

C. Shuttle Mechanical Disturbances

Several mechanical systems on the Orbiter induce transient or oscillatory disturbances. The most familiar to investigators is the previously mentioned Ku Band antenna which is used for communications between the vehicle and the Tracking Data Relay Satellite. Other sources of unwanted noise are compressor motors associated with refrigerators, and fans in payloads. The most complex disturbance originates from remote manipulator system (RMS). This system is the jointed arm located in the Shuttle's cargo bay and used for grappling satellites or other pieces of space hardware which need to be manipulated by the crew from within the flight deck.

Disturbances in the raw accelerometer data, such as the one shown in the upper right box in Fig. 7, are readily visible when the RMS is operated. Although the disturbances were generally expected, their analysis revealed some unusual properties. The main section of the plot of Fig. 7 shows these characteristics over a fifteen minute stretch of data while the unit was being operated. The upper trace in this plot is the one second averages of the raw accelerometer data from the vehicle's z-axis. The most

unusual feature is the steady offset lasting for about a minute in the 50 to 100 micro-g range starting about 9 minutes into the plot. The second trace in the figure is the telemetered data on the motion of the RMS elbow joint. As can be seen, the steady offset correlates (almost) with a robust movement of this joint. On the other hand, it is difficult to understand why movements of the arm would instigate this type of acceleration. The indicated acceleration is sufficient to impart a net change of several centimeters per second in the velocity of this relatively heavy vehicle (about 100000 kg), in a situation in which there is nothing for the arm to push against.

The answer to the puzzle becomes evident when the record of the vehicle attitude control thrusters is examined. The bottom trace in the figure plots a small triangle each time the thrusters fired during the data interval. It is evident that the operation of these thrusters correlates exactly with the interval of the steady offset acceleration. The explanation then, is that the movement of the arm is sufficient to "rock" the vehicle beyond its in-flight stability control limit, generally of the order of 0.1 degree in pitch, yaw, and roll. When this occurs, the thrusters begin operating to steady the attitude. The thrusters do not form a perfect couple and always provide a residual thrust along the z-axis. Clearly, one means of reducing this type of motion would be to open the control limits to minimize the operation of the attitude control system during arm maneuvers.

A second unusual feature of the averaged acceleration data is the large ringing seen in the plot seen at about eight minutes, and again at about nine minutes into the data interval. Although it is not shown here, the initiation of this ringing correlated exactly with short, rapid movements of the RMS shoulder joint. This ringing has been traced to a natural oscillation of the arm in response to short dynamic impulses. Thruster firings alone can induce the response, however at the relatively low amplitude of a few micro-g's.

D. Exercise vibration and isolation

Specific crew exercise related measurements were carried out during STS-50. During the mission, two approaches for minimizing the effects of crew exercise on the acceleration environment in the vehicle were undertaken. One was a special exercise device called EVIS (Ergometer Vibration Isolation System) located in the Orbiter middeck and the other was the suspension of the exercise ergometer from elastic bungee cords on the flight deck. The reader is referred to reference 9 for more detail on these devices. The EVIS system is an upright bicycle ergometer that incorporates three-axis vibration isolation. The second system resembled a recumbent bicycle suspended by a system of elastic bungees (in the X and Y directions) that also affords some form of vibration isolation. The exercise sequence required a warm-up interval and an interval of high exertion for a total time of 20 to 40

minutes. During the exercise, crew members attempted to maintain a constant pedaling rate of about 70 rpm, or approximately 1.2 Hz.

Some measurements on the ergometer were also made during the STS-40 mission in the Spacelab module. Qualitative analysis of the exercise period acceleration data shows that the fundamental pedaling frequency is observed in the accelerometer measurements. Interestingly, the fundamental is not the most intense signature of the exercise; see Fig. 6, panel 3. The 1.2 Hz frequency is just visible on the compressed scale in the x-axis. The first harmonic at 2.45 Hz is at a somewhat higher magnitude and the largest signature is at the vehicle structural resonance mode of 3.6 Hz.

For the STS-50 mission, the accelerometers were placed at three specific locations in the Spacelab module while crew exercise was carried out on the flight deck and middeck. A cursory look at the data (not shown) during bungee cord isolated exercise routines show that the character of the exercise signature is significantly different. With the bungee isolation, the vehicle modes are no longer excited above their steady state level, but the level of the fundamental exercise frequency is enhanced. For a more rigorous quantitative comparison of the data, four sections of accelerometer data (frequency range dc-5 Hz) corresponding to 1) no exercise or post exercise, 2) EVIS exercise, 3) bungee exercise, and 4) hard mounted exercise, were selected and a separate analysis performed. These plots each represent 10 minutes of activity to average down transient effects and changes in the exercise rate by the same individual. The power spectral density (PSD) from each of the four sections of data is shown in Fig. 8 on a log scale. The PSD is calculated such that

$$RMS = \left[\int_0^f (PSD) df \right]^{1/2} \quad (1)$$

This implies that the RMS of the time domain signal is equal to the square root of the integral of the PSD of that signal. For this analysis, the upper limit on the integral was set to 6 Hz. The accelerometer's 5 Hz filter is affecting the data at about the 10% level beyond the 3 Hz point⁹.

The fundamental frequency of the exercise is visible in all exercise cases near 1.2 Hz. As one progresses from the case of no exercise through the hard-mounted case, the energy in the vehicle structural modes is seen to steadily increase. There appears to be no large effect by the exercise on the environment below 1 Hz. Additional insight into the data can be gleaned by evaluating the RMS in equation (1) as a function of the upper limit on the integral. This plot labeled *Cumulative RMS* is shown in Fig. 9. At 6 Hz, the value of the integral is equal to the RMS of the original time domain signal. At lower frequencies, the value of the cumulative RMS calculation represents the RMS which would be obtained if there were a sharp low-pass filter in effect at the frequency. The result is one measure of the

effectiveness of the various exercise systems on STS-50. Table 3 summarizes the numerical values at end points corresponding to 2 Hz and 6 Hz, respectively, of this plot.

Based on the data, the distinct reduction in disturbance levels due to vibration isolation is clear. Based on the particular set of exercise sessions used for the plot, the bungee system reduced the integrated disturbance level between 0 and 6 Hz to about one-third of the non-isolated case, while the EVIS reduced the level by about one fourth. From an alternative viewpoint, EVIS allowed the disturbance background to rise by about a factor of two over the no-exercise case (post-exercise on the plot), while the bungee system allowed an approximate 50% additional increase over the EVIS. Considering the relative complexity, expense, and operational difficulties of the EVIS, the present analysis suggests that a bungee system is adequate.

CONCLUSIONS

An overview of the Space Shuttle acceleration environment is provided. Measurements from OARE are used to characterize the residual or quasi-steady environment and measurements from SAMS are used for evaluating the acceleration components at higher frequencies.

The measurement of the quasi-steady environment (frequencies below 0.01 Hz.) by the OARE instrument determined that this portion of the environment can be influenced at a fraction of the micro-g level by forces other than drag and gravity gradients. On STS-50, a persistent acceleration of approximately 0.5 micro-g, thought to be Orbiter induced, was present for much of the mission. Therefore, earlier speculation that this portion of the spectral range could be handled by analytic modeling have been proven incorrect. It is now known that experiments sensitive to forces of this nature will have to depend on a measurement system with the demonstrated capabilities of the OARE (of the order of 0.1 micro-g absolute) to supply environmental data for post-flight analysis.

In the lower frequencies (1 to 10 Hz), it has been determined that the dominant pattern of the STS environment is the presence of enhanced disturbances levels at a set of vehicle resonance modes which form a fairly common background from mission to mission. Above this frequency range (10 to 100 Hz), disturbances to the environment are primarily generated by noisy equipment. A notable exception is the 17 Hz dither of the STS Ku-band TDRSS communication antenna. On occasion, this disturbance has been found to account for a major portion of the total noise power in the 0-100 Hz frequency range.

The disturbance contributions originating from crew activity arise mostly in the 1 to 10 Hz frequency band. They range from a gentle rocking of the vehicle during intervals when the crew is performing routine duties, to fairly violent shaking and excitation of the structural modes during robust exercise periods. Tests show however, that the exercise disturbances can be substantially reduced by combining the exercise equipment with vibration isolation techniques.

REFERENCES

1. Ostrach, S., 1982, "Low Gravity Fluid Flows, Annual Review of Fluid Mechanics, Vol. 14, pp. 313-345.
2. Hamacher, H. and U. Merbold., "Microgravity environment of the Material Science Double Rack on Spacelab-1," J. Spacecraft, Vol. 24, No. 3, pp. 264-269, 1987.
3. Baugher, C. R., *Acceleration Characterization and Analysis Project (ACAP) - 1992 Annual Report*, NASA Marshall Space Flight Center, 1993.
4. Baugher, C. R., Martin, G. L., and DeLombard, R., "Review of the Shuttle Vibration Environment," AIAA Aerospace Sciences Meeting, Reno, Nevada, AIAA 93-0832.
5. Rogers, M. J. B., Alexander, J. I. D., 1992, "Residual Acceleration Data Analysis for Spacelab Missions," *Microgravity Sci. Tech.* V, pp. 43-49, 1993.
6. Blanchard, R. C., Nicholson, J. Y., Ritter, J. R., "STS-40 Orbital Acceleration Research Experiment Flight Results During a Typical Sleep Period," NASA Technical Memorandum 104209, 1992.
7. Ramachandran, N, Baugher, R. C., and Rogers, M, J. B., "Acceleration Environment of the Space Shuttle and its Impact on Thermo-Solutal Fluid Mechanics," ASME Winter Annual Meeting, New Orleans, Nov. 28 - Dec. 3, AMD-Vol. 174, FED Vol. 175, pp. 155-171, 1993.
8. Blanchard, R. C., Nicholson, J. Y., and Ritter, J. R., "Preliminary OARE Absolute Acceleration Measurements on STS-50," NASA TM 107724, Feb. 1993.
9. Baugher, C. R., *Early Summary Report of Mission Acceleration Measurements from STS-50*, 1992.
10. Baugher, C. R., *Early Summary Report of Mission Acceleration Measurements from STS-40*, 1991.

Table 1: OARE Missions

Mission Id.	Launch Date	Mission
STS-40	June 5, 1991	First Life Science Laboratory
STS-50	June 25, 1992	First US Microgravity Laboratory
STS-58	Oct. 18, 1993	Second Life Science Laboratory
STS-62	March 4, 1994	Second US Microgravity Payload

Table 2: Specific Space Shuttle missions and SAMS Configuration

Mission Id.	Launch Date	Mission
STS-40	June 5, 1991	First Life Science Laboratory
STS-42	Jan. 22, 1992	First International Laboratory
STS-43	Aug. 2, 1991	TDRSS Launch
STS-47	Sept. 12, 1992	Spacelab - Japan
STS-50	June 25, 1992	First US Microgravity Laboratory
STS-52	Oct. 22, 1992	First US Microgravity Payload
STS-54	Jan. 13, 1993	TDRSS Launch
STS-57	June 23, 1993	First Spacehab Mission
STS-60	Feb. 3, 1994	Second Spacehab Mission
STS-62	March 4, 1994	Second US Microgravity Payload

Table 3: Cumulative RMS Values

Exercise Mode	RMS 0-2 Hz (micro-g)	RMS 0-6 Hz (micro-g)
Hard Mounted	42.2	456
Bungee	38.6	159
EVIS	26.3	110
No Exercise	22.1	73

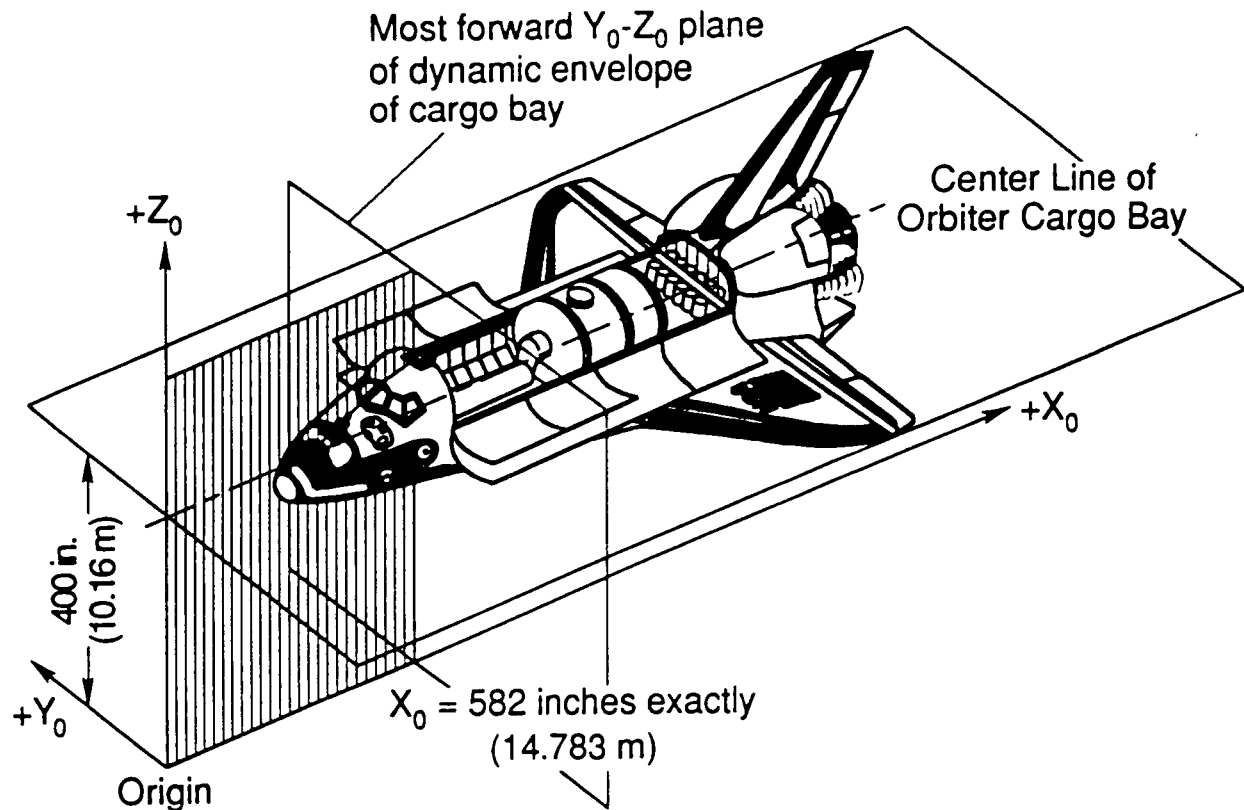


Figure 1 The Orbiter Structural Coordinate System (X_0 , Y_0 , Z_0).

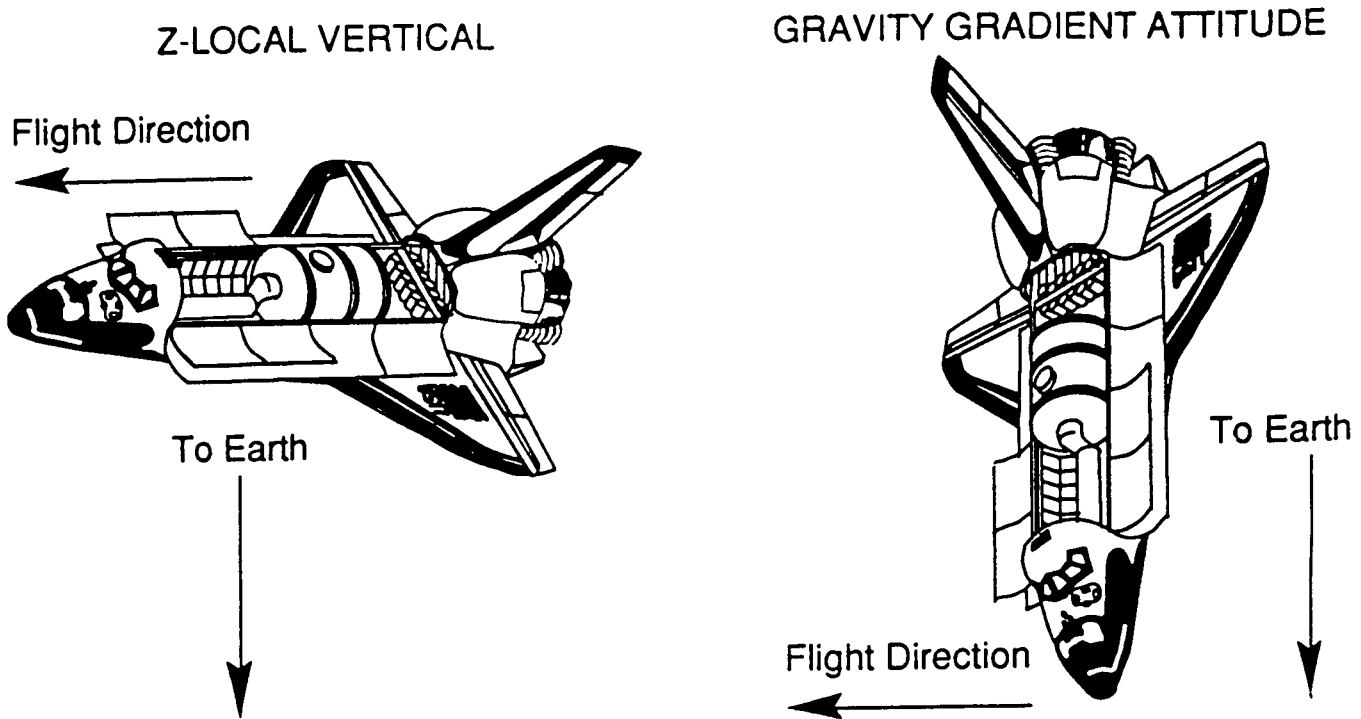


Figure 2 Space Shuttle flight attitudes.

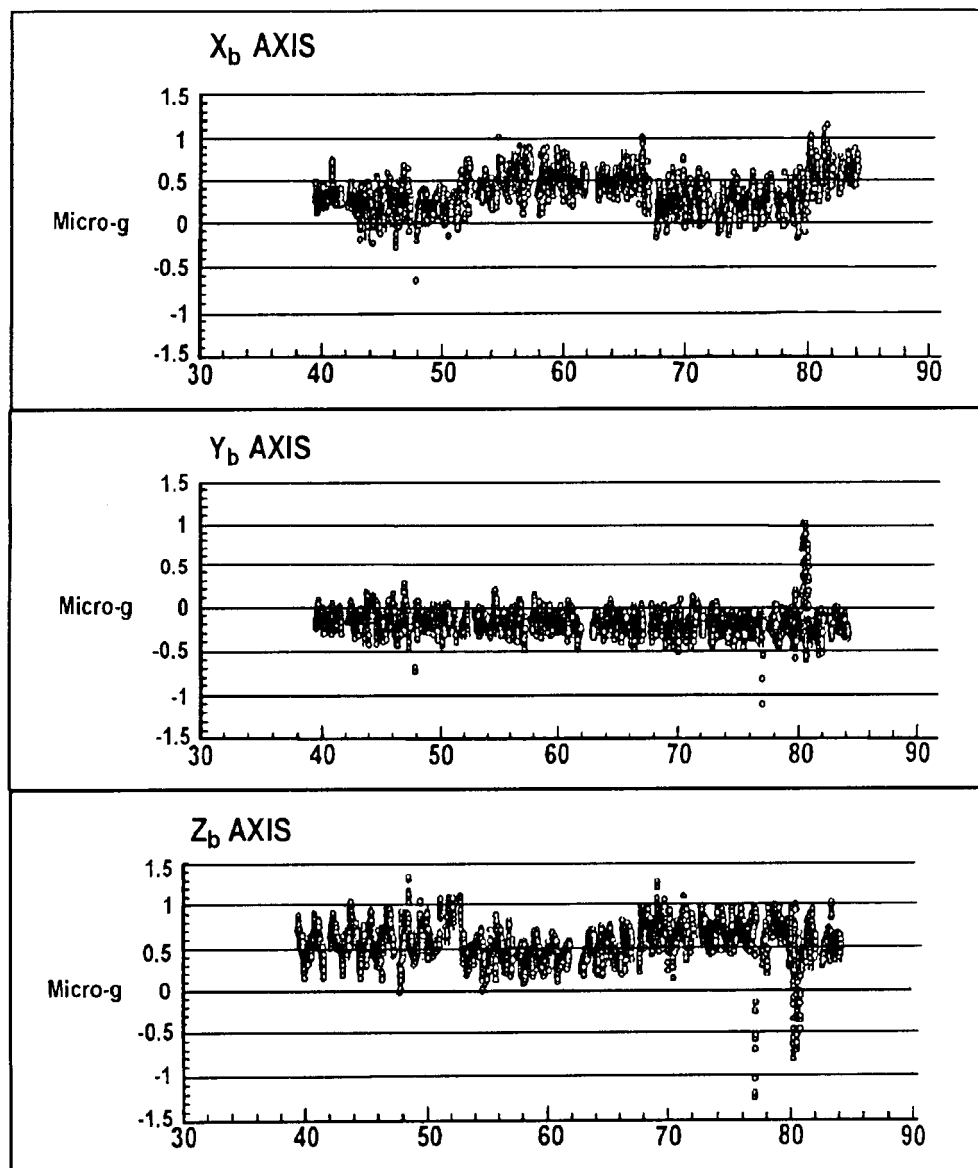


Figure 3 Quasi-steady measurements from OARE on USML-1 (Ref. 8).

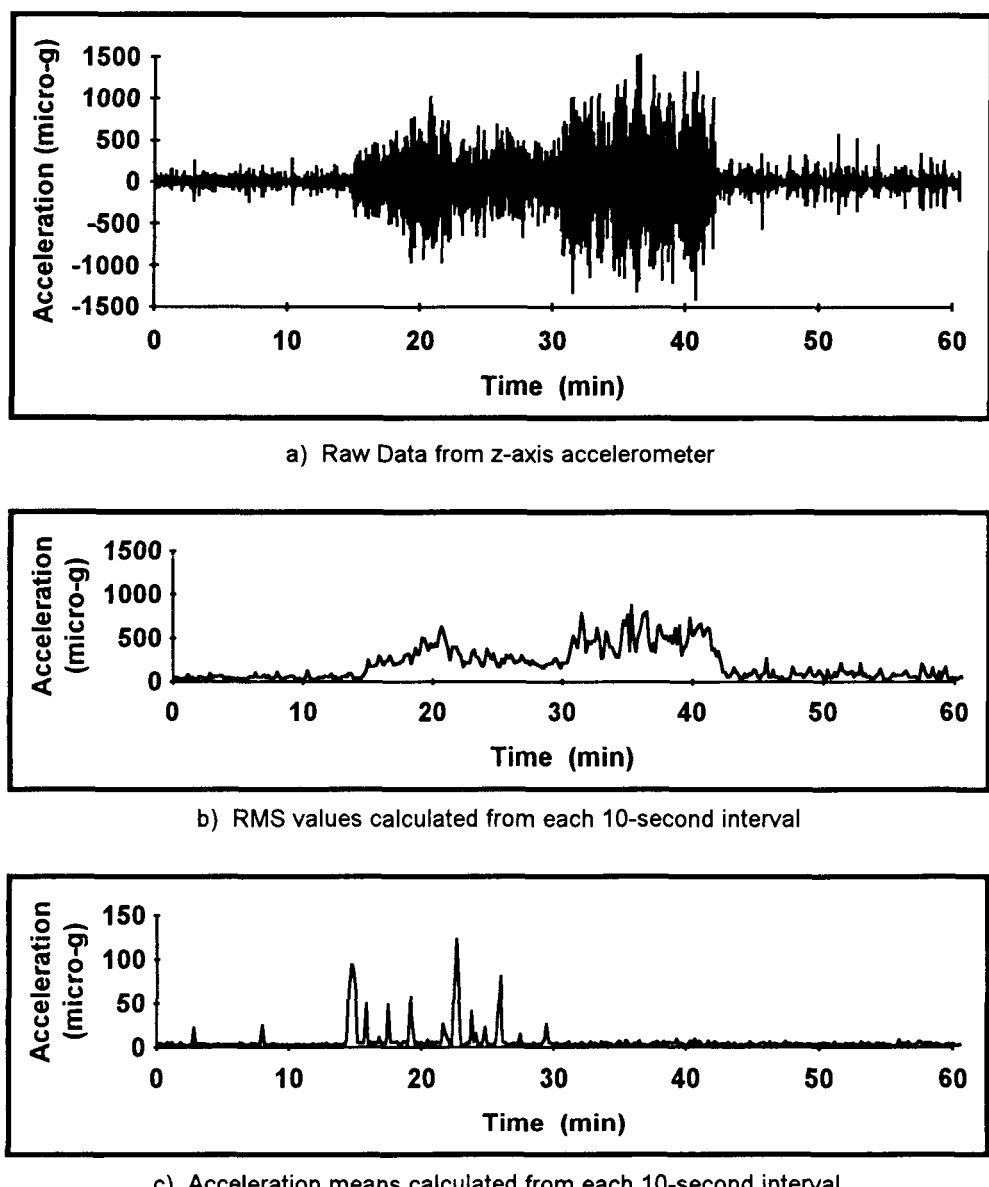


Figure 4 Summary Processing of Raw Acceleration Measurements

The initial analysis of SAMS data was designed to reduce the large volume of data, yet preserve its salient features. The raw data in 4a) contains approximately 90,000 measurements over the one-hour interval. The two sets of processed data contain 360 data points each. This data was selected from a period in which there were two dissimilar events in progress. The predominate was an approximate thirty-minute crew exercise session evident in the center portion of the raw data and the RMS processing. Coincident with the beginning of the exercise, a vehicle attitude maneuver was implemented which involved thruster firings. The residuals from these firings are clearly evident in the acceleration means in 4c). Note the expansion of the scale by a factor of ten in 4c) and the "disappearance" of the large perturbations due to the crew activity since it does not impart net forces on the 10-second averaging basis.

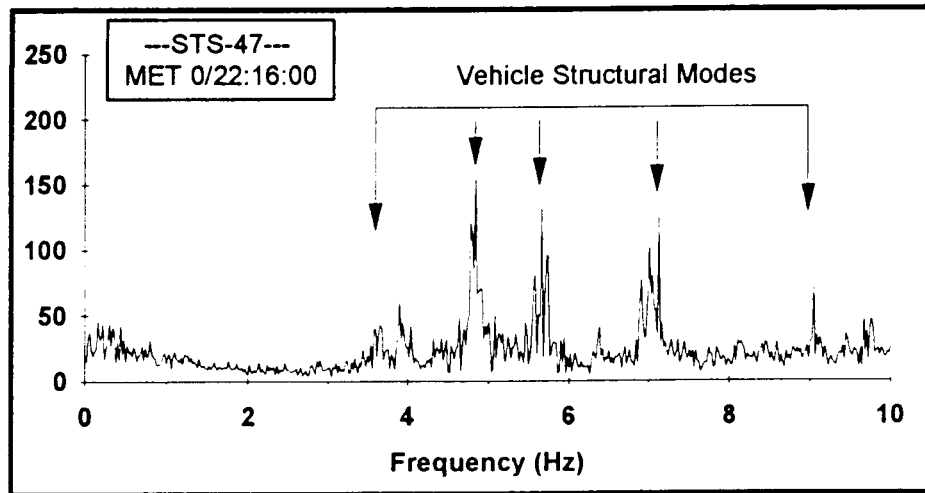


Figure 5 Typical low frequency STS structural modes.

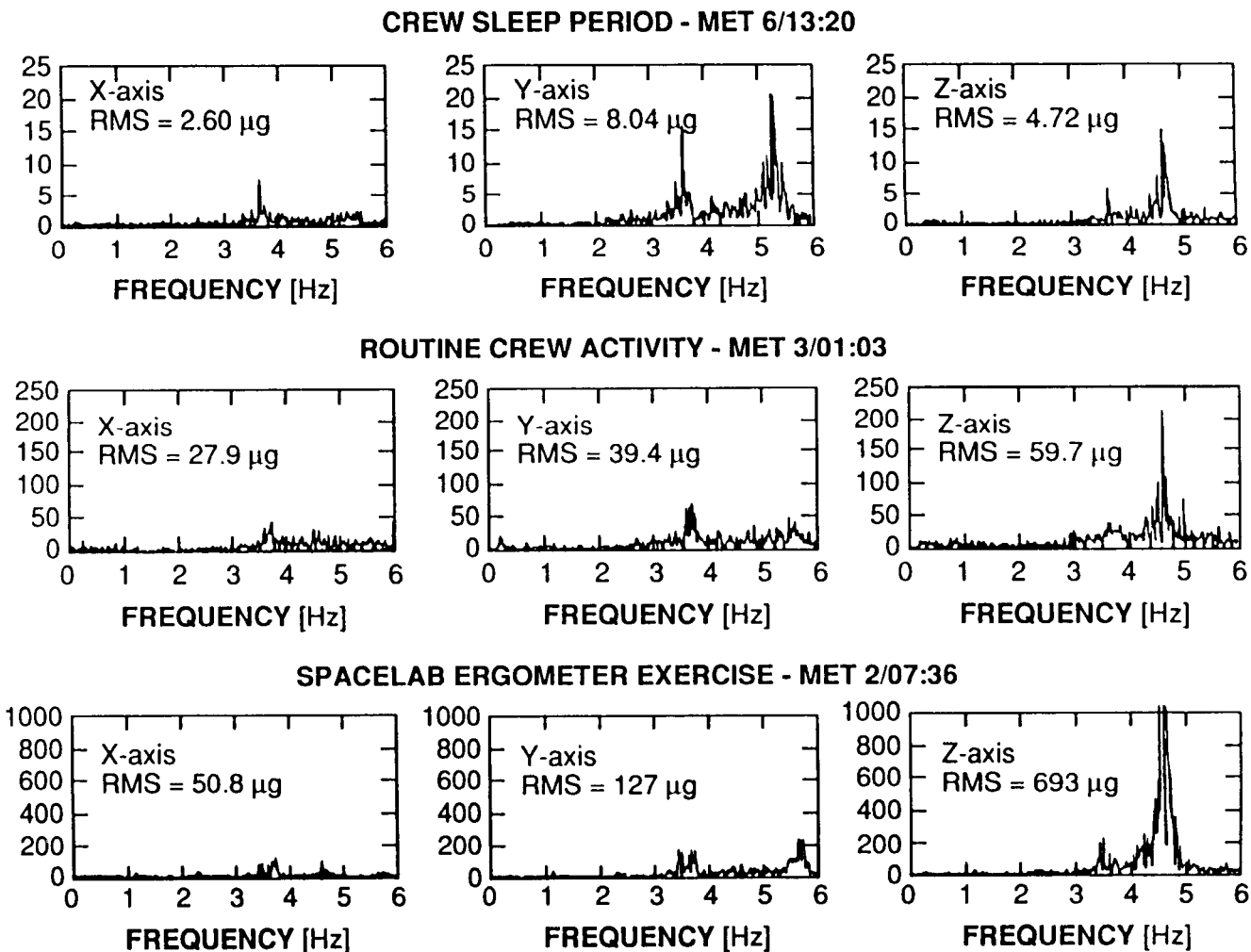


Figure 6 Power Spectral Density of the Acceleration environment on STS-40 - Spacelab module. Units of $\mu\text{g}/\sqrt{\text{Hz}}$.

STS-52
Time Referenced to MET 7/17:31

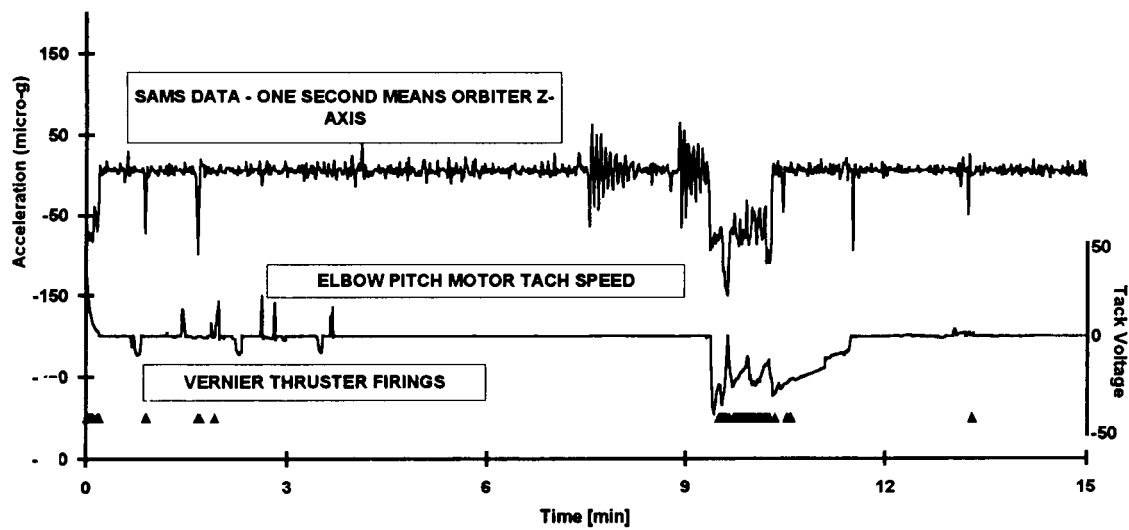
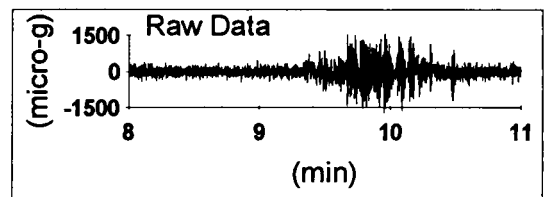


Figure 7 Analysis of Acceleration Disturbances from the Remote Manipulator arm.

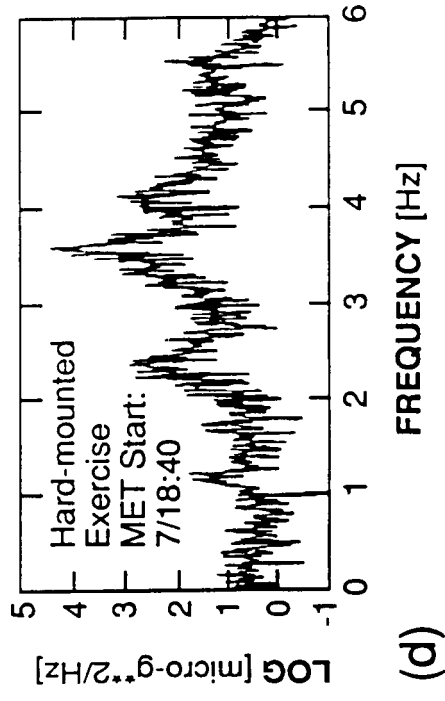
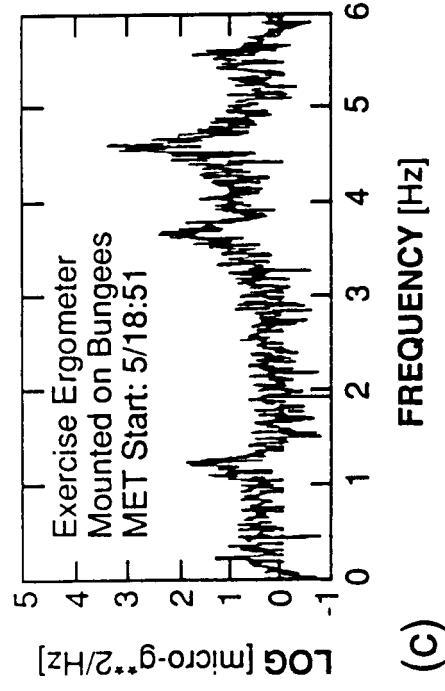
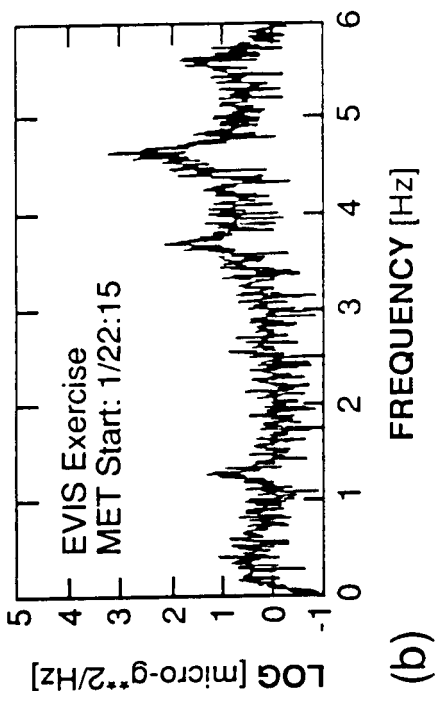
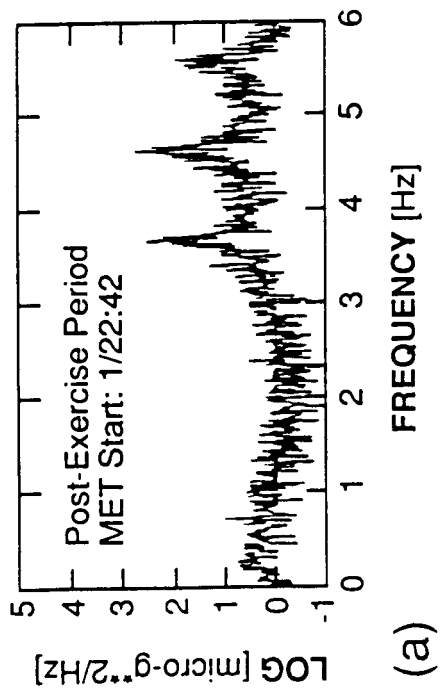


Figure 8 Power spectral density analysis of crew exercise, STS-50.

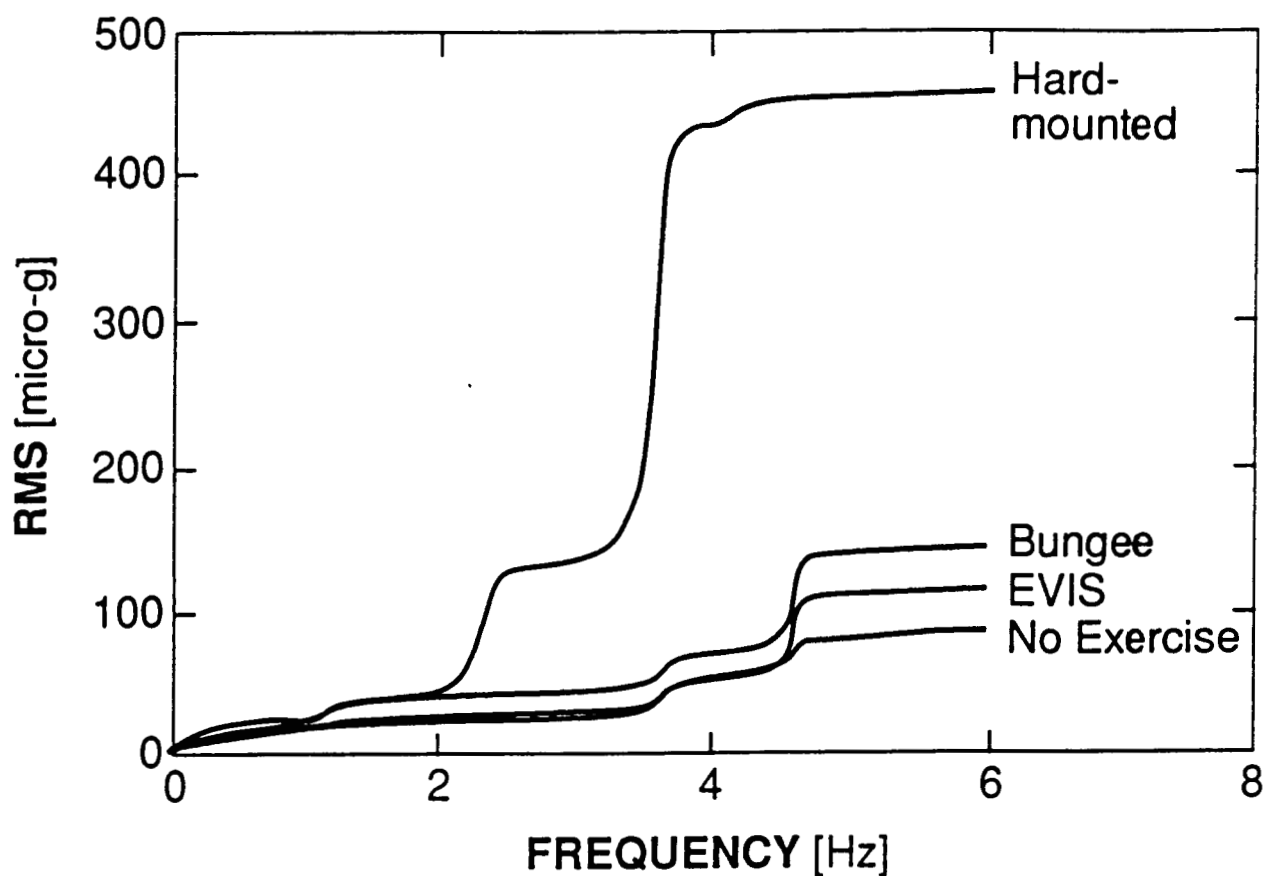


Figure 9 Cumulative RMS analysis of crew exercise, STS-50.

Discussion

Question: *This question is directed towards the previous two speakers. Having seen the data presented here by Charles Baugher, do they feel they are in any position to comment on if their particular experiments would be sensitive to either a) the described crew environment or b) to the disturbances in the upper two frequency bands that were described; 1 to 10 and 10 to 100 Hz ?*

Answer: In fact in the Lambda Point Experiment, we were very sensitive to the heating effects from vibration and were particularly concerned with the 51 Hz second harmonic from the TDRSS antenna because we have structural resonances quite close to that frequency. And as it turned out, because of the problems with the thermometry, we saw very little direct impact of the acceleration environment. On the next flight we expect to have that problem solved so we would be back in the situation where it would be significant again.

With regard to the MEPHISTO Experiment, acceleration effects on the experiment were clearly seen and the investigators are in the process of really vigorously looking at accelerometer data and correlating it with the Seebeck signals. As a matter of fact, Charles Baugher and Jean-Jacques Favier will be doing that for the next couple of months. As Favier showed in his presentation, there was definite correlation between acceleration and the experiment response.

18 pg

1993-10-17
3240617015
P. 17

REVIEW OF EUROPEAN MICROGRAVITY MEASUREMENTS

H. Hamacher

German Aerospace Research Establishment (DLR), Cologne, Germany

ABSTRACT

European efforts to characterize the microgravity (1/19) environment within a space laboratory began in the late seventies with the design of the First Spacelab Mission SL-1. Its Material Science Double Rack was the first payload element to carry its own tri-axial acceleration sensor package. Even though incapable for any frequency analysis, the data provided a wealth of novel information for optimal experiment and hardware design and operation for missions to come. Theoretical investigations under ESA contract demonstrated the significance of the detailed knowledge of μg data for a thorough experiment analysis. They especially revealed the high sensitivity of numerous phenomena to low frequency acceleration. Accordingly, the payloads of the Spacelab missions D-1 and D-2 were furnished with state-of-the-art detection systems to ensure frequency analysis between 0.1 and 100 Hz. The Microgravity Measurement Assembly (MMA) of D-2 was a centralized system comprising fixed installed as well as mobile tri-axial packages allowing real-time data processing and transmission to ground. ESA's free flyer EURECA carried a system for continuous measurement over the entire mission. All EURECA subsystems and experiment facilities had to meet tough requirements defining the upper acceleration limits. In a French / Russian cooperation, CNES developed a microgravity detection system for analyzing the Mir space station μg -environment for the first time. An approach to get access to low frequency acceleration between 0 and 0.02 Hz will be realized by QSAM (Quasi-steady Acceleration Measurement) on IML-2, complementary to the NASA system Spacelab Acceleration Measurement System SAMS. A second flight of QSAM is planned for the Russian free flyer FOTON.

INTRODUCTION

Experimentation under microgravity has been a focal point in Europe's space utilization since the late seventies when NASA and ESA agreed to develop Spacelab and to fly it in a first joint Mission SL-1 in 1983. About two-thirds of the European experiments carried out in SL-1 were investigations in materials science and fluid physics which made use of the greatly reduced level of gravitation. Even more microgravity experiments were performed in the Spacelab missions with European involvement which followed SL-1. The German Spacelab missions D-1 and D-2 (1985 and 1993, respectively) were especially dedicated to microgravity experimentation. ESA designed the unmanned free flier EURECA

(European Retrievable Carrier) which was launched by the Space Shuttle in 1992 to stay in a 500 km orbit for about a year. EURECA-1 carried a nearly 100% microgravity payload. European scientists also participate with microgravity experiments in the IML flights, USML and USMP. They also contribute μ g-experiments to the Russian space station Mir and other flight opportunities like the free flying capsule FOTON.

Almost all European microgravity investigations have been accompanied by efforts to measure the residual acceleration occurring during the experiment's running time. It started with a single measuring device within the Materials Science Double Rack (MSDR) of SL-1. In contrast to that, the payload of D-2, brought into orbit a decade later, was equipped with the centralized Microgravity Measurement Assembly (MMA) which comprises fixed installed as well as mobile sensors packages. It allowed to transmit real time acceleration data to ground during the mission enabling the experimenters to judge whether the experimental conditions have been met or not. This is the concept ESA anticipates to apply on Columbus.

It was recognized very soon that microgravity analysis must be guided by the needs of the physical phenomena to be investigated. Like NASA, ESA supported studies to analyze the susceptibility of the physical phenomena to residual acceleration [1-5]. Chief results were sensitivity curves indicating the level of continuous sinusoidal acceleration which is tolerated by an experiment versus frequency. Examples are shown in Fig. 1. The investigations yielded the following results:

1. Experiments are only sensitive to accelerations within a limited bandwidth. A range between 0 (d.c.) and 100 Hz is regarded to cover the requirements for all Spacelab type experiments.
2. The tolerated acceleration is lowest at low frequencies and increases towards higher frequencies.

These results have been applied for the definition of measurement and characterization requirements which usually consist of the following steps:

i) ***On-board Measurement***

The *low frequency range* is characterized by low level acceleration typically $< 10^{-6}$ g, (Fig. 1). It requires

- (i) sensor sensitivity better than 10^{-7} g
- (ii) in-orbit calibration and sufficient zero point stability between the calibrations.

Since the low frequency range is usually below the spacecraft's fundamental frequency f_f , a single point measurement is sufficient to determine the entire low frequency field from rigid body dynamics. To characterize the *high frequency regime*, ranging from the vicinity of the fundamental frequency to the upper limit, local measurements as close to the experiments as possible are indispensable.

ii) ***Modeling***

Microgravity characterization cannot be accomplished by measurement alone. Some locations within the spacecraft might not be accessible, e.g. a materials sample within a furnace. In such cases the

mechanical transfer function between the location of the perturbing force and the sample has to be known to calculate the acceleration at the location of interest from the on-board measurements.

The microgravity activities in Europe either directed by ESA or by national agencies aim to contribute to these tasks. In the following, some of the activities are described in more detail.

I. MICROGRAVITY MEASUREMENT ACTIVITIES

A. Spacelab

SL-1 Mission (1983): The Material Science Double Rack (MSDR) was one of the first payload elements to be equipped with an accelerometer package for monitoring the microgravity environment [6]. Even though operated in a peak detection mode to reduce the amount of data, the system provided valuable data for scientists as well as for design and system engineers. These early data revealed the order of magnitude of residual acceleration attainable in Spacelab experiment rack. Some results were truly unique. Owing to the fact that the Space Shuttle in its early (verification) flights was equipped with extensive auxiliary measurement devices, it was possible to correlate the data of the MSDR sensor to these measurement results. As an example, a stick-slip event, monitored by a strain gauge at the flange connecting the Transfer Tunnel with the Spacelab module, could be correlated to a sharp spike in the μg -recording within the MSDR as shown in Fig. 2. This occurrence is an example of a stochastic event which cannot be explained in nowadays Spacelab missions. SL-1 also gave the first valuable experience on how to correlate acceleration data to the disturbing sources. It turned out that continuous onboard video recordings are indispensable means for microgravity data interpretation.

D-1 Mission (1985): Each microgravity payload element of that mission carried at least one accelerometer [7,8]. High frequency signal sampling ensured frequency sufficient for all experiments and, in combination with extensive onboard video recordings, data correlation to perturbations for many events. It gave some novel insights into Spacelab's in-orbit dynamics and the spectral composition of its acceleration (Fig. 3). The achievements effectively forwarded our knowledge to improve experiment hardware design and operation. It demonstrated Spacelab's excellent capability as a carrier for microgravity payloads.

D-2 Mission: Despite these accomplishments, D-1 also indicated difficulties in the analysis of data measured by different autonomous systems especially if, for example, exact time correlation is required. Various investigations, such as transfer function measurements for structural dynamics experiments, call for precise time correlation and accuracy of the data. It was for this and some other fundamental reasons that Spacelab D-2 was equipped with a centralized system, the Microgravity Measurement Assembly

(MMA) [9]. It comprises six triaxial sensors, four of which permanently mounted in experiment racks and two mobile sensor packages which allowed investigation of the acceleration across the entire Spacelab module (Fig. 4). The MMA makes use of a new generation of small size micro-mechanical accelerometers developed by CSEM (Centre Suisse d'Electronique et de Microtechnique S.A.), Switzerland, under ESA contract [10]. This development is aimed at a miniaturization of the sensor to allow its installation as closely to the experiment as possible. The key element is an electromechanical silicon chip as shown in Fig. 5. A movable plate, suspended by flexure bars, deflects from its neutral position under the action of acceleration applied perpendicular to the plate. This deflection is transformed to an electrical signal by measuring the change in capacitance between the plate and the electrodes placed on either side of the housing walls. The chip itself has a dimension of 7 mm x 3.6 mm x 1.4 mm. Its resonance frequency is 700 Hz near critical damping. Another novel feature of the MMA was real-time data transfer capability to ground. During the mission, processed μ g data were available for the experimenters in the Payload Operations Control Center in Oberpfaffenhofen, Germany to judge whether the experimental condition had been met. This principle is intended by ESA to be applied on Columbus for interactive experimentation. The MMA also comprised an impulse hammer to measure the structural transfer function under microgravity conditions [11]. The D-2 μ g characterization program also included acceleration measurements on ground on the integrated Spacelab prior the mission during the Mission Sequence Test. The intention was to investigate to what extend the spacecraft in-orbit vibration behavior can be predicted from ground measurements.

The lower detection limit of the MMA was 0.1 Hz which excluded the measurement of low frequency acceleration. For that reason a calculation program has been applied to estimate the main contributions by atmospheric drag, gravity gradient (tidal) and rotational acceleration (Fig. 6) [12]. An instrument (QSAM: Quasi-steady Acceleration Measurement) is under development for the IML-2 mission allowing access to the low frequency range between 0 and 0.02 Hz. Continuos zero-offset elimination is achieved by periodic signal modulation. This is achieved by flipping the sensor sensitive axis every 10 sec [13].

B. EURECA

This automated platform allowed to perform long lasting microgravity experiments in its first mission EURECA-1 (Fig. 7). To minimize the orbit decay during the eleven month flight the carrier was flown in a 500 km orbit which ensured a level of drag acceleration in or below the $10^{-6}g$ range. An upper limit of residual acceleration was defined between 0 and 1000 Hz as shown in Fig. 8. Various design features had been determined to minimize EURECA's residual acceleration level in the low frequency as well as in the high frequency range. For the first time in microgravity experimentation, all subsystems

and experiment facilities had to meet stringent requirements which defined maximum acceleration limits at their interfaces. This had to be verified by analysis and test. The platform itself was equipped with a Microgravity Measurement System (MMS) which allowed continuous measurement over the entire mission duration with a bandwidth between 0 and 5 Hz [14]. Figure 9 shows a plot of the acceleration which occurred during a thruster firing. Preliminary data are given in [15].

C. Russian Missions

European scientists also participate with microgravity experiments on Russian flight opportunities like the space station Mir and the free flying capsule FOTON. In a French / Russian cooperation, CNES developed and provided the technology experiment "Microaccelerometre" which was especially dedicated to characterize the residual acceleration. It was the first systematic effort to analyze the Mir μ -g - environment. Measurements were taken at some 80 locations across the station during characteristic operation phases like working and sleeping periods, orbit maintenance and docking maneuvers. The bandwidth was between 0.1 and 400 Hz [16].

The German Space Agency DARA anticipates to fly a QSAM-type measurement system on the free flying capsule FOTON in 1995. This carrier is expected to provide a very low μ -g-level. All experiment facilities provided by DARA for the EuroMir Mission 1995 will also be equipped with accelerometer packages.

II. STUDIES

Quite a number of studies have been performed or are under way dealing with modeling, prediction and measures to prevent or to reduce residual acceleration. A great number of the studies supported by ESA are related to the Columbus microgravity environment. As an example, an active suspension system (Microgravity Isolation Mount, MGIM) has been designed under ESA contract to isolate sensitive experiment facilities from the vibrating spacecraft structure. Other studies deal with systematic identification of the perturbation sources and their reduction, and the computational modeling to predict the broad band vibration response spectra [11, 17].

III. OUTLOOK

The European activities in the field of microgravity measurement were always characterized by close cooperation with international partners. Microgravity data of Spacelab Missions are extensively exchanged between NASA and ESA. The upcoming Spacelab Mission IML-2 (Second International Microgravity Laboratory) is an excellent demonstration of the intensive international cooperation in this field. Scientists from the United States, Japan and Europe participate in that mission to measure the

residual acceleration and to test novel sensor systems and means to isolate vibrations. NASA's Space Acceleration Measurement System SAMS and the European QSAM are complementary instruments for characterizing the residual acceleration of the entire Spacelab. A great deal of these fruitful collaborations has been initiated by the Microgravity Measurement Group (MGMG) an international advisory group established and organized by NASA. It is our pleasure to acknowledge the outstanding contribution of Gary Martin of NASA Headquarters and Charles R. Baugher of NASA Marshall Space Flight Center.

REFERENCES

- [1] *Langbein, D., Tiby, C.*, "Allowable g - levels for microgravity payloads", Final Report for ESA, Contract No. 5.504/83/F/FS(SC), Batelle Frankfurt, 1984, pp 1 -24.
- [2] *Alexander, J. I. D.*, "Low gravity experiment sensitivity to residual acceleration: a review", Microgravity Science and Technology, 3, 1990, pp 52 - 68
- [3] *Naumann, R.J.*, "Susceptibility of materials processing experiments to low-level accelerations, NASA CP 2199, 1981, pp 63 - 68
- [4] *Monti, R., Langbein, D., Favier, J., J.*, "Influence of residual accelerations on fluid physics and materials science experiments", in: "Fluid Sciences and Materials Science in Space", H. U. Walter (ed.), Springer-Verlag, Berlin, 1987
- [5] *Feuerbacher, B., Hamacher, H., Jilg, R.*, "Compatibility of microgravity experiments with spacecraft disturbances", ZfW 12, 1988, pp 145 - 15
- [6] *Hamacher, H., Merbold, U.*, "The microgravity environment of the Material Science Double Rack During Spacelab-1", J. Spacecraft & Rockets, 24, 1987, pp 264 - 269
- [7] *Hamacher, H., Jilg, R., Merbold, U.*, "Analysis of microgravity measurements performed during D1 ", ESA SP-256, 1987, pp 413-420
- [8] *Hamacher, H., Fitton, B., Kingdon, J.*, "The environment of Earth-orbiting systems" in: "Fluid Sciences and Materials Science in Space", H. U. Walter (ed.), Springer-Verlag, Berlin, 1987, pp 1 - 50
- [9] *Eilers, D., Gerhard, I., Hofer, B., Rudolf, F., Brungs, W.*, "Microgravity Measurement Assembly (MMA) for Spacelab Module missions", IAF-88-343, 1988, 8 p
- [10] *Rudolf, F., Jornod, A., Bergqvist, J., Leuthold, H.*, "Precision accelerometers with 1!9 resolution", Sensors and Actuators, A21 -A23, 1990, pp 297-302
- [11] *Stark, H. R., Stavrinidis, C.*, "ESA microgravity and microdynamics activities - an overview", 1st Space microdynamics and accurate control symposium, Nice, France, Nov. 1992
- [12] *Hamacher, H.*, "Spacecraft low frequency residual acceleration", IAF-92-0970, 1992, 10 p

[13] *Hamacher, H., Jilg, R., Feuerbacher, B.*, "QSAM - A measurement system to detect quasi - steady accelerations aboard a spacecraft", IAF-90-377, 1990, 7 p

[14] *Heffs, W., Andresen, R.D., Eilers, D.*, "The measured and predicted micro-g EURECA environment", IAF-88-341, 1988, 18 p

[15] *Eilers, D., Stark, H. R.*, "EURECA microgravity environment - preliminary flight data", Microgravity Measurement Group Meeting, Huntsville, Alabama, ESP. 1993 (this publication).

[16] *Granier, J., Dancet, Y., Faucher, P., Riaboukha, S.*, "Microaccelerometre' experiment Mir microacceleration characterization", 1st Space microdynamics and accurate control symposium, Nice, France, Nov. 1992, 10 p

[17] *Jones, D. I., Owens, A., R., Owen, R., G.*, "A microgravity isolation mount", IAF-86270, 1986, 8 P

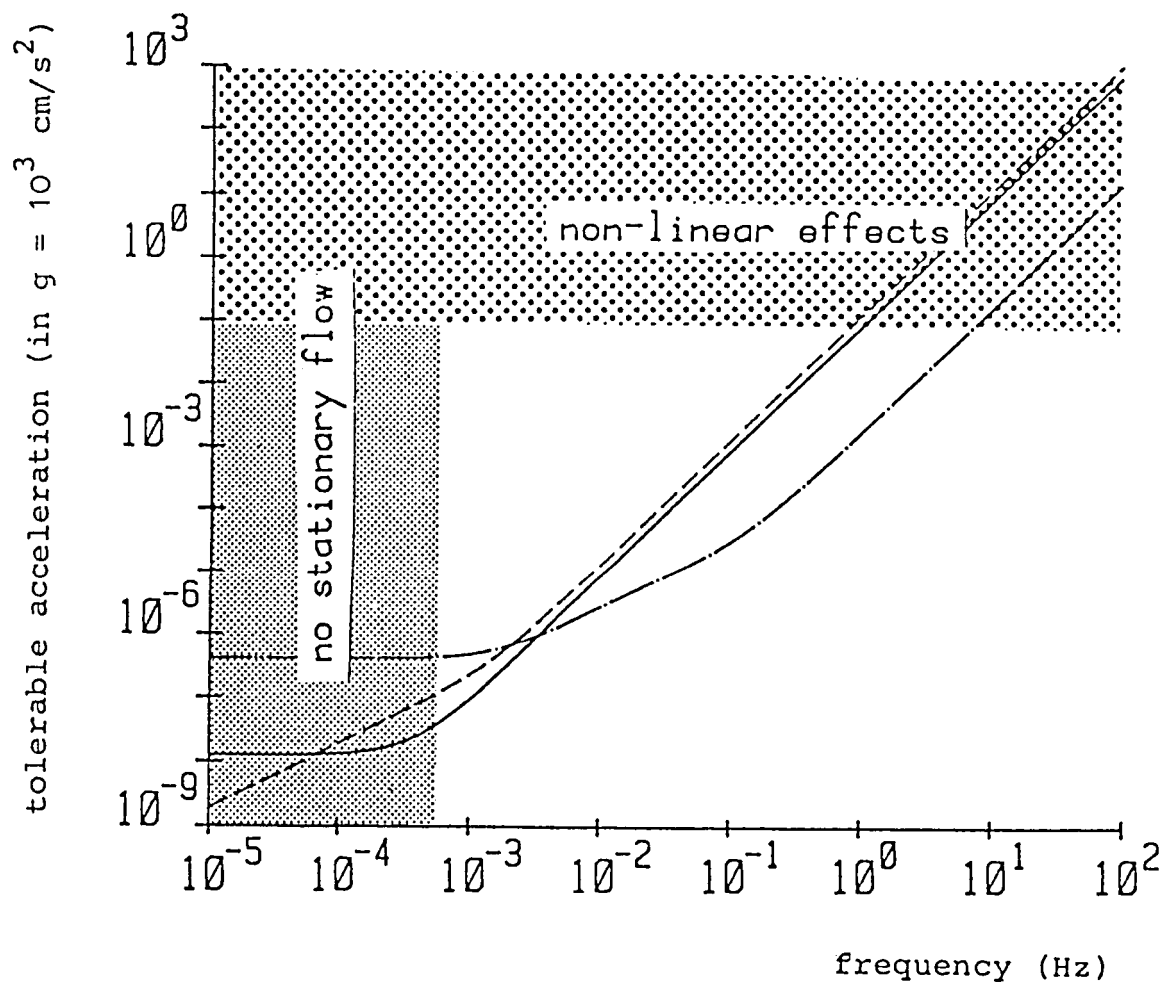


Figure 1 The tolerable residual acceleration in

- a fluid physics experiment involving a temperature gradient,
- - - a crystal growth experiment by the THM method,
- · - · - an experiment on thermodiffusion; [1]

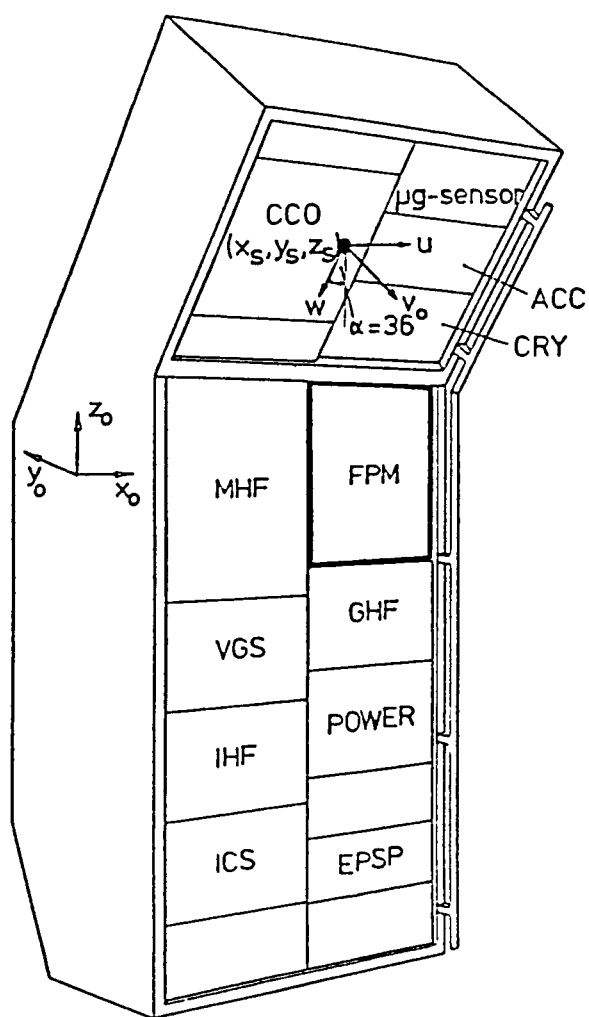


Figure 2 Material Science Double Rack (MSDR) and coordinate system of the μ -sensor of SL1.

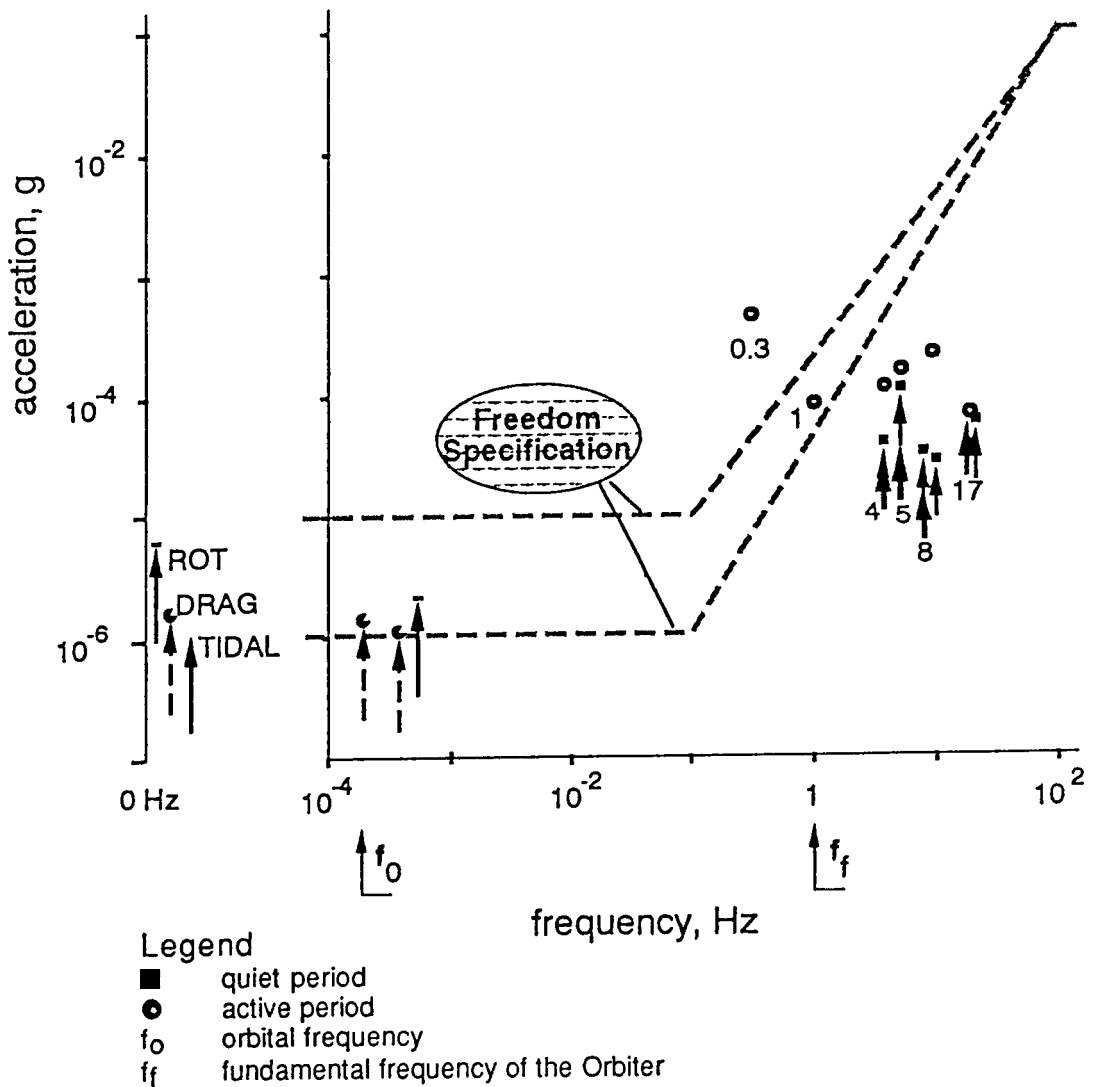


Figure 3 Spectral composition of the Spacelab's acceleration (D-1 mission) compared to the space station.

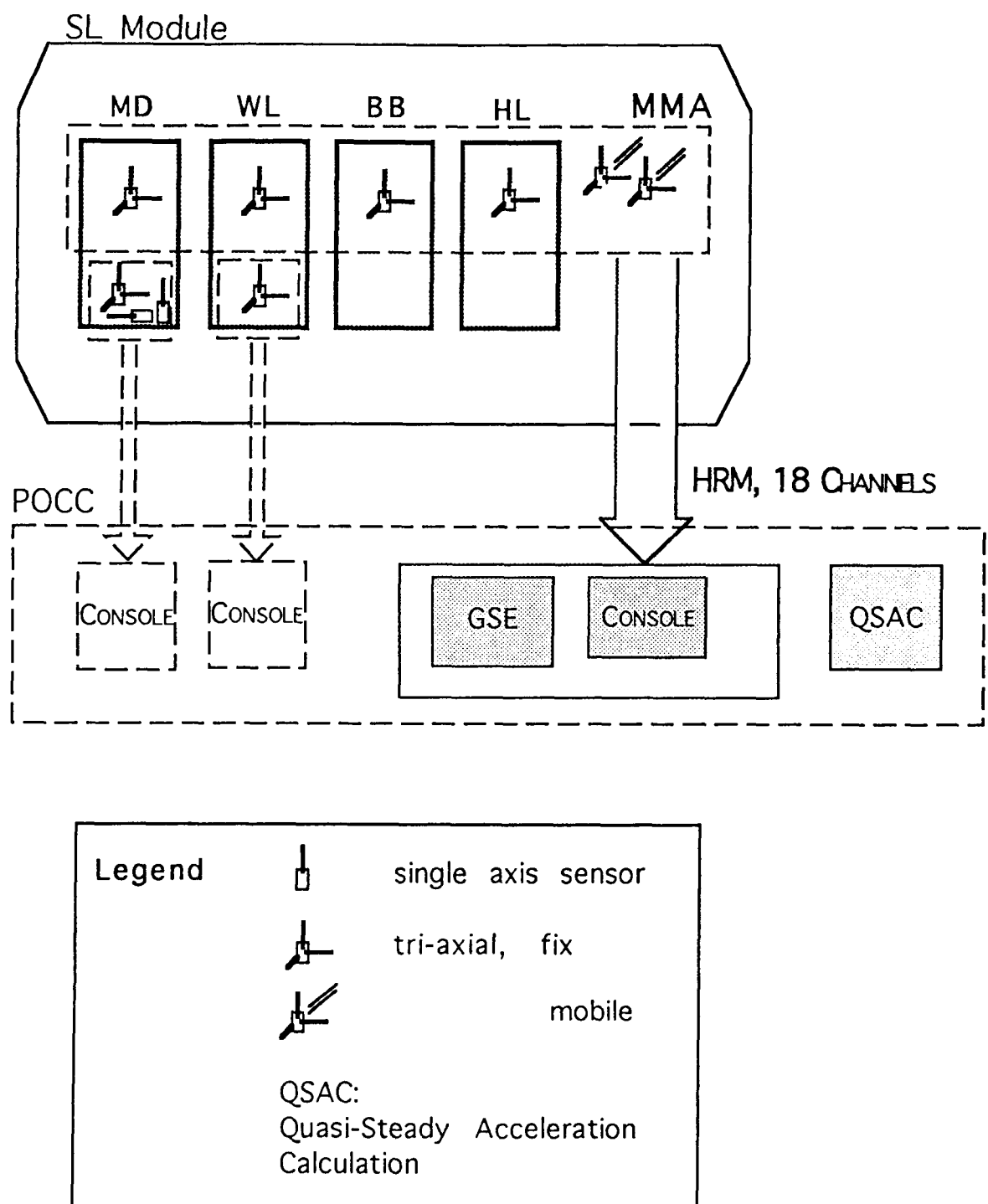


Figure 4 MMA sensor location and data transmission.

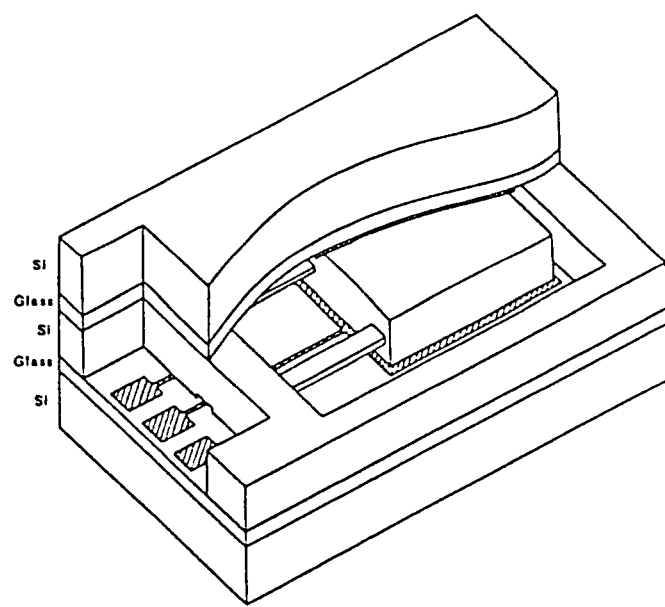


Figure 5 The CSEM accelerometer applied to the MMA. The top plates have been partially cut away to show the spring-mass system and the fixed electrodes.

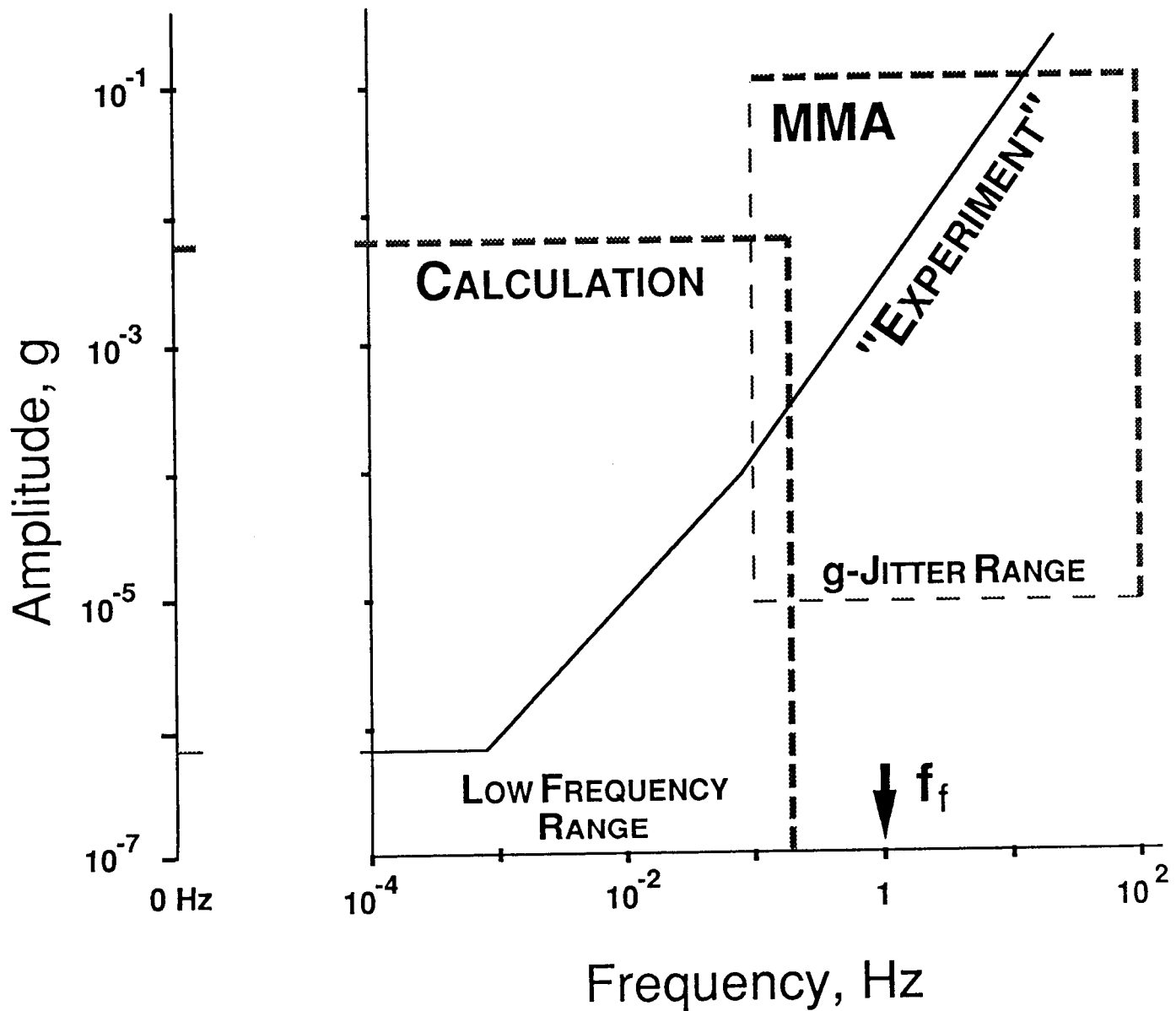


Figure 6 Detection Range of the MMA and low frequency range to be calculated.

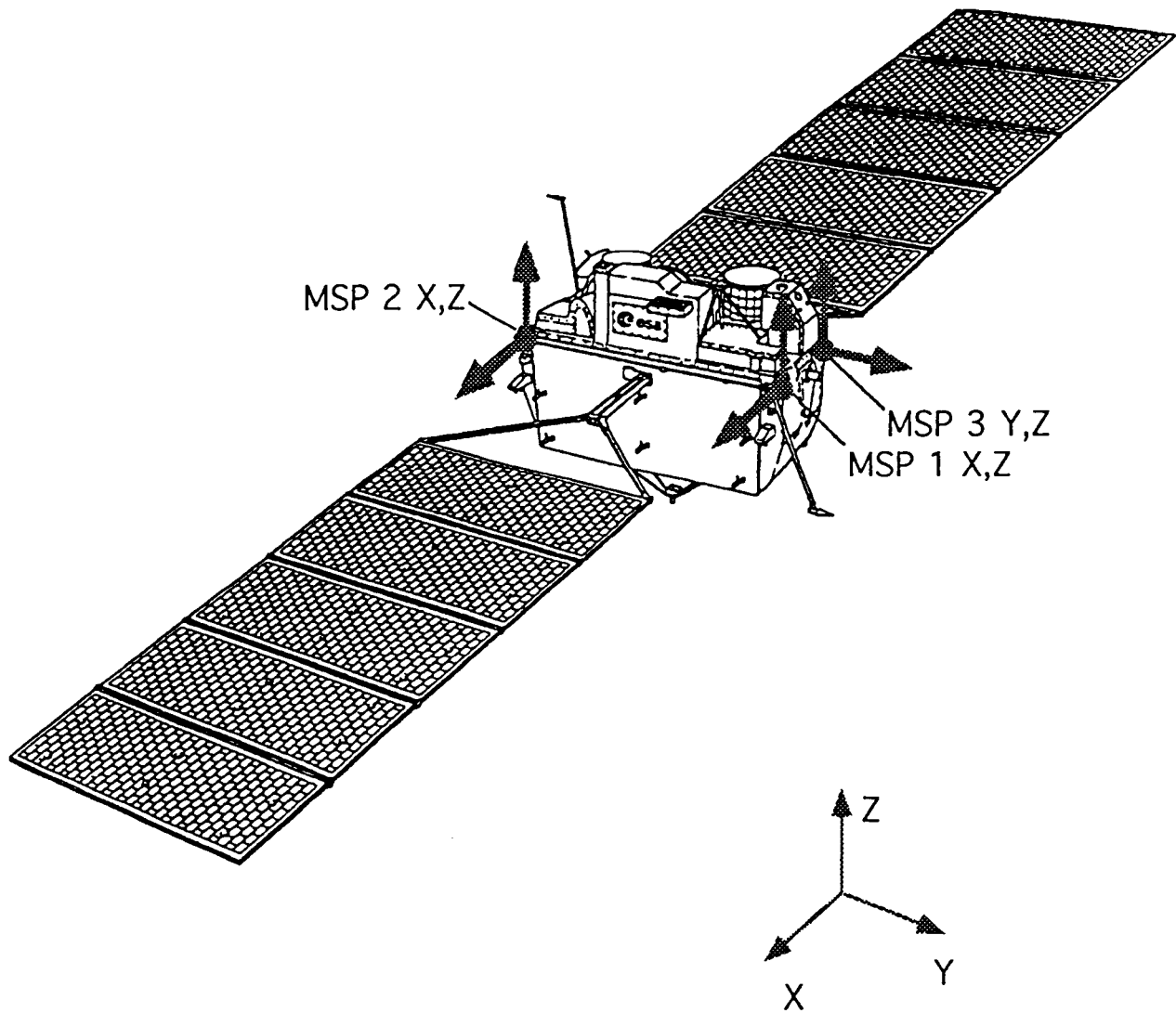


Figure 7 EURECA configuration and MMS sensor location and orientation of sensitive axes.

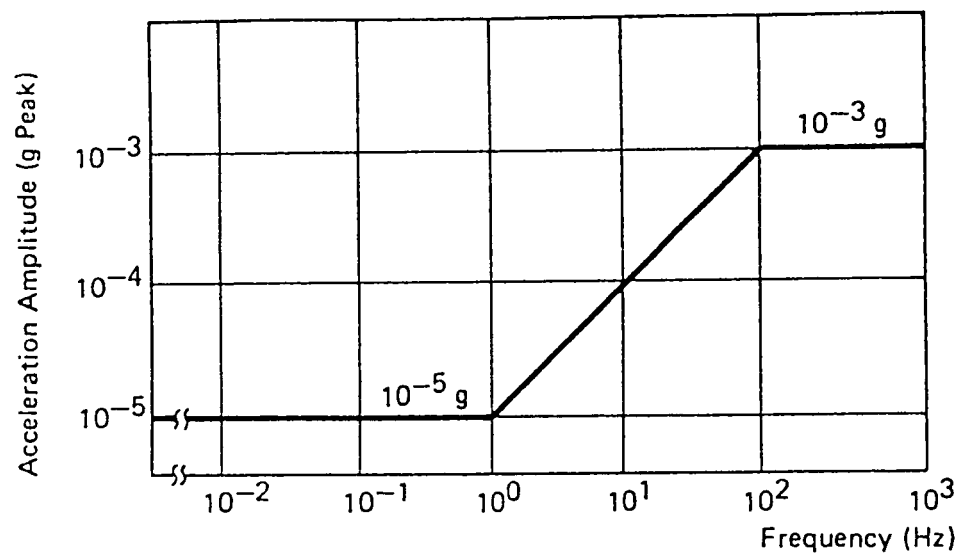


Figure 8 EURECA microgravity environment design specification [14].

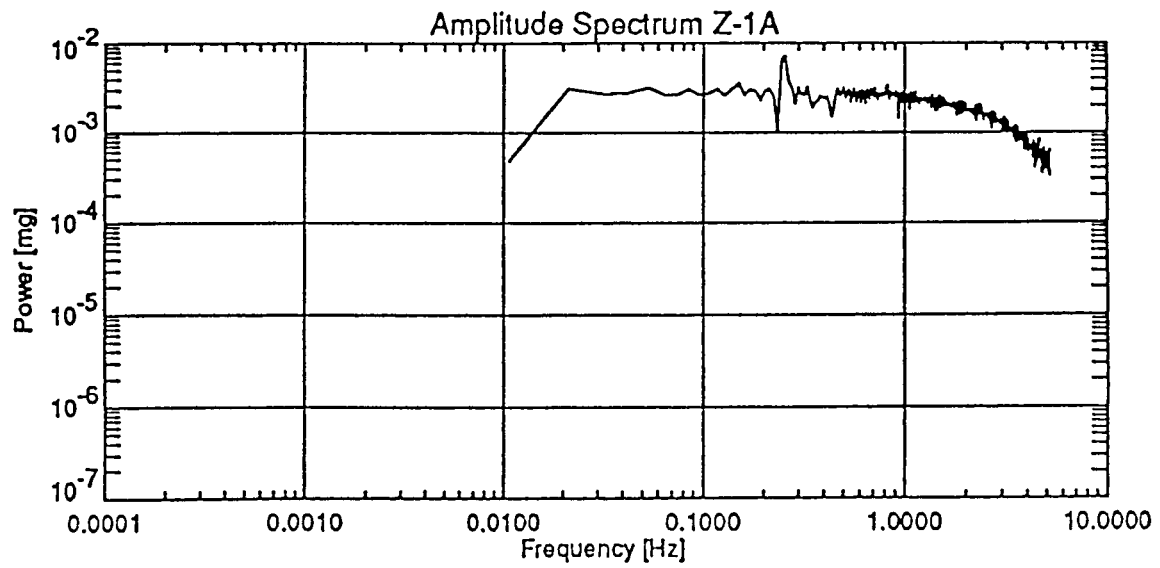
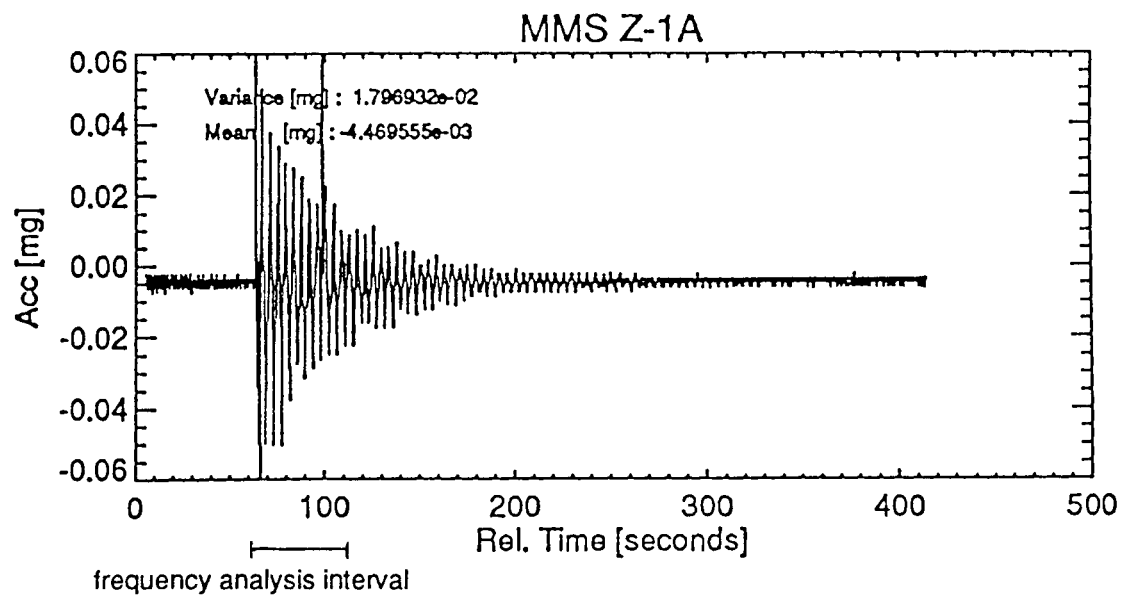


Figure 9 EURECA acceleration during a hydrazine thruster firing.

Discussion

Comment: (Dr. Bonnie Dunbar) *When we take the measurements during a flight on crew activity it is probably going to be helpful to interview the crew afterwards about their approach to it and I can give you some insights to it on D-1 versus USML-1. First of all, going back to D-1 and to Spacelab-1. Spacelab-1 was a 10 day flight. D-1 was a 7 day flight. D-1 also had a mix of disciplines. We did have the vestibular sled on that flight and we had the SPARS palette in the back which required Earth pointing. So the mission attitude was split about half and half, between the gravity gradient attitude and the other half bay to the Earth attitude and that rotation occurred at least once a day. And although the crew were sensitive to the microgravity experiments needs (environment wise) there wasn't an understanding of the relationship (of the experiment response) to the (acceleration) magnitude, so as I recall being on the mission, we operated in a laboratory environment but we weren't aware that closing locker doors for instance put in spikes into the structure that actually ran through. On USML-1 mission, we were much more aware of that environment particularly because of the results of D-1 and we were particularly sensitive to things like that; for example in areas where we had drawers that were sticking we simply did not close those lockers during particular experiments. So the results that you see may indicate different values for what is called crew activity because of that sensitization.*

Question : *The question I have deals with EURECA which was a solar inertial platform and as such had a rotational residual g vector even though it might be very small. My question is, what kind of effect did that have on your directional solidification experiment or do you have that correlation yet ?*

Answer: Yes. We have to calculate the effect of the rotating vector, but all the details have still to be worked out. The rotation of the residual vector introduces a low frequency acceleration that is very important to experiments sensitive to that range and most experiments are sensitive to low frequency accelerations.

46

Pg

1995-14212-48

324069

N95-14212

25-29

THE SOLID SURFACE COMBUSTION EXPERIMENT
ABOARD THE USML-1 MISSION

P 19

Robert A. Altenkirch*, Kurt Sacksteder**, Subrata Bhattacharjee***,
Prashant A. Ramachandra*, Lin Tang*, and M. Katherine Wolverton*

* Department of Mechanical Engineering and the National Science Foundation Engineering Research Center for Computational Field Simulation
Mississippi State University
Mississippi State, MS 39762

** NASA Lewis Research Center
Cleveland, OH 44135

*** Department of Mechanical Engineering
San Diego State University
San Diego, CA 92182

ABSTRACT

An experiment was conducted aboard STS-50/USML-1 in the solid Surface Combustion Experiment (SSCE) hardware for flame spread over a thin cellulosic fuel in a quiescent oxidizer of 35% oxygen / 65% nitrogen at 1.0 atm. pressure in microgravity. The USML-1 test was the fourth of five planned experiments for thin fuels, one performed during each of five Space Shuttle Orbiter flights. Data that were gathered include gas- and solid-phase temperatures and motion picture flame images. Observations of the flame are described and compared to theoretical predictions from steady and unsteady models that include flame radiation from CO₂ and H₂O.

Experimental results from the five experiments indicate that flame spread rate increases with increasing ambient oxygen content and pressure. The brightness of the flame and the visible soot radiation also increase with increasing spread rate. Steady-state numerical predictions of temperature and spread rate and flame structure trends compare well with experimental results near the flame leading edge while gradual flame evolution is captured through the unsteady model.

INTRODUCTION

Flame spread over solid fuels is a phenomenon of fundamental, scientific interest as well as one that has practical implications. The behavior of spreading flames is dependent on the environment and the flow field in which the phenomenon occurs, and so it is important to understand these effects in order

to develop effective fire suppression strategies. A unique environment in which flame spreading has importance to fire safety issues is that of spacecraft in which the gravitational acceleration is low compared to that of the Earth, here referred to as microgravity.

In normal gravity, induced flows due to buoyancy are present, and so it is difficult to control the flow field in which a spreading flame is embedded. Additionally, extrapolation of experimental and modeling results obtained from an environment in which buoyancy is present to one in which it is not is difficult if not impossible because the physics dominant in the two environments are not quite the same. Buoyancy induced flows are generally strong enough to suppress radiative effects, which prove to be important in the low-flow environments that is obtained in microgravity. As a result, a program of conducting flame spreading experiments in a quiescent, microgravity environment was established so that the physics of the flame spread process in that environment could be delineated without having to contend with the complicating effects of buoyancy.

The experiments were designed to be conducted aboard Space Shuttle Orbiter flights. Keeping in mind crew safety and development costs, the experimental hardware was designed for a single experiment per flight. Here we summarize results from the USML-1 experiment and provide some comparison with both steady and unsteady flame spread models and earlier experiments. Detailed results from and analyses of earlier flights can be found in several of the references listed here.

I. HARDWARE DESCRIPTION

The experiment described here was conducted aboard STS-50/USML-1 on 2 July 1992 using the Solid Surface Combustion Experiment (SSCE) payload specifically designed for these tests [1]. The SSCE chamber has a contained gas volume of 0.039 m^3 , two orthogonal windows, and a centrally located sample holder. The sample holder supports the fuel, three thermocouples, and a pressure transducer and was designed to withstand the stresses of a Shuttle launch.

A camera module includes two 16 mm motion picture cameras, using Kodak 7296 color negative film, ASA rated 500, an electronics box, and a battery box. The cameras are positioned so spreading flames cross the fields of view, one axis normal to the sample surface (top view), the other parallel (side view). The cameras provided a timing light strobe on the margin of the film to measure the framing rate, and a 1 Hz strobe light was used to illuminate the fuel surface to observe the propagation of the surface pyrolysis front. The experiment was filmed using a lens aperture of f/1.4.

The test sample, 11.0 cm long by 3.0 cm wide, was made from Whatman #1 filter paper, 0.0825 mm half-thickness with an area density, based on the half-thickness, of $4.282 \times 10^{-2}\text{ Kg/m}^2$. The sample was clamped between two thin metal sheets with both sides of the fuel exposed to the atmosphere. A nichrome ignitor wire with a webbed pattern, 1.0 cm long, was clipped over one end of the sample. A

solution of nitrocellulose in acetone was applied to the sample over the ignitor wire and allowed to dry. Three Type R thermocouples of 0.13 mm wire diameter were installed: 7.0 mm above the center of the sample, embedded in the center of the sample, and 2.3 mm below the sample 2.54 cm farther from the ignitor than the first two.

The experiment sequence is automated beginning with a five-second camera acceleration to 24 frames per second. The ignitor is then energized with 2 amps of current for five seconds. The thermocouple and pressure signals are recorded digitally at 20 Hz, and camera operation and data acquisition continue for 68 s after the ignitor is energized.

The film was forced-processed two f-stops. A color frame grabber was used to digitize the flame images, frame by frame. The images were spatially filtered to smooth the film grain, and an edge detection scheme based on the brightness of the blue component of the image was used to measure the flame position and calculate the flame spread rate. The experiment was conducted at 35% oxygen/65% nitrogen and 1.0 atm pressure, the lowest oxygen percentage. Earlier flight tests were conducted at 50% oxygen and 1-2 atm.

II. CONDUCT OF THE EXPERIMENT

The USML-1 flight of the SSCE hardware was its fourth. Payload Commander Bonnie Dunbar began the experiment on schedule, with assistance from Pilot Ken Bowersox. In earlier flights, STS-41 and STS-43, the crew used the Orbiter CCTV for a real-time down link of the flame image. Time was provided during the USML-1 mission to use the CCTV for real-time coverage of the top view of the fuel sample. The photographic shroud used to ensure a darkened chamber for the cine film worked well enough to saturate the CCTV automatic gain control. In consultation with the SSCE team in the POCC, Payload Commander Dunbar used a penlight to reflect enough light off the chamber exterior and into the CCTV to bring the detector out of saturation and provide a good video exposure. Ignition and flame spread was initiated, proceeded nominally, and the SSCE team was able to observe the pyrolysis front propagation in real time.

The flight film was recovered early from the Spacelab and taken by the SSCE team to the Johnson Space Center (JSC). The cine films were processed by the Imaging Sciences Division (ISD) at the JSC, using a procedure customized for this project. The JSC-ISD also provided a video transfer from the original film.

III. MODELING

Because details of the steady model have been described before [2,3], and the extension of the steady model to include unsteady effects is conceptually straightforward, although not without practical

difficulty [4], the discussion here is abbreviated. The model consists of the unsteady, two-dimensional continuity, momentum, species (fuel, oxygen, nitrogen), and energy equations in the gas, written in the common form

$$\frac{\partial(\rho\phi)}{\partial t} + \frac{\partial(\rho u\phi)}{\partial x} + \frac{\partial(\rho v\phi)}{\partial y} = \frac{\partial}{\partial x}\left[\Gamma_\phi \frac{\partial\phi}{\partial x}\right] + \frac{\partial}{\partial y}\left[\Gamma_\phi \frac{\partial\phi}{\partial y}\right] + S_\phi \quad (1)$$

where ϕ , Γ_ϕ and S_ϕ for the different equations are listed below,

	ϕ	Γ_ϕ	S_ϕ
<i>continuity</i>	1	0	0
<i>x-momentum</i>	u	μ	$-\partial P/\partial x$
<i>y-momentum</i>	v	μ	$-\partial P/\partial y$
<i>fuel</i>	m_f	μ/Pr	$-B_g P^2 m_f m_{ox} e^{-E_g/(RT)}$
<i>oxygen</i>	m_{ox}	μ/Pr	$s S_f$
<i>nitrogen</i>	m_{N_2}	μ/Pr	0
<i>energy</i>	T	μ/Pr	$[-\Delta H_c S_f + \dot{q}_{ign}''' - 4a_p \sigma (T^4 - T_\infty^4)]/C_p$

and the continuity and energy equations in the solid.

$$\dot{m}'' = \frac{d(\rho_s \tau)}{dt} = -A_s \rho_s \tau e^{-E_s/RT_s} \quad (2)$$

$$\frac{\partial(\rho_s C_s T \tau)}{\partial t} = -\dot{m}'' L_v + \lambda_g \frac{\partial T}{\partial y} l_g + \dot{q}_{ign}''' \tau \quad (3)$$

The term \dot{q}_{ign}''' in the gas- and solid-phase energy equations is the transient ignition term, and other symbols in Eqns. (1)-(3) are usual ones [2-4].

Viscosity and thermal conductivity at 700 K are $0.0515 \text{ W m}^{-1} \text{ K}^{-1}$ and $2.46 \times 10^{-5} \text{ kg m}^{-1} \text{ s}^{-1}$, respectively, for 50% oxygen, and $0.0508 \text{ W m}^{-1} \text{ K}^{-1}$ and $2.63 \times 10^{-5} \text{ kg m}^{-1} \text{ s}^{-1}$, respectively, for 35% oxygen and are varied with the square root of temperature for a fixed Prandtl number of 0.7 and unit Lewis number. Chemical reaction is a one-step, second-order Arrhenius process with a pre-exponential factor of $1.58 \times 10^{11} \text{ m}^3 \text{ kg}^{-1} \text{ s}^{-1}$ [2], activation energy of $1.167 \times 10^5 \text{ kJ kmol}^{-1}$ [2], and heat of combustion of $1.674 \times 10^4 \text{ kJ kg}^{-1}$ [5]. The specific heat of the gas is $1.465 \text{ kJ kg}^{-1} \text{ K}^{-1}$ [6] for 50%

oxygen and $1.352 \text{ kJ kg}^{-1} \text{ K}^{-1}$ for 35% oxygen. The source term in the gas-phase energy equation contains the chemical heat-release term, the transient ignition-energy input term, and a radiation loss term. The gas-phase radiation is modeled using a Planck absorption coefficient obtained from a detailed radiation calculation in the steady-state model that accounts for radiation from CO_2 and H_2O [3].

First-order Arrhenius kinetics, with pre-exponential factor of $7.8 \times 10^{16} \text{ s}^{-1}$ [2], and activation energy of $2.494 \times 10^5 \text{ kJ kmol}^{-1}$ [2], describe the fuel pyrolysis. The specific heat of the solid fuel and heat of vaporization are $1.256 \text{ kJ kg}^{-1} \text{ K}^{-1}$ [5] and $368.45 \text{ kJ kg}^{-1}$ [5], respectively. Surface reradiation and gas-to-surface radiative feedback are taken to balance for purposes here [7]. Unsteady fuel heating and the energy required for pyrolysis then are provided by conduction from the gas and from the transient ignition source.

The solid- and gas-phase equations are solved simultaneously and numerically, using the SIMPLER algorithm [8], for a 10 cm long sample in a domain 15 cm long by 10 cm above one side of the fuel. The domain is extended 2.3 cm behind the ignition end of the fuel sample, which allows oxygen to diffuse into this region to give rise to a trailing-edge flame. The other end of the fuel sample is extended by 2.7 cm and is inert with the properties of the metal holder in the experiment. The numerical domain is represented by a 92x40 uniform grid and a time step of 0.0165 s, except during the ignition transient when the time step is halved.

Computationally the flame spreads left to right across the domain atop the fuel surface. Boundary conditions on the left, right, and top of the domain are ambient pressure and zero gradients for all field variables. The fuel is within the computational domain such that the boundary condition at the bottom is that the fuel is insulated at its half-thickness; behind the fuel burnout is a slip plane. At the fuel gas interface, there is a no slip condition and diffusion-convection balances normal to the fuel for energy and species.

The 1 cm-long ignition source, $2 \times 10^8 \text{ W/m}^2$, is at the left end of the fuel sample and is turned on at the beginning of the simulation. The source is turned off once the flame develops, which is approximately at 1.2 s into the computation. The mean Planck absorption coefficient is increased linearly with time from zero until steady spread of the leading edge is achieved.

IV. RESULTS

A. Description of the Flame

Filmed images of the SSCE flames were recorded during each flight. The apparent brightness of the flames varies from nearly undetectable in this 35% oxygen case to near saturation, indicating enhanced soot production both with increasing atmospheric oxygen content and pressure, particularly at 50% oxygen. For 35% oxygen a flame image from the top is not detectable on film, but the 1 Hz strobe

light in the chamber allows the progress of the apparent pyrolysis front across the sample to be seen.

For the USML-1 experiment at 35% oxygen, the shape of the visible flame is symmetrical about the midpoint of its length, and, after the ignition transient, becomes steady with a maximum visible height of 0.5 cm and a length of 1.4 cm. A black-and-white print from one frame of the film is shown in Fig. 1.

Unlike the flames at 50% oxygen, which behind the leading edge curve away from the surface to a maximum distance (height) from the surface and then curve back toward the surface near the trailing edge, the 35% oxygen flame is nearly flat, curving very slightly toward the fuel surface near the leading and trailing edges as seen in Fig. 1. Additionally, the leading edge and trailing edge are equally bright, although the presence of the thermocouple in the frame of Fig. 1 obscures this fact somewhat.

In the top view, there is evidence that the fuel was not entirely consumed as the flame passed, as it would have been at 35% oxygen in normal gravity. This observation suggests that pyrolysis products may be available far behind the flame leading edge.

B. Spread Rate and Temperature Measurement

In the recorded flame images, the leading edge of the flame reaches a steady spread rate almost immediately following ignition, while the trailing edge, in general, develops more slowly. The nominal leading-edge spread rate determined from the film for the 35% oxygen/1.0 atm experiment here is 0.092 cm/s, while at 1.5 atm it is 0.150 cm/s, and at 50% oxygen, for 1.0, 1.5, and 2.0 atm it is 0.358, 0.454, and 0.547 cm/s, respectively. The measured temperatures are shown as a function of time in Fig. 2. Following an earlier error analysis of the thermocouple measurements [9], the reported temperatures are uncorrected. Because it was farther from the ignitor, the temperature history of the gas-phase thermocouple 2.3 mm from the surface is shown shifted in time by an amount equal to the displacement divided by the steady flame spread rate.

The surface temperature increases as the leading edge of the flame approaches the thermocouple, a plateau in temperature is nearly reached as the fuel pyrolyzes, and the temperature rises again as the trailing edge of the flame approaches. Following passage of the trailing edge, the temperature decreases. Because the maximum height of the visible flame above the surface is less than the distance of the thermocouple farthest (7.0 mm) from the surface, that thermocouple signal shows only a single peak in temperature. The thermocouple 2.3 mm from the surface senses only the leading edge of the flame prior to the time at which data taking ceases.

C. Steady-State Model Comparisons

The steady-state model developed in detail elsewhere [2,3,7] describes well the overall

characteristics of the leading edge of the flame, the flame region responsible for establishing the spread rate. Predicted surface temperatures there match well with experiment [7], the model predicts an increase in spread rate with pressure [7] and with increasing oxygen concentration, and a slight increase of pyrolysis temperature with increasing pressure [7]. As seen later, measured pyrolysis temperature increases with pressure for 35% oxygen, although that behavior is not quite as clear for 50% oxygen. In comparison, the expression for spread rate given by de Ris for heat-conduction-limited-spread over a thermally thin fuel [10] predicts a decrease in spread rate with increasing pressure due to the prediction from the steady model of a increase in vaporization temperature with pressure.

The predicted increase in spread rate with pressure, consistent with experiment and opposite of the thermal theory of de Ris, can be explained from gas-phase radiation effects. An increase in pressure results in an increase in Planck mean absorption coefficient computed as described in Ref. [3] and taking into account the distribution of temperature, CO₂, and H₂O, but neglecting the presence of soot. Predicted absorption coefficients, used in the radiative source term in the gas-phase energy equation, increase from 1.9 m⁻¹ at 1.0 atm, to 2.4 m⁻¹ at 1.5 atm, to 3.0 m⁻¹ at 2.0 atm and 50% oxygen, but a thinning of the reaction zone occurs with an increase in pressure such that the optical thickness of the flame decreases [7]. As a result, flame cooling due to radiation decreases with increasing pressure causing an increase in spread rate. Although this result was obtained neglecting radiative feedback to the surface, inclusion of radiative feedback as described in Ref. [3] did not change this conclusion. Neglecting that feedback is equivalent to assuming that the gas radiation to the surface is balanced by the surface reradiation or that the surface emittance and absorption are set equal to zero.

The steady model qualitatively predicts the overall size of the flame adequately. Temperature contours, in the units of the ambient temperature of 298 K, are shown in Fig. 3 for flames spreading left to right. For 35% oxygen, the dimensionless temperature of 3.0 encloses the experimental flame shown in Fig. 1. Superimposed on the temperature contours in Fig. 3 are the computed velocity vector fields for the 50%/2.0 atm flame and the 35%/1.0 atm USML-1 flame. The velocities are shown in units of computed spread rate. As in the experiments, the 50%/2.0 atm flame extends away from the surface the farthest, and the 35%/1.0 atm flame the least. Additionally, the experimental 35%/1.0 atm flame is nearly symmetrical about the midpoint of its length, which is evident in Fig. 1. The asymmetry evident for the 50%/2.0 atm case is consistent with the higher spread rate, which results in a higher relative velocity of oxidizer into the flame at the leading edge.

D. Unsteady Model Comparisons

While the steady model describes the character of the leading edge of the flame properly, it is unable to describe a trailing edge structure and the evolution of the trailing edge after the ignition

transient. The tendency of the flame to curve back toward the surface near the trailing edge is never adequately captured by the steady model. Increases in gas and surface temperature found experimentally as the trailing edge of the flame passes over the thermocouples are not predicted.

Predicted surface temperatures from the unsteady model for 35% oxygen are compared to the flight measurements in Fig. 4, and gas-phase temperatures are compared in Fig. 5. The structure of the profiles is generally captured by the unsteady model. Like the steady model, the unsteady results were obtained neglecting radiation feedback to the surface. For calculations of radiative loss to the surroundings, absorption coefficients at 35% were estimated from the computed values at 50%, correcting for the differences in CO_2 and H_2O produced from stoichiometric reaction at 35% as compared to 50%, to be 1.46 m^{-1} and 1.84 m^{-1} at 1.0 and 1.5 atm, respectively.

The flight experiments show that a substantial amount of solid fuel remains following the initial spreading of the gas-phase flame, while in normal gravity the same fuel is entirely consumed. The one-step, Arrhenius, pyrolysis model requires a dimensionless fuel density at burnout, defined as the ratio of the solid density at burnout to that of the virgin fuel. Reflecting the flight experiment observations, the burnout density was chosen to be 0.7 for 35% oxygen, i.e., only 30% of the potentially pyrolyzable fuel is converted to gas-phase fuel. This value of burnout density is much higher than the value of 0.27 than the pyrolysis experiments of Kushida *et al.* suggest [11], but burnout densities below 0.7 do not allow the observed structure of the trailing edge to evolve and result in flames that in the calculation are too long. With a burnout density of 0.27, the model predicts that the trailing edge does not move from the point of ignition for the entire experiment time, contrary to the observations.

Surface temperature and heat flux distributions computed from the unsteady model are shown in Fig. 6 for comparison to the experimental values, derived from the spread rate and temperature measurements, shown in Fig. 7. Surface radiation in both figures was computed from the surface temperature assuming a surface emittance of 0.5, and the remaining details of the data reduction scheme used to compute the experimental heat fluxes is described elsewhere [9]. In both figures, each distribution is normalized with its peak value, which is shown in parentheses in the figure legend.

Computationally, conduction constitutes the net heat flux to the solid, because surface radiation and gas-to-surface radiation are taken to balance. The computational net heat flux profile shows a single peak near the flame leading with a magnitude comparable to the experimental conduction peak, the two differing by about a factor of two. Experimentally, the net flux shows two peaks near the leading edge, which is due to the influence of radiation; conduction alone cannot account for this behavior. Surface radiation and gas-to-surface radiation are at least comparable in Fig. 7, consistent somewhat with the model assumption of a balance between the two. The magnitude of the radiative fluxes compared to conduction clearly indicates their importance, and the fact that the conduction flux and the gas-to-surface

radiative flux do not peak at the same location gives rise to the net heat flux profile observed experimentally.

For further comparison, computational results for 50% oxygen and 1.5 atm pressure are shown in Fig. 8, with the corresponding experimental results shown in Fig. 9. Behavior similar to the 35% oxygen flame is obtained, although more experimental data are available in the pyrolysis region, because of the higher spread rate, showing that surface radiation and gas-to-surface radiation there are comparable. The separation of the peaks of the conduction and gas-to-surface radiation fluxes, and the importance of the radiative flux near the leading edge, is evident in Fig. 9, which again gives rise to the character of the net heat flux profile different from a pure conduction process.

CONCLUSIONS

Flame spread over a thin solid fuel in a quiescent, microgravity environment was studied in one atmosphere aboard USML-1 in a continuing series of flight tests. Experimental results, along with results from a steady and an unsteady model, show generally that the flame elongates after ignition, forming a trailing edge that follows the leading edge at a slower speed. After a lengthy ignition transient, the flame shape is steady. The spread rate of the leading edge becomes steady almost immediately after ignition and increases with increasing pressure and oxygen content.

The brightness of the flames increases as the spread rate increases with atmospheric conditions, and the color of the flame changes from blue to orange, indicating increased soot production. The faster spreading flames are elongated and asymmetric, while the slower spreading flames, such as the USML-1 flame, are symmetrical about the midpoint of their length.

Trends in flame size, temperature, and spread rate are reproduced by the steady and unsteady models when radiation loss from the flame is included. However, trailing-edge phenomena, which appear to be inherently unsteady, are only captured by the unsteady model. The experiment observations suggest that the fuel is not completely pyrolyzed after the flame passes, and the fuel density at burnout, treated as a parameter, must be relatively high in order to obtain qualitative agreement between model and experiment.

Experimental heat flux profiles demonstrate the importance of radiative processes in these low-gravity flames. Conduction and radiative fluxes are comparable in magnitude, and although model predictions of conduction fluxes are quite comparable to experiment, coupling between surface and gas radiative processes is generally needed to predict the behavior of the experimental heat flux profiles near the flame leading edge. With basic flame structure and evolution predictable, submodel refinement, e.g., the degree of radiative coupling, will allow for more quantitative agreement between model and experiment to be pursued.

ACKNOWLEDGMENTS

This work was supported by NASA through Contract NAS3-23901. We thank Prof. S. V. Patankar for providing to us an initial version of the gas-phase software. We gratefully acknowledge the contributions of Ralph Zavesky, John Koudelka, and the SSCE flight hardware team at the NASA-Lewis Research Center and the program support of NASA Headquarters, Microgravity Division, Office of Space Science and Applications.

REFERENCES

1. Vento, D., Zavesky, R., Sacksteder, K., and Altenkirch, R. A., *The Solid Surface Combustion Space Shuttle Experiment Hardware Description and Ground-Based Test Results*, NASA TM 101963, 1989.
2. Bhattacharjee, S., and Altenkirch, R. A., *Twenty-Fourth Symposium (International) on Combustion*, The Combustion Institute, Pittsburgh, 1992, pp. 1669-1676.
3. Bhattacharjee, S., and Altenkirch, R. A., *Twenty-Third Symposium (International) on Combustion*, The Combustion Institute, Pittsburgh, 1990, pp. 1627-1633.
4. Bullard, D.B., Tang, L., Altenkirch, R. A., and Bhattacharjee, S., *Advances in Space Research.*, 13:(7)171-(7)184 (1993).
5. Altenkirch, R. A., Eichhorn, R. and Shang, P. C., *Combustion and Flame*, 37: 71-83, (1980).
6. West, J., Bhattacharjee, S., and Altenkirch, R. A., *Combustion Science and Technology*, 83: 233-244, (1992).
7. Bhattacharjee, S., Altenkirch, R. A., and Sacksteder, K., *ASME Winter Annual Meeting*, 1993.
8. Patankar, S. V., *Numerical Heat Transfer and Fluid Flow*, Hemisphere Publishing Corporation, New York, 1980.
9. Bhattacharjee, S., Altenkirch, R. A., and Sacksteder, K., *Combustion Science and Technology*, 91:225-242 (1993).
10. de Ris, J.N., *Twelfth Symposium (International) on Combustion*, The Combustion Institute, Pittsburgh, 1969, pp. 241-252.
11. Kushida, G., Baum, H. R., Kashiwagi, T., and di Blasi, C., *Journal of Heat Transfer*, 114: 494-502 (1992).

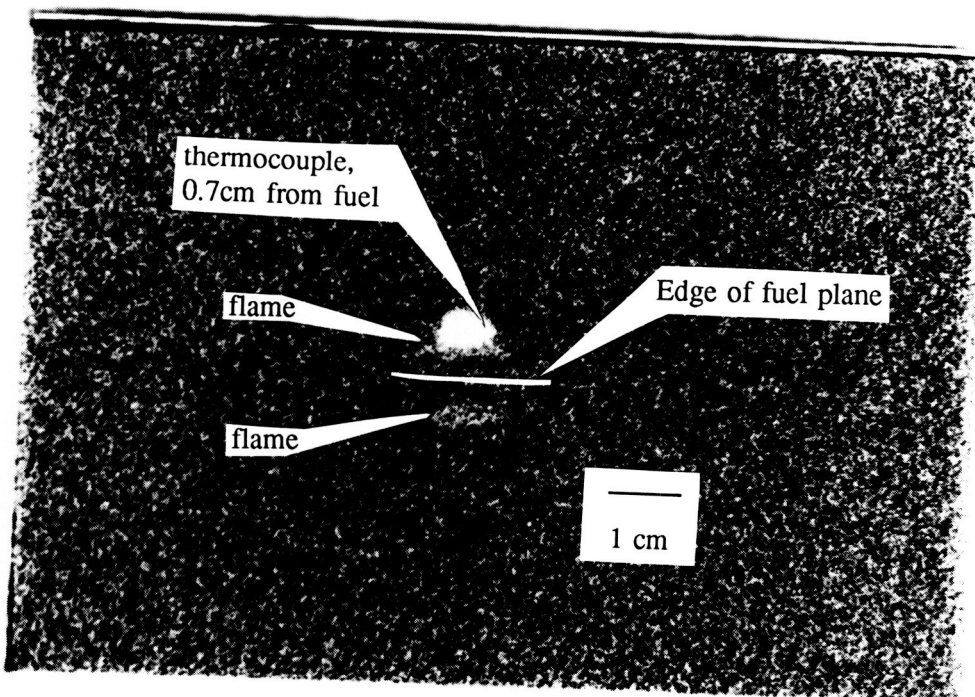


Figure 1 Black-and-white photograph of the flame spreading left to right at approximately half way along the sample.

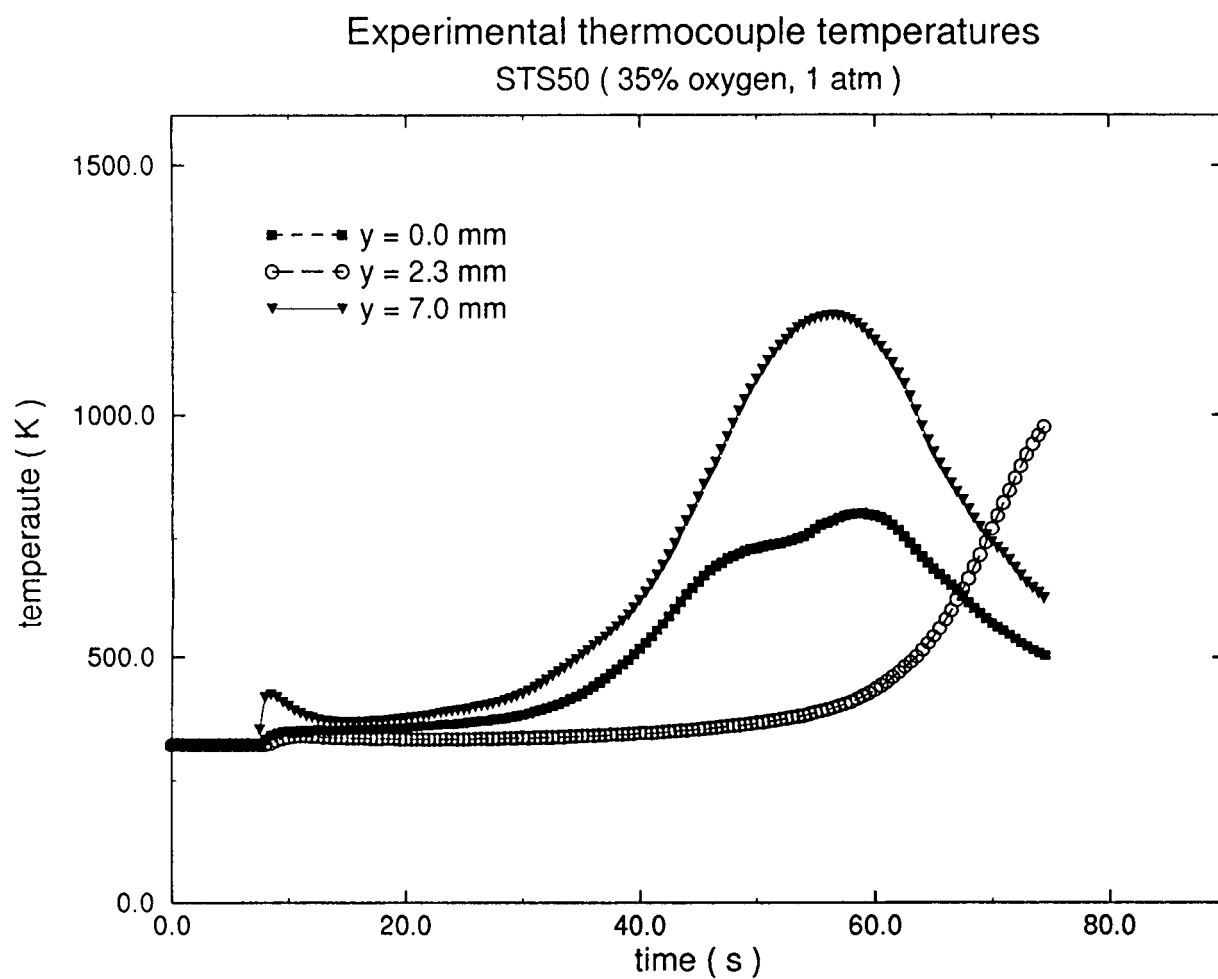
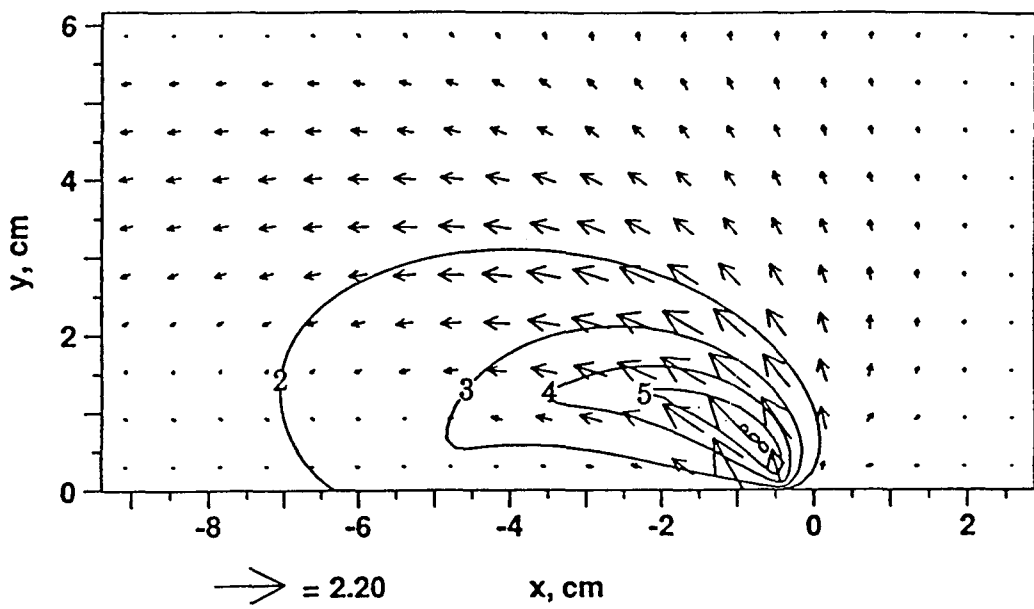


Figure 2 Measured surface and gas-phase temperatures for 35% oxygen, 1.0 atm.

50% oxygen/2.0 atm



35% oxygen/1.0 atm

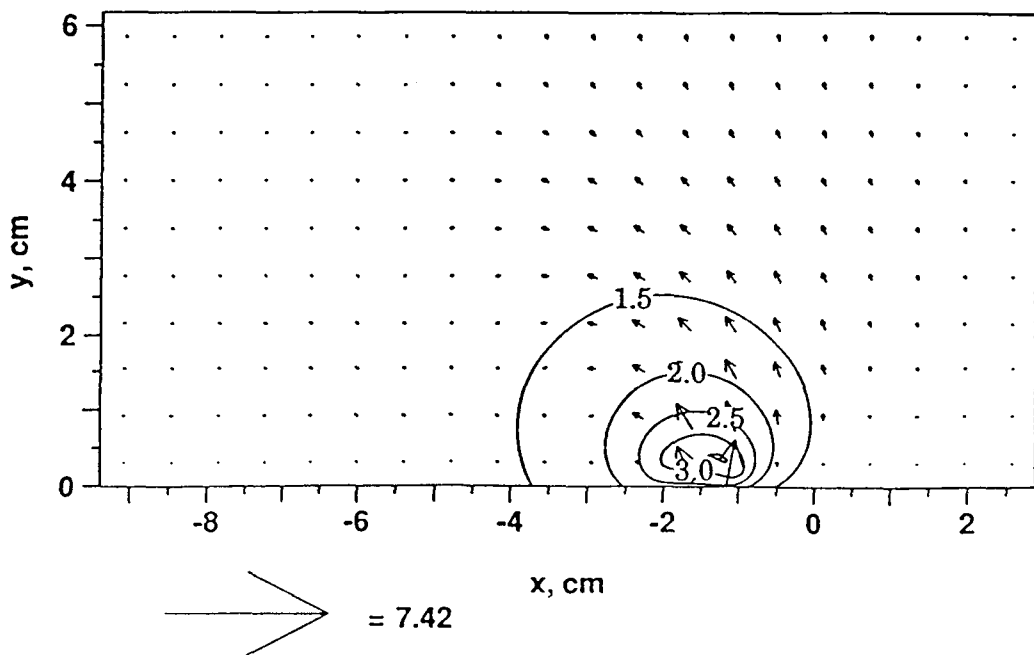


Figure 3 Temperature contours predicted from the steady model with temperatures in the units of the ambient superimposed on the computed vector velocity field relative to the ambient with the vector scale in units of computed spread rate.

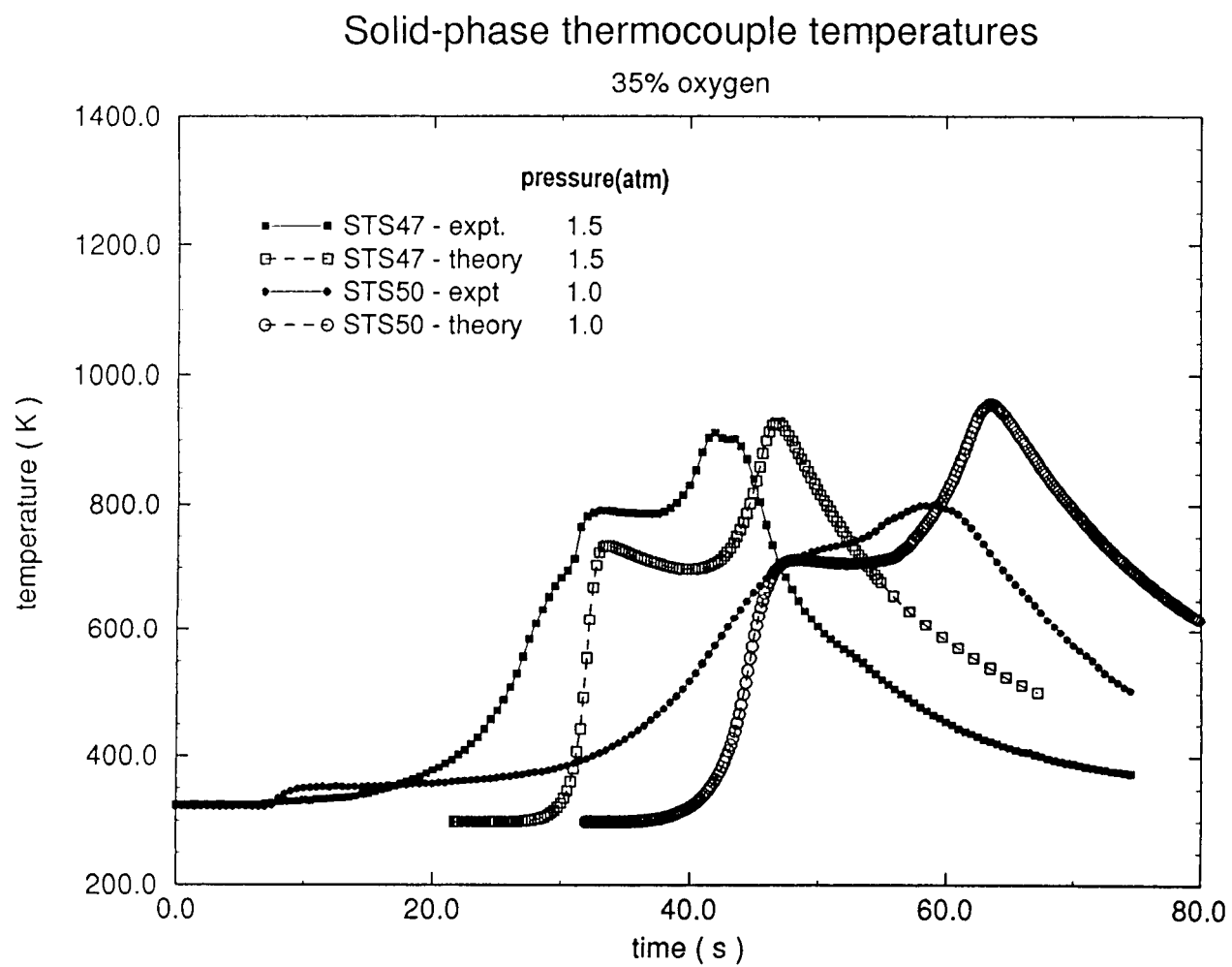


Figure 4 Comparison of measured and predicted surface temperatures from the unsteady model formulation for 35% oxygen.

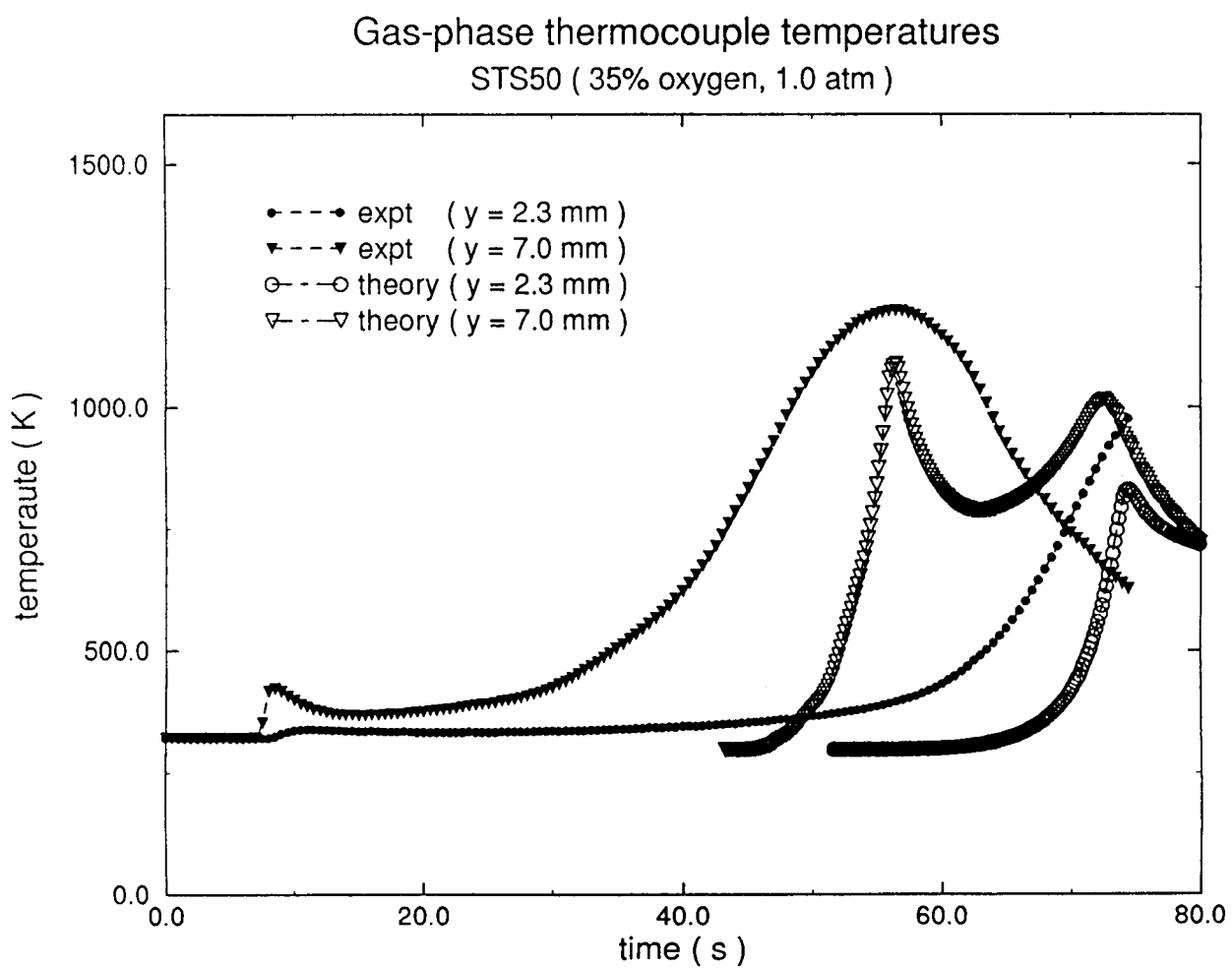


Figure 5 Comparison of measured and predicted gas-phase temperatures from the unsteady model formulation for 35% oxygen.

Surface parameters

STS50 (35% oxygen, 1.0 atm, emis = 0.5, flame location = 5 cm)

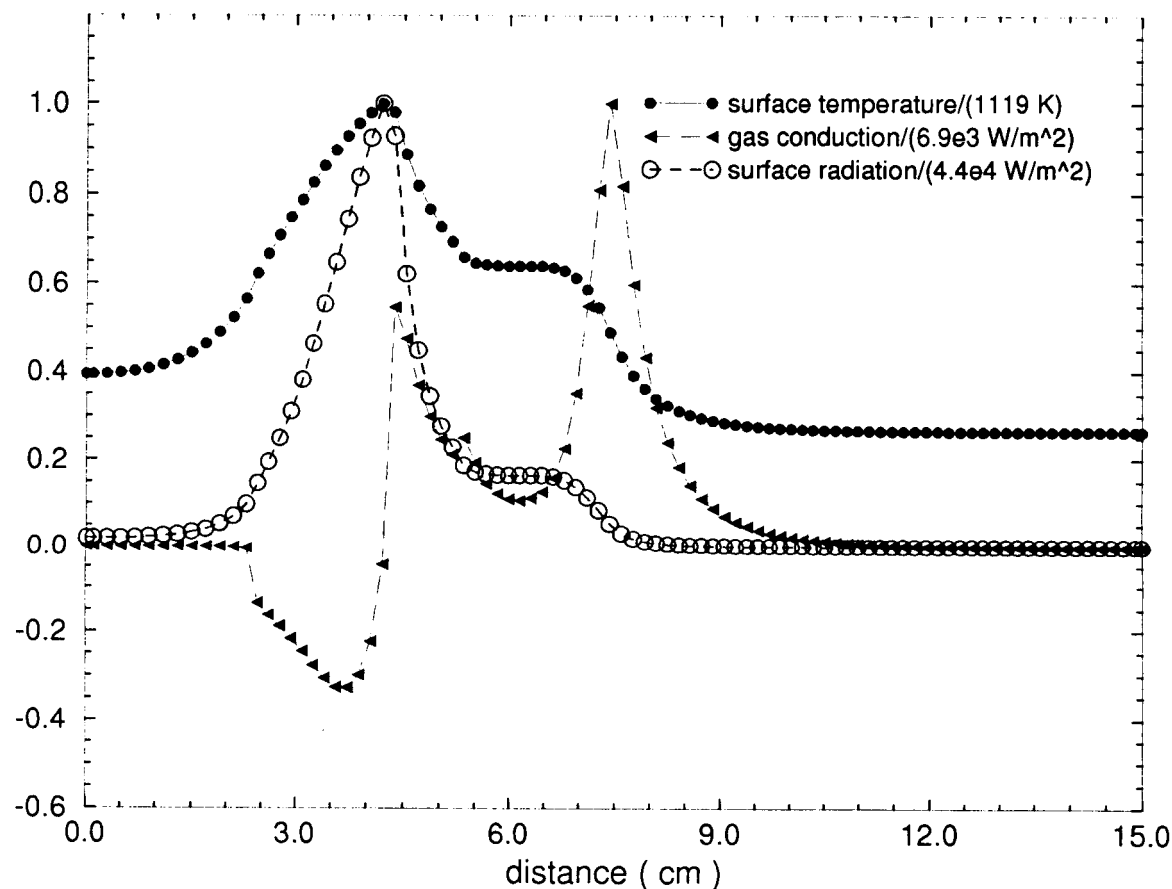


Figure 6 Computed heat fluxes for 35% oxygen, 1.0 atm.

3010

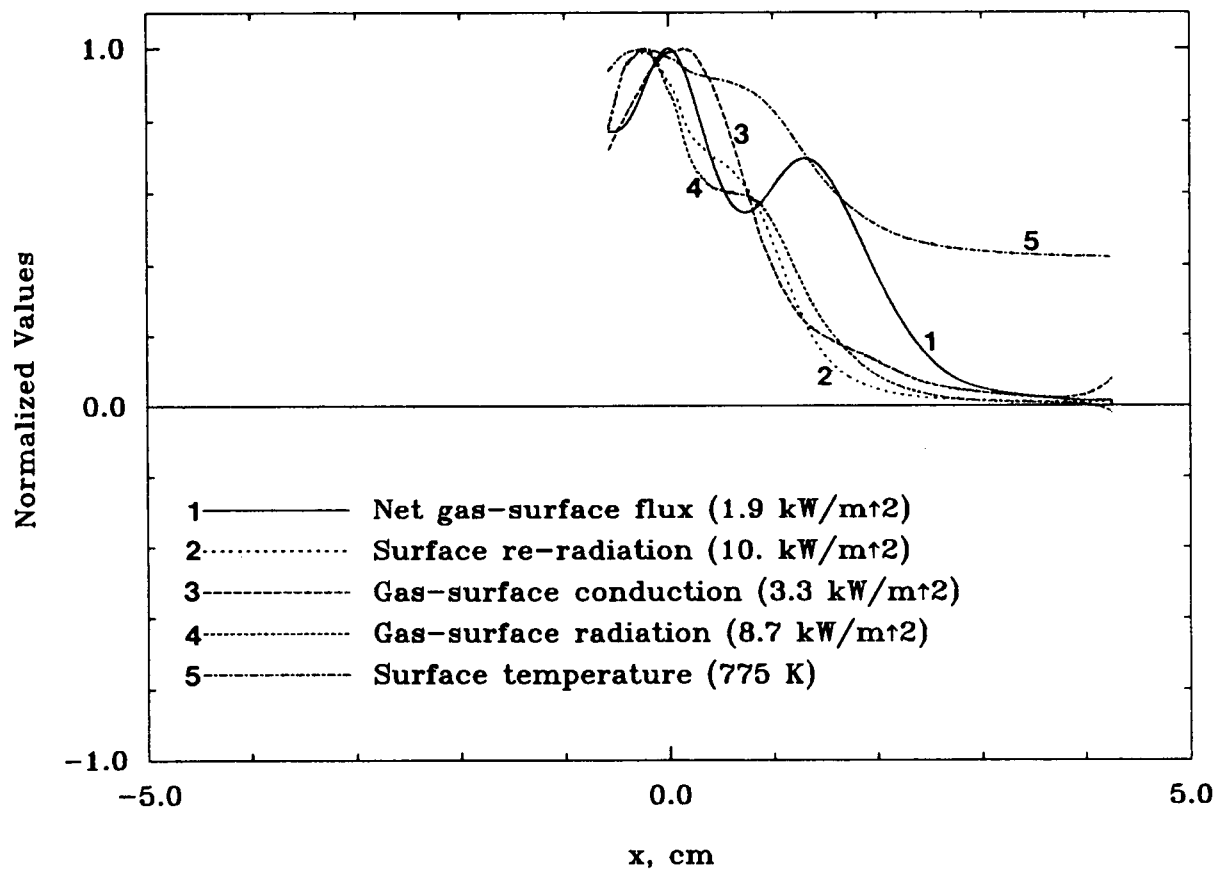


Figure 7 Experimental heat fluxes for 35% oxygen, 1.0 atm.

Surface parameters

STS41 (50% oxygen, 1.5 atm, emis = 0.5, flame location = 5 cm)

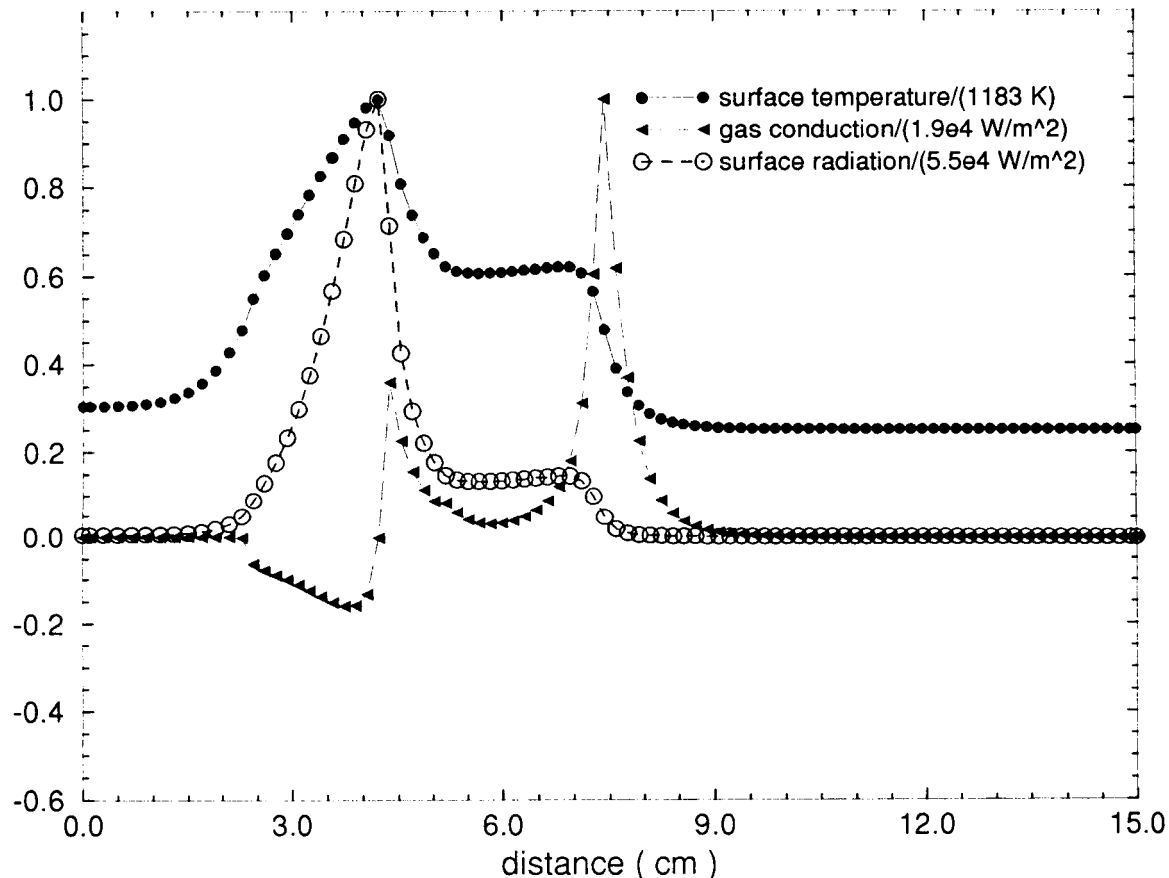


Figure 8 Computed heat fluxes for 50% oxygen, 1.5 atm.

5015

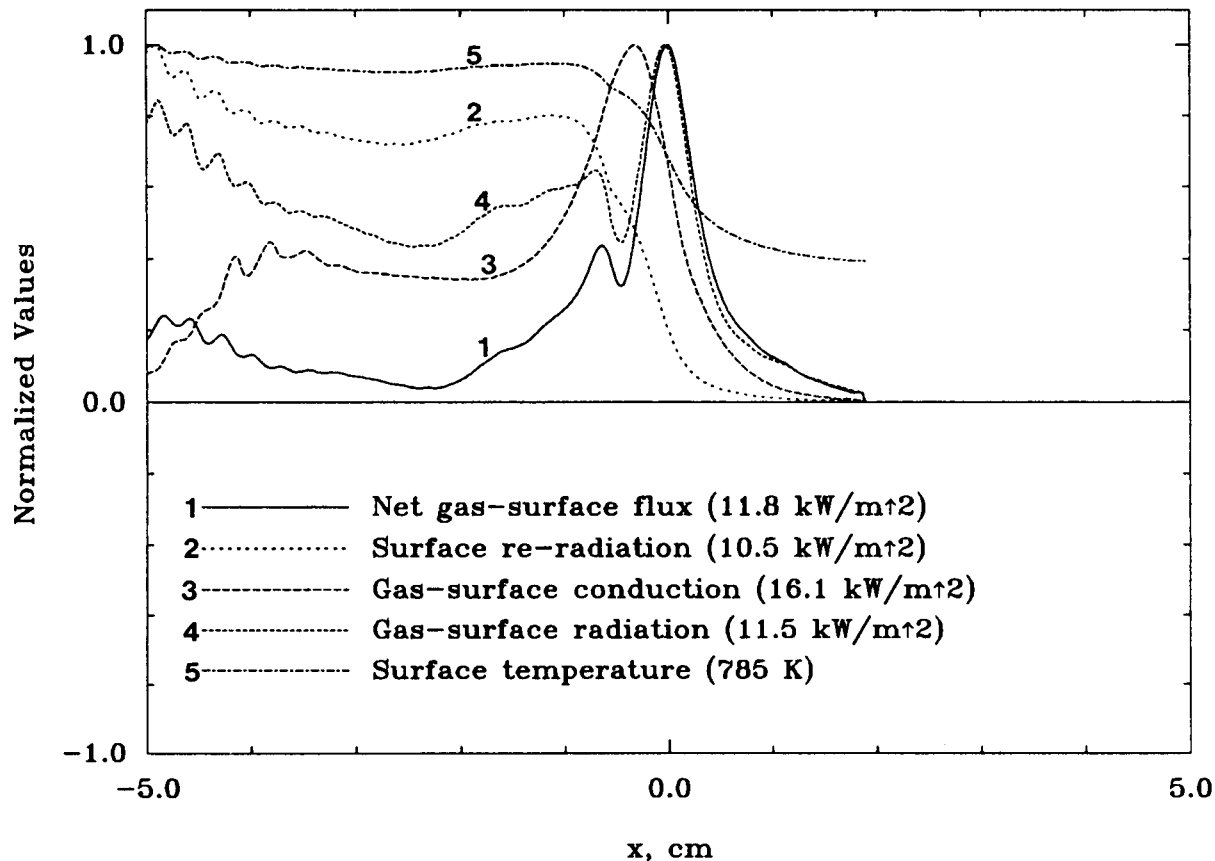


Figure 9 Experimental heat fluxes for 50% oxygen, 1.5 atm.

S K P
5
P-
11/20/87

PRELIMINARY OARE ABSOLUTE ACCELERATION MEASUREMENTS ON STS-50

Robert C. Blanchard*, John Y. Nicholson⁺, and James R. Ritter[^]

*NASA Langley Research Center, Hampton, Virginia 23681-0001

⁺ViGYAN, Inc., Hampton, Virginia 23666-1325

[^]Lockheed Engineering & Sciences Co., Hampton, Virginia 23666-1339

ABSTRACT

Orbital Acceleration Research Experiment (OARE) data on STS-50 have been examined in detail during a 2-day time period. Absolute acceleration levels have been derived at the OARE location, the Orbiter center-of-gravity, and at the STS-50 Spacelab Crystal Growth Facility.

The tri-axial OARE raw acceleration measurements (i.e., telemetered data) during the interval have been filtered using a sliding trimmed mean filter in order to remove large acceleration spikes (e.g., thrusters) and reduce the noise. Twelve OARE measured biases in each acceleration channel during the 2-day interval have been analyzed and applied to the filtered data. Similarly, the *in situ* measured x-axis scale factors in the sensor's most sensitive range were also analyzed and applied to the data. Due to equipment problem(s) on this flight, both y- and z- axis sensitive range scale factors were determined in a separate process (using the OARE maneuver data) and subsequently applied to the data. All known significant low-frequency corrections at the OARE location (i.e., both vertical and horizontal gravity-gradient, and rotational effects) were removed from the filtered data in order to produce the acceleration component at the Orbiter's center-of-gravity, which are the aerodynamic signals along each body axes. Results indicate that there is a force of unknown origin being applied to the Orbiter in addition to the aerodynamic forces. The OARE instrument and all known gravitational and electromagnetic forces have been reexamined, but none produce the observed effect. Thus, it is tentatively concluded that the Orbiter is creating the environment observed.

NOMENCLATURE

A	acceleration
g	gravitational acceleration at sea level ($9,8065 \text{ m/s}^2$)
MET	mission elapsed time (i.e., time from lift-off)
nano-g	$1 \times 10^{-9}g$
p,q,r	body axes angular rates
T	temperature
u,v,w	air relative velocity body axes components
V	velocity
V_{air}	air relative velocity
X,Y,Z	sensor axes
X_b, Y_b, Z_b	body axes
α	angle-of-attack
β	side-slip angle
μg	$1 \times 10^{-6}g$

Subscripts

o	Orbiter spacecraft coordinates
L	with respect to the center-gravity
rot	rotational

Acronyms

CAS	Calibrated Ancillary System
CGF	Crystal Growth Facility
HiRAP	High Resolution Accelerometer Package
IMU	Inertial Navigation unit
OARE	Orbital Acceleration Research Experiment
STS	Space Transportation System

INTRODUCTION

The orbital acceleration Research Experiment (OARE) consists of a three axis, state-of-the-art accelerometer with an electrostatically suspended proof mass, a full in-flight calibration station, and a microprocessor which is used for in-flight experiment control, processing, and storage of flight data. The experiment system is designed to measure low-frequency($<1 \text{ Hz}$) low-level acceleration (i.e., nano-g sensitivity). An in-depth description of the experiment goals, equipment design characteristics, and capabilities is given in Ref. 1.

The first Shuttle flight of the OARE was June 5, 1991, on the *Columbia* during STS-40. Orbital data were collected for about 3.5 days beginning approximately 5.5 days after launch for this mission. Some equipment problems were noted on the first OARE flight; however, limited results were obtained. These results are given in reference 2.

After the STS-40 flight, the OARE was removed and the problems were isolated and repaired prior to the STS-50 flight. STS-50 is the first flight which employs an operating nano-g sensor coupled with a calibration capability which allows for the measurement of absolute acceleration levels. Over 13 days of orbital data were collected on STS-50. This included over 60 full calibrations sequences which provided both bias and scale factor measurements for 3 axes and 3 ranges. A problem, however, was noted in the most sensitive range for the scale factor measurements on the y -and z-axes. To circumvent the anomaly, OARE maneuvers (three separate rotations about each of the Orbiter's body axes) have been used to provide scale factors for all three axes in the sensor's most sensitive range.

This paper presents the analysis of the OARE data taken during the time period $1d14^h$ to $3d14^h$ MET. The analysis of this orbital time segment was selected in order to provide low frequency, low acceleration information for Spacelab furnace experimentation application, e.g. the Crystal Growth Facility. The on-orbit calibration measurements and their applications to the OARE acceleration signals to produce absolute accelerations are discussed. Also presented is the transformation of the data from the OARE location to the Orbiter's center-of-gravity, which provides acceleration data on the drag aerodynamics along each axis.

I. FLIGHT DATA ANALYSIS

A. Orbiter State parameters

Ancillary flight data of the Orbiter's inertial position, velocity vector, and orientation (Aries mean 1950 coordinate system) are received from Goddard Space Flight Center in the form of Calibrated Ancillary System (CAS) tapes. In general, these data give the conditions under which the OARE acceleration measurements were taken. Specifically, the CAS data are interpreted in order to validate the OARE data and to transform the OARE data to other locations (e.g., the center of gravity). The CAS data are transformed into other useful quantities, such as distance from the center of Earth, latitude, longitude, and relative velocity. For relative velocity calculations, it is assumed that the atmosphere is rotating with the Earth. On the CAS tapes, the orientation of the Orbiter is given in quaternions. These are combined with the velocity components to calculate angle of attack, α , and slideslip angle, β . This section gives some of the results from the Orbiter CAS tapes.

Figure 1 shows the relative velocity and the altitude variations as a function of MET in hours. The altitude is referenced to a spherical Earth with a radius of 6356.766 km. As seen, the orbit is very

circular; a difference of only 9 km exists between perigee and apogee. The altitude range is about 325 km to 316 km and the orbit is slightly changing with time. The expected mean aerodynamic drag is very small and the 90 min, variation due to the slightly elliptical orbit is even smaller (e.g., using the 1976 US standard atmosphere³, the acceleration signal is estimated at about 275 ng with a variation of ± 25 nano-g).

Based upon the CAS data, the Orbiter is oriented with the payload bay doors toward the velocity vector with the right wing tilted about 12° into the velocity vector (i.e., forward of a line perpendicular to the orbital plane). The orientation is shown in Fig. 2 where the engines are pointed toward Earth and the payload doors are open. The insert graph in Fig 2 shows the α and β flight data for entire period. Both angles are tightly held to $\pm 1/2$ deg centered around $\alpha=-90^\circ$ and $\beta= 12^\circ$. For completeness, the definitions⁴ of α and β are as follows:

$$\alpha = \tan^{-1}(w/u) \text{ and}$$

$$\beta = \sin^{-1}(v/V_{\text{air}}),$$

where u , v , and w are body axes velocity components of V_{air} and V_{air} is the magnitude.

In this orientation, it is anticipated that the majority of the aerodynamic effect is along the positive z-body axis. The y-body axis acceleration should be negative and very small due to an aerodynamic force produced on the right side of the Orbiter facing into the velocity vector. The x-body axis acceleration signal should be positive, almost entirely due to gravity-gradient and rotational effects. Figure 2 also shows the body axis coordinate system.

Figure 3 shows the Orbiter's three body rates during the entire period. Clearly, roll rate, p (the angular rate about the x-body axis) is on the average nearly zero. If the Orbiter y-body axis were held perpendicular to the orbital plane, the pitch rate, q , (the angular rate about the y axis) would be equivalent to rotating the Orbiter 360° over the orbital period of 90 minutes (i.e., 0.067 deg/s). The y axis is not quite perpendicular to the orbital plane so that this rate component is slightly reduced. The yaw rate, r , (the angular rate about the z axis) shows an approximate value of 0.014 deg/s due to the 12° offset mentioned earlier.

B. In-flight calibrations

The success of making low frequency, low amplitude acceleration measurements at orbital altitudes relies heavily on providing reliable calibration factors. The OARE plays a unique role in the technological development of systems for making these calibration measurements. It has a complete calibration station providing both *in situ* bias and scale factor measurements. This section of the report discusses the instrument operating conditions and shows the calibration data taken during the interval.

The instrument was programmed to perform a calibration sequence approximately every 4.75 hours. The calibration sequence includes up to nine separate bias calibrations (three axes, three ranges) and up to six scale factor calibrations (two table rate/axis, with y and z axes scaled simultaneously). A bias calibration consists of collecting 50 s of data in one position, rotating the sensor 180°, and then collecting data for another 50 s period. The sum of the average of each interval is twice the bias, while the difference is twice the average input signal. A scale factor calibration consists of rotating the sensor at a pre-programmed rate and measuring the acceleration difference between the sensor at rate and the average output at rest. This difference is scaled to the known centripetal acceleration which is a function of the square of the rate (which is measured) and the location of the sensor on the table (which is known). Two table rates are used for each sensor range for linearity checks.

Figure 4 shows the temperature measurements from two thermocouples, one inside the sensor package and one mounted on the base, adjacent to the rotary table surface. Throughout the entire period, the temperature varied by about 4°C, getting cooler as the mission progressed. It is interesting to observe the diurnal variation of about 1°C. This type of variation has the potential to seriously limit the interpretation of pendulous type accelerometer drag variations because typical bias temperature sensitivity coefficients are 20 to 60 $\mu\text{g}/^\circ\text{C}$ for these instruments. That is, for these accelerometers, it is difficult to separate diurnal drag variations from sensor temperature effects since both effects are in phase. It has been demonstrated that ground based calibrations of these instruments in a 1-g environment produce significant errors when applied to the micro-gravity environment produce significant errors when applied to the micro-gravity environment encountered on orbit.⁵ There are two important reasons why OARE is not seriously affected by this phenomenon. First, *in situ* calibrations are made and thus no extrapolations to space are necessary. Secondly, the OARE bias temperature sensitivity coefficients are very small, typically much less than 1 $\mu\text{g}/^\circ\text{C}$.

Figures 5, 6, and 7 show the results of the x, y, and z body axes bias calibrations, respectively. Included in each figure is the temperature at each calibration point. In addition, each time a bias is performed, the true (i.e., bias independent) signal is simultaneously measured and is shown along with the bias on each graph, labeled "signal". From the graphs, it is clear that the bias correction is only a few μg except for the y axis which is about 7 μg . This is within OARE design specifications. The x axis has the largest temperature sensitivity, about 0.2 $\mu\text{g}/^\circ\text{C}$, while both y and z are an order of magnitude smaller. The discrete signal measurements on each axis give a 12 point sample of the expected Orbiter residual acceleration environment, except for scale factor adjustments. Clearly, the x axis has a relatively large, almost constant 1.0 μg signal, while y axis is less than .5 μg and z axis varies about 0.8 μg . This is useful information for checking the adjustments to the measured signals which are discussed later.

The scale factors for the x-axis in its most sensitive range were successfully measured *in situ* using the two programmed calibration table rates. The low and high table rates produce calibration accelerations of approximately $20 \mu\text{g}$ and $45 \mu\text{g}$, respectively. Figure 8 shows the scale factor results along with the instrument temperature as a function of time. The scale factor temperature sensitivity for this axis, in this temperature interval is about $0.3\%/\text{^{\circ}C}$. As noted earlier, the *in situ* scale factor measurements for the y- and z-axes in the most sensitive range were unsuccessful. These scale factors were determined using data taken during the OARE data to solve for the scale factors on all three axes. Table 1 summarizes the scale factor results.

The *in situ*-axis scale factor compares moderately well with the one derived from the maneuvers. Several facts are worth mentioning about the possible source for the differences. First, the OARE maneuver occurred late in the mission (on day 12 MET) when the instrument was at a different temperature (cooler). Second, typically each maneuver involves rotating the spacecraft 360° . Rate motion is obtained from gyro processing during the scale factor extraction process. The gyros require calibration factors which introduce errors,

II. OARE GROUND PROCESSING

OARE collects tri-axial data at the rate of 10 samples/s. The data are filtered thorough an analog filter and a 6 pole Bessel filter with a cutoff frequency of about 1 Hz. This raw data are too noisy for use in detailed characterization of low frequency analysis.

By design, the raw data are telemetered to ground stations and simultaneously processed on-board by the OARE computer using a 'trimmed-mean' filter. Briefly, this filter consists of ordering a window of data (for STS-50, the window size was set at 500 samples) from low to high values. Then, a 'q statistic' is calculated which gives a measure of outlier content. From this, a percentage of the 'tails' of the data is eliminated. The remainder of the data are averaged and the window slides in time (for STS-50, 25 seconds was chosen). Examination of this data revealed that it was still slightly noisy for the purpose of this report. In addition, a check was required to determine whether the on-board computer was handling the data correctly. Thus, it was decided to ground process the raw telemetered data in the same manner as the on-board computer, except vary the window size. However, after the study, it was evident that the flight data processing algorithm performed as planned.

A. OARE Location Environment

Figure 9 shows the OARE measured x, y, and z acceleration levels in the Orbiter's body axes system at the OARE location. The data in this figure are the OARE 10 samples/sec telemetered raw (unprocessed) data which have been averaged using a trimmed-mean technique with a window of 200 sec sliding at 25 sec intervals. This digital filter essentially limits frequency observability to less than

about 0.0025 Hz. However, this introduces no problems since this frequency is much larger than those associated with orbital phenomena of interest. The data have been corrected with the OARE biases and scale factors.

The x-axis appears to produce the largest signal of about $1 \mu\text{g}$ with an oscillatory wave of period 26 hours. The y-axis signal is positive and smaller than the x-axis (about $0.6 \mu\text{g}$), and also has an oscillatory signal of about 26 hours which is 180° out of phase with the x-axis data.

B. Center of Gravity Environment

The location of the OARE sensor in body axes coordinates relative to the Orbiter's center-of-gravity is $X_b = -1.536 \text{ m}$, $Y_b = -0.0234 \text{ m}$, $Z_b = 1.435 \text{ m}$. Based upon this lever arm and the Orbiter orientation data discussed earlier, the magnitude of the major adjustments, namely, gravity-gradient and rotational effects, is shown in Fig. 10. The gravity-gradient effect includes both vertical and horizontal displacements from the Orbiter center-of-gravity. Clearly, the largest correction is on the x axis, about $0.65 \mu\text{g}$, with components from gravity-gradient and rotational effects. The total of the y axis corrections is an order of magnitude smaller and its source is mostly rotational effects. The net correction for the z axis is practically zero due to the cancellation of the gravity-gradient effects with the rotational contributions. Applying these adjustments to the data shown in Fig 9 should theoretically give the accelerations at the Orbiter center-of-gravity which are the drag measurements. The results are shown on fig. 11. Clearly, the value of the residual acceleration along the x axis is much too large to be attributable to the x axis, the aerodynamics should be very nearly zero. Further, the signal also has an obvious 26 hours oscillation. The z axis also has this oscillation at about the same frequency. The z axis data contain the 90 min drag oscillation similar to that observed during STS-40². The y axis appears about as expected: namely, a small slightly negative acceleration which is mainly attributable to aerodynamics.

Several physical phenomena associated with a 24-hour period have been investigated, such as oblate Earth, geomagnetically induced forces, solar radiation pressure, etc. However, none of the considerations to date have produced the proper amplitude and frequency. Thus, a possible alternative is that the Orbiter itself is producing the environment being measured by the OARE sensor. Of course, this requires further investigations.

C. CGF Location Environment

The accelerations caused by this force of unknown origin and the aerodynamic forces are given in Fig. 11. This represents the external forces exerted on the Orbiter at the center-of-gravity. The corresponding accelerations at any other location can be obtained by adding to these measurements the predictions due to gravity-gradient and rotational effects at this location.

The location of the Crystal Growth Facility (CGF) melt location,⁶ in Orbiter Project spacecraft coordinates, is $x_0 = 1086.00$ in., $y_0 = -44.39$ in., $z_0 = 395.45$ in. This corresponds to a lever arm about the center-of-gravity of $X_l = 0.173$ m, $Y_l = 1.117$ m, $Z_l = -0.537$ m. Using this lever arm with the orientation and Orbiter rotation rate data from the CAS tapes, the corrections to the CGF location have been calculated and the results are shown in Fig. 12. Shown are the individual is about $-0.16 \mu\text{g}$ in the y axis due to gravity-gradient horizontal displacement effects. Both x and z axis corrections are fairly small, namely about -0.07 and $-0.035 \mu\text{g}$, respectively.

Figure 13 shows the final results of the low frequency acceleration environment at the CGF melt location. This is obtained by applying the results shown in Fig. 12 to Fig. 11. The acceleration along the x-axis ($\sim 0.5 \mu\text{g}$) is dominated by the acceleration created by the unknown force, possibly the Orbiter itself. The expected acceleration due to drag in this axis is much smaller, approximately an order of magnitude less. The acceleration along the y-axis is slightly negative ($\sim 0.2 \mu\text{g}$) due to aerodynamics and horizontal displacement effects. The z-axis acceleration shows the diurnal atmospheric effect. This effect is seen in Fig. 13 as the higher frequency variation within the 26 hour variation caused by the component of the unknown force in the z direction.

III. ERROR ESTIMATION

The largest and most important error source along all three axes would be from incorrectly estimating the bias. Consequently, care has been taken with this quantity throughout the analysis. For this study, a simple straight line was fit through the measured bias values. The average value and slope will cause no consistent error greater than $0.05 - 0.07 \mu\text{g}$. (it's entirely possible that a given bias could be in error more than this, but it is likely that the biases on either side would not.) In addition, uncertainties in scale factors, knowledge of the center-of-gravity, and rotation rates contribute to errors. These errors could be cumulative, but most probably are not. Estimates of their error contributions are listed in Table 2.

At this time, there remain two unresolved questions from the analysis. First, what is the source of the unpredictable acceleration in the x direction? The x axis signal offset is clearly too large to be attributable to aerodynamics based upon an assessment using data from Ref. 7. In order for gravity-gradient and rotational effects to generate the unforeseen acceleration, the center-of-gravity would have to move about 40 in., which is unrealistic. However, it would take only a few ounces of force exerted on the Orbiter to produce this effect (since 1 oz. = $0.26 \mu\text{g}$). A component of this force has to be exerted in the positive x direction, which would occur with a gas leak in the opposite, i.e., negative x direction.

The second question (which is most likely related to the first) is: What is the cause of the 26 hour oscillations seen in both the x- and z- axes? This oscillation in the z direction would certainly require that

a gas leak has a component in the z direction. Since the phase of the oscillation in the z axis 180° with respect to the x axis, the z force component has to be exerted on the Orbiter from its underside. Therefore, the leak would be directed downward as well as backward from the Orbiter. Of course, if there is a continuous leak in the plane of the orbit, then the orbit itself would undergo a slight change. There is a slight change in orbit conditions (see Fig. 2). But, at this time, it is not known if the observed change in orbit is due to a leak, a result of cumulative attitude-keeping jet firings, or simply natural phenomena such as tidal effects, etc.

Rechecking the data, its processing, and calibration revealed no errors. The bias values for both x- and z-axes show no anomalies. Also, the signals calculated concurrently with the biases are in good agreement with the data once the data signals are adjusted for bias. Although no definitive explanation exists at the present time, all evidence indicates that both effects are real and should be included in the acceleration environment.

SUMMARY

The OARE data on STS-50 during the time period 1d 14h to 3d 14h MET (38h to 86h MET) have been examined in detail and absolute acceleration levels have been derived at the location of the OARE, the Orbiter center-gravity, and the STS-50 Spacelab at the location of the OARE, the Orbiter center-of-gravity, and the STS-50 Spacelab Crystal Growth Facility.

The tri-axial OARE raw acceleration measurements (i.e., telemetered data) during the interval have been filtered using a 2000 point trimmed mean filter moved every 250 points (OARE sample rate is 10 samples/s). This process removes large acceleration spikes due to thrusters, etc. and reduces the noise. The 10 OARE measured biases in each channel during the 2d interval were analyzed and applied to the filtered data. Similarly, the x-axis scale factors were also analyzed and applied to the data. Both y- and z- axis scale factors were determined in a separate process(using the OARE maneuver data) and subsequently applied to the data. All known significant corrections at the OARE location (i/e., gravity - gradient effects from both vertical and horizontal displacements, and rotational effects) were removed from the filtered data in order to produce the aerodynamic signals along the 3 body axes. However, the results indicate that there is a force of unknown origin being applied to the Orbiter in addition to the aerodynamic forces. The force characteristics are such that they produce a cyclic acceleration with a period of ~26 hours and an amplitude of 0.1 to 0.2 μg residing on top of a magnitude of about 0.5 μg , in the plane of the orbit. Upon re-examination of the OARE instrument, there is no evidence that the equipment is malfunctioning. Further, all known gravitational and electromagnetic forces have been reexamined and none produce the observed effect. Thus, it is tentatively concluded that the Orbiter is

creating the environment observed (e.g., an oscillatory gas leak of a few ounces of force in the aft direction could produce the effect). Obviously, this situation requires further investigation.

The aerodynamics data (with the unknown force mapped to the Crystal Growth Facility (CGF) location by adding the adjustments to the measurements for gravity-gradient and rotational effects. The enclosed Fig. 13 shows the final results. The acceleration along the x-axes ($\sim 0.5 \mu\text{g}$) is dominated by the acceleration created by the unknown force, possibly the Orbiter itself. The acceleration along the y-axis is slightly negative ($\sim 0.2 \mu\text{g}$) mostly due to aerodynamics and gravity-gradient horizontal displacement effects. The z-axis acceleration shows the diurnal atmospheric effect, about $0.6 \mu\text{gs}$. This effect is observed in conjunction with the 26-hour oscillation caused by the z-component of the unknown force.

REFERENCES

1. Blanchard, R. C., Hendrix, M. K., Fox, J. C. Thomas, D. J., and Nicholson, J. Y., "The Orbital Acceleration Research Experiment," *Journal of Spacecraft and Rockets*, Vol. 24, No. 6, Nov-Dec. 1987, pp. 504-511.
2. Blanchard, R. C., Nivholdon, J. Y., and Ritter, J. R., "STS-40 Orbital Acceleration Research Experiments Flight Results During a Typical Sleep Period." *Microgravity Science and Technology* Vol. 2, 1992, pp. 86-93.
3. U.S. Standard Atmosphere, 1976, NOAA, NASA. USAF, Oct. 1976.
4. Etkin, Bernard, *Dynamics of Atmospheric flight*, John Wiley and Sons, Inc., New York, 1972, p. 114.
5. Blanchard, R. C., Larman, K. T., and Moats, C.D., "Flight Calibration Assessment of HiRAP Accelerometer Data," AIAA paper 93-0836, January 1993.
6. C. Baugher, MSFC, *Private communications*.
7. Aerodynamics Design Data Book-Vol. I: Orbiter Vehicle, NASA CR-160386, 1978.

Table 1

AVG. SCALE FACTORS*		
axis	in situ	maneuvers
x	1.03	0.93
y	—	1.06
z	—	0.96

*actual SF($\mu\text{g}/\text{count}$)/design SF($\mu\text{g}/\text{count}$)

Table 2

ACCELERATION ERRORS			
Quantity	x_b (μg)	y_b (μg)	z_b (μg)
scale factor	.030	.020	.060
center-of-gravity	.035	<.020	.022
rotation rates	.070	.020	.060

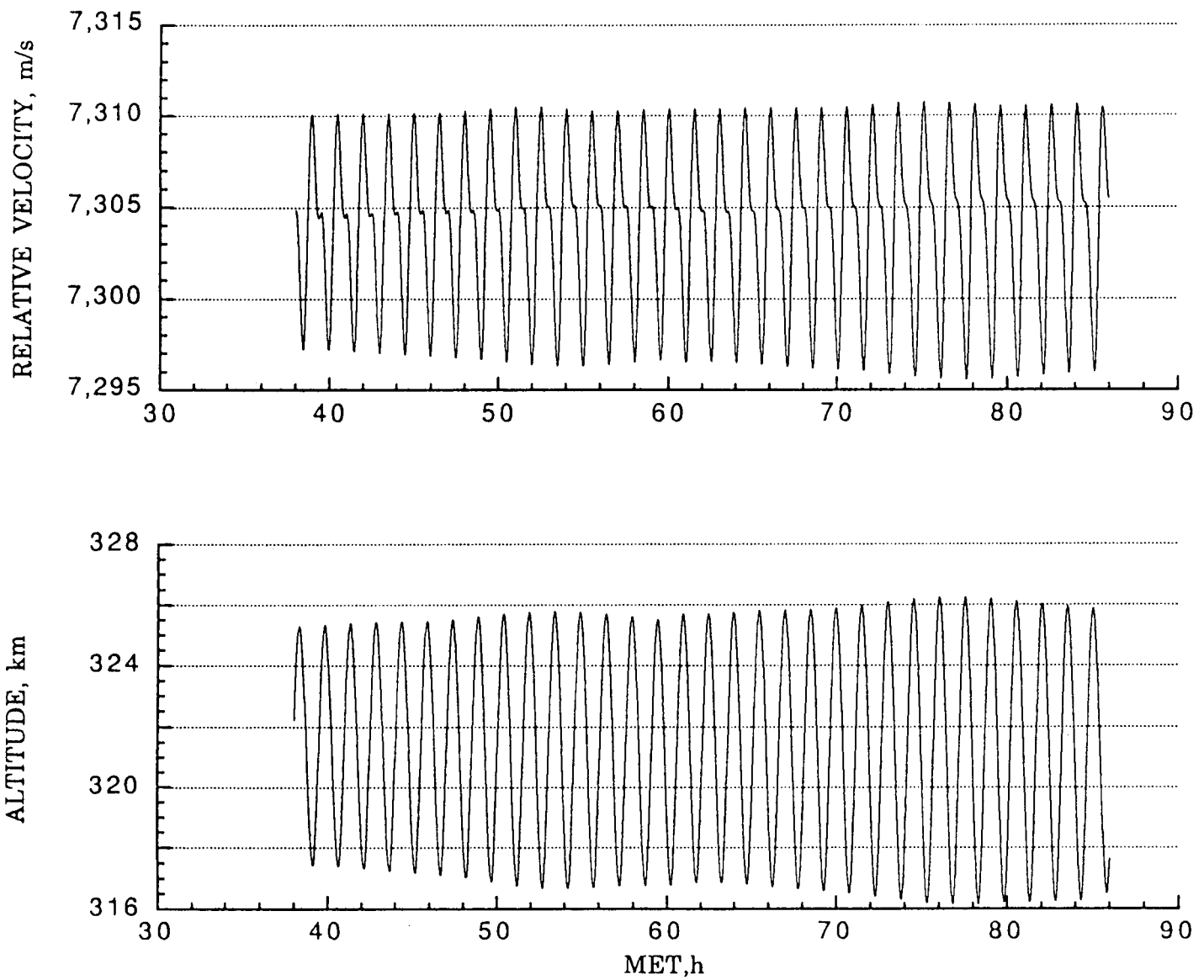


Figure 1 Orbiter relative velocity and altitude time history.

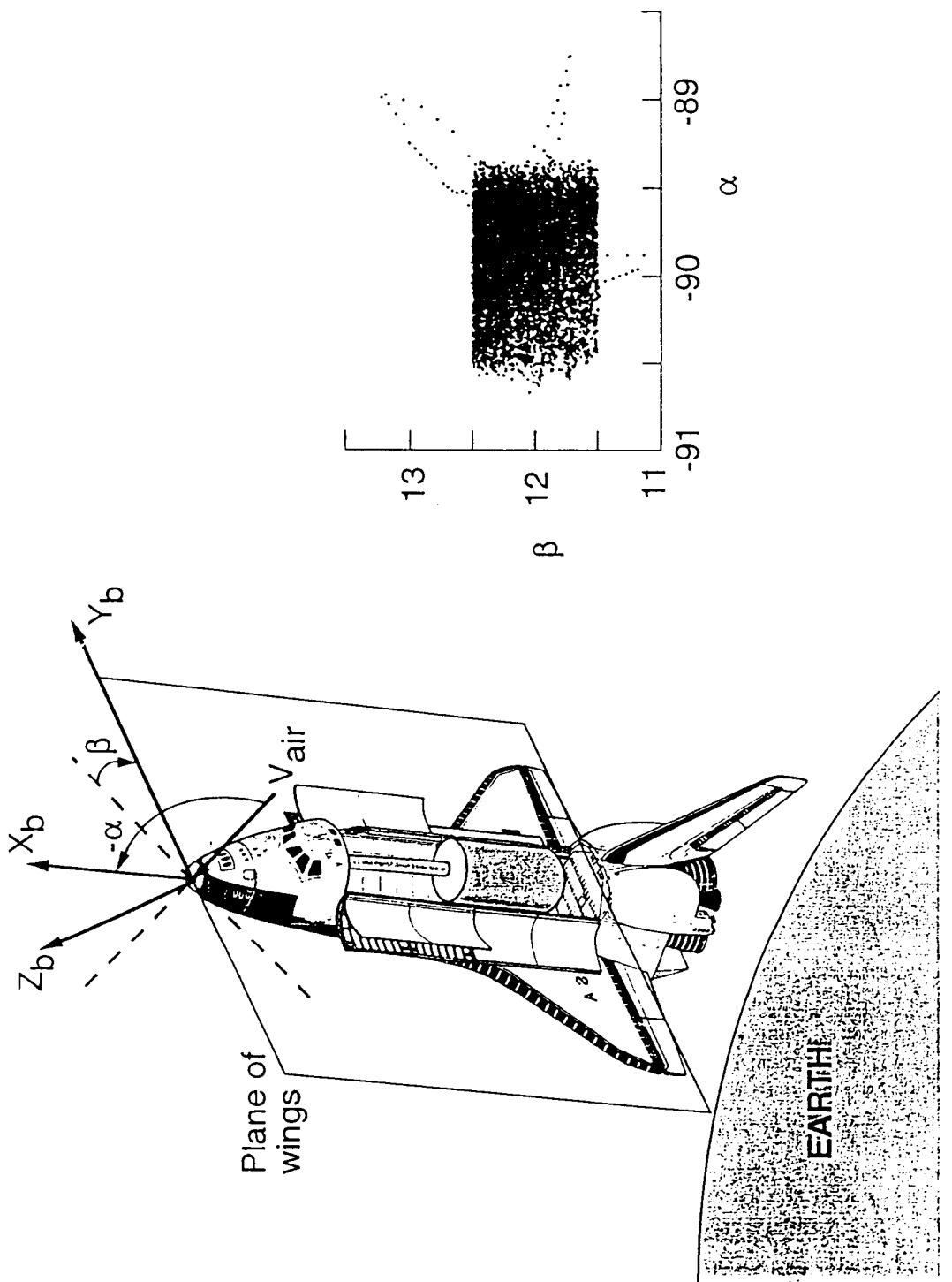


Figure 2 Orbiter orientation and measurements.

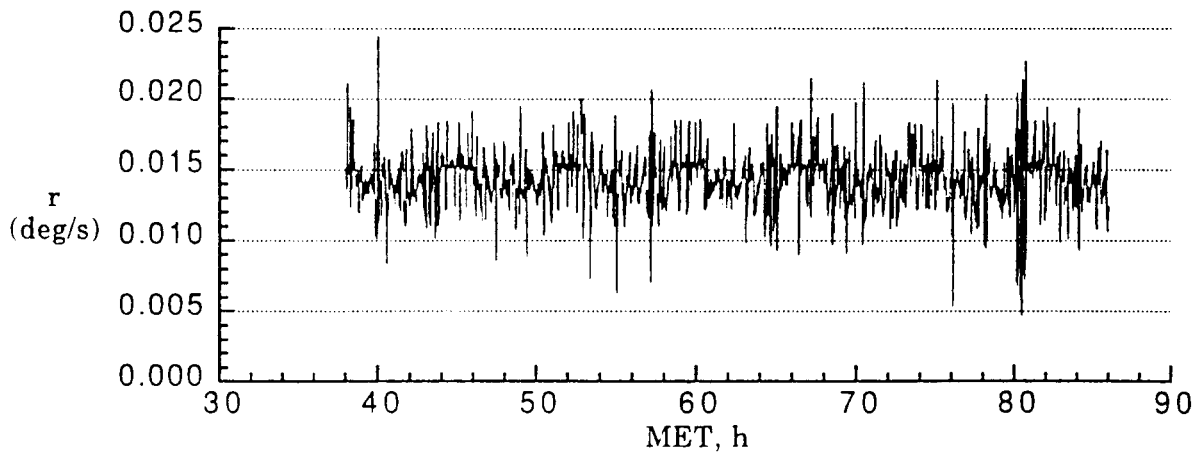
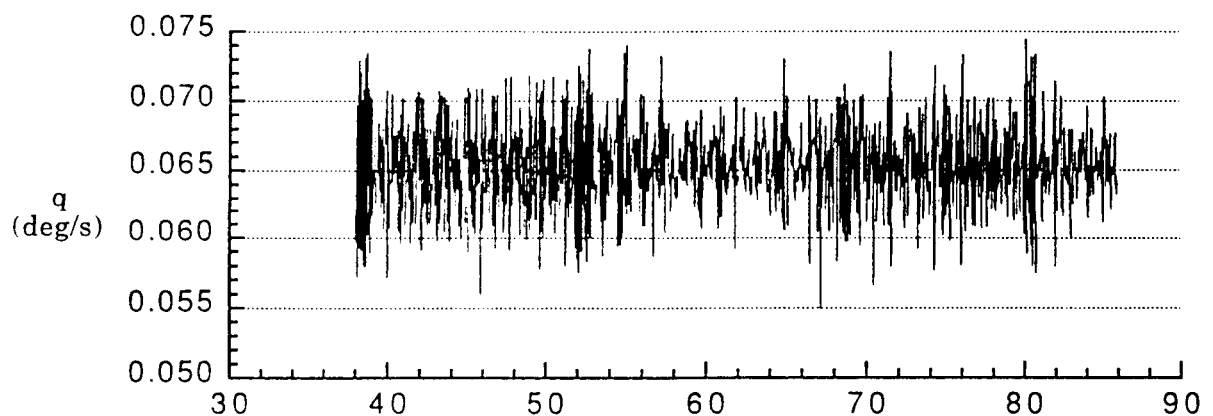
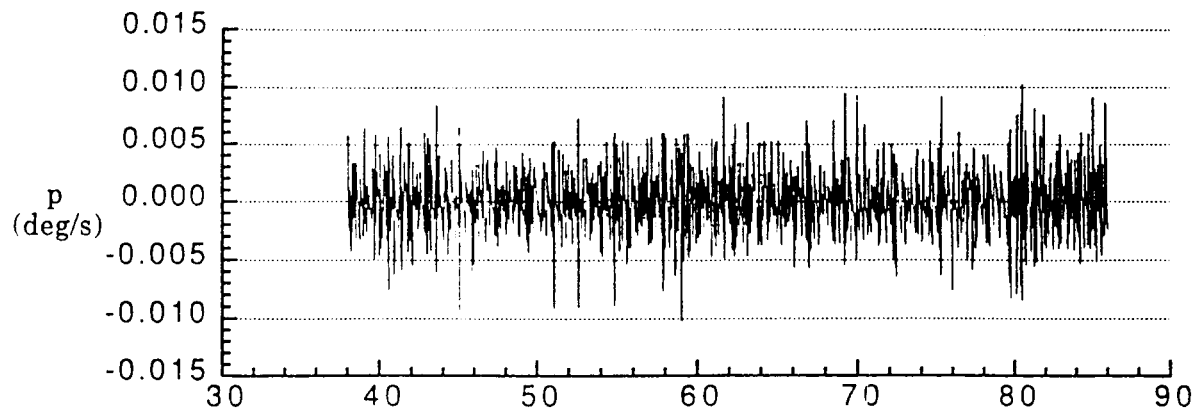


Figure 3 Orbiter angular body rates.

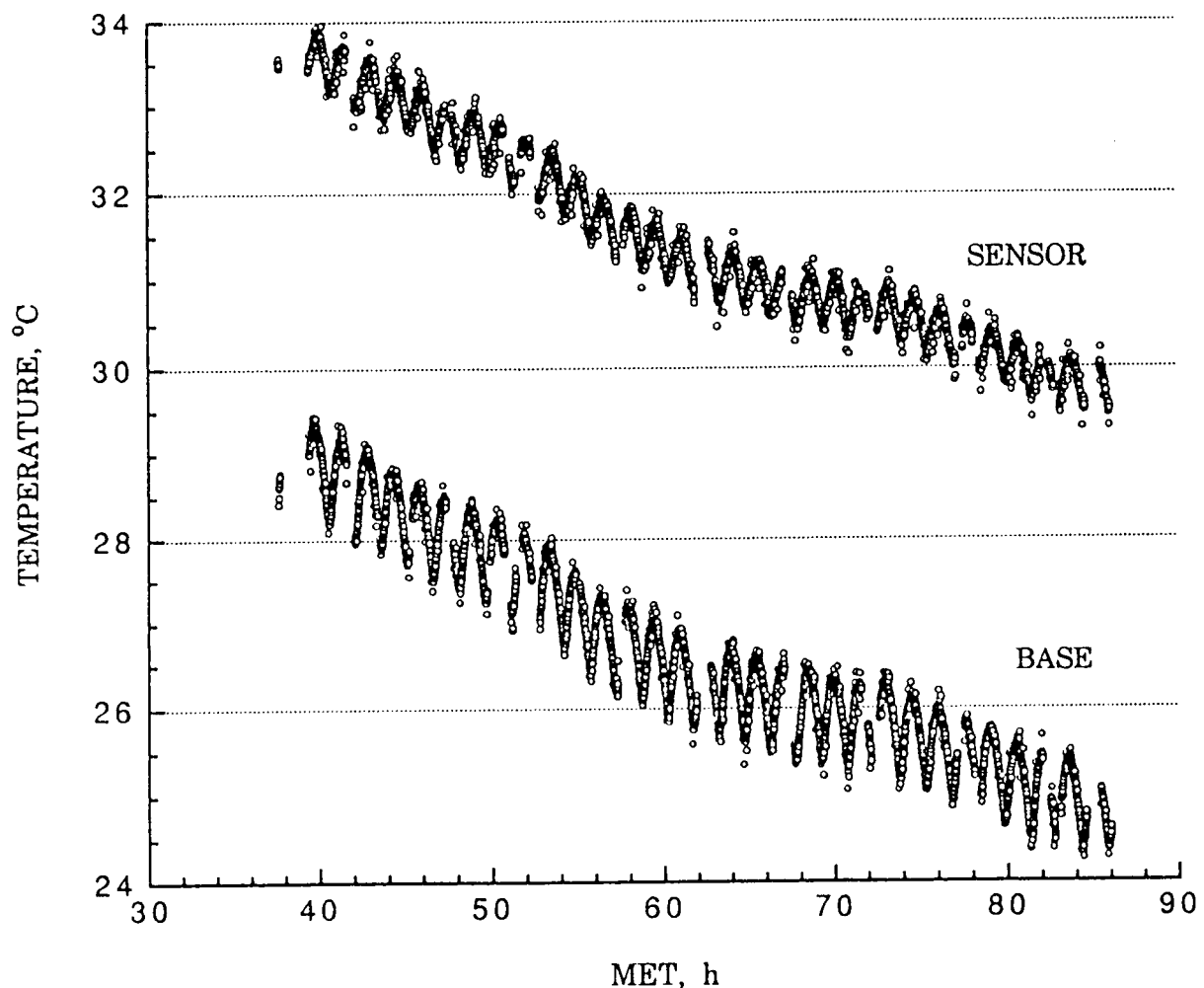


Figure 4 OARE Sensor temperature measurements.

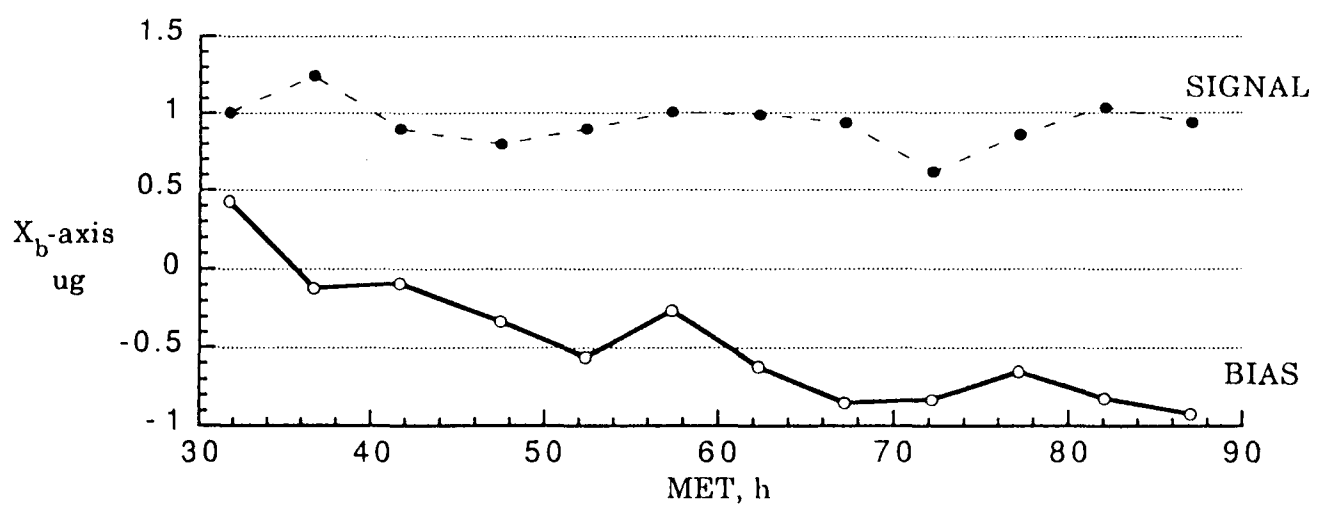
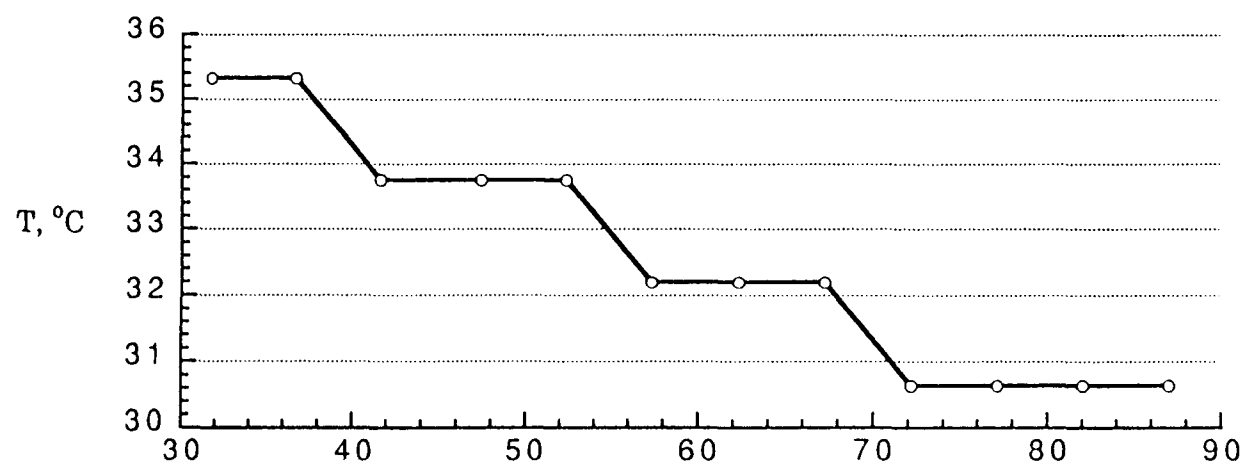


Figure 5 X-body axis sensor temperature, bias, and signal measurements.

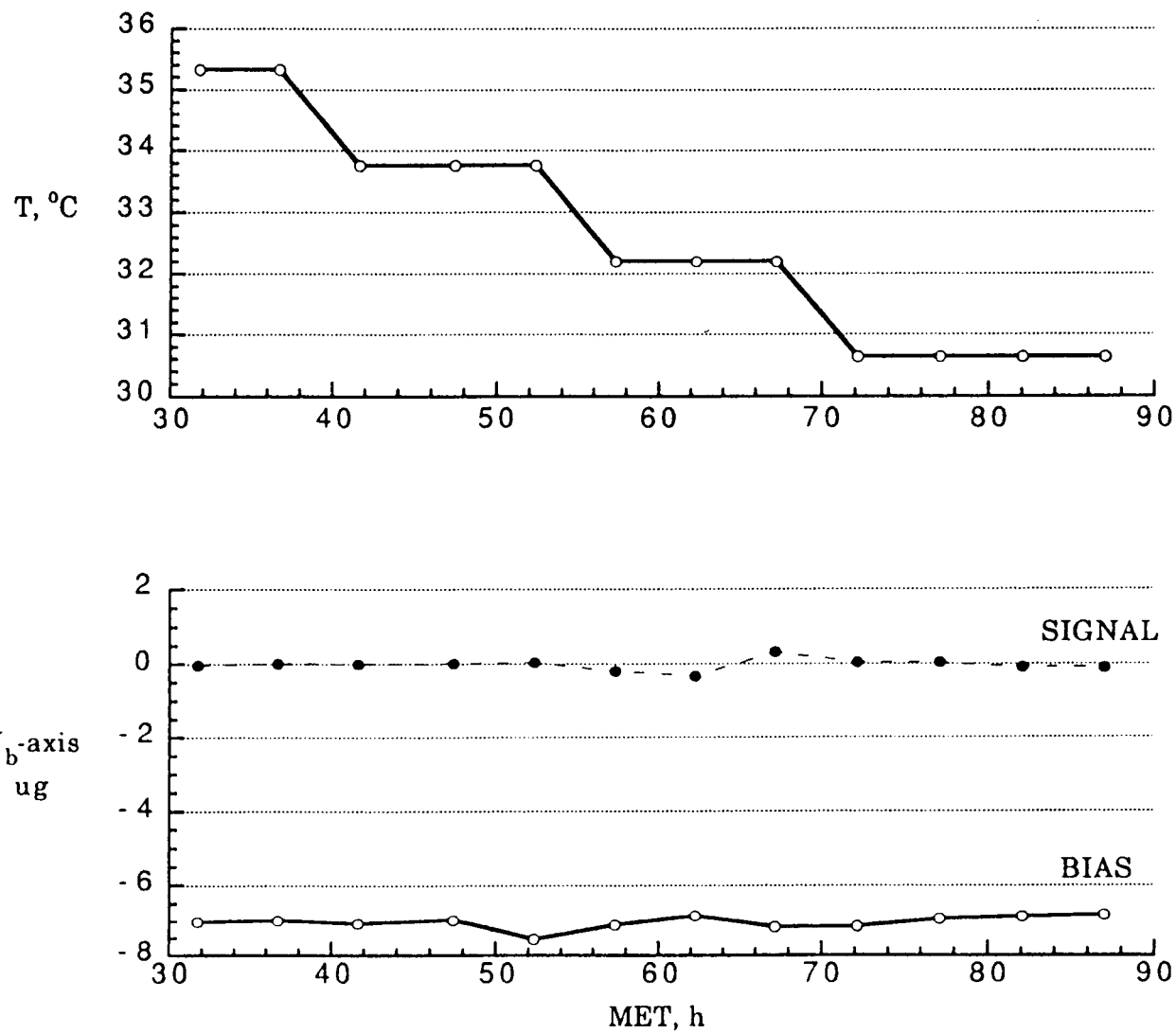


Figure 6 Y body axis sensor temperature, bias, and signal measurements.

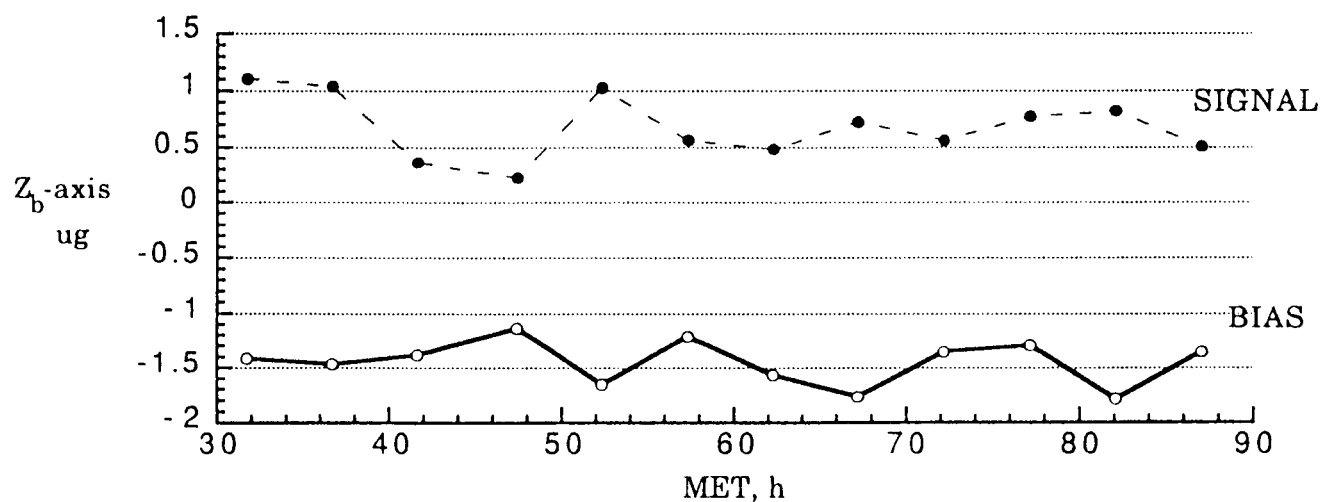
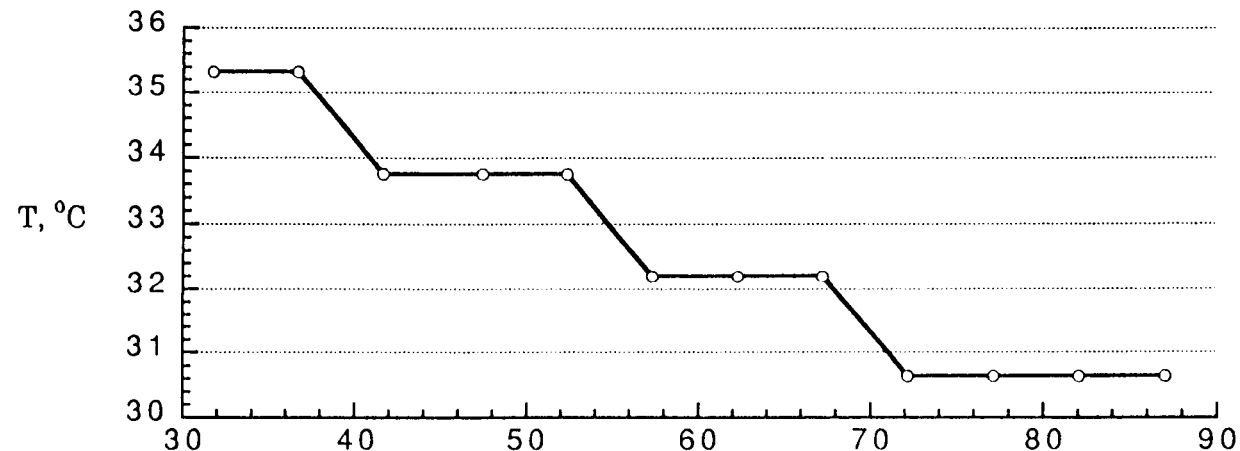


Figure 7 Z body axis sensor temperature, bias, and signal measurements.

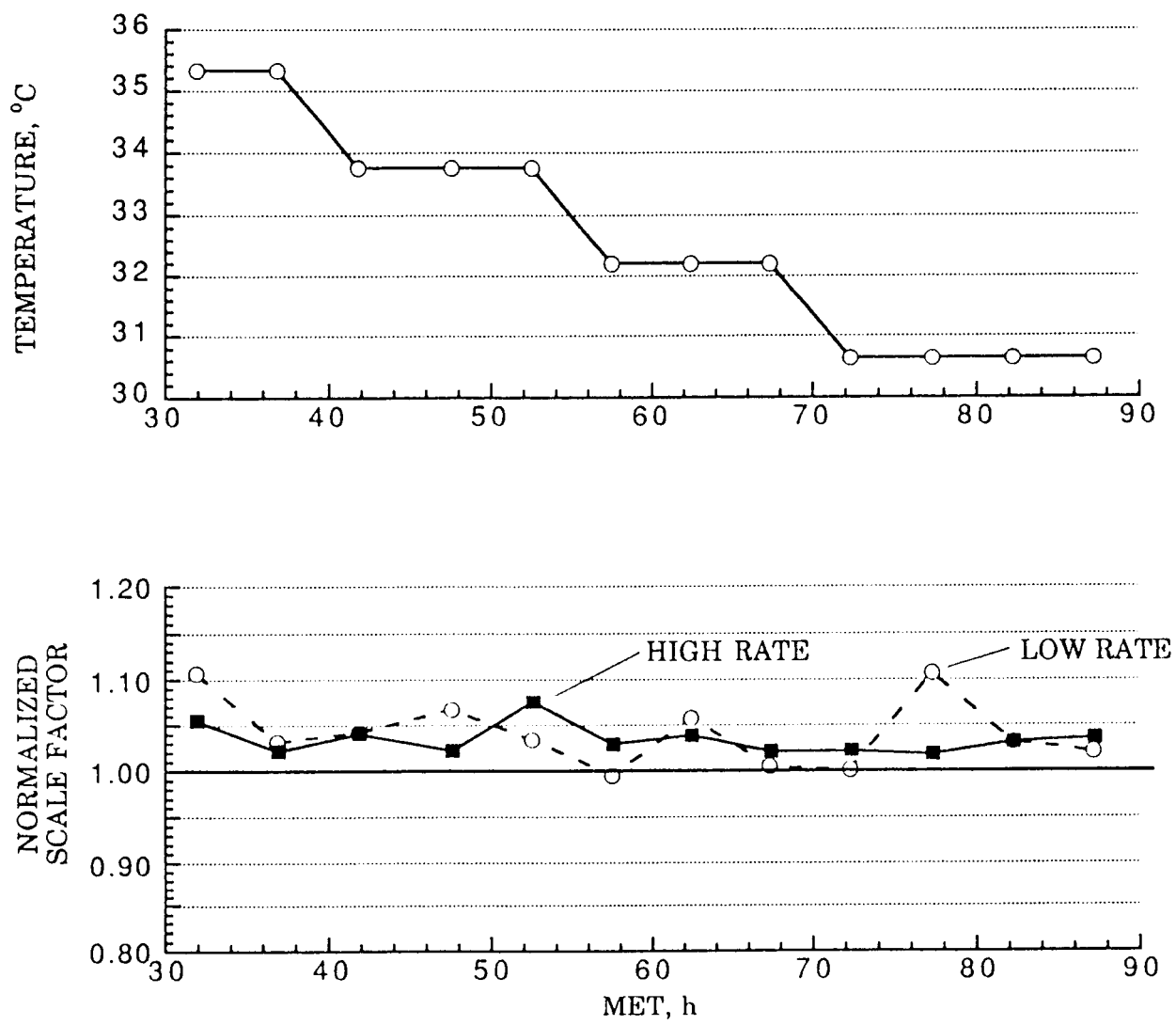


Figure 8 X-axis C-range scale factor measurements.

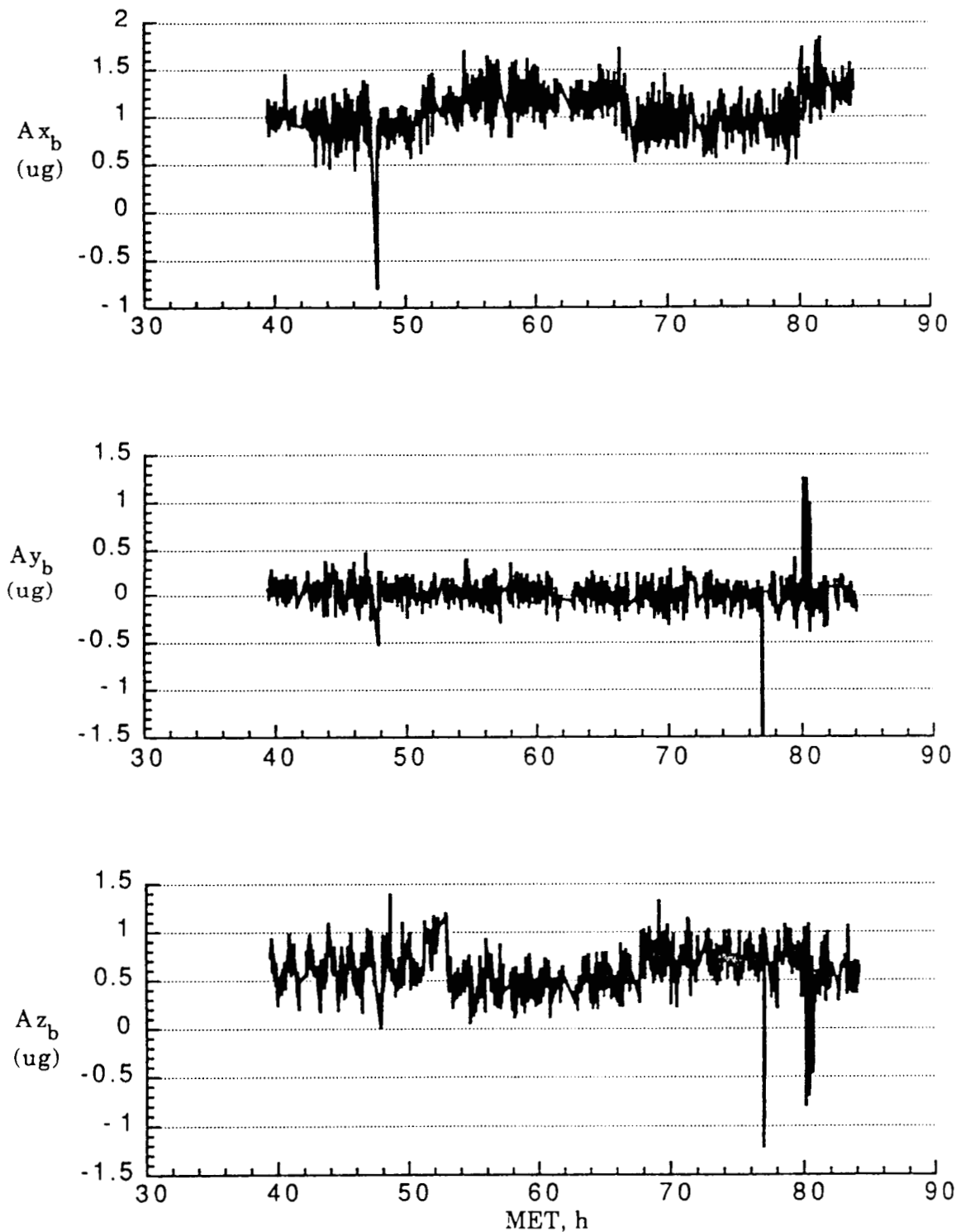


Figure 9 OARE body axes measurements at the OARE location.

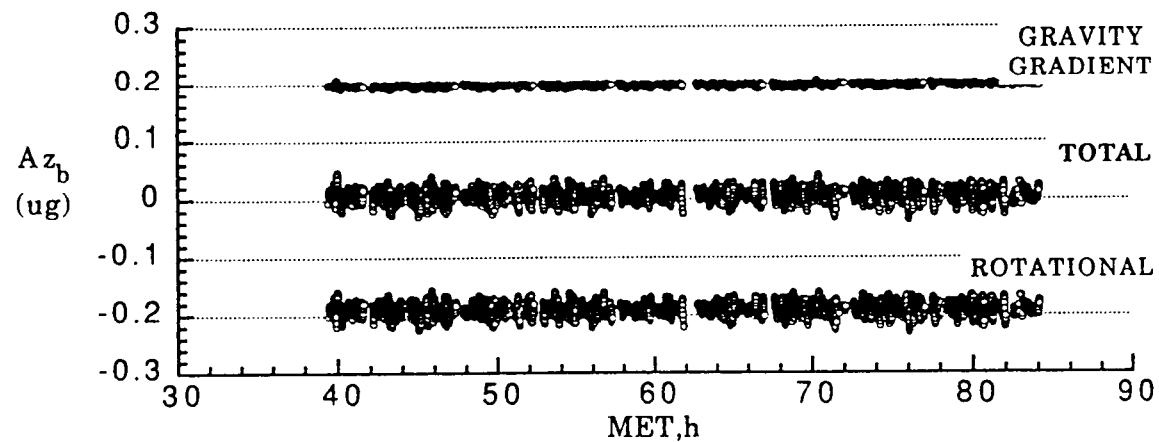
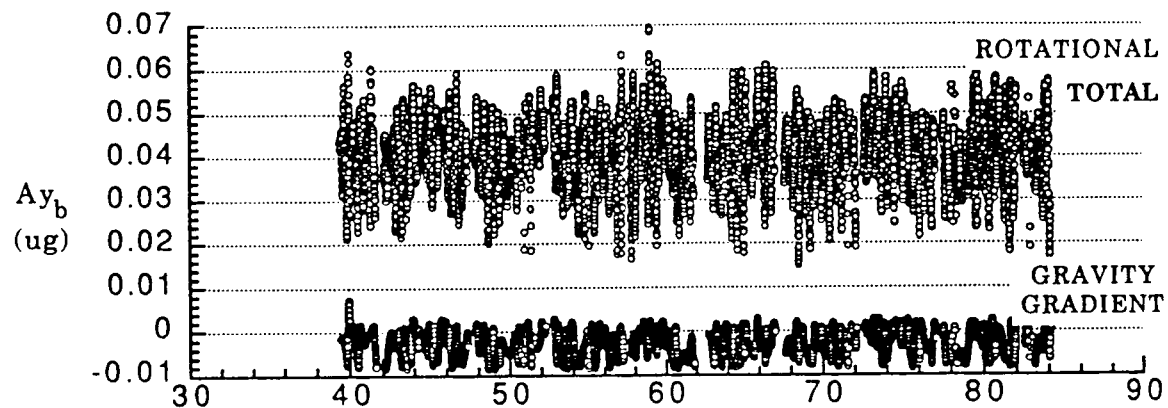
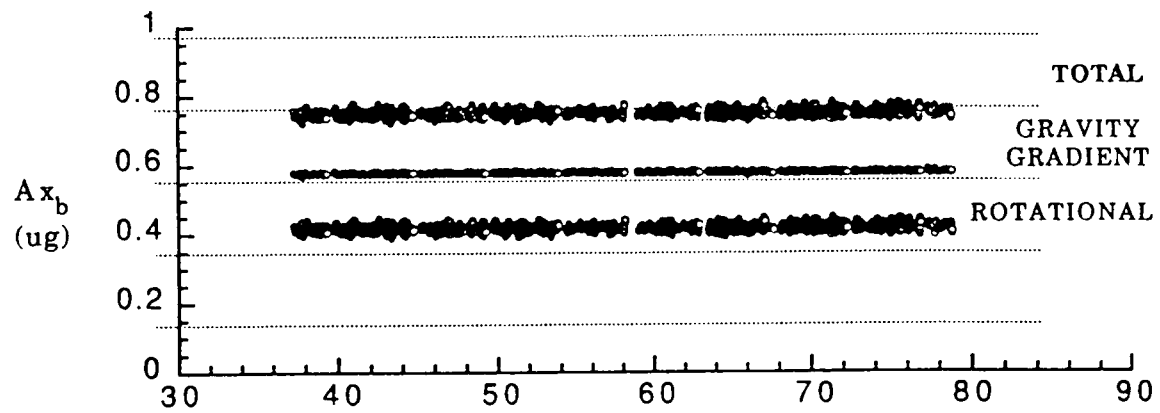


Figure 10 Gravity gradient and rotational accelerations from Orbiter measurements at the OARE location.

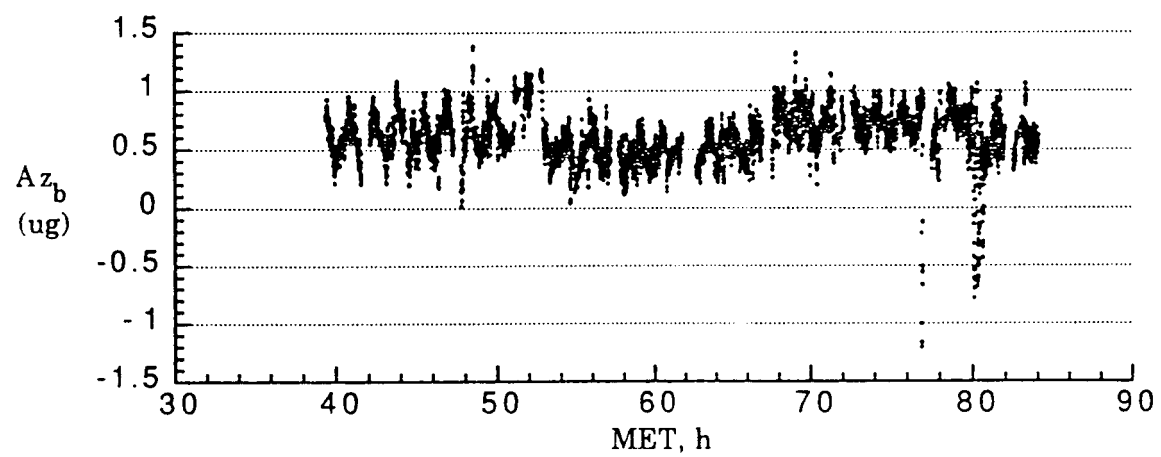
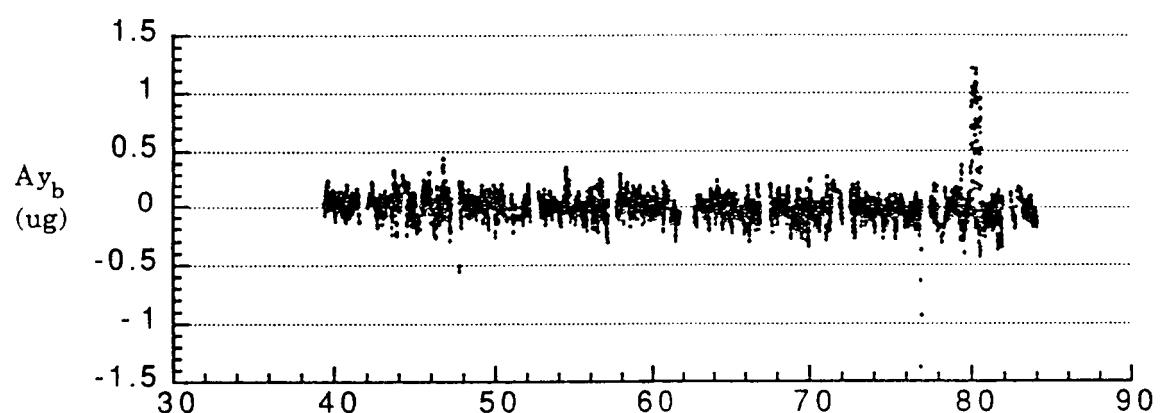
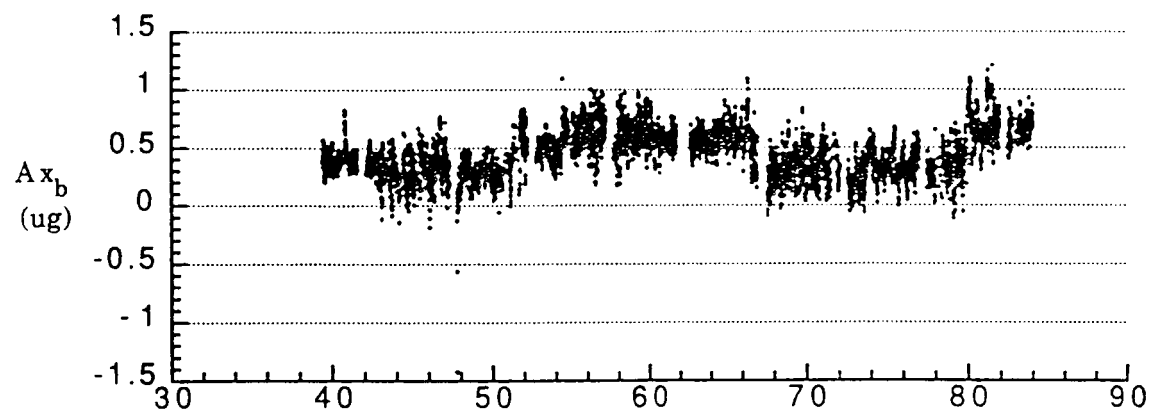


Figure 11 OARE measurements at the center of gravity.

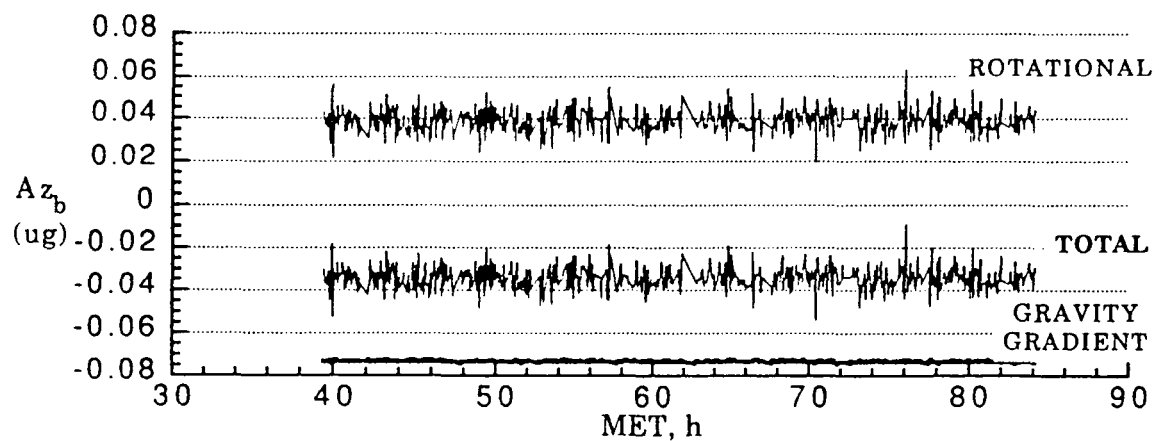
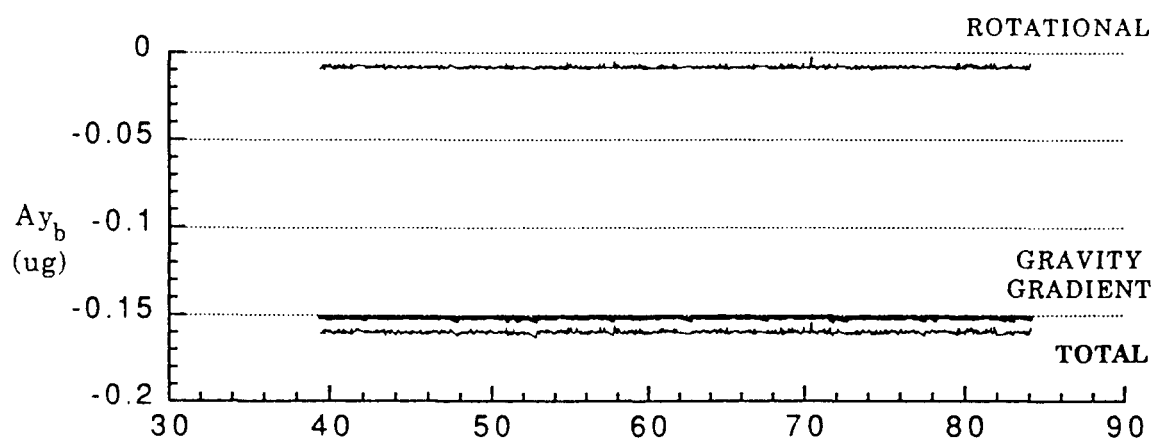
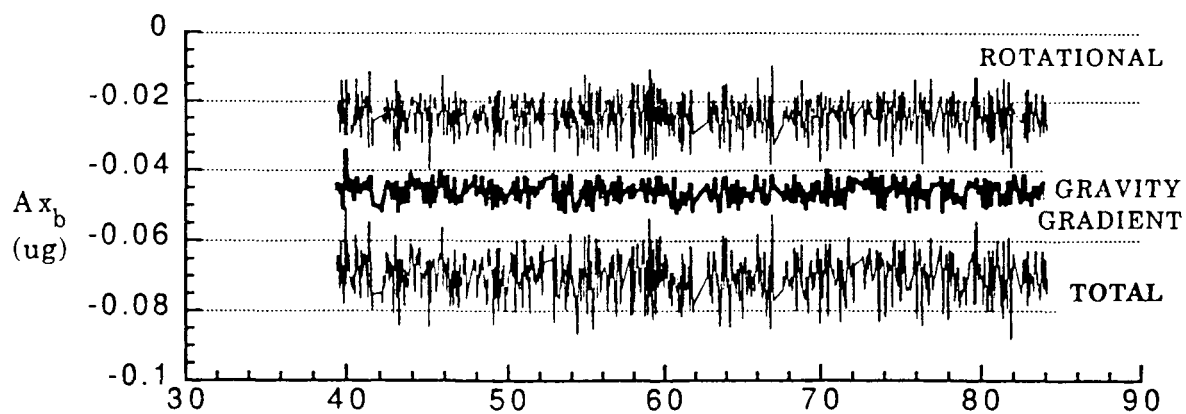


Figure 12 Gravity gradient and rotational accelerations from Orbiter measurements at the CGF location.

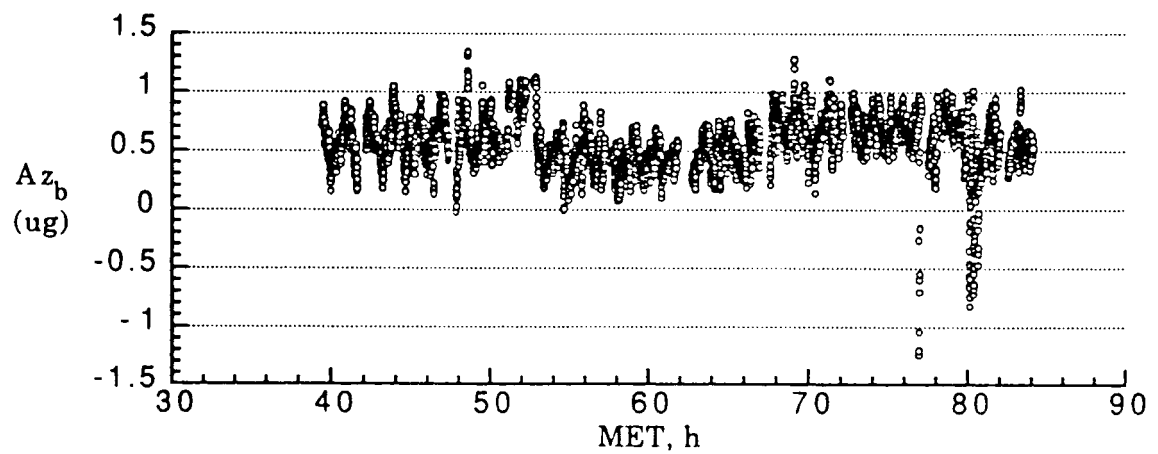
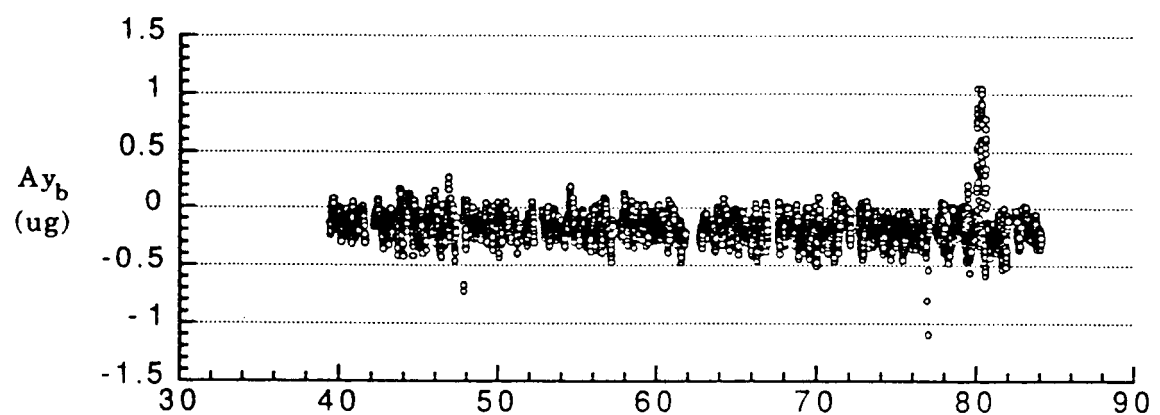
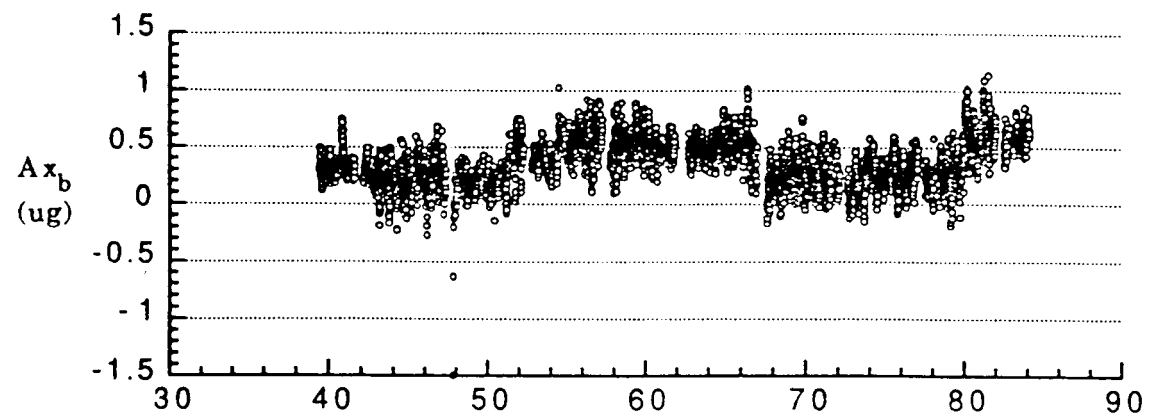


Figure 13 Body axes accelerations at the CGF location ($X_0 = 1086.00$, $Y_0 = 44.39$, $Z_0 = 395.45$) using OARE data.

Discussion

Question: *Is the Flash Evaporation System (FES) the only contributing factor or are there several others that contributed to the measured residual g-levels ?*

Answer: Yes. There is more than just the FES. There are more things that are happening that need to come out and you could not see it on the charts that I showed you because the chart showed you 14 days of data. But if you look at details at various sections on the flight you see that there are more activities ongoing.

Question: *On the z axis data, especially the drag component, were they pretty well what you thought they should be ? Have you looked at that ?*

Answer: Well they are off because of the FES; we have yet to take it out. You saw on the chart I had up earlier, it was off by a factor of 2 or 3 because of the FES.

Question: *If that variation (z-axis data) is in phase with the day/night variation, it could be induced by different rates of out-gassing produced by the sun, i.e. temperatures. Have you examined that scenario ?*

Answer: Yes. That is a good observation. We modeled out gassing as best we can but the values you get are much too big. These values are tenths of a micro-g whereas out-gassing, we feel, will be less than that number, about an order of magnitude less.

Question: *What value of C_D did you pick for your model; 2.3 for all directions ?*

Answer: Yes we used a value of 2.3 but not for all directions. We used a complex model which has all angle of attack variations.

Question: *Do you know enough about the FES to know whether a quick fix will be the feasible thing to do or would you have a recommendation for that ?*

Answer: It doesn't bother me now that I know about it. Now I know where to look so I can look at those moments of the mission when the FES system was off and probably get enough data to satisfy myself and do the calculations I wanted to do. Certainly for people who are worried about the d.c. acceleration levels, that are on the order of 0.2 μg and that affects their experiments, they had better know when that system (FES) is operating because it may produce results that they are not happy with, for that experiment. For my experiment I can go and find the time when it was not operating but I am not sure that is true about everybody's experiment.

34PG

324073

NASA

N95-14213

1995107799

ORBITAL PROCESSING OF
HIGH-QUALITY CdTe COMPOUND SEMICONDUCTORS

P. 33

D. J. Larson, Jr.*, J. I. D. Alexander[†], D. Gillies[‡], F. M. Carlson[§], J. Wu[¶] and D. Black[★]

*Grumman Aerospace Corporation, Bethpage, NY.

†Center for Microgravity and Materials Research, University of Alabama in Huntsville, Huntsville, AL.

‡NASA Marshall Space Flight Center, Huntsville, AL.

§Dept. of Mechanical and Industrial Engineering, Clarkson University, Potsdam, NY.

¶University of New York - Stony Brook, Stony Brook, NY.

★National Institute of Standards and Technology, Gaithesburg, Washington, D.C.

ABSTRACT

CdZnTe crystals were grown in one-g and in μ -g for comparative analysis. The two μ -g crystals were grown in the Crystal Growth Furnace during the First United States Microgravity Laboratory Mission (USML-1). The samples were analyzed for chemical homogeneity, structural perfection, and opto-electronic performance (infrared transmission).

FTIR transmission of both ground and flight materials showed that the infrared transmission was close to theoretical, 63% versus 66%, suggesting that the material was close to the stoichiometric composition during both the ground and flight experiments. Infrared microscopy confirmed that the principal precipitates were Te and their size (1-10 μ m) and density suggested that the primary flight and ground base samples experienced similar cooling rates.

Macrosegregation was predicted, using scaling analysis, to be low even in one-g crystals and this was confirmed experimentally, with nearly diffusion controlled growth achieved even in the partial mixing regime on the ground. Radial segregation was monitored in the flight samples and was found to vary with fraction solidified, but was disturbed due to the asymmetric gravitational and thermal fields experienced by the flight samples.

The flight samples, however, were found to be much higher in structural perfection than the ground samples produced in the same furnace under identical growth conditions except for the gravitational level. Rocking curve widths were found to be substantially reduced, from 20/35 (one-g) to 9/20 (μ -g) for the best regions of the crystals. The FWHM of 9 arc seconds is as good as the best reported terrestrially for this material. The ground samples were found to have a fully developed mosaic structure consisting of subgrains, whereas the flight sample dislocations were discrete and no mosaic

substructure was evident. The defect density was reduced from 50-100,000 (one-g) to 500-2500 EPD (μ -g). These results were confirmed using rocking curve analysis, synchrotron topography, and etch pit analysis.

The low dislocation density is thought to have resulted from the near-absence of hydrostatic pressure which allowed the melt to solidify with minimum or no wall contact, resulting in very low stress being exerted on the crystal during growth or during post-solidification cooling.

INTRODUCTION

CdZnTe is a technologically important member of the family of II-VI compound semiconductors. The most important application of CdZnTe is as a lattice-matched substrate for the epitaxial growth of HgCdTe infrared detectors. The requirements for large area infrared devices have led to increased reliance on epitaxial processes to provide detector-grade material and a concomitant demand for high quality substrates. These substrates are typically grown using unseeded, modified horizontal and vertical Bridgman crystal growth techniques.

Presently, HgCdTe epilayers are most frequently fabricated using liquid phase epitaxy (LPE). However, to achieve abrupt device/substrate junctions, epitaxial growth of HgCdTe has been driven to lower temperatures, using chemical vapor deposition or molecular beam techniques. These techniques minimize interdiffusion, but they are much more sensitive to wafer quality, particularly at the surface. In addition, fast diffusion of Hg along dislocation cores has resulted in demands for the minimization of extended defects. This requirement has led to a demand for reduced defect densities in the substrates, as these extended defects are likely to project from the wafer surface into the epilayer.

One solution is to lattice-match the substrate and the epitaxial layer at the growth temperature in order to minimize interfacial strains and dislocation generation, propagation, and/or multiplication at the substrate/epilayer interface. The lattice-matched substrate of choice is CdZnTe. The primary needs for these CdZnTe applications are therefore (1) increased structural perfection (reduced defect density) within the bulk crystals and substrates, and (2) more uniform lattice parameters (chemical homogeneity) within the substrates, which better match those of the specific HgCdTe composition at the epitaxial growth temperature.

The program described in this paper was initiated to investigate quantitatively the influences of gravitationally dependent phenomena on the growth and quality of compound semiconductors as a means of improving crystal quality (structural and compositional) and to better understand and control the variables within the production process. The empirical effort entailed the development of a one-g experiment baseline for quantitative comparison with the microgravity results. This empirical effort was supported by the development of high-fidelity process models of heat transfer, fluid flow and solute

redistribution, and thermomechanical stress occurring in the furnace, safety cartridge, ampoule, and sample throughout the melting, solidification, and post-solidification processing.

The models were initially used to predict the impact of process parameter variation (trend analysis), allowing us to design critical one-g growth experiments. Subsequently, as the models were empiricized, correlation and optimization experiments in one-g and in microgravity experiments were conducted. Finally, the models were utilized to assist in the interpretation of the flight results and the quantitative comparison of flight and ground base results.

I. EXPERIMENTAL TECHNIQUE

The samples on USML-1 were processed in the Crystal Growth Furnace (CGF) using the seeded Bridgman-Stockbarger method of crystal growth. Bridgman-Stockbarger crystal growth is accomplished by establishing isothermal hot zone and cold zone temperatures with a uniform thermal gradient in between. The thermal gradient spans the melting point of the material (1095°C). After sample insertion, the furnace's hot and cold zones are ramped to temperature (1175°C and 980°C, respectively), establishing a thermal gradient (30°C/cm) in between and melting the bulk of the sample. The furnace is then programmed to move farther back on the sample, causing the bulk melt to come into contact with the high-quality seed crystal, thus seeding the melt. The seed crystal prescribes the growth orientation of the crystal grown. Having seeded the melt, the furnace translation is reversed and the sample is directionally solidified at a uniform velocity (1.6 mm/hr) by moving the furnace and the thermal gradient over the stationary sample.

The CGF samples were characterized and the results from one-g and μ -g were quantitatively compared with respect to chemical homogeneity and structural quality. These 'internal' results were then quantitatively compared with the best results accomplished terrestrially as an 'external' comparison. The 'external' samples were fabricated using the same growth method and the Grumman Programmable Multi-Zone Furnace (PMZF) operated in a low gradient configuration (<10°C/cm). This PMZF material has been shown in the ARPA Infrared Materials Producibility Program to compare favorably with the best CdZnTe crystals grown terrestrially.

The characterization techniques employed in this study included x-ray double crystal rocking curve (DCRC), x-ray precision lattice parameter (PLP), energy dispersive x-ray analysis (EDX), photoreflectance (PR), synchrotron white beam topography (SWBT), and synchrotron monochromatic beam topography (SMBT). Both SWBT (Ref. 1) and SMBT were performed at the National Synchrotron Light Source (NSLS) at the Brookhaven National Laboratory (BNL). The DCRC and PLP measurements were made at Grumman using Blake Instruments custom systems, with Copper radiation and a spot size of $\sim 1\text{mm}^2$. The EDX and microprobe measurements were made at the Marshall Space Flight Center.

PR (Ref. 2) was carried out at 300K using a He-Ne laser chopped at 200 Hz, a monochromator resolution of about 25 Angstroms and a typical spot size of ~1mm. The energy gap was determined from a lineshape fit using the low-field approximation (Ref. 3,4); the zinc content (x) in $\text{Cd}_{(1-x)}\text{Zn}_x\text{Te}$ was derived from the "calibration curve" of Ref. 2, assuming a constant energy shift in the curve to account for our use of 300K rather than 77K. For DCRC, PLP, and PR the sample was mounted on a micropositioner stage which allowed manual or automatic scanning over the sample surface. All samples were identically chemomechanically polished using a dilute Br-methanol solution (Ref. 5).

II. EXPERIMENTAL PLAN

A. Ground

Ground-base qualification and developmental tests were conducted in the CGF Ground Control Experiments Laboratory (GCEL) to confirm hardware designs for the sample/ampoule, ampoule/cartridge, and the interfaces between these components and instrumentation within the Sample/Ampoule Cartridge Assembly (SACA). Figure 1 shows the ampoule design and location of the instrumentation thermocouples. In addition, timeline compatibility between the four experiments that were to run in series in the CGF on USML-1 and the flight timeline was confirmed. Lastly, the test results served to empiricize the process models and optimized the processing parameters for the flight experiment.

The final CGF ground sample, grown under the optimized process conditions, duplicated the anticipated flight conditions and served as a 'ground truth' sample for quantitative comparison with the primary flight sample. Since we were fortunate to have the opportunity to conduct a second experiment with the flight back-up (secondary) sample, the 'ground truth' experiment for the secondary sample was conducted post-flight. Analyses of these samples focused on the chemical homogeneity and the structural quality of the crystals.

In addition to the CGF 'internal' baseline, an additional 'external' baseline was established using the Programmable Multi-Zone Furnace at the Grumman Corporate Research Center. This furnace system employed lower thermal gradients (<10°C/cm) and slower heating and cooling rates (1°C/min) in order to minimize the thermo-elastic stresses imposed on the sample during processing. These samples were 38mm in diameter as compared to the CGF samples which measured 15mm in diameter. These results were intended to serve as an external comparative baseline representative of the best CdZnTe produced terrestrially. This material has been shown in the ARPA Infrared Materials Producibility Program to compare favorably with the best CdZnTe crystals grown terrestrially.

B. Flight

The USML-1 Mission was planned to process one primary sample, with a back-up sample in stowage outside of the CGF Furnace. The primary sample was successfully processed and due to the premature termination of one of the other experiments, a second flight experiment was possible, but of shorter duration. The furnace heat-up rate, seeding and thermal equilibration time, temperature profile, and cooling rate were identical for both experiments; the primary difference being the duration of the experiments. Since the samples were of identical lengths, this meant that the secondary sample was furnace cooled prior to the completion of solidification of the sample, and a substantial amount of material was solidified under non-plane-front growth conditions. The secondary sample served to confirm the successful seeding technique and to provide additional material from the shouldering region that solidified without wall contact.

Conducting the second experiment demanded unprecedented actions on the part of the crew, particularly: Payload Specialist Eugene Trinh to install the flexible glove box on the CGF, which enabled the processed SACAs to be removed from the CGF; Alternate Payload Specialist Al Sacco to develop the SACA exchange procedures; and Payload Commander Bonnie Dunbar and Pilot Ken Bowersox who exchanged the SACAs, demonstrating for the first time in the US program the ability to exchange potentially toxic materials in the closed environment of the Spacelab. These actions proved the feasibility of conducting similar necessary operations on Space Station, greatly increasing the productivity.

III. EXPERIMENT RESULTS

The Temperature/Time/Position history of the optimized ground experiment is shown as Figure 2. The heat-up rate ($2^{\circ}\text{C}/\text{min}$), thermal equilibration time (2 hrs), solidification velocity (1.6 mm/hr), applied thermal gradient ($33^{\circ}\text{C}/\text{cm}$) and cool-down rates ($2^{\circ}\text{C}/\text{min}$) were determined to give the best quality crystals that were consistent with the available flight time and the performance characteristics of the CGF. A ground sample with good crystallinity, grown on the Grumman PMZF in the NASA flight geometry, is shown as Figure 3. This sample is dominated by a large single crystal with a localized twin and a secondary grain nucleated late in the growth process.

The scaling analysis done by Alexander et al (Ref. 7) suggested that the macrosegregation in this system should be relatively low, even in one-g. Chemical mapping of the one-g samples using EDX, microprobe, PR and PLP measurements confirmed this prediction. A typical fit is shown as Figure 4. The shape of the curve suggests that fluid flow is relatively benign and transport is close to diffusion controlled growth, even though still within the partial mixing regime in one-g. The emphasis in analyzing the chemical homogeneity of the flight samples was thus be placed on evaluation of the radial

segregation, since diffusion controlled growth was anticipated. The PMZF 38 mm diameter samples exhibited a solute redistribution coefficient K_e of 1.10, as compared to the equilibrium redistribution coefficient of 1.22. This strongly suggested that the partial mixing in the melt was benign and that diffusion controlled growth could be approached on the ground in large diameter ingots solidified under optimized thermal control longitudinally and radially.

Electro-optical analysis of the CGF ground-base samples indicated that the FTIR transmission was approximately 63% and uniform from 2.5 to 25 microns. This is quite good, as theoretical transmission is approximately 66%. The PMZF material, approached 66%. The flight material was found to be almost identical to the CGF ground material.

Structural analysis indicated that the sample morphology consisted of a mosaic of cells defined by subgrains. Typical rocking curve widths varied systematically from 20 to 35 arc seconds, full width half maximum (FWHM), with the maximum widths at the periphery of the wafer, the minimum midway between the center and the periphery, and the expected 'W' shape from edge to edge.

The Temperature/Time/Position history of the primary flight sample is shown as Figure 5. The major differences between the flight samples and those processed identically on the ground was a measurable difference in the amount of heat flux due to gravitational 'draining' of the liquid volume toward the seed crystal as the sample melted. No thermal surge in temperature at the seed crystal was noted in the flight experiments, suggesting that the transport of the bulk liquid toward the seed was slower and that less fluid volume was transported.

The processed flight ampoules are shown in Figure 6, and radiographs of the interior of the flight ampoules are shown in Figures 7a (primary sample, GCRC-1) and 7b (secondary sample, GCRC-2). It should be noted that the separate bulk liquid was brought in contact with the seed crystal due to the residual gravitational vector, and since the liquid will always wet its own solid, the seeding operation was successful in both instances.

Careful inspection of the radiographs in Figures 7 shows that both of the crystals grown are separated from the ampoule wall in the shoulder region. This was anticipated and is referred to as 'dewetting', though this term is not strictly correct. Wall contact is not reestablished until the full ampoule cross-section is reached in the steady state region of growth.

It was anticipated that the residual g-vector pointed down the axis of the CGF would result in a thermally and gravitationally symmetric geometry that was thermally stabilizing for our experiment. The orientation of the calculated residual g-vector relative to the Spacelab and the CGF is shown in Figure 8 (Ref. 7). Inspection of the flight samples suggested that this was not correct in the actual experiment. Figure 9 shows the actual primary flight sample after sand blasting the surface. It may be seen that the

sample has a high degree of crystallinity, with a bubble at the top of the shoulder which initiated a twin, and porosity later in the experiment when the sample was furnace cooled.

Analysis of the acceleration data from the mission suggested that there was an unanticipated gravitational component that resulted in gravitational asymmetry at the CGF location (Ref. 7). This was due to the operation of the Shuttle Flash Evaporator System (FES), which operated on approximately a 28 hour cycle (14 hours on and 14 hours off). Figures 10a and 10b show the average orientation of the residual acceleration vector when FES was on, recorded by (a) OARE at the OARE location and extrapolated to the CGF location and (b) PAS on the Flight Deck and extrapolated to the CGF location. It is clear that this is significantly asymmetric relative to the CGF furnace bore axis and could result in thermal and gravitational asymmetry in the flight samples.

The color pattern and surface texture pattern on the surface of the GCRC-1 flight sample, shown in Figures 11 (prior to sand blasting the surface), suggest that each sample solidified without wall contact throughout the shoulder and that when wall contact was resumed, it was only on one side of the ampoule. Partial wall contact would be expected to result from gravitational asymmetry, which was not anticipated and would be expected to cause significant disturbance thermally, possibly solutally, and possibly mechanically because of the absence of hoop stresses during cooling on the free surface side of the sample.

Examination of the surface topography of the primary flight sample, Figure 11a, shows that the areas in full contact with the ampoule wall mirror the surface topography of the wall and appear visually to be very bright surfaces. The topography of the free surfaces shows some thermal etching, but is relatively smooth and has the blue-grey appearance of most semiconductors. The region of partial wall contact, however, is a highly textured matte finish. The surface was found to be comprised of a honeycomb of interconnected hexagonal cells that are nearly perfect hexagons nearest the region of full wall contact and which get progressively more elongated circumferentially as the liquid moves away from the wall. This pattern of contact is shown in Figure 11(b).

Synchrotron White Beam Topography was used to evaluate the surface condition of the flight samples in the three regions of varying wall contact. The regions of total wall contact gave very poor topographic images (not shown), suggesting high levels of surface strain. The regions of no wall contact, however, gave high quality topographs which suggested that the residual strain levels were very low and images of the defect structure suggested the possibility that the defect density was low and that dislocations present were discrete rather than in a fine subgrain or mosaic structure. The regions of no wall contact showed no sign of twinning at the surface. The regions of partial contact, however, showed strong evidence of cross slip, and occasional twinning. Deformation of this type was restricted to the regions of partial wall contact and suggested that the honeycomb surface structure may have acted as a

series of stiction points for the solidification interface resulting in much higher local stresses and concomitant plastic deformation by dislocation and twinning mechanisms.

A topograph of a region of the primary sample that solidified with no wall contact is shown as Figure 12a and a region of the same sample solidified with partial wall contact is shown as Figure 12b. Note the discrete dislocation pattern and low dislocation density in 12a and the high density of dislocations manifested as occasional twinning and extensive slip and in 12b.

Having thoroughly analyzed the surfaces of the samples, the crystals were then oriented using x-ray techniques and wafered such that the wafer surfaces were $\{111\}$ planes, which is the industry standard. The sectioning plan for the secondary flight sample, which was cropped to remove the portion of the sample that was not plane-front solidified, is shown schematically in Figure 13. The primary sample was sectioned on a $\{111\}$ plane that was closer to the growth axis of the crystal. The series of real wafers is shown in Figure 14a and the etched wafer surfaces are shown as Figure 14b. The wafers were etched with a lactic acid etchant that differentiates between the A and B faces; A (Cd, Zn) appearing dark and B (Te) appearing light. X-ray synchrotron Bragg reflection topography confirmed that the sample surfaces are entirely $\{111\}$, however, there is 180° rotational twinning such that the left third of the wafers are predominantly A faces whereas the remaining portion consists of a single B face. The left side experienced wall contact whereas the right did not. The flight samples were analyzed using DCRC mapping as a measure of residual strain in the crystal. The results suggest that the quality of the flight material, as judged by the full width half maximum (FWHM) of the $\{333\}$ Bragg diffraction peak, is substantially better than that recorded for the ground truth samples. Area maps of the FWHM for flight wafer 7 is shown as Figure 15. It should be noted that appreciable areas of the flight samples average FWHM values between 10 and 15 arc-seconds, whereas the same regions in the ground truth samples averaged 20 to 35 arc seconds. The strain in the best regions of the flight samples, as indicated by the FWHM of the $\{333\}$ rocking curve is as low as 9.2 arc seconds. This is fully comparable to the best material that has been grown on the ground using the PMZF technology or any other commercial technology.

The peak distributions are also much different in that the best material is found close to the sample periphery whereas the ground samples evidenced maximum strain and peak width at the periphery. This suggests that unlike the ground samples that were forced to be in mechanical contact with the ampoule walls during processing, the flight samples were not, with a resultant significant reduction in strain. Post flight modeling of this process confirms this suggestion, with the stress experienced by the free surface significantly lower than that at the wall. This is shown in Figure 16.

A further difference between the flight samples and the ground base samples appears in the shape of the DCRC peaks. Figure 17a shows a typical DCRC peak and Gaussian fit for a good region of

a ground sample. The FWHM is about 20 arc-seconds and the fit at the base of the peak, the 'tail' of the curve, is quite poor. This indicates that agreement between diffraction theory and real diffraction is not good. This deviation occurs because the 'tails' of the curve represent the defect structure of the real samples and the defect distribution in these samples is not the ideal distribution that the theory assumes. Figure 17b shows the same peak and fit, except that it is plotted on a log plot which emphasizes the tails of the curve and focuses attention on the lack of agreement between theory and practice. Figure 18 is a ground sample from a complementary study, where the tails of the curve are well described by kinematic diffraction theory. This sample region had a well developed mosaic substructure that conforms well to the description of an 'ideally imperfect' crystal. Figure 19 shows a typical {333} rocking curve peak from a low strain region of the flight material. In this case the tails of the curve are very well described by the Gaussian fit and, taken in concert with the low density discrete dislocation regions imaged on the flight sample surfaces (see Figure 12a), suggested the possibility that this material was 'ideally perfect' material rather than the aforementioned 'ideally imperfect' material which we commonly encounter.

The critical test for this hypothesis was to image the samples topographically in transmission, so that the dislocation structure is imaged directly. Samples of the flight and ground-base materials were chemo-mechanically polished to $\leq 180\mu\text{m}$ in thickness and were exposed to monochromatic synchrotron radiation. Only the flight sample could be brought into diffraction; insufficient transmission resulting in no topographic imaging for the ground samples. This suggested the possibility that the higher strain content of the ground samples prevented sufficient transmission whereas the flight sample permitted transmission due to greater crystalline perfection and lower strain. Figure 20 shows the result of this test and clearly shows that the dislocations are low in density and are discrete over large (relative) areas. The singular bright spots are thought to be Te precipitates and the two long straight lines are two variants of {111}[110] twins. This micrograph confirms the discrete nature of the dislocations in the flight material and subsequent dislocation etching of this surface suggested that the dislocation density of this material varied between 500 and 2500 EPD with no mosaic substructure whereas the ground truth material was typically 50,000 to 100,000 EPD and the dislocations formed a continuous mosaic structure.

CONCLUSIONS

FTIR transmission of both ground and flight materials showed that the infrared transmission was close to theoretical, 63% versus 66%, suggesting that the crystals grown were close to the stoichiometric composition in both the ground and flight experiments. Infrared microscopy confirmed that the principal precipitates were Te and their size ($<1\text{-}10\ \mu\text{m}$) and density suggested that the primary flight and ground-base samples experienced similar cooling rates and were similar in composition.

Macrosegregation was predicted, using scaling analysis, to be low even in one-g crystals and this was confirmed experimentally. Nearly diffusion controlled growth was achieved even in the partial mixing regime on the ground. Radial segregation was monitored in the flight samples and was found to vary with fraction solidified, but was disturbed due to the asymmetric gravitational and thermal fields experienced by the flight samples.

The flight samples were found to be much higher in structural perfection than the ground samples produced in the same furnace under identical growth conditions except for the gravitational level. The flight material was properly described as 'ideally perfect' material from a diffraction standpoint, whereas ground material was described as ideally imperfect material. The rocking curve width of the best flight material matched the best achieved terrestrially, 9.2 arc-seconds, using any growth technique. The dislocation density was reduced from 50-100,000 in the ground samples, to 500-2500 in the flight samples. The low dislocation density completely eliminated the dislocation substructure that is typical of all ground material. The dislocation reduction is thought to have resulted from the near-absence of hydrostatic pressure in μ -g, which allowed the melt to solidify with minimum or no wall contact, resulting in very low stress being exerted on the crystal during growth and during post-solidification cooling.

ACKNOWLEDGMENTS

We gratefully acknowledge financial support under NASA Contract NAS8-38147. Further, we acknowledge the following Grumman personnel: Andre Berghmans, Frank Chin, and Nils Fonneland, who rendered valuable assistance in growing and characterizing the CdZnTe crystals. We also thank Dr. Louis Casagrande for valuable advice on polishing the wafers and Dr. Donald DiMarzio for assistance in making x-ray measurements. We would also like to acknowledge the technical contributions and generosity of Dr. Michael Dudley, and Dr. Bruce Steiner in conducting synchrotron topography studies.

REFERENCES

1. J. Miltat and Dudley, Chapter 3 in "Applications of Synchrotron Radiation," C. R. A. Catlow and G. N. Greaves (Eds), Blackie and Son Ltd, Glasgow, UK, 65-99, (1990).
2. J. J. Kennedy, P. Amirtharaj, Boyd, Qadri, R. C. Dobbyn, and G. Long, *J. Cryst. Growth*, v. 86, 93, (1988).
3. D. E. Aspnes, *Surf. Sci.* v.37, 418, (1973).
4. F. H. Pollak and H. Shen, *J. Electronic Materials*, v.19 (5), 399, (1990).
5. L. G. Casagrande, D. DiMarzio, M. B. Lee, D. J. Larson, Jr., M. Dudley, and T. Fanning, submitted to the *J. Crystal Growth*, (1992).
6. C. Parfeniuk, F. Weinberg, I. V. Samarasekera, C. Schvezov, and L. Li, *J. Cryst. Growth*, v. 119, 261, (1992).
7. J. I. D. Alexander, Orbital Processing of High Quality CdTe Compound Semiconductors: Numerical Modeling and Acceleration Data Analysis, Final Report on Contract Number PO 21-69118, CMMR, University of Alabama in Huntsville, March, 1994.

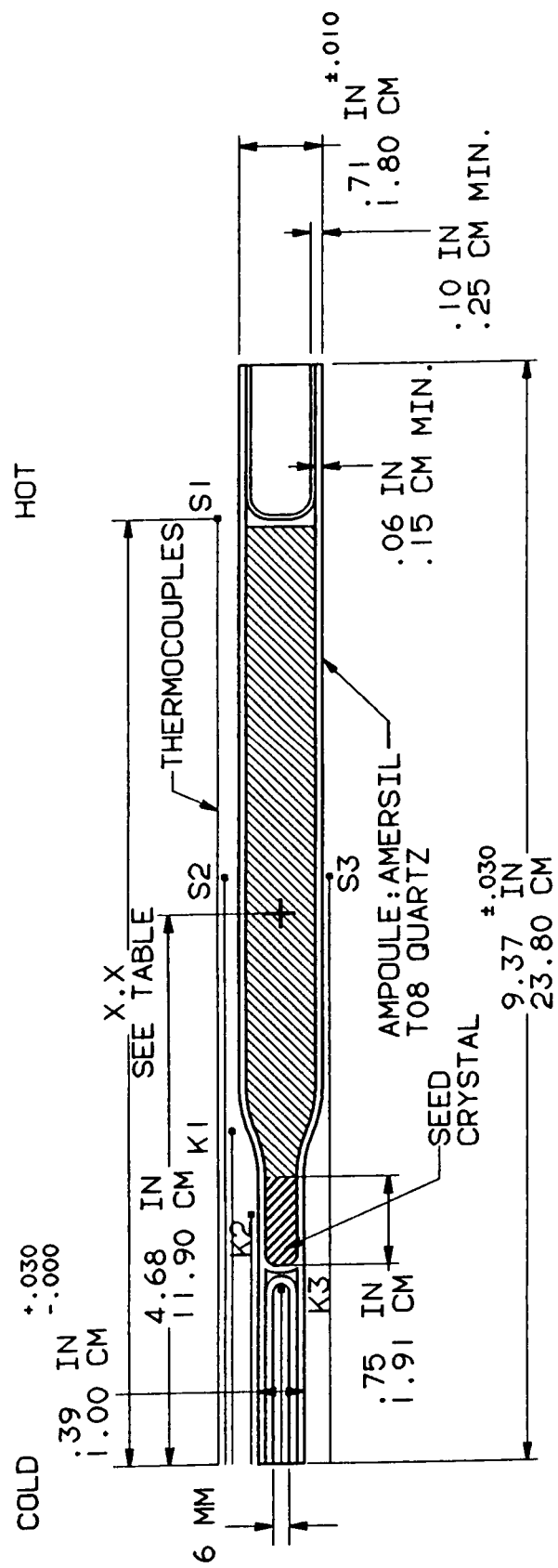


Figure 1 Ampoule Design (Schematic) with Instrumentation Thermocouples.

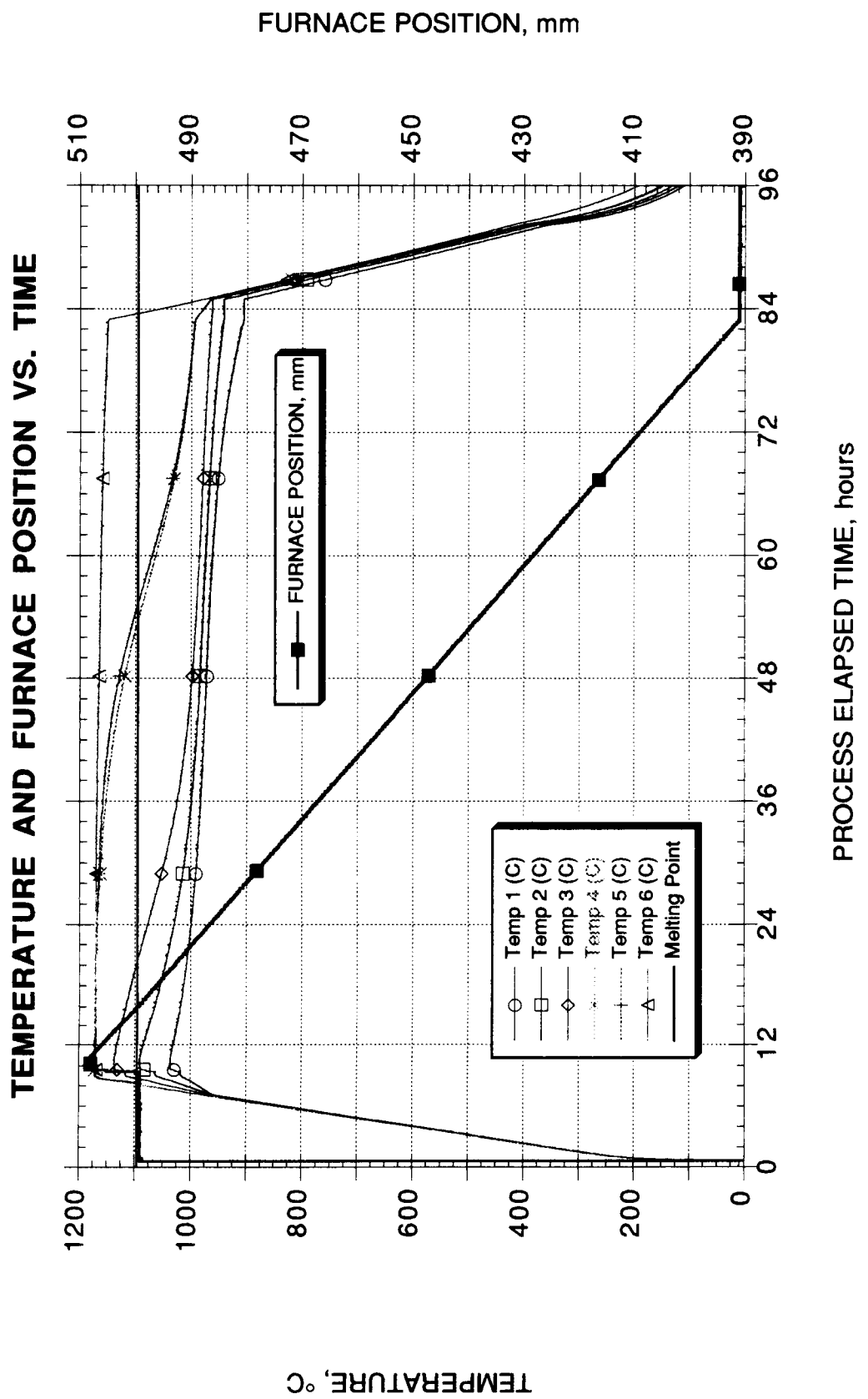


Figure 2 Primary Ground Truth Sample Temperature/Time/Distance History.

GRUMMAN FLIGHT OPTIMIZATION TEST - 1

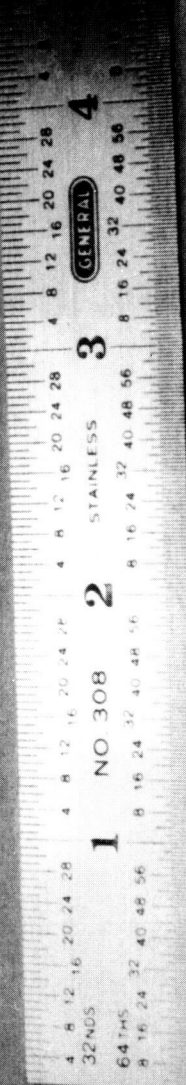


Figure 3 Ground Sample Grown in Grumman PMZF Showing a Dominant Single Crystal Grain.

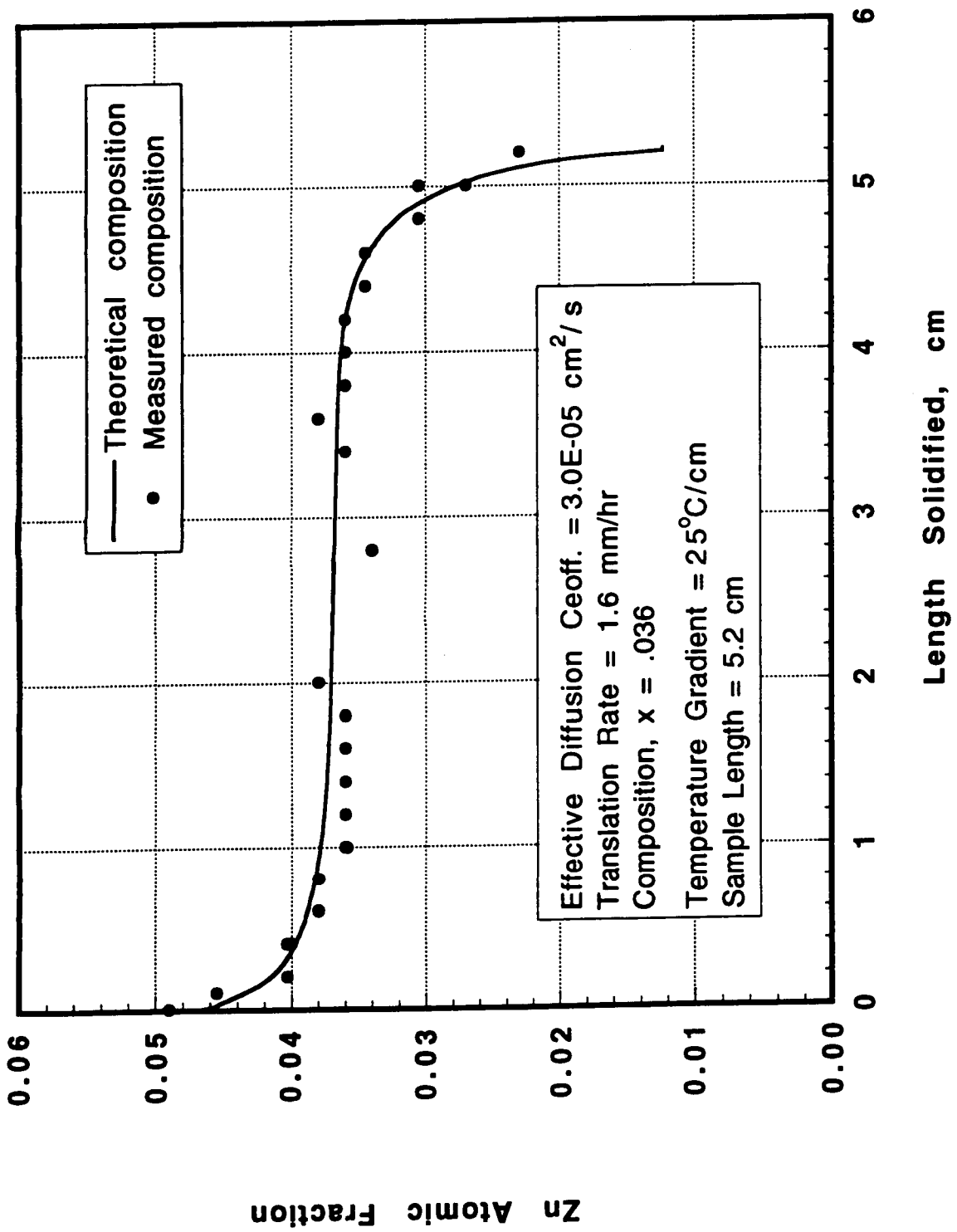


Figure 4 Composition versus Length Solidified, with Calculated Solute Redistribution and Fitting Parameters Superimposed.

USML-1/CGF/GCRC-1 TEMPERATURE AND FURNACE POSITION VS. TIME

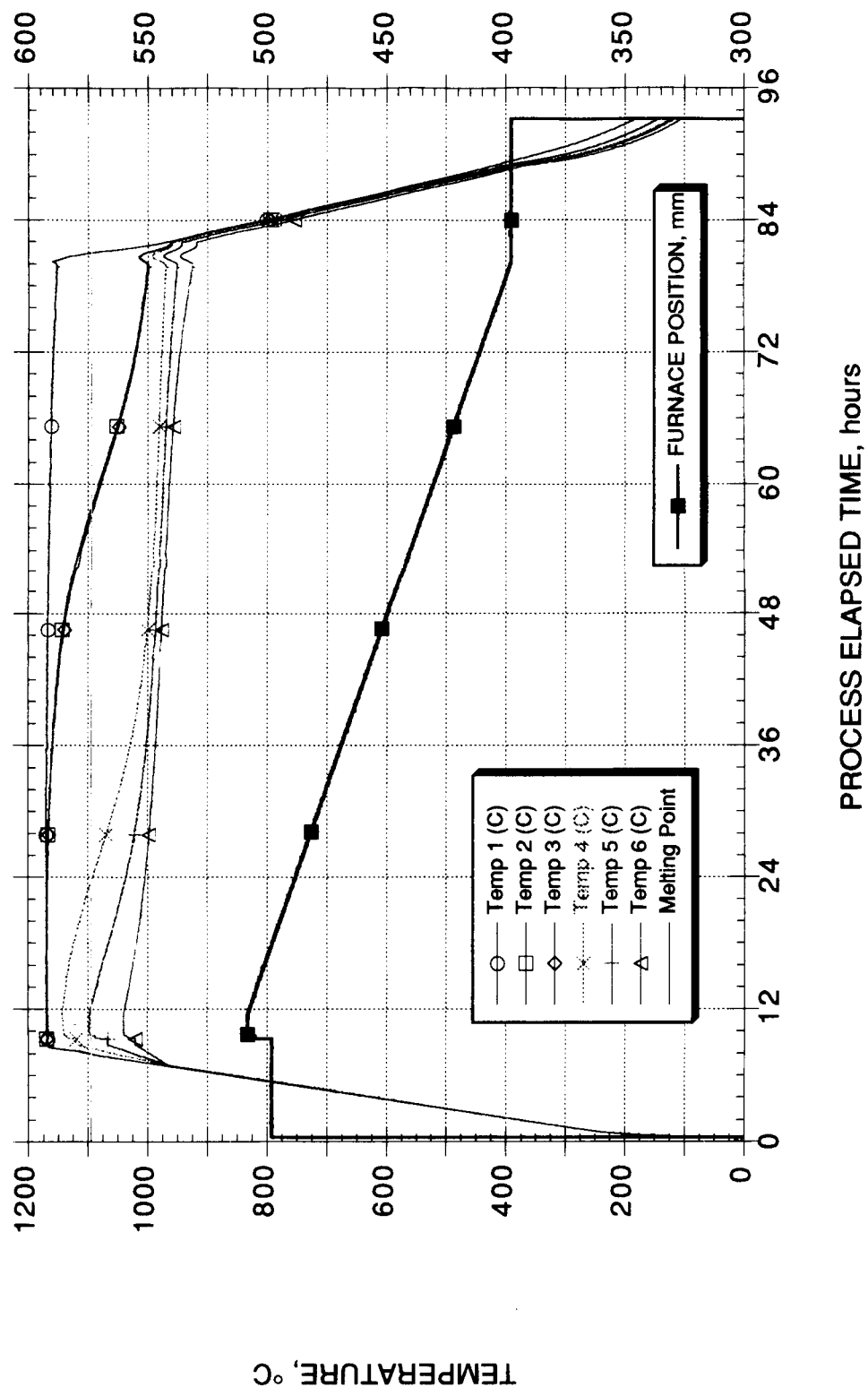


Figure 5 Time/Temperature/Distance History of the Primary Flight Sample, GCRC-1.



Figure 6 Photograph of Primary and Secondary Flight Ampoules (Post-flight).

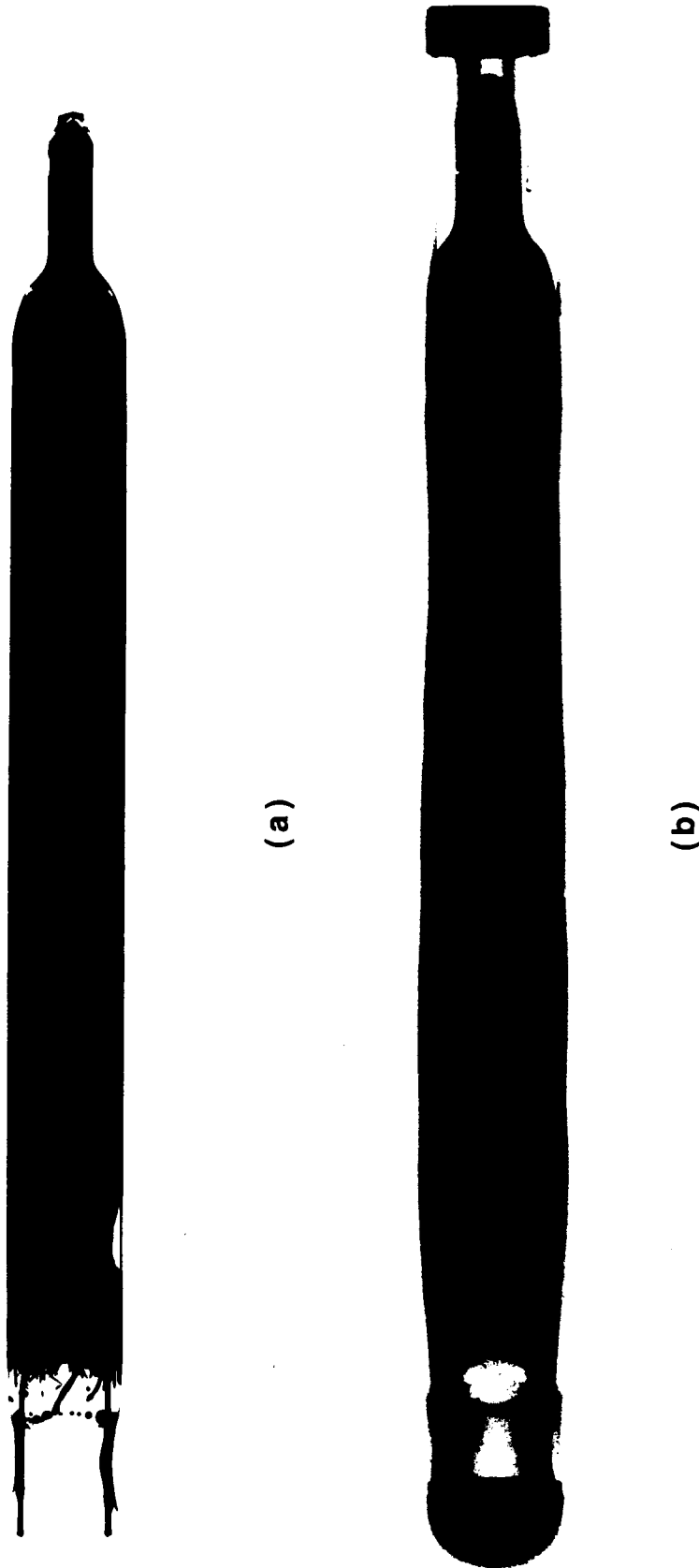


Figure 7 Post-flight X-Radiographs of (a) the Primary Flight Sample, GCRC-1 Ampoule and (b) the Secondary Flight Sample and Ampoule.

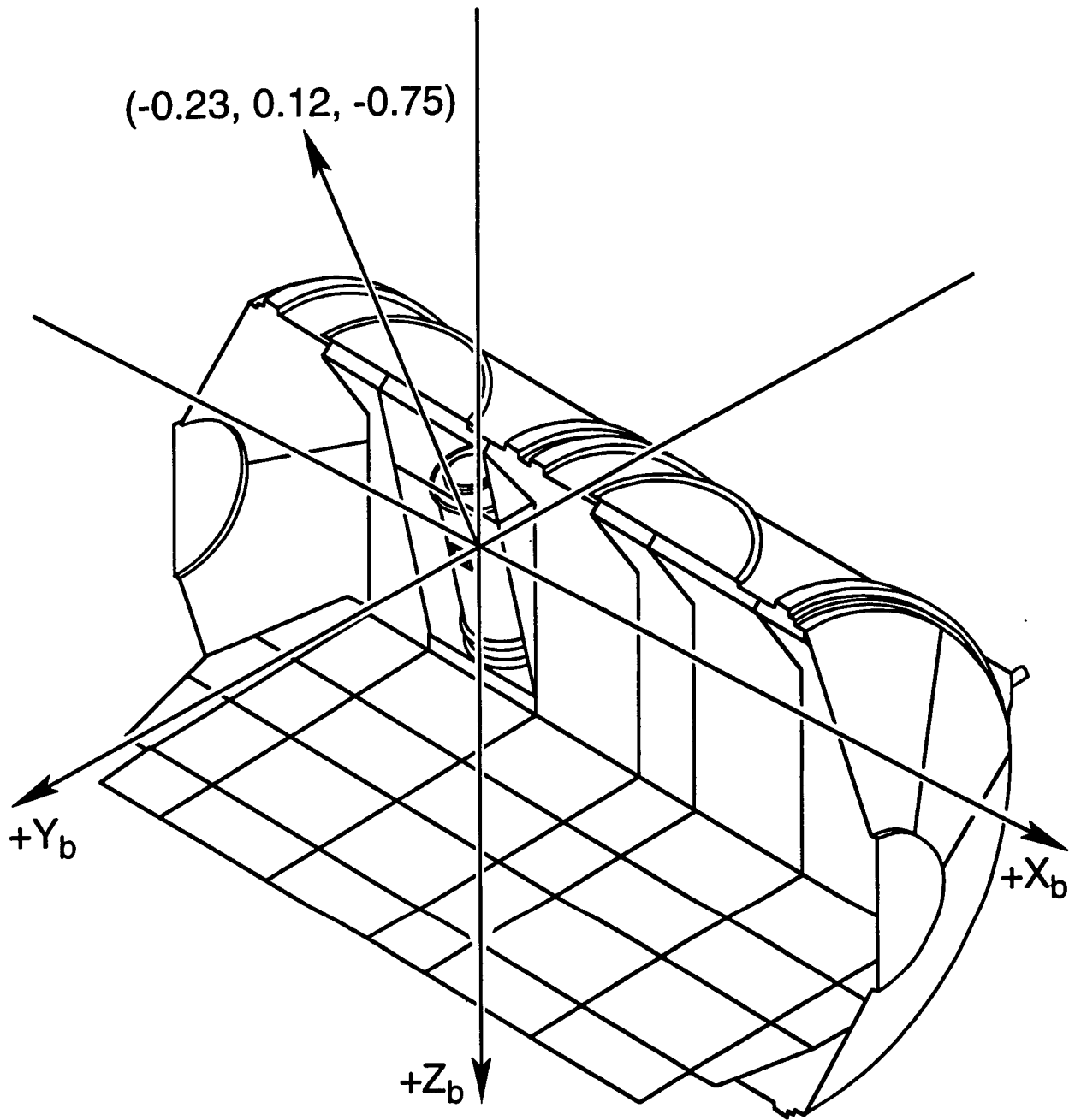


Figure 8 Calculated g-Vector at the CGF location, Without the Flash Evaporator System, (Ref. 7).

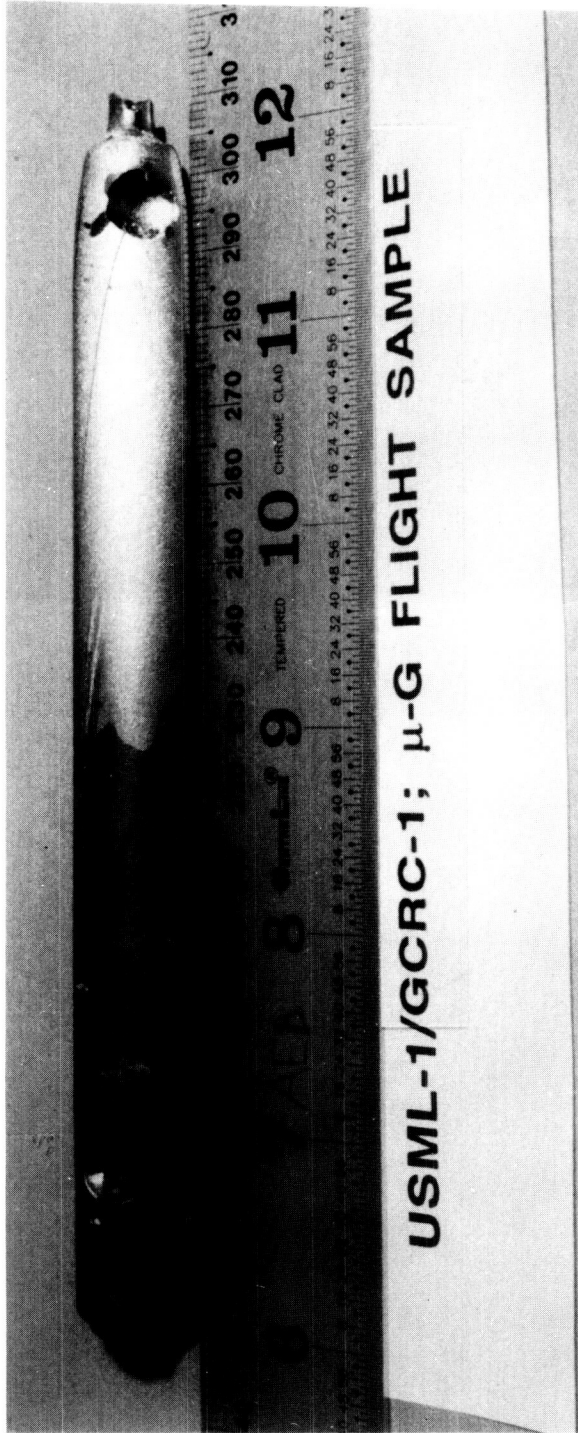


Figure 9 Photograph of the Primary Flight Sample, GCRC-1.

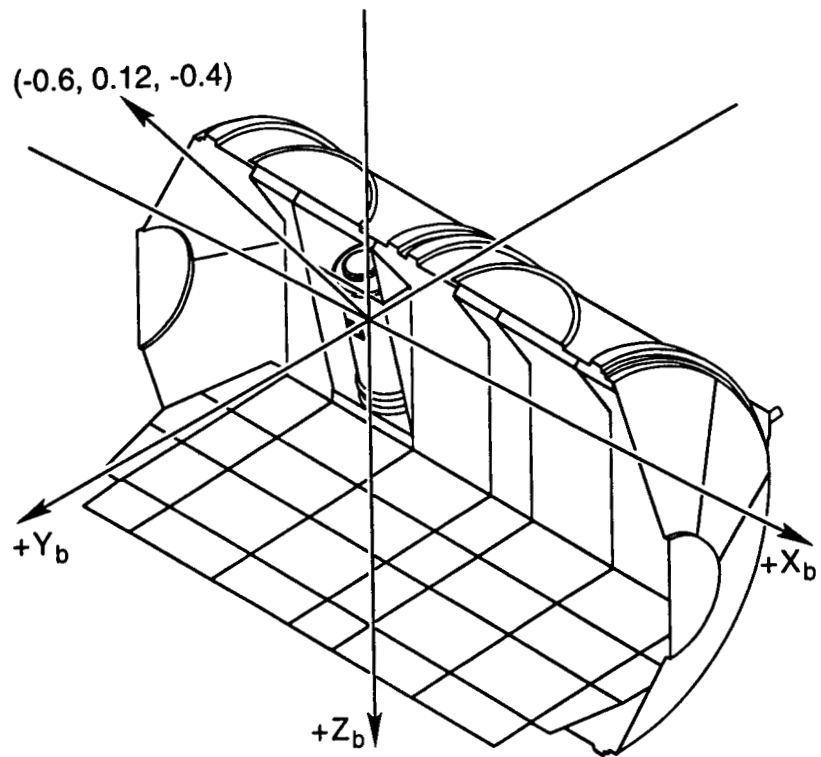


Figure 10a G-Vector at the CGF Location, Calculated from OARE Data.

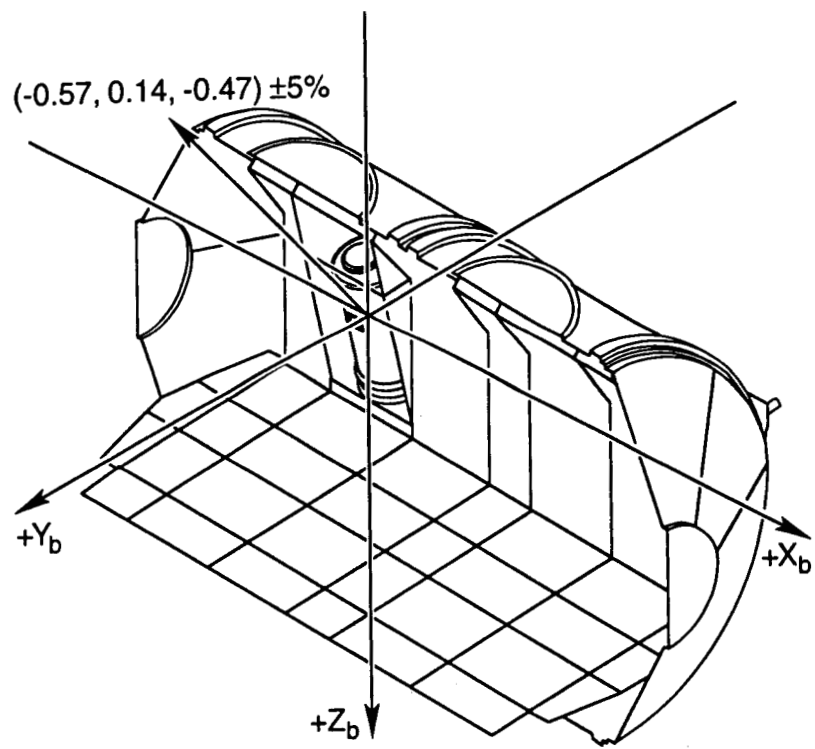
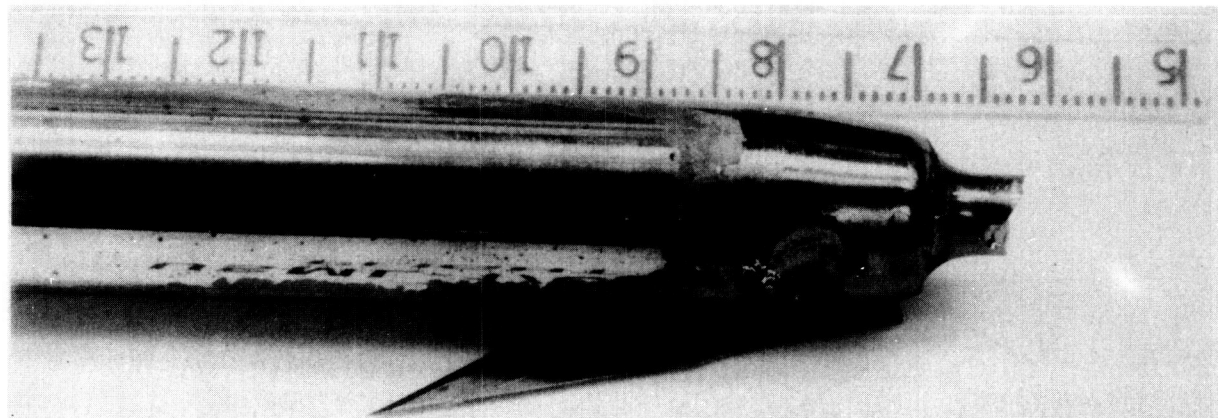


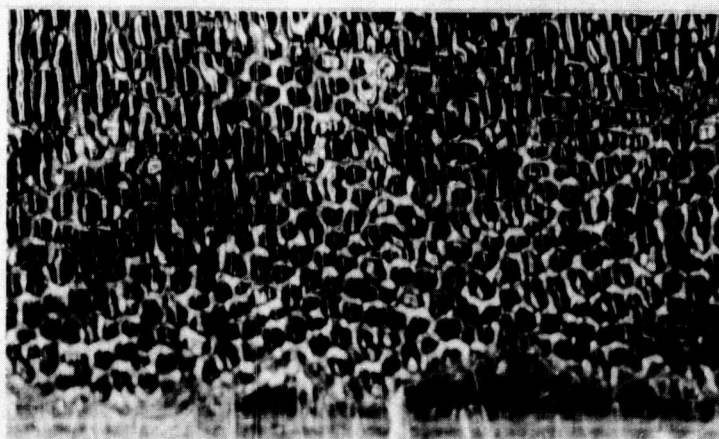
Figure 10b G-Vector at the CGF Location, Calculated from PAS Data.



USML-1/CGF/GCRC-1 FLIGHT SAMPLE

(a)

partial wall contact



full wall contact

(b)

Figure 11 Surface Texture on the GCRC-1 Flight Sample, (a) Seed/Shoulder/Steady State Transition, and (b) Partial Contact Region Showing 'Honeycomb' Surface Structure.

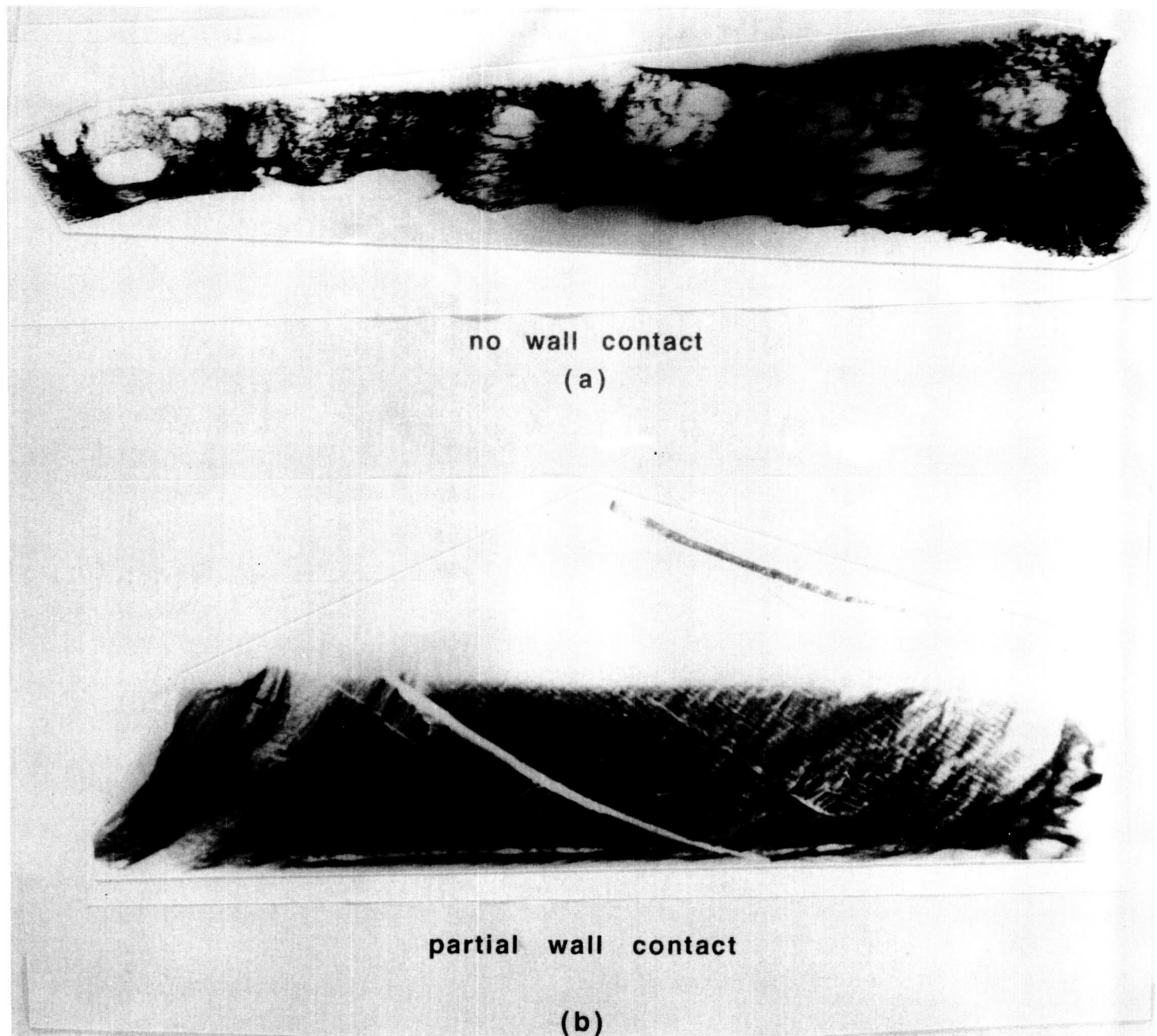


Figure 12 Synchrotron White Beam Topographs of the GCRC-1 Flight Sample Surfaces, a) Region Solidified Without Wall Contact Showing Discrete Dislocations, and b) Partial Contact Region Showing Slip and Twinning.

GCRCF2 μ g Sample

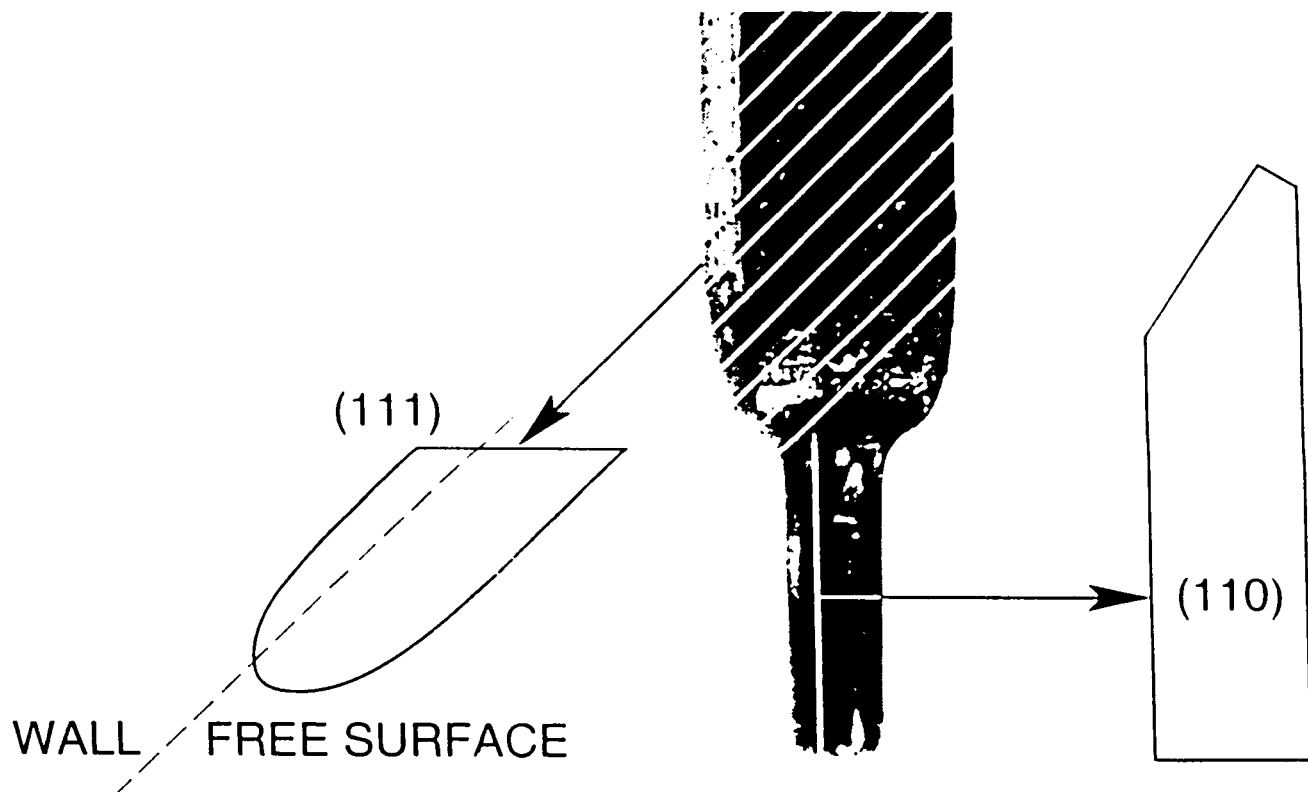
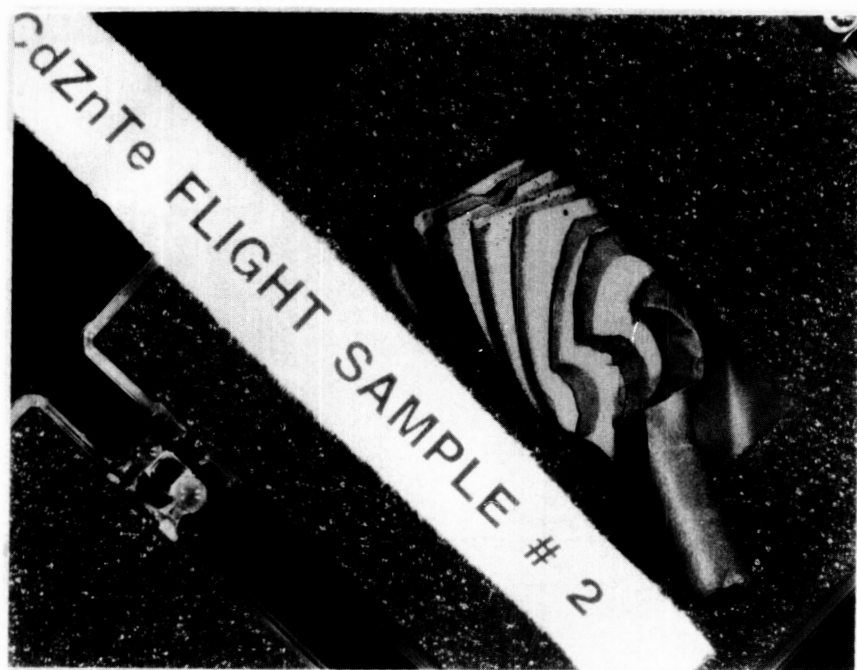
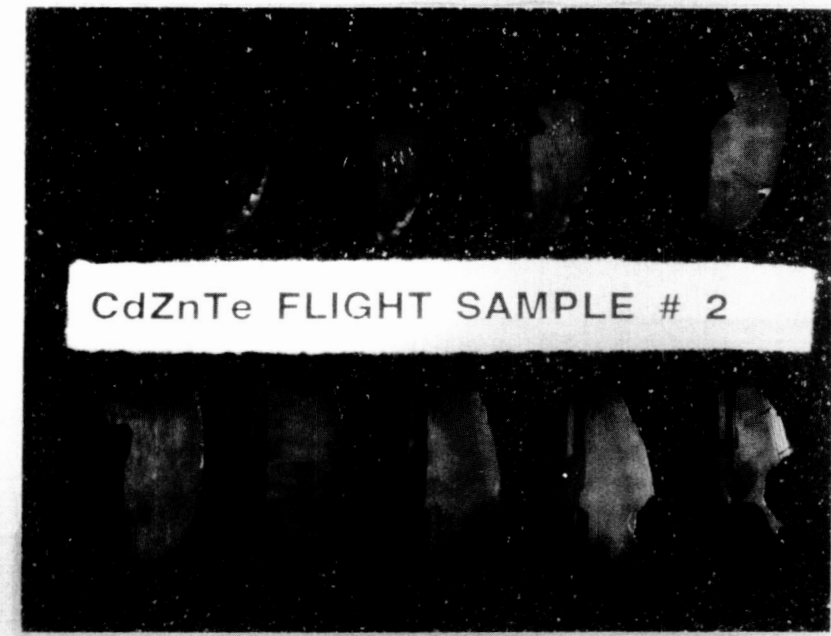


Figure 13 Wafer Sectioning Plan for the Secondary Flight Sample Boule and Seed (Schematic).



(a)



(b)

Figure 14 {111} Wafer Set Cut from the Secondary Flight Sample, GCRC-2, a) As Cut, and b) Polished/Etched.

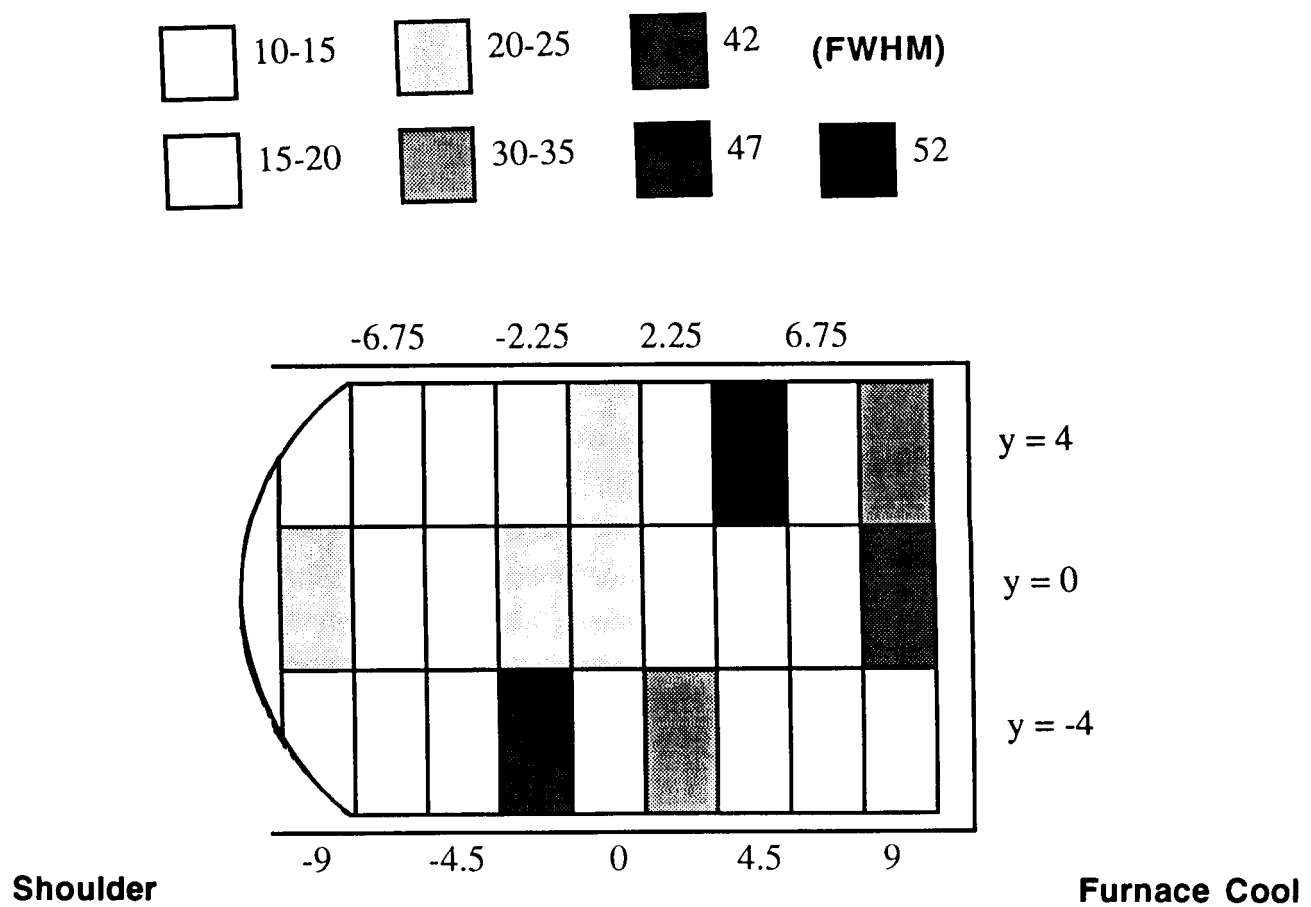


Figure 15 X-Ray Rocking Curve Map (FWHM Vs Position) for GCRC-2 Wafer 7. The Highest Strain Regions do not Originate at the Periphery and the Best Material Coincides with the Regions of No Wall Contact.

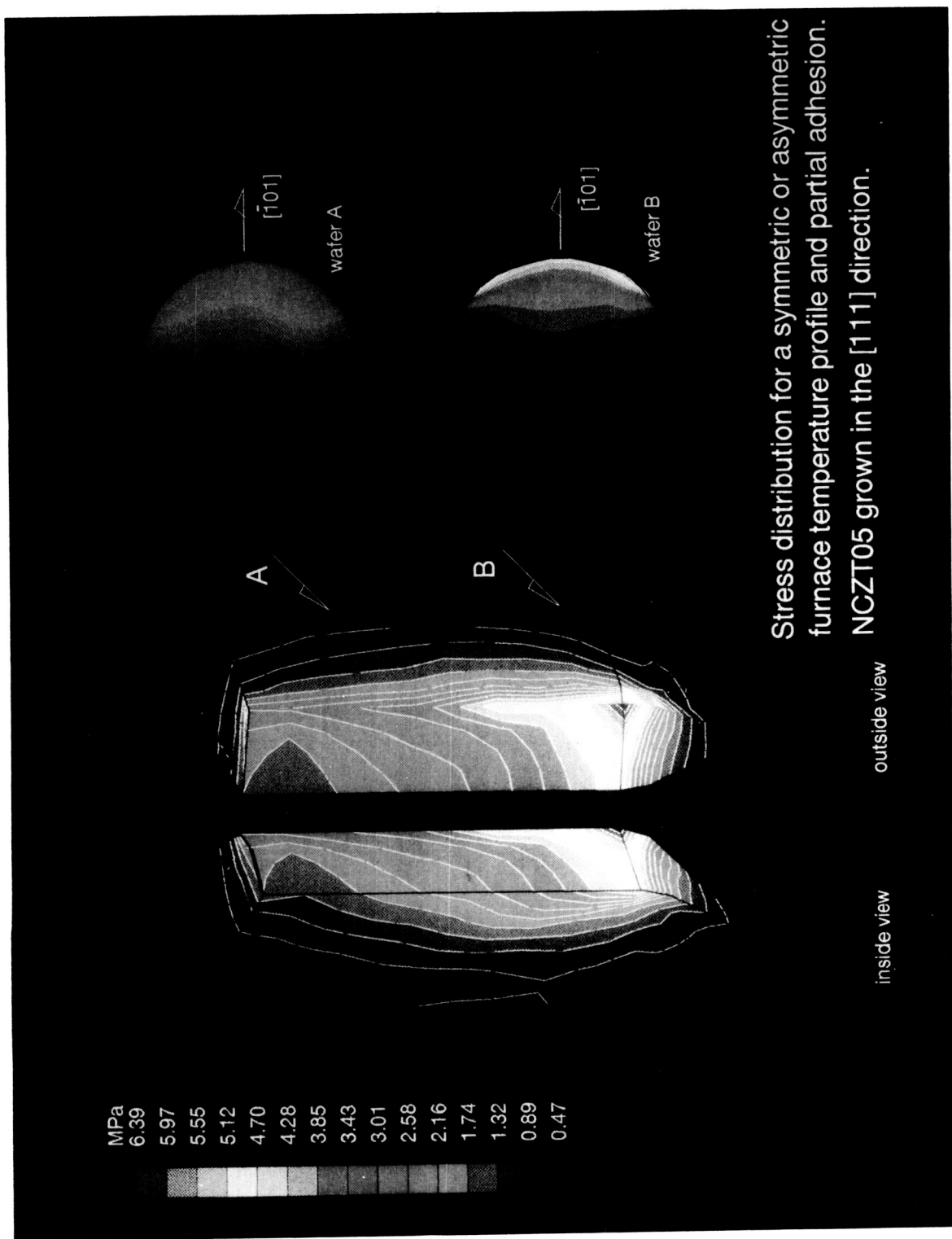
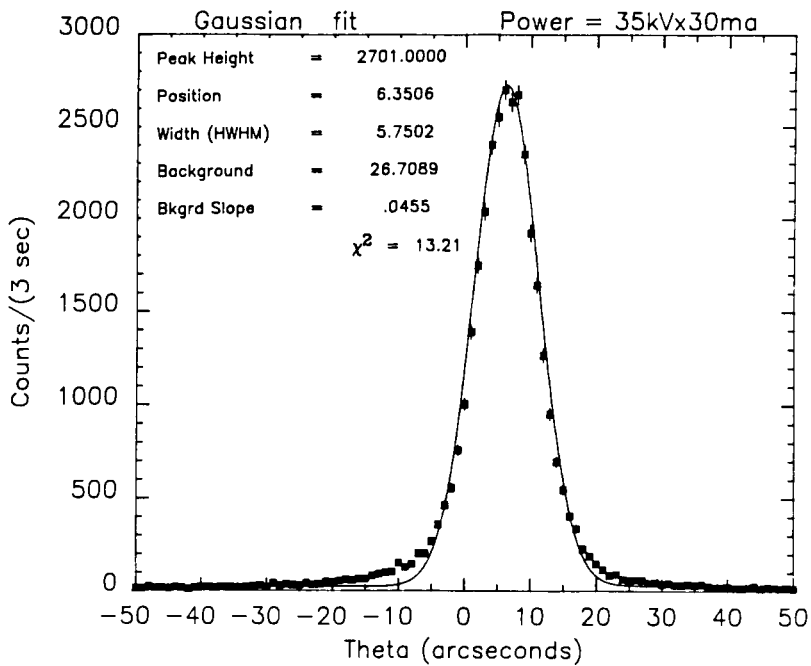
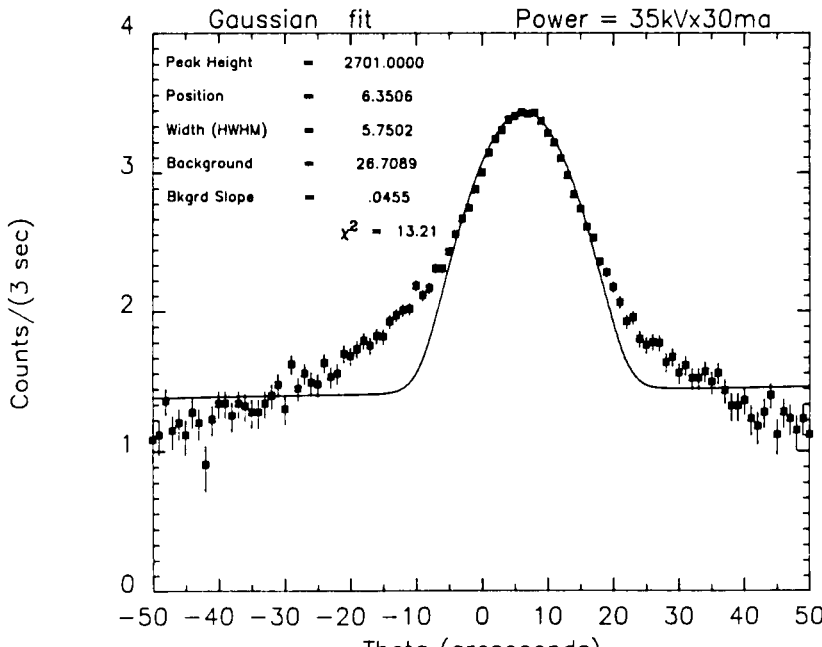


Figure 16 Calculated Stress Distribution for Flight Samples with Partial Wall Contact, Asymmetric Temperature Profile, and No Wall Adhesion.



(a)



(b)

Figure 17 DCRC Curve from PMZF One-g Sample Showing Deviation from Ideal Kinematic Diffraction in the Tails of the Curve, (a) Linear Scale, and (b) Log Scale.

Peak Height = 48186.8500

Position = -5.7064

Width (HWHM) = 77.2925

Background = 3934.9880

Bkgrd Slope = -10.5792

$\chi^2 = 21.12$

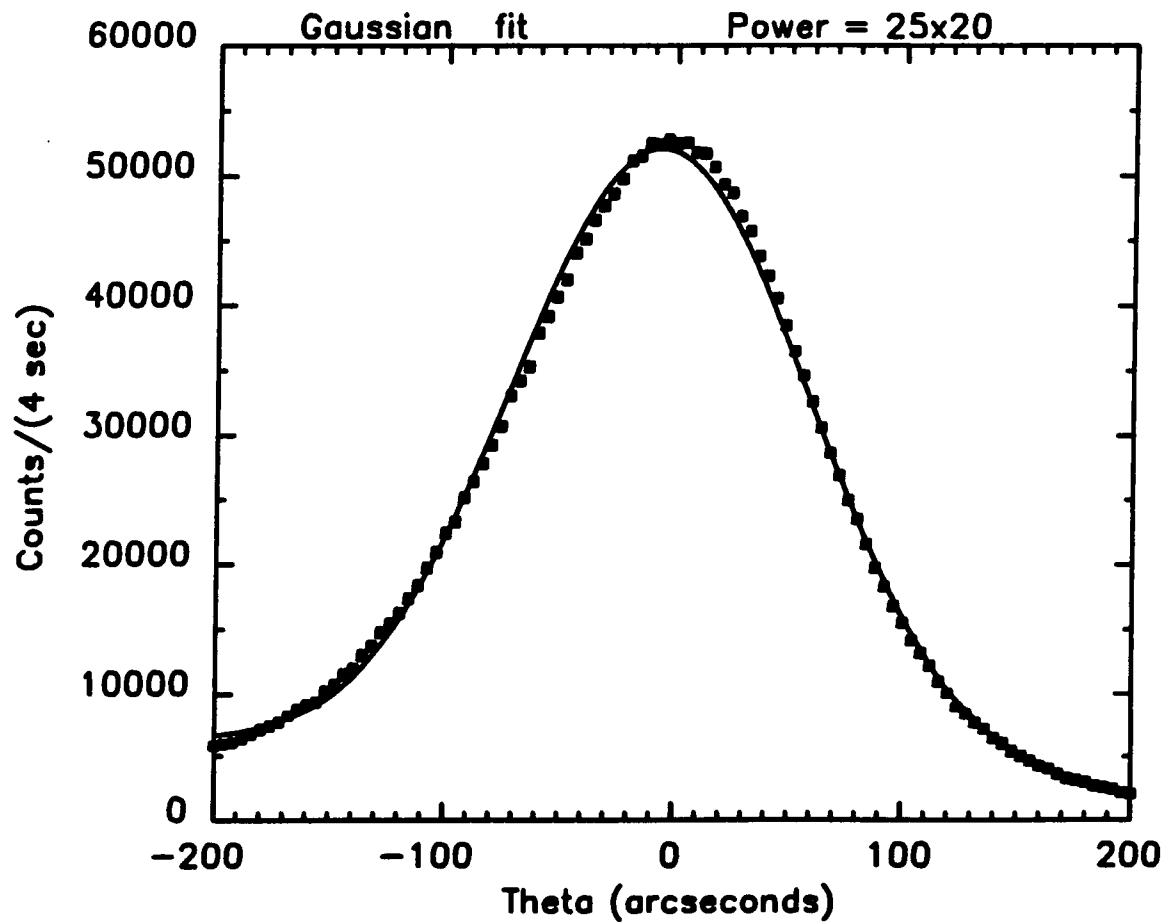


Figure 18 Ideally 'Imperfect' Rocking Curve Peak Described by Kinematic Diffraction Theory.

Peak Height = 1643.5000 ± .0000
 Position = -40.7409 ± .1417
 Width (HWHM) = 10.1820 ± .1048
 Background = 13.5773 ± 1.6134
 Bkgrd Slope = -.0326 ± .0385
 χ^2 = 2.96

X trans (Millimeter) = 8.2500

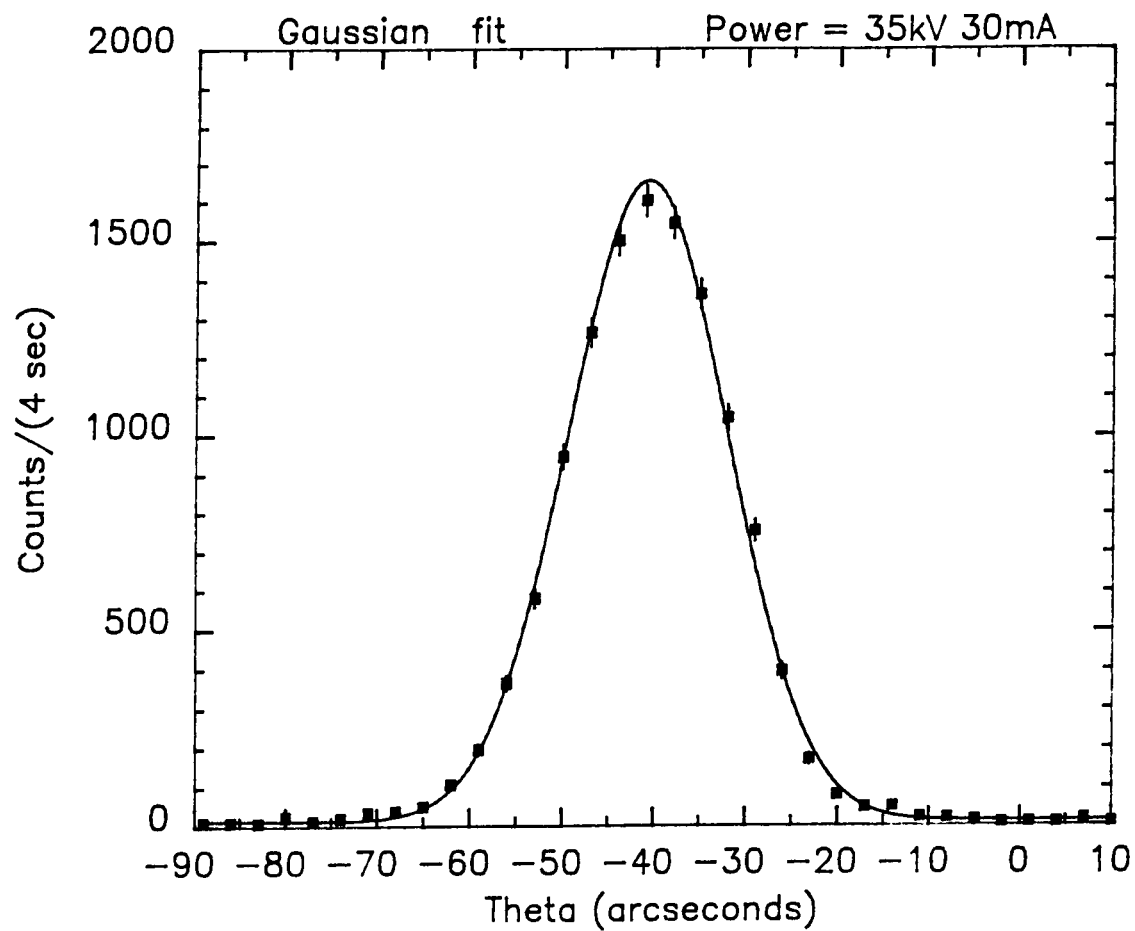


Figure 19 Ideally 'Perfect' Rocking Curve Peak Described by Dynamic Diffraction Theory.

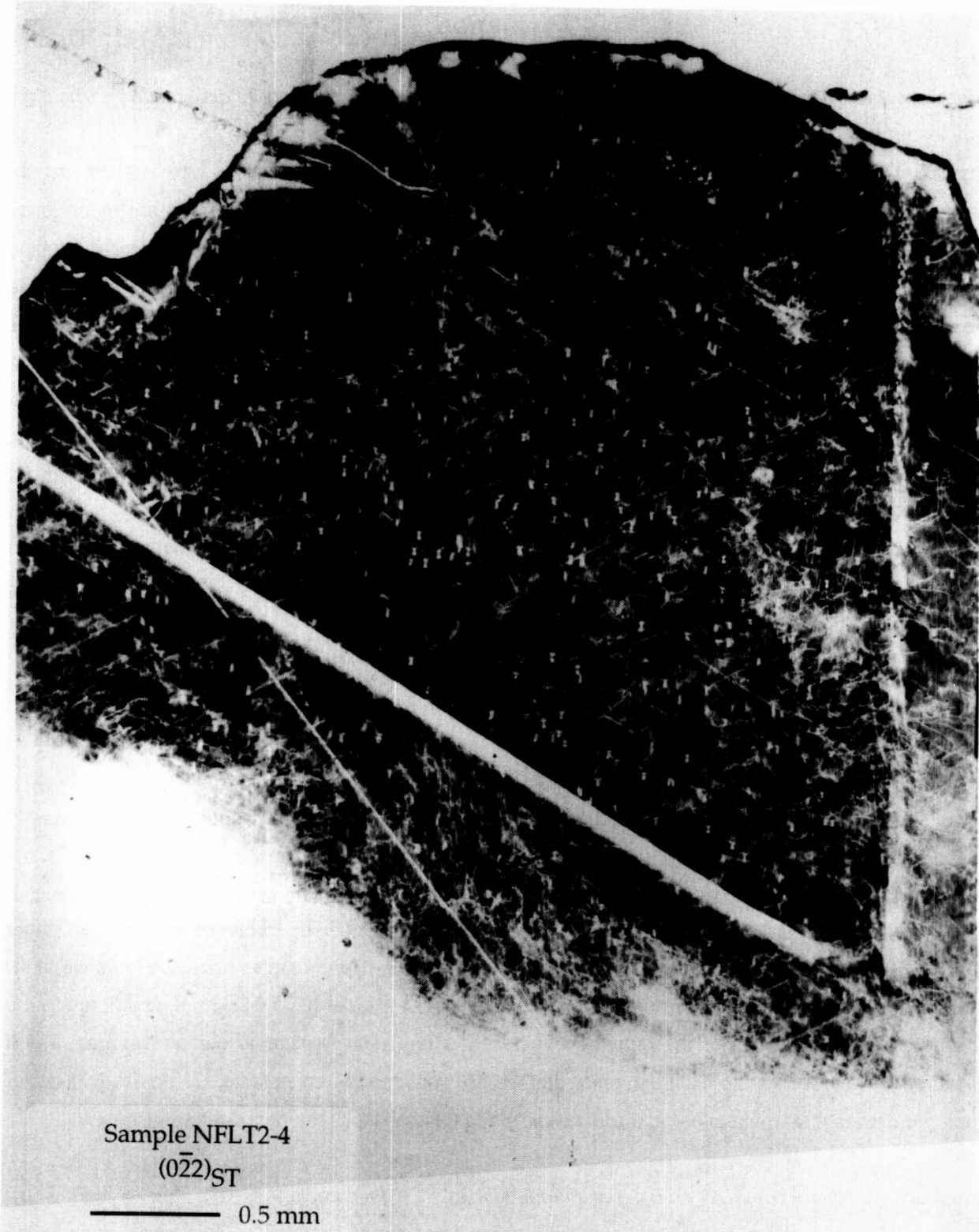


Figure 20 Synchrotron Monochromatic Transmission Topograph Showing an Array of Discrete Dislocations Within the Flight Crystal, GCRC-2.

Discussion

Question: *I wonder if you could make a comment or two about why the mobility dislocations of the flight samples appear to have been lower ?*

Answer: I think it is just a numbers game to the extent that I think the dislocations were mobile, just not many of them are there. That is somewhat surprising. The twin interfaces in general are much lower strain interfaces and have fewer twins in their vicinity at least as these are depicted from an etching standpoint. But I think it is just a numbers game as far as accumulating into, or, migrating into a substructure. You reach a point where even if they migrate, they are not accumulating into a substructure which is on a scale, which we are not used to looking at. It is a rather coarse structure. We can only find one sub-grain or sub-boundary in those wafers that we have imaged so far. It obligated us to map each of the wafers now sequentially so that we can build a three dimensional map of everything that is going on inside of that crystal. That's time consuming. It's only when we finish that and reconstruct that, for instance, we can get a true measure of the radial segregation, a true measure of the dislocation distribution because all of these are oblique sections right now that we are projecting. But to get back to the original question, I think that there are just fewer defects there. They have not accumulated into a substructure that we are used to seeing.

Question: *Is it possible to keep the free surfaces away from the wall container ?*

Answer: To get it away from the wall, basically. We have looked at two geometries. The initial geometry that we have looked at, recent calculations suggest was the wrong geometry to use. Calculations at UAH, if they are correct, suggest that in fact we can have an aspect ratio virtually what we please and that what we should do is perhaps offer additional support for that sample by using a thin liquid encapsulant to keep it away from the wall. I think that is feasible and in fact we will have to talk to the COTR to see if in fact, that is considered within our statement of work, to pursue that concept rather than the taper. The taper that we had measured on the previous flight samples were such that we knew from actual measurements that we could stay from the wall of a taper as low as 8°. It could have put a big burden on the direction of the original g vector; how large the transverse component was; and it placed a lot of burden on the flight dynamics that we felt would not be acceptable. So we are looking for other geometries that would allow us more flexibility and this one looks the best right now.

Question: *Could you comment on the Tellurium motion in the flight sample ?*

Answer: We normally map the Tellurium precipitate. Because of the high cooling rates, even in the standard sample, the Tellurium precipitates are usually quite small. In industry usually there is reference

to two different precipitates. The ones that occur on cooling frequently are referred to as inclusions, which is completely misleading, but that is jargon. These are deadly in the industry because they are typically larger by an order of magnitude and they will frequently generate dislocations around them because of the mismatch and external expansion between that inclusion (one that solidifies and its surrounding solid. It actually precipitates as a liquid). Below the final solidification there is additional precipitation that usually occurs on a sub micro scale. It is very hard to pick up. With respect to the side to side comparison we probably have not done enough of it with regard to infra-red microscopy. I think Don took a look at it. The sample I sent down last week. What we found typically in the previous samples, and the quick look that we have taken of the flight material, is that, the infra-red precipitate size is quite small typically on the order of sub-micron whereas in the slow cooled samples it is typically on the order of 1 to 10 microns. The distribution density I have to go back and look at the numbers, I don't know right off hand what it is.

Question: *I was just wondering there have been some publications done by the Soviets a few years ago where they looked at microscopic surface roughening as a way to try to minimize contact between the melt and the surface and I was wondering if any of that was being looked into and if that would affect your strain density because of the point to point contact ?*

Answer: There has been a lot of work on how to properly contain, if you will, a reactive melt. The roughening of the ampoule inner surfaces is something that has been done frequently and universally on the ground. Most commonly in quartz ampoules and basically what it serves to do is to keep at least a portion, as I think Favier described it, of the melt away from the wall at all times. It minimizes the contamination from the wall diffusion of oxygen and silica for instance. We have taken a somewhat different approach in trying to use a nonreactive monolithic inner coating, which is non-wetting, which is in this case graphite or carbon rather. They all have a limitation to the extent that where there is a local failure, and you get contact with the wall, that would be considered a reaction and you get stiction at that wall.

60 pg

1995.07.11 NASA
324035

N95-14214

4019

P-60

CRYSTAL GROWTH OF SELECTED II-VI SEMICONDUCTING ALLOYS
BY DIRECTIONAL SOLIDIFICATION

S. L. Lehoczky, F. R. Szofran, D. C. Gillies and S. D. Cobb
NASA Marshall Space Flight Center

C.-H. Su and Y.-G. Sha
Universities Space Research Association

R. N. Andrews
University of Alabama at Birmingham

ABSTRACT

A $Hg_{0.84}Zn_{0.16}Te$ alloy crystal was back-melted and partially resolidified during the first United States Microgravity Laboratory (USML-1) mission in the Marshall Space Flight Center's Crystal Growth Furnace. The experiment was inadvertently terminated at about 30% of planned completion. Nonetheless, it was successfully demonstrated that HgZnTe alloy ingots partially grown and quenched on the ground can be back-melted and regrown in space under nearly steady state growth conditions. An identical "ground-truth" experiment was performed following the mission. Preliminary results are presented for both crystals, as well as for a series of other crystals grown prior to the mission for the purposes of optimizing in-flight growth conditions.

INTRODUCTION

The growth of homogeneous crystals of mercury-based II-VI alloys, such as mercury zinc telluride ($Hg_{1-x}Zn_xTe$, $0 \leq x \leq 1$), from the melt is a particularly challenging problem because their liquidus and solidus temperatures (see for example Figure 1) are widely separated. Consequently, their interface segregation coefficient (k) is large (Figure 2). Generally the density of the mercury compound is larger than the other II-VI alloying compound, e.g. ZnTe. This, when combined with the large change in the thermophysical properties upon phase change, makes the achievement and control of the desired solidification interface shape an extremely difficult task in a gravitational environment.

On Earth the Hg-rich component rejected during solidification is denser than the original melt and the vertical Bridgman-Stockbarger melt growth process would appear to be both gravitationally and thermally stable against convection. However, this is not generally the case. Due to the peculiar relationships between the thermal conductivities of the melt, solid, and ampoule, it is not practical to

completely avoid radial temperature gradients in the growth region for alloys of this type [1-4]. Because of the high Hg partial vapor pressures involved at the processing temperatures [5-8], the confinement of the alloys requires the use of very thick fused silica ampoules which have thermal conductivities compared to those of the alloys. This, when combined with the large (a factor of 4 to 10) decrease in the thermal conductivities of Hg-alloys upon freezing [9-11], leads to isothermal surfaces near the melt/solid interface that are bowed into the solid. Although the interface under this condition is neither an isothermal nor an isocompositional surface, it is bowed in the same direction as the adjacent isotherm. A method that relies on a careful control of radiation heat transfer near the growth interface can minimize this effect [1,4,12]; nonetheless, because the interface temperature undergoes large changes during growth, the complete elimination of radial temperature gradients in the vicinity of the interface is nearly impossible. Thus, in spite of the stabilizing influence of solutal density gradients, intense thermally-driven gravity-induced fluid flows will always occur near the interface [13-16]. Recent theoretical calculations [17] suggest that such flows should have only a small effect on the solidified alloy composition. On the other hand, alteration of the flow field by growth in a magnetic field yielded significant changes in the axial and radial compositional distribution in HgCdTe and HgZnTe alloys for the growth rates and temperature distributions employed [18]. One of the aims of this and other on-going flight experiments [19] is to evaluate the relative importance of various gravity and non-gravity related effects.

The specific objectives for the USML-1 phase of the investigation were:

1. To back melt a preprocessed $Hg_{0.84}Zn_{0.16}Te$ solid solution alloy ingot and grow a 2 cm alloy crystal under nearly diffusion limited and stabilizing gravity conditions using a modified Bridgman growth method.
2. To establish whether preprocessed alloy crystals can be successfully quenched, back-melted, and regrown maintaining nearly steady-state compositions.
3. To freeze the diffusion boundary layer essentially without disturbing it, and from analysis of the boundary-layer composition to establish a value for the HgTe-ZnTe interdiffusion coefficient for the $x=0.16$ alloy composition.
4. To perform detailed microstructural, electrical, and optical characterization on both the ground-grown and space-grown portion of the crystal, and evaluate the effects of reduced gravity for the USML-1 crystal growth conditions.
5. To perform detailed characterization of the rapidly frozen portions of the ingot to assess the potential benefits of casting alloy ingots in space.

The required duration time for the successful completion of the experiment was approximately 150 hours. Unfortunately, because of the loss of power to the Crystal Growth Furnace (CGF), the experiment was prematurely terminated at about 56 hours into the timeline. This significantly reduced the

science return of the experiment. Nonetheless, an approximately 5.7 mm-long crystal was grown during this time period. A summary of the results for the flight as well as the ground based portion of the experiment are described in the following sections.

I. RESULTS FROM THE GROUND-BASED PORTION OF THE INVESTIGATION

A series of $Hg_{0.84}Zn_{0.16}Te$ crystal ingots (Table 1) have been grown from pseudobinary melts by the Bridgman-Stockbarger type directional solidification using a MSFC/Space Science Laboratory (SSL) heat-pipe furnace [20] and the CGF Ground Control Experiment Laboratory (GCEL) furnace (Figure 3). A number of translation rates and a series of hot and cold zone temperatures were employed to assess the influence of growth parameters on crystal properties.

The ingots were sectioned longitudinally and transversely, polished, and etched appropriately to reveal macroscopic and microscopic defects including cracks, grain boundaries, voids, second-phase inclusions, and dislocations. Typically the ingots contained about 2×10^{-5} dislocations/cm² including dislocations that formed large numbers of sub-grain boundaries (Figure 4). An analysis of transmission electron micrographs (Figures 5 and 6) for selected wafers indicated the dislocation had 110-type Burger's vectors.

Precision mass density, wavelength-dispersive and energy-dispersive x-ray analyses were used to generate detailed compositional maps for the ingots. The fitting of the measured axial compositional variations to a one-dimensional diffusion model that includes changes in the interface temperature and segregation coefficient during the transient phase of solidification [21-24] was used to obtain an estimate for the effective HgTe-ZnTe liquid diffusion coefficient (D) and the fit for an $x=0.18$ alloy is shown in Fig. 7. A best estimate of $D = 6.0 \times 10^{-6}$ cm²/s and the data in Figures. 1 and 2 were used to obtain $G/R = 9.6 \times 10^{-6}$ °C·sec/cm² (G = temperature gradient in the melt ahead of the interface and R = solidification rate), the criterion for the prevention of interface breakdown resulting from constitutional supercooling. For optimum CGF operation conditions G was estimated to be about 35°C/cm, which allowed a maximum growth rate of about 3.8 mm/day. The time scale in Figure 7 illustrates the time consuming nature of growing significant lengths of crystals under steady state, and constant x conditions, and therefore the impossibility of meeting one of the major objectives within the 150 hours mission elapsed time allocated for the experiment. We decided therefore to grow the first part, the initial transient segment in Figure 7, of the crystal on the ground, and then rapidly freeze (quench) the remaining liquid to preserve the melt compositional distribution needed for the continuation of steady-state growth following back-melting on orbit. A series of growth runs was performed to establish the required protocols. Four precisely located thermocouples (See Figure 8) were used to establish the proper

back-melting position. The quench was initiated when the appropriate thermocouple read the solidus temperature of the $x=0.16$ alloy, i.e., 695°C.

Figure 9 depicts the grain structure following a typical back-melting/regrowth sequence. As can be inferred from the figure, grain growth usually proceeded as would have been expected had there been no growth interruption. Figure 10 shows the behavior of the axial composition distribution prior to and after regrowths for one of the ingots. The data indicate that nearly steady state growth resumed following back melting without any significant composition transients.

Figure 11 and 12 show the interface region for two different temperature settings. As can be seen the melt/solid interface shapes are highly dependent on the exact temperature settings used. A hot zone temperature of 800°C and a cold zone temperature of 350°C were selected as optimum for the flight experiment. The radial compositional variations for the two cores are illustrated in Figures 13 and 14.

II. FLIGHT AND GROUND-TRUTH SAMPLE RESULTS

1. USML-1 Experiment

The flight experiment on USML-1 was performed from June 26 to 28, 1992 on shuttle mission STS-50. Figure 15 shows the scheduled timeline for the experiment. The five-zone CGF illustrated in Figure 3 was heated to its set points in 5 hours and the furnace was translated at a rate of 10 mm/hr to the melt-back position as planned. After about 7.5 hours Process Elapsed Time (PET), the back-melting was completed, the furnace translation stopped and the sample was soaked for 10 hours before the directional solidification started at about 17.5 hours PET. The experiment was inadvertently terminated at 56.5 hours PET. The furnace lost its power and cooled in a passive mode. With a translation rate of 3.5 mm/day, a 5.7 mm long crystal was grown during the 39-hour growth period. A ground-truth growth experiment was performed after the flight mission using exactly the same timeline as the flight experiment including the power outage and the passive cool-down .

2. Sample Properties

a. Surface morphology

Figure 16 shows the radiograph of the returned flight sample and Figure 17 shows a flight sample inside the fused silica ampoule. The surface features before and after 4.7 cm from the sample tip are markedly different. From the quenched-in interface determined later, this position (4.7 cm) was the back-melt interface. As opposed to the sample grown on Earth, the portion of the sample melted in space showed partial separation from the ampoule wall. A scanning electron microscope (SEM)

photomicrograph of the surface of the space-grown region is shown in Figure 18 and the counterpart for the ground-truth sample is given in Figure 19.

b. Quenched-in interface shape

Figure 20 shows the quenched-in melt/solid interface in a longitudinal section cut from the flight sample. The interface was slightly concave toward the solid as was expected from previous ground based results. However, it was significantly more asymmetric when compared to the quenched-in interfaces seen for the GCEL samples. The sectioned area of the ground-truth sample shows more symmetric interface as depicted in Figure 21.

c. Space-grown crystal microstructure

A photomicrograph of the polished and etched slab from the flight sample is shown in Figure 22. The quenched-in interface can be easily seen and at 5.7 mm from this interface a discontinuity delineated by a concave boundary in the microstructure can also be observed. This boundary is believed to be the melt back interface. As shown in the figure, the space-grown crystal continued to grow in the same crystal orientation as the ground-grown part, and the first 2 to 3 mm crystal grown in space has a dense distribution of subgrain boundary structures which might have been caused by the applied thermal gradients and/or the abrupt changes in the local lattice constants due to the change in the axial composition as discussed later. However, when the crystal had grown to about 4 mm, as measured from the melt-back interface, the microstructure improved considerably with significant reduction in the density of subgrain boundaries, indicating that steady-state growth was nearly achieved. As can be seen an additional crystal grain was nucleated from the ampoule wall at about 2 mm from the melt-back interface.

d. Radial compositional distribution of the grown crystals

The radial compositional distributions at various axial locations were measured by using microprobe analysis. Figures 23 to 30 illustrate the sequence of the evolution of the radial composition distribution of the flight sample. The compositional distribution shown in Figure 26 is at an axial position of 6 mm in front of the quenched-in interface. The usual concave shape is distorted in the middle because only the central portion of the sample was back-melted due to the concavity. Figures 24 and 25 suggest that the initial resolidification phase passed through a transient period and, as shown in Figures 26 to 29, approached a steady-state growth about 3 mm from the quenched-in interface. This is consistent with the evolution of the microstructure shown in Figure 22. The asymmetry in the radial compositional profile at 1 mm in front of the quenched-in interface is also consistent with the asymmetry in the shape of the quenched-in interface. The asymmetry could have been caused by either an asymmetric temperature distribution or by residual transverse accelerations. Although we cannot completely rule out the first possibility, we believe that the more likely cause was residual transverse

accelerations. Data provided by the Orbital Acceleration Research Experiment (OARE) test project [25] tend to support this supposition. Although the residual acceleration along one of the transverse axes (Y) was about $0.15\text{--}0.2\mu\text{g}$, as had been expected, along the other transverse axis (X), the measured accelerations were a factor of 2 to 3 larger and varied with time. As shown in Figure 31 as a function of mission elapsed time, these accelerations ranged from 0.4 to about $0.8\mu\text{g}$. We have indicated in the figure the estimated times at which the growth translation started, as well as, when the growth interface was at various positions (5, 4, ... 1 mm) as measured from the quenched-in interface location. There appears to be a definite one-to-one correlation between the development of the compositional asymmetries shown in Figs. 24-28 and the changes in the magnitude of the residual acceleration X-component.

A rough estimate of the relative diffusion-limited radial segregation ($\Delta C/C_0$) resulting from non-planar interface geometries may be obtained as described in Figure 32. The measured and estimated values for $\Delta C/C_0$ and $\Delta C_2/C_0$ corresponding to the quenched-in interface geometry are summarized in Table 2. The fact that the experimental values are 4 to 6 times larger than these estimated is not consistent with the assumption of purely diffusive mass transport.

The radial compositional distributions in the "ground-truth" sample are shown in Figures 33 to 37. Similar to the flight sample, the compositional distributions suggest a transient region followed by near steady state growth. Consistent with its interface shape, the radial composition distribution was highly asymmetric at 1 mm from the quenched-in interface. The relative radial segregation based on diffusive mass transfer was estimated to be 0.05 versus the measured value of about 0.18, suggesting significant flow contribution to the overall mass transfer process.

e. Axial compositional distribution of the grown crystals

The axial compositional variations along the grown crystal were measured by energy dispersive x-ray spectroscopy (EDS) on the sample surface as well as along the centerline of the ingot by microprobe, and are illustrated in Figures 38 and 39. The surface compositional profile shows an initial increase in the ZnTe mole fraction and then a gradual decrease to a steady state value. The centerline data were somewhat scattered and such a trend is not as clear. From the surface compositional profile and the radial compositional distributions shown in Figures 23 to 30, a slight excessive back-melting of 0.5 mm is estimated. Figures 40 and 41 show the similar data along the surface and the centerline, respectively, for the "ground-truth" sample. For both cases in the measurements of the "ground-truth" sample, an initial increase and a gradual decrease in the ZnTe mole fraction is indicated; suggesting slightly excessive back-melting.

f. Microstructure of the quenched-in sections

The quenched-in section of the flight sample was polished, etched and examined by the SEM using the back scattering mode. The back scattering photomicrographs of the quenched-in section of the flight sample (Figure 41) clearly show an array of long parallel dendritic structures originating at the quenched-in interface and extending into the melt at an angle of about 50 to 60° from the growth axis. This lack of symmetry is consistent with the observed asymmetries in the interface shape and in the radial compositional distribution. A similar micrograph for the "ground-truth" sample is shown in Figure 42. The major dendritic structures near the interface were rather short compared to the flight case, and show a nearly symmetric distribution about the growth axis as was the case for the radial compositional distribution.

g. Axial compositional distribution in the quenched-in sections

The axial compositions along the centerline of the flight sample in the quenched-in section were measured by microprobe and are plotted in Figure 44. The large fluctuation in the data is caused by the dendritic nature of the sample. Subsequently, the sample was annealed at 580°C for 114 hours and the composition distribution re measured and is shown in Figure 45. The annealing time and temperature were chosen to accelerate local diffusion between the dendritic core (high ZnTe content) and the last to freeze section (high HgTe content) while minimizing the effect on the axial compositional distribution. As expected, the annealing procedure greatly reduced the data scatter. The results show an initial increase in the mole fraction of ZnTe to a steady value of about 0.05. The axial data for the ground-truth sample for the as-quenched and the annealed cases are given in Figures 46 and 47, respectively. The data were taken 2 mm from the centerline to avoid large shrinkage cavities. The as-quenched sample shows much larger scatter than that of the flight sample. This is probably the result of the differences in the dendritic structure in the two cases. The profile for the annealed "ground-truth" sample is similar to that of the flight sample except the steady-state composition is somewhat higher.

Repeated annealing of the quenched samples generally resulted in an increase in the size of the larger shrinkage cavities and a reduction of the size of the smaller ones. This interesting behavior seems to provide strong evidence for the importance of a surface-energy driven ripening effect for the moderate temperatures and short time intervals used.

A back scattering micrograph of the very top portion of the as-quenched ground-truth sample is shown in Figure 48. The presumed high ZnTe content in the several bright areas seen in the figure was confirmed by EDS analysis which indicated a ZnTe content of over 60%. It is believed that during the rather slow cooling process a significant portion of the solid particles of high ZnTe content that formed in the melt just in front of the freezing interface floated to the top of the sample. As expected, no such areas of high ZnTe content were found in the top portion of the flight sample.

III. Summary of Preliminary Flight Results

Because of the loss of power to the CGF, the experiment was terminated after approximately 39 hours into the growth period. About 5.7 mm of sample had been grown at that point. X-ray radiographs of the returned cartridges did not show any features for either the primary or the secondary (not heated in orbit) sample that indicated off-nominal behavior. It is very likely, therefore, that the experiment would have met its objectives for this mission if it had proceeded to conclusion.

Detailed surface photomicrographs of the removed sample clearly showed significant topographical differences between the space- and ground-grown portions. Measurements of the Zn content of the sample along the growth direction indicated that the back melting portion of the experiment was successfully accomplished as planned. The meltback interface location was within 0.5 mm of the desired value. Compositional measurements along the sample axis indicated that the desired steady-state growth for the axial composition was reached at about 3 mm into the growth. An X-ray diffraction and SEM survey of the sample showed that both the ground- and flight-portions of the ingot contained only a few grains, i.e., were nearly single crystals, and the crystallographic orientation was maintained following back-melting and space growth. The interface shape, radial compositional variations, and the quenched-in dendritic structures of the flight sample all have shown an asymmetric behavior. At least the compositional data strongly suggest that the most likely cause was unanticipated transverse residual accelerations.

ACKNOWLEDGMENTS

We would like to thank R. K. Crouch and J. Kearns of NASA/HQ and D. A. Schaefer of NASA/MSFC for programmatic support, J. Mark Jones, NASA/MSFC for sample preparation, Greg Jerman for electron microprobe analysis and Shirley A. Buford, NASA/MSFC, for typing the manuscript for publication. We are also grateful to Robert E. Blanchard of NASA/LeRC for providing his OARE data prior to publication, and C. R. Baugher of NASA/MSFC and to the ACAP project for acceleration data reduction. The work was supported by the Microgravity Science and Applications Division of NASA

REFERENCES

1. Szofran, F.R., and Lehoczky, S.L., J. Crystal Growth 70, 349 (1984).
2. Naumann, R.J., and Lehoczky, S.L., J. Crystal Growth 61, 707 (1983).
3. Jasinski, J., Rohsenow, W.M. and Witt, A.F., J. Crystal Growth 61, 339 (1983).
4. Dakhoul, Y.M., Farmer, R., Lehoczky, S.L. and Szofran, F.R., J. Crystal Growth 86, 49 (1988).
5. Steininger, J., Strauss, A.J., and Brebrick, R.F., J. Electrochem. Soc. 117, 1305 (1970).
6. Steininger, J., J. Electron. Mater. 5, 299 (1976).
7. Kelly, J.D., Martin, B.G., Szofran, F.R., and Lehoczky, S.L., J. Electrochem Soc. 129, 2360 (1982).
8. Yu, T.C. and Brebrick, R.F., J. Phase Equilibria 13, 476 (1992).
9. Holland, L.R., and Taylor, R.E., J. Vacuum Sci. Technol. A1, 1615 (1983).
10. Su, C.-H., J. Crystal Growth 78, 51 (1986).
11. Szofran, F. R. and Lehoczky, S . L., Bull. APS 28, 1313 (1983).
12. Cobb, S.D., Andrews, R.N., Szofran, F.R. and Lehoczky, S.L., J. Crystal Growth, 110, 415 (1991).
13. Lehoczky, S.L. and Szofran, F.R., NASA Technical Paper 2787 (December 1987).
14. Lehoczky, S.L. and Szofran, F.R., "Growth of Solid Solution Single Crystals," in The Nation's Future Materials Needs, International SAMPE Technical Conference Series, Lynch, T., Persh, J., Wolf, T., and Rupert N., eds., (SAMPE: Technical Conference, Arlington, Virginia, October 13-15, 1987).
15. Cobb, S. D., Szofran, F. R. and Lehoczky, S. L., "Growth Rate Dependence of the Radial Segregation in Directionally Solidified $Hg_{1-x}Cd_xTe$ Alloys," MCG/West 10th Conference on Crystal Growth, Fallen Leaf Lake, California, June 7-10, 1988.16. Kim, D.H. and Brown, R.A., Massachusetts Institute of Technology, private communication, to be published in J. Crystal Growth.
17. Kim, F.H., Brown, R.A., J. Crystal Growth 114, 411 (1991).
18. Su, C.-H., Lehoczky, S.L., and Szofran, F.R., J. Crystal Growth 109, 392 (1991).
19. Experiment to be flown on the Second United States Microgravity Payload (USMP-2) mission.
20. Lehoczky, S.L., Szofran, F.R., and Martin, B.G., NASA CR-161598, (1980).
21. Clayton, J.C., NASA CR-162049, (1982).
22. Clayton, J.C., Davidson, M.C., Gillies, D.C., and Lehoczky, S.L., J. Crystal Growth 60, 374 (1982).
23. Andrews, R.N., Szofran, F.R. and Lehoczky, S.L., J. Crystal Growth, 92, 445 (1988).

24. Szofran, F.R., Chandra, D., Wang, J.-C., Cothran, E.K., and Lehoczky, S.L., *J. Crystal Growth* 70, 343 (1984).
25. Blanchard, R.E. and Baugher, C.R., private communication (to be published).

Table 1: Ground-Based $Hg_{0.84}Zn_{0.16}Te$ Alloy Crystals Grown

Sample	Preprocessed Furnace	Growth Furnace	Hot Zone Temp (°C)	Cold Zone Temp (°C)	Growth Rate (mm/day)	Length Grown (mm)
B16-L	SSL	-	790	530	3.8	101.3
*B18-K	SSL	SSL	790	550	3.8	29.6
+B16-1	SSL	GCEL (1) GCEL (2)	800 800	375 375	3.5 3.5	10.8 10.4
+B16-2	SSL	GCEL (1) GCEL (2)	780 780	350 350	3.5 3.5	8.9 11.6
+B164	SSL	GCEL (1) GCEL (2)	800 800	555 555	3.5 3.5	21.7 7.1
B16-8	GCEL	GCEL	800	350	3.5	17.7
B16-33	SSL	GCEL	800	350	3.5	17.9

* $Hg_{0.82}Zn_{0.18}Te$ sample

+For samples B16-1, 2 and 4, the samples were preprocessed in SSL furnace and back-melted, regrown, and quenched in GCEL (labeled as GCEL (1)), and then back-melted, and regrown again in GCEL (labeled as GCEL (2))

Table 2: Measured and Estimated Radial Segregation

Measured	Estimated
$\frac{\Delta C_1}{C_o} = 0.40$	$\frac{\Delta C_1}{C_o} = 0.068$
$\frac{\Delta C_2}{C_o} = 0.18$	$\frac{\Delta C_2}{C_o} = 0.046$

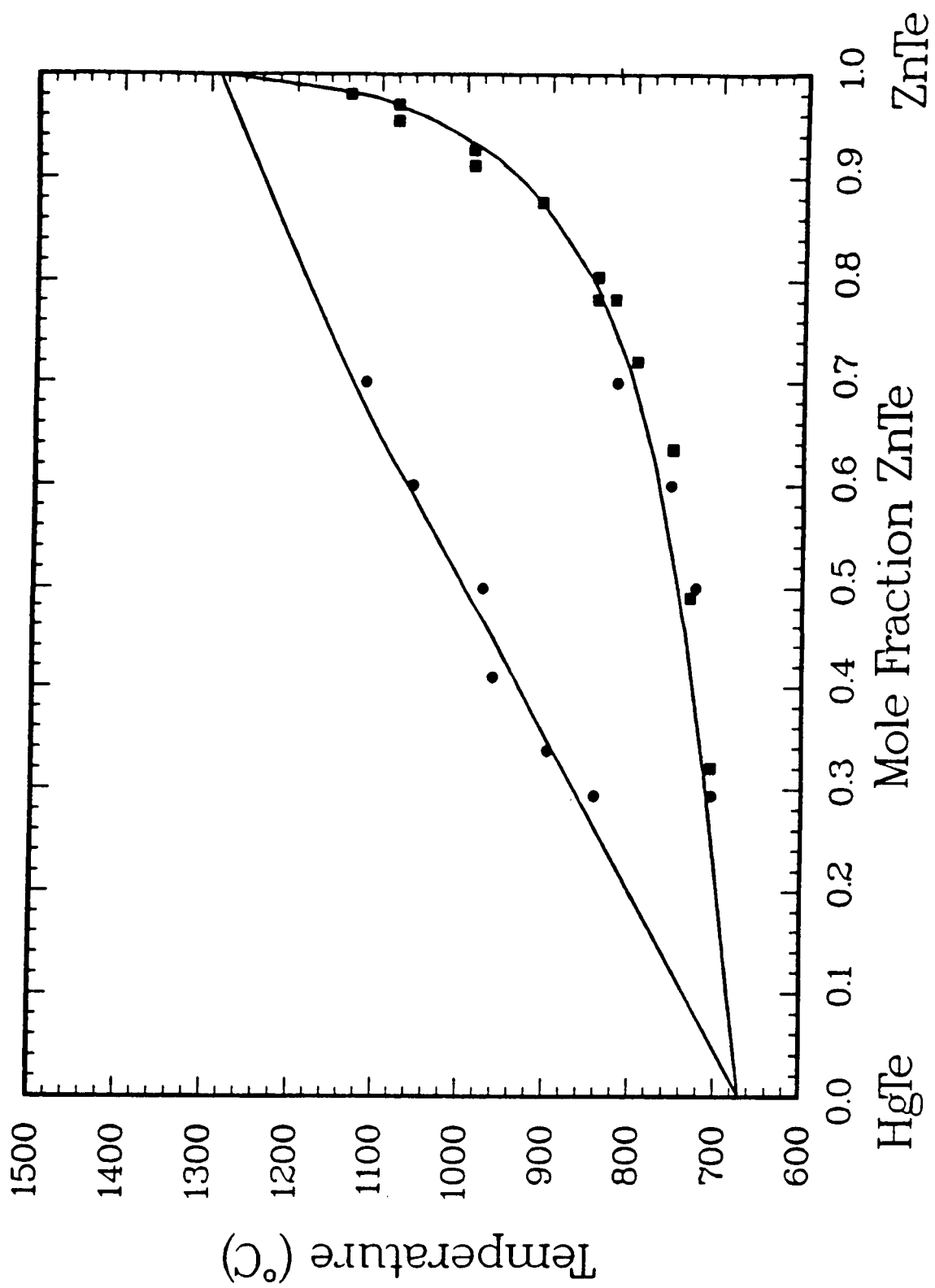


Figure 1 $\text{Hg}_1\text{x}\text{ZnTe}$ pseudobinary constitutional phase diagram.

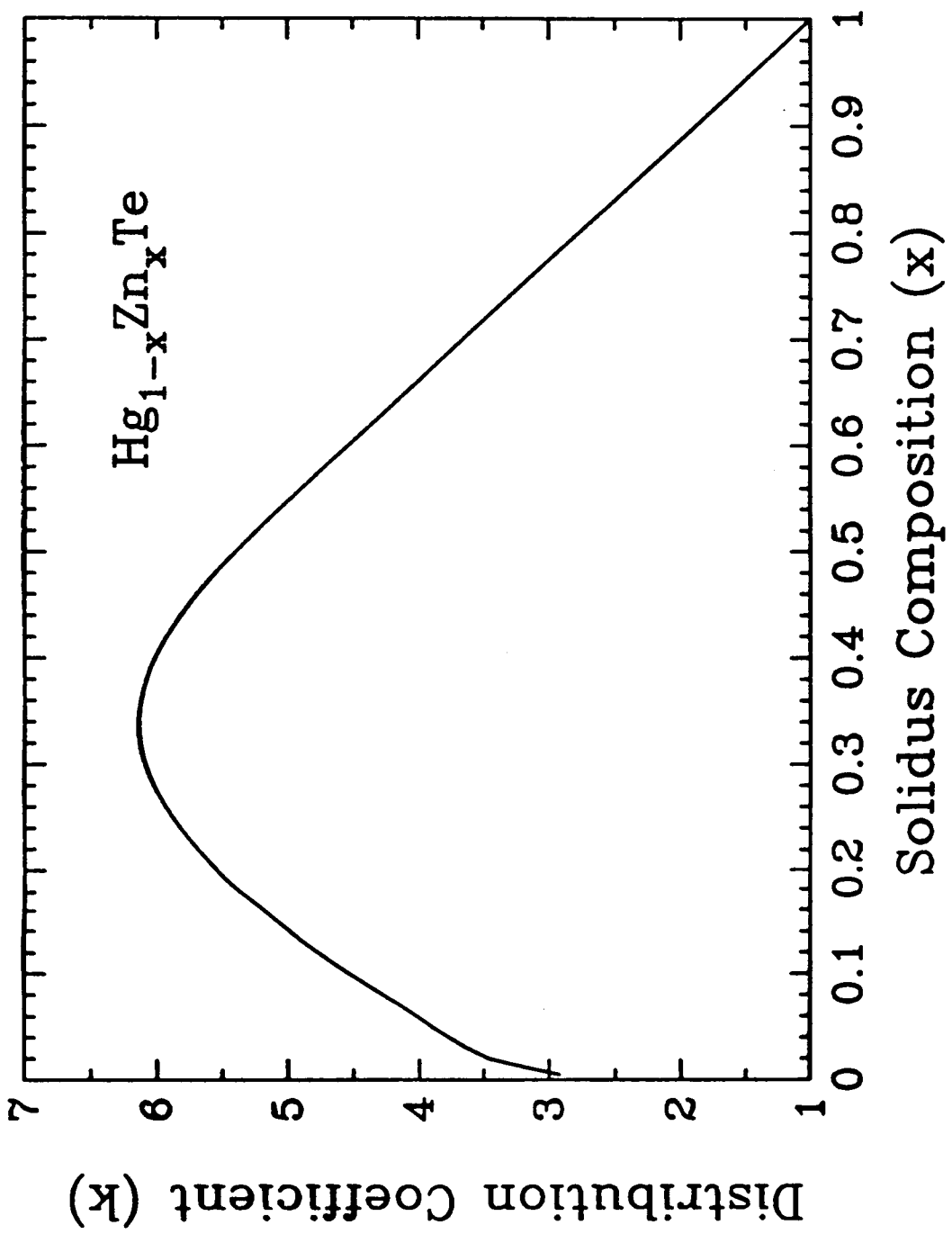
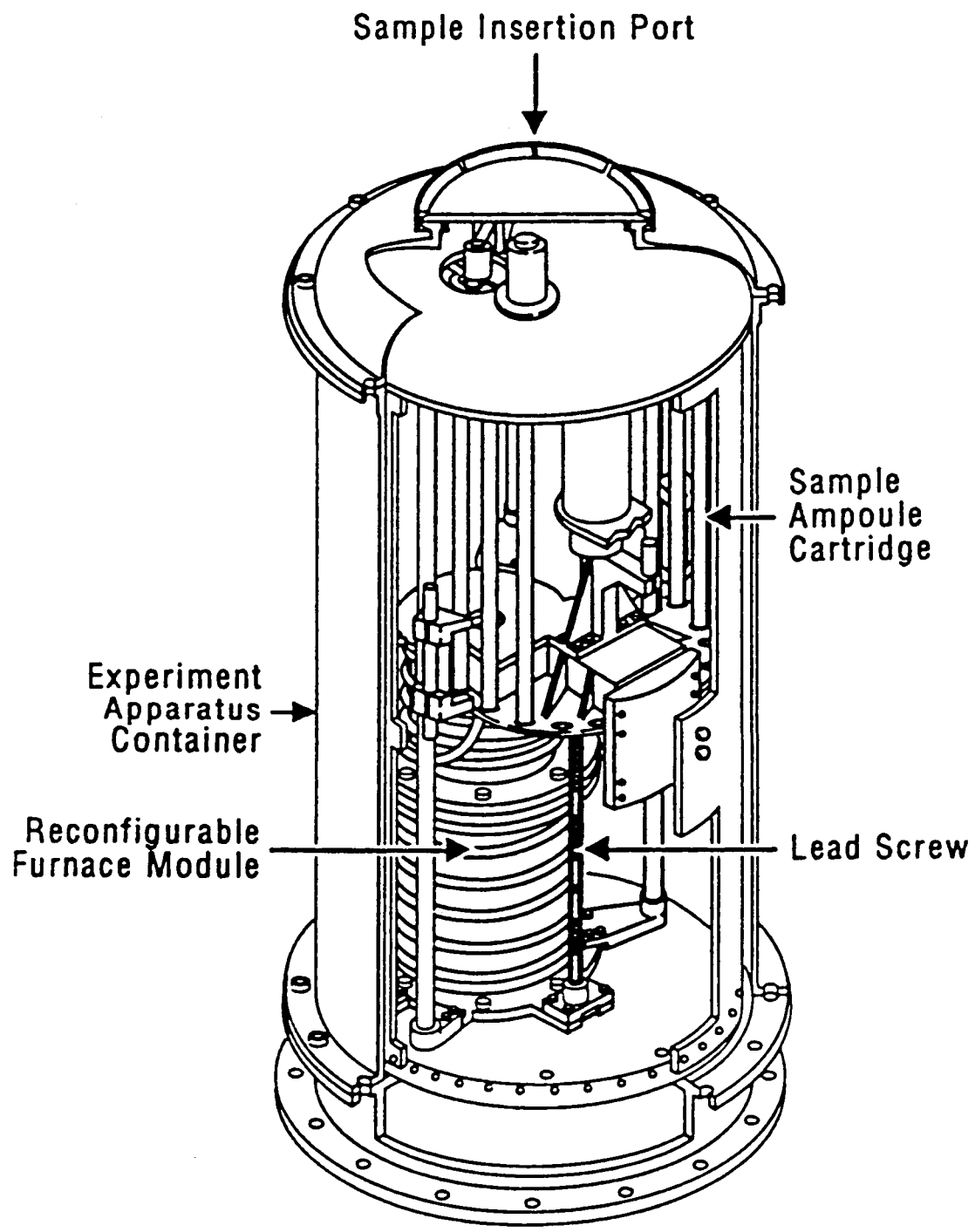


Figure 2 Composition dependence of the solidification interface segregation coefficient.



The Crystal Growth Furnace

Integrated Furnace Experiment Assembly (IGEA)

Figure 3 Crystal Growth Furnace schematic

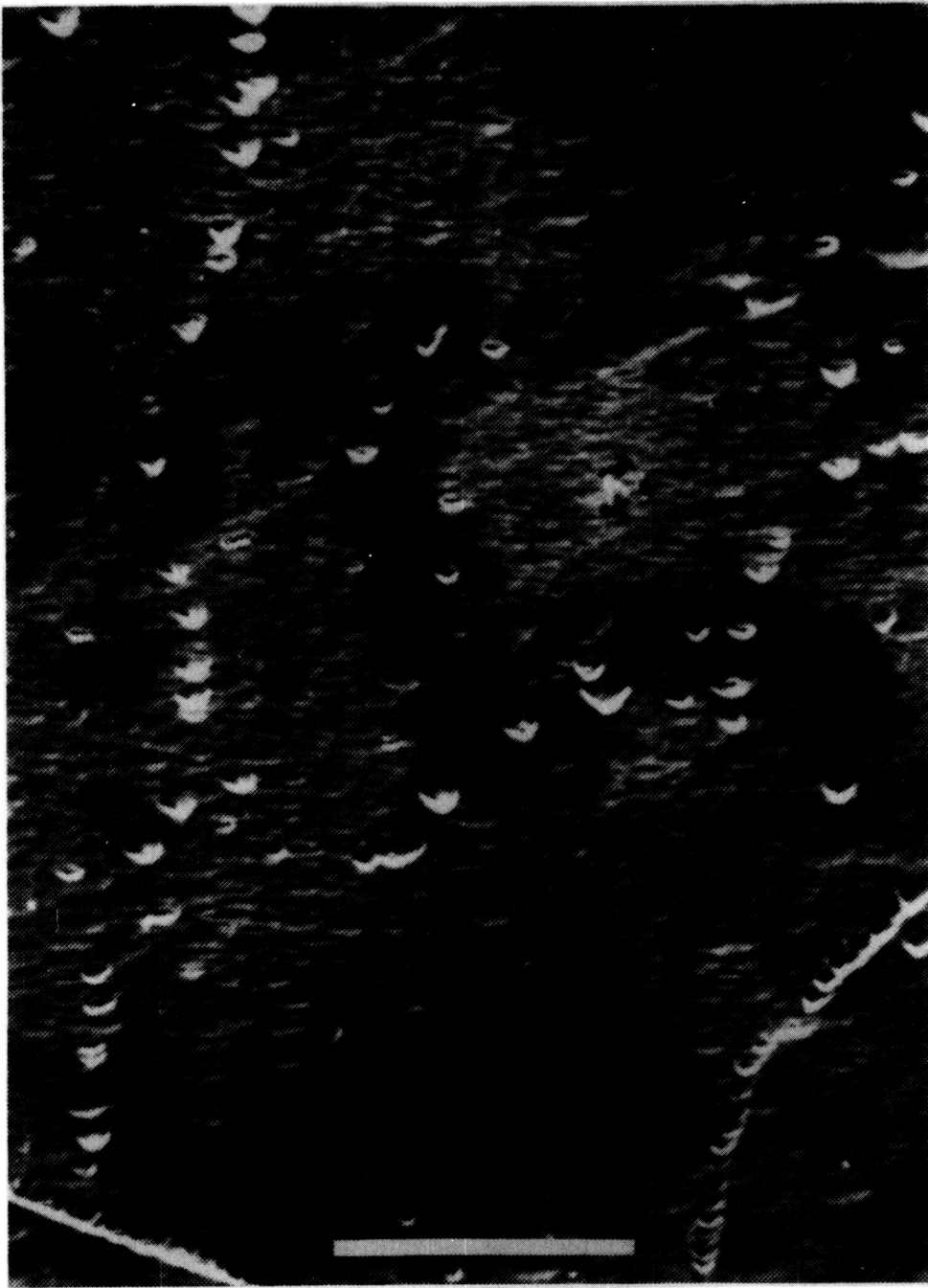


Figure 4 Typical dislocation etch pits showing individual dislocations and sub-grain boundaries. Marker represents 50 μm .

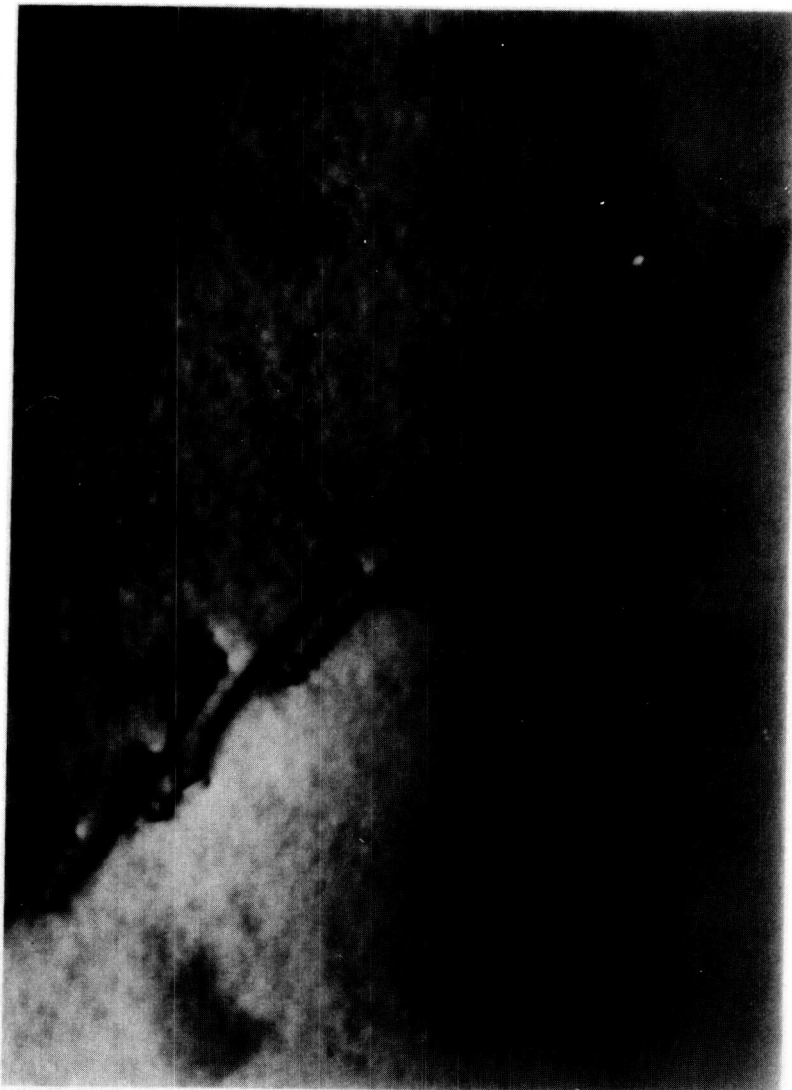


Figure 5 Transmission electron micrograph for a $\text{Hg}_{0.84}\text{Zn}_{0.16}\text{Te}$ wafer showing a subgrain boundary.



Figure 6 Transmission electron micrograph for a Hg_{0.84}Zn_{0.16}Te wafer showing individual dislocations with 110-type Burger's vectors.

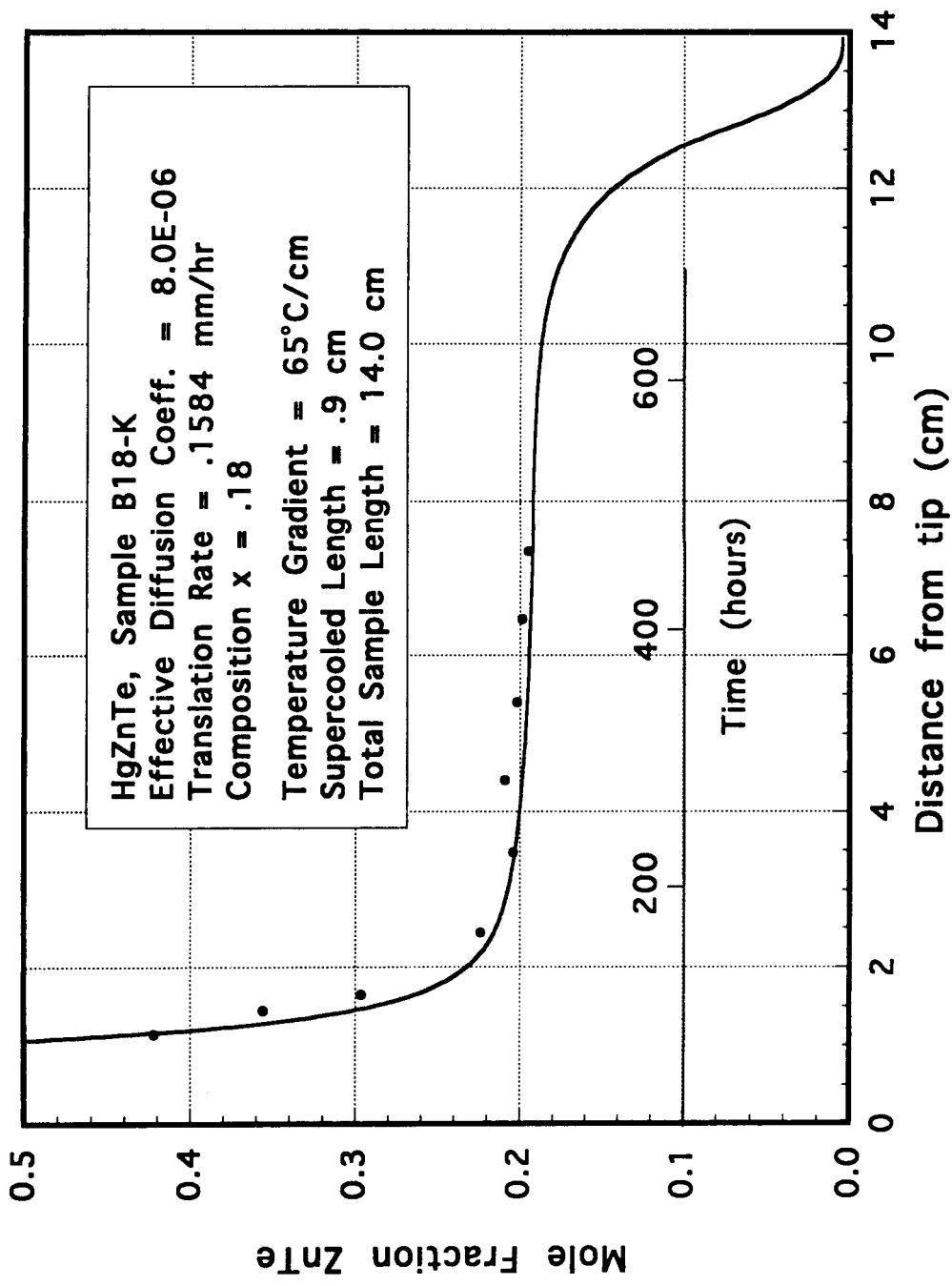
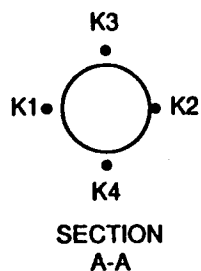
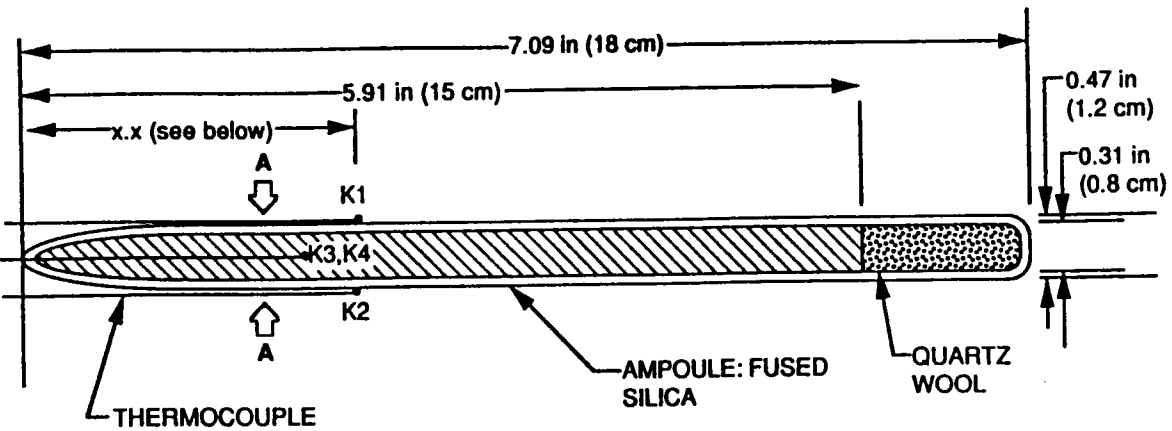
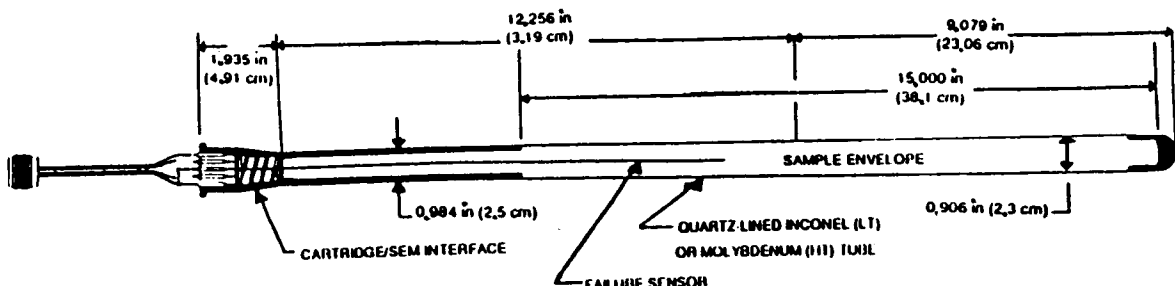


Figure 7 Axial variation in an $\text{Hg}_{0.82}\text{Zn}_{0.18}\text{Te}$ alloy crystal showing measured and calculated results.



Thermocouple	x.x (Nominal Distance From Ampoule End)
K1	2.36 in (6 cm)
K2	2.36 in (6 cm)
K3	1.97 in (5 cm)
K4	1.97 in (5 cm)

(a)



(b)

Figure 8 Schematic drawing of sample ampoule (a) and cartridge (b) configurations.

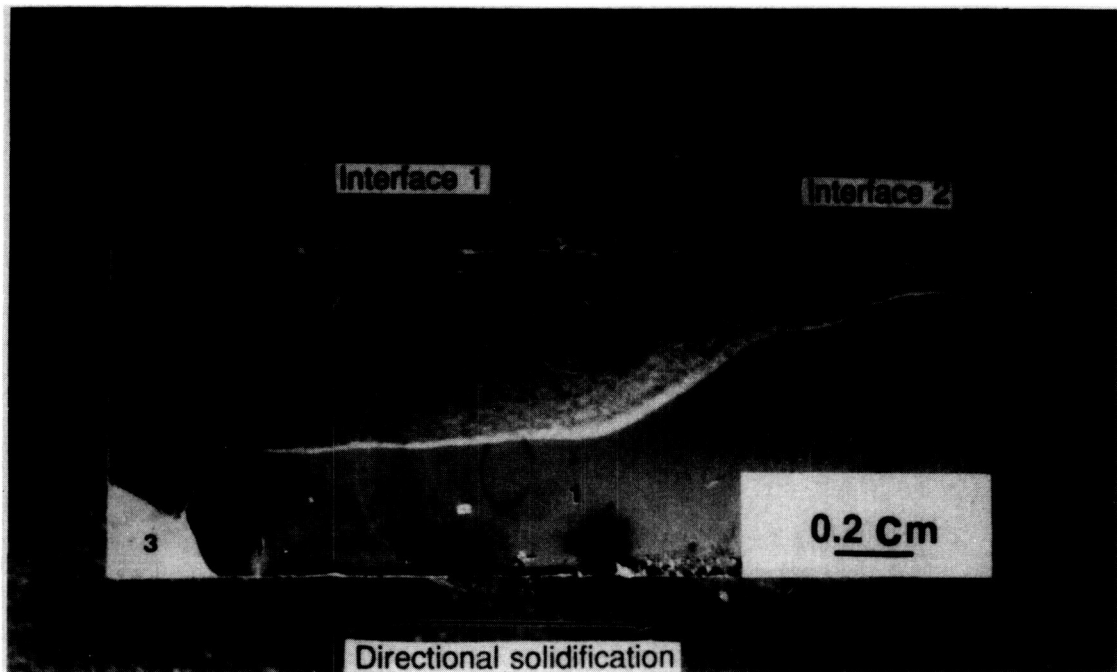


Figure 9 Grain structure near the quenched, back-melted and regrowth interface.

Zn Content in $Hg_{1-x}Zn_xTe$ B16-1A-B

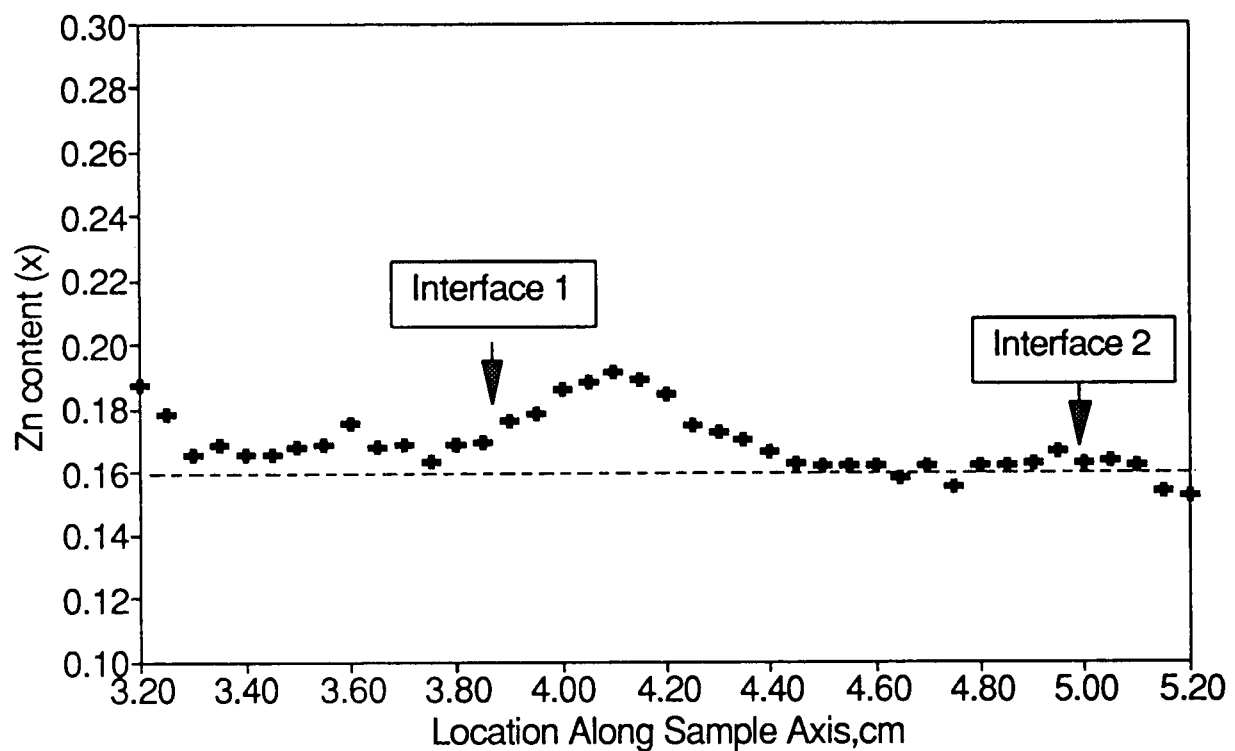


Figure 10 Axial compositional distribution following back-melt/regrowth sequence.

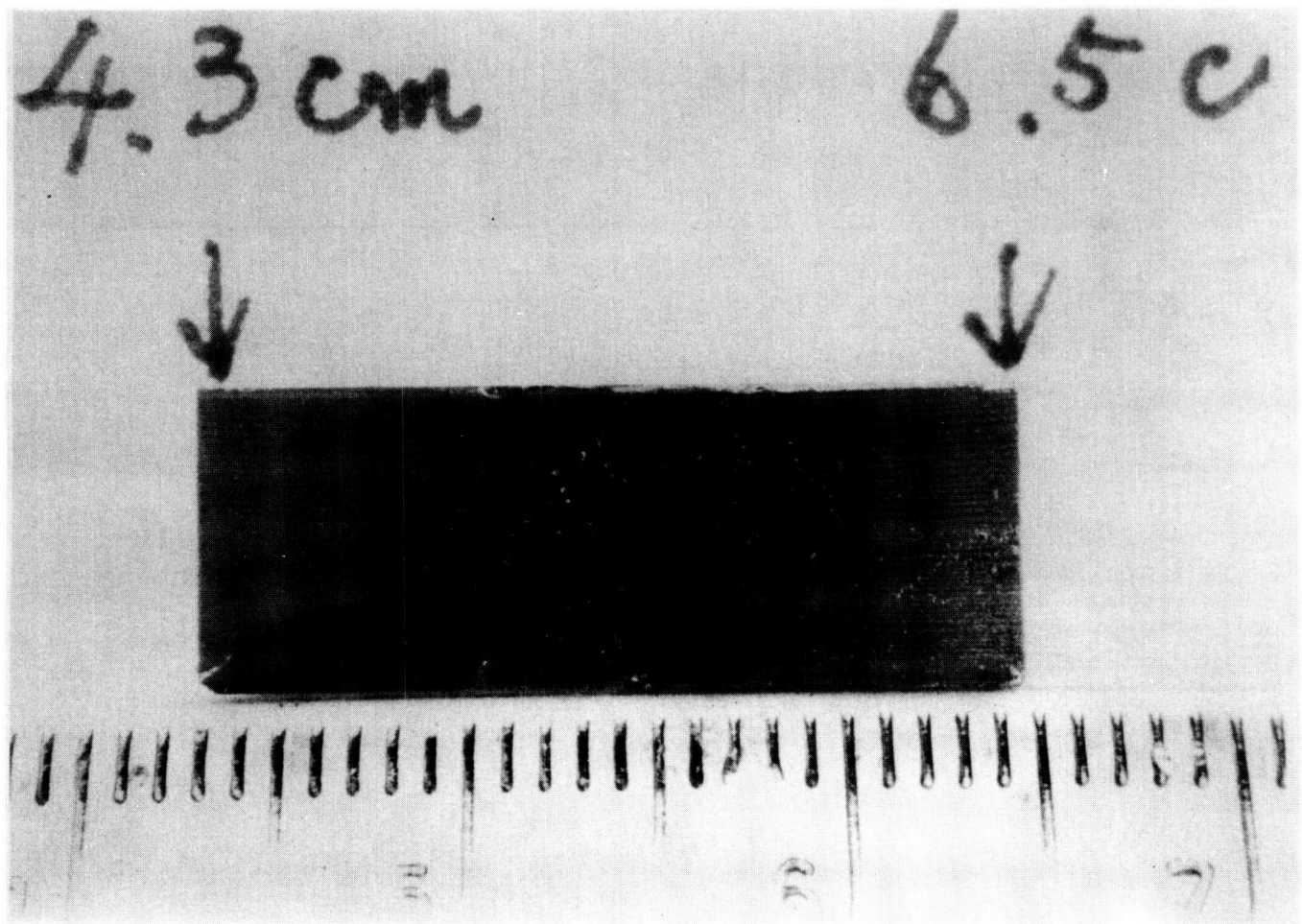


Figure 11 Interface shape for a hot zone temperature of 800°C and a cold zone temperature of 555°C.

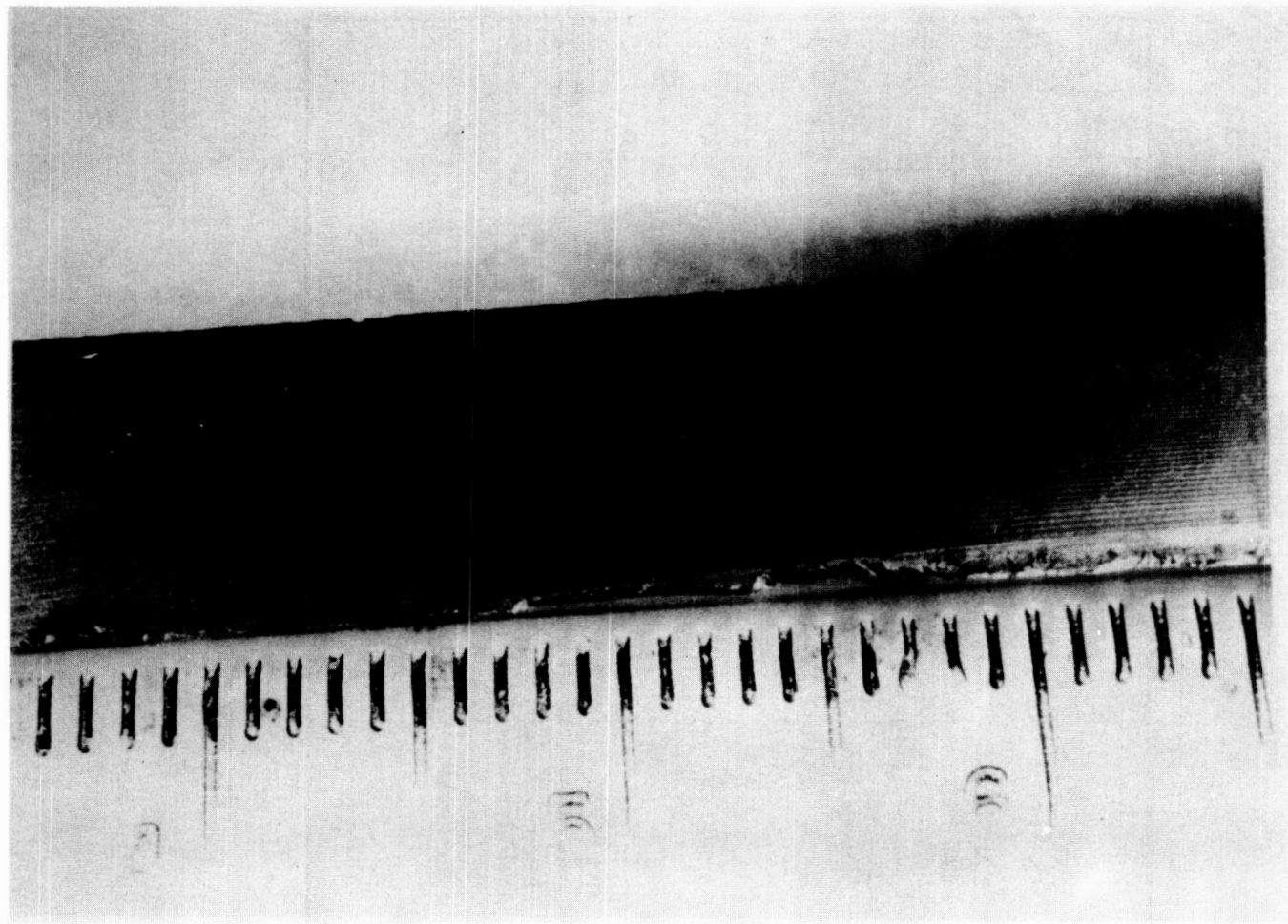


Figure 12 Interface shape for a hot zone temperature of 780 °C and a cold zone temperature of 350 °C.

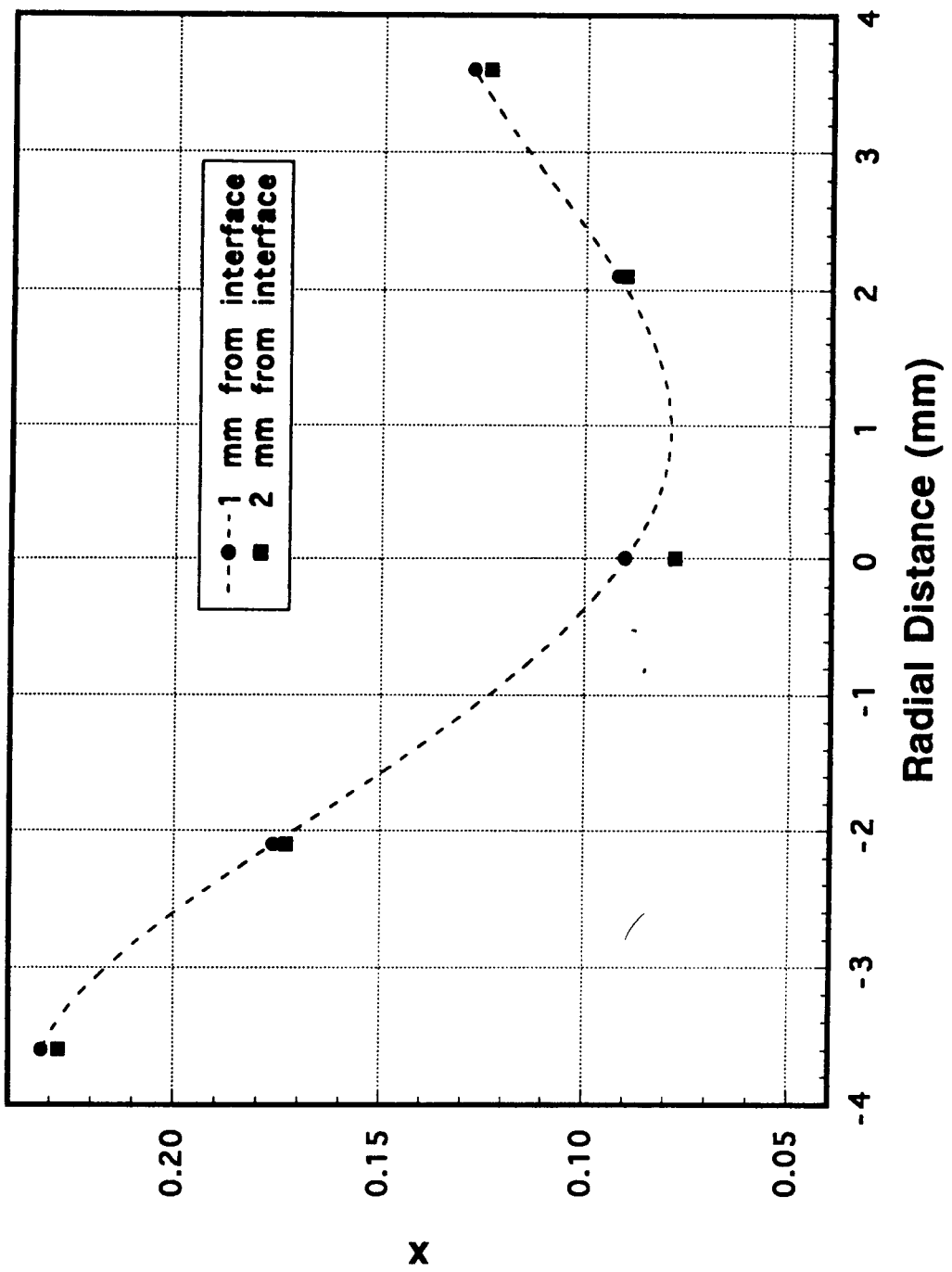


Figure 13 Radial compositional variation for ingot shown in Figure 11.

Radial Distribution

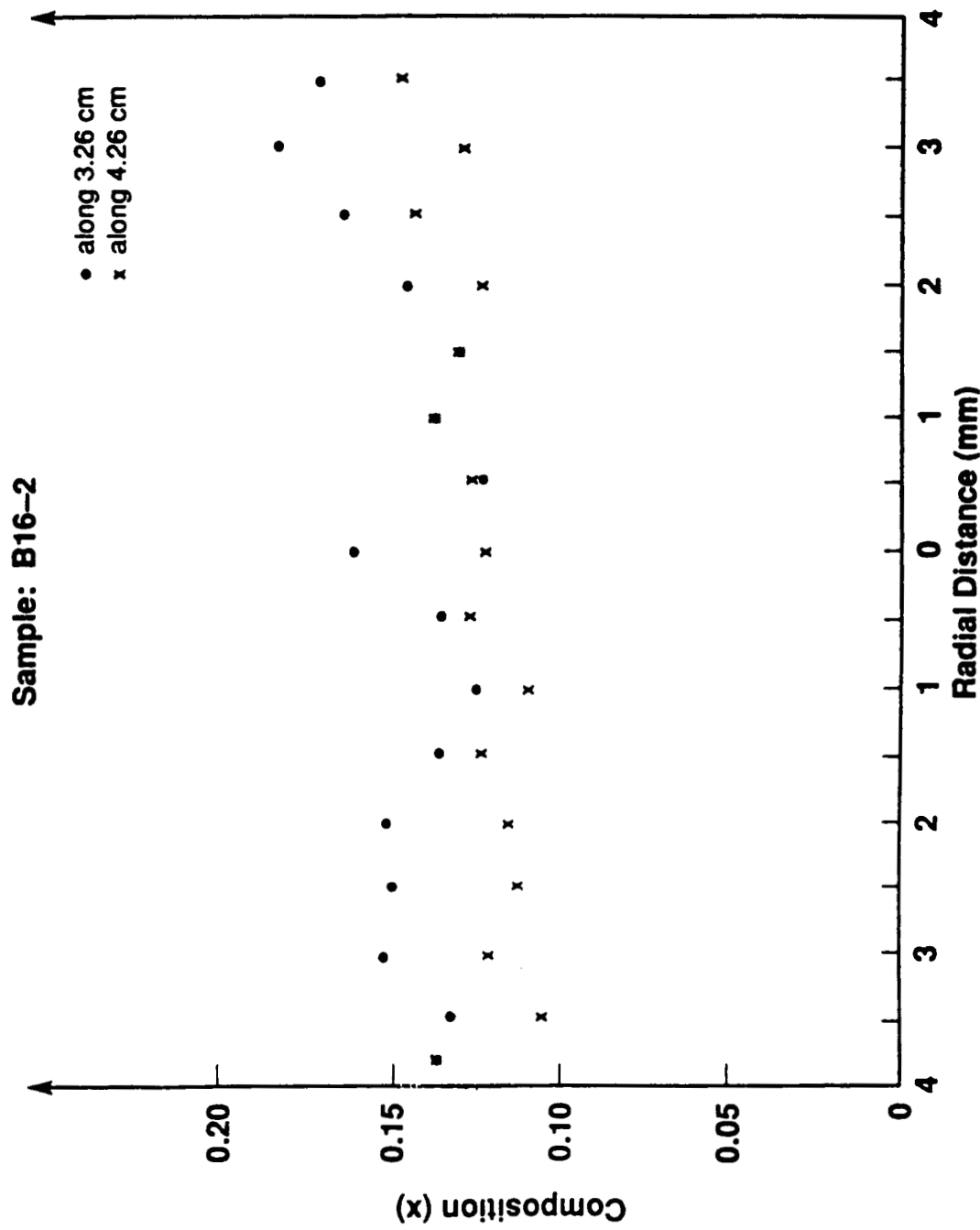


Figure 14 Radial compositional variation for ingot shown in Figure 12. The data were measured along 3.26 and 4.26 cm from the first freeze (the interface is at about 5.3 cm from the first freeze).

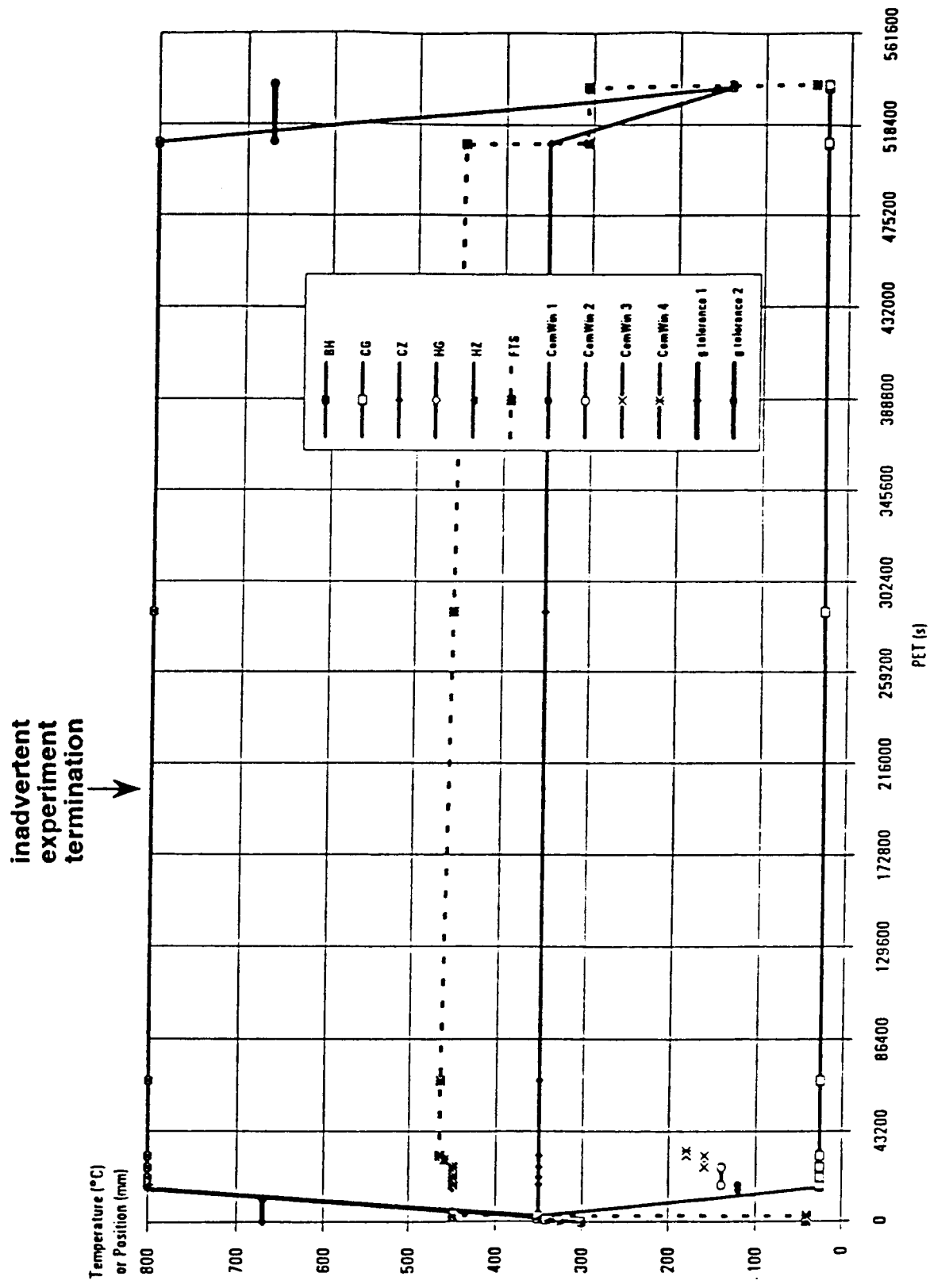


Figure 15 Scheduled USML-1 timeline.

270

180

90

MSFC JULY 14 92

SIN08 B16-7

0

Figure 16 Radiograph of returned flight sample.

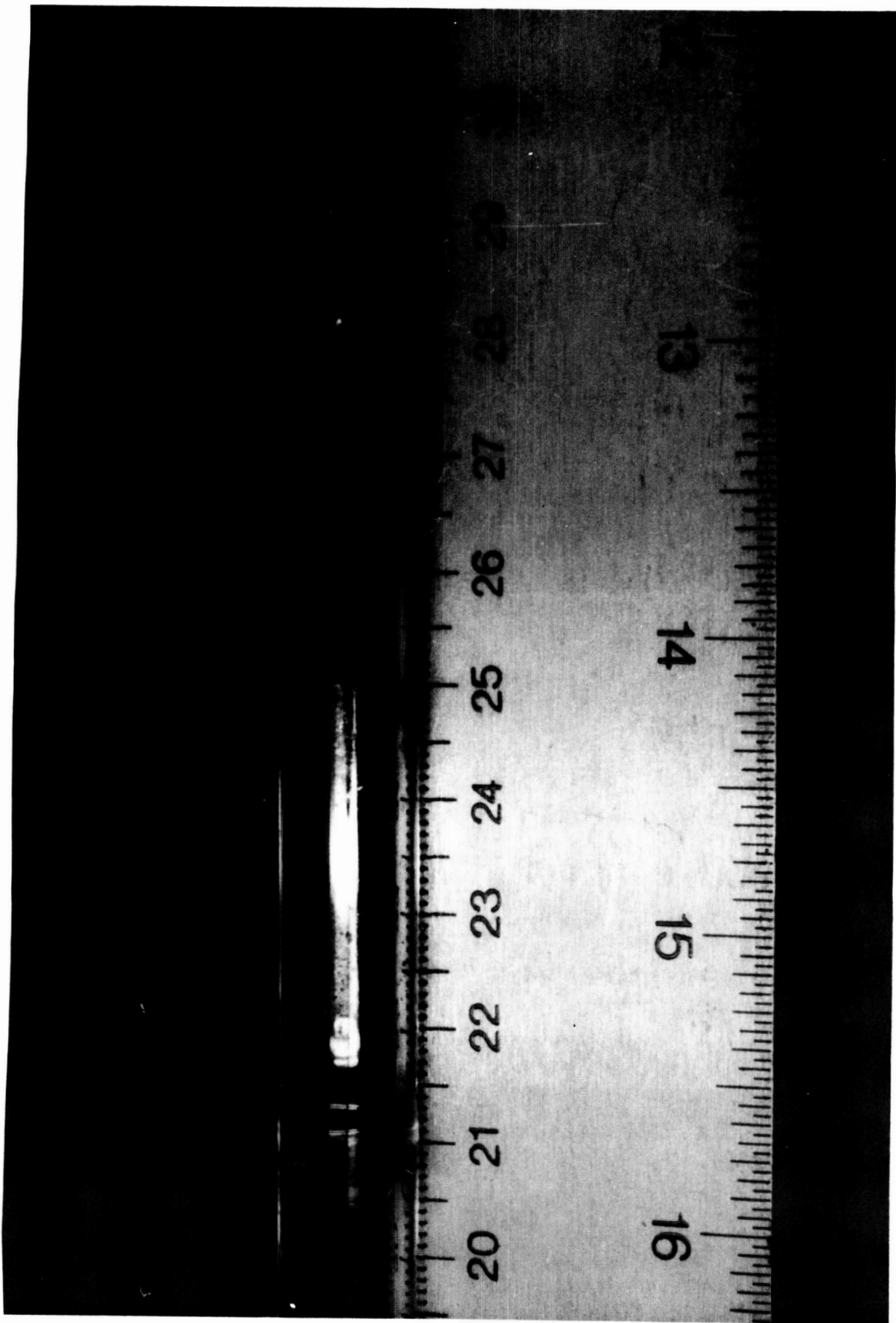


Figure 17 Flight sample photograph inside fused-silica ampoule.

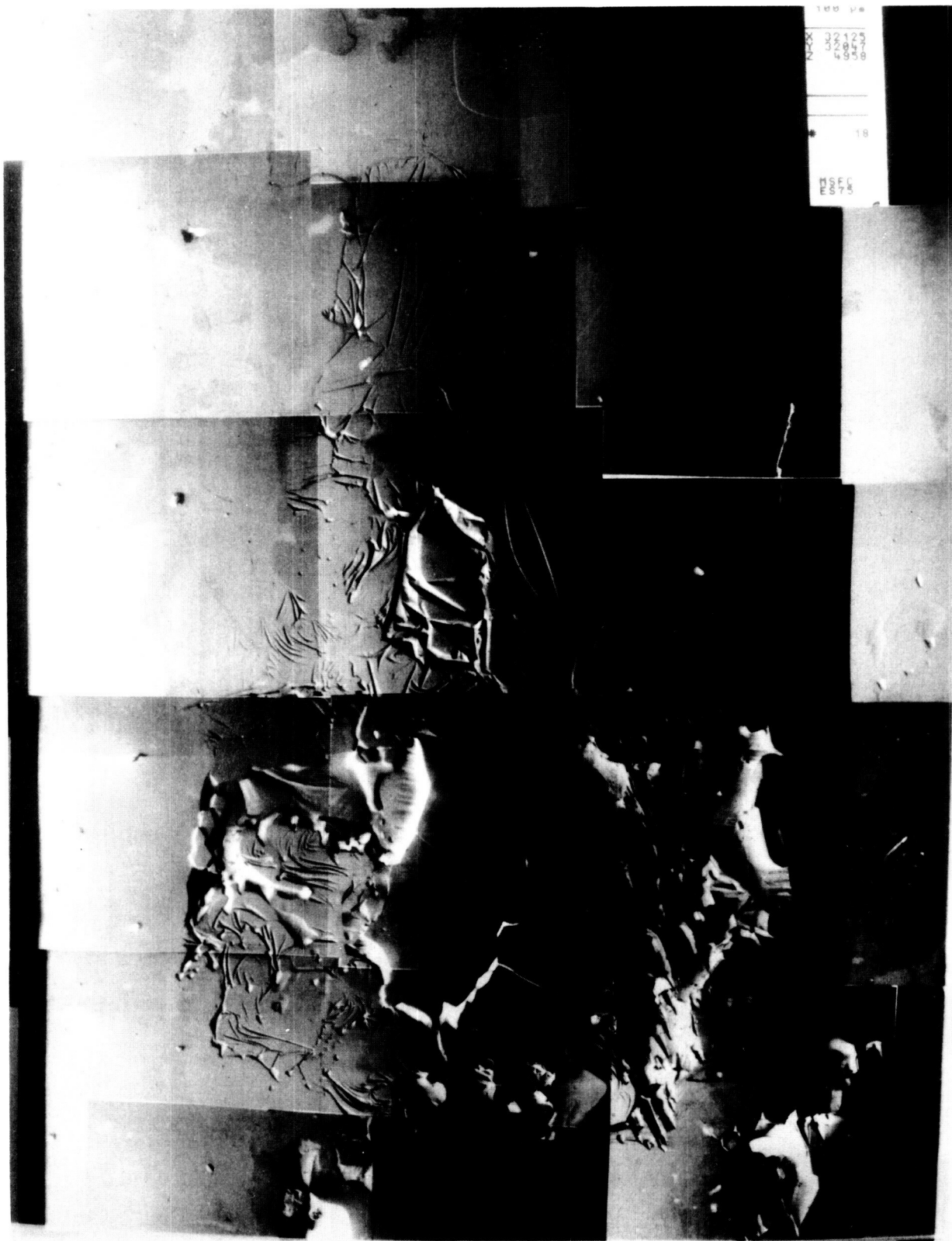


Figure 18 Surface photomicrograph of space grown region.



Figure 19 Surface photomicrograph of ground-truth sample for same axial location as for flight sample shown in Figure 18.

USML-1 CGF

2

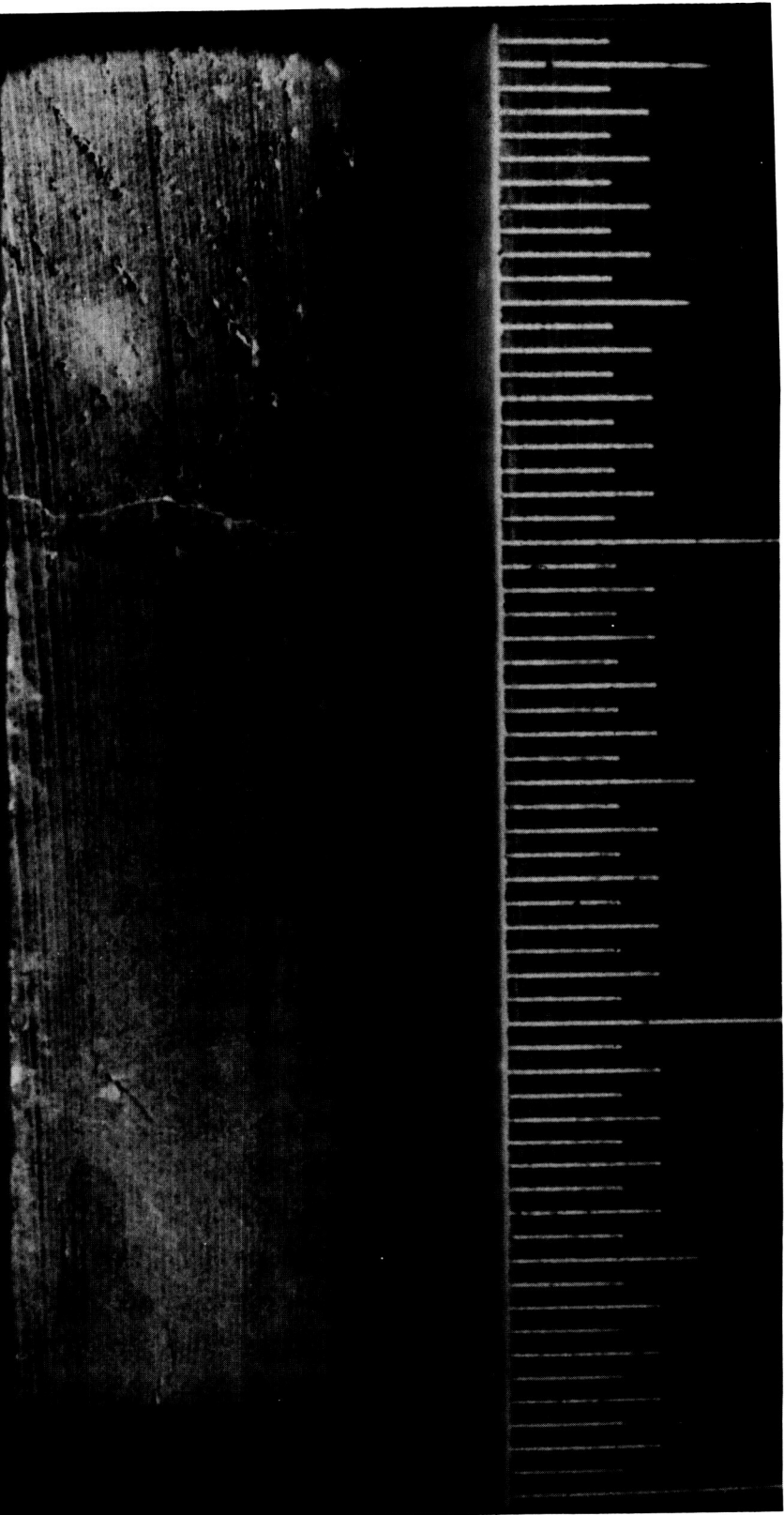


Figure 20 Quenched-in melt/solid interface shown in a longitudinal section cut from the flight sample.

HgZnTe Ground Truth Sample

4.7 – 6.3 cm from FTF



Figure 21 Quenched-in melt/solid interface shown in a longitudinal section cut from “ground-truth” sample after annealing. (Note that the cut is not exactly perpendicular to the crystal axis.)

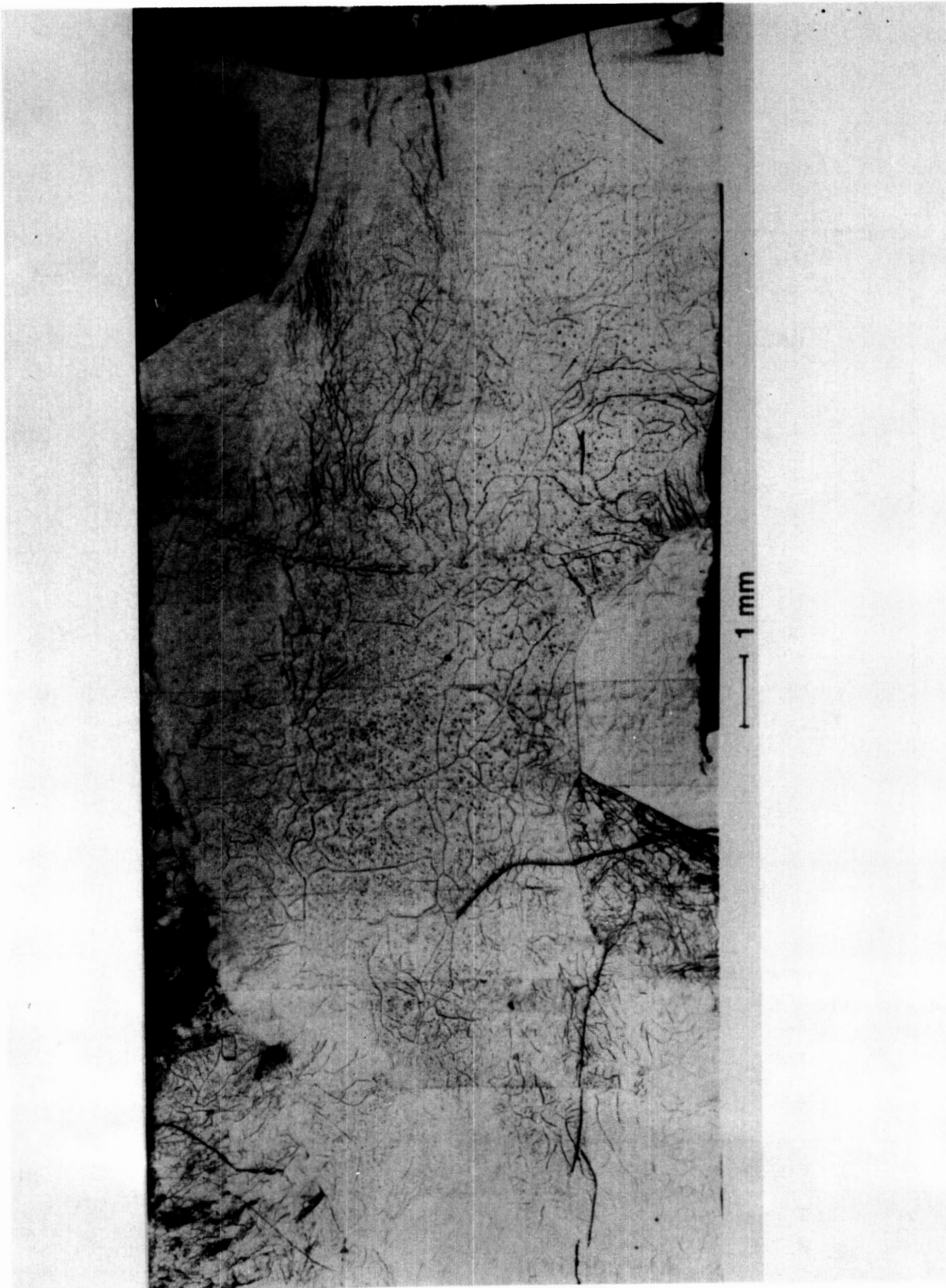


Figure 22 Photomicrograph of polished and bromine-etched slab from flight sample.

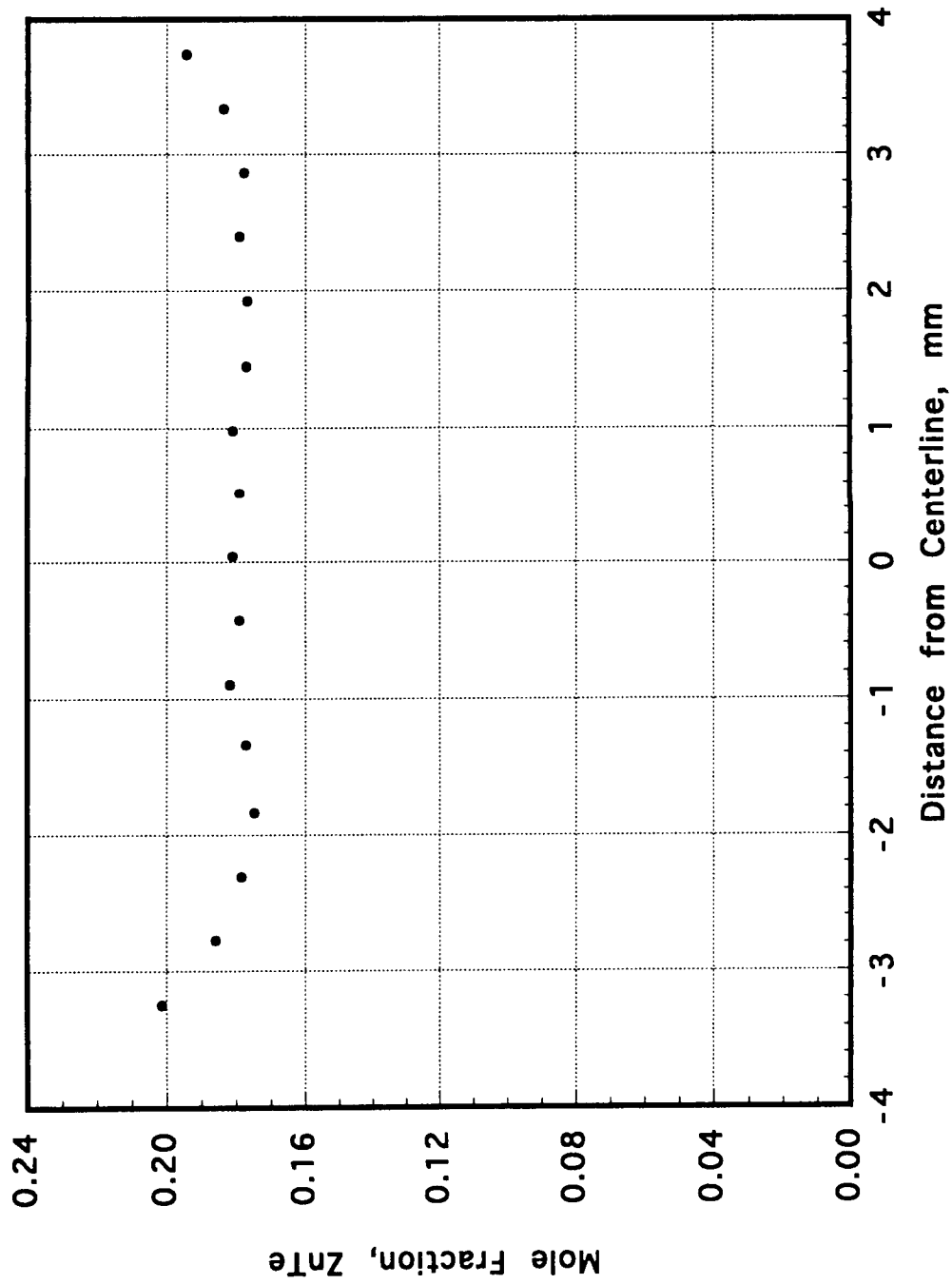


Figure 23 Flight sample radial compositional distribution 6 mm from quenched-in interface.

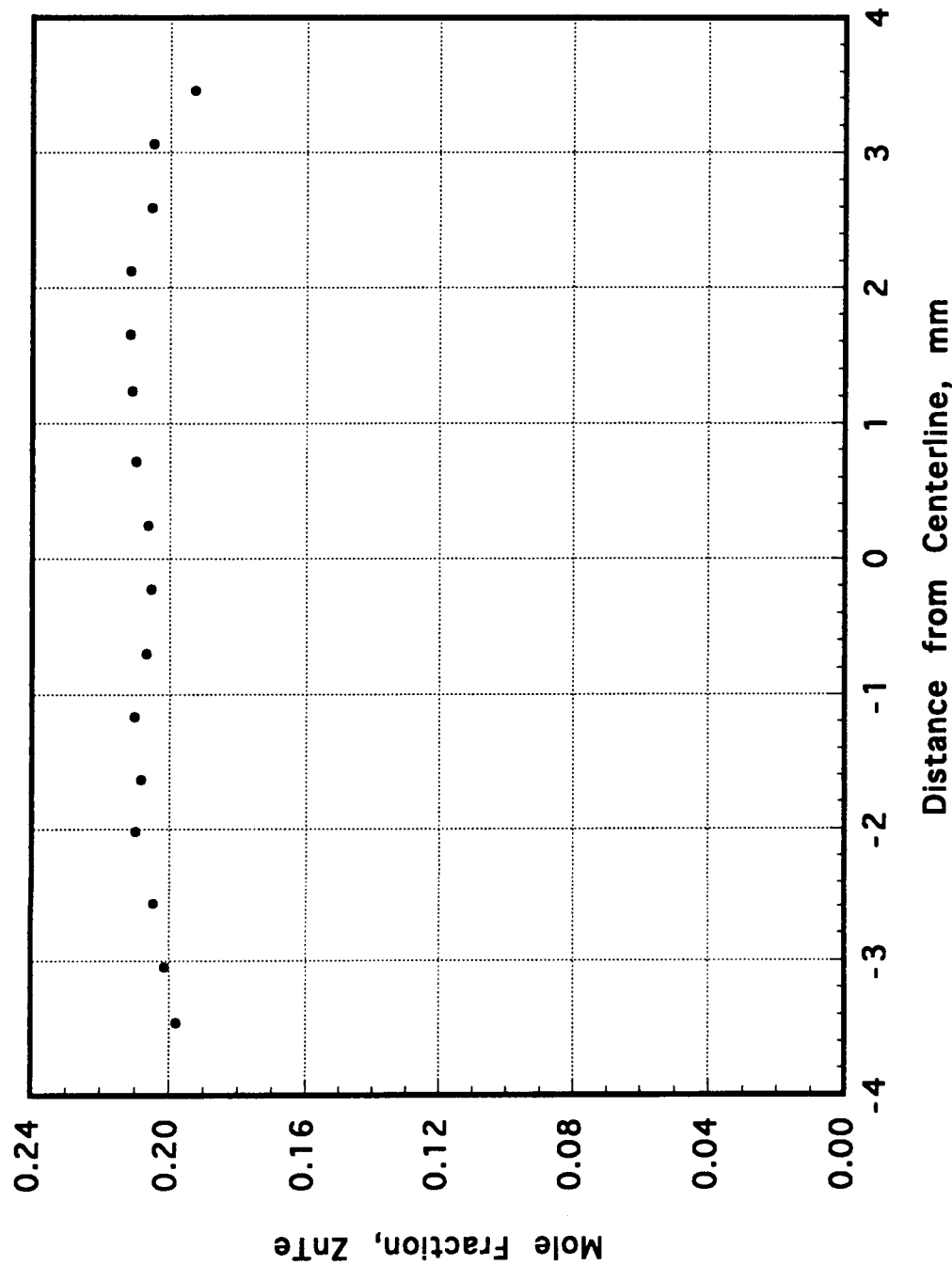


Figure 24 Flight sample radial compositional distribution 5 mm from quenched-in interface.

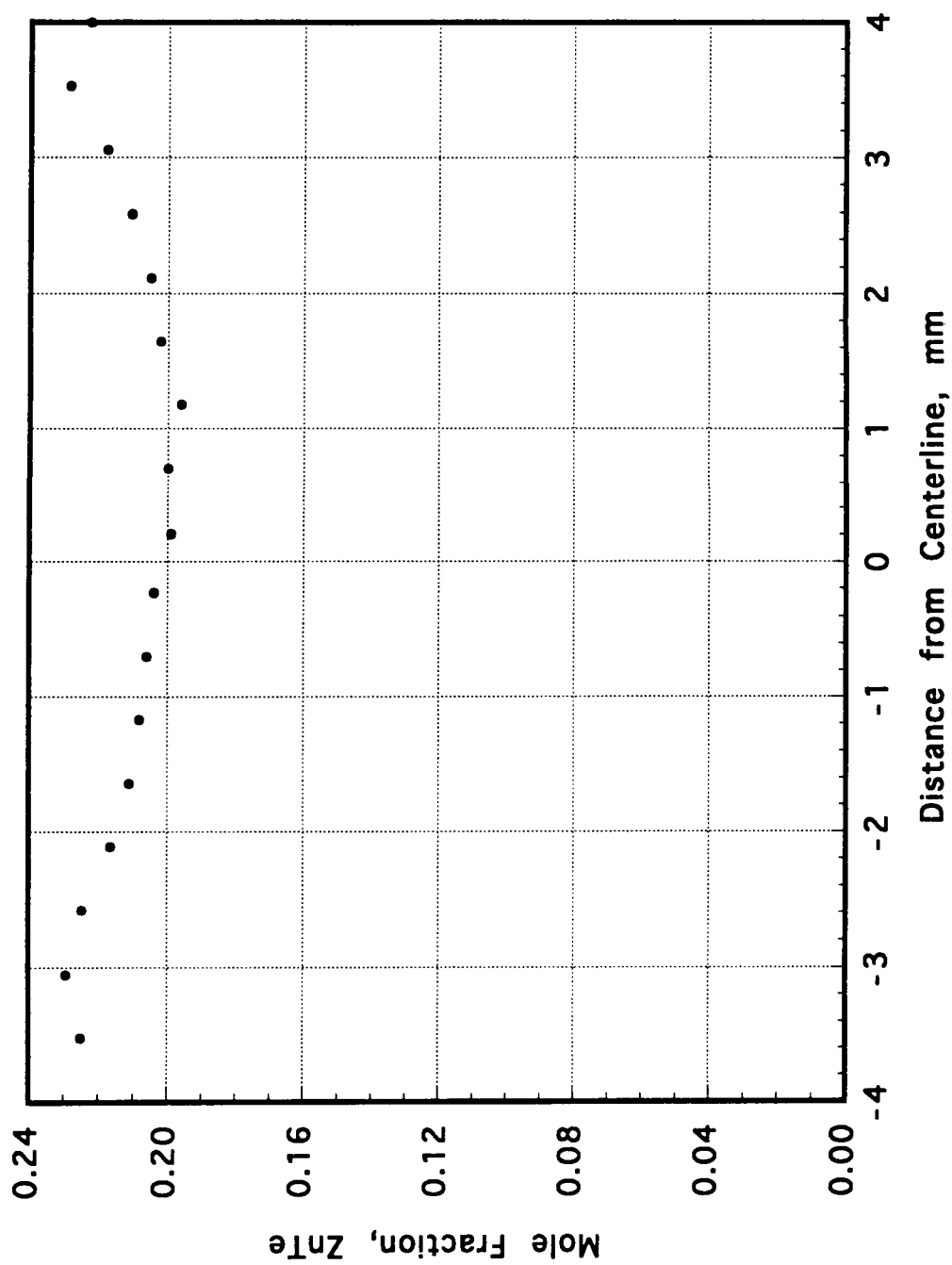


Figure 25 Flight sample radial compositional distribution 4 mm from quenched-in interface.

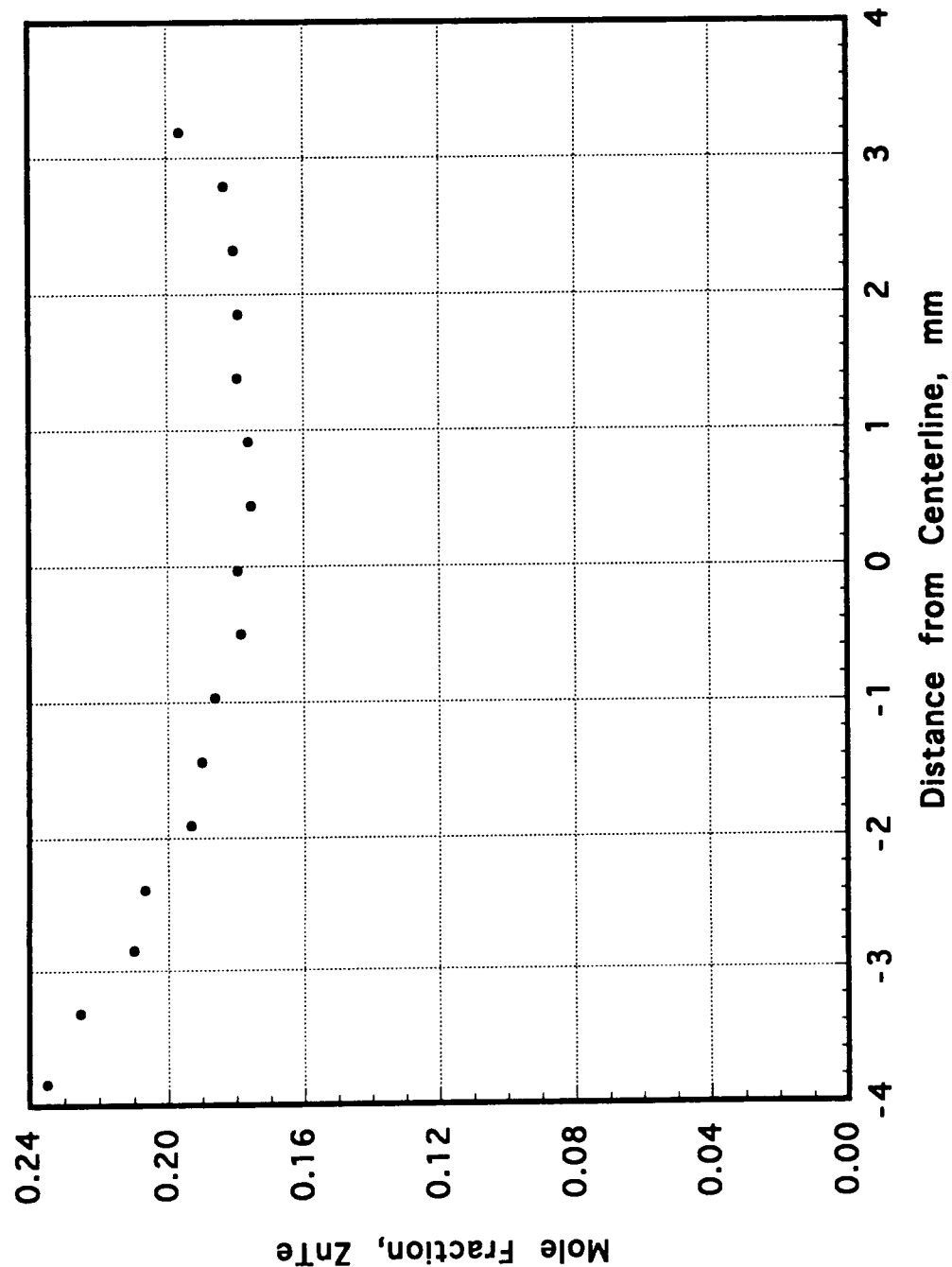


Figure 26 Flight sample radial compositional distribution 3 mm from quenched-in interface.

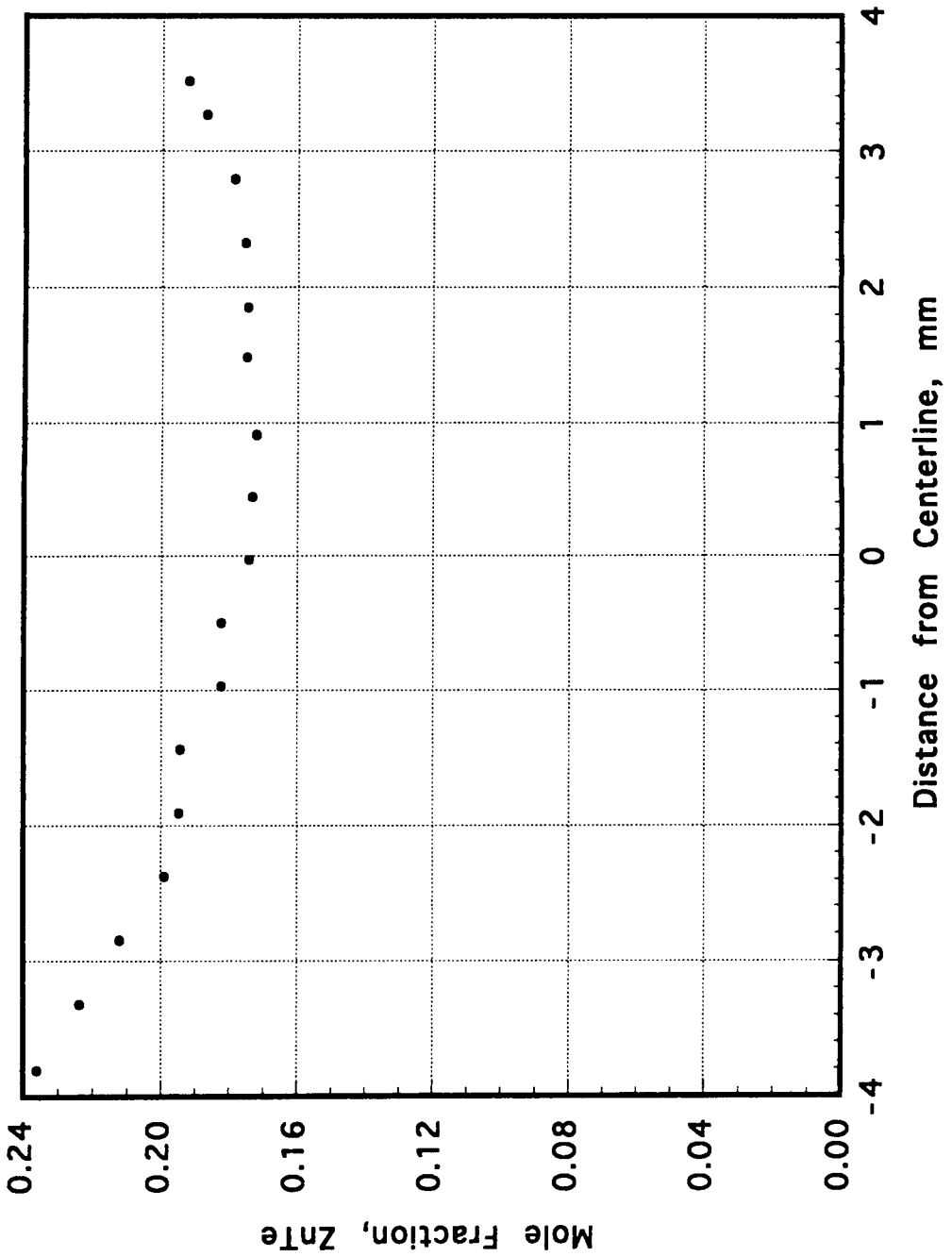


Figure 27 Flight sample radial compositional distribution 2 mm from quenched-in interface.

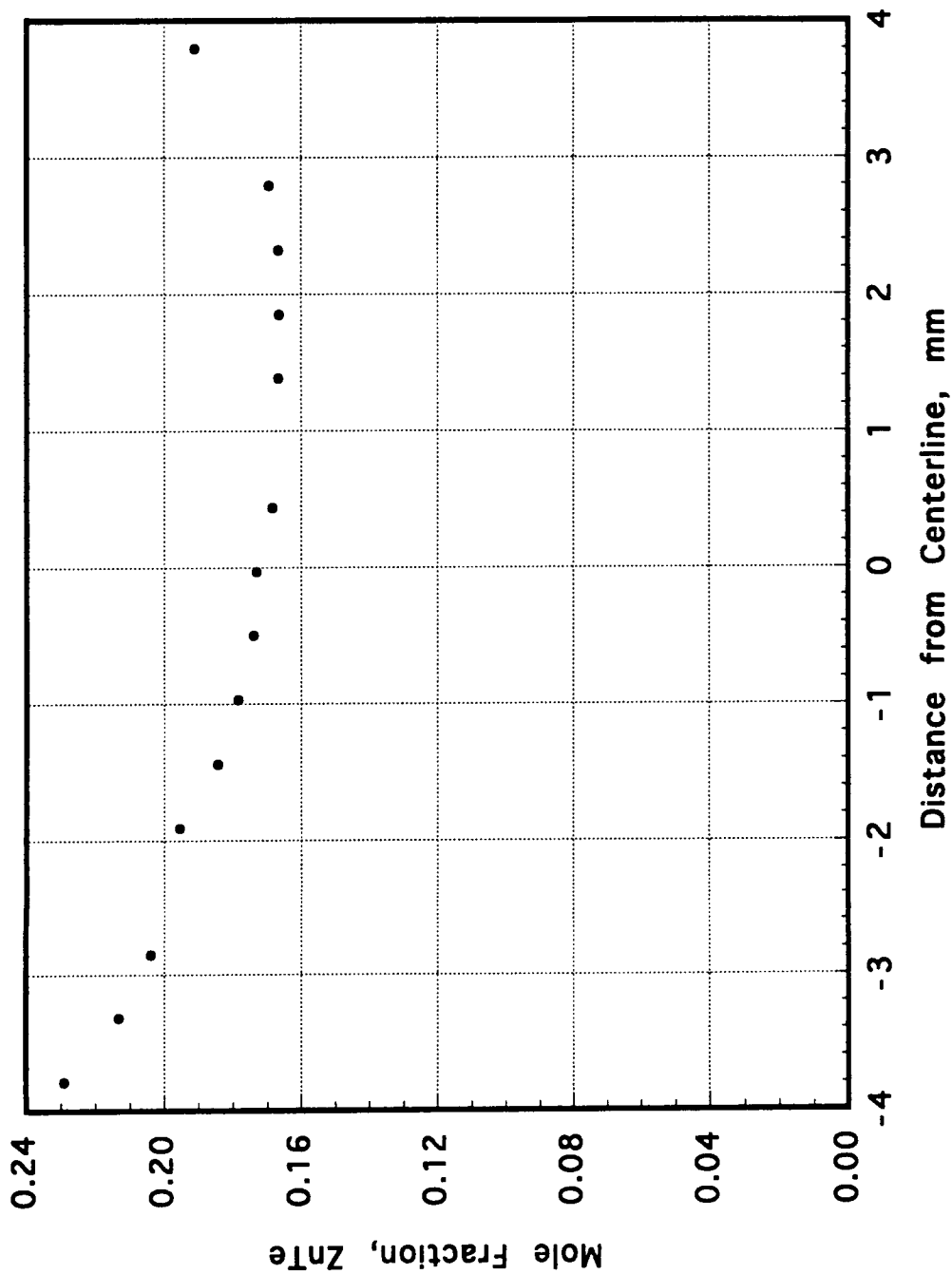


Figure 28 Flight sample radial compositional distribution 1 mm from quenched-in interface.

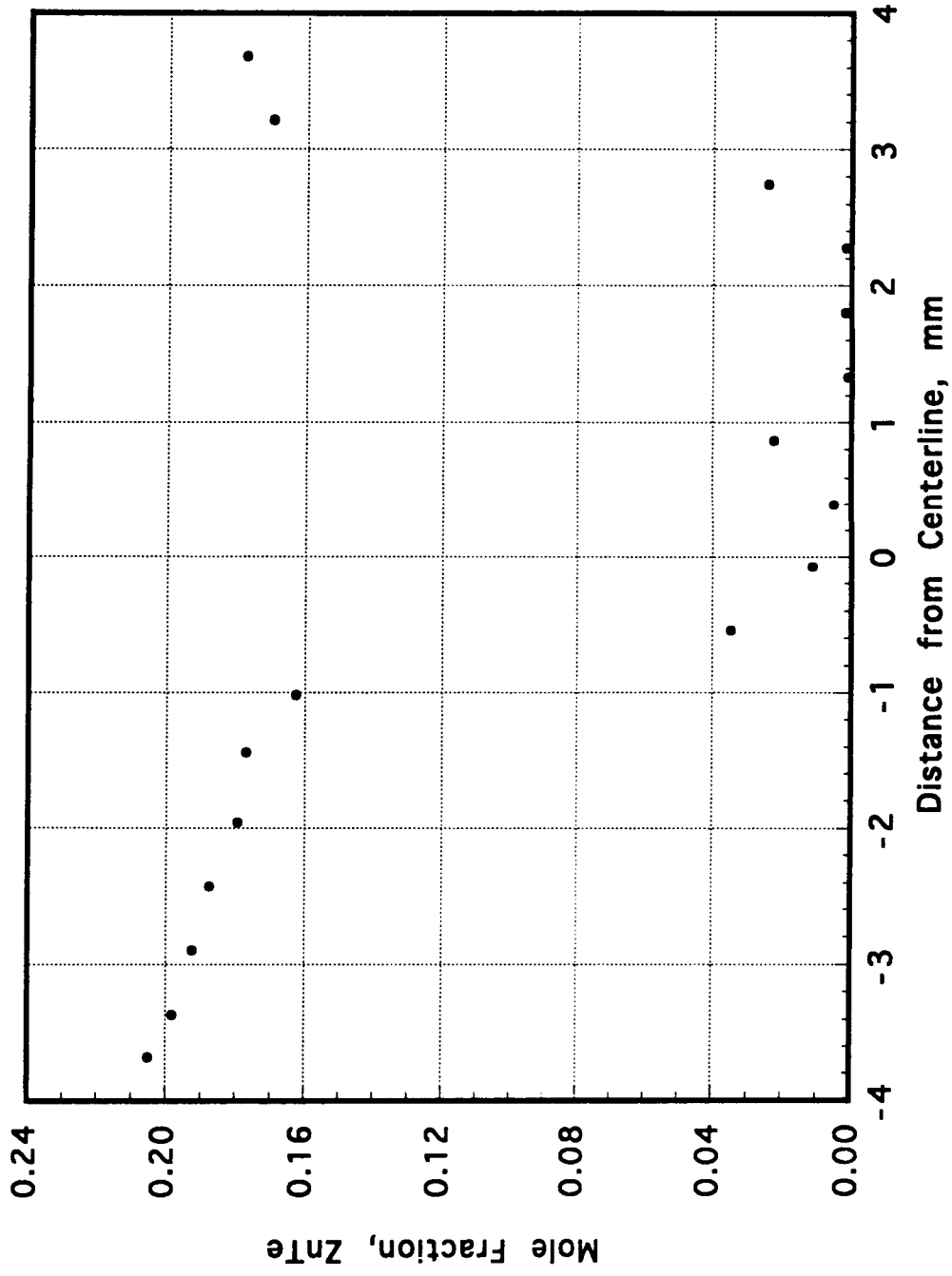


Figure 29 Flight sample radial compositional distribution at the interface.

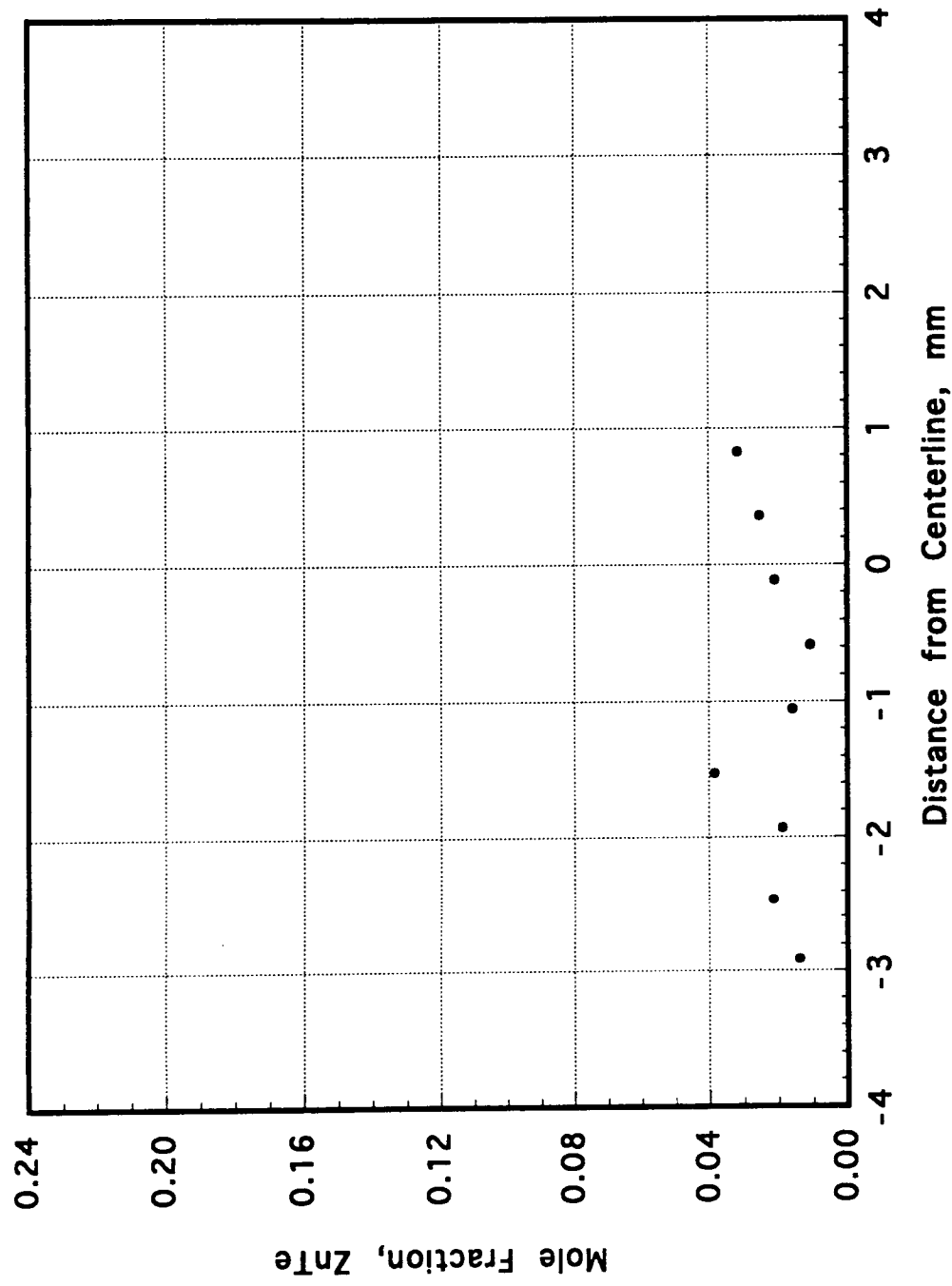


Figure 30 Flight sample radial compositional distribution 1 mm past interface.

A_x , ug

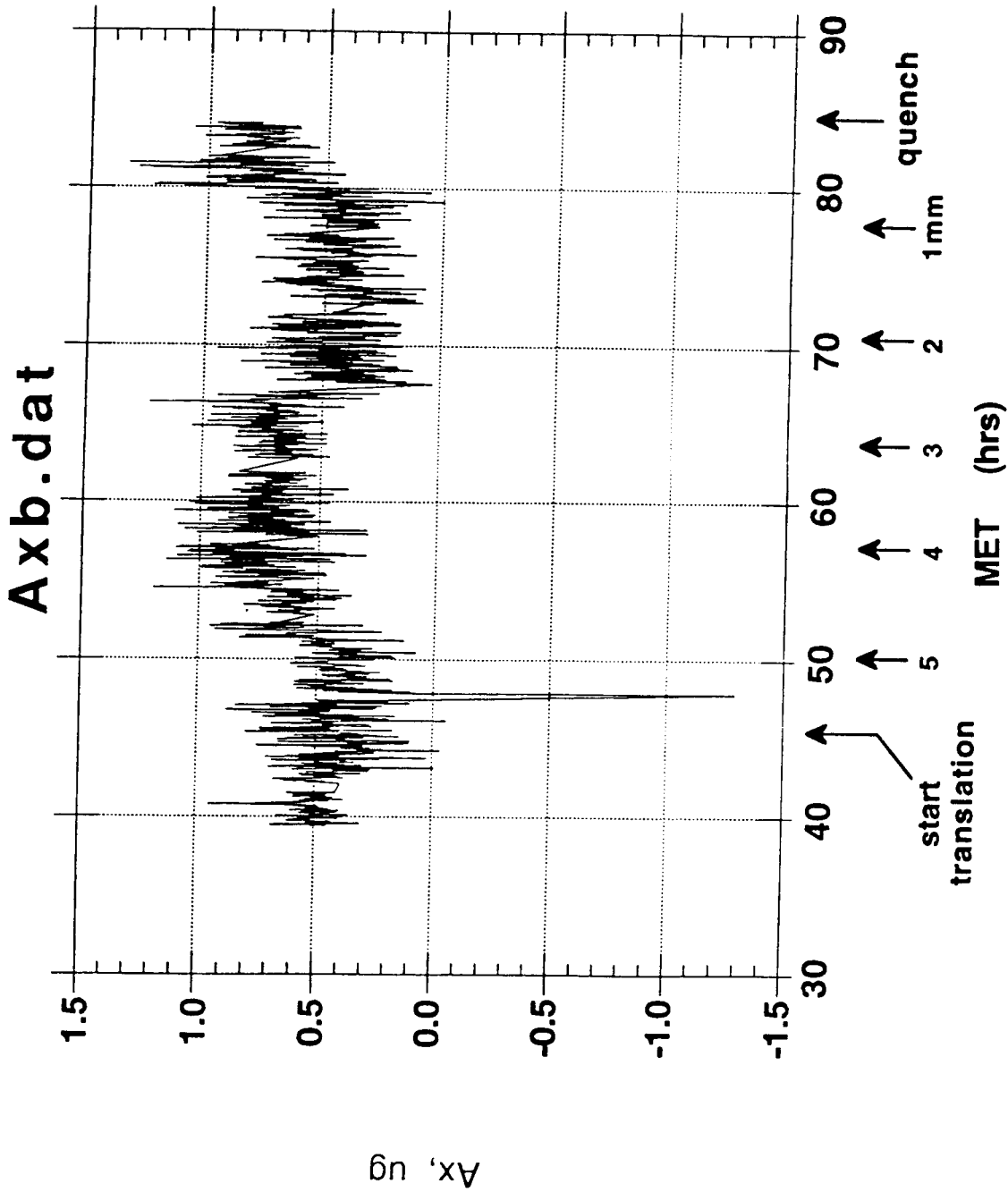
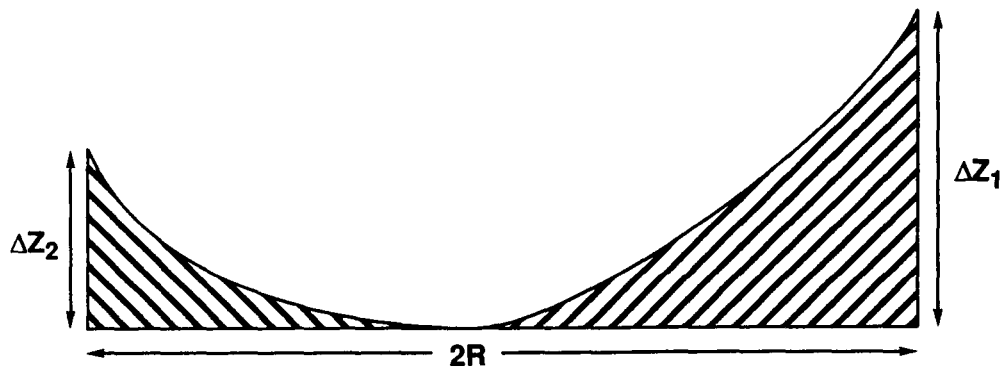


Figure 31 OARE acceleration data for the growth duration.

Interface Deflection and Radial Segregation



$$\frac{\delta C}{C_0} = \frac{(k-1)}{k} \frac{R}{D} \Delta Z$$

k = Segregation Coefficient = 4.0

D = Effective ZnTe - HgTe Liquid Diffusion Coefficient
 $= 6 \times 10^{-6} \text{ cm}^2/\text{s}$

R = Growth Rate = $4.0 \times 10^{-6} \text{ cm/s}$

Figure 32 Correlation between interface deflection and relative radial segregation.

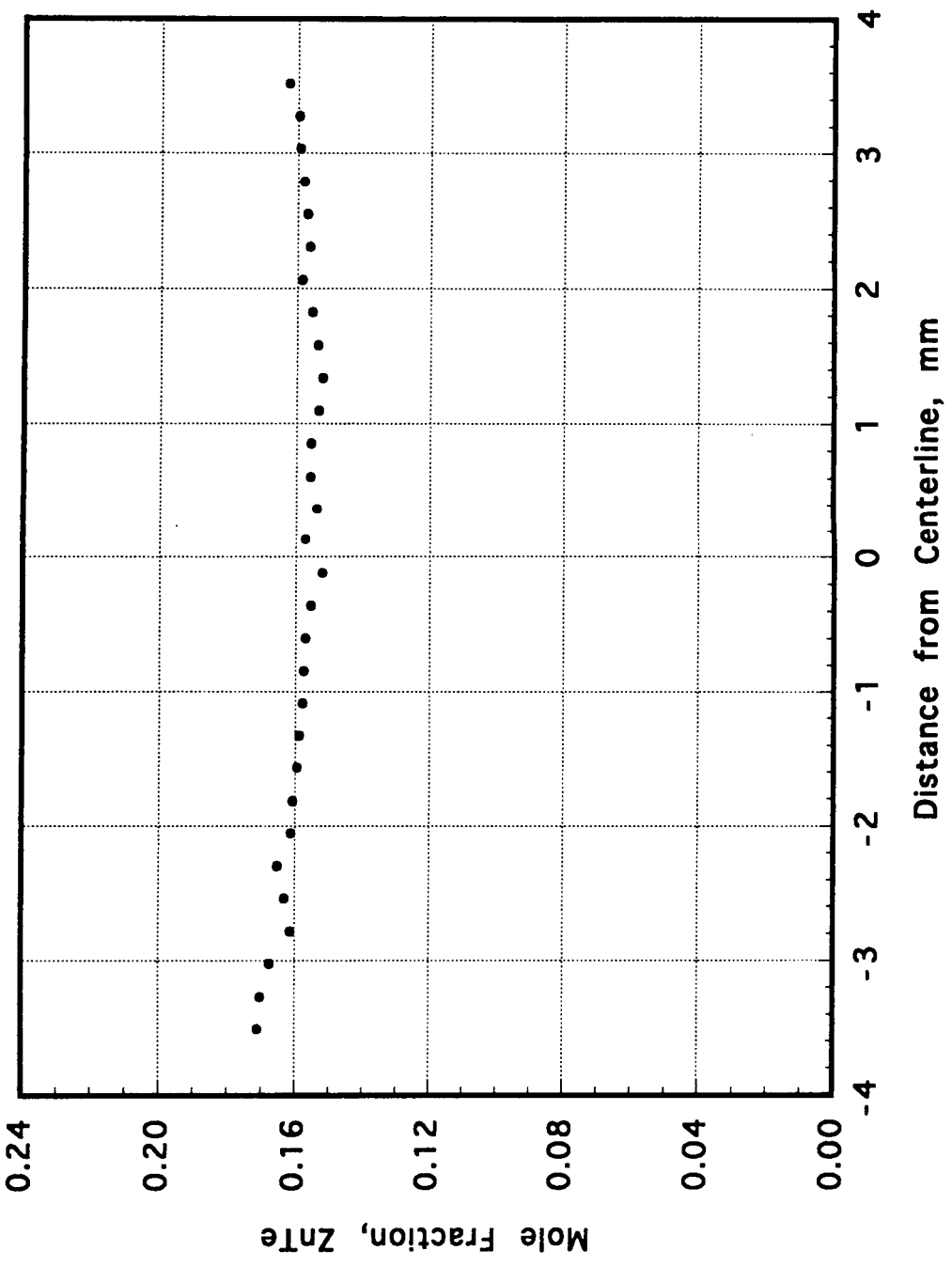


Figure 33 Ground-truth sample radial composition 6 mm from quenched-in interface.

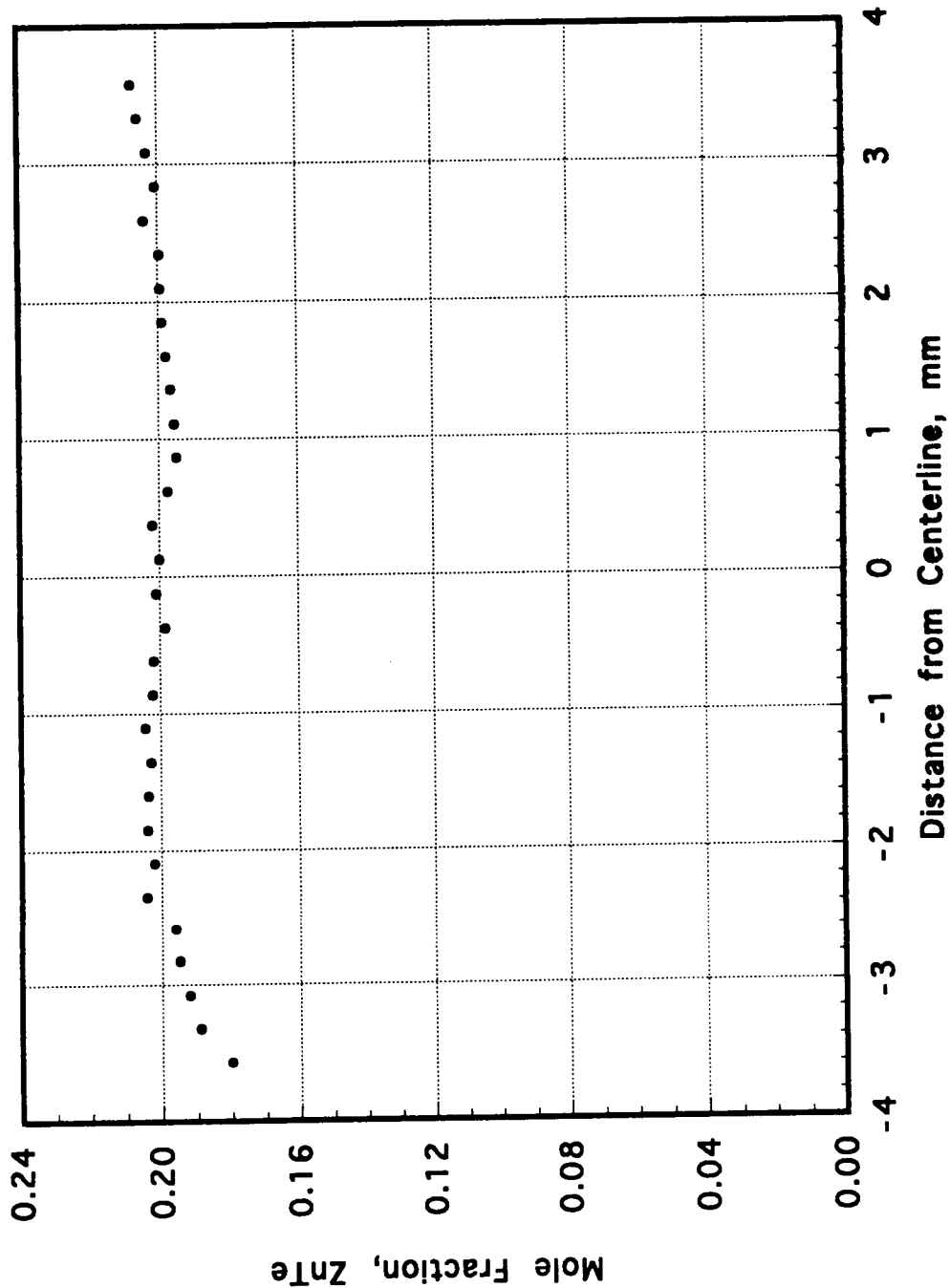


Figure 34 Ground-truth sample radial composition 4 mm from quenched-in interface.

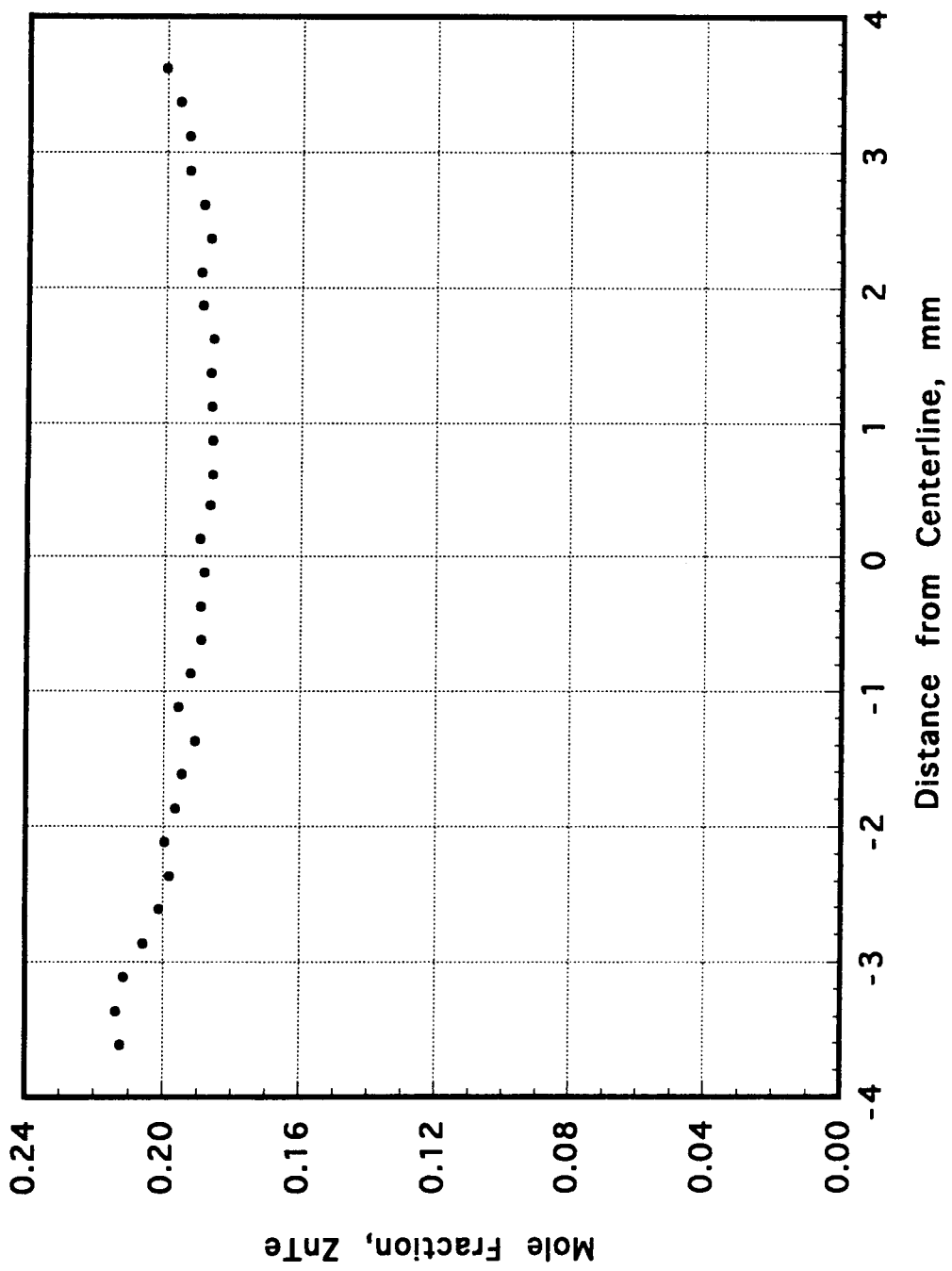


Figure 35 Ground-truth sample radial composition 3 mm from quenched-in interface.

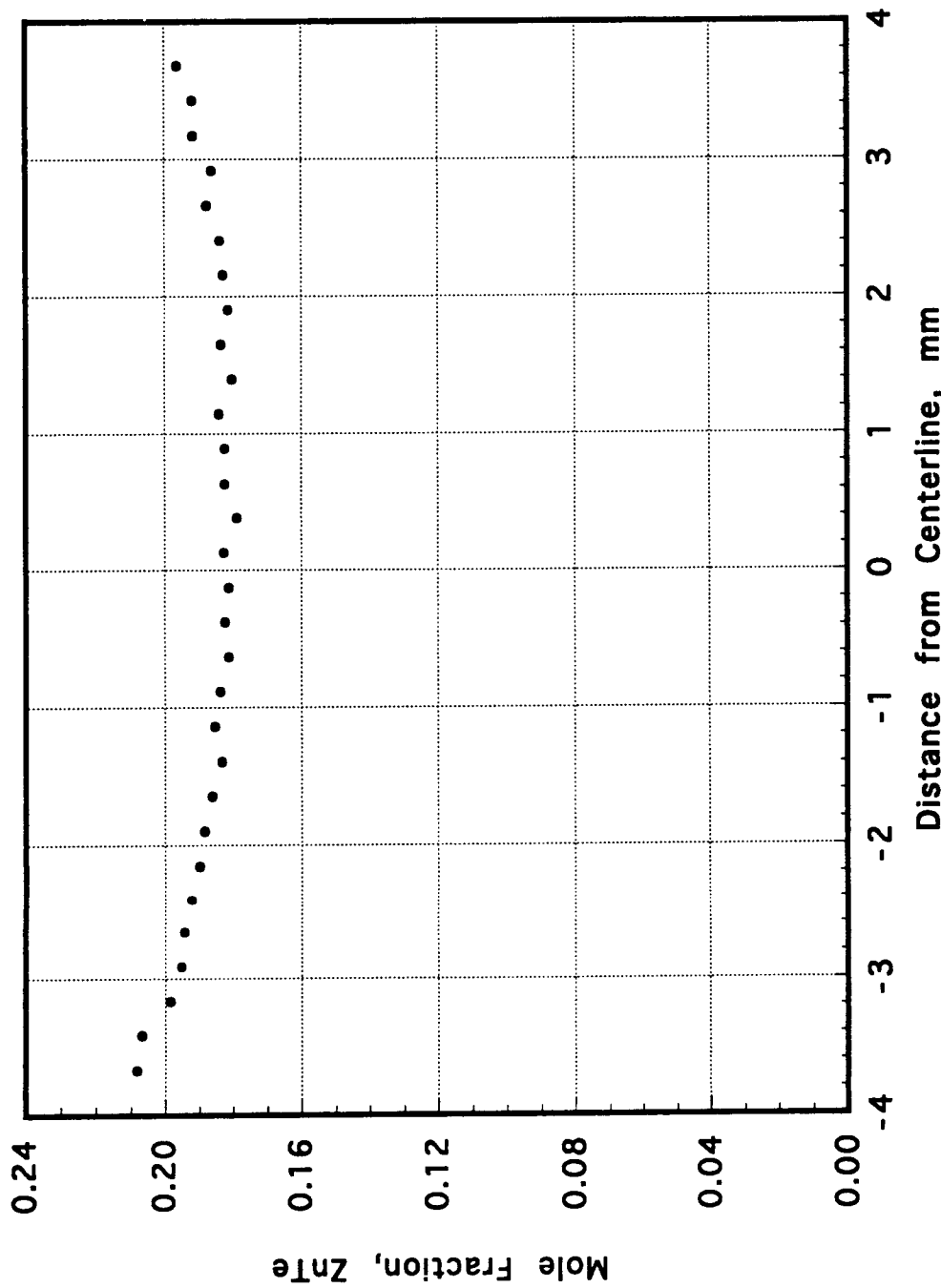


Figure 36 Ground-truth sample radial composition 2 mm from quenched-in interface.

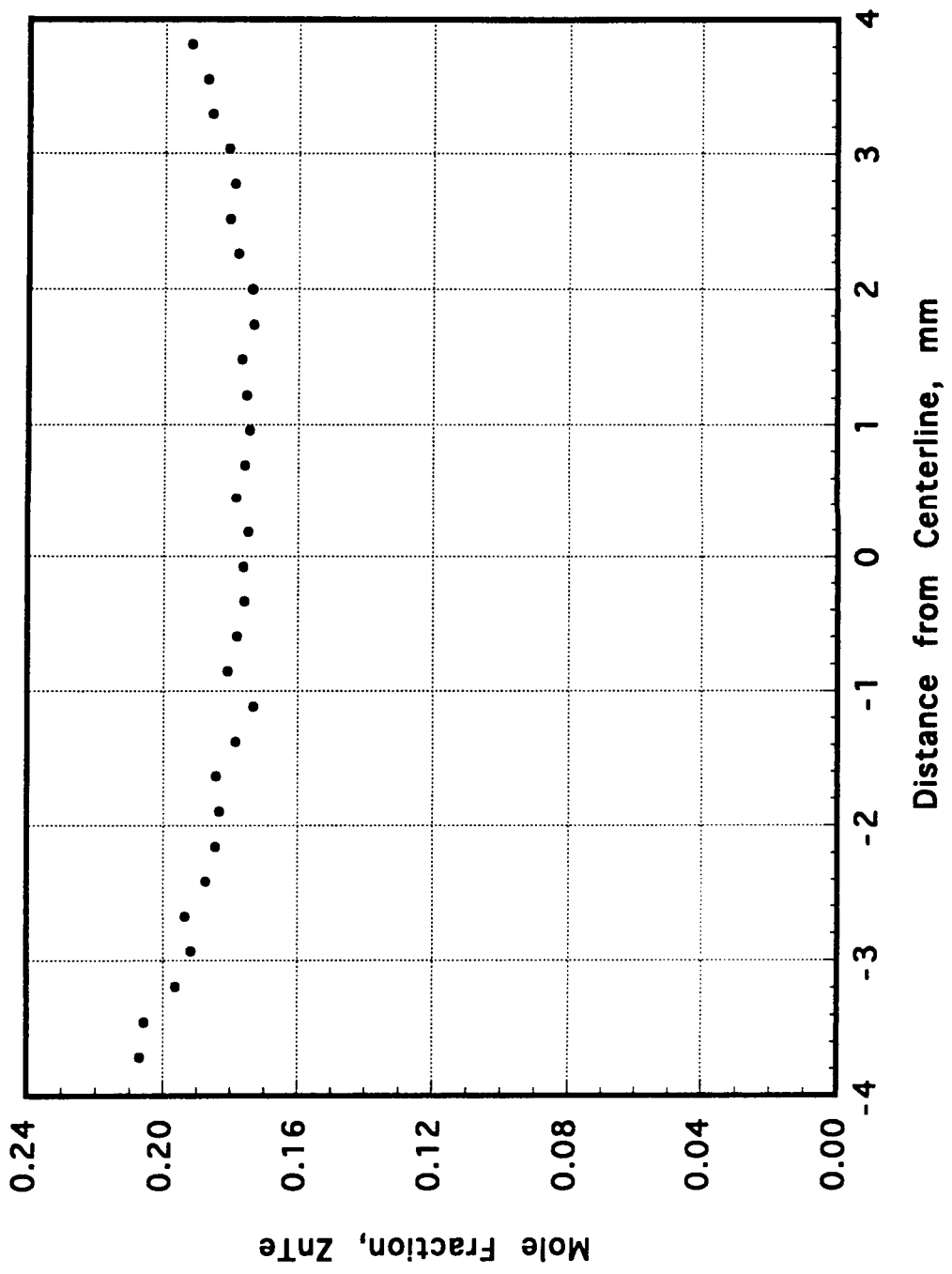


Figure 37 Ground-truth sample radial composition 1 mm from quenched-in interface.

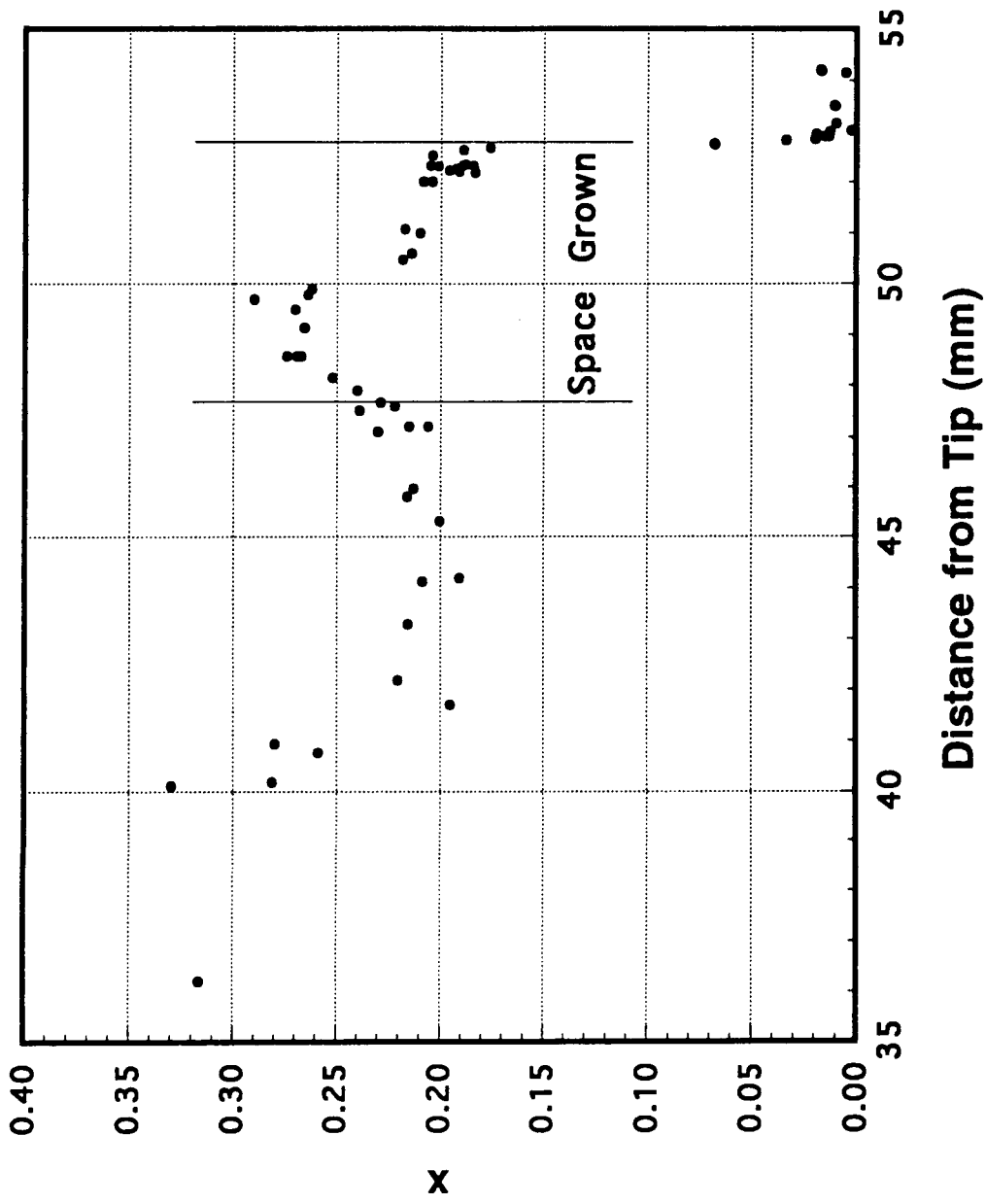


Figure 38 Surface composition distribution along flight sample axis.

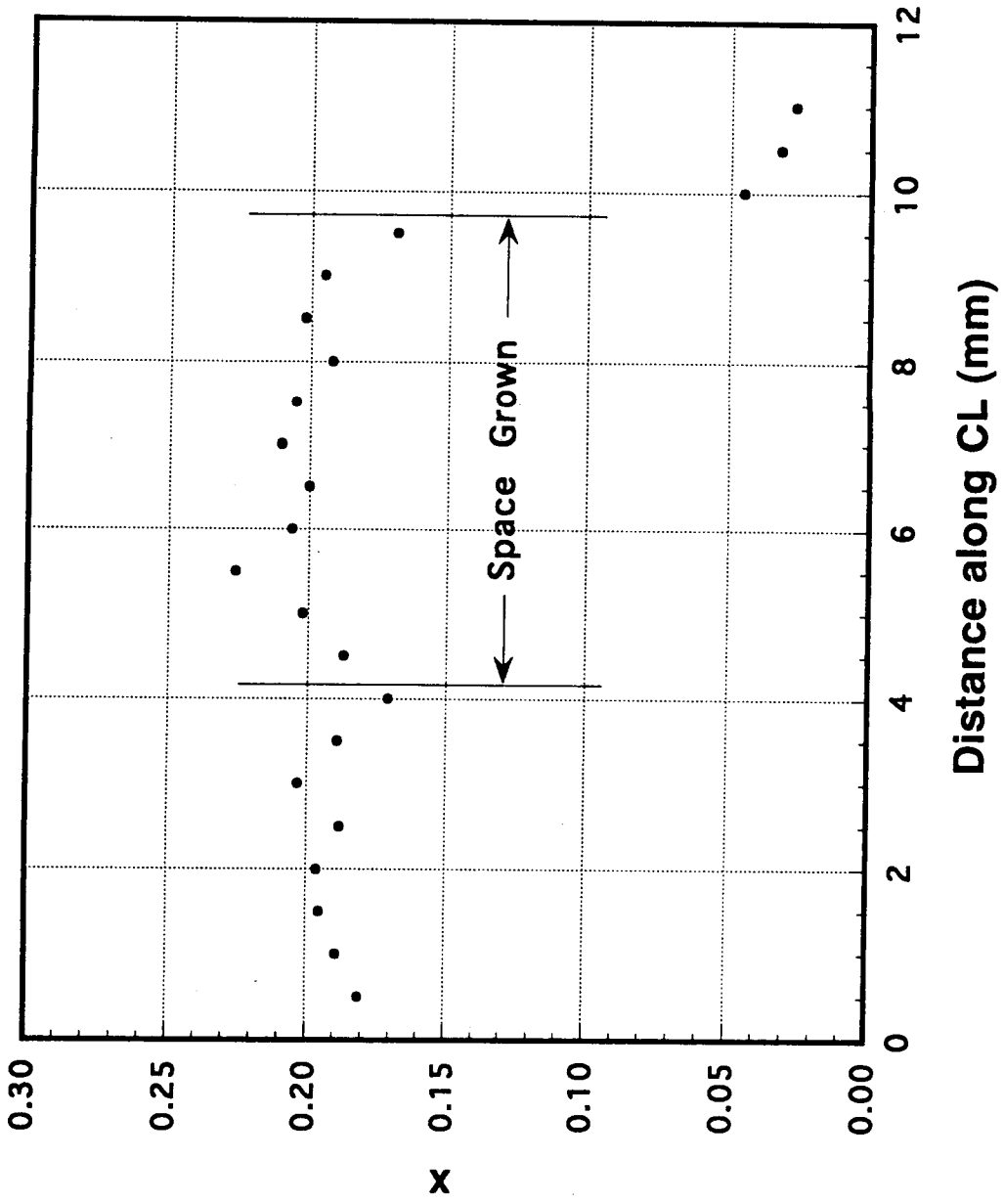


Figure 39 Center-line compositional distribution along flight sample axis.

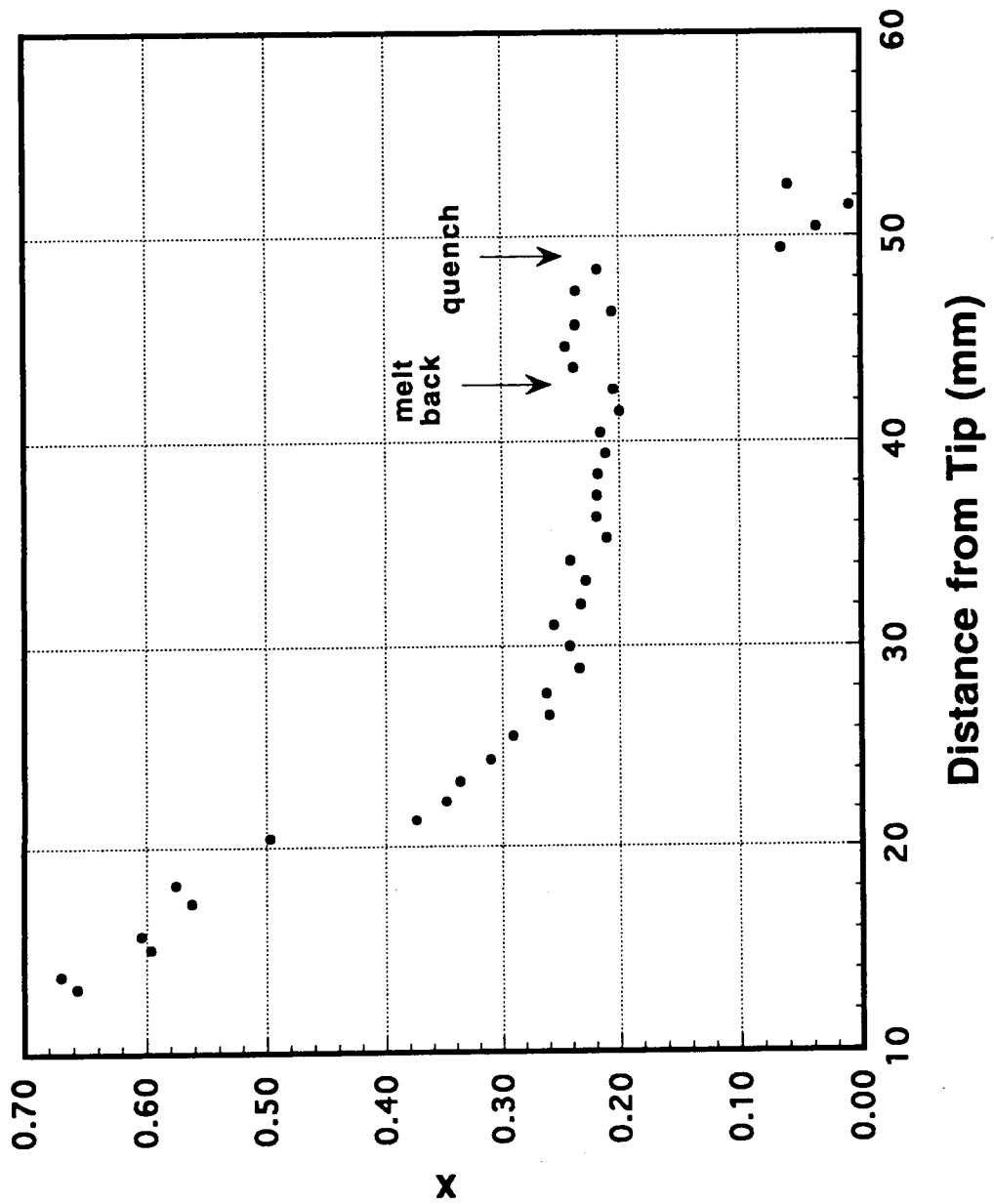


Figure 40 Surface compositional distribution along ground-truth sample axis.

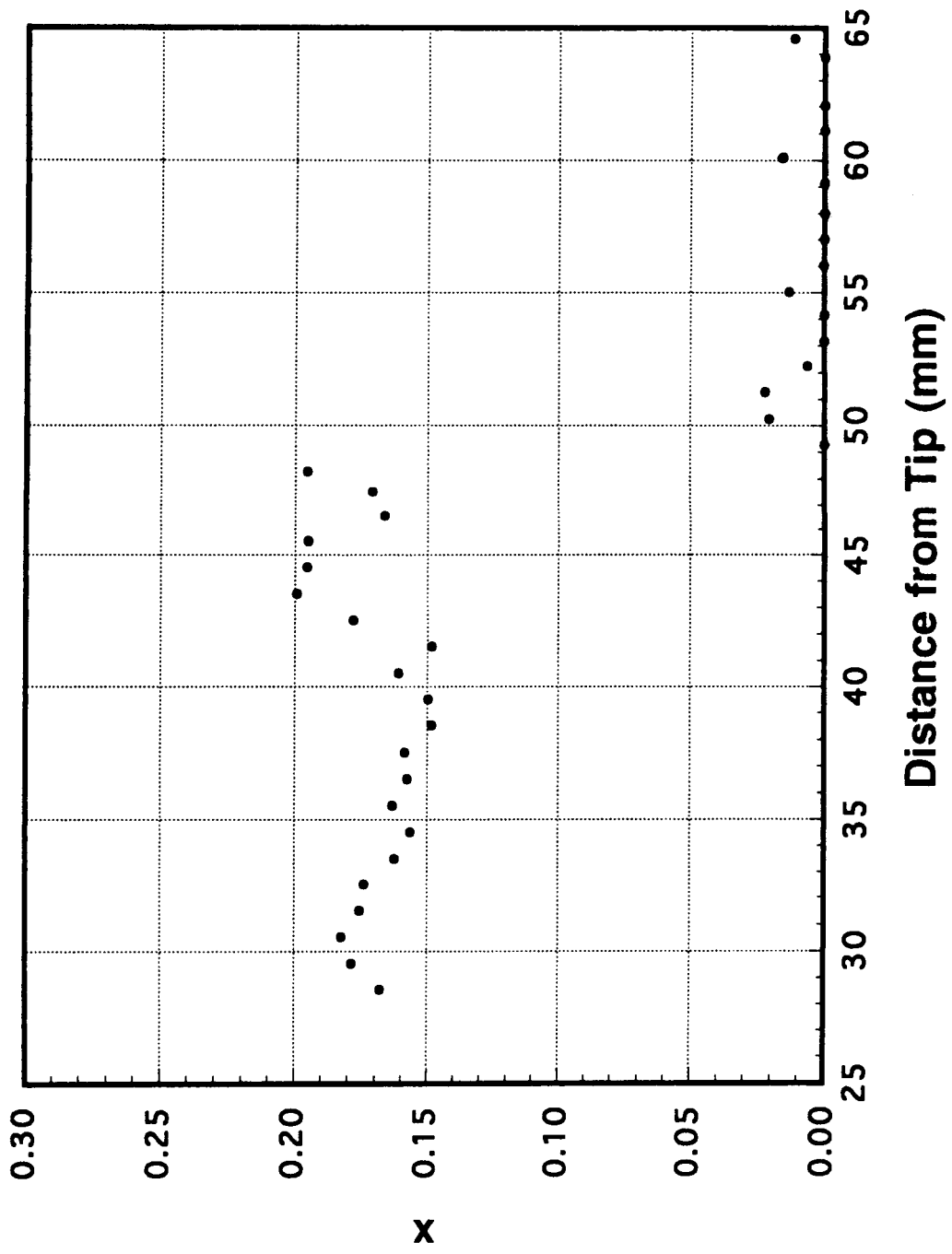


Figure 41 Center-line compositional distribution along ground-truth sample axis.

USM-1 QUENCHED MATERIAL HgZn4
Near Interface

500 μ m

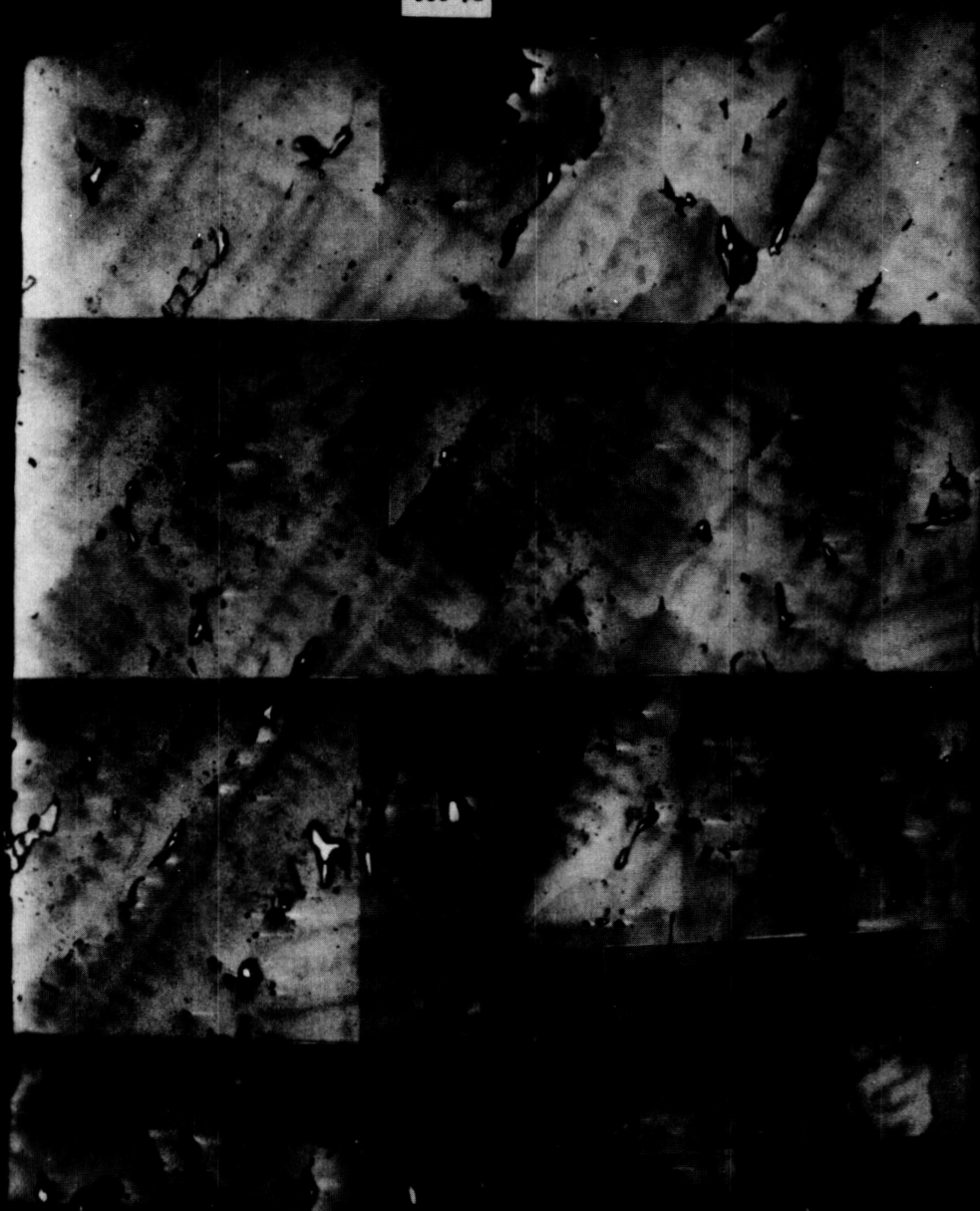


Figure 42 Back scattering SEM micrograph of part of the quenched in portion of flight sample.

B16-34 Ground Truth Sample Quenched HgZnTe
Near Interface



Figure 43 Back scattering SEM micrograph of part of the quenched in portion of the ground truth sample.

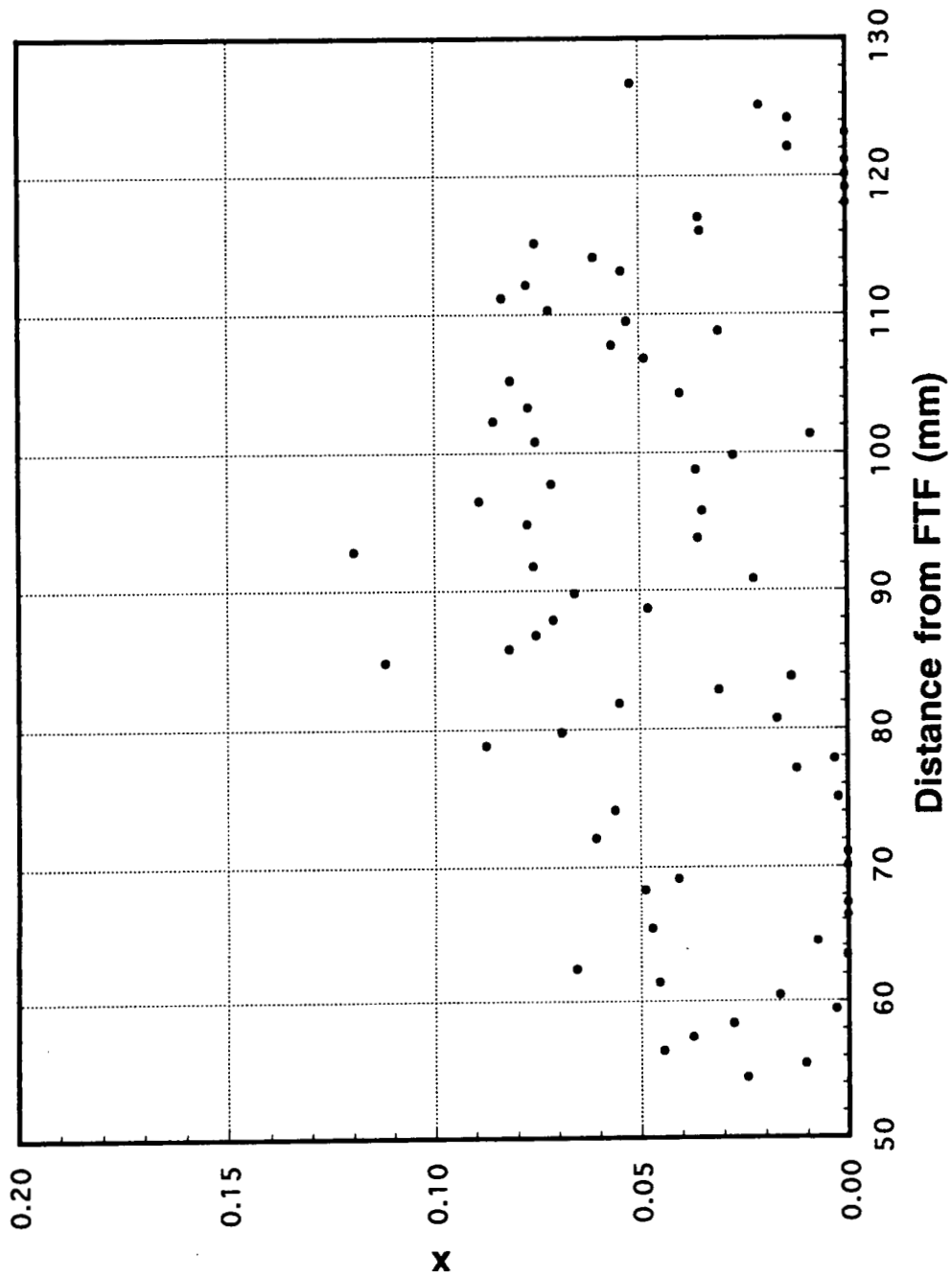


Figure 44 As-grown center-line compositional distribution along a quenched-in portion of the flight sample.

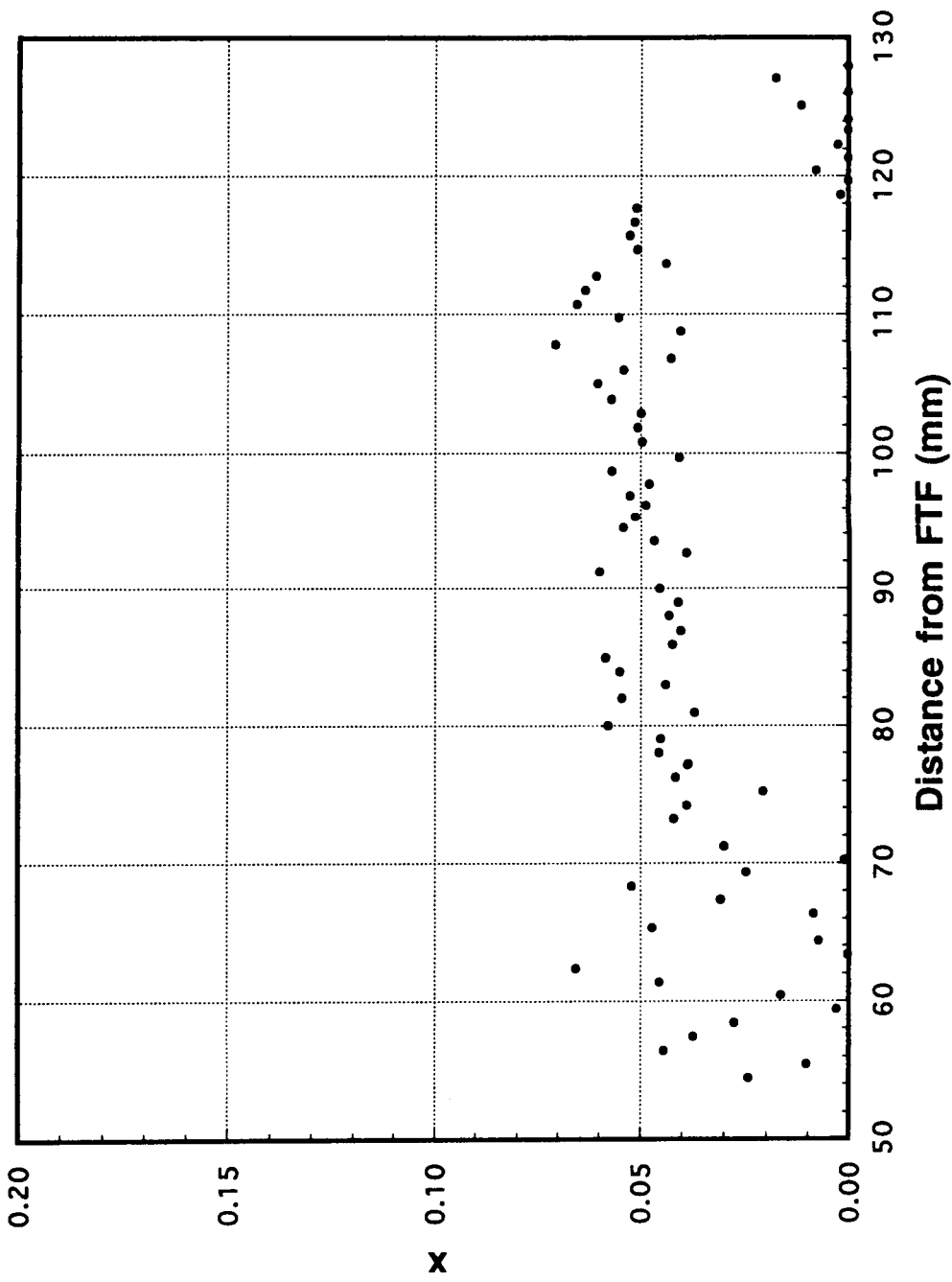


Figure 45 After-anneal center-line compositional distribution along a quenched-in portion of the flight sample.

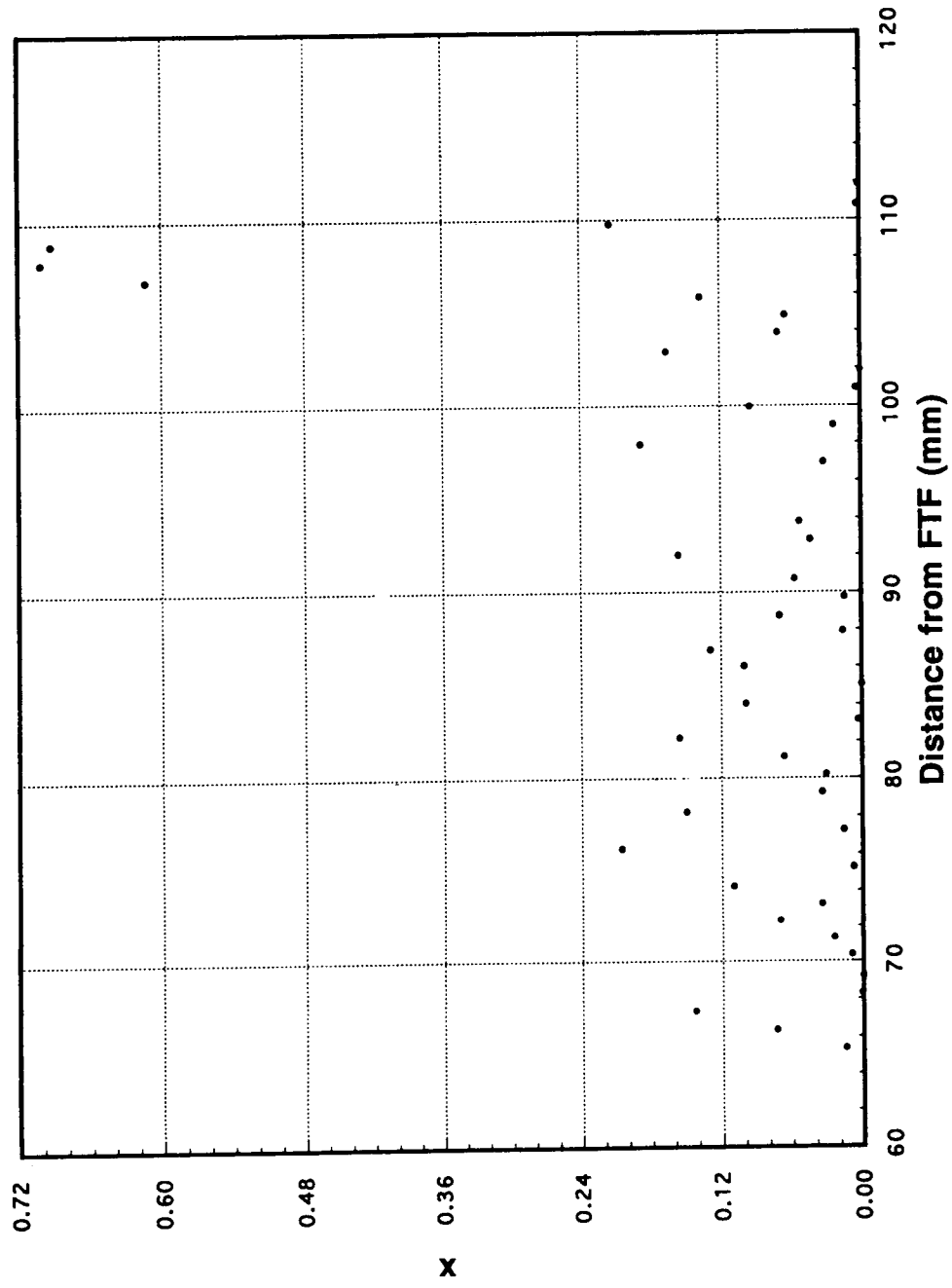


Figure 46 As-grown off-center-line compositional distribution along a quenched-in portion of the ground truth sample.

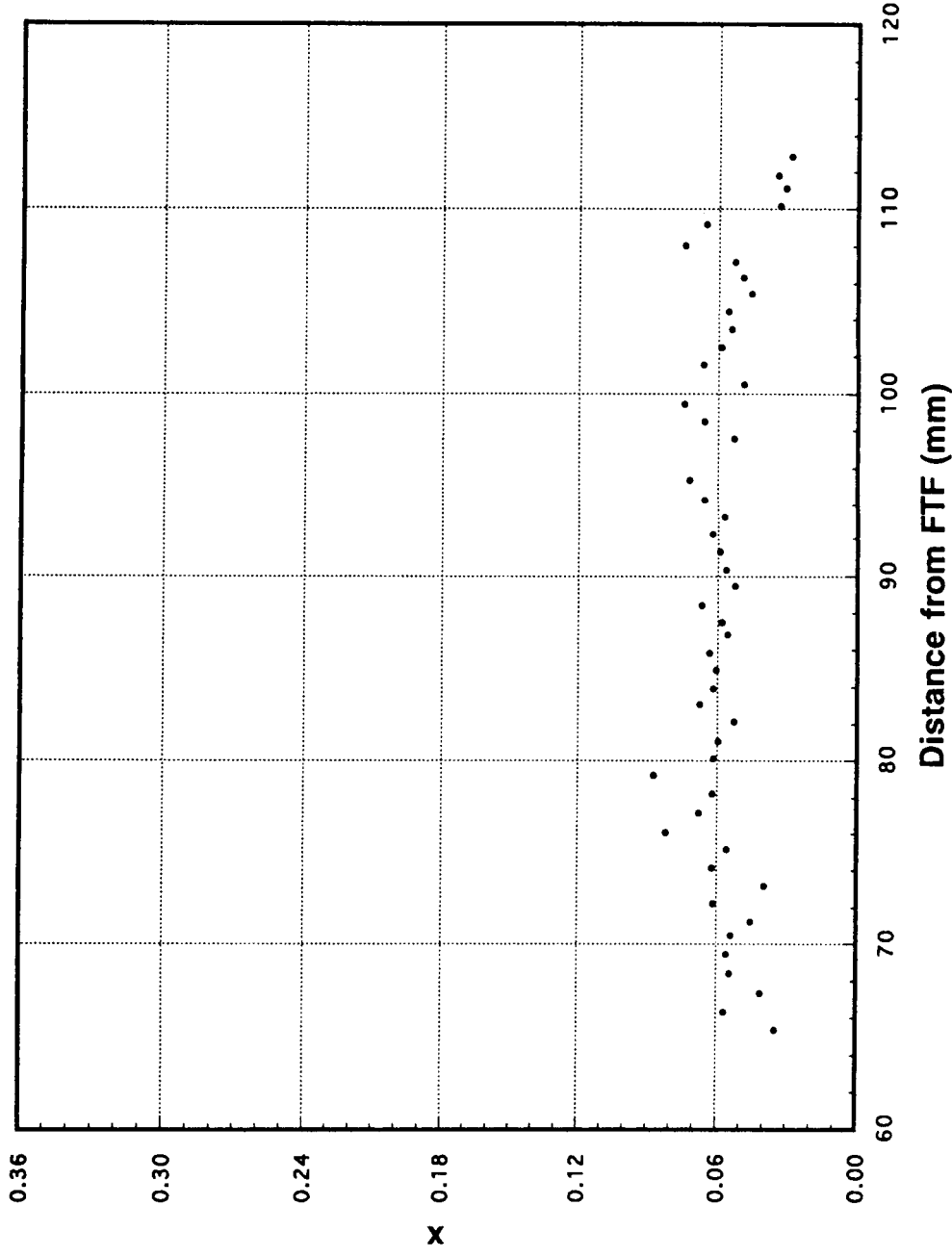


Figure 47 After-anneal off-center-line compositional distribution along the quenched-in portion of the ground truth sample.

B16-34 Ground Truth Sample Quenched HgZnTe
49 mm from the Interface

500 μ m



Figure 48 Back scattering SEM micrograph of the top portion of the quenched-in part of the ground truth sample.

Discussion

Question: *How did you decide where to cut the axial slides? Because the correspondence between the radial segregation profile and the interface morphology I agree is remarkable. How do you decide what angle to cut them ?*

Answer: Fortuitous. As a matter of fact, I thought it was truly remarkable and for one thing we never thought we would see non-symmetry. So, when we cut the crystal, we were not sensitive to how exactly to cut. Another interesting thing to note was as you watched the composition evolution, it was rather flat and then started to distort in correspondence to the acceleration data. When you saw the transverse component going in, there is one to one correlation as to how the composition evolved.

Question: *The axial (z) acceleration was of the same order as the x component, was it not ?*

Answer: Matter of fact, that is the problem. You would like to have the stabilizing gradient to be much larger. In that situation, the axial component will be much larger than the transverse component.

Question: *Could you give some estimates of this ratio ?*

Answer: As a matter of fact, I am glad you asked that question. Bob Naumann made some estimates on the optimum value. If you do not have any transverse component then you like to have zero axial acceleration but if you have a transverse component of about 0.1 to 0.2 μg then you would like to have a drag of 1 μg or a little bit more to have a stronger axial stabilizer.

Question: *What about the orientation ?*

Answer: What you would like to do is to have the primary acceleration axis line up with the sample axis.

40 Pg

1975.07.01

N95-14215

324078

58-29

THE STUDY OF DOPANT SEGREGATION BEHAVIOR DURING
THE GROWTH OF GaAs IN MICROGRAVITY

17020

P. 40

D. H. Matthiesen and J. A. Majewski

Department of Materials Science and Engineering
The Case School of Engineering
Case Western Reserve University, Cleveland, OH 44106

ABSTRACT

An investigation into the segregation behavior of selenium doped gallium arsenide during directional solidification in the microgravity environment was conducted using the Crystal Growth Furnace (CGF) aboard the first United States Microgravity Laboratory (USML-1). The two crystals grown were 1.5 cm in diameter and 16.5 cm in length with an initial melt length of 14 cm. Two translation periods were executed, the first at 2.5 $\mu\text{m/s}$ and after a specified time, which was different between the two experiments, the translation rate was doubled to 5.0 $\mu\text{m/s}$. The translation was then stopped and the remaining sample melt was solidified using a gradient freeze technique in the first sample and a rapid solidification in the second experiment. Measurement of the selenium dopant distribution, using quantitative infra-red transmission imaging, indicates that the first sample initially achieved diffusion controlled growth as desired. However, after about 1 cm of growth, the segregation behavior was driven from a diffusion controlled growth regime to a complete mixing regime. Measurements in the second flight sample indicated that the growth was always in a complete mixing regime. In both experiments, voids in the center line of the crystal, indicative of bubble entrapment, were found to correlate with the position in the crystal when the translation rates were doubled.

INTRODUCTION

Axial Segregation Theory

When an alloy of composition C_0 is solidified, segregation of the solute occurs and is described by the alloy's equilibrium phase diagram [1]. The equilibrium segregation coefficient k_0 , is defined as the ratio of the solute concentration at the interface in the solid to that in the liquid,

thus:

$$k_0 = \frac{C_s^{\text{eq}}}{C_l^{\text{eq}}} \quad (1)$$

If $k_o < 1$ for an alloy, then solidification causes rejection of solute into the liquid at the solid-liquid interface. There are two limiting theoretical cases: (1) complete convective mixing of the solute in the liquid; and (2) diffusive mixing of the solute in the liquid in the absence of convection.

The solute distribution for the first limiting case of complete mixing in the melt, has been derived by many investigators, most notably by Scheil [2] and Pfann [3]. In their one-dimensional analysis they assume that: (1) there is no diffusion of solute in the solid; (2) the segregation coefficient k_o is constant; and (3) there is complete mixing in the liquid. By considering a mass balance of the solute, the composition of the solid as a function of the fraction solidified was derived to be:

$$C_s = k_o C_o (1 - f_s)^{(k_o - 1)} \quad (2)$$

where:

C_s = concentration of the solute in the solid

k_o = equilibrium segregation coefficient

C_o = initial concentration in the melt

f_s = fraction solidified

Figure 1 shows the resultant solute distribution in the solid when complete mixing due to convection was present during solidification.

The solute distribution for the second limiting case of diffusion controlled growth, was originally treated by Tiller, Jackson, Rutter and Chalmers [4]. They derived an approximate, time-independent expression to describe the solute concentration in the solid for steady state growth as a function of the distance grown, growth rate, and diffusion coefficient of the solute in the liquid:

$$C_s = C_o \left[1 - (1 - k_o) \exp\left(-\left(\frac{k_o R x}{D_l}\right)\right) \right] \quad (3)$$

where:

R = microscopic growth rate

x = distance grown

D_l = diffusion coefficient in the melt

This expression assumes: (a) there is a planar interface; (b) there is no diffusion in the solid; (c) k_o is a constant; (d) there is no convection in the melt; and (e) that solute is conserved. Also, it is assumed that the rate at which C_s approaches C_o is a function of growth distance and is proportional to $(C_s - C_o)$.

As Fig. 1 illustrates, growth under these conditions results in a uniform composition profile, except for initial and final transients. The characteristic length for the initial transient D_I/R_{k_0} , represents the build up of the solute boundary layer. The characteristic length for the final transient D_I/R , represents the impingement of the solute boundary layer on the end of the crystal.

As can be seen in Fig. 1, a major portion of the crystal grown in a diffusion controlled growth regime would have the desired composition of C_0 . This compares to the complete mixing case, seen in Fig. 1, in which only a small portion of the crystal has the desired composition. Thus, a higher yield of commercially useful crystal would be achieved if diffusion controlled growth could be realized.

Diffusion Controlled Growth

Having established that diffusion controlled growth is desirable from a materials engineering point of view, how can this be achieved? In other words, how can convection in the melt be suppressed or eliminated? A review of this subject is given by Carruthers [5] in which he discusses the factors that influence the stability and types of thermal convective flow patterns and presents the methods employed to control convection. Carruthers examines in detail the importance of thermal boundary conditions and the degree of confinement in determining the nature of thermal convective instabilities. In all types of crystal growth, the factors that influence the type and amount of thermal convection can be characterized by the dimensionless Rayleigh number, N_{Ra} :

$$N_{Ra} = N_{Gr} \times N_{Pr} = \left(\frac{\beta \bar{g} \Delta T L^3}{\alpha v} \right) \quad (4)$$

where:

N_{Ra} = Rayleigh number

N_{Gr} = Grashof number

N_{Pr} = Prandtl number

β = thermal expansion coefficient

g = effective gravitational constant (g/g_0)

ΔT = change in temperature across L

L = characteristic distance

α = thermal diffusivity

v = kinematic viscosity

The Rayleigh number is the ratio of buoyancy forces, which lead to the development of convective flow, to the viscous forces, which oppose flow. For small values of the Rayleigh

number, where the viscous forces opposing convection are large, the fluid is stable and thermal convection is absent. At some critical value of the Rayleigh number, the onset of laminar flow occurs and, for increasingly larger Rayleigh numbers, this flow becomes oscillatory and then turbulent in nature. Engineering control of the nature and velocity of these convective flows is achieved by manipulating and controlling the variables described in the Rayleigh number, namely; the characteristic distance; the temperature gradient; and gravity.

The characteristic distance, with a third power dependence, is an obvious starting point as a variable to manipulate in order to eliminate convection in the melt. Kim *et al.* manipulated the melt-to-diameter aspect ratio to control the type and intensity of convection in Te-InSb [6] and Ga-Ge [7] in a top seeded Bridgman system using a gradient freeze growth technique. Holmes and Gatos [8] were able to achieve diffusion controlled growth in small diameter, capillary sized crystals of Ga-Ge in a bottom seeded Bridgman system using a gradient freeze growth technique. As they increased the diameter to larger than 1 mm, the segregation behavior quickly approached the complete mixing regime. Reduction of the characteristic distance then, does not allow for achieving diffusion controlled growth in bulk crystals.

Another variable to manipulate would be the temperature difference across the characteristic distance. In order to solidify single crystals from their melts, it is necessary to remove the heat of solidification from the melt-solid interface during growth. Thus, temperature gradients are required during crystal growth, and the limited manipulation of these temperature differences are typically ineffective in reducing or eliminating convection in the melt. There have however, been several one-dimensional models developed to predict the axial temperature gradients [9], and several two-dimensional models to predict the axial and radial temperature gradients present in the growth system [10]. Although manipulation of temperature gradients has limited effectiveness in eliminating convection in the melt it is an important variable in the generation and multiplication of dislocations and other defects [11].

The final variable in Eq. 4 which can be manipulated to eliminate convective flows in the melt and thus achieve diffusion controlled growth, is the effective gravity term. Experimentation in this area began during the translunar portions of the Apollo 14, 16 and 17 flights [12]. These efforts were continued during the Skylab program with several crystal growth experiments [13].

During the Apollo-Soyuz Test Project (ASTP), Professors Witt and Gatos directed efforts to grow bottom seeded gallium doped germanium using a gradient freeze technique [14]. During growth, current pulses were used to demarcate the melt-solid interface at known time intervals (Peltier Pulsing). These pulses allowed for determination of the interface shape and the growth rate. Single point spreading resistance measurements were used to determine the dopant distribution.

Since there were three growth chambers, none of them were in the thermal center of the furnace, and thus, the melt-solid interface shapes of the crystals were not symmetric. In addition, it was determined that the interface shapes changed throughout growth due to changing thermal loads in the system. Also, it was determined that the growth rate slowly increased during growth and never achieved a steady state value.

The measured dopant distribution quickly increased in value over the first centimeter of growth and then slowly increased throughout the rest of growth. By averaging the measured left periphery, right periphery, and center values, an overall axial distribution was determined. By using the best available material property values from the literature, combined with the measured growth rate data, Witt and Gatos showed that diffusion controlled growth was achieved in the axial direction. In contrast, the ground based experiments showed that the segregation behavior approached that of complete mixing.

The radial dopant distribution data for the crystals grown in space varied by a factor of 3 greater than the radial dopant distribution data for the crystals grown on Earth. This increased radial segregation in the presence of diffusion controlled axial segregation behavior was an unexpected result.

Radial Segregation Theory

The unexpected radial segregation behavior measured in Professors Witt and Gatos's experiment has lead to several analytical and numerical investigations into radial segregation behavior. Coriell and Sekerka [15] assumed an interface shape with a radius of curvature expressed as:

$$R = \frac{1}{2} \left(\frac{L^2}{4\Delta d} + \Delta d \right) \quad (5)$$

where:

R = radius of curvature

L = diameter of the crystal

Δd = the interface deflection

With this assumed interface shape, they were able to solve analytically for the radial segregation due to a slightly curved interface, a small Peclet number and a flat interface shape at the ampoule wall. When data from the Witt and Gatos experiment were used, their solution predicted approximately 10 percent radial segregation, which is in qualitative agreement with the measured 300 percent radial segregation data.

Coriell, Sekerka and coworkers [16] followed this paper with a paper in which they combined analytical and numerical results to predict the radial segregation behavior due to large interface deflections, a large Peclet number and a flat interface shape at the ampoule wall.

As part of this program Korpela, Chait and Matthiesen [17] developed an analytic expression for the radial segregation due to small interface deflections, large Peclet numbers and an arbitrary interface shape at the ampoule wall.

Computer Modeling

Numerical investigations were then initiated to provide further insight into the radial segregation behavior. The numerical simulations of Kim, Adornato and Brown [18] have recently shed some insight into the problem of axial and radial segregation behavior with respect to the convection present in the melt. They predict that, initially in a bottom seeded Bridgman-Stockbarger growth system, a two cell toroidal flow pattern will exist, with an intense flow cell near the melt-solid interface. As the flow velocities are decreased, either by microgravity or applied magnetic fields, or both, the two flow cells gradually merge into one large cell. As the flow velocities are further decreased, this one flow cell eventually disappears and diffusion controlled growth is achieved.

An important conclusion of their analysis is that when the two cell patterns become one cell, the axial dopant distribution approaches that of diffusion controlled growth, but the radial segregation increases. It is only after the flow velocities are further reduced that the radial segregation finally decreases, as shown in Fig. 2. When the convective flows are finally suppressed, the radial segregation is controlled by the interface shape, as predicted by Coriell and Sekerka.

I. GROWTH OF Se DOPED GaAs IN MICROGRAVITY

A. Motivation and Goals

Although the work of Professor Brown and his co-workers has provided useful insight to the segregation behavior during the growth of electronic materials, there has been little experimental verification. In fact, the Witt and Gatos experiment is the only experiment which has had all the appropriate data necessary for comparison to these numerical simulations.

The question then arises, can these simulations be used to predict the growth of other materials in microgravity? In 1978 the Committee on Scientific and Technological Aspects of Materials Processing in Space (STAMPS) of the National Research Council [19] issued a report which reviewed the materials processing in space programs done to that date. Among their many conclusions was that, although the growth of germanium on ASTP provided a firm foundation for

the growth of electronic materials in space, it was not possible *a priori* to extrapolate these results to the more technologically interesting III-V and II-VI materials. In addition, the necessary material property values needed to perform applicable numerical simulations that would predict the outcome of processing these materials in space have not been precisely determined, and in some cases, not determined at all.

B. Scientific Objectives

The scientific objectives of these experiments were to determine the following under microgravity conditions:

- 1) to investigate techniques for obtaining complete axial and radial dopant uniformity during the crystal growth of selenium doped gallium arsenide
- 2) to use a large melt length-to-melt diameter aspect ratio (9.3:1) initially to investigate steady state segregation behavior and
- 3) to use a small melt length-to-melt diameter after the above to study the transient segregation behavior during the gradient freeze growth

The third scientific objective would provide a baseline to other experiments which have been conducted in microgravity with this material system.

II. EXPERIMENTAL PROCEDURE

A. Crystal Growth of Sample Charges

The Liquid Encapsulated Czochralski (LEC) grown crystals were oriented <111> and doped to achieve an average dopant concentration in the grown crystal of $\approx 10^{17}/\text{cm}^3$. These charges were prepared from the *in situ* synthesis and growth of ≈ 800 gm charges of selenium doped gallium arsenide. A layer of boric oxide was used as an encapsulant and a pyrolytic boron nitride (PBN) crucible was used for the growth. An argon overpressure was maintained in the Malvern High Pressure crystal growth system. Typically the seed rotation rate was 10 rpm and the crucible rotation was 0 rpm. The pulling rates were typically $1 \mu\text{m/s}$.

The single crystal LEC boules were then annealed in flowing argon at 600°C for a 3 hour period and then slowly cooled to room temperature. The boules were then machined to the desired diameter using a diamond coring drill. Typically three cored samples could be obtained from a two inch diameter boule. After coring the samples were cut to length, typically 5-7 cm long, and again annealed to relieve any stresses from the machining process. These crystals were sized to the PBN sleeve by etching with 1:1:1 sulfuric:peroxide:acetic acid to the final diameter.

For the science samples and the first flight and ground truth samples, a total charge would consist of three single crystal doped samples totaling 16.5 cm in length. For the second flight and ground truth samples, which were actually part of the ampoule qualification test program, the charge consisted of a doped single crystal seed and two undoped polycrystalline sections.

B. Ampoule Design and Fabrication

As shown in Fig. 3, each charge consisted of three Liquid Encapsulated Czochralski (LEC) grown crystals. These 1.5 cm in diameter crystals were contained within a pyrolytic boron nitride crucible (sleeve). This sleeve had a 0.035 inch wall and was 18 cm long. The cold end contained a graphite pedestal for positioning the seed crystal. The hot end contained a graphite plunger, which in turn contained a PBN leaf spring assembly. This spring allowed the plunger to advance and retreat as the crystal contracted upon melting and expanded upon freezing. The crystal, graphite and PBN were hermetically sealed into a fused quartz envelope, which minimized the arsenic losses from the GaAs crystal. The ampoule was heated to 250°C under 10 millitorr vacuum before it was finally sealed.

The ampoule was then positioned into a cartridge. This cartridge was made of WC-103 and had an Fe silicide coating on the outside to inhibit thermal oxidation. As shown in Fig. 3, there were six open bead, type-S thermocouples located between the ampoule and the cartridge. The ampoule was positioned to the correct seeding position using zirconia insulation pedestals.

Since the ampoule was determined to contain 2.2 atm of arsenic pressure at the processing temperature of 1260°C [20], the cartridge was filled with argon gas and hermetically sealed to balance this internal ampoule pressure. Thus, even though the fused quartz of the ampoule was in viscous flow at the processing temperature no deformation of the ampoule was expected since the pressure forces on the ampoule balanced one another.

Before delivery each sample ampoule-cartridge assembly (SACA) was X-rayed to determine the exact location of the thermocouples relative to the seed end of the crystal.

C. Experimental Timelines

The experimental timeline for the first experiment is shown in Fig. 4. The experiment consisted of establishing a desired thermal gradient of 15°C/cm across the 2 cm gradient zone of the CGF, with the melt/solid interface located in the center of the gradient zone. The initial location of the crystal in relation to the gradient zone is shown in Fig. 3. Ideally at the fully inserted position, thermocouple T2 would read 1238°C and the seeding melt-solid interface position would be in the center of the gradient zone. This would result in a 14 cm melt length. After a thermal soak, two translation periods were executed, the first at 2.5 $\mu\text{m/s}$ for 4.05 cm and the second at

$5.0 \mu\text{m/s}$ for 4.05 cm. The translation was then stopped and the remaining 5.9 cm sample melt was solidified using a gradient freeze technique, which in a 4 hour period would have an average growth rate of $5.0 \mu\text{m/s}$.

The experimental timeline for the second experiment is shown in Fig. 5. The experiment consisted of establishing a desired thermal gradient of 15°C/cm across the 2 cm gradient zone of the CGF, with the melt/solid interface located in the center of the gradient zone. The initial location of the crystal in relation to the gradient zone is shown in Fig. 3. Ideally at the fully inserted position, thermocouple T2 would read 1238°C and the seeding melt-solid interface position would be in the center of the gradient zone. This would result in a 14 cm melt length. After a thermal soak, two translation periods were executed, the first at $2.5 \mu\text{m/s}$ for 3.15 cm and the second at $5.0 \mu\text{m/s}$ for 3.15 cm. The translation was then stopped and the remaining 7.7 cm sample melt was solidified using a rapid quench by issuing a power off command to the heaters.

In an attempt to measure the growth interface shape and microscopic growth rate, a mechanical pulse was initiated by a solenoid attached to the top of the cartridge at specified times. These times were selected to occur during the steady state growth periods and are indicated in Figs. 4 and 5.

D. Sample Analysis Preparation

After flight each SACA was X-rayed after which the ampoule was removed from the cartridge and inspected. The ampoules were then opened and the GaAs crystals removed. After inspection the GaAs crystals were oriented such that an axial cut made down the axial center of the crystal was parallel to the (211) plane. A 0.070 inch thick (1.778 cm) axial slice was then cut from the crystal and polished both sides to yield a 0.050 inch (1.27 cm) sample. The smaller of the two half cylinders or 'D' sections was cut perpendicular to the axial direction. This yielded approximately 150 0.050 inch (1.27 cm) thick 'D' shaped samples, which are being used for Hall effect measurements. The remaining large half cylinders or 'D' section were lapped with $1 \mu\text{m}$ alumina.

III. RESULTS AND DISCUSSION

A. As Grown Surface Characterization

All crystals grown in space and on Earth could readily be removed from the PBN sleeve. The surface of the seed could readily be differentiated from the remelt region because the seed had a bright specular finish from the etch used in charge preparation while the remelt region had a dull, matte finish indicative of contact with the PBN sleeve. No free surfaces were observed and the

diameter of the remelt region was constant, thus it is concluded that the PBN spring-graphite plunger did in fact work.

B. Axial Slice Characterization: Lapped Surface

The lapped surface from the first space flight and ground truth experiments are shown in Fig. 6. Here it can be seen that polycrystalline breakdown occurs in both samples during the first translation period. In addition, several large voids appear in the centerline of the flight sample. The first occurrence of these voids corresponds to the translation rate change.

The lapped surfaces from the second space flight and ground truth experiments are shown in Fig. 7. Here too it can be seen that a central void appears in the flight sample. The position of the first occurrence of this void again corresponds to the translation rate change. In addition, during the rapid quench period, voids can be seen in both samples. However, in the flight samples there are only a few large voids while in the ground truth sample there is a distribution of small voids.

The segmented nature of these voids is suggestive of bubbles and it is expected that they were arsenic bubbles at their formation. One explanation of why the bubbles are in the central axis of the flight crystal is that they were formed there, i.e. as the melt-solid interface moved along, arsenic gas came out of solution at the 'cold' interface. In the ground test, the arsenic gas would rise to the top (all ground samples were run in a vertically stabilizing configuration) but in flight the arsenic gas would not and was therefore captured at the growth interface. Following this logic, if the ground tests were run at very large growth rate, then the arsenic bubbles could be trapped at the interface also. There is evidence of this in the rapid quench section of the second ground based sample, shown in Fig. 7.

C. Axial Slice Characterization: Infra-red Transmission

The axial slices were polished on both sides and imaged using a macroscopic infra-red transmission imaging system [21]. Figures 8-11 are montages of the infra-red transmission through the ground truth 1, space flight 1, ground truth 2 and space flight 2 samples.

The meltback position in each sample is clearly seen in the left hand side of each sample. A small portion of each sample is lost due to the presence of the sample holder. The meltback positions for the four samples are compared in Fig. 12. Although the meltback positions of the four samples varied from 3.2 cm to 2.0 cm (i.e. remaining seed material) an analysis of the relative position differences of the seeding thermocouples to that of the thermocouple temperature readings indicates that these differences are strictly due to the relative position differences of the thermocouple and are not due to being processed on the ground or in space.

None of the samples show any evidence of demarcation lines, with the exception of two lines in the first flight sample, Fig. 9. In Fig. 13 the relative position of the seeding interface (s), thermocouples (TCx), translation periods (Tx) and the mechanical pulses (Pxy) are shown. Although a comparison of Fig. 13 with Fig. 9 shows that the relative position of the two demarcation lines are close to P22 and P23, measurement of the growth rate, assuming the time difference between the two pulses, yields a growth rate of $7.5 \mu\text{m/s}$ not $5.0 \mu\text{m/s}$, which was the translation rate during that period. Since these two demarcation line are at the beginning of a void, it is believed instead that they are artifacts from the entrapment of the bubble into the growing crystal.

D. Seeding Interface Shape Measurements

The seeding interfaces are clearly seen in the left hand portion in each sample shown in Figs. 8-11. All seeding interfaces are curved into the liquid. Using an infra-red microscope, a photomicrograph montage of the seeding interface can be constructed, as shown in Fig. 14 for the second space flight and ground truth samples. The seeding interface shape can then be measured.

The four seeding interface shapes are shown in Fig. 15. All the interfaces deflections are approximately the same and are symmetric about the growth axis. This is to be expected since the seeding interface shape is the result of the steady state heat transfer and for a lower Prandtl number fluid the fluid flow does not contribute much to the overall heat transfer. Thus, it is expected that the interface shape and growth rate from the space experiments will be similar to the ground truth experiments.

E. Dopant Distribution Measurements

In Figs. 8-11 variations in the photographic contrast can be seen. Since this is a photograph of an infra-red transmission image, these contrast differences are due to differences in transmission of light through the sample. Since these samples were doped at $1 \times 10^{17}/\text{cm}^3$ with selenium, which is several orders of magnitude larger than any unintentional impurity, it is assumed that these variations in transmission are due to variations in selenium distribution in the samples.

A macro-imaging system based on these assumptions has been developed and a detailed description can be found in the literature [21]. In essence, this system used a CCD camera at a known wavelength on infra-red light ($1.05 \mu\text{m}$) to measure the transmission of the sample. By measuring calibration samples of known transmission with the system, then a transformation can be made from gray level output from the camera to transmission. The transmission can be converted to absorption coefficient by knowing the wavelength (and thus the index of refraction) and the sample thickness. The absorption coefficient can then be converted to free carrier concentration and at room temperature it is assumed that all the free carriers are due to the selenium.

The resultant image of the selenium distribution is approximately 100 pixels wide by 400 pixels long. This corresponds to an area approximately 0.015 cm wide by 0.02 cm long. To determine the average axial dopant distribution the 100 values are averaged across the sample. The overall average free carrier concentration for ground truth 1 and space flight 1 are shown in Figs. 16 and 17. The area of interest in each of these figures is only the first translation period, since the presence of the voids invalidates this measurement technique. Also shown in Figs. 16 and 17 are selected radial distribution plots.

F. Axial Segregation Analysis

In Fig. 18, the average selenium distribution for the first ground based sample is compared to the predicted distribution made using the complete mixing equation (Eqn. 2). As can be seen there is fair agreement in these data.

In Fig. 19, the average selenium distribution for the first flight sample is compared to the predicted distribution made using the diffusion controlled growth equation (Eqn 3). Also plotted is the distribution predicted from the complete mixing equation. As can be seen, the growth starts out following the diffusion controlled growth prediction within the error associated with the precision that the thermal physical property values are known. However, after approximately 0.5 cms the distribution is slowly driven into the complete mixing regime.

G. Radial Segregation Analysis

The radial dopant distributions shown in Figs. 18 and 19 show that for the ground base sample the radial segregation is about 30% - 50%, which would be expected in a sample of this size. In Fig. 19 however, the radial distribution starts out slightly above 20%. This is in excellent agreement with Coriell and Sekerka's second paper (C&S II) as shown in Fig. 20. However, as the growth continues beyond 1 cm, where the axial segregation indicates that the axial distribution is moving to a complete mixing regime, the radial segregation increases to the 30% - 50% range typical of the ground based sample. Thus, the radial segregation completely supports the conclusions derived from the axial segregation data.

I. Comparison to Acceleration Data

Three acceleration measurement experiments were flown as part of this mission: OARE, SAMS and PAS. All of them are experiments in their own right, were conducted for their own reasons and the final data from these experiments has not been released. However, the Principal Investigators [22-24] from these experiments have shared some preliminary data. Of particular interest is, of course, the time period after the start of growth for the first flight experiment.

The data from OARE with an approximate growth scale is shown in Fig. 21. As can be seen there is a large gap in the data in the region of interest. This is because the OARE data analysis

program filters out any large data excursions. This conclusion is confirmed with the data from SAMS shown in Fig. 22 where a large acceleration event occurred at the one hour (≈ 1 cm) point of the experiment.

Although it is left to identify what this particular acceleration event was, it is sufficient to conclude that one did occur. This acceleration event was sufficiently large in amplitude and duration that it drove the segregation behavior of the sample from diffusion controlled growth to that of complete mixing.

CONCLUSIONS

Measurement of the selenium dopant distribution, using quantitative infra-red transmission imaging, indicates that the first sample initially achieved diffusion controlled growth as desired. However, after about 1 cm of growth, the segregation behavior was driven from a diffusion controlled growth regime to a complete mixing regime. Measurements in the second flight sample indicated that the growth was always in a complete mixing regime. In both experiments, voids in the center line of the crystal, indicative of bubble entrapment, were found to correlate with the position in the crystal when the translation rates were doubled.

ACKNOWLEDGMENTS

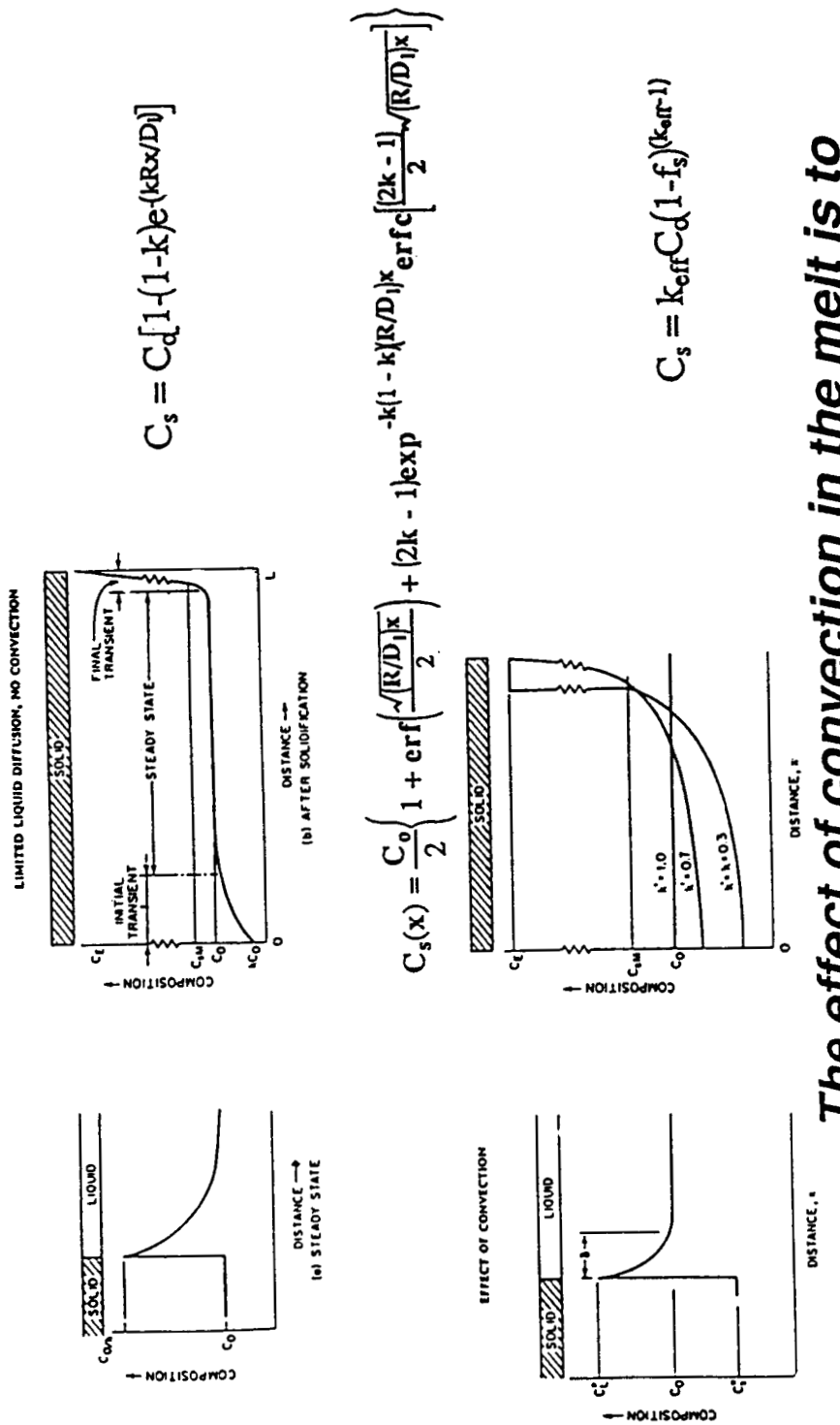
The authors would like to thank the National Aeronautics and Space Administration for their cooperation and enthusiastic support during all stages of these experiments. The following individuals are especially noted for their unwavering efforts in achieving the success of these experiments: Mr. David Schaefer, Project Manager and Dr. Frank Szofran, Project Scientist from the Marshall Space Flight Center and Mr. Joel Kearns, Program Manager from the Microgravity Science and Applications Division of NASA Headquarters. This work was sponsored under NASA-MSFC contract NAS8-39695.

REFERENCES

1. M.C. Flemings, *Solidification Processing*, McGraw-Hill, Inc (1974).
2. E. Schiel, Z. Metallk., 34 (1942) 70.
3. W.G. Pfann, J. Metals, 4 (1952) 763.
4. W.A. Tiller, K.A. Jackson, J.W. Rutter and B. Chalmers, Acta. Met., 1 (1953) 428.
5. J.R. Carruthers, in *Preparation and Properties of Solid State Materials*, vol. 3, (1973) 1.

6. K.M. Kim, A.F. Witt and H.C. Gatos, J. Electrochem. Soc., 119 (1972) 1218.
7. K.M. Kim, A.F. Witt, M. Lichtensteiger and H.C. Gatos, J. Electrochem. Soc., 125 (1978) 475.
8. D.E. Holmes and H.C. Gatos, J. Electrochem. Soc., 128 (1981) 429.
9. see for instance
C.E. Chang and W.R. Wilcox, J. Crystal Growth, 21 (1974) 135.
R.J. Naumann, J. Crystal Growth, 58 (1982) 554.
T. Jasinski, W.M. Rosenow and A.F. Witt, J. Crystal Growth, 61 (1983) 710.
10. see for instance
T.F. Fu and W.R. Wilcox, J. Crystal Growth, 48 (1980) 416.
R.J. Naumann, J. Crystal Growth, 58 (1982) 569.
T. Jasinski, W.M. Rosenow and A.F. Witt, J. Crystal Growth, 67 (1984) 173.
T. Jasinski, W.M. Rosenow and A.F. Witt, J. Crystal Growth, 71 (1985) 295.
11. see for instance
S. Motakef, J. Crystal Growth, 98 (1989) 711.
A.S. Jordan, J. Crystal Growth, 49 (1980) 631.
12. R.J. Naumann and H.W. Herring, *Materials Processing in Space: Early Experiments*, NASA SP-443, Washington, DC (1980).
13. Proceedings Third Space Processing Symposium, *Skylab Results: Volume 1*, NASA-Marshall Space Flight Center, M-74-5, June (1974).
14. A.F. Witt, H.C. Gatos, M. Lichtensteiger and C.J. Herman, J. Electrochem. Soc., 125 (1978) 1832.
15. S.R. Coriell and R.F. Sekerka, J. Crystal Growth, 46 (1979) 479.
16. S.R. Coriell, R.F. Boisvert, R.G. Rehm and R.F. Sekerka, J. Crystal Growth, 54 (1981) 167.
17. S.A. Korpela, A. Chait and D.H. Matthiesen, J. Crystal Growth, accepted for publication (1993).
18. D.H. Kim, P.M. Adornato and R.A. Brown, J. Crystal Growth, 89 (1988) 339.
19. Committee on Scientific and Technological Aspects of Materials Processing in Space, *Materials Processing In Space*, National Academy of Sciences, Washington DC, (1978).
20. D.H. Matthiesen, J. Crystal Growth, accepted for publication (1994).
21. J.A. Majewski and D.H. Matthiesen, J. Crystal Growth, accepted for publication (1994).
22. R. Blanchard, OARE Principal Investigator, private communication.
23. R. Delombard, SAMS Principal Investigator, private communication.
24. I. Alexander, PAS Principal Investigator, private communication.

Axial Segregation



The effect of convection in the melt is to increase the segregation in the solid

Figure 1 Solute redistribution during solidification with limited liquid diffusion and no convection. Composition profile during steady-state solidification and composition profile after solidification, top. Solute redistribution during solidification with limited liquid diffusion and convection in the melt. Composition profile during steady-state solidification showing d , the mass boundary layer and composition profile after solidification, bottom. (After Flemings [1]).

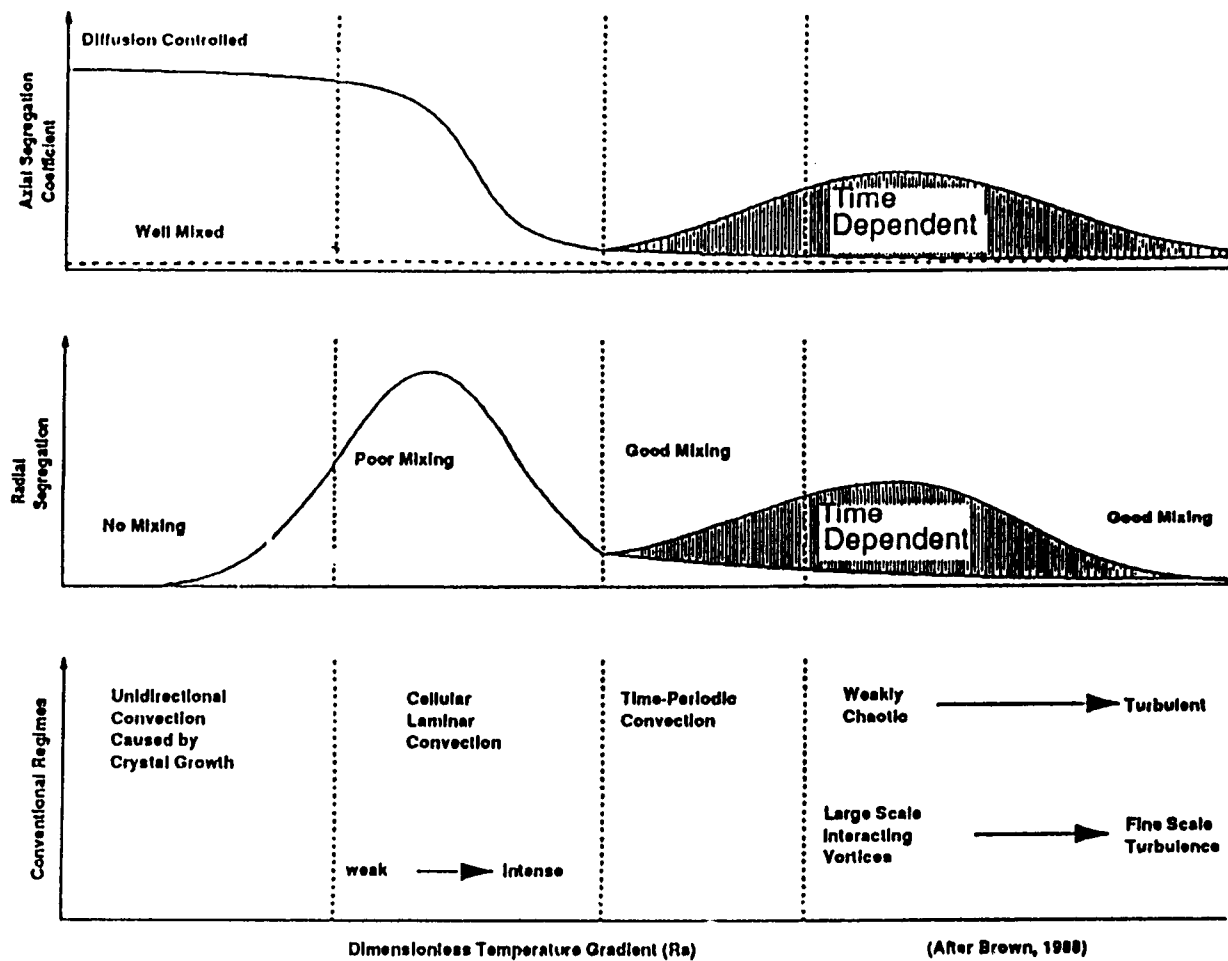


Figure 2 The effect of convection on the axial and radial segregation in a dilute binary system (after Brown [18]).

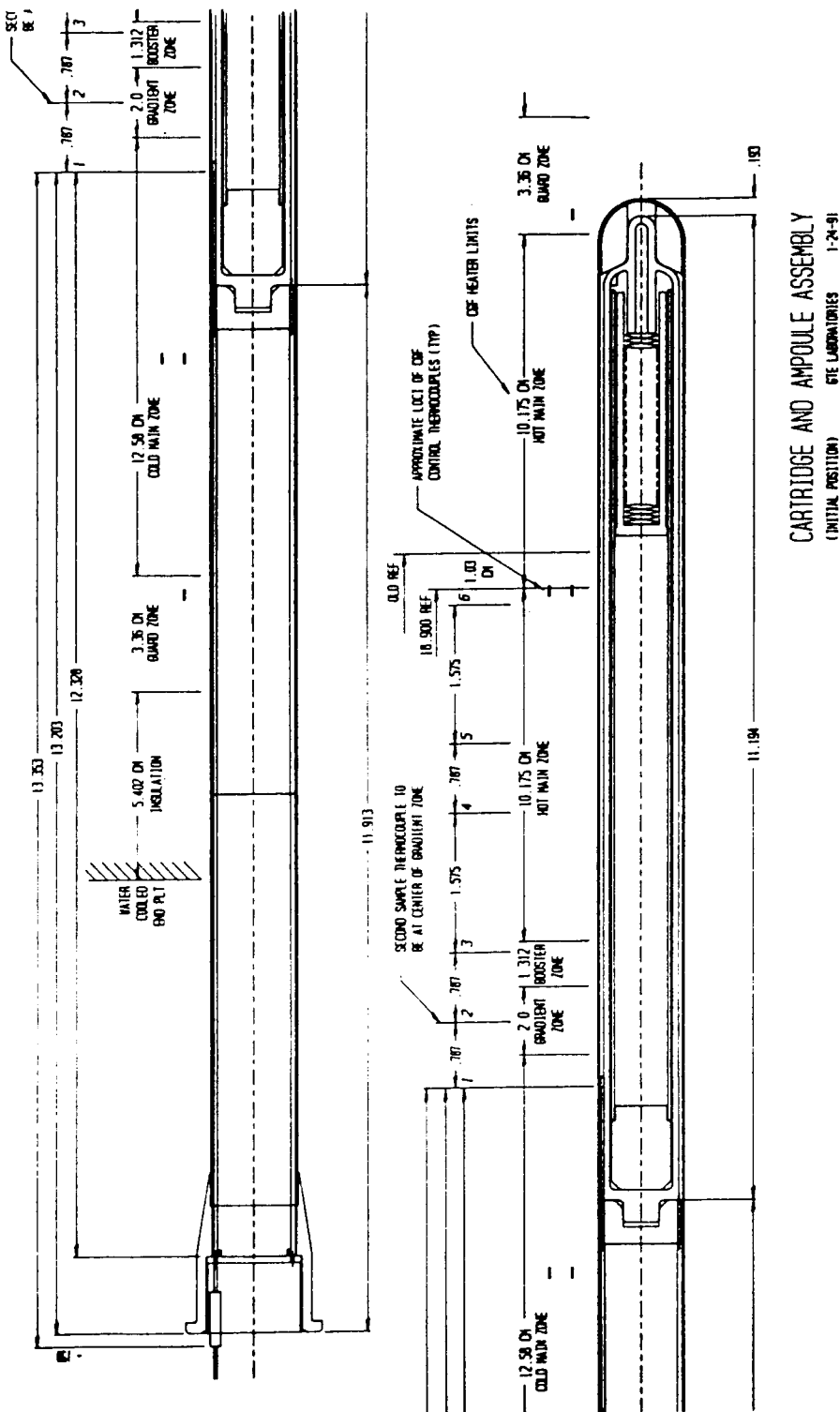


Figure 3 Cross-sectional drawing of the ampoule within the cartridge, together these form the Sample Ampoule Cartridge Assembly (SACA), at the initial seeding position. Also shown are the relative relationship of the sample thermocouples and furnace zone positions.

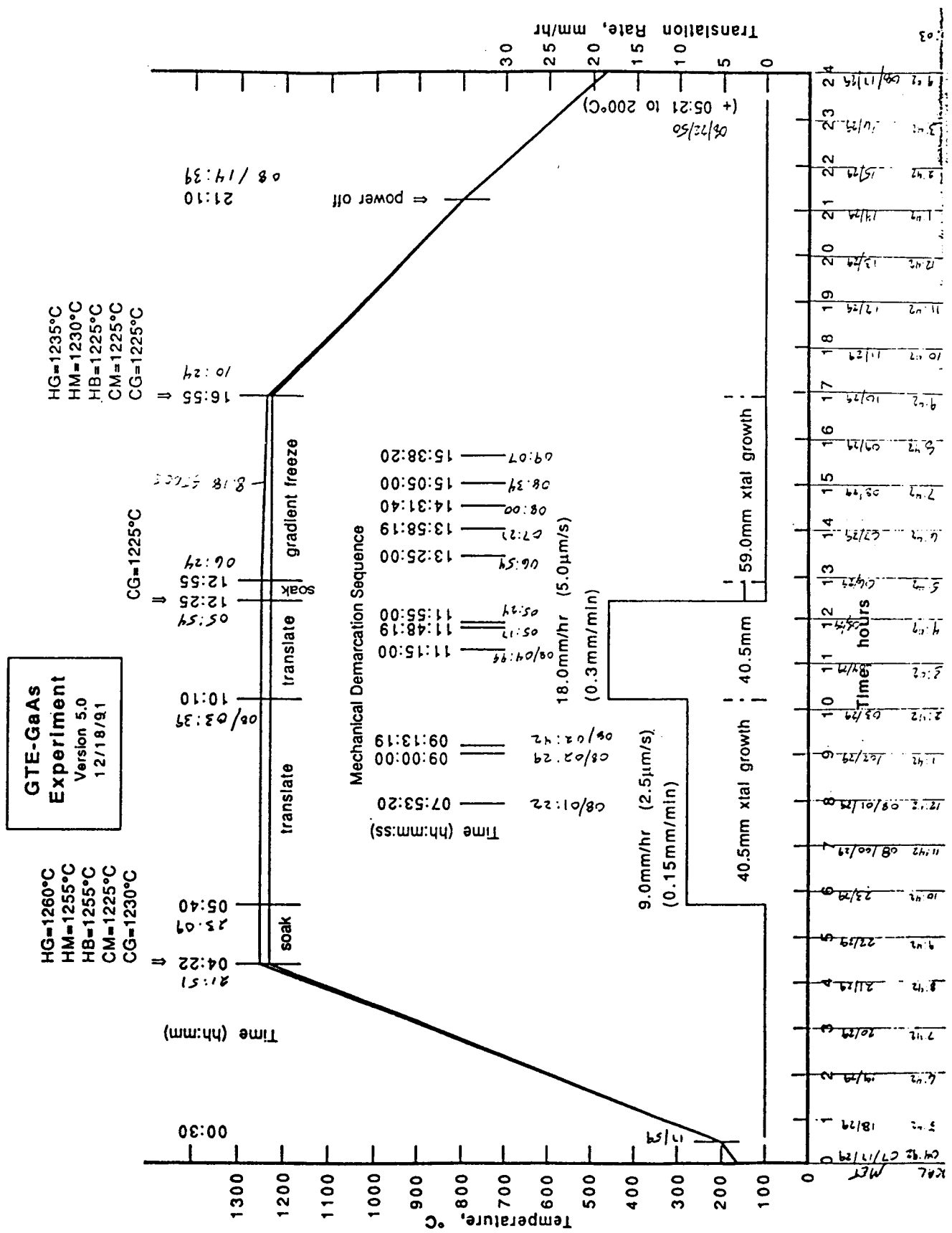
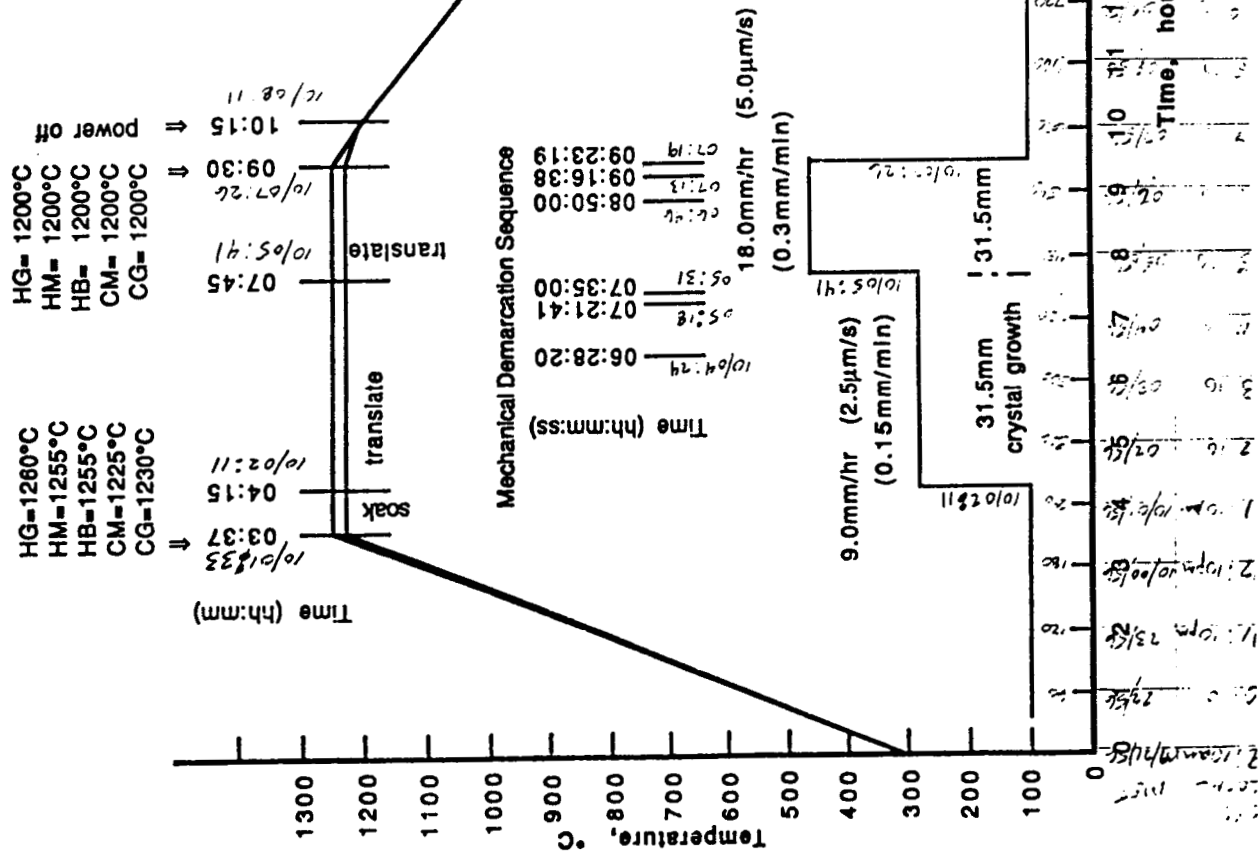


Figure 4 Experimental timeline for the first flight and ground truth experiments. MET times are listed for the flight experiment.

**CWRU-GaAs
Experiment**
Version 6.2
07/04/92



ORIGINAL PAGE IS
OF POOR QUALITY

Figure 5 Experimental timeline for the second flight and ground truth experiments. MET times are listed for the flight experiment.

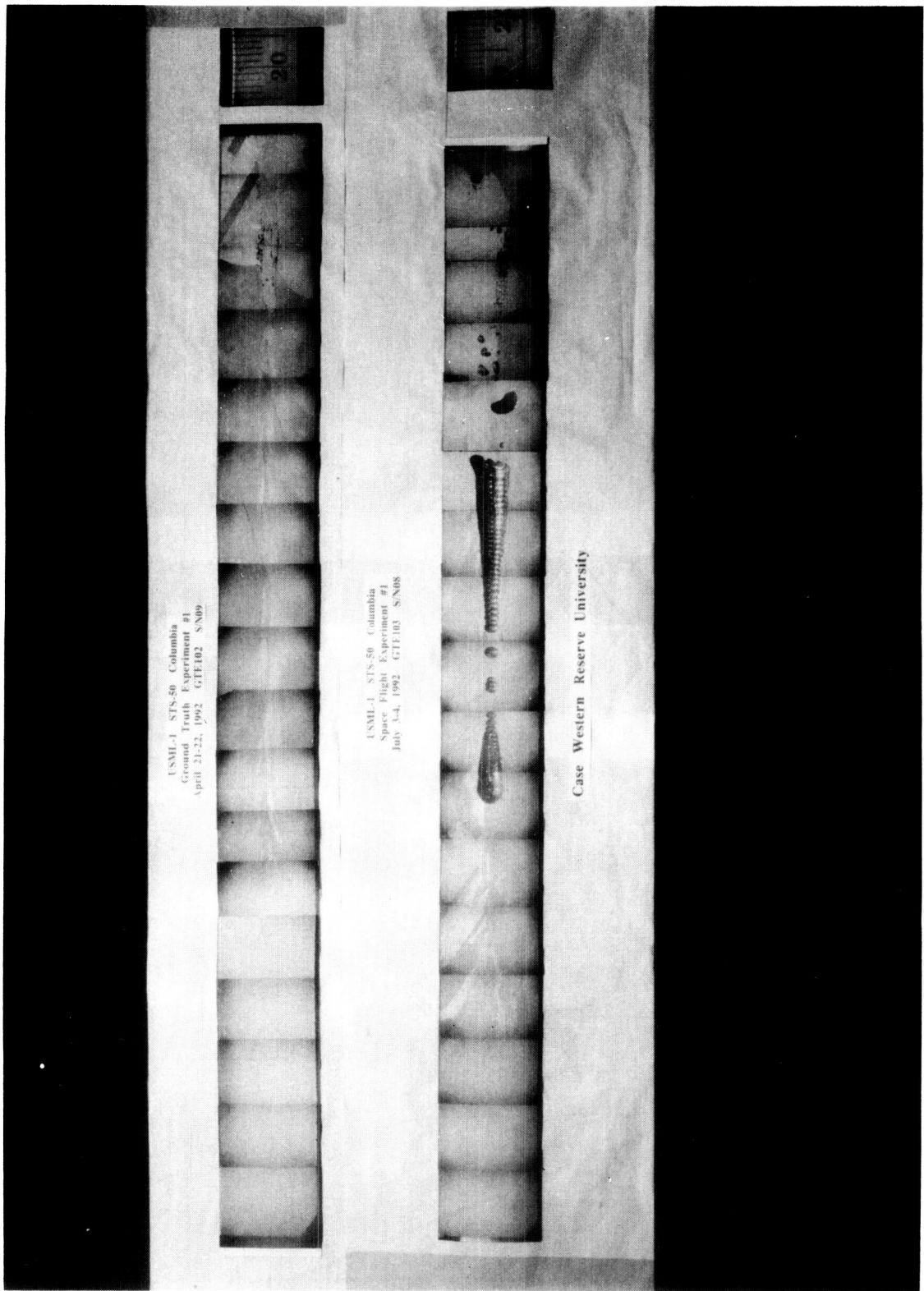


Figure 6 Lapped surface samples from the first flight and ground truth samples.

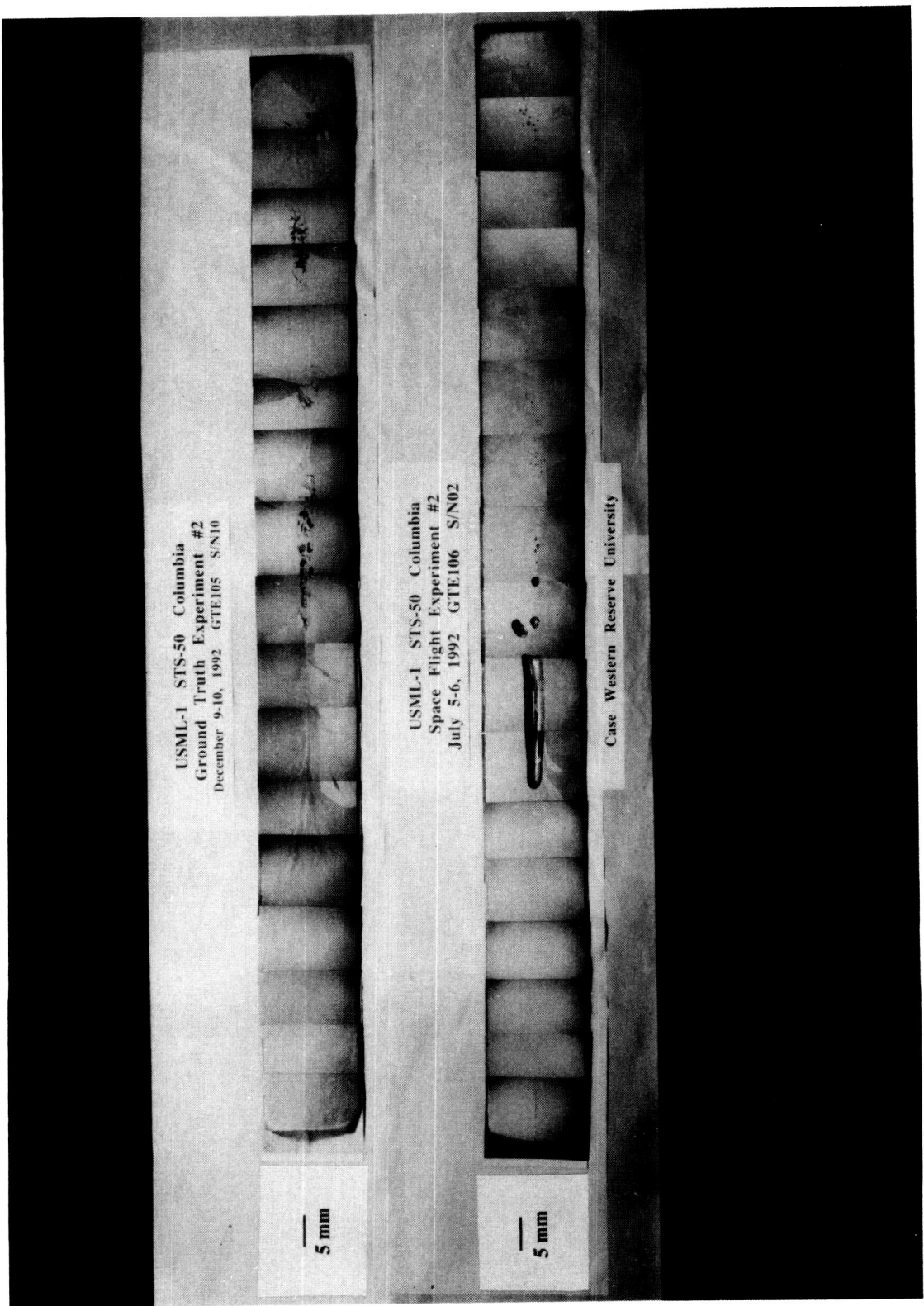


Figure 7 Lapped surface samples from the second flight and ground truth samples.

USML-1 STS-50 Columbia
Ground Truth Experiment #1
01/21/92 011102 S-N09
Case Western Reserve University

Bridgeman growth-->

seed crystal

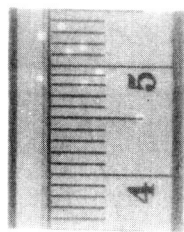
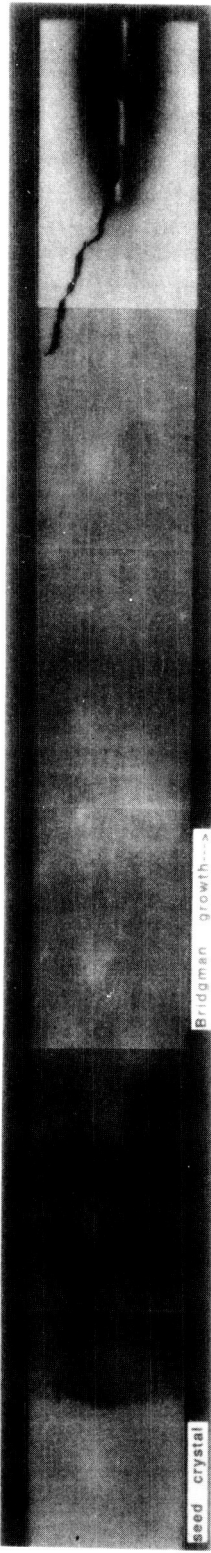


Figure 8 Montage of the infrared transmission imaging for the axial slice from the first ground truth sample.

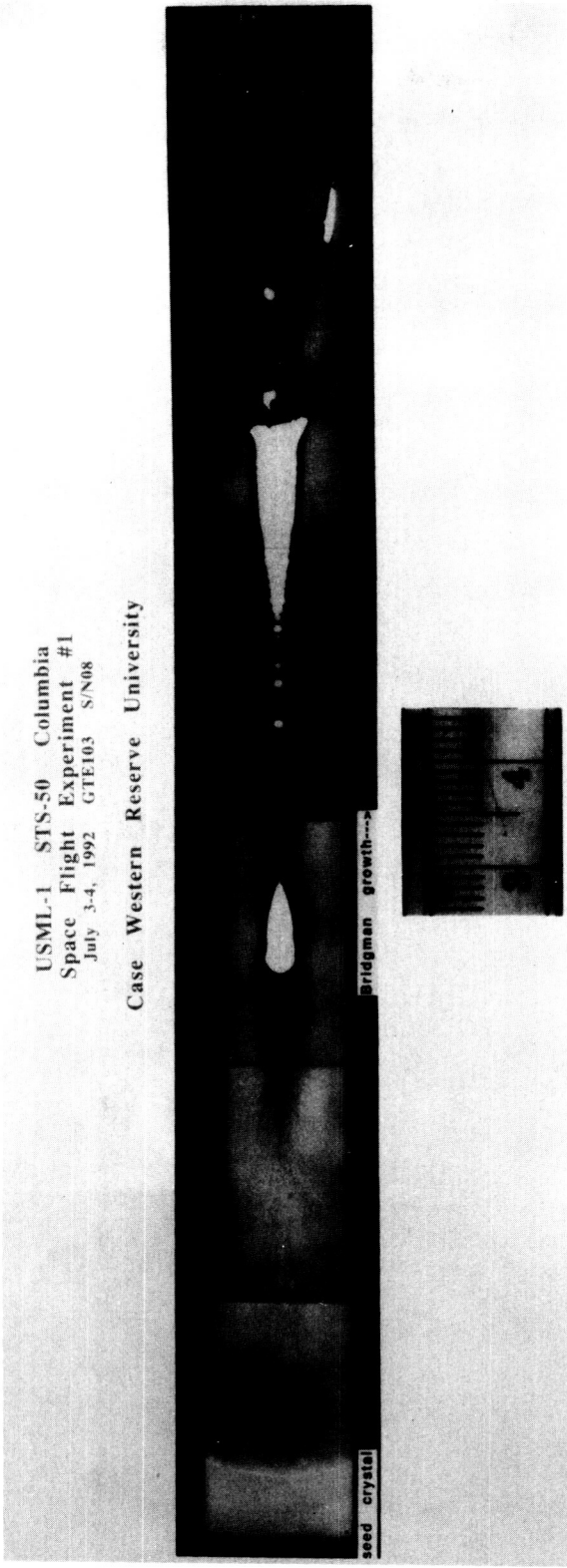


Figure 9 Montage of the infrared transmission imaging for the axial slice from the first flight sample.

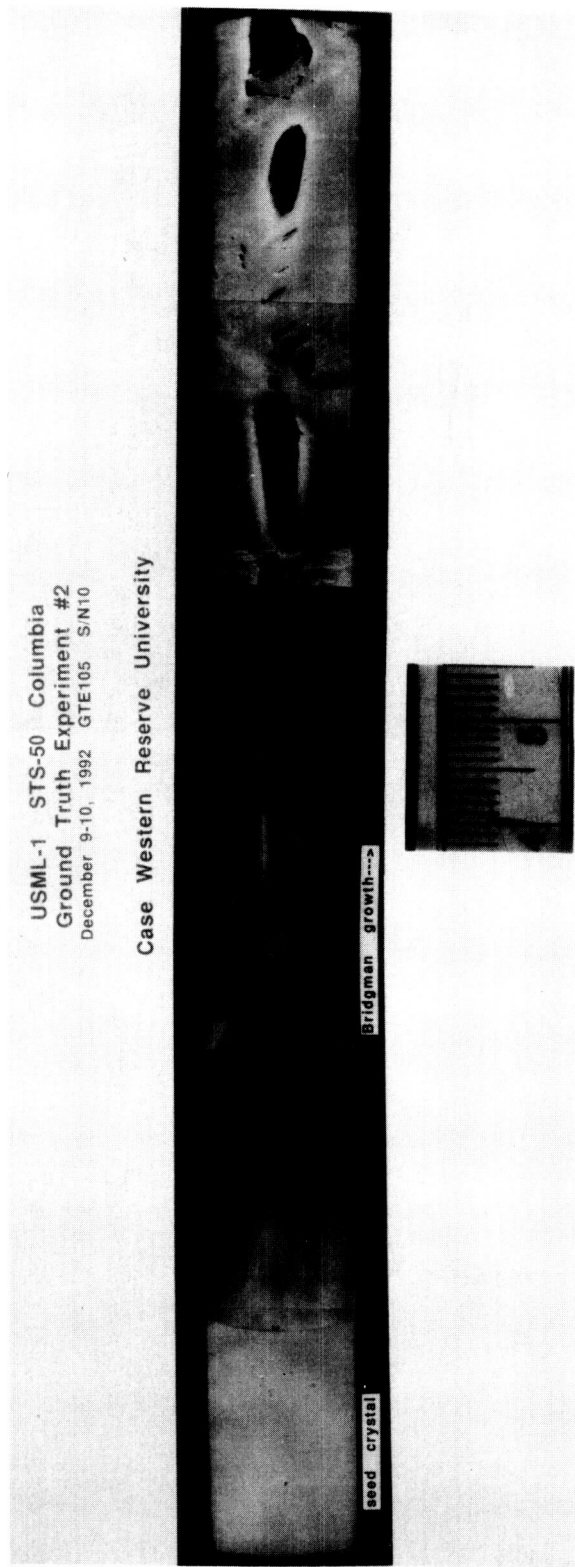


Figure 10 Montage of the infrared transmission imaging for the axial slice from the second ground truth sample.

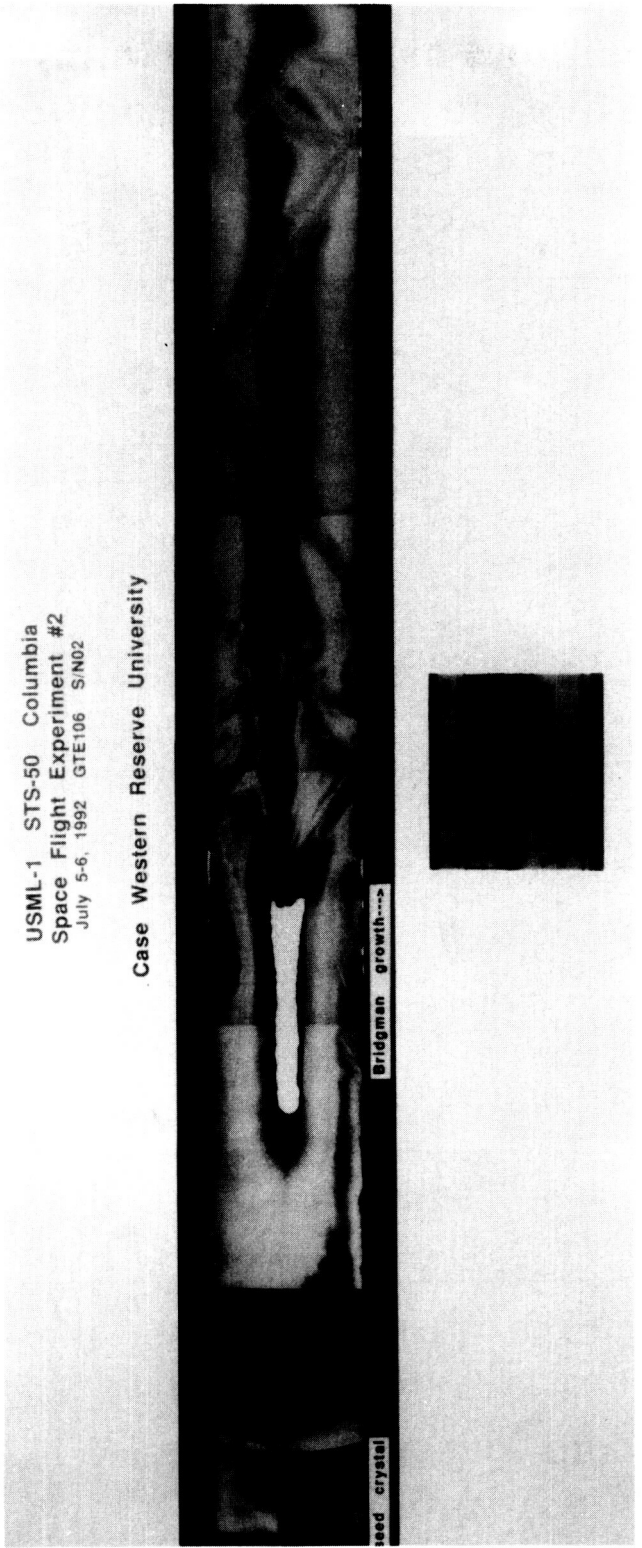


Figure 11 Montage of the infrared transmission imaging for the axial slice from the second flight sample.

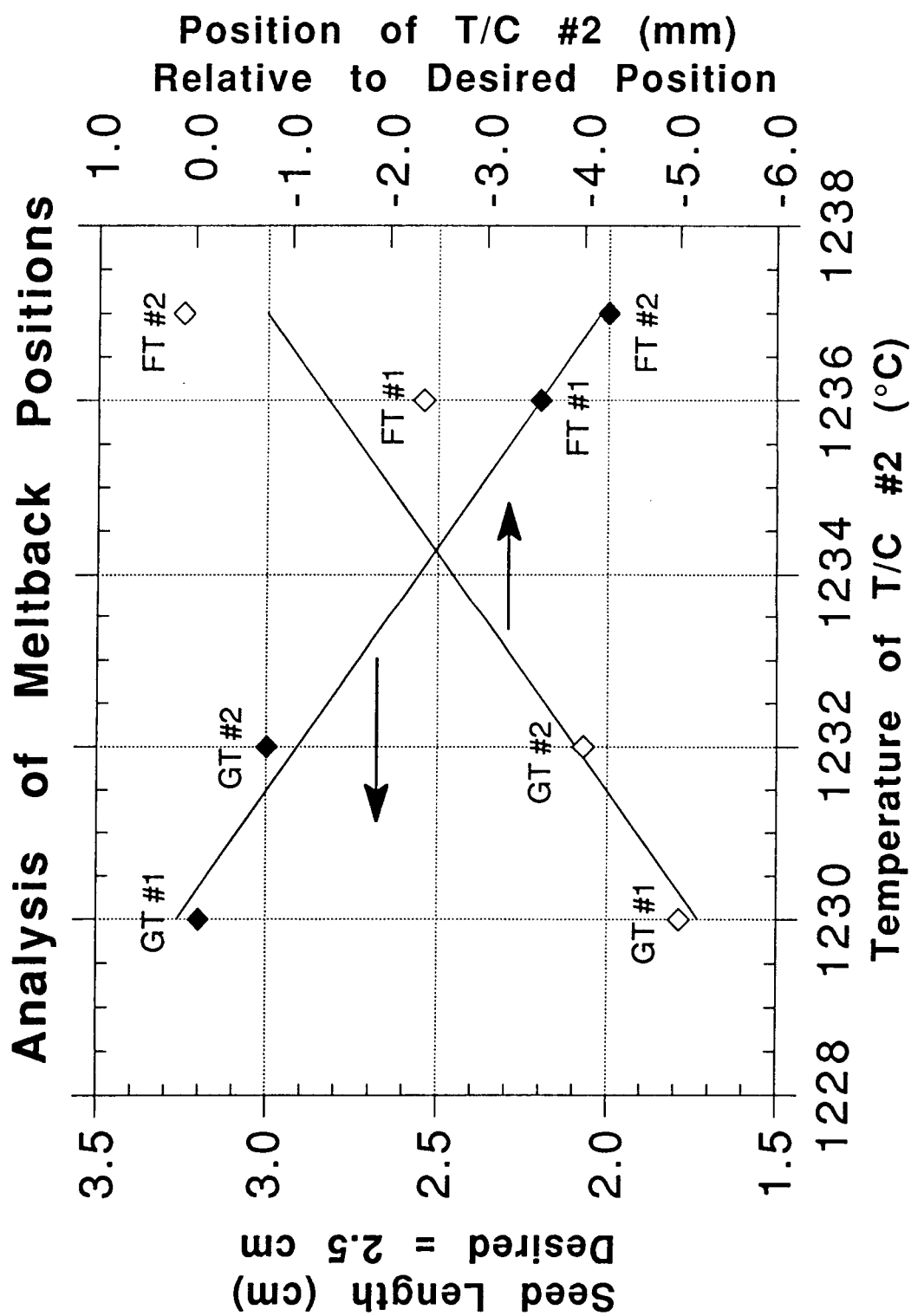


Figure 12 Analysis of the meltback position from the first ground truth (GT#1), first flight (FT#1), second ground truth (GT#2), and second flight (FT#2) samples.

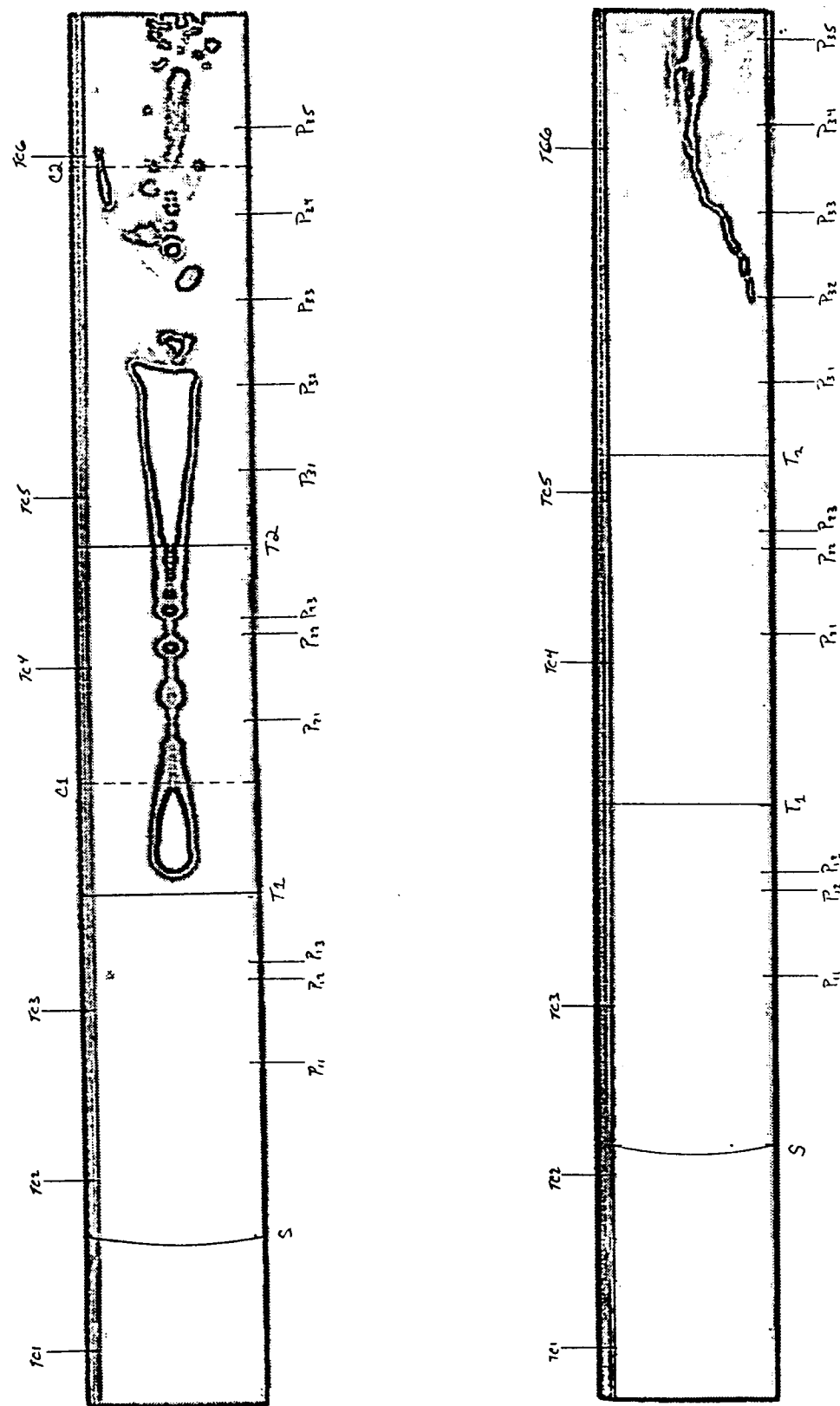


Figure 13 Edge detection image processing of Fig. 8 and Fig. 9. Also shown are the relative positions of the seeding interface (*s*), initial sample charge positions (*Cx*), sample thermocouples (*TCx*), translation rate changes (*Tx*), and mechanical pulsing events (*Pxy*).

USML-1 STS-50 Columbia
Ground Truth Experiment #2
December 9-10, 1992 GTE105 S/N10
Case Western Reserve University

USML-1 STS-50 Columbia
Space Flight Experiment #2
July 5-6, 1992 GTE106 S/N02
Case Western Reserve University

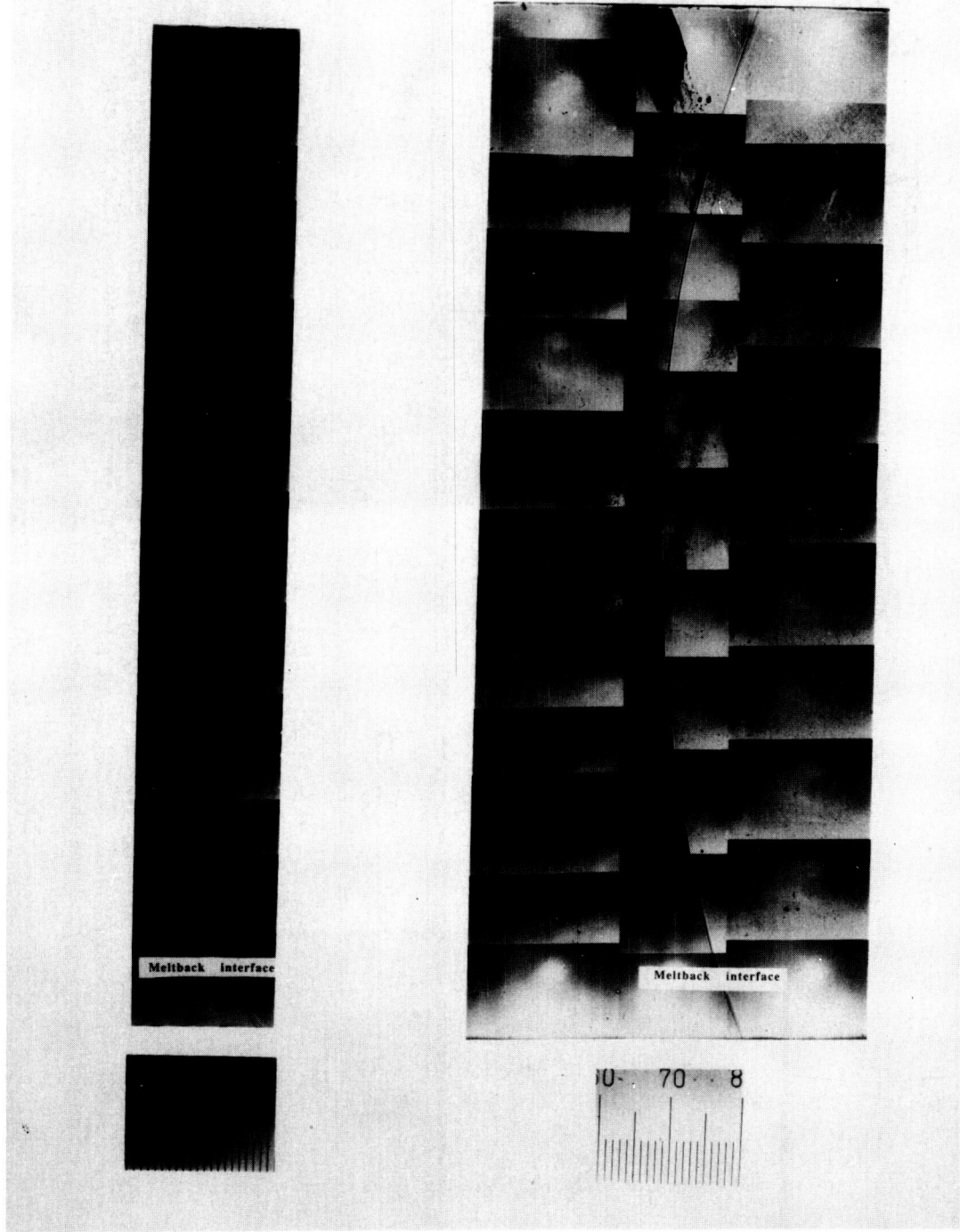


Figure 14 Montage of the infra-red microscope imaging of the seeding interface shapes for Fig. 10 and Fig 11.

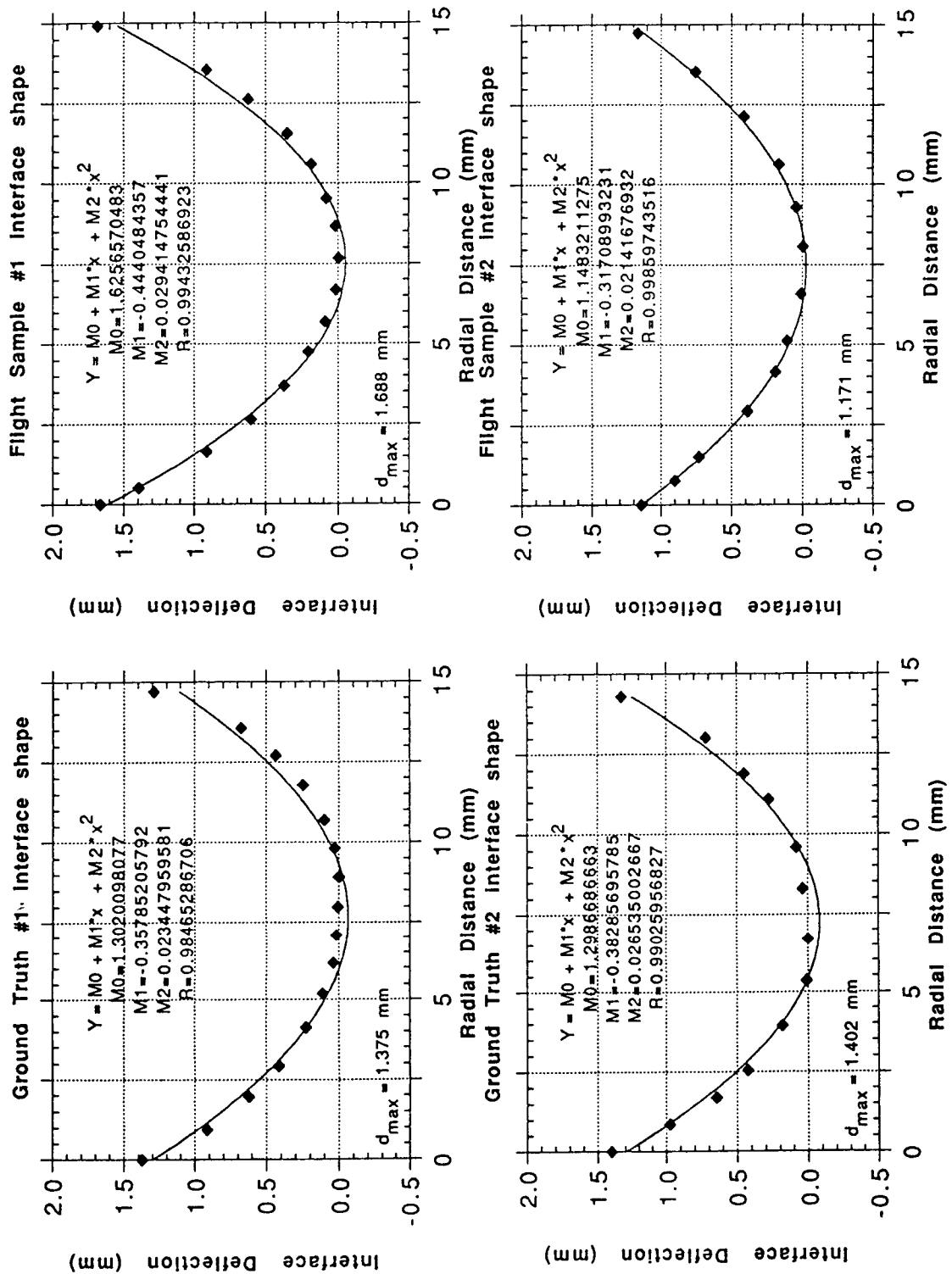


Figure 15 Measured interface shapes for all four samples. Interface shapes are parabolic and symmetric about the growth axis.

Ground Truth Experiment #1
Overall Average Free Carrier Concentration
for 1st Translation

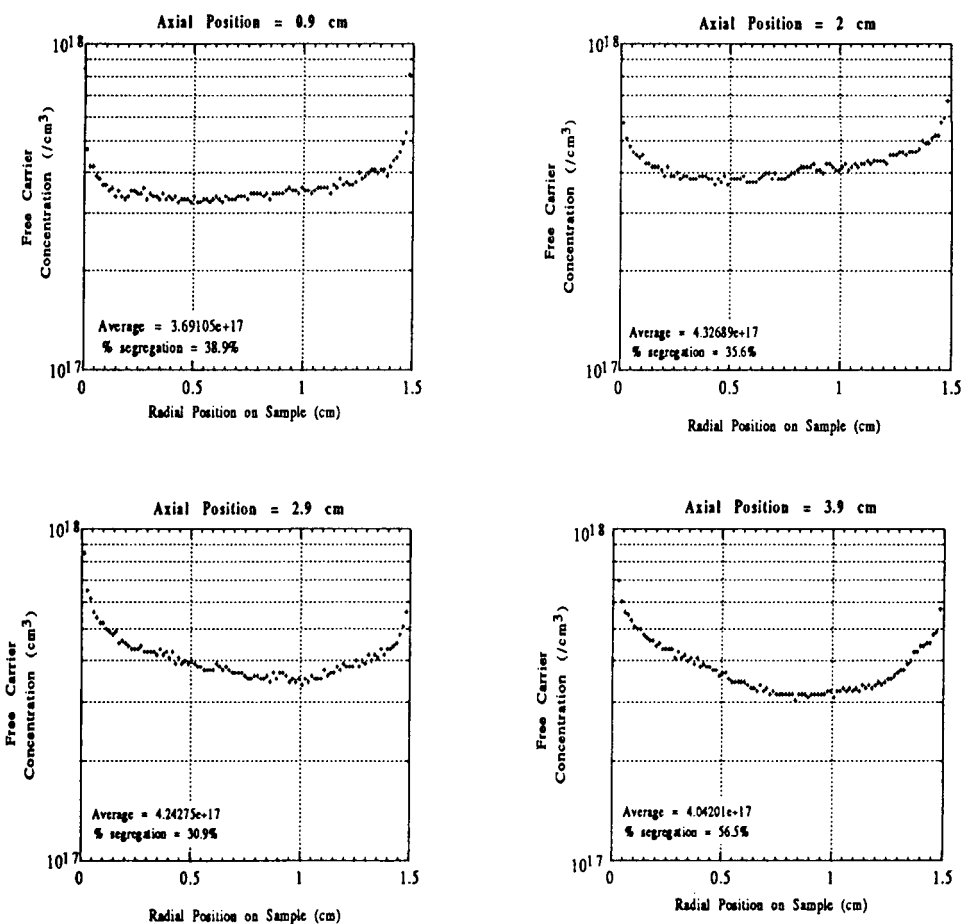
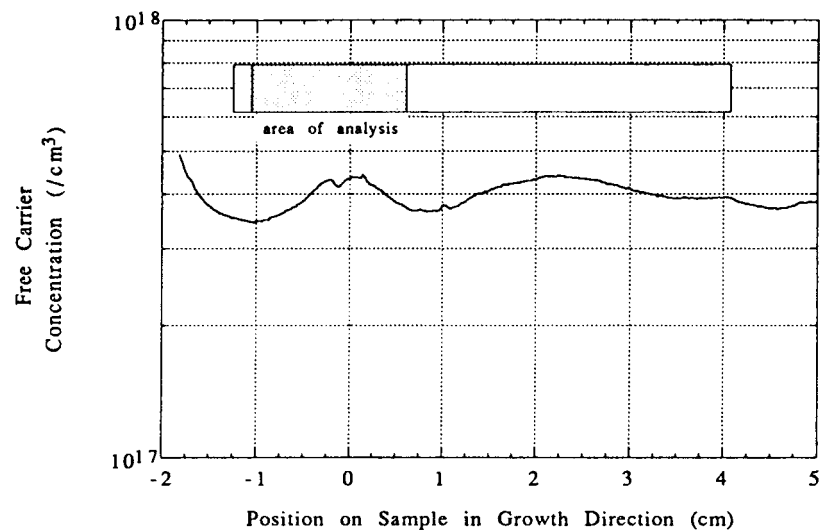


Figure 16 Free carrier concentration (selenium dopant) distribution for the first ground truth sample at the averaged axial positions (top) and for individual radial positions (bottom).

Space Flight Experiment #1
Overall Average Free Carrier Concentration
for 1st Translation

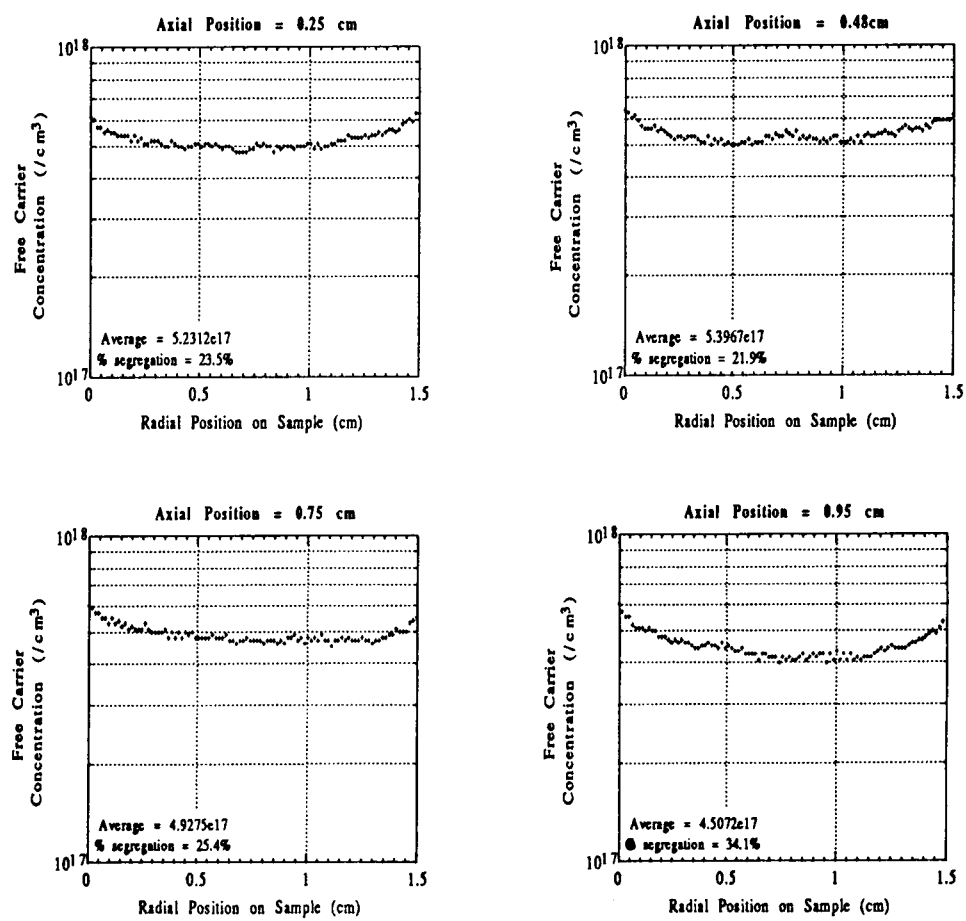
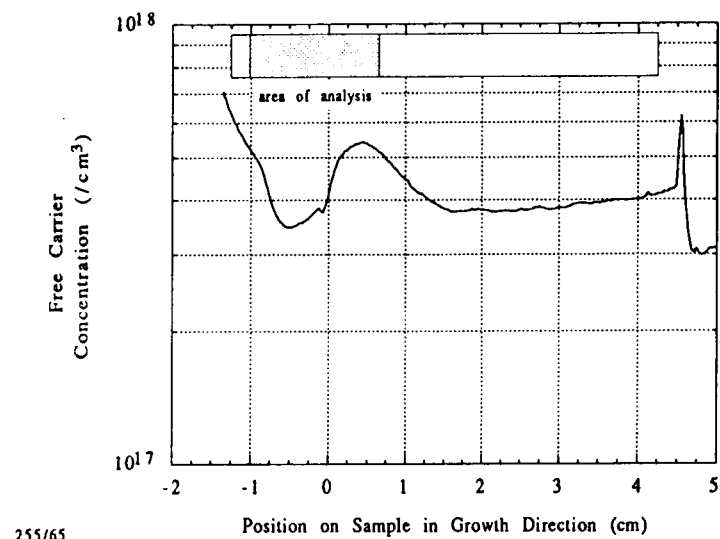


Figure 17a Free carrier concentration (selenium dopant) distribution for the first flight sample at the averaged axial positions (top) and for individual radial positions (bottom).

Space Flight Experiment #1
Overall Average Free Carrier Concentration
for 1st Translation

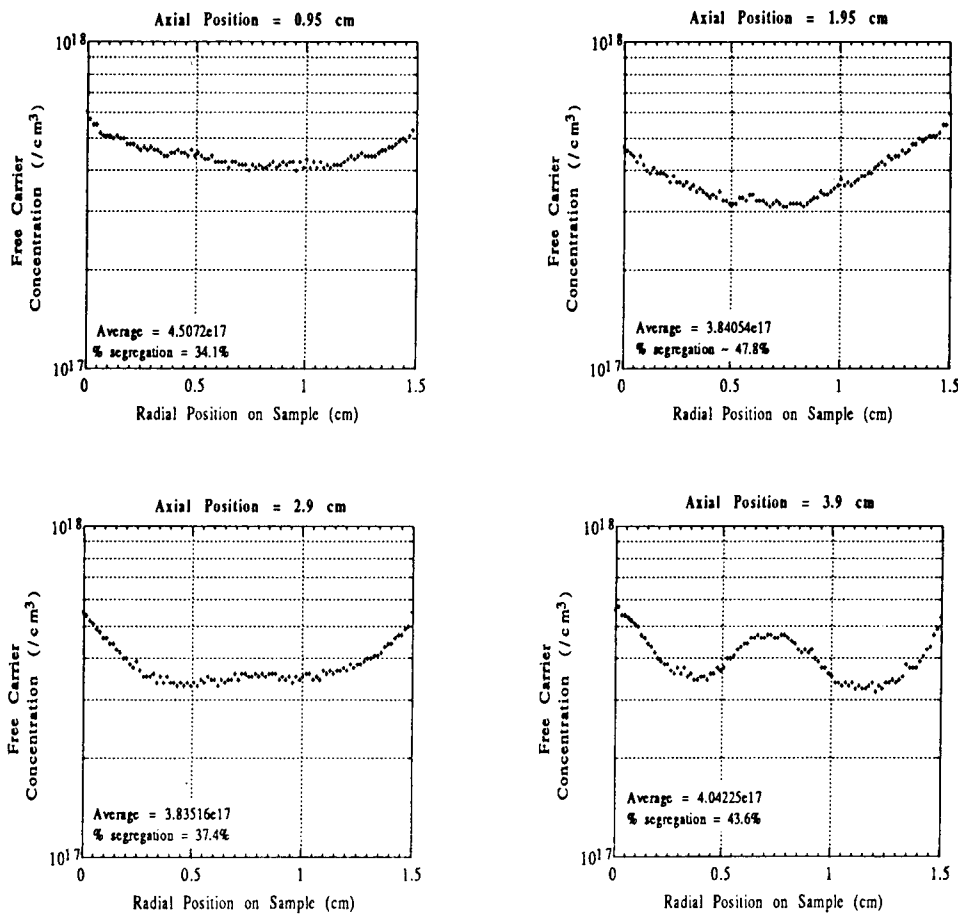
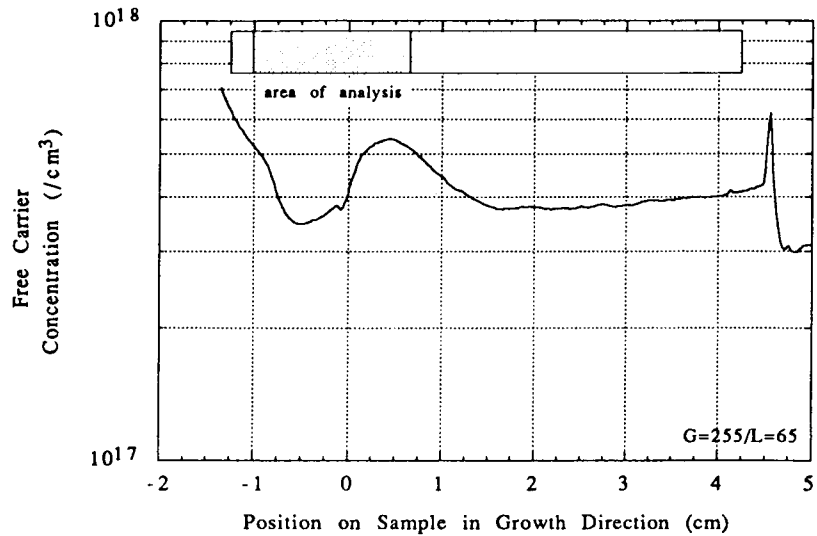


Figure 17b Free carrier concentration (selenium dopant) distribution for the first flight sample at the averaged axial positions (top) and for individual radial positions (bottom).

Ground Truth Experiment #1
Calculated Results from Complete Mixing Equation
Compared to Results from Infrared Imaging

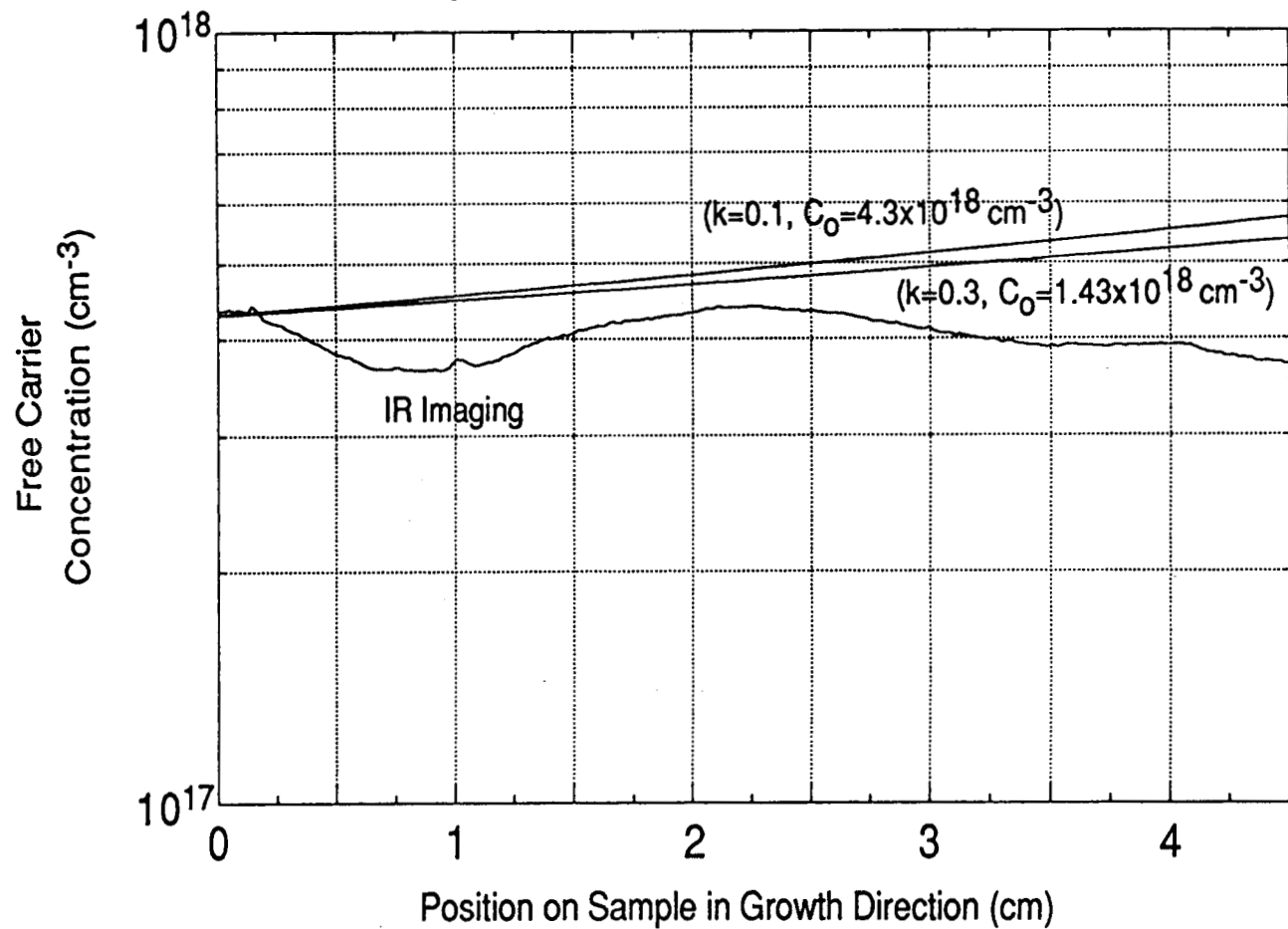


Figure 18 Segregation analysis for the first ground truth sample. Also shown is the segregation behavior for the complete mixing case using the labeled values.

Space Flight Experiment #1
 Theoretical Results from Diffusion-Controlled Growth (DCG)
 and Complete Mixing (CM) Equations Compared with
 Results From Infrared Imaging

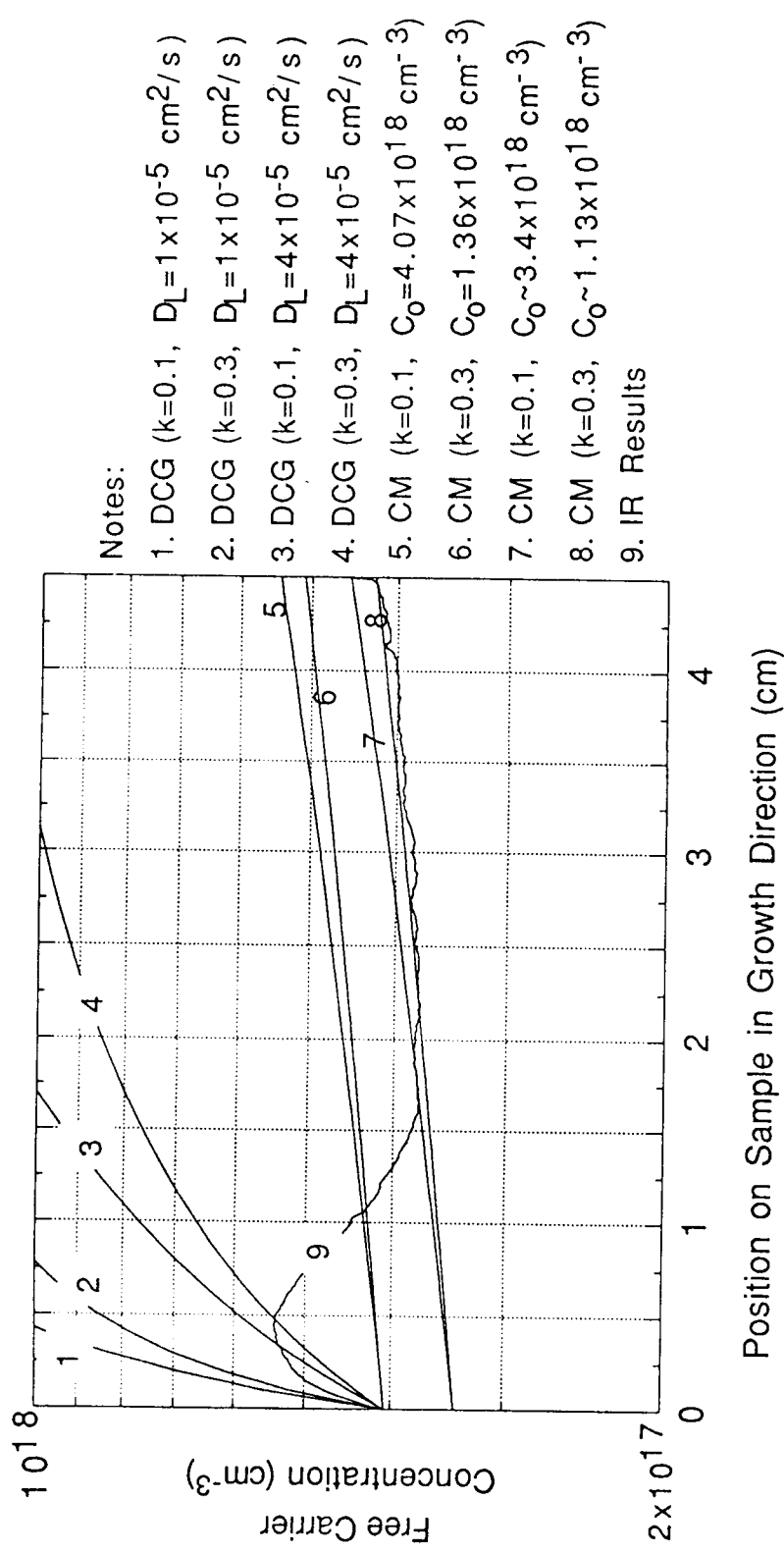


Figure 19 Segregation analysis for the first flight sample. Also shown is the segregation behavior for the complete mixing case and the diffusion controlled growth case using the labeled values.

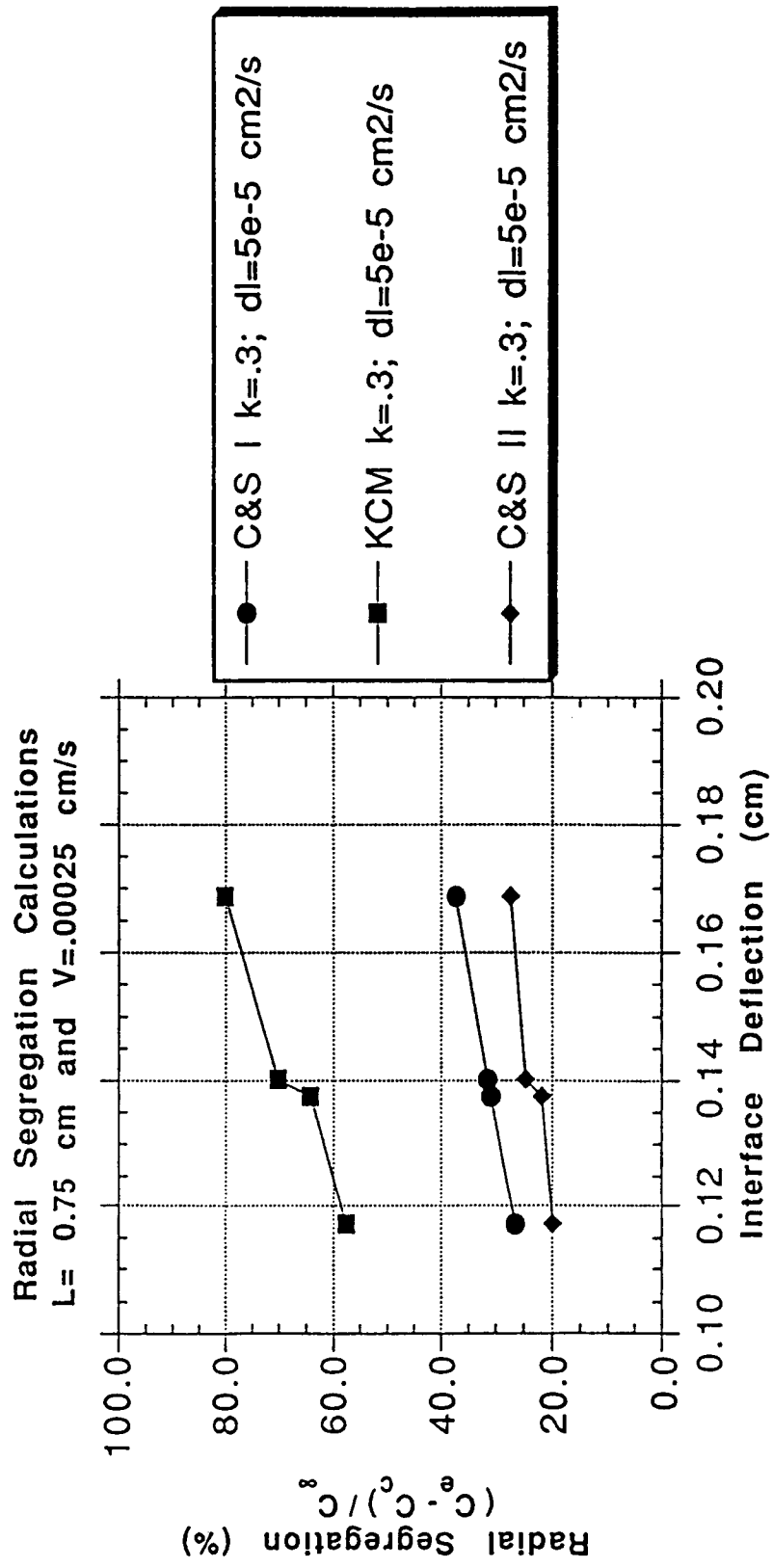


Figure 20 Calculated values for the radial segregation using the various theories (see text).

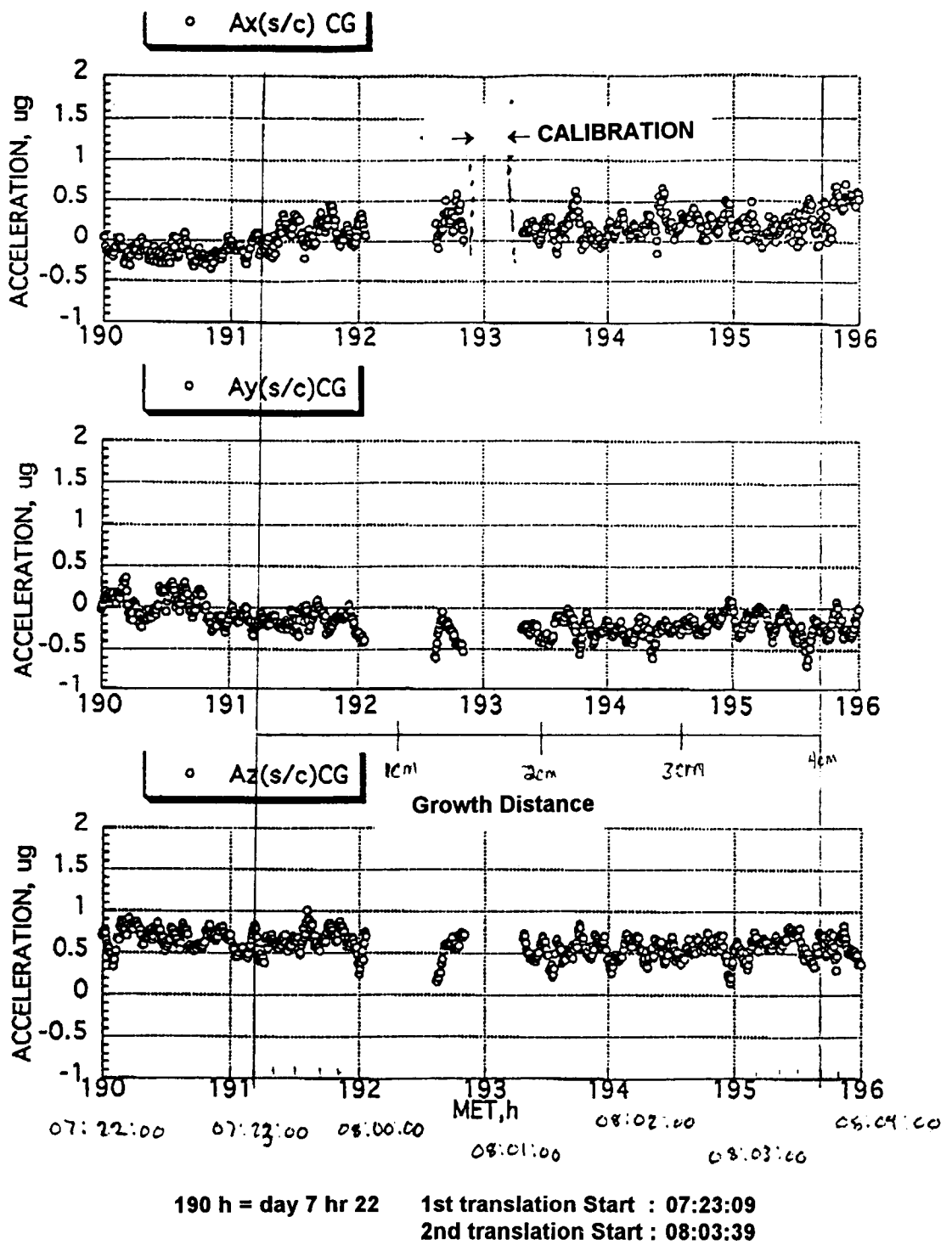


Figure 21 Preliminary acceleration data from the OARE experiment for the first translation period of the first flight sample [22]. Gap in data is due to analysis filtering out of large acceleration deviations.

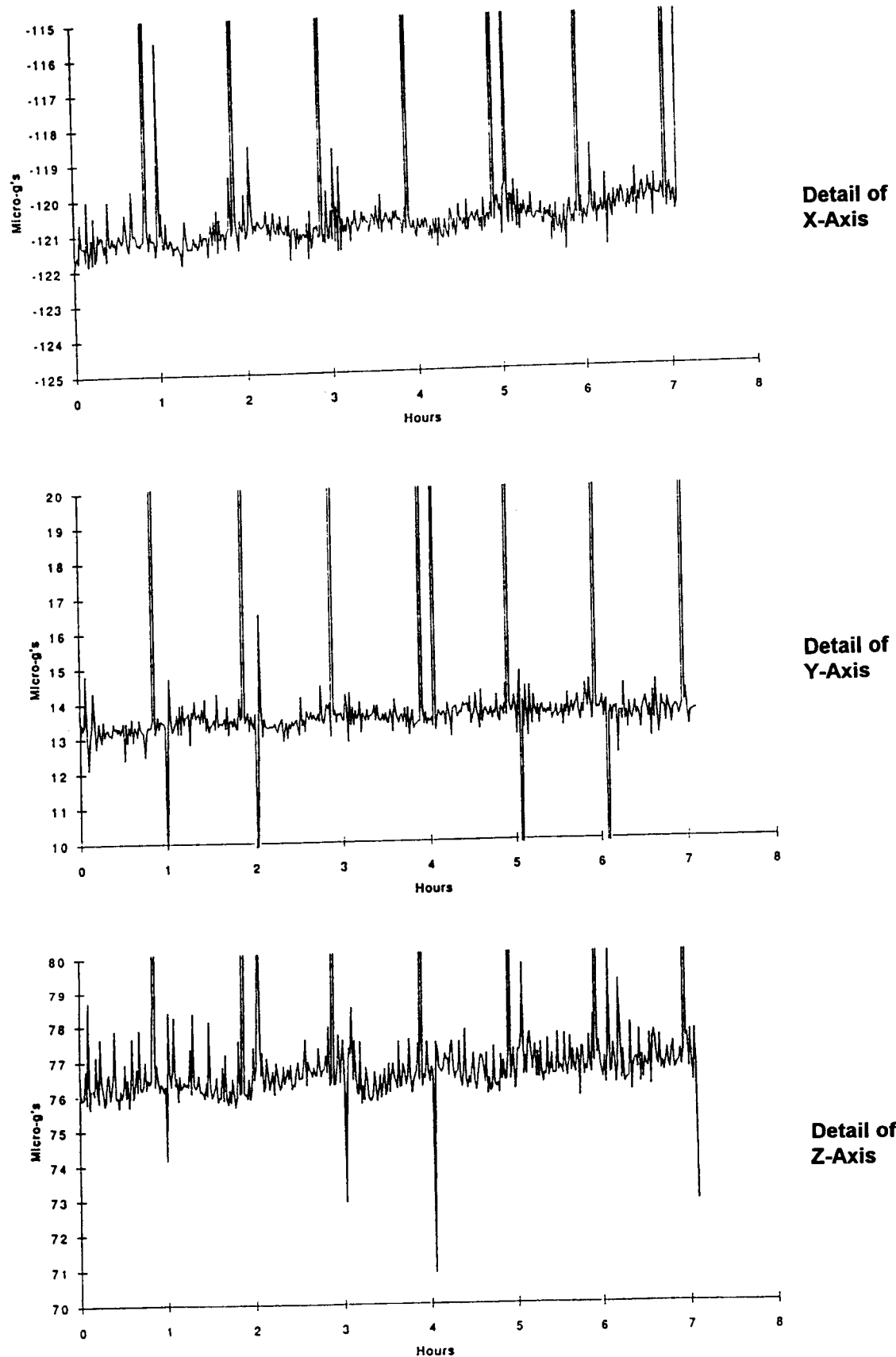


Figure 22 Preliminary acceleration data from the SAMS experiment for the first translation period of the first flight experiment [23]. Note large acceleration peak at the one hour mark.

Discussion

Question: *This smoke plume as you described it, I think, in the second flight sample, can you elaborate or say anything about how that came about ?*

Answer: We are trying to. We have seen it before in a sample when we core the sample. You take a diamond drilling core which is a rather aggressive technique and after we core it, we anneal it, and we have seen in the past that on the slip planes you get precipitates. We are trying to hit one of those with an ogive to find out exactly what it is. Whether it is gallium or whether it is carbon are the two guesses you have and, typically, when we melt back, those don't propagate into the samples. In this case, they did. There was evidence that those precipitates came off on that, indicative of a flow pattern and the dopant distribution measurements also agree that there is a flow pattern. The radial segregation seen is very similar in magnitude to what the ground base was. So to try to alleviate that problem is a problem because we cannot see in the sample externally before we use it. To alleviate that we are working on machining the USML-2 samples with EDM (electro discharge machining).

Question: *Is there any indication of flow in the sample ?*

Answer: I am saying that the plume is indicative of the flow.

Question: *So you do not understand or can't tell us why it (the plume) has that shape ?*

Answer: Right.

Question: *You suggested that an element of a better experiment would be the accurate measurement of the acceleration environment at the experiment. Have you thought, has anybody thought, of going one step beyond that and actually designing an experiment where the acceleration environment is controlled ? Seems like everything is aimed at how good you can do with lesser and lesser micro-g but there seems like there would be value in finding out what small number micro-g's do to you.*

Answer: Well in fact on USML-2, I forgot the name of the engineering test demonstration. On USML-2 there will be an attitude change from wings forward to the CGF attitude. It is intended that in that period they will be growing gallium doped germanium crystals with interface demarcation and that crystal will be analyzed to see what does that attitude change do. So yes we have learned that and yes we are going to do that.

Question: *Could you comment on the dopant distribution of those crystals you grow on ground? Do they fit into a diffusion model and things like that ?*

Answer: They follow complete mixing.

Question: *On the ground ?*

Answer: Yes. With interface curvature we have radial segregation around 30-40%.

Question: *This is with regard to your comment about bubble generation. The most common geometry to grow gallium arsenide is the Czochralski geometry which is inverted which you would think would trap bubbles if they were there. Most bubbles that I have read about in cadmium telluride or gallium arsenide seem to show up when there is an abrupt change of rate. What do you think of that possibility ?*

Answer: We have several, we have a theory of the week on bubbles. One theory presented to me was that when you do that growth rate change we are in a rather low gradient situation. You generate such a large heat of fusion that you boil the liquid and you get an arsenic bubble. In generating that arsenic bubble, you change the heat transfer and if you follow the logic, you sort of get to a step growth rate, where it grows rapidly and stops and then grows rapidly and stops. That is a good explanation for why the bubbles are segmented they look like worms actually. They have body segments. And that sort of agrees with the idea, that you had a start and stop growth rate. We are struggling with a way to come up with a definitive experiment to explain it.

Comment: There has been some work done looking at the trapping of inclusions and bubbles and so forth. I think that a theory has been worked out to determine what the critical velocity should be to trap those. I need to go back and refresh myself on that but I sort of thought that looked familiar.

Answer: Yes. In fact we went back to that particular thesis. Yes, we are aware of that and it is a heat transfer problem. When you get the bubble you have to know your heat transfer coefficients which we don't know. Yes, we are aware of that and we are kind of struggling with what numbers do you plug into the theory. .

Question: *Can you say for a certainty whether or not these bubbles are actually voids or whether or not there is some kind of gas inside the bubbles like hydrogen etc. ?*

Answer: I am sure it is a gas and I am sure it is arsenic.

Question: *How are you sure ?*

Answer: Can I prove that statement ? Your comment was am I sure and yes I am sure. Now if you are asking if I can prove that statement the problem you have at temperature is that you have a volatile component in gallium arsenide and that is arsenic. You look at what else we knew we put in there. We put a vacuum on the ampoule and sealed it up. So you have got the graphite, PbN, gallium, arsenic, and you have got the selenium and that's it. You look at what could create that type of bubble.

Question: *That's at room temperature. Is that correct ?*

Answer: Yes, after a low temperature bake out. We do bake it out to make sure we get rid of water vapor. If it was arsenic gas at temperature, it cools down and condenses, it leads back to Don's question, have we gone along to the inside surface to try to find these few micrograms of arsenic that you would expect, and no we haven't and we haven't because we have doubted that we would find it. But we will eventually look. We will see arsenic for sure. Right. But do we see little plates or chunks of arsenic is the question ?

8 pg

1995107802

N95-14216

324079

59-29

VAPOR TRANSPORT CRYSTAL GROWTH OF
MERCURY-CADMIUM-TELLURIDE IN MICROGRAVITY
(INTERIM REPORT)

7021
P- 8

Heribert Wiedemeier

Department of Chemistry
Rensselaer Polytechnic Institute, Troy, New York

ABSTRACT

Two epitaxial growth experiments of $Hg_{1-x}Cd_xTe$ layers on (100) CdTe substrates in closed ampoules using HgI_2 as a transport agent have been performed during the USML-1 Mission. The characterization results to date demonstrates a considerable improvement of the space-grown epitaxial layers relative to ground-control specimens in terms of morphology, compositional uniformity, and structural micro homogeneity. These results show the effects of microgravity and of fluids dynamic disturbances on ground on the deposition and growth processes. The continued analysis of this technologically important system is designed to further elucidate the observed crystallographic improvements and their relation to mass flow.

INTRODUCTION

Our earlier chemical vapor transport (CVT) experiments of germanium-chalcogenide systems in microgravity environment demonstrated the feasibility of the closed tube vapor transport method for crystal growth in space. The results of the Skylab [1] and Apollo-Soyuz [2] experiments yielded GeSe and GeTe crystals of considerably improved chemical and structural micro homogeneity. The space grown crystals were also larger than ground based specimens. An important observation of these early experiments were quantitative mass transport rates significantly greater than predicted for diffusion limited conditions in microgravity. As a hypothesis, we proposed that these mass flux anomalies were related to thermal effects of homogeneous gas phase reactions in these multi-component-multi reaction CVT systems [2]. The physical vapor transport (PVT) of the GeSe-Xenon system represents a two-component-single-reaction system essentially without any chemical homogeneous gas phase reactions. Vapor transport crystal growth experiments of the GeSe-Xenon system during the STS-7[3] and D-1[4] missions yielded mass transport rates in excellent agreement with theoretical predictions of diffusive flow and with experimental data for vertical, stabilizing conditions on ground. These observations strongly

support the validity of our hypothesis concerning the effects of homogeneous gas phase reactions on mass flow. In addition, the STS-7 and D-1[3,4] experiments yielded GeSe single crystals of considerably improved quality and much larger sizes than observed under ground-based conditions.

A more recent reevaluation of the mass transport properties of the GeSe CTV and PVT systems on ground and in microgravity [5] reconfirmed the above conclusions and observations. In addition, the results of numerical modeling of related transport systems [6,7] are consistent with our experimental observations and theoretical explanations of the earlier transport experiments.

The investigation of the vapor transport and crystal growth properties of the $Hg_{1-x}Cd_xTe$ alloys is based on the above experience with such systems on ground and in microgravity environment. The technologically useful electro-optical properties of $Hg_{1-x}Cd_xTe$ alloys in the 3-5 and 8-14 μm range are based on the formation of continuous series of solid solutions with a nearly linear change in lattice parameters and corresponding changes in the band gap energy of this material. Because of the significant differences in vapor pressure of the constituent elements and binary components of this system, and because of the solid-liquid phase diagram of the $Hg_{1-x}Cd_xTe$ solid solution system, growth of $Hg_{1-x}Cd_xTe$ single crystals presents considerable problems. Growth from the melt is associated with inherent segregation effects. Physical vapor transport requires the use of multiple sources to adjust the vapor pressures. And the employment of CVD and MOCVD techniques requires complex instrumentation which is presently not suitable for space experimentation. Based on our extensive experience in vapor transport properties of metal chalcogenide systems, the concept of chemical vapor transport of $Hg_{1-x}Cd_xTe$ in closed ampoules using a single source material and a transport agent was developed in our laboratory.

I. SCIENTIFIC AND TECHNOLOGICAL BASIS

Our earlier chemical vapor transport and crystal growth studies of the $Hg_{0.8}Cd_{0.2}Te$ system [8] demonstrated that bulk crystals could be grown in closed ampoules using a single source material and HgI_2 as a transport agent. Mass transport rate studies of the $Hg_{1-x}Cd_xTe-HgI_2$ system ($x=0.2$ for the source material) as a function of transport agent pressure and for different orientations of the density gradient relative to the gravity vector were performed [8]. The results showed that the chemical structural microhomogeneity of the crystals are considerably affected by gravity-driven convection. The growth of single crystals of $Hg_{1-x}Cd_xTe$ from the vapor phase appears to be very sensitive to even relatively small fluid dynamic disturbances. A first order thermodynamic analysis of the $Hg_{0.8}Cd_{0.2}Te$ -Iodine transport system for different compositions of the source material [9,10] yielded estimations of the diffusive mass transport rates. The computed and experimental mass transport rates [9,10] are in close agreement. In connection with additional CTV studies of the $Hg_{0.8}Cd_{0.2}Te-HgI_2$ vapor transport system

[11], the transport model developed earlier [9,10] was further tested and extended for different conditions. Experimental results in terms of mass transport rates and compositions of the grown crystals are in close agreement [11]. This confirms the validity of the model applied to the CVT process of this system.

The above observations and results [8-11] provided the basis for the growth of epitaxial layers of $Hg_{1-x}Cd_xTe$ by the closed tube chemical vapor transport technique. Exploratory studies of the epitaxial growth of $Hg_{1-x}Cd_xTe$ demonstrated the feasibility of the chemical vapor transport technique for this purpose [12]. The characterization of the $Hg_{1-x}Cd_xTe$ layers grown on CdTe substrates [13,14] revealed good single crystallinity of the layers and electrical properties comparable to reported data.

More recent detailed investigation under this program of the vacancy concentration and P-T phase diagrams of the $Hg_{0.8}Cd_{0.2}Te$ and $Hg_{0.6}Cd_{0.4}Te$ systems were performed employing dynamic mass-loss measurements [15]. The results of these investigations yielded quantitative Hg partial pressures at the phase boundaries and within the homogeneity region. In addition, the enthalpy of formation of singly-ionized metal vacancies was obtained from these measurements[15]. Analogous investigations of the $Hg_{0.8}Zn_{0.2}Te$ system yielded the corresponding Hg partial pressures and enthalpy of formation of singly-ionized metal vacancies for this system [16]. From a comparison of the $Hg_{0.8}Cd_{0.2}Te$ and $Hg_{0.8}Zn_{0.2}Te$ systems, the influence of Cd and Zn on the bonding in HgTe could be ascertained. Theoretical predictions of the bond strengthening (weakening) effects of alloying HgTe with Zn or Cd are consistent with our observations [15,16]

The above information was used for the further improvement of the crystal growth of $Hg_{1-x}Cd_xTe$ by chemical vapor transport. Employing a combined CVT-seeding technique, bulk crystals of $Hg_{0.8}Cd_{0.2}Te$ of good chemical and structural homogeneity could be grown [17]. Possible origins of the subgrain structure were examined

Continued detailed investigations of the epitaxial growth of $Hg_{1-x}Cd_xTe$ on CdTe substrates [18] revealed the influence of growth temperature, of substrate orientation, and of HgI_2 pressure. Layers of nearly uniform composition and low etch pit densities were obtained. The growth temperature and HgI_2 pressure have significant effects on the layer morphology and composition [18].

Similar investigations of the epitaxial growth of $Hg_{1-x}Cd_xTe$ were performed using different source material compositions, different growth temperatures and HgI_2 pressures [19]. As predicted from the above vapor pressure measurements [15], the source composition has a significant effect on the mass transport and growth rates of the system [19]. From these measurements, suitable experimental parameters for the growth of epitaxial layers of desired composition can be deduced.

The combined results of the above ground-based investigations provide the scientific and technological basis for microgravity experiments of this system. The ground based results can be summarized as follows:

1. Bulk single crystals of $Hg_{0.8}Cd_{0.2}Te$ can be grown by CVT using a single source material in closed ampoules.
2. Convection effects on the chemical and structural microhomogeneity of bulk crystals are established.
3. Epitaxial layers of $Hg_{0.8}Cd_{0.2}Te$ on CdTe substrates have been grown by CVT using a single source and HgI_2 as a transport agent.
4. Convection effects on uniformity and properties of epitaxial layers have been observed.
5. Based on a thermodynamic analysis of the $Hg_{0.8}Cd_{0.2}Te-HgI_2$ system, diffusion controlled mass fluxes and the composition of bulk crystals can be predicted.
6. The above results have been used for the development of crystal growth experiments in microgravity environment.
7. The above results provided the basis for the definition of experimental parameters for the vapor growth of $Hg_{1-x}Cd_xTe$ epitaxial layers on CdTe substrates during the USML-1 Mission.

II. USML-EXPERIMENTS

A. Experimental Conditions and Procedures

The growth ampoule consisted of a fused silica tube of about 15 mm outer diameter and 10 cm length. The source material slug was located at the rounded end of the ampoule and was firmly attached to the ampoule wall. The (100) CdTe substrate was located at the other flat end of the ampoule on a very flat sapphire disc. In order to maintain the substrate in its proper position and to seal the loaded growth ampoule under high vacuum, a double-ampoule configuration was employed for these experiments. The loaded and sealed ampoule was inserted into a metal cartridge and instrumented with five K-type thermocouples to monitor the temperature of the source, and in between at all times.

The ampoule-cartridge assembly was inserted in the crystal growth furnace (CGF) where the heat-up, crystal growth and cool-down occurred according to time-lines developed during the ground-based studies and GCEL test experiments. The proper positions of the thermocouples and the physical integrity of the entire cartridge-ampoule assembly were confirmed by X-ray diffraction photography before and after the flight experiments.

The growth conditions of the flight experiments are as follows:

Flight Experiment RPI-1:

Source Material:	$Hg_{0.4}Cd_{0.6}Te$
HgI_2 Pressure	~0.01 atm
Growth Time:	8.1 hours
Nominal Growth Temperature:	545°C
Nominal Source Temperature:	593°C

Flight Experiment RPI-2:

Source Material:	$Hg_{0.4}Cd_{0.6}Te$
HgI_2 Pressure:	~0.01 atm
Total Growth Time:	6.4 hours
Nominal Growth Temperature:	545°C
Nominal Source Temperature:	593°C

B. Results and Discussion

The results to date of our two USML-1 experiments are based on optical and scanning electron microscopy, on IR spectroscopy, on electron microprobe (WDS) analysis, on X-ray diffraction Laue and rocking curve measurements, and on Synchrotron investigations.

The present results are summarized below.

B1 Surface Morphology of Epitaxial Layers

A microscopic comparison of the epitaxial layers obtained under ground-control conditions and in microgravity demonstrates an unexpected degree of improvement in surface morphology of the space-grown crystals. The surfaces of the ground-control epitaxial layers have a "wavy" type step-terrace structure. The step heights are in the order of several microns and the widths vary from 20 to about 200 μm . Even the flattest regions of the epitaxial layer obtained during the flight simulation test on ground show uneven and irregular growth steps. At the same magnifications (100-500 X) the epitaxial layers grown in space appear mirror-smooth, i.e., the growth steps cannot be resolved. These differences in surface morphology remain even at much higher magnifications under SEM conditions.

B2 Compositional Homogeneity of Epitaxial layers

Employing infra-red spectroscopy techniques, the overall chemical compositions of the space-grown epitaxial layers are consistent with those of the ground test samples. These observations indicate

that any fluid dynamic disturbances on ground are not very large. However, a detailed investigation of the spatial composition distribution (map) reveals considerable differences in uniformity between the ground and space-grown layers. For the entire layers, the compositional differences between local regions are about two to three times smaller for the space than for the ground-control samples. These differences indicate the effects of fluid dynamic disturbances on the deposition and growth processes on ground.

The results of several compositional depth profiles of the (011) cross section of epitaxial layers based on electron microprobe (WDS) analysis show a high degree of composition uniformity of the space-grown layers. In terms of absolute composition, the WDS results are consistent with those of the IR measurements performed in our laboratory.

B3 Structural Homogeneity of Epitaxial Layers

The crystallographic identity of the epitaxial layers grown on ground and in space was determined by X-ray diffraction Laue patterns. The epitaxial layers have a (100) orientation showing a substrate parallel layer growth as expected.

A considerable difference between the crystallographic perfection and uniformity of the space and ground-grown layers was observed based on X-ray diffraction rocking curves. The values of the full-width-half-maximum (FWHM) for the native surfaces of the space-grown layers range from 90-120 arc seconds. Those of the ground-based sample range from about 200-240 arc seconds. The FWHM-values observed for our space-grown layers are equal to or smaller than the best value reported for $Hg_{1-x}Cd_xTe$ epitaxial layers grown by MOCVD techniques on ground. Typical FWHM-values reported in the literature for $Hg_{1-x}Cd_xTe$ are in the order of several hundred arc seconds. In view of the chemical and structural complexity of this growth system, these observations represent a significant crystallographic improvement of the space-grown epitaxial layers relative to those obtained on ground.

B4 Synchrotron Measurements

The results of Synchrotron measurements of the space and ground-grown epitaxial layers reveal a cellular type morphology for both. This kind of structure has been observed for other II-VI and III-V compound crystals. The origin of the cellular structure is not understood at this time for this and other materials. However, it is important to recognize that the material must have a very high degree of crystallographic perfection in order to observe the cellular structure by Synchrotron measurements. This requirement is consistent with the above results of the X-ray diffraction rocking curves which yielded relatively small FWHM-values for the space-grown epitaxial layers. Also consistent with the rocking

curve results are the Synchrotron observations of a much larger area of uniform crystallinity of the space grown epitaxial layer compared to the ground sample,

Because of the basic scientific and technological importance of these particular observations, it is highly desirable to continue the Synchrotron measurements on the flight and ground-based epitaxial layers of this material.

III. CONTINUED ANALYSIS AND CHARACTERIZATION OF THE USML-1 Experiments

For several of the above discussed, non-destructive characterization procedures (IR mapping, X-ray diffraction rocking curves, Synchrotron measurements) the facilities employed are not under our control. Therefore, additional analyses of the flight and ground-based samples, involving partly destructive techniques, had to be delayed. These measurements, including cross-section analysis, electrical measurements, and chemical etching, are in progress.

As indicated above, in view of the rather interesting structural investigation and results, it is very desirable to perform additional studies with the objective to further elucidate the origin of the cellular structure.

IV. PRELIMINARY SUMMARY AND CONCLUSIONS

Epitaxial growth experiments of $Hg_{1-x}Cd_xTe$ layers on (100) CdTe substrates by chemical vapor transport in closed ampoules using HgI_2 as a transport agent were performed during the USML-1 Mission in microgravity environment. The results to date demonstrate considerable improvements of the flight samples in terms of surface morphology, chemical microhomogeneity and the degree of crystallographic perfection and uniformity relative to ground-based samples. These improvements are consistent with our earlier predictions concerning the sensitivity of the $Hg_{1-x}Cd_xTe-HgI_2$ vapor transport system to even minute fluid dynamic disturbances on ground. The combined results to date justify the conclusion that these experiments were successful.

Continued analysis and characterization efforts are designed to further investigate the effects of microgravity on the epitaxial growth of this system. Ongoing detailed investigations of the substrate-layer interface revealed new information concerning the effects of microgravity during the initial periods of epitaxial growth. The further elucidation of these phenomena is of basic scientific value and of technological significance. These are important objectives of our experiments proposed for the USML-2 Mission.

REFERENCES

1. H. Wiedemeier, F.C. Klaessig, E.A. Irene and S.J. Wey, *J. Crystal Growth*, **31**, 36 (1975).
2. H. Wiedemeier, H. Sadeek, F.C. Klaessig, M. Norek and R. Santandrea, *J. Electrochem. Soc.* **124**, 1095 (1977).
3. H. Wiedemeier, S.B. Trivedi, X.R. Zhong and R.C. Whiteside, *J. Electrochem. Soc.*, **133** 1015 (1986).
4. H. Wiedemeier and S.B. Trivedi, *Naturwissenschaften* **73**, 376 (1986).
5. W. Palosz and H. Wiedemeier, *J. Crystal growth* **89**, 242 (1988).
6. B. Zappoli and D. Bailly, *Phys. Fluids A* **2**(10), 1771, 1990.
7. B. Zappoli, *Phys. Fluids A* **3**(4), 578 (1991).
8. H. Wiedemeier and D. Chandra, *Z. anorg. allg. Chem.* **488**, 137 (1982).
9. D. Chandra and H. Wiedemeier, *Z. anorg. allg. Chem.* **545**, (1986).
10. H. Wiedemeier and D. Chandra, *Z. anorg. allg. Chem.* **545**, 109, (1987).
11. H. Wiedemeier and W. Palosz, *J. Crystal growth* **96**, 933 (1989).
12. H. Wiedemeier and A.E. Uzpurvis, *J. Electrochem. Soc.* **130**, 252 (1983).
13. H. Wiedemeier and A.E. Uzpurvis, and D. Wang, *J. Crystal growth* **65**, 474, (1983).
14. H. Wiedemeier and A.E. Uzpurvis, *Z. anorg. allg. Chem.* **510**, 199 (1984).
15. H. Wiedemeier and Y.G. Sha, *J. Electron. Mater.* **19**, 761 (1990).
16. Y.G. Sha and H. Wiedemeier, *J. Electron. Mater.* **19**, 1303 (1990).
17. H. Wiedemeier and G.H. Wu, *J. Electron.* **20**, 891 (1991).
18. H. Wiedemeier and Y.G. Sha, *J. Electron. Mater.* **21**, 563 (1992).
19. Y.G. Sha and H. Wiedemeier, *J. Electron. Mater.* **21**, 613 (1992).

30 Pg

199707803
324081

N95-14217

IV/1/11

SURFACE TENSION DRIVEN CONVECTION EXPERIMENT (STDCE)

S. Ostrach* and Y. Kamotani* and A. Pline⁺

*Department of Mechanical and Aerospace Engineering,
Case Western Reserve University, Cleveland, Ohio.
⁺NASA Lewis Research Center, Cleveland, Ohio.

5/029

17022

P-30

ABSTRACT

Results are reported of the Surface Tension Driven Convection Experiment (STDCE) aboard the USML-1 Spacelab which was launched on June 25, 1992. In the experiment 10 cSt silicone oil was placed in an open circular container which was 10 cm wide by 5 cm deep. The fluid was heated either by a cylindrical heater (1.11 cm dia.) located along the container centerline or by a CO₂ laser beam to induce thermocapillary flow. The flow field was studied by flow visualization. Several thermistor probes were placed in the fluid to measure the temperature distribution. The temperature distribution along the liquid free surface was measured by an infrared imager. Tests were conducted over a range of heating powers, laser beam diameters, and free surface shapes. In conjunction with the experiments an extensive numerical modeling of the flow was conducted. In this paper some results of the velocity and temperature measurements with flat and curved free surfaces are presented and they are shown to agree well with the numerical predictions.

INTRODUCTION

Surface tension variations along a liquid free surface caused by non-uniform temperature distributions induce so-called thermocapillary flows in the bulk liquid. In a terrestrial environment such flows are usually overshadowed by buoyancy-driven flows, except in configurations of small dimension (less than several mm). In the reduced gravity environment of space, however, buoyancy is greatly reduced and thermocapillarity becomes an important driving force for fluid motion (Ostrach, 1982). In such applications as crystal growth from melts, two-phase flows with heat transfer, and thermocapillary migration of bubbles and droplets, thermocapillary flow is known to play an important role. For that reason much attention has been given in recent years to thermocapillary flow analysis. Much of past work was done numerically. Since thermocapillary flow experiments in one-g must be conducted in very small systems to minimize buoyancy effects, they can cover only limited ranges of parameters.

Therefore, it is necessary to perform experiments in microgravity over a wide range of conditions to investigate and describe thermocapillary flows fully and to validate numerical analyses.

It is also known that thermocapillary flows become oscillatory under certain conditions but its cause is not yet completely understood. The least understood part is the role free surface deformability plays in the oscillation mechanism. Based on our past ground-based experimental work we suggested a physical model which emphasized the importance of deformable free surface and proposed a surface deformation parameter to represent its role in the oscillation mechanism (Kamotani et al., 1984). On the other hand, some investigators consider the oscillation phenomenon to be the result of instability that could occur even with an undefinable free surface (reviewed in Davis, 1987). According to the latter concept, only one dimensionless parameter, called Marangoni number (Ma), specifies the critical condition for the onset of oscillations. Therefore, we sought to obtain further evidence to determine the importance of free-surface deformation by conducting experiments in space over a wide range of conditions.

For those reasons we conceived a series of experiments to study thermocapillary flows in microgravity. The first experiment, called the Surface Tension Driven Convection Experiment (STDCE), was conducted on the first U.S. Microgravity Laboratory Mission (USML-1) on the Space Shuttle Columbia (STS-50) which was launched on June 25, 1992. The main objectives of the STDCE were to study the velocity and temperature fields in detail in non-oscillatory thermocapillary flows and to determine if Ma alone can specify the onset of oscillations. In a second series of experiments (STDCE-2), which is scheduled to be conducted aboard USML-2 in 1995, we will focus on the oscillation phenomenon including the measurement of free surface deformation.

In order to complement the space experiments, as well as to help design them, an extensive numerical analysis of thermocapillary flow was conducted for both flat and curved free surfaces and under steady and transient (non-oscillatory) conditions. In this paper some results of the velocity and temperature measurements with flat free surfaces are presented and compared with the numerical results. It was also found that despite the fact that Ma in the STDCE was as large as 5 times that of the critical Ma determined in one-g tests, no oscillations occurred.

I. DESCRIPTION OF STDCE

The specific objectives of the STDCE were to determine the extent and nature of thermocapillary flows, the effect of heating mode and level, the effect of the liquid free-surface shape, and the onset conditions for oscillatory flows. The detailed requirements of the experiment are given by Ostrach and Kamotani (1987). Its design and important considerations behind it are discussed by Kamotani and Ostrach (1987). The development of the STDCE flight hardware is described by Pline et al. (1990).

A. Experimental System

The basic experimental configurations are illustrated in Figs. 1 and 2. 10 cSt silicone oil was used as the test fluid in a circular container, 10 cm in diameter and 5 cm in depth. The container side was made of 5 mm thick copper with copper tubing coiled around the outside of the side wall for cooling water circulation. The top rim of the side wall had a sharp edge to pin the fluid. The bottom wall was made of plexiglass of uneven thickness (average thickness 8 mm) because of a filling hole and the attachment of lens assembly for flow visualization through the bottom wall. In order to minimize the contamination of the test fluid the container inner surface was kept clean and dry until the experiment and the fluid and the air above it were both contained within the fluid loop. Two heating modes were employed: CO₂ laser heating (called the Constant Flux Experiment (CF)) and heating by a cylindrical heater placed along the container centerline (called the Constant Temperature Experiment (CT)). The diameter of the submerged heater was set at 1.11 cm but the laser beam diameter was variable. The laser power was adjustable from 0.2 to 3 watts and the submerged heater power from 1 to 20 watts. The mean absorption length of CO₂ laser (10.6 μm wavelength) by the test fluid was measured to be 0.060 mm (Pline et al., 1990), so the laser beam was absorbed within a relatively very short distance from the free surface. The emissivity of the fluid surface was determined to be 0.9 (Pline et al., 1990). The free surface shape was varied by adjusting the total volume of fluid in the container. Fig. 2 shows flat and curved surfaces for the baseline tests but in the actual experiment additional tests with other curved surfaces, including a convex shape in the CF configuration, were conducted. Fig. 3 shows those surface shapes. Each shape was set within 1 mm of the prescribed location. The temperature field in the bulk fluid was studied by thermistors. Nine probes were used to measure temperature at various locations in the fluid and in the container walls. Their positions are shown in Fig. 4. The top of the thermistor No. 1 touched the free surface. In addition, one probe measured the ambient temperature above the fluid free surface and thermistors monitored the submerged heater shell temperature. The three probes along the container centerline were removed during the CT tests. The diameter of the thermistors in the fluid was 0.5 mm. The temperature data were taken once every 100 milliseconds during tests, digitized, and stored. They were downlinked during certain times to the ground station where we monitored the experiment. The resolution of the digital data was 0.1 °C and the accuracy of thermistor sensors was 0.1 °C.

To obtain information on the temperature distribution along the free surface, which is important because it is directly related to the driving thermocapillary force, a thermographic technique was employed. The infrared imaging system used in the STDCE is described by Pline and Butcher (1990). The operating wavelength was 8-14 μm and the mean absorption length of the fluid in that range was

measured to be 0.012 mm. As will be discussed later, the thermal boundary layer thickness along the free surface can become comparable to the above absorption length in certain relatively small areas but along most of the free surface the boundary layer is much thicker than the absorption length, so the infrared data represents the surface temperature well. The minimum detectable temperature difference was 0.1°C and the spatial resolution was 1 mm. Its feasibility and accuracy were checked in the ground-based experiment (Pline, 1988). This technique was also found to be very useful in studying the oscillation phenomenon (Kamotani et al., 1992).

The flow field was studied by flow visualization. Fifty micron alumina particles were used as tracers. They were illuminated by a 1 mm thick laser light sheet to study the flow in one cross-sectional plane of the container. Since the container side wall was made of copper to obtain a uniform wall temperature, a CCD camera was attached to the transparent bottom wall (see Fig. 1) for recording. Because of the bottom viewing the video image of the illuminated cross-section was distorted (keystone effect). The video record of the flow is being analyzed using a particle image velocimetry (PIV) technique. The technique is explained by Wernet and Pline (1991). The keystone effect is corrected in the analysis.

The hardware for the STDCE is discussed in more detail by Pline, et al. (1993).

B. Parametric Ranges

The important dimensionless parameters for the present experiment in the case of flat free surface are: Ma (Marangoni number) = $\sigma_T \Delta T H / \mu \alpha$, Pr (Prandtl number) = ν / α , Ar (aspect ratio) = H/R , Hr (relative heater size) = D_H / D , where σ_T is the temperature coefficient of surface tension, ΔT the net temperature variation along free surface, H the fluid depth, D the container diameter, R the radius, D_H the heating zone diameter, ν the kinematic viscosity of the fluid, μ the dynamic viscosity, and α the thermal diffusivity. In the CT configuration ΔT is the temperature difference between the heater and the side wall. Since total heat input is specified in the CF tests, the ΔT is not known a priori. However, because the thermocapillary flow driving force is closely related to ΔT and to make comparisons between the CT and CF tests convenient, a Ma based on ΔT is used in both cases in the present paper, ΔT being determined from the numerical analysis for the CF tests.

In one-g heat loss occurs at the free surface mainly through natural convection in the surrounding air but in microgravity radiation loss to the enclosure wall becomes important. Since the temperature difference between the free surface and the surroundings is relatively small compared to their absolute temperatures, the radiation loss can be represented by Ra (radiation parameter) = $\epsilon \sigma T_a^3 H / k$, where ϵ is the emissivity of the fluid free surface, σ the Stefan-Bolzmann constant, T_a the temperature of the surroundings, and k the thermal conductivity of the fluid.

The range of each parameter covered in the STDCE was as follows: $3.6 \times 10^4 \leq Ma \leq 3.1 \times 10^5$, $78 \leq Pr \leq 97$, $Ar = 1.0$, $Hr = 0.11$ for CT and 0.05, 0.1, and 0.3 for CF, and $Ra = 0.5$. The physical properties are evaluated at the mean fluid temperature in the container. The range of Pr reflects the fact that the fluid viscosity varies with temperature. In our ground-based tests in the CT configuration using a small container (4 mm dia.), the critical Ma for the onset of oscillations was found to be 6.5×10^4 (Kamotani et al., 1992), so the maximum value of Ma in the STDCE was about 5 times of that. As discussed in the Introduction, we found that the deformability of the free surface is important in the oscillation mechanism and proposed the surface deformation parameter S , which is defined as $S = \sigma_T \Delta T / (\sigma(1/Pr))$, to represent it, when Pr is larger than unity (Kamotani et al., 1984). The critical value of S determined in our one-g tests was 9×10^{-3} for $Ar = 1$ (Kamotani et al., 1992) but in the STDCE the maximum value of S was 2.5×10^{-3} , so based on our concept the flow in the STDCE should not oscillate.

II. NUMERICAL ANALYSIS

The program for flat free surface is based on the SIMPLER algorithm by Patankar (1980). The flow is assumed to be laminar, incompressible, and axisymmetric. The fluid properties are considered to be constant except for viscosity which varies with temperature. The program analyzes both transient and steady states. It turns out that all the temperature data taken in the STDCE were in transient state although we had planned to obtain some steady state data.

In the CT configuration the measured temperatures of heater and side wall are used as inputs. Both temperatures changed with time during the tests. In the CF case the measured values of laser power and side wall temperature, and the beam diameter are the inputs. The emissivity and the absorption length are also taken into account. The coordinate system used in the analysis is defined in Fig. 4. The velocity components (u, v) and stream function ψ are made dimensionless by $\sigma_T \Delta T / \mu$ and $\sigma_T \Delta T R H / \mu$, respectively. The temperature T is non-dimensionalized as $\theta = (T - T_c) / \Delta T$, where T_c is the side wall temperature.

A non-uniform grid system is adopted with meshes graded toward the hot and cold walls and toward the free surface. In the CT cases due to the presence of a thin thermal boundary layer along the heater surface the free surface temperature varies very sharply near the heater. As a result the free surface velocity increases very sharply in that region and an accurate resolution of the surface velocity distribution near the heater is the most important requirement for the numerical grid. In Fig. 5a the surface velocity distributions computed with three different grids are shown. The computed case corresponds to the main CT test and is discussed in detail below. The 46×41 (radial x vertical) grid with the smallest radial mesh size of 0.001 next to the heater is not adequate. The 58×51 and 67×60 grids

with the smallest mesh sizes of 0.0005 and 0.0003, respectively give nearly the same distribution. With all three grids the maximum stream function and the total heat transfer rate are all within 1% of each other. Therefore the 58×51 grid is used both for the steady and transient CT computations. In the CF configuration there exists a very thin thermal boundary layer along the free surface in the region heated by the laser beam, so an accurate prediction of the surface temperature distribution near the heated region becomes important. In Fig. 5b the surface temperature distributions computed with three different grids, 37×40 , 46×51 , and 58×60 with the smallest axial mesh sizes next to the free surface of 0.005, 0.001, and 0.0005, respectively are shown for the main CF test. Based on Fig. 5b the 46×51 grid is used for the CF transient and steady analysis.

The program for curved free surfaces is explained in Kamotani and Platt (1992). The computational domain with curved free surfaces is transformed into a rectangular domain by a coordinate transformation and the velocity and temperature fields are solved by a finite-difference scheme.

III. RESULTS AND DISCUSSION

In the STDCE a total of 20 CF and 18 CT tests were conducted with flat and curved free surfaces but many of them were run only for 10 minutes to study if the flow became oscillatory. It had been estimated that it takes about one hour after the flow is started to obtain hydrodynamic as well as thermal equilibrium. Considering that relatively long transient period we had decided to conduct only one CF and one CT 1-hour test with flat free surfaces to study the complete transient flow and thermal development. Those two tests are discussed first.

A. CT One-hour Test

Before the test we made sure that the free surface was flat and no appreciable motion existed in the fluid through video downlink. Fig. 6 shows how the heater and side wall temperature varied during the one-hour period after the heating started. The power to the heater was boosted for the first 90 seconds to shorten the warm-up time of the heater. Judging from the heater temperature overshoot in Fig. 6 the power boost was slightly too large. After the boost period the heater power was fixed but the heater temperature increased gradually throughout the one-hour period. The side wall temperature variation was relatively small, about 0.6°C increase after one hour. The readings of the two thermistors in the side wall were the same within the resolution of the data acquisition system (0.1°C). As for the 6 thermistors in the heater shell 4 of them, which are positioned in the top 2/3 of the heater length, read within 0.2°C of each other (the data in Fig. 6 is the average of those) but 2 thermistors near the heater bottom read about 0.5°C below the above average probably due to the end loss. The solid lines in Fig.

6 are the inputs to the numerical analysis.

Fig. 7 shows the computed streamlines and isotherms at t (time) = 2 min. The streamline pattern shows that the whole fluid is already in motion at this time. The observed streamline pattern at the same time is shown in Fig. 8, which was obtained by superposing several video frames of the flow. The observed pattern agrees well with the computed one in Fig. 7 in terms of the overall flow structure (unicellular motion) and the location of the cell center. The overall flow pattern changes little beyond this time. In comparison, in one-g the flow in this large system is confined to a thin region near the surface because of stratification. The isotherms in Fig. 7 suggest that over most of the flow field the temperature is basically equal to the initial temperature. The liquid initial temperature was about 0.5 °C below the side wall temperature.

The development of temperature field with time is shown in Fig. 9 based on the numerical analysis. One can see that heat is transferred from the heater by convection first along the free surface and then into the interior region. The steady state profile in Fig. 9 is computed based on the thermal boundary conditions at $t = 60$ min., which shows that the temperature field at $t = 60$ min. (Fig. 9c) is not yet steady. One reason why it did not become steady by $t = 60$ min. (we had estimated the transient period to be about 60 min.) was because the heater temperature kept increasing as seen in Fig. 6. Fig. 9 also shows the presence of a thin thermal boundary layer along the heater. In the CT tests thermistors No. 1 - No. 3 (Fig. 4) measured the fluid temperature. The outputs from those probes are compared with the numerically predicted values in Fig. 10 and good agreement is shown. For some reason the No. 3 probe output seemed to be too high because, although it was placed below the No. 2 probe (Fig. 4), its reading was always above that of No. 2, which does not seem to be correct (see the isotherms in Fig. 9). In any case the difference between the No. 3 probe reading and the numerical prediction is at most 0.4 °C, which is only 3% of ΔT . As shown in Fig. 10b, relative to the overall temperature variation in the liquid agreement between the analysis and data can be said to be excellent (for clarity only Nos. 1 and 2 readings are shown in Fig. 10b). As mentioned above, the fluid temperature was still increasing after the one-hour period.

The infrared imager did not require in situ calibration but for a reason not yet fully understood its readings seemed to have shifted judging from a comparison of its measurement of the fluid initial temperature with that measured by the thermistors. It was calibrated before and after the flight but no drifting was found. For that reason instead of determining the absolute temperature of the free surface we computed the surface temperature increase above the initial temperature. Fig. 11 shows the relative surface temperature distributions at $t = 10$ and 60 min. The data and numerical prediction agree very well. As seen in Fig. 11 the surface temperature drops sharply near the heater and, as a result, the surface velocity increases very sharply and attains its peak near the heater as Fig. 5a shows. By

comparing the profiles at $t = 10$ and 60 min., one sees that the overall profile does not change much with time, only it shifts as the fluid warms up, which explains why the velocity field does not change much with time, the driving force being dependent on the slope of the profile.

The total heat transfer at the heater is calculated to be 1.18 W while the total power input to the heater was measured to be 1.2 W, so about 2% of the input is lost by conduction through the base of the heater. Of 1.18 W of the net heat input to the fluid 14% is lost by radiation from the free surface according to the numerical analysis. The ratio of the net heat input to the total heat out from the fluid (radiation loss plus conduction at the cold wall) is computed to be 1.19 at $t = 60$ min., showing again that the temperature field was not in equilibrium at that time.

The velocity vectors determined from the particle motions at $t = 10$ min. are presented in Fig. 12. The velocity is relatively large in the region near the top half of the heater. Although there is a very strong flow along the free surface close to the heater (see Fig. 5a), the present flow visualization did not detect it because the tracer particles did not go into that small corner region.

The measured velocity distributions are compared with the computed ones in Fig. 13. The axial velocity distribution at $Z/H = 0.89$ (Fig. 13a) and the radial velocity distribution at $r/R = 0.23$ (Fig. 13b) are shown. Those locations cover the region of large velocity in Fig. 12. At present the velocity field analysis is not yet complete and the data presented herein are still preliminary. Fig. 13 shows two sets of data, one from the right cross-section in Fig. 12 and the other from the left. In Fig. 13a the data and the prediction differ as much as 40% but the predicted general trend agrees with the data. We have to analyze much more data before we can make a definite statement about the comparison. The agreement in Fig. 13b is better except near the free surface where, as discussed above, the measurement did not show a large velocity region close to the surface.

B. CF One-hour Test

The thermal conditions for the CF test are shown in Fig. 14. The laser beam power remained constant at 0.48 W throughout. The beam diameter was 1.0 cm. However, the side wall temperature kept increasing and changed by 1.5 °C (15% of ΔT) after one hour. Since in the above CT test the side wall temperature did not change that much despite the fact that the heat input to the fluid was greater, the side wall temperature increase in the CF test was not because of the heat input from the laser beam. Considering the fact that the air temperature above the fluid also increased by the same rate as Fig. 14 shows, the increase is considered to be due to the ambient temperature increase due probably to an increase in thermal loading of the Shuttle avionics air system. In all other tests the side wall temperature remained at about 25 °C. The solid lines in Fig. 14 are the inputs to the numerical analysis. The air temperature is assumed to represent the surrounding wall temperature in the calculation of the radiation

loss from the free surface.

Fig. 15 shows the computed and measured streamlines at $t = 2$ min. They agree well. The flow structure is unicellular as in the CT configuration.

The computed isotherm patterns at various times are presented in Fig. 16. The steady state pattern is based on the thermal conditions at $t = 60$ min. The initial liquid temperature was about 0.6°C below the side wall temperature. At $t = 10$ min., heat was spread only along the free surface and most of the fluid temperature remained unheated. Even at $t = 30$ min., a large portion of the fluid had a temperature below the side wall but convection was beginning to heat up the interior. At $t = 60$ min., most of the fluid had a temperature just above the side wall temperature but the temperature distribution was not yet close to the steady profile. The main reason why the fluid temperature remained low compared to the side wall for that long time was the continuous increase of the latter temperature as discussed above. Also compared to the CT case the total heating area was smaller in the CF test, so the bulk temperature remained relatively low in the latter case.

Fig. 17a shows the computed maximum fluid temperature and comparison between the Nos. 1 and 2 thermistor readings and the numerical prediction. The maximum temperature kept increasing partly because of the side wall temperature increase and partly because the temperature field was not in equilibrium. The figure shows good agreement between the data and the prediction. In Fig. 17b the temperature scale is expanded to show three thermistor readings. As discussed in the CT case, the reading of No. 3 thermistor seemed to be slightly too high (nearly close to the reading of the probe at the free surface) but the difference between the data and the prediction is about 0.4°C which is only 4.5% of ΔT . In the CF test the three thermistors along the container centerline gave additional data and their readings are given in Fig. 17c along with the numerical prediction. Their readings are all close and the predicted temperature variations follow the data closely. According to the isotherms in Fig. 16 the thermal boundary layer thickness along the free surface is less than 1.5 mm near the center, so the No. 5 thermistor, which was located at 2 mm from the surface, was just outside the boundary layer.

The infrared imager data are compared with the predicted relative surface temperature distributions at $t = 10$ and 60 min. in Fig. 18. They agree well but near the heated region the imager data was lower than the prediction because of the presence of a very thin thermal boundary layer there. Because of the thin boundary layer practically there is no accurate way to measure the surface temperature near the middle. The data at $r/R = 0.5$ agrees with the No. 1 thermistor data.

As for the overall thermal balance based on the numerical analysis, 14% of the total heat input to the fluid is lost by radiation from the free surface at $t = 60$ min. The ratio of the total heat input to the total heat out from the fluid is 3.4 at $t = 60$ min. so that the temperature field is still very far away from equilibrium even after one hour. The overall ΔT is 10°C when a steady state is reached as seen in Fig.

5b but ΔT at $t = 60$ min., is still about 9°C according to Fig. 17a.

The velocity vectors at $t = 10$ min., are given in Fig. 19 and Fig. 20 shows the measured and computed velocity distributions at selected locations. The agreement between them is better than that in the CT configuration (Fig. 13) and in this particular instance a few particles gave large velocities near the surface.

By comparing the results of the CT and CF tests presented above one can say that although the flow structures are similar (simple unicellular structure), the temperature fields are different: In the CT case the overall fluid temperature is higher and there exists a very noticeable thermal boundary layer all along the heater surface while in the CF case a thermal boundary layer exists along the free surface mainly in the heated region. In both cases the free surface temperature drops sharply in a relatively small region near the center (the so-called hot-corner region) and the flow is driven mainly in the hot-corner region. Although no oscillations were found in the present experiment, our ground-based tests have shown that the oscillation phenomenon is very much influenced by the heating mode.

C. Curved Free Surface Tests

The analysis of the data from the curved free surface tests has just begun, so not much data can be presented herein. An example of streamline pattern with a curved free surface is presented in Fig. 21 and it is compared with the numerical result. The predicted flow pattern agrees well with the data. The flow structure is still unicellular. One major objective herein is to study how the free surface shape affects the flow structure. One aspect studied so far is given in Fig. 22, where the location of the cell center is shown for various surface shapes. The predicted locations are in general agreement with the measured ones. When the free surface is flat or convex, the cell center is located around mid-radius. When the surface is concavely curved, the flow along the free surface turns around sooner because the flow passage toward the top cold wall region narrows and consequently the cell center moves toward the centerline. However, when the surface is highly concave, the fluid height near the center becomes small and consequently the fluid speed decreases rapidly when the fluid moves away from the center because of increasing flow area. Therefore, the main motion is seen only near the center, which produces one cell. The fluid speed is quite small away from the center but since the fluid volume involved in the weak motion is very large, a second cell is produced in the region (Fig. 22). The fluid rotation direction is the same in both cells. A more detailed flow analysis is in progress.

CONCLUDING REMARKS

Some of the velocity and temperature data taken in the STDCE experiment conducted aboard the USML-1 Spacelab in 1992 are presented. The results for one-hour CT (Constant Temperature) test

and also for one-hour CF (Constant Flux) test and some preliminary results for curved surface tests are given and compared with the results of the numerical analysis conducted in conjunction with the experiment. The tests covered a range of Ma up to 3.1×10^5 . Aside from some problems discussed above, the hardware performed well generally and a large amount of valuable data were collected. Much of the data are still being analyzed. The temperature data shown in the present paper agree well with the numerical predictions. A validation of a numerical analysis for thermocapillary flow in such a high Marangoni range has not been done in the past. A total of 20 CF and 18 CT tests were conducted with flat and curved free surfaces under varieties of conditions. No oscillations or instabilities were observed in any of the tests. G-jitter caused by thruster firings induced small but visible free surface disturbances but did not change the flow field appreciably.

ACKNOWLEDGMENTS

The authors wish to express their appreciation to many people, especially the NASA Lewis Research Center engineering and operations teams, who contributed to make the STDCE a successful and important experiment. Special thanks to Dr. Eugene Trinh who, as a payload specialist aboard the USML-1, conducted the STDCE tests tirelessly and expertly for many hours. We also gratefully acknowledge the financial support of NASA for this experiment. The work done at Case Western Reserve University was supported by NASA under contract NAS3-25973 with Mr. T. P. Jacobson of the NASA Lewis Research Center as the Project Manager and Dr. R. Thompson as the Project Scientist.

REFERENCES

1. Davis, S. H., 1987, *Thermocapillary Instabilities*, Annual Review of Fluid Mechanics, Vol. 19, pp. 403-435.
2. Kamotani Y., Ostrach, S., and Vargas, M., 1984, *Oscillatory Thermocapillary Convection in a Simulated Floating-Zone Configuration*, Journal of Crystal Growth, Vol. 66, pp. 83-90.
3. Kamotani, Y. and Ostrach, S., 1987, *Design of a Thermocapillary Flow Experiment in Reduced Gravity*, Journal of Thermophysics and Heat Transfer, Vol. 1, pp. 83-89.
4. Kamotani, Y. and Platt, J., 1992, *Effect of Free Surface Shape on Combined Thermocapillary and Natural Convection*, Journal of Thermophysics and Heat Transfer, Vol. 6, No. 4, pp. 721-726.
5. Kamotani, Y., Lee, J. H., and Ostrach, S., 1992, *An Experimental Study of Oscillatory thermocapillary Convection in Cylindrical Containers*, Physics of Fluids A, Vol. 4, pp. 955-962.
6. Ostrach, S., 1982, *Low-Gravity Fluid Flows*, Annual Review of Fluid Mechanics, Vol. 14, pp. 313-345.
7. Ostrach, S. and Kamotani, Y., 1989, *Science Requirements Document for the Surface Tension Driven Convection Experiment in Reduced Gravity*, Case Western Reserve University, Cleveland, Ohio.
8. Patankar, S. V., 1980, *Numerical Heat Transfer and Fluid Flow*, Hemisphere Pub., Washington.
9. Pline, A., 1988, *Surface Temperature Measurements for the Surface Tension Driven Convection Experiment*, NASA TM 101353.
10. Pline, A. and Butcher, R. L., 1990, *Spacelab Qualified Infrared Imager for Microgravity Science Applications*, Thermosense XII, SPIE Vol. 1313, pp. 250-258.
11. Pline, A., Jacobson, T. P., Wanhaninen, J. S., and Petrarca, D. A., 1990, *Hardware Development for the Surface Tension Driven Convection Experiment*, Journal of Spacecraft and Rockets, Vol. 27, pp. 312-317.
12. Pline, A., Jacobson, T. P., Kamotani, Y., and Ostrach, S., 1993, *Surface Tension Driven Convection Experiment*, AIAA Paper 93-4312.
13. Wernet, M. and Pline, A., 1991, *Particle Image Velocimetry for the Surface Tension Driven Convection Experiment Using a Particle Displacement Tracking Technique*, NASA TM 104482.

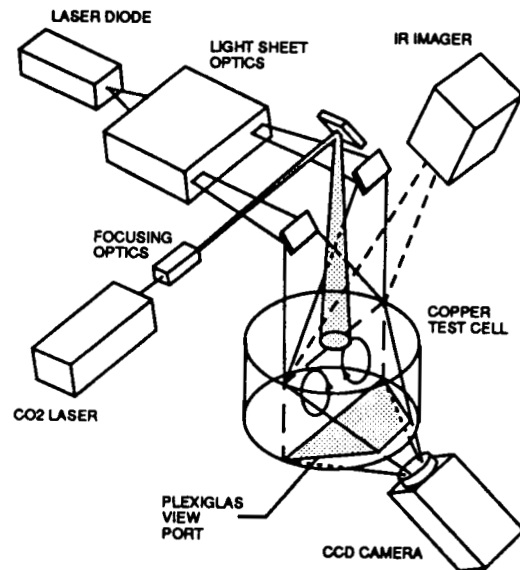


Figure 1 Experimental setup for STDCE

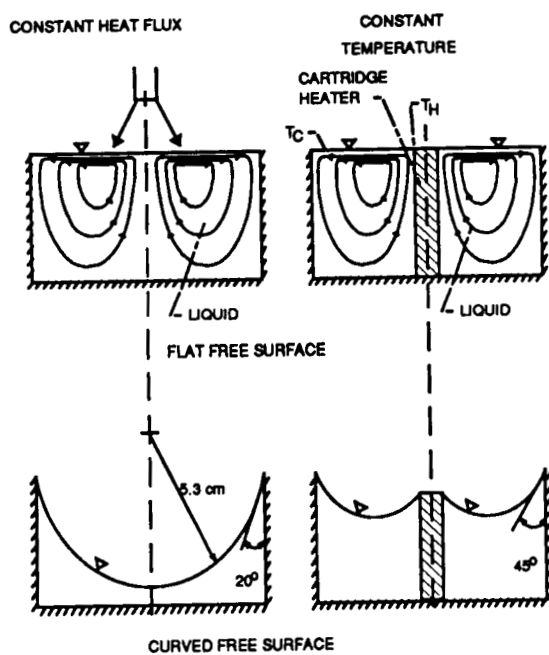


Figure 2 Basic configurations of STDCE

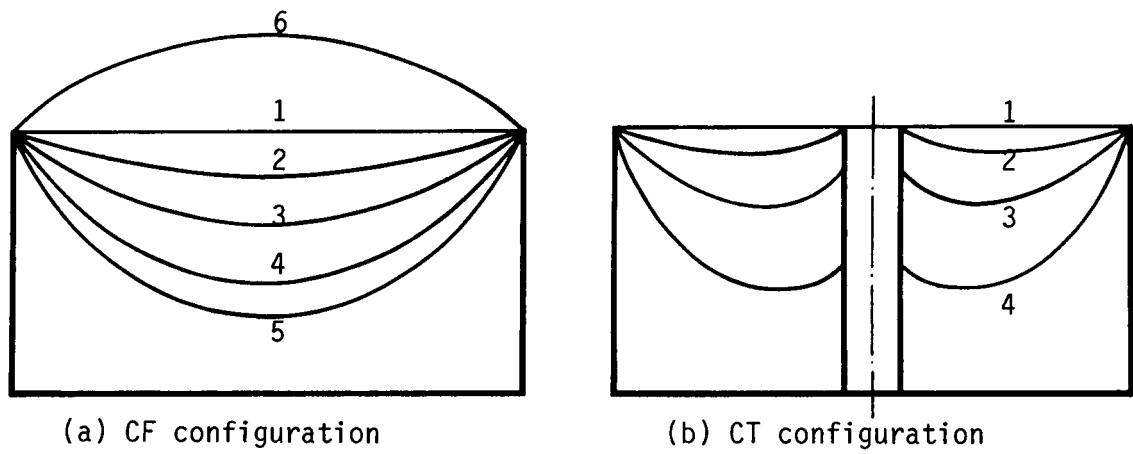


Figure 3 Free surface shapes

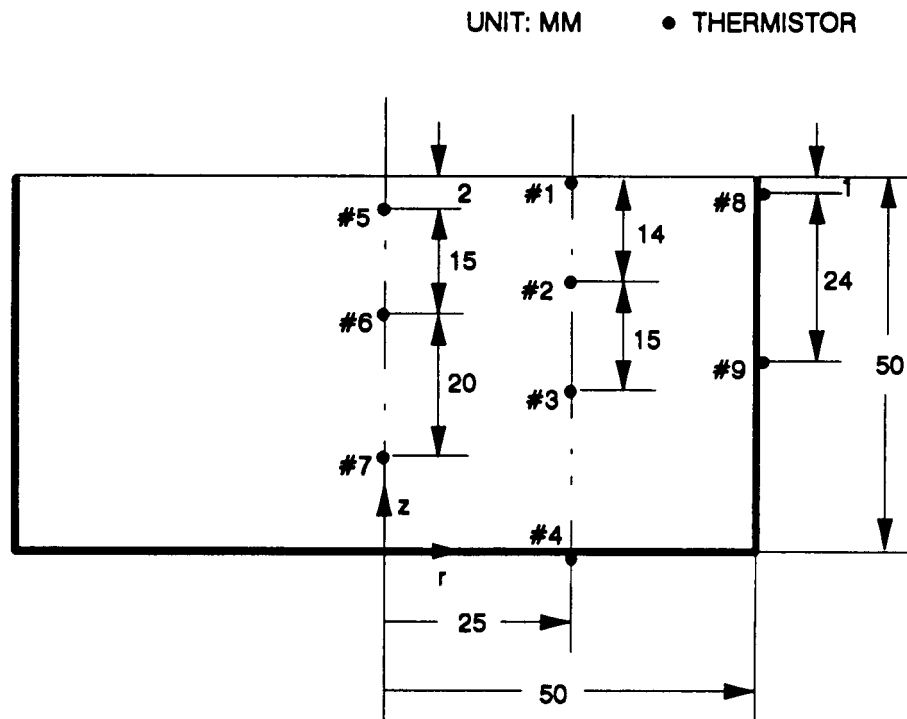


Figure 4 Location and numbering of thermistors

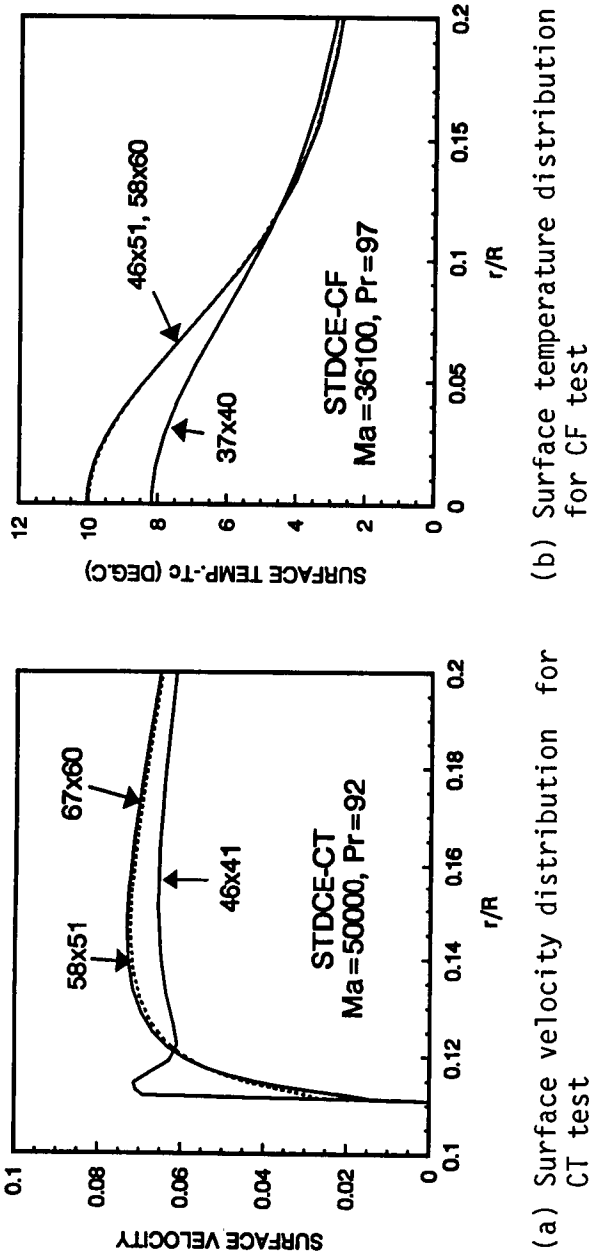


Figure 5 Comparison of results obtained with various grid systems

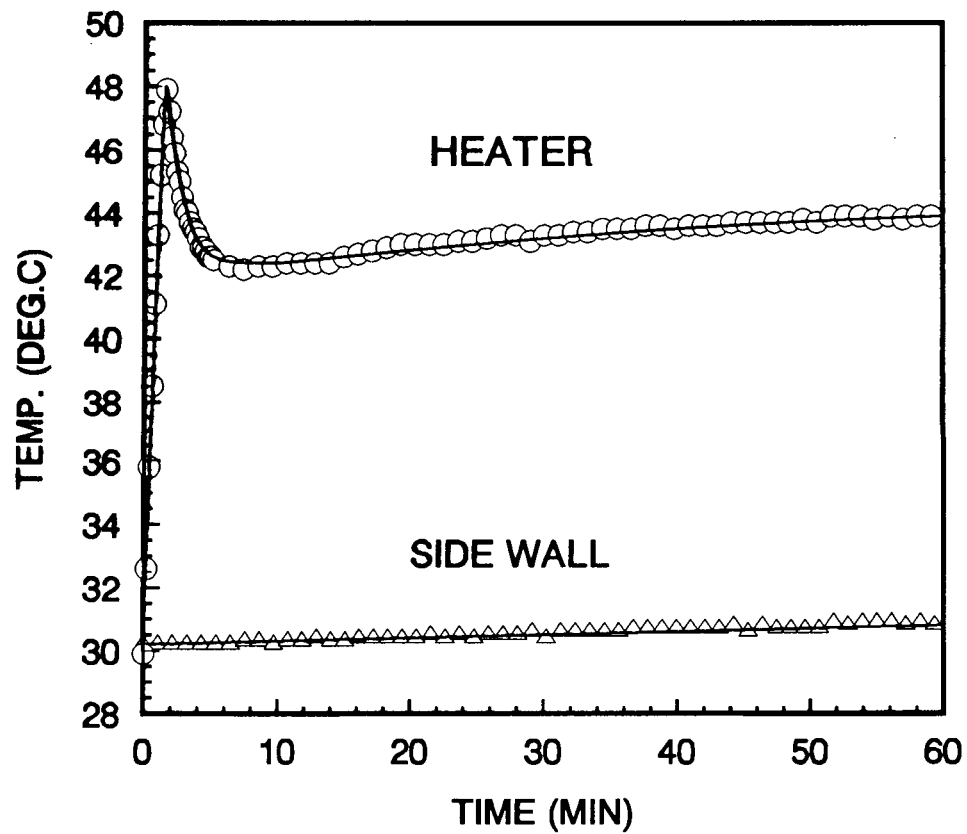
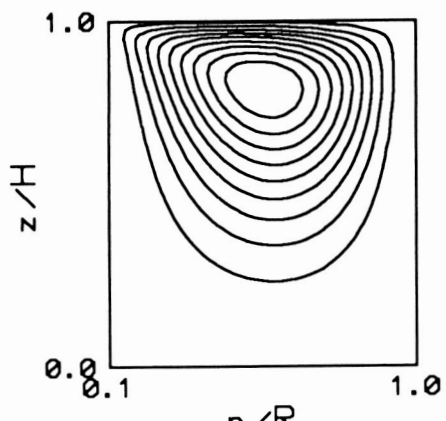
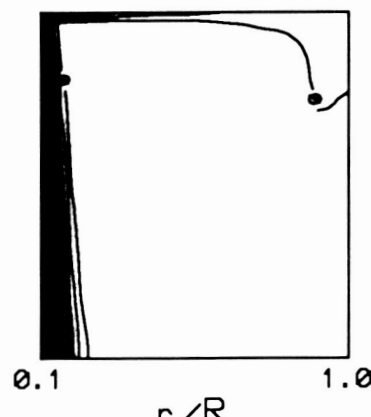


Figure 6 Variation of heater and side wall temperatures with time for CT test (symbols denote experimental data and solid lines are inputs to numerical analysis)



(a) Streamlines



(b) Isotherms

Figure 7 Streamlines and isotherms at t = 2 min. for CT test

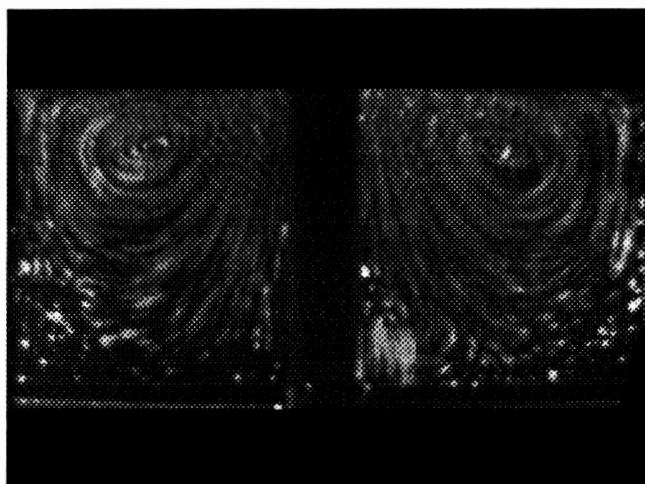


Figure 8 Observed streamlines at $t = 2$ min. for CT test

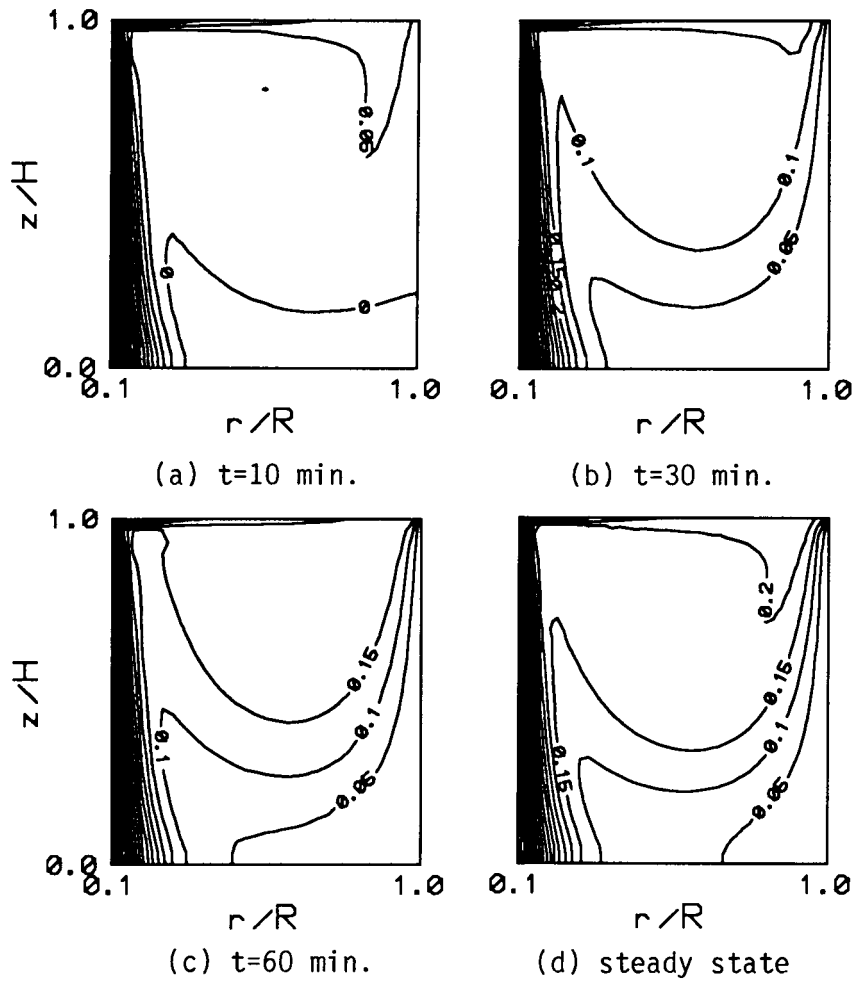
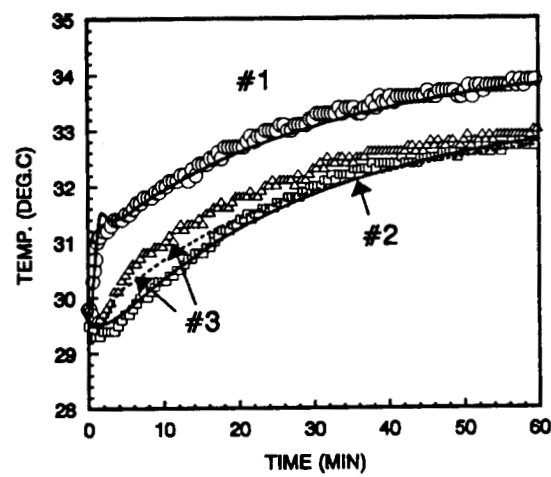
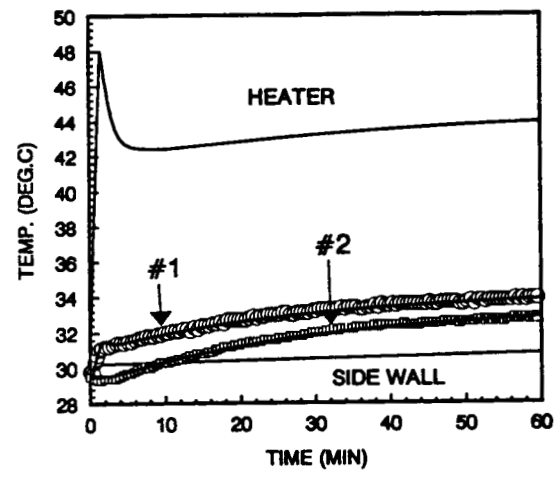


Figure 9 Isotherms at various times for CT test



(a) Fluid temperature variation



(b) Fluid temperature in comparison with boundary temperatures

Figure 10 Comparison of thermistor data with numerical result for CT test

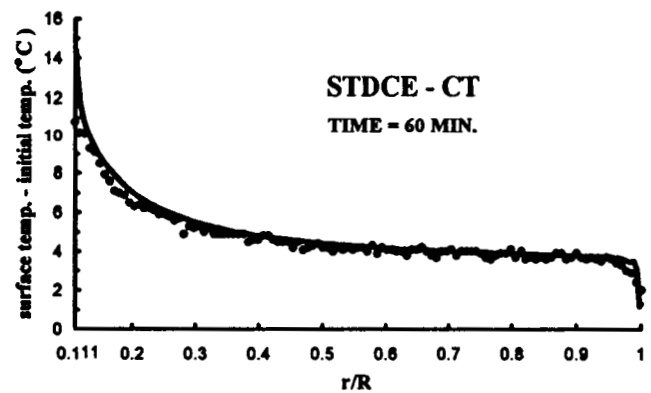
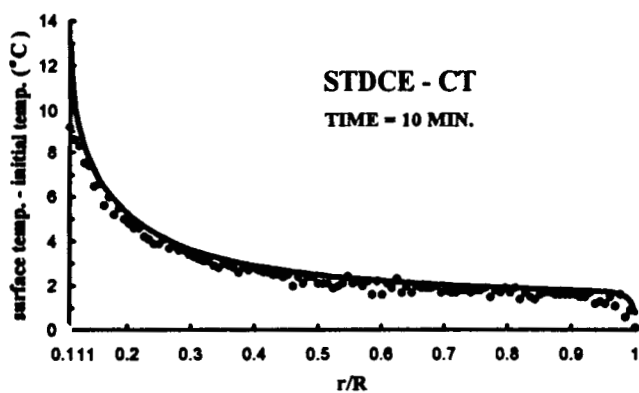


Figure 11 Comparison of infrared imager data with numerical result for CT test (points are experimental data and lines are numerical results)

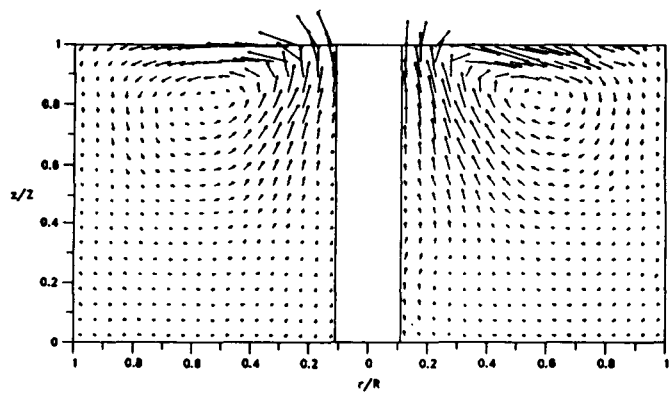
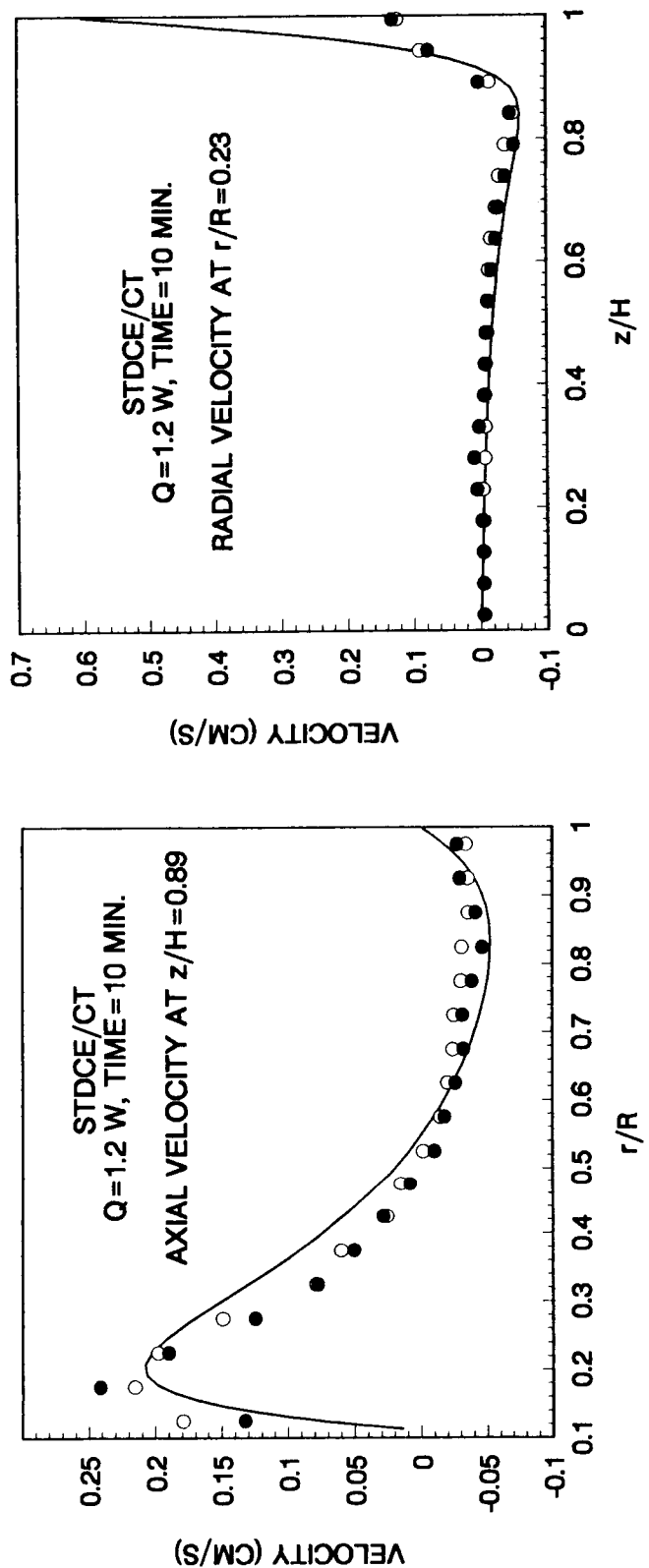


Figure 12 Measured velocity vectors at $t = 10$ min. for CT test

Figure 13 Measured and computed velocity distributions at $t = 10$ min. for CT test



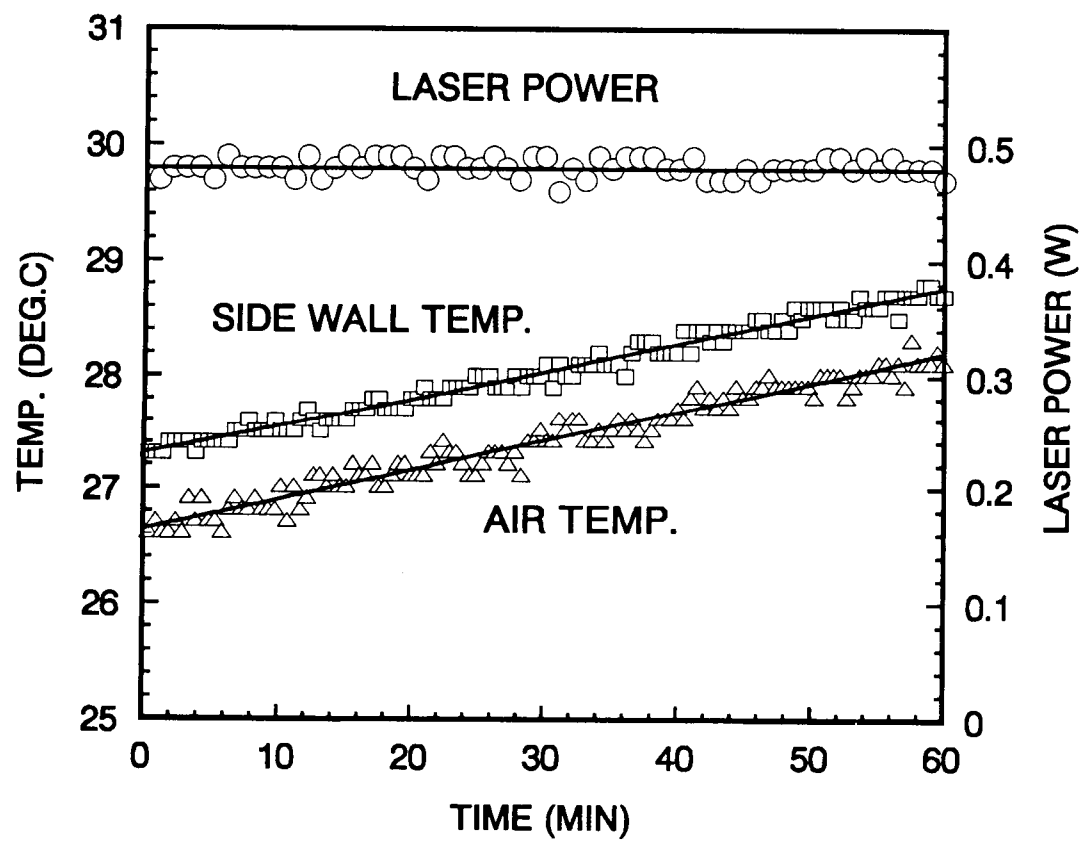


Figure 14 Thermal boundary conditions for CF test (symbols denote experimental data and solid lines are inputs to numerical analysis)

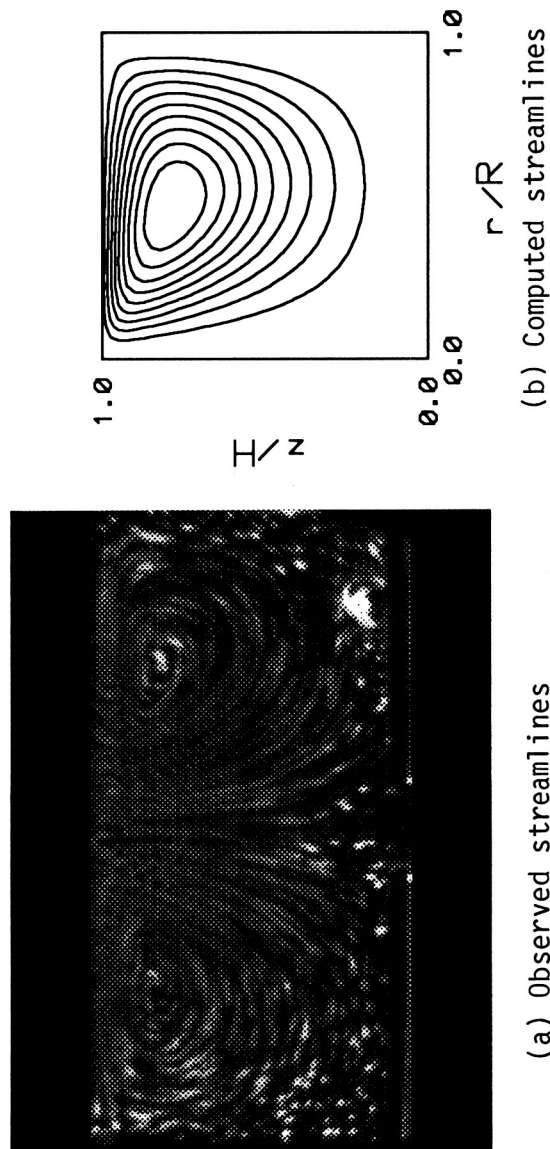


Figure 15 Observed and computed streamlines at $t = 2$ min. for CF test

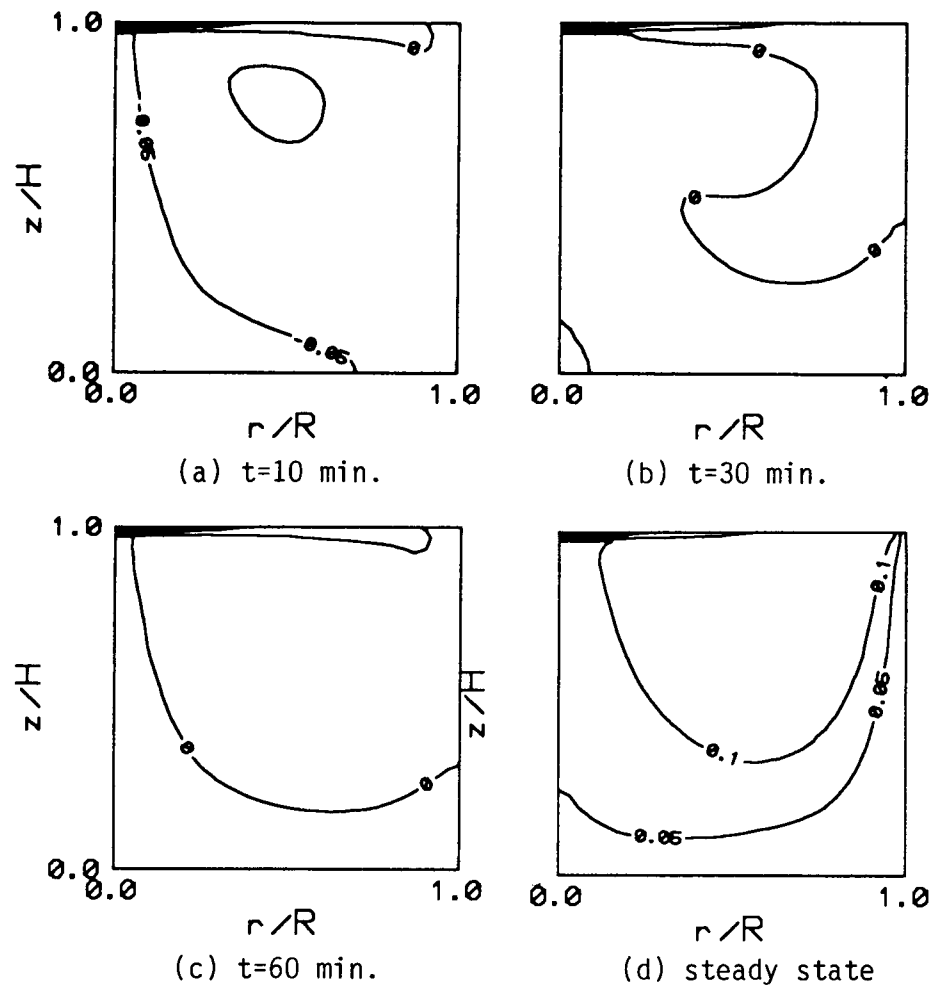
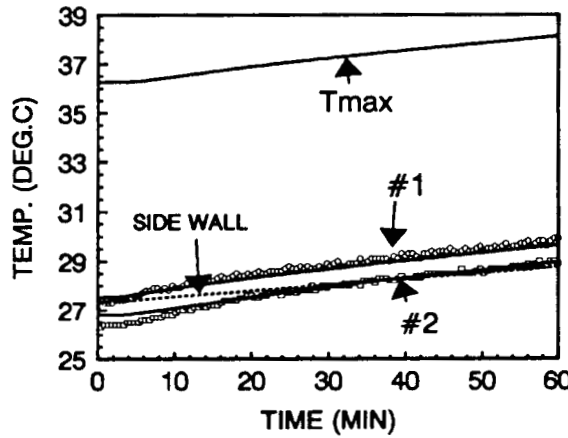
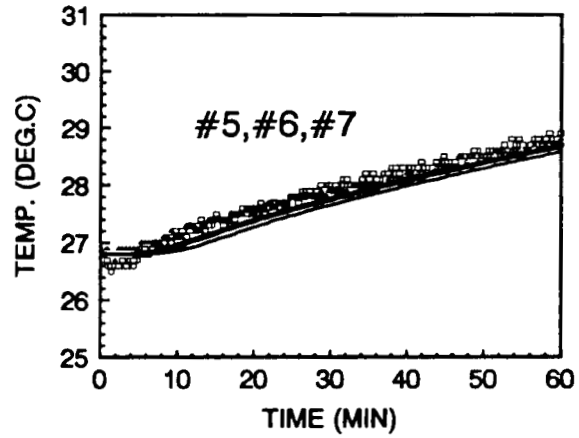


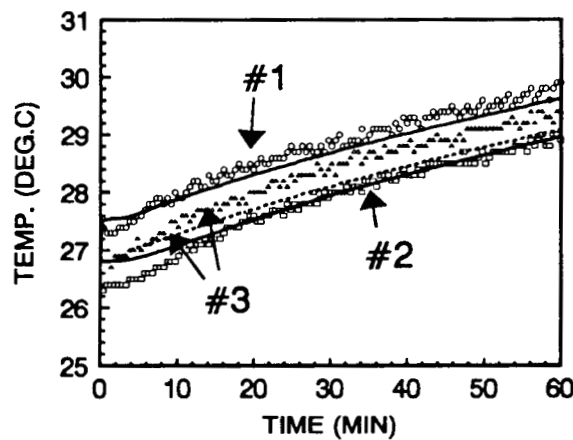
Figure 16 Isotherms at various times for CF test



(a) Fluid temperature variation



(c) Fluid temperature at $r/R=0$



(b) Fluid temperature at $r/R=0.5$

Figure 17 Comparison of thermistor data with numerical result for CF test

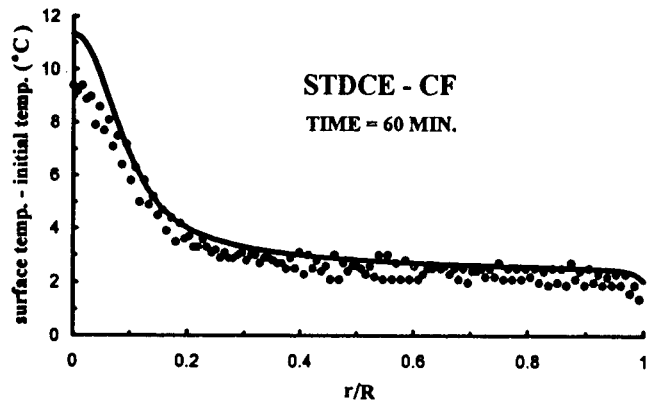
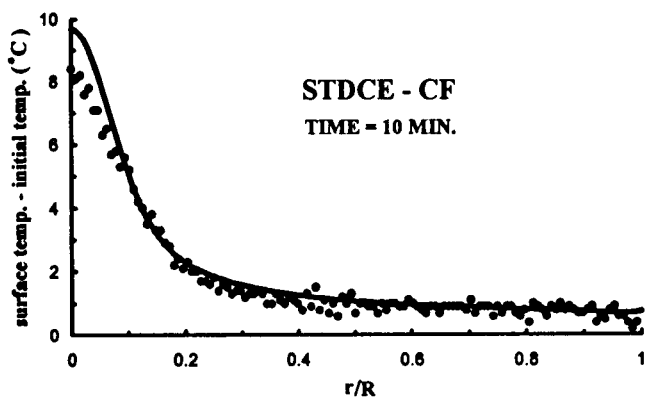


Figure 18 Comparison of infrared imager data with numerical result for CF test

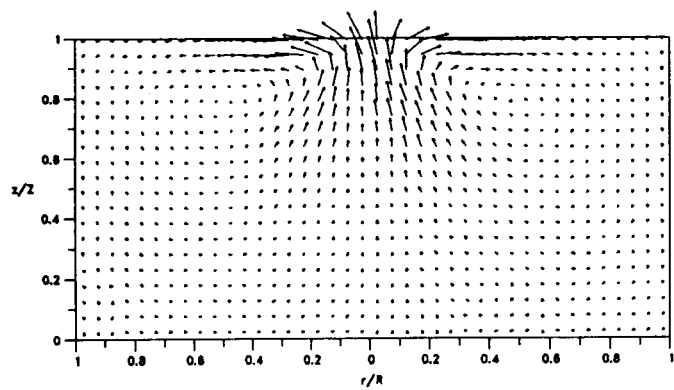


Figure 19 Measured velocity vectors at $t = 10$ min. for CF test

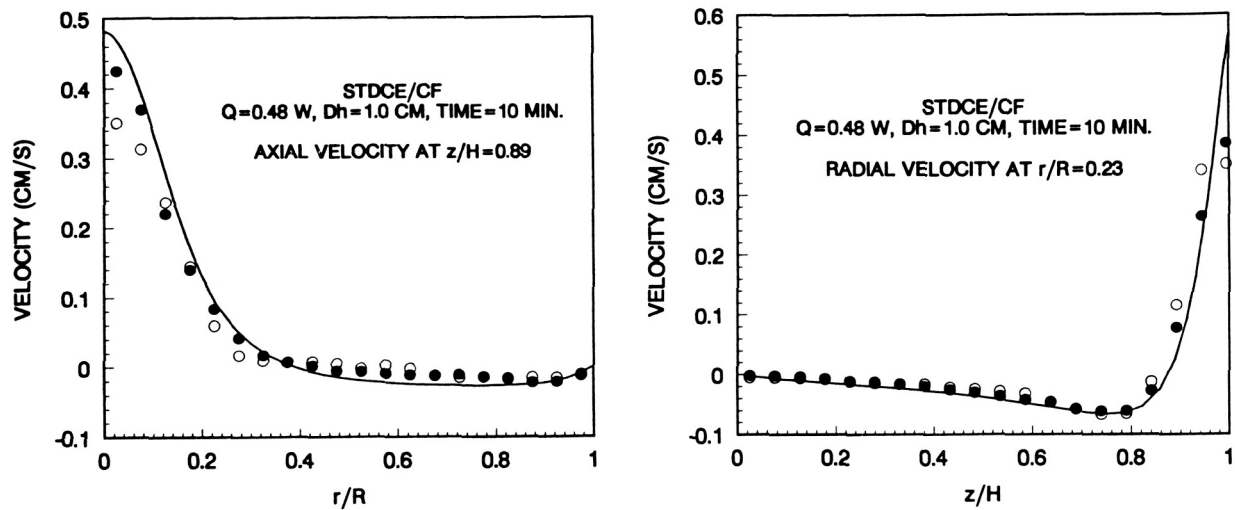


Figure 20 Measured and computed velocity distributions at $t = 10$ min. for CF test

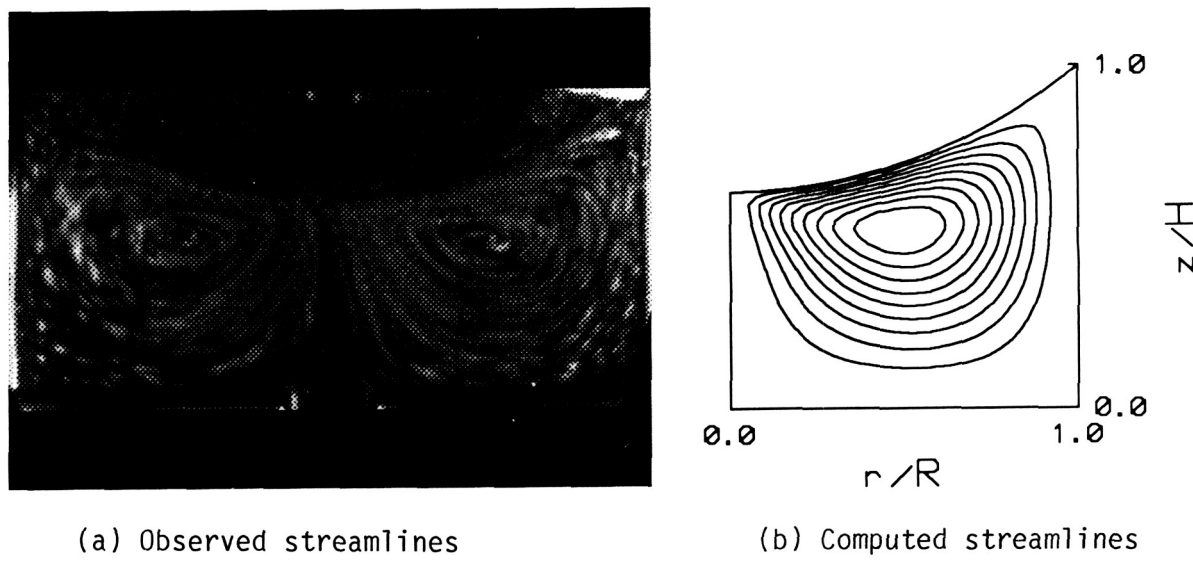


Figure 21 Observed and computed streamlines for a curved free surface test in CF configuration ($Q = 1.4$ W, beam dia. = 5 mm)

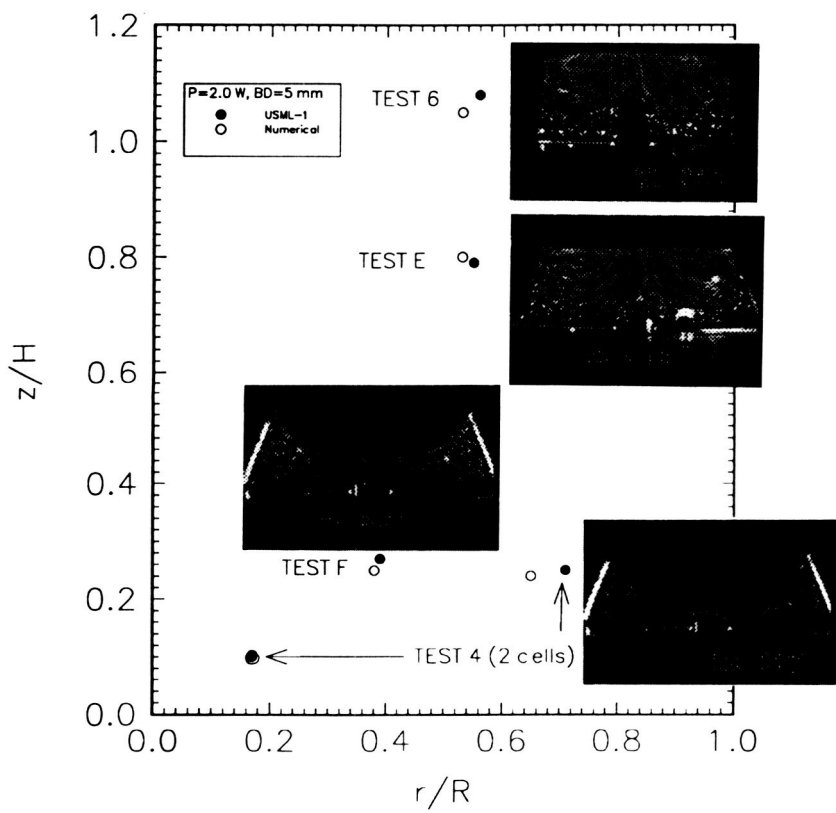


Figure 22 Experimental and numerical comparison of cell center locations for CF tests

Discussion

Question: Could you make a comment as to what you think is wrong in terms of the prediction for oscillatory onset that does not seem to happen. Where do you think the problem is ?

Answer: Well, the problem is in the physics. You know there was just always this assumption that was an instability. Usually if you think of an instability you can see a physical mechanism for an instability, that you have a heavy fluid overlaying a lighter one. When the thing (oscillatory behavior in surface tension flows) was called an instability, I did not see that physics. We went along with it and it became apparent to us that we could not correlate the onset conditions with a single parameter. The only other, if you believe in similitude theory which I do, I am a strong advocate of it, you say there is another parameter missing. Well what is the other parameter ? From the boundary conditions and the normal stresses there is a capillary number. Now everybody was taught to evaluate the capillary number. The capillary number, if you evaluate it, is very small. So you say that surface deformation cannot be important. We had a heated discussion about this here in Huntsville in the early days before any experiments were done. There had been some numerical studies where people had assumed a linear temperature profile along the free surface and I as an applied mathematician said, the surface temperature distribution has to be part of the solution. We got into this argument, and also considered the shape, and people said that since the capillary numbers are very small, it was not important. But when we could not correlate the data, we knew we needed another parameter, and asked the question what can that be ? The answer is the capillary number, which immediately said surface deformation must be important and so we said that. As we continue to do experimental and numerical work we feel, and we have described this, that the oscillations are due to a three way coupling, part of the inherent dynamics of the situation. In other words, you impose a temperature gradient on the free surface, when the Marangoni number gets effectively high so the convection is important, that is why you have got to exceed the Marangoni number like 10^4 . What happens is that profile begins to change and the imposed signature changes. For high Prandtl number fluids it actually becomes S-shaped so that all the driving ends up in the end. Now this fluid moves to the end, hits the end wall and because the surface can deform, even if it deforms a little bit, there is a time lag. So the return flow that comes back and starts to cool has that time lag in it. You say this S parameter, which is a modified capillary number, is kind of small but that S parameter is a measure of the deformation of the free surface to the radius. Well that is a very small number but the fact is that the thermal boundary layer thicknesses here are 100 microns. So these deformations are on that order. So what is happening is that the driving force is being modulated through this time lag. And now everybody in the world sees these deformations of the free surface. Our feeling is that it is not an instability. All the instability theories have to date left off the end

effects, they have dealt with doubly infinite regimes and they claim quantitative agreement. They will agree with a wave number but be off 3 orders of magnitude on the frequency. The wave forms are wrong and so this has been some sort of a controversy that has been going on. At the same time I hear people saying we understand the physics of Marangoni convection. Maybe the physics of Marangoni flow they understand but thermocapillary flows, the physics, has been a problem. And I think we have gone a long way to delineate it. And I think unequivocally, our measurements have shown the importance of the ends in driving this whole mechanism.

Question: *Was it the stream function maximum that you compared from the experiment to the calculations?*

Answer: Yes.

Question: *In your numerical code how did you input the shape of the surface ? Was that calculated or was that a constant? And did you get that from the experiment ?*

Answer: Knowing the contact angle the shape is determined and input to the code.

Question: *What are your reasons for the marginal, at best, comparisons ? I did not understand why your numerical prediction of the circulation center point did not agree with the experiment ?*

Answer: Because these rotating cells, these sub-region flows which occur in buoyancy driven flows as well, have velocities that are sometimes orders of magnitude off the mean velocity. So if your computer doesn't know where these cells are and what high resolution to use, they miss it just like experimentally you would miss it if you didn't have the right resolution. That has been the problem in trying to do confined flows by buoyancy driven or by surface tension driven force where the driving is being done on the surface. What happens in the interior can be all kind of crazy things like what I call flow sub-regions. If you don't have the proper resolution numerically or experimentally you are going to miss those and that is the problem.

Question: *That means it is not a converged solution. It has to be grid independent. Is that correct ?*

Answer: True. That is an inherent difficulty. People think all you have to do is compute everything. When I have people computing 3 dimensional, unsteady, turbulent everything I give them a little problem of a box, heat one wall and then cool one wall. I'll show you what the data looks like. I never hear from those guys again. So it is not that easy.

20 PG

148707804

N95- 14218

324082

17023

P 20

CORE-CENTERING OF COMPOUND DROPS IN CAPILLARY OSCILLATIONS: OBSERVATIONS ON USML-1 EXPERIMENTS IN SPACE

T. G. Wang, A. V. Anilkumar, C. P. Lee, and K. C. Lin

Center for Microgravity Research and Applications
Vanderbilt University, Nashville, Tennessee.

SUMMARY

Experiments on liquid shells and liquid-core compound drops were conducted using acoustic levitation, in a low-gravity environment during a Space Shuttle flight. It was observed that their inner and outer interfaces became concentric when excited into capillary oscillations. Using the existing inviscid theories, an attempt is made to explain the centering of the oscillating liquid shell. It is concluded that viscosity needs to be considered in order to provide a realistic description of the centering process.

INTRODUCTION

A compound drop¹ consists of a fluid drop enclosed inside another liquid drop. The inner drop, the outer drop and the external medium are called the core, shell, and host, respectively. When the core is a gas bubble, the compound drop is referred to as a *liquid shell*. In our studies, we are only interested in air as the host medium, and its dynamics can be neglected compared with that of the drop. In principle, any liquid can enclose any other liquid. But in practice, the compound drop system prefers to have the liquid with a lower surface tension on the outside because this configuration carries less total surface energy², e.g., it is much easier to enclose a water drop inside an oil drop than vice versa. The opposite arrangement is metastable: as long as the inner and outer interfaces do not touch it is neutrally stable. However, as soon as the two interfaces touch, the liquid inside will prefer to move completely or partially to the outer surface such that the system can adopt a lower total surface energy.

Like a compound pendulum, a compound drop exhibits two types of oscillations due to the surface tensions on its inner and outer interfaces: (1) the lower frequency slosh mode in which the two interfaces move opposite to each other and, (2) the higher frequency bubble mode in which they move in the same direction as each other³. In the idealized situation of a thin shell, in the slosh mode, the shell liquid mostly shuffles back and forth along the interfaces, whereas in the bubble mode, the shell liquid mostly moves in and out normally to the interfaces. For a liquid shell, neglecting the dynamics of air, the motion of the drop is essentially the motion of the shell liquid only. But for a liquid-core compound drop,

the densities of the shell and core fluids are comparable such that the two motions are equally important. Moreover, for a low-viscosity liquid, with its two stress-free interfaces, the oscillation of a liquid shell can be considered as inviscid to a first approximation. But for a liquid-core compound drop, the shear between the shell and core liquids makes it unrealistic to neglect their viscosities.

In the absence of gravity, the core can sit anywhere inside the shell. When the drop oscillates, it has been observed, with no detailed documentation, that the core tends to go to the center of the drop for both the liquid shell⁴ and the liquid- or solid core compound drop⁵. From a theoretical point of view, in the linear regime, the core is still neutrally stable anywhere inside the shell. Taking into account the non-linearity, the centering mechanism for an inviscid liquid shell has been studied in the thin shell limit⁶ and for the finite shell thickness⁷. The two theories are formulated completely differently, but their essential results agree with each other. Their main conclusion is that in the presence of a pure mode of capillary oscillation, the bubble of the liquid shell undergoes a slow translational oscillation inside the shell, with a frequency that is proportional to the amplitude of the capillary oscillation. It should be emphasized that an oscillation about the center of the shell is not exactly the same as centering the latter implying that the bubble goes to and settles at the center. The present study provides a close observation of the centering phenomenon for both liquid shells and liquid-core compound drops.

Acoustic levitation is used. It is known that a standing sound field, through its acoustic radiation pressure, can provide a potential well at a pressure node for levitating a small sphere⁸. It is also known that if the sound amplitude is modulated at the resonant frequency of a drop, the latter can be excited into capillary oscillations⁹. These are the main principles behind the apparatus to be used for this experiment.

I. APPARATUS, MATERIALS, AND EXPERIMENTAL PROCEDURE

The experiments were performed in the Drop Physics Module (DPM) of the United States Microgravity Laboratory-1 (USML-1) on board the Space Shuttle Columbia (STS-50) during its flight from June 25 to July 9, 1992, by, astronauts Eugene Trinh and Bonnie Dunbar.

In the DPM, the injection system for deploying the drops consists of two similar arms sticking from the middle of the two opposite vertical sides of the walls, to meet at the center of the chamber when demanded. Each arm contains the injector tube for injecting the liquids or air, as desired. The arm tips provide the mechanical means to hold a drop during the injection.

Three types of liquids were used for the experiments: a silicone oil (Dow Corning 200 series, 2 cSt.), water, and water/glycerine (72/28) mixture (Table 1). The silicone oil and the water/glycerine mixture were chosen to have about the same viscosity (2 cSt). Since the liquids have different wetting properties they are handled slightly differently.

For deploying a water shell, a needle type injector is used (Figure 1). A water drop of the desired volume is first held between the tips, then an air bubble of the desired volume is injected. The tips are finally withdrawn, suddenly, leaving the liquid shell levitated at the center of the chamber. For deploying a silicone oil water/glycerine compound drop, a flat-tip injector is used. A silicone oil column of a desired volume is sandwiched between two flat tips during injection. Then water/glycerine mixture of a desired volume is injected into the oil drop. The flat tips are similarly withdrawn suddenly, leaving the compound drop in levitation.

The sound wave is modulated in amplitude at a modulation frequency that sweeps past the n=2 bubble or slosh mode frequency of the liquid shell or compound drop, looking for a resonant response from the drop and the expected centering of its core.

II. RESULTS AND DISCUSSION

The resonances of a liquid shell are far apart such that most of the time a pure n=2 mode can be excited. But for a liquid-core compound drop, the modes are closely packed. Also, their resonance peaks are less sharp due to dissipation by viscosity such that a lot of mode overlapping and coupling occurs. Visually, the excited shape oscillation of a liquid-core compound drop by-and-large consists of more than one mode.

A. Water Shell

The deployed drop had a volume of 4.15 ± 0.1 cc, consisting of 2 cc of water and 2.15 cc of air. The average operating temperature was 25°C. The water contained some pliolite tracers (50 μm , Goodyear Chemical Co.) for monitoring any uncontrolled rotation of the drop.

Following deployment, it was found that the levitation of the drop was not easy, with the air bubble sloshing with respect to the shell when the drop oscillated translationally in the acoustic potential well. The bubble moved opposite to the drop translation, such that the center of mass of the drop moved back and forth, in the same direction as that of the motion of the drop, rather than staying still (Figures 2 a,b,c). The levitated drop had a small deformation along the z-axis of about 1 % ($(a/b-l) \times 100\%$, where a and b are the equatorial and polar radii, respectively), and an uncontrolled rotation of about 0.15 rps. along the y-axis. The side-view was the most suitable for observation of the interface. In a liquid-air interface, which is furthermore curved, optical distortion is an issue; however no corrections have been made for this in the measurements.

The amplitude of the sound wave in the z-direction was varied at a modulation frequency, sweeping through the n=2 bubble mode oscillation resonance of the drop from 9 to 11 Hz in 200 seconds. It was observed that the bubble was centered quickly in the first eight seconds, i.e., about 60

shape oscillation cycles. When this occurs (Figures 2 d,e), the translational oscillation of the drop in the z-direction also stopped. The translations along the x- and y-axes persisted, although the shell looked centered in those directions. It is noted that after the drop was excited into oscillation, there was a slight additional average flattening due to the modulated radiation stress averaged over a capillary wave cycle, such that a becomes a' and b becomes b'. The shape oscillation amplitude 'e' during centering ($e = (L'/W' - b'/a') \times 100\%$; L' and W' are the height and width of the drop in maximum prolate shape), was very small, an average of about 1.2 %. Once the core was centered, it did not go off-center easily.

In Figure 3, L/W (L and W being the height and width of the oscillating drop) is plotted over time for certain intervals before and after initiation of shape oscillations. The first cluster of data points represents, with some scatter, the flattening before oscillation. The second cluster (points connected) represents the drop in a forced oscillation by the modulation radiation stress, giving the mean additional deformation, mainly due to the modulation stress. The third cluster represents a similar situation at the end of centering, showing a slightly higher oscillation amplitude.

In Figure 4, the percentage eccentricity ($\Delta L/L \times 100$) is plotted versus time, where ΔL is the thickness of the shell on one side of the shell (see inset of Figure 4), and L is the height of the drop, both being dependent on time as the drop oscillates. The initial oscillation of this quantity (region I, Figure 4) arises from the fact that the drop is translating oscillatorily in the acoustic potential well, predominantly along the z-axis at a frequency of about 0.76 rad/sec. As the drop is oscillated, the translational oscillations in the potential well die out (region II) and the drop is centered (region III). The damping of the amplitude of the translational oscillations, provides unambiguous evidence of centering.

During the n=2 bubble mode sweep, the shape oscillation amplitude increased as the drop approached resonance. The amplitude 'e' peaked at 12% at around a frequency of 10 Hz (fig. 2 e,f), approximately 100 seconds following the start of the oscillation.

The experiment was repeated with the same drop with an n=2 slosh mode sweep, from 1.5 to 3.5 Hz in 200 seconds. This experiment was started following the bubble mode sweep. Prior to initiating the slosh mode sweep, the shell was almost centered along the vertical z-axis, but was off-center along the y-axis. Figure 5 is the eccentricity plot ($\Delta L/L\%$ versus time; z-axis) showing the shell almost centered prior to starting the shape oscillations (region I). As the oscillation was started, at an average amplitude of about 2.4%, the core moved off-center for about 8 seconds or about 12 oscillation cycles (region II), before becoming centered again (region III). This off-centering is probably a transient readjustment resulting from the centering along the y-axis.

During the n=2 slosh sweep, as the oscillation amplitude further increased to about 11%, with the drop approaching resonance around 2.4 Hz, the core went off center, and sloshed around violently. Eventually, the bubble got lodged on one side of the shell which, being thin, disintegrated by atomization

from capillary ripples forced by the acoustic radiation pressure¹¹⁻¹³. The loss of centering, at large amplitudes, is not well understood at this time.

B. Liquid-Core Compound Drop

The silicone oil contained pliolite tracers, and the water/glycerine mixture contained green food coloring (0.5% by volume). The tracers were used for monitoring any uncontrolled rotation of the drop. The dye helped to make the inner interface more visible. For an $n=2$ slosh mode oscillation of a liquid-core compound drop (as opposed to a liquid shell), the shell liquid tends to pile up at the equator during the oblate phase of the oscillation, forming a protrusion along the equator, which is susceptible to outward stretching by the acoustic suction stress¹¹. Hence in the top view, the shell size is a little magnified. The top view was most suitable for studying the dynamics of the interfaces of the compound drop.

The drop had a volume of 3.55 ± 0.08 cc, with 1.55 cc of oil. The average temperature during the experiments was about 24.5°C. To keep the drop from uncontrollably rotating during levitation, the drop was acoustically flattened at the poles. The resulting flattening was about 20%. In addition, an acoustic torque¹⁰ was used to cancel any residual rotation.

The modulation frequency was swept from 2.8 to 3.8 Hz in 132 seconds, through the $n=2$ bubble mode, which was also close to the $n=4$ slosh mode of the compound drop. Four sweeps were conducted with different drive amplitudes. Initially some complex mode, mostly $n=4$ slosh mode, with its non-axisymmetric components up to $m=\pm 4$, appeared. Then the $n=2$ and $m=0$ mode appeared, followed by a strong $n=2$ and $m=\pm 2$ component, and next by a strong $n=2$ and $m=+1$ component. It seems that not a pure mode, but a superposition of modes with a dominant one appeared at any time. The order of the appearances did not seem to be related to the oscillation amplitude. The ease at which the highest non-axisymmetric modes occur, e.g. $m=\pm 2$ for $n=2$ and $m=+4$ for $n=4$, can be explained by the fact that they are of the longest average wavelength among their co-modes for the same n , which implies that they are the least suppressed by viscosity. Their occurrence probably has to do with some slight biases imposed by the x- and y-drives: the slight deviation of the static shape from axisymmetry leads to a similar deviation in the modulation stress felt by the drop.

From the top-view, centering was effective with the $m=\pm 2$ mode, but not much centering was seen for the $m=0$ and $m=\pm 1$ modes. It may be concluded here that in order for centering in the equatorial plane to be effective, the shell liquid has to set up an uneven average pressure distribution through Bernoulli effect in the equatorial plane, which requires the $m=\pm 2$ mode. Once the core was centered, it did not go off center, even as the amplitude of oscillation increased.. Figure 6 shows the progressive stages of centering when the $m=\pm 2$ mode came into effect. Figure 7 shows a complete oscillation of the

centered compound drop. A plot of percentage eccentricity $\Delta W/W \times 100$ versus time is given in Figure 8, showing strong evidence for centering.

The experiment was repeated for the $n=2$ slosh mode. The modulation frequency was swept in the range 1 to 2 Hz for 132 seconds. A few sweeps were conducted with different drive amplitudes. The drop was flattened by about 30% for levitation stability, and for driving larger amplitudes. At high oscillation amplitudes, mode coupling of $n=2$ mode with $n=2$, $m=\pm 2$ mode was seen. Good, centering was achieved at small and moderate amplitudes, but at extremely large amplitudes ($e > 100\%$) the core went off center, because the protrusion at the equator became asymmetric due to uneven stretching by the acoustic suction stress (Bernoulli suction) at the edge. The shell finally disintegrated on the thin film, following the excitation of small capillary ripples there. The thin film is probably an outcome of the loss of stability at the edge of the protrusion¹¹.

The decay of the slosh mode oscillation of the compound drop, of which the inner and outer liquids had the same viscosity of 2 cSt, occurred on a time scale about 10 times shorter than the corresponding simple drop with the same viscosity, implying a strong dissipation at the inner interface.

III. THEORETICAL CONSIDERATIONS

We are interested in the centering of a liquid shell, which has been a subject of theoretical studies. Lee and Wang⁶ have studied the centering of a liquid shell undergoing capillary oscillation in the thin shell limit. In this limit, the dimensionless shell thickness parameter $\delta = t_S/R_S$ is assumed to be much less than 1, where t_S is the concentric shell thickness, and R_S is the mean radius of the shell ($R_S = (R_0 + R_i)/2$; R_i is the inner radius R_0 is the outer radius). Because of the disparity between the frequencies of the bubble mode and the slosh mode for a given shape oscillation mode ($n=2$ for most studies), in the thin shell limit, different scalings are applied to the two modes.

For a liquid shell of density ρ and surface tension σ , for the bubble mode of oscillation, time is scaled by the inverse of $\omega_S/\delta^{1/2}$, where $\omega_S = (\sigma/\rho R_S)^{1/2}$. The wave amplitude is characterized by ε_1 , which is the surface displacement amplitude scaled by R_S as in the initial condition $\tilde{R} = R_S(1 + \varepsilon_1 P_n(\cos\theta))$ relative to the geometrical center of the two surfaces (\tilde{R} is the position of the mid-surface between the inner and outer oscillating surfaces, P_n is a Legendre polynomial, and θ is the polar angle). The initial displacement of the core is represented by Δ in $t = t_S(1 - \Delta \cos\theta)$, where t is the thickness distribution of the shell. It was found that for a shell with an off-center gas core, the core position undergoes a fast oscillation with the same frequency as the wave, together with a slow oscillation, about the center of the drop due to the nonlinearity of the wave; the latter being interpreted as a manifestation of the Bernoulli

effect. In this study, the dimensionless frequency of the slow oscillation of the core for the n=2 bubble mode is about 1.3 times ε_1 .

For the slosh mode, time is scaled by the inverse of $\omega_S \delta^{1/2}$. The wave amplitude is characterized by a ε_2 (different from ε_1), which is the amplitude of the variation in the thickness of the shell scaled by t_S , as in the initial condition $t = t_S(l - \Delta \cos\theta + \varepsilon_2 P_n(\cos\theta))$, where t is the shell thickness distribution, and Δ represents the core displacement. It was again found that for a shell with an off-center gas core, the core position undergoes a fast oscillation with the same frequency as the capillary wave, together with a slow oscillation, about the center of the drop due to the nonlinearity of the wave. The dimensionless frequency of the slow oscillation of the core for the n=2 slosh mode is about 0.6 times ε_2 . For both the bubble and the slosh mode, the results do not depend on Δ except for the extreme case of Δ close to 1, and do not depend on, or are not very sensitive to, δ as long as it is small.

Pelekasis et al.⁷ considered a liquid shell with a finite thickness. Their results agree with those of Lee and Wang in the thin shell limit. Pelekasis et al. do not discriminate between the bubble mode and the slosh mode in their scalings; time is scaled with $\omega_0 = (\sigma/\rho R_0^3)^{1/2}$, and lengths are scaled with R_0 . For both modes, the wave amplitude is characterized by ε as in the initial condition $F_2 = 1 + \varepsilon P_n(\cos\theta) + \dots$ for the position of the outer surface. With R^* being the ratio R_i/R_0 , their results for the slow oscillation frequency can be written in the dimensionless form $\Omega^* = C_b(R^*)\varepsilon$ for the bubble mode and $\Omega^* = C_s(R^*)\varepsilon$ for the slosh mode, where the coefficients C_b and C_s are functions of R^* .

Converting Lee and Wang's results into the scaling system of Pelekasis et al., C_b and C_s , from both works, are plotted against R^* in Figure 9 and Figure 10, respectively (the data for Ω^* of Pelekasis et al. are taken from their Figure 9 (a), (b) and (c) for the bubble mode, and from their Figure 16 and their text after their equation (7.3b) for the slosh mode). From Figure 9, it is seen that C_b depends on R^* but its value from Pelekasis et al. approaches the constant value of Lee and Wang asymptotically as the shell gets thin. From Figure 10, it is seen that C_s is insensitive to R^* , and its value from the two works are approximately equal, considering the numerical errors involved. It is noted that the calculation of Pelekasis et al. is more prone to numerical difficulty when R^* approaches 1; being unable to finish one slow cycle, such that the values of the slow frequencies there are not very accurate. With C_b and C_s given by Figure 9 and Figure 10 respectively, the slow frequency in rad/sec for the bubble mode is given by

$$\Omega = C_b(R^*)\varepsilon \left(\frac{\sigma}{\rho R_o^3} \right)^{1/2} \quad (1)$$

and that for the slosh mode by

$$\Omega = C_s (R^*) \varepsilon \left(\frac{\sigma}{\rho R_o^3} \right)^{1/2} \quad (2)$$

where it is recalled that ε is the surface displacement amplitude scaled by R_o .

IV. COMPARISON WITH EXPERIMENTAL RESULTS

The translational oscillation in the potential well, before the liquid shell is excited into shape oscillations, has a frequency about 0.76 rad/sec (Figure 4). After it is excited into the bubble mode, the translational frequency is about 1.6 rad/sec. The average oscillation amplitude ($e\%$) for centering from Figure 3 is about 1.2%. For the current liquid shell $R^* \sim 0.8$ and thereby C_b is ~ 6.5 from Figure 9. Imposing this onto equation 1, while noting that ε is $\sim 2/3 e$, we arrive at a frequency of about 0.44 rad/sec. There is no strong evidence for the presence of this frequency. However, the time scale over which centering occurs is about 8 seconds. It is very tempting to consider this as an over damped slow oscillation, representing a one-half period, leading to a frequency of about 0.4 rad/sec. The bottom line is that the result questions the validity of inviscid assumption in the context of centering of the liquid shell.

Similarly in the context of Figure 5, for centering in the slosh-mode, the average oscillation amplitude is about 2.4 %. For the current drop, C_s is ~ 4 , from Figure 10. Imposing these onto equation 2, we arrive at a frequency of about 0.54 rad/sec. Again, it is very tempting to consider the transient re-adjustment of the core (Figure 5), over a time scale of about eight seconds, as representing a half-period of slow oscillation.

CONCLUDING REMARKS

We have seen that when centering of a compound drop in capillary oscillation occurs, the core stays at the center after a few oscillations. For a liquid-core compound drop, this is reasonable because of the viscous friction between the core and shell fluids. But for a liquid shell, in the inviscid limit, it has been predicted by two independent theories that the core should go through a slow oscillation with a frequency proportional to the wave amplitude. In view of the discrepancy between the theoretical prediction and the experimental observation, the obvious question is: should the liquid shell be considered inviscid? The observation seems to suggest that as far as the nonlinear effect called centering is concerned, viscosity should be taken into account in order to obtain a realistic prediction.

We have also observed that the liquid shell can become decentered at large wave amplitude, for the case of the $n=2$ slosh mode. This effect could be a result of the coupling between the translational

oscillation of the shell, in the acoustic potential well, and the shell centering force of the capillary wave, and needs to be investigated further.

REFERENCES

1. R.E. Johnson, and S.S. Sadhal, *Ann. Rev. Fluid Mech.* 17, 289 (1985).
2. S. Torza, and S.G. Mason, *J. Colloid Interface Sci.* 33, 67 (1970).
3. M. Saffren, D.D. Elleman, and W.K. Rhim, in *Proceedings of the Second International Colloquium on Drops and Bubbles, Monterey, California, November 1981*, D.H. Le Croisette, Ed., p.7, Jet Propulsion Laboratory, California Institute of technology, Pasadena, California (JPL Publication 82-7) (1982).
4. T.G. Wang and D.D. Elleman, private communication about an experiment on water shells on board a KC-135 plane flying parabolically to simulate zero gravity.
5. M.C. Lee, I.A. Feng, D.D. Elleman, T.G. Wang, and A.T. Young, in *Proceedings of the Second International Colloquium on Drops and Bubbles, Monterey, California, November 1981*, D.H. Le Croisette, Ed., p.107, Jet Propulsion Laboratory, California Institute of Technology, Pasadena, California (JPL Publication 82-7) (1982).
6. C.P. Lee, and T.G. Wang, *J. Fluid Mech.* 188, 411 (1988).
7. N.A. Pelekasis, J.A. Tsamopoulos, and G.D. Manolis, *J. Fluid Mech.* 230, 541, (1991).
8. L.V. King, *Proc. Roy. Soc. (London)* A147, 212 (1934).
9. P.L. Marston, *J. Acoust. Soc. Am.* 67, 15 (1980).
10. F.H. Busse, and T.G. Wang, *J. Acoust. Soc. Am.* 69, 1634 (1981).
11. C.P. Lee, A.V. Anilkumar, and T.G. Wang, *Phys. Fluids A* 3, 2497 (1991).
12. S.D. Danilov and M.A. Mironov, *Sov. Phys. Acoust.* 33, 141 (1987).
13. A.V. Anilkumar, C.P. Lee and T.G. Wang, (submitted to Physics of Fluids A).

Table I

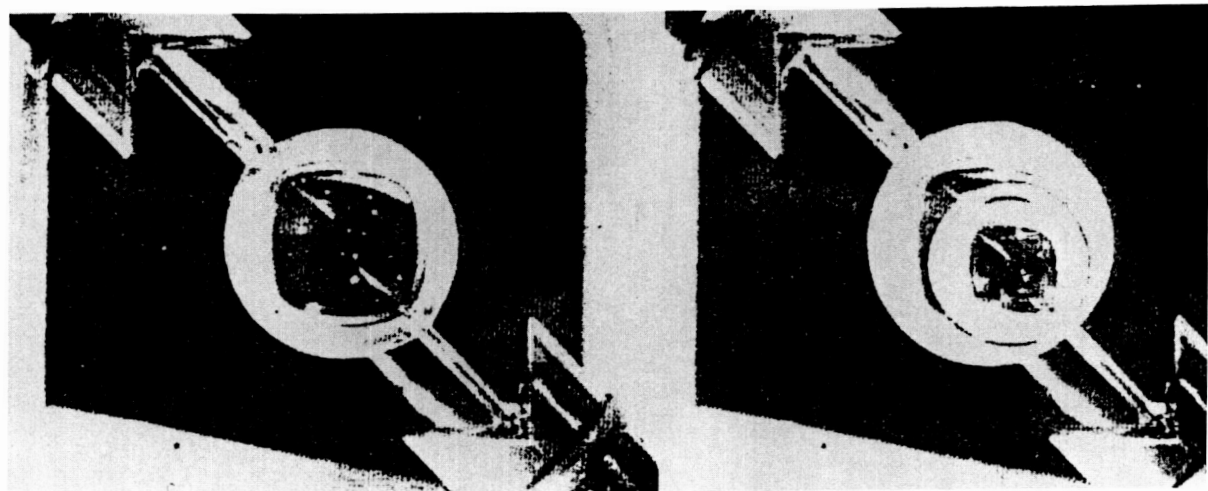
Properties of the Liquids Used in the Experiments at 25°C

* measured from the leftover flight fluids

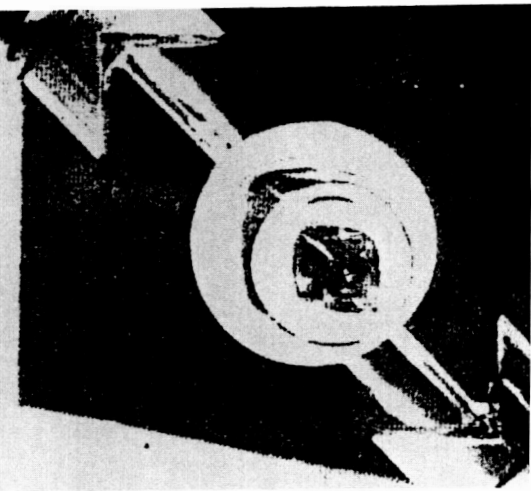
measured from retained samples of the flight fluids

Liquids	ν (cSt) #	ρ (gm/cc) #	σ (dyn/cm)*
silicone oil (DC 200 series)	2.0	0.962	21±0.2
water	0.9	0.997	71.2±0.4
water/glycerine (72/28) (with 0.5% by volume green dye)	1.9	1.064	68.0±0.4

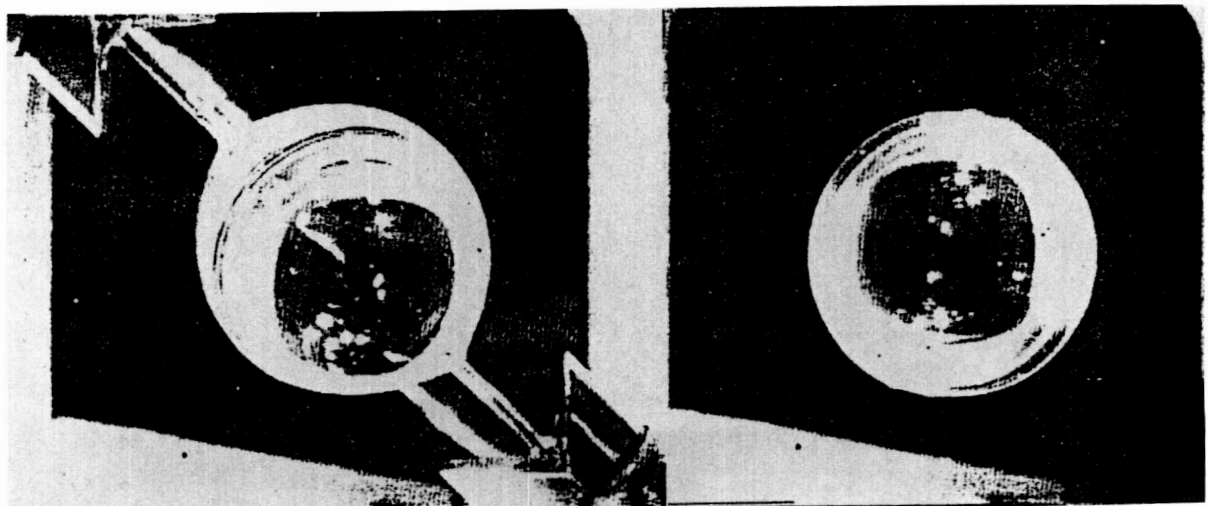
Interfacial tension between silicone oil (2 cst) and water/glycerine (72/28) is 33±0.3 dyn/cm#



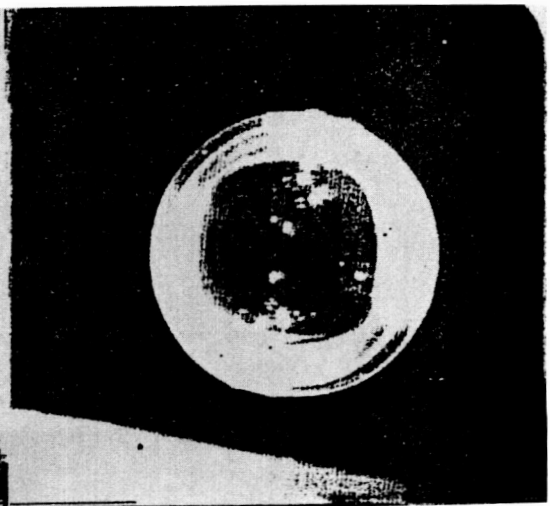
1a



1b



1c



1d

Figure 1 Deployment of a water shell (top-view): a) injected water drop held between needle tips, b) injection of air bubble, c) bubble injection complete, d) deployed water shell.

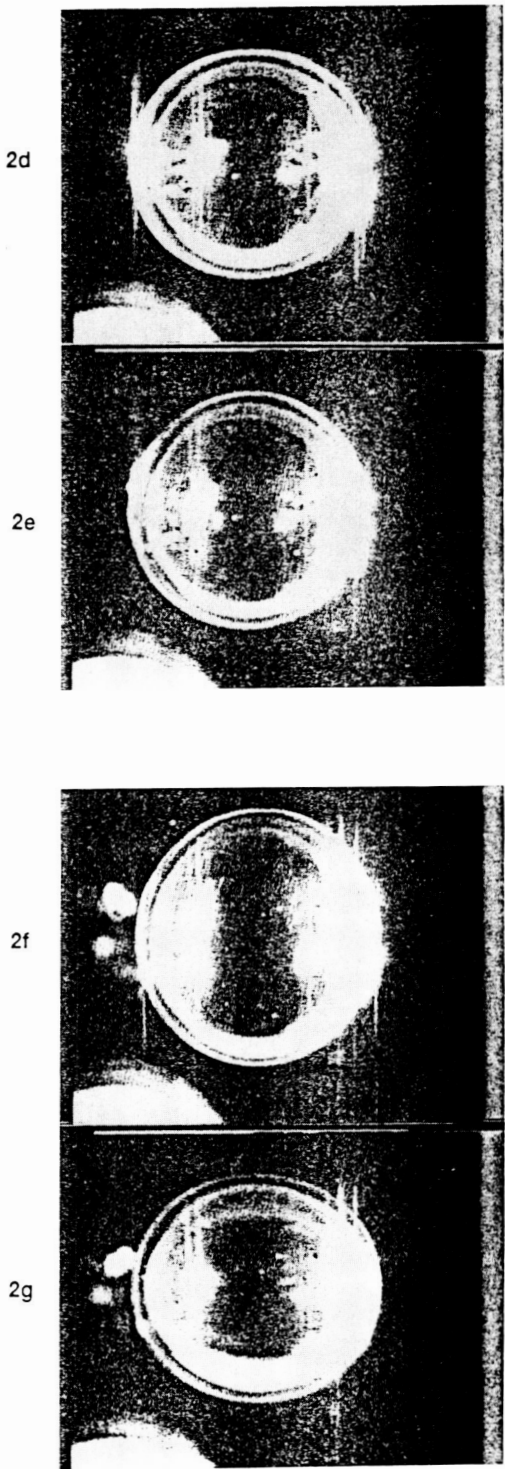
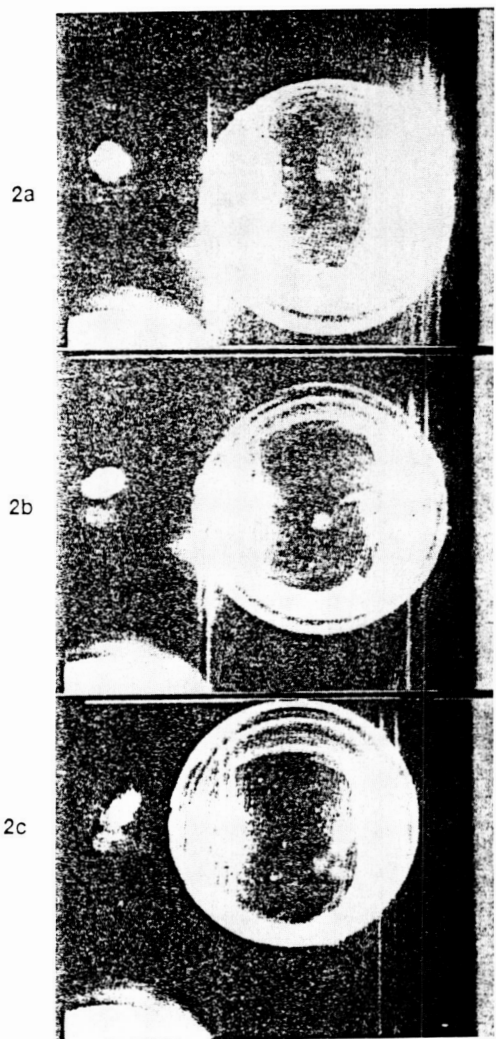


Figure 2 Centering of water shell by $n=2$ bubble mode: a, b, c) initial sloshing of the core due to translational oscillations of the drop in the potential well., d, e) core centered during small amplitude oscillations, f,g) centering during large amplitude oscillations.

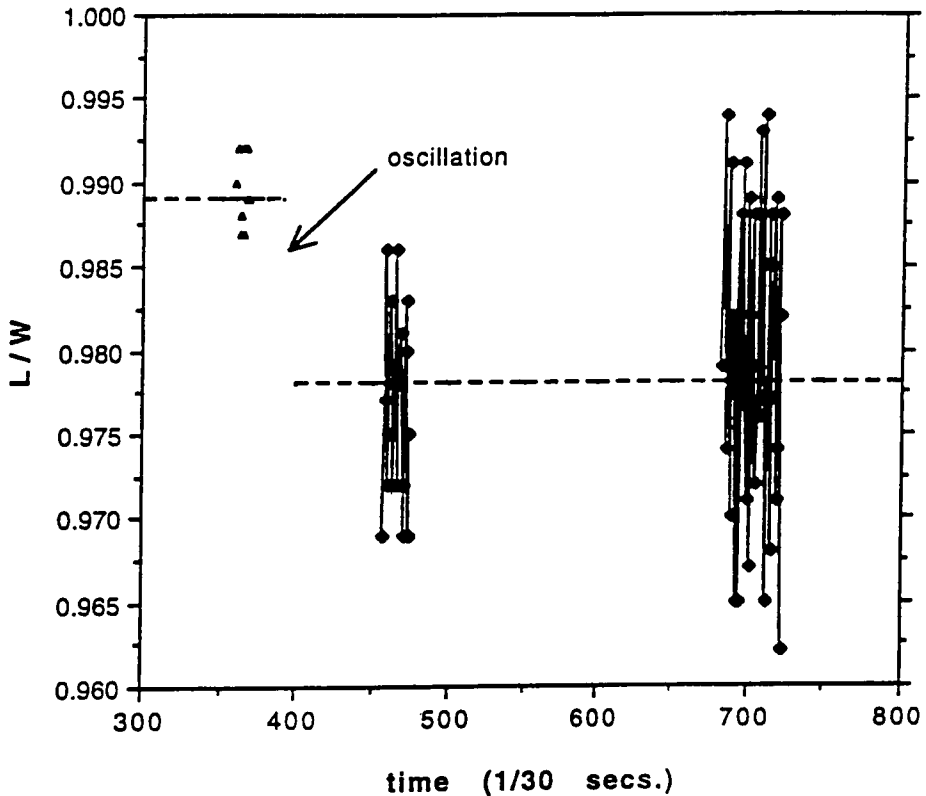


Figure 3 L/W versus time for $n=2$ bubble mode of the water shell.

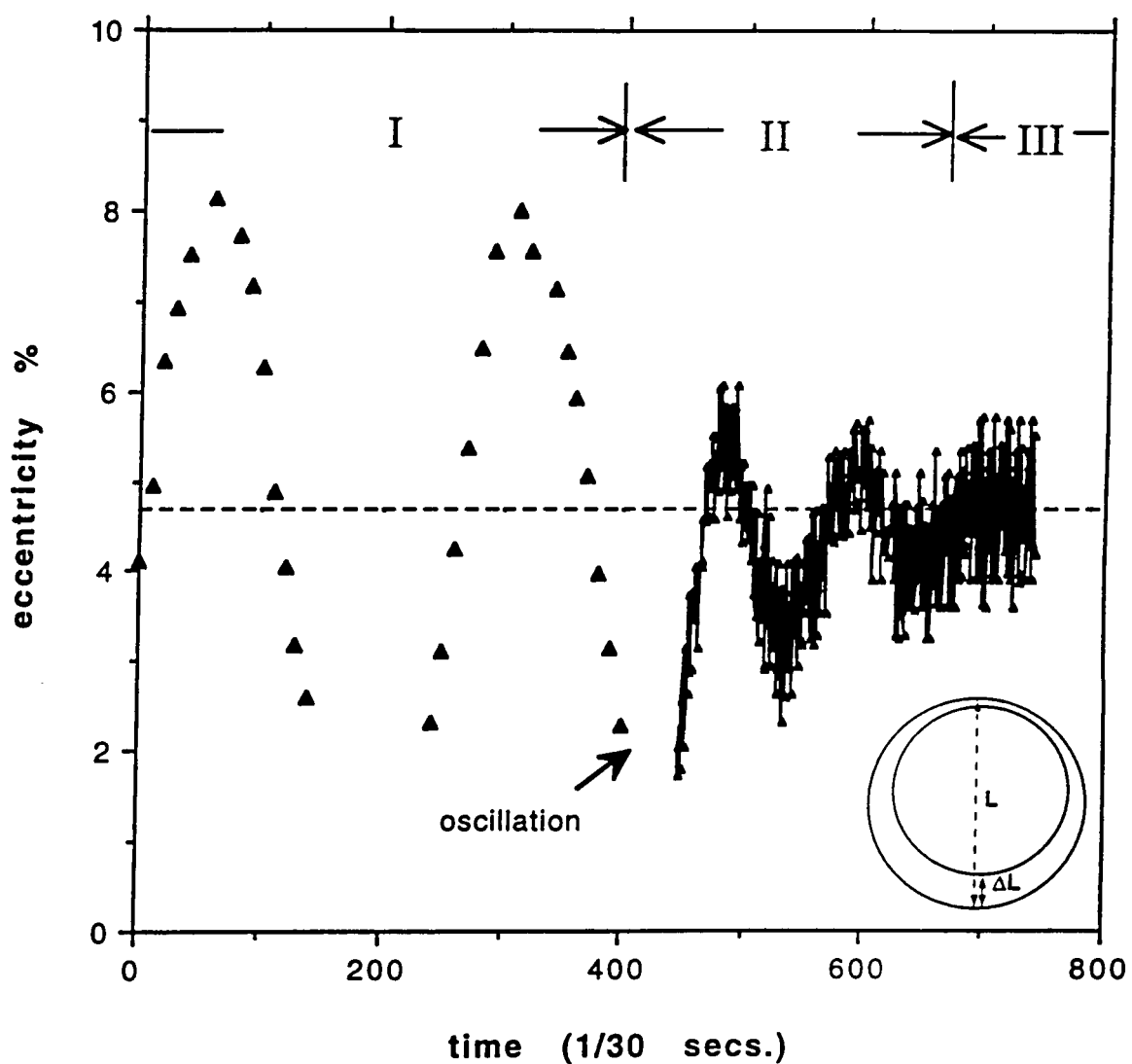


Figure 4 Plot of percentage eccentricity ($\Delta L/L * 100$) versus time for $n = 2$ bubble mode of the water shell.

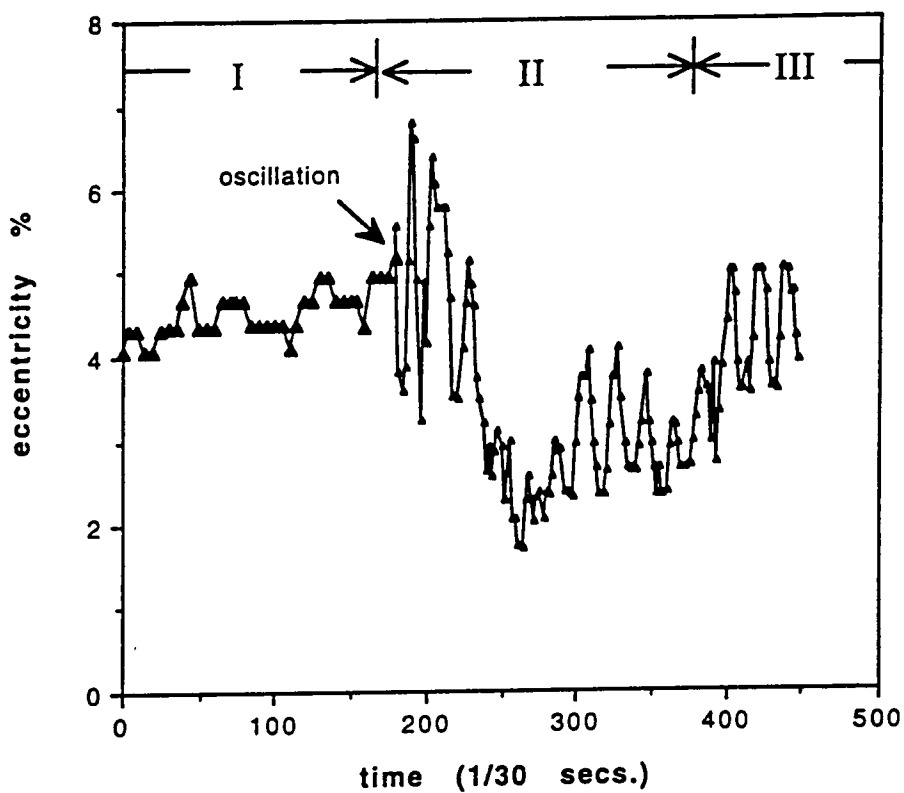


Figure 5 Plot of percentage eccentricity ($\Delta L/L * 100$) versus time for $n = 2$ slosh mode of the water shell.

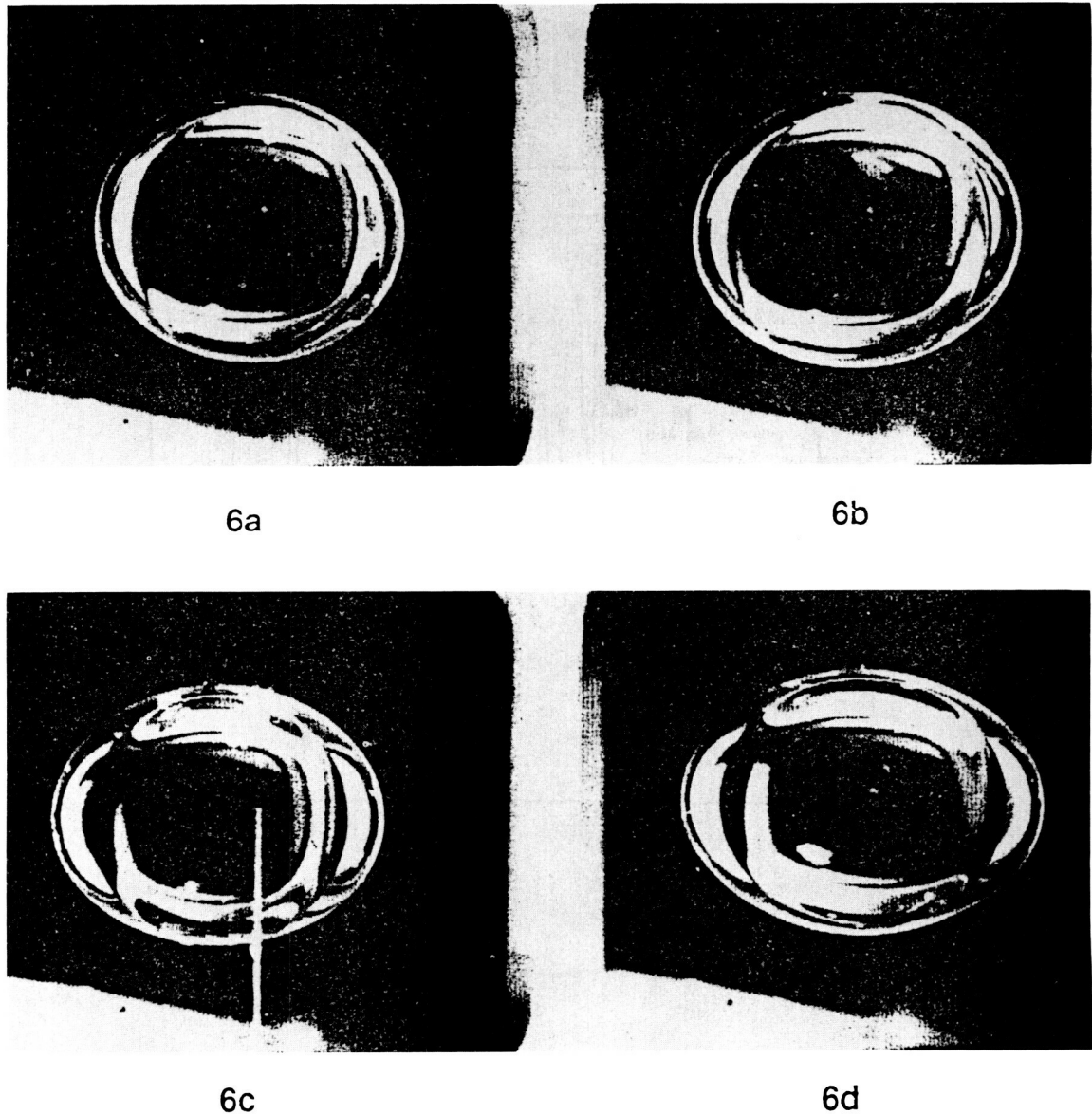


Figure 6 Progressive centering of the liquid-core compound drop during $n = 2$ bubble mode oscillations with a strong $m = \pm 2$ component (Figures a, b, c, d represent the shapes during the extremum of the oscillations).

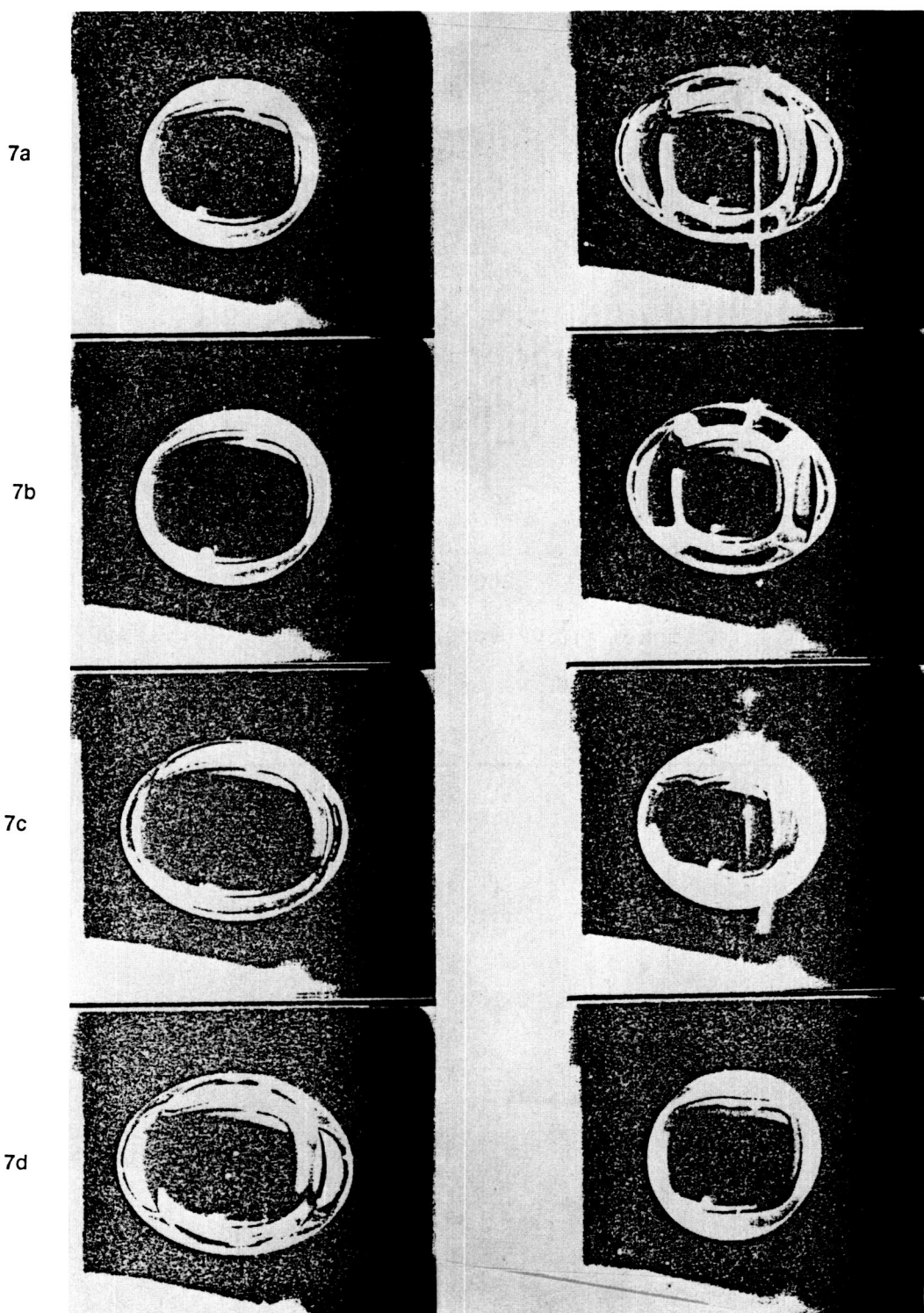


Figure 7 A complete $n = 2$ bubble-mode oscillation following centering of the liquid core.

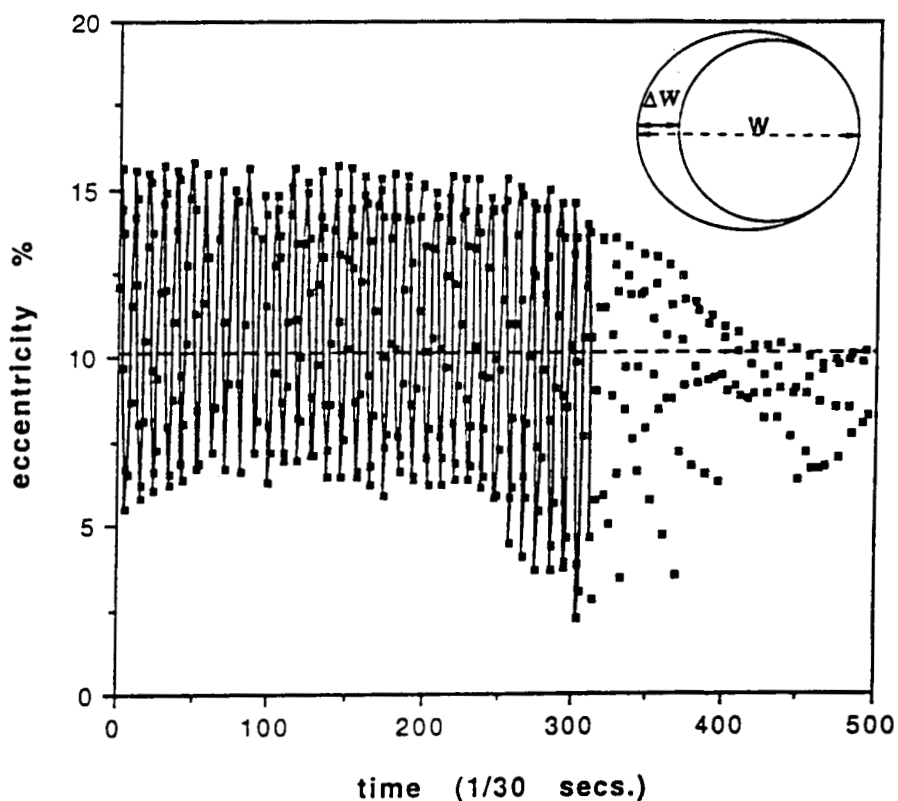


Figure 8 Plot of percentage eccentricity ($\Delta W/W * 100$) versus time for Figure 6 (a, b, c, d).

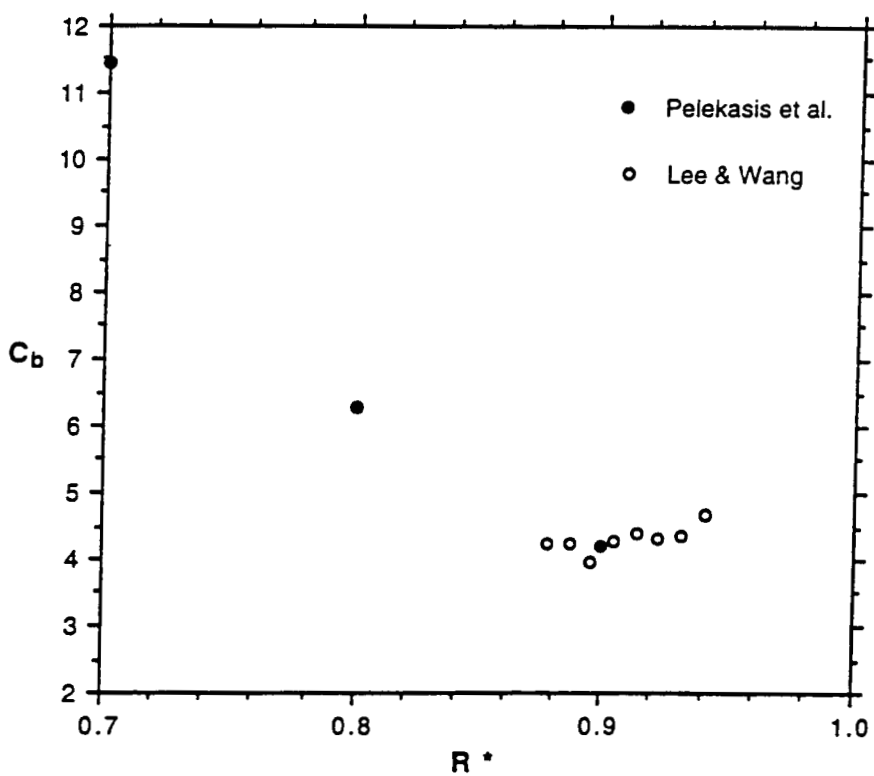


Figure 9 C_b versus R^* . White squares: Lee and Wang 1988, black squares: Pelekasis et al. 1990.

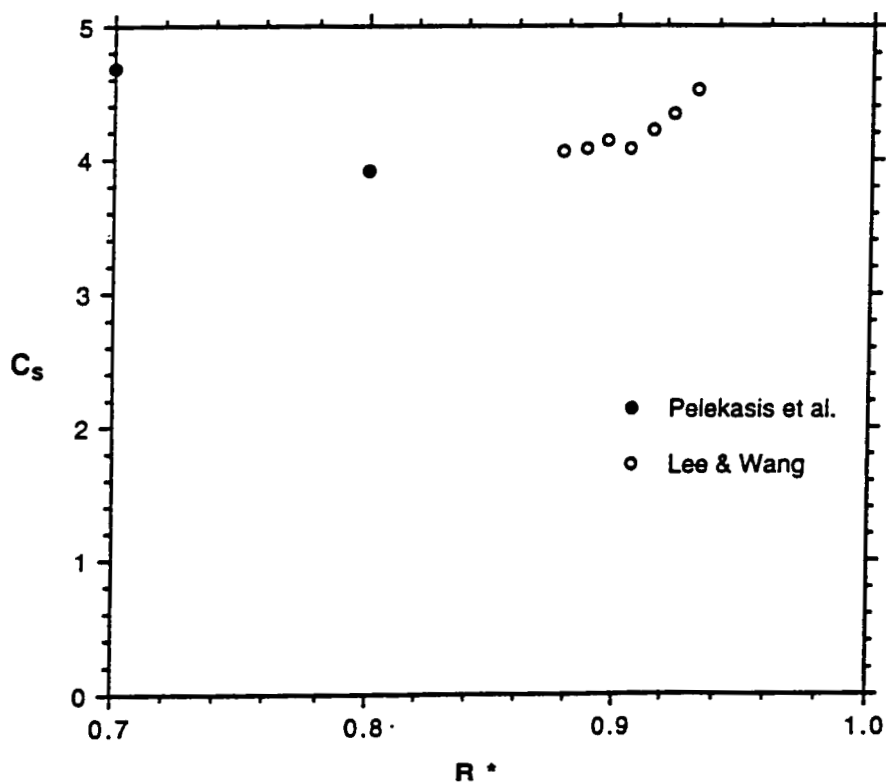


Figure 10 C_s versus R^* . White squares: Lee and Wang 1988, black squares: Pelekasis et al. 1990.

Discussion

Question: Could you comment on the interplay between viscous and inertial forces in the centering process?

Answer: We don't know how to comment. We are looking at it. We think that the viscous force is very important. I believe that all the calculations currently assuming viscosity as a perturbation are probably incorrect. That is what the data suggests to us but not the calculations, but we are looking at it.

Question: Wouldn't that be particularly important if the density difference is only a couple percent and could that sabotage your whole program?

Answer: It won't sabotage my program. We will just have to find a more ingenious way to do it, that's all. No. Actually the viscous force, we believe, manifests itself both in the liquid core as well as in the liquid shell. The data shows us that those are both equally important and if I had to draw a tentative conclusion, the tentative conclusion is the viscosity effect is very much stronger than predicted.

Question: In the data you showed, where you did a compound liquid droplet what were the two liquids that you used and what were their viscosities?

Answer: Silicon oil, water, and glycerin.

Question: In order to be able to see your data better why don't you color the inside droplet, so that when you are trying to do your data reduction you can see it a whole lot better?

Answer: We did, but it did not do any good on USML-1. We will try it again with a different color. We were using a green color and the sensor recordings did not come out very well. Part of the reason is that we have a lighting problem, the light was just not bright enough and that made life very difficult. During the investigation, I got a little bit involved in the medical-biotechnology and then I started to appreciate it. The human body is a remarkable system, particularly the eye and the eye could just barely make it out. We are hoping on USML-2 it will be better.

18pg

19751071305

N95-14219

324084

11024

BIFURCATION OF ROTATING LIQUID DROPS: RESULTS FROM USML-1 EXPERIMENTS IN SPACE

P. 17

T. G. Wang, A. V. Anilkumar, C. P. Lee, and K. C. Lin

Center for Microgravity Research and Applications
Vanderbilt University, Nashville, Tennessee.

SUMMARY

Experiments on rotational bifurcation of liquid drops, in which the drops were levitated and spun using acoustic fields in a low-gravity environment, were conducted during the USML-1 Space Shuttle flight. The experiments have successfully resolved the discrepancies existing between the previous experimental results and the theoretical predictions. In the case of a spherical drop, for which theory exists, the results agree well with the predictions. In the case of flattened drops, the experiments have established a family of curves, with the spherical drop as the limiting case.

INTRODUCTION

The phenomenon of bifurcation of a rotating liquid drop was first observed by Plateau (1863), as a model for a rotating liquid mass held by self-gravity. In his experiment, liquid drops were held and rotated by a shaft in a liquid medium of almost the same density. Beside the solid supporting device, his drops were necessarily influenced by the viscous friction with the outer liquid. We have performed the experiments for liquid drops in air without these limitations, using acoustic force for positioning and acoustic torque for rotation, in the microgravity environment of space.

When a spherical liquid drop, held together by surface tension, undergoes a solid body rotation about an axis in a less dense medium, its shape becomes oblate, with its liquid displaced away from the axis due to centrifugal force in the new equilibrium configuration. With increasing rotation rate, the equilibrium shape becomes more and more flattened, then becomes concave at the top and bottom surfaces, until eventually the two surfaces merge and the central membrane breaks. In reality, however, the drop finds a non-axisymmetric route to equilibrium, which leads to two-lobed ($n=2$) bifurcation, as the rotation rate reaches a certain critical value before the drop becomes concave (Chandrasekhar 1965). The $n=2$ bifurcation branch, of the maximum dimension versus rotation rate curve, has been calculated, among others, by Brown and Scriven (1980). With increasing angular momentum, as the drop

approaches the other end of the bifurcation branch, at one point, the two-lobed shape turns from stable to neutrally stable, and then unstable, with the drop eventually fissioning.

The experiments have been conducted using acoustic fields. It is known that a standing sound field, through its acoustic radiation pressure, can provide a potential well at a pressure node for levitating a small sphere (King 1934). It is also known that two sound fields vibrating in perpendicular directions, at the same frequency but out of 2-phase to generate a circular motion in the medium, can exert a viscous torque on the sphere (Busse and Wang 1981). These are the main principles behind the present apparatus as well as the Drop Dynamics Module (DDM) used in the previous space experiments (Wang et al. 1986).

In the previous space-based experiments, while there was a general qualitative agreement with the theory, there was also some discrepancy between the data and the theoretical curve which needs to be resolved. Rhim et al. (1988) performed the experiments in a ground-based study using charged drops levitated in an electrostatic field and rotated using an acoustic torque, obtaining an $n=2$ bifurcation point close to the theoretical prediction. But the use of electric charge and field introduces some uncertainty into the validity of the comparison. Biswas et al. (1991) studied the bifurcation of ground-based acoustically levitated and rotated drops in comparison with the 1986 space experiments. Although the outcome of their experiments was necessarily biased by gravity, their data has a signature that seems to corroborate that of the earlier space flight results. We shall address this point later.

For the bifurcation study, the results are conveniently displayed in a plot of the dimensionless radius R^* ($R^* = R_{\max}/R$) with the dimensionless rotation rate Ω^* ($\Omega^* = \Omega/\omega_0$). Here, R_{\max} is the maximum radial position of the axisymmetric or nonaxisymmetric drop surface in the equatorial plane from its central axis in gyrostatic equilibrium, R is the spherical radius of the drop, Ω is the drop rotation rate and $\omega_0 = (8\sigma/\rho R^3)^{1/2}$ is the $n=2$ oscillation frequency of the drop; with σ being the surface tension and ρ being the density of the drop liquid.

I. EXPERIMENTAL APPARATUS AND PROCEDURE

The experiments were performed in the Drop Physics Module (DPM; Figure 1) of the United States Microgravity Laboratory-1 (USML-1) on board the Space Shuttle Columbia (STS-50) during its flight from June 25 to July 9, 1992, by astronauts Eugene Trinh and Bonnie Dunbar.

In the DPM, an injector for deploying drops consists of two similar arms sticking from the middle of two opposite vertical edges to meet at the center of the chamber when demanded, one of which contains the injector tube for the liquid while the other provides the mechanical means to hold the drop during the injection. Two types of liquids are used for the experiments: (1) silicone oil and (2) water-glycerine mixtures. Since they have different wetting properties, they are handled slightly

differently. For deploying a silicone oil drop, a flat-tip injector is used such that a liquid column is sandwiched between two flat plates during injection (Figure 2). When the desired amount of liquid has been put into place, the arms are suddenly withdrawn, leaving the drop levitated at the center. The same procedure is used for water-glycerine drops, except that a needle-tip injector is used, such that the drop is held between two needle tips initially (Figure 3). A simple tip-to-tip deployment is the desired method, whereby a quiescent spherical drop can be deployed at the center of the chamber, and trapped by the acoustic potential well.

Since this is mainly a study of the solid body rotation of drops, transient dynamic situations such as those during the spin-up or spin-down process must be minimized as much as possible. Since the relaxation time for a drop to adjust to a new rotation rate is estimated to be R^2/v , where R is the radius of the drop and v is the kinematic viscosity of the liquid, high-viscosity liquids were used. The practical absence of gravity allows for the study of large drops, and the drop sizes are only limited by how much of a drop can remain in view through the windows while it is deformed by rotation.

Silicone oil is the best choice since, unlike water, for example, its surface tension is not very sensitive to contamination. This fact is important, considering that because of the flight planning, the liquids had to be prepared and stored for months before the flight. Pure water was also not used because of its low viscosity, which means long relaxation time. Glycerine/water (82/18 and 87/13 by weight) solution was used instead. The properties of the liquids used are listed in Table 1. Pliolite tracer particles (Goodyear Chemical Co.), about 50-100 μm in size, are mixed with the liquids during preparation, for the purpose of identifying solid body rotation and determining the rotation rate. The volume of the drop is calibrated against a perfectly machined 2.54 cm plastic ball when the latter is held at the center of the chamber by the injector arms. The uncertainty in the volume determination is less than 3%.

For the bifurcation study, a drop is levitated and rotated about the z-axis using about 145 dB of sound pressure level along each of the axes. Minimum acoustic pressures are used to avoid deforming the drop. The rotation rate is increased stepwise a bit at a time, allowing plenty of time for the drop to relax in order to ensure solid body rotation. Experimentally, the drop stays at a fixed position and rotates steadily in gyrostatic equilibrium after its rotation rate has increased past a certain point; thereafter, usable data can be taken. Most measurements of the drop size R_{\max} were made using the top-view (z-view), where the measurements were insensitive to any small movements of the drop. Most experiments were conducted at temperatures between 23.5° to 26.5° C. The average temperature for each of the drop, has been indicated below.

II. RESULTS

A. Data from glycerine/water drop (82/18)

This solution was colored with a green food-coloring dye (McCormick), 0.1% by volume. The measurements shown in Table 1 for this 82/18 solution were made on the ground from the leftover samples.

In Figure 4 we show the data by plotting R^* versus Ω^* for controlled spin-up and controlled spin-down of a 2.5 cc drop, where 'controlled' means 'changing the torque in small steps one at a time,' with the rotation rate scaled with the measured value of ω_0 . The experiment actually involved many spin-ups, spin-downs and bifurcations of the same drop, and the data points shown in Figure 4 represent the runs in which we are satisfied that the drop was in stable levitation and gyrostatic equilibrium. The axisymmetric curve lies slightly above, and the bifurcation branch lies slightly to the left, of the curves predicted by Brown and Scriven (1980).

In Figure 5 we show the data for a similar experiment with another drop in this session, with the drop significantly flattened by the z-drive during spin-up. The drop has a volume of 1.55 ± 0.05 cc, and was deployed by a tip-to-tip injection between fresh tips (Figure 3). The average temperature during the experiments was 24°C. The deformation before the rotation started, defined as $(a/b-1) \times 100\%$, where a and b are the equatorial and polar radii, respectively, was about $25 \pm 2\%$. For the spin-up, the axisymmetric curve lies well above, and the bifurcation branch lies well to the left, of the predicted ones. The value of Ω^* at bifurcation from the spin-up curve is about 0.47, which is significantly lower than the theoretical value. The bifurcation branch shoots vertically upward such that R^* increases by 10-15% at constant Ω^* before bifurcation; it is noteworthy that bifurcation does not occur at the turning point but a bit above it. Thus the bifurcation point is not well-defined for such a drastically flattened drop. The bifurcation branch continues to rise vertically to intersect the theoretical bifurcation curve until fission occurs. The spin-down was achieved by lowering the z-drive close to (but slightly above) the x- and y-levels, and releasing the torque as opposed to a controlled spin-down. Since the torque was released when the drop was high up on the bifurcation curve, the drop, with its high viscosity, has enough time to relax back to equilibrium not too far down the curve. The rest of the spin-down curve and the associated bifurcation point agree well with the theory.

B. Data from silicone oil drop (DC 200 series, 100 cst)

The first silicone oil drop had a volume of 2.90 ± 0.05 cc. The average temperature during the experiment was 22.5°C (for which the surface tension is corrected from its value at 25°C in Table 1 at -0.08 dyn/cm/°C). The initial deformation of the drop due to the z-drive was about $5 \pm 1\%$. The torque was carefully raised in the spin-up. Starting from an axisymmetric shape, the drop went through bifurcation to the two-lobed shape, and then all the way to fission. As seen in Figure 6, the agreement with the theory

is good; except in the unstable two-lobed region where fission occurs. This issue will be taken up in the future.

The experiment was repeated with a second silicone oil drop of volume 2.80 ± 0.05 cc at an average operating temperature of 25°C (Figure 7). In one run, the drop was spun step-by-step beyond bifurcation and then allowed to spin down with all acoustics turned off, starting from a point on the bifurcation curve about the same as that for the last run. The data, with all acoustics off, cannot be plotted because the dimension of the drop changed as it moved out of the field of view of the cameras in the absence of a restraining force. But the bifurcation point is estimated to be $\Omega^* = 0.563$, in good agreement with the theory. Finally, the drop was trapped and spun up past bifurcation to fission, with an initial flattening of $11 \pm 1\%$. As expected, there is a deviation from the theory as a consequence of the flattening (Figure 7).

In Figure 8, we show the photographs of the top view of a typical drop being spun up from rest, going through bifurcation to fission. During the fission (Figures 6,7), it is noted that $R^* \Omega^*$ is approximately constant, as is required by conservation of angular momentum.

The experimental uncertainty in Ω^* is 2%, and that in R^* is 2%. It is necessary to flatten the drops to impose a controlled rotation; however, if the imposed deformation is less than 5%, the uncertainty for Ω^* and R^* are within the aforementioned error bars.

III. COMMENTS

The experiments have been successful in resolving the discrepancies existing between the previous experimental results and the theoretical predictions. In the case of a spherical drop, for which theory exists, the results agree well with the predictions. In the case of flattened drops, the experiments have established a family of curves, with the spherical drop as the limiting case.

In the previous Spacelab experimental results (Wang et al. 1986; cf. Fig. 3), for the spin-up and fission of a 1 cc glycerine-water drop of 100 cSt viscosity, the bifurcation branch is well to the left of the ideal one, and crosses it later. The value of Ω^* at bifurcation is about 0.47 ± 0.04 , which is below the theoretical value of 0.56. Considering the qualitative similarity between these earlier results and the present results, shown in figure 5 for the flattened drop, and also those from the ground-based study using a single-axis levitator (Biswas et al. 1991), it is felt that the discrepancy in the earlier Spacelab results is due to drop flattening along the rotation axis by the acoustic radiation pressure. This has been confirmed by a re-examination of the initial non-rotating shape of the drop used in the earlier space experiments, the flattening being estimated to be about the same as that in the current Figure 5.

In a general context, a rotating drop with its 'elasticity' characterized by the $n=2$ oscillation frequency is not easily deformed by the acoustic pressure when it is still almost spherical. On the other

hand, at the bifurcation point where the stability is neutral, the oscillation frequency is zero and the drop is 'plastic' rather than 'elastic.' Therefore as the drop flattens with rotation when approaching the bifurcation point, it also becomes more susceptible to deformation by the acoustic pressure. In other words, the bias shows up at higher rotation rate. The bias tends to make the drop flatter even if the three waves are of the same amplitude, because after the drop becomes oblate with rotation, it scatters more z-wave than others with its larger projection on the equatorial plane, and thus sees the z-wave as the dominant wave.

With such a bias, it is obvious that the axisymmetric curve should shift upward. Since the angular momentum balance of an axisymmetric drop is not affected by flattening, it seems reasonable to assume that the bifurcation angular momentum is insensitive to the flattening. Also, for the same angular momentum, the axisymmetric drop has a higher R^* , thus a higher moment of inertia and a lower Ω^* . This possibly explains the leftward shift of the bifurcation point. Furthermore, when the drop becomes elongated, the acoustic radiation pressure continues to flatten it such that R^* rises more rapidly with decreasing rotation rate than the non-flattened counterpart. This possibly explains why the bifurcation curve for the flattened drop rises to intersect the ideal one on the Ω^*-R^* plane.

Another question is why the bifurcation point from the ground-based study (Biswas et al. 1991) of about $\Omega^*=0.44$ for an initial deformation of 21 % due to the levitating sound field, is lower than 0.47 for a drop of an even greater deformation of 25% in Figure 5, if we believe that the bifurcation point should go down with deformation. A reasonable explanation is that although gravity is much weaker than surface tension in the ground-based study, it can easily tip the energy balance at the bifurcation point, where surface tension is counteracted by centrifugal force to the point that the system is neutrally stable. Gravity tends to spread the drop out horizontally (like a drop on a table), increasing R^* and reducing Ω^* for the same angular momentum.

REFERENCES

1. A. Biswas, E. W. Leung and E. H. Trinh, "Rotation of ultrasonically levitated glycerol drops," J. Acoust. Soc. Am. 90, 1502-1507 (1991).
2. R. A. Brown and L. E. Scriven, "The shape and stability of rotating liquid drops," Proc. R. Soc. Lond. A 371, 331-357 (1980).
3. F. H. Busse and T. G. Wang, "Torque generated by orthogonal acoustic waves theory," J. Acoust. Soc. Am. 69, 1634-1638 (1981).
4. S. Chandrasekhar, "The stability of a rotating liquid drop," Proc. R. Soc. Lond. A 286, 1 -26 (1965) .

5. L. V. King, "On the acoustic radiation pressure on spheres", Proc. Roy. Soc. Lond. A147, 212-240 (1934).
6. J. A. F. Plateau, "Experimental and theoretical researches on the figures of equilibrium of a liquid mass withdrawn from the action of gravity," Annual Report of the Board of Regents of the Smithsonian Institution, pp. 270-285 Washington, D.C. (1863).
7. W. K. Rhim, S. K. Chung and D. D. Elleman, "Experiments on Rotating Charged Liquid Drops," AIP Conference Proceedings 197: *Drops and Bubbles 3rd International Colloquium, Monterey, CA, 1988*, ed. T.G. Wang (American Institute of Physics, New York 1989).
8. T. G. Wang, E. H. Trinh, A. P. Croonquist and D. D. Elleman, "Shapes of rotating free drops," Spacelab experimental results, Phys. Rev. Lett. 56, 452-455 (1986).

Table 1

Properties of the Liquids Used in the Experiments at 25°C

- measured from leftover flight liquids
- # measured from retained samples of the flight liquids
- ^ nominal values suggested by the manufacturer, or from standard tables

Liquids	ν (cSt)	ρ (gm/cc)	σ (dyn/cm)
Silicone Oil (DC 200 series)	100^	0.962#	21±0.2*
Glycerine/Water (82/18) (with 0.1% vol. green dye)	47^	1.209#	64.8±0.4*
Glycerine/Water (87/13)	87^	1.222#	64.4±0.4#

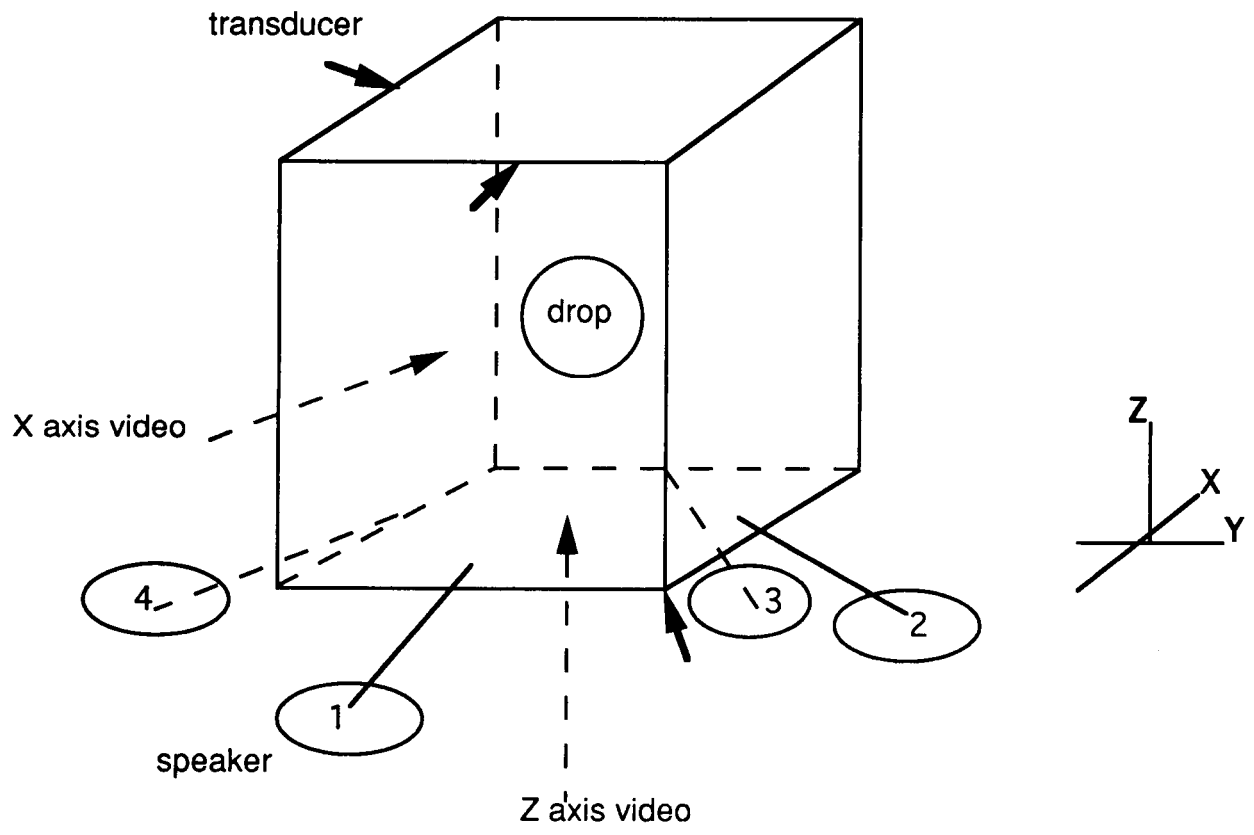


Figure 1 Schematic of the Drop Physics Module.

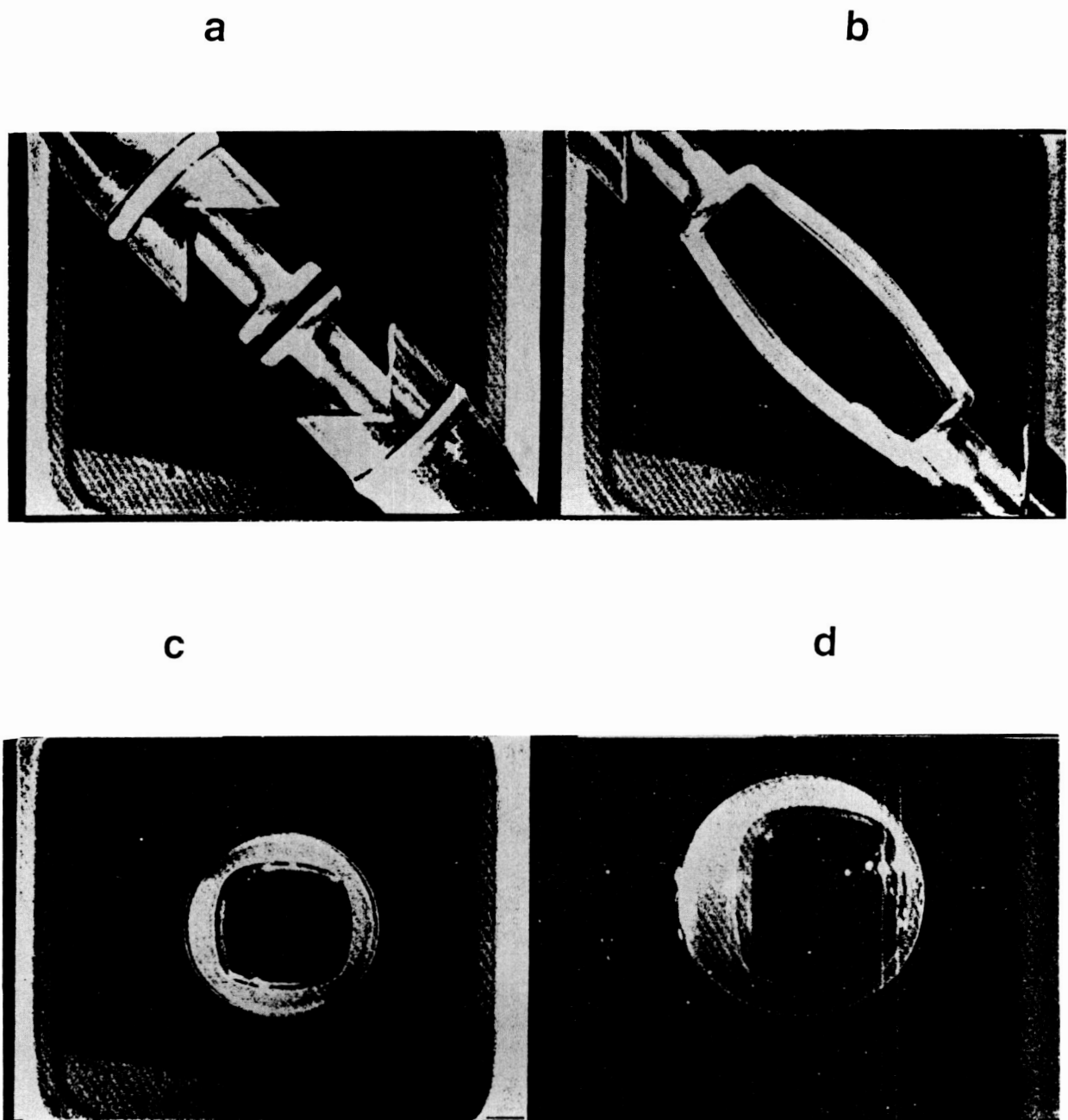


Figure 2 Deployment of a silicone oil drop: a) top view showing the flat injector tips, b) the injected liquid column, c) the deployed drop, d) side view of the deployed drop.

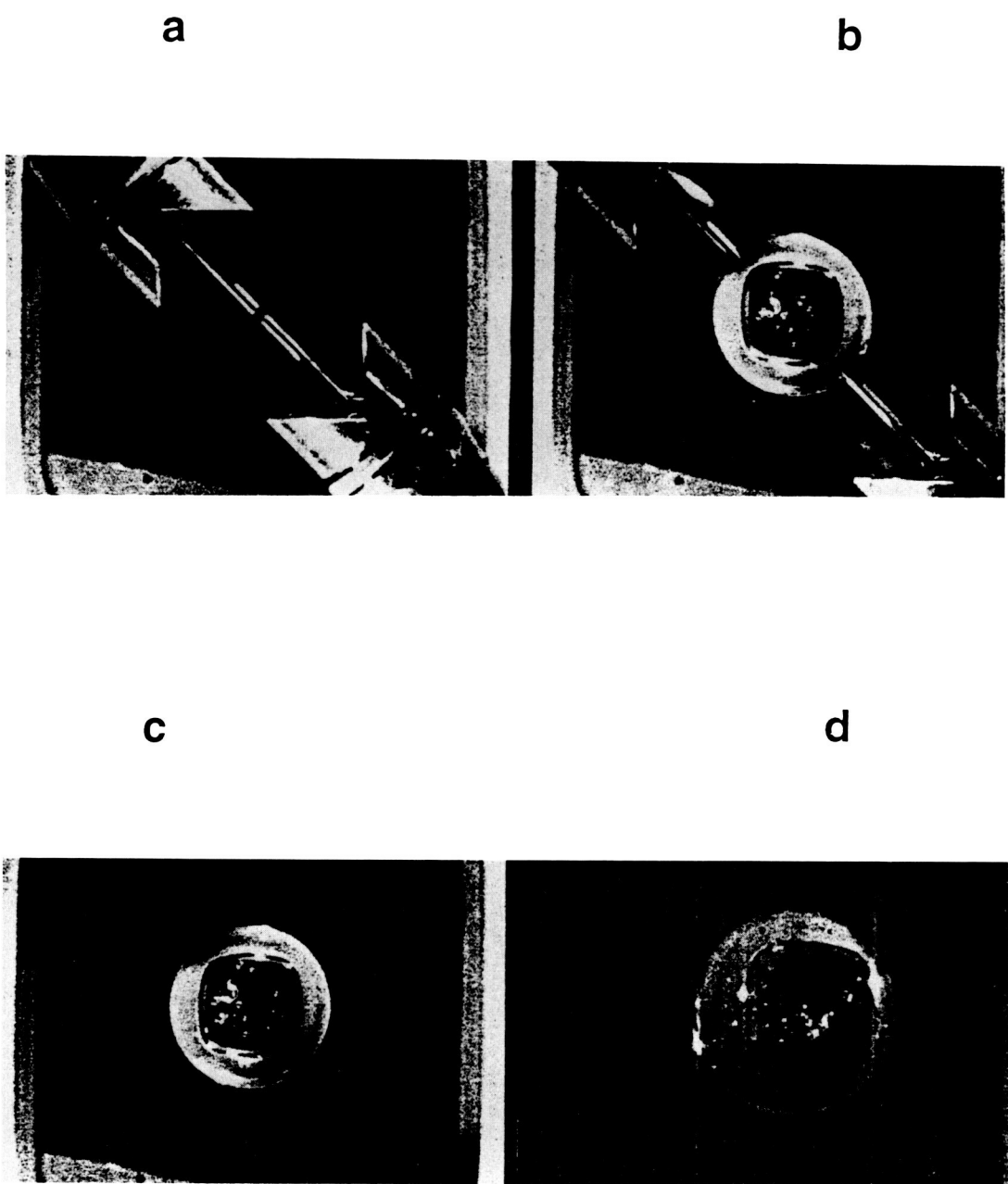


Figure 3 Tip-tip deployment of a glycerol-water drop: a)top view showing the needle tips, b) the injected liquid drop, c) the deployed drop, d) side view of the deployed drop.

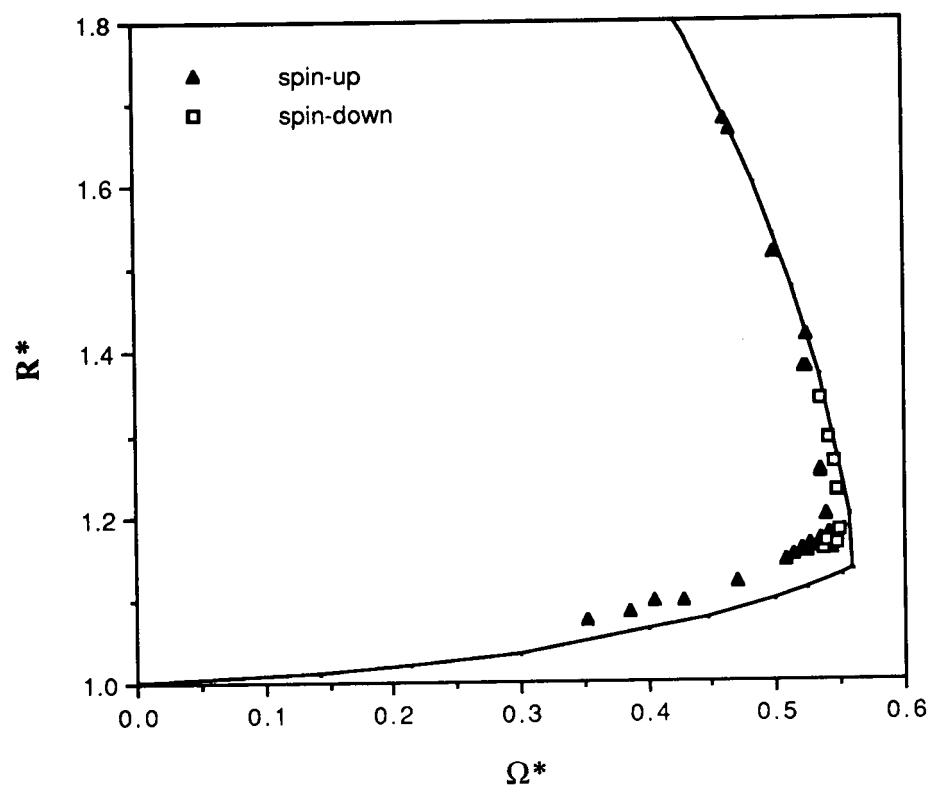


Figure 4 Bifurcation of 82/18 glycerine/water drop of 2.5 cc.

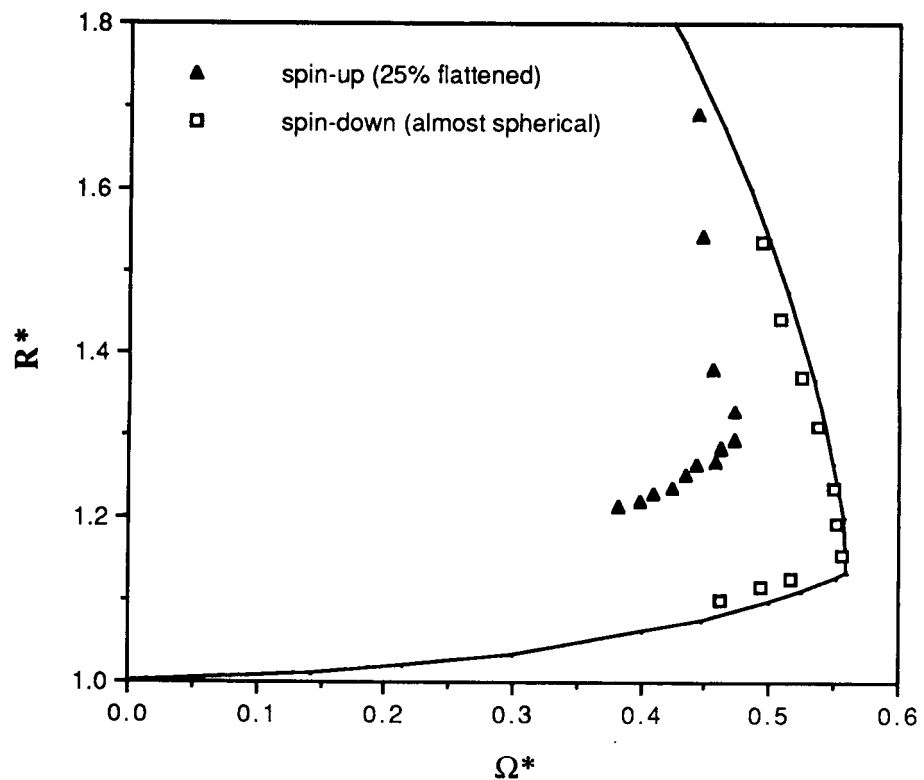


Figure 5 Bifurcation of 82/18 glycerine/water drop of 1.5 cc, the left curve was obtained by deliberately flattening the drop with the z-drive by 25%.

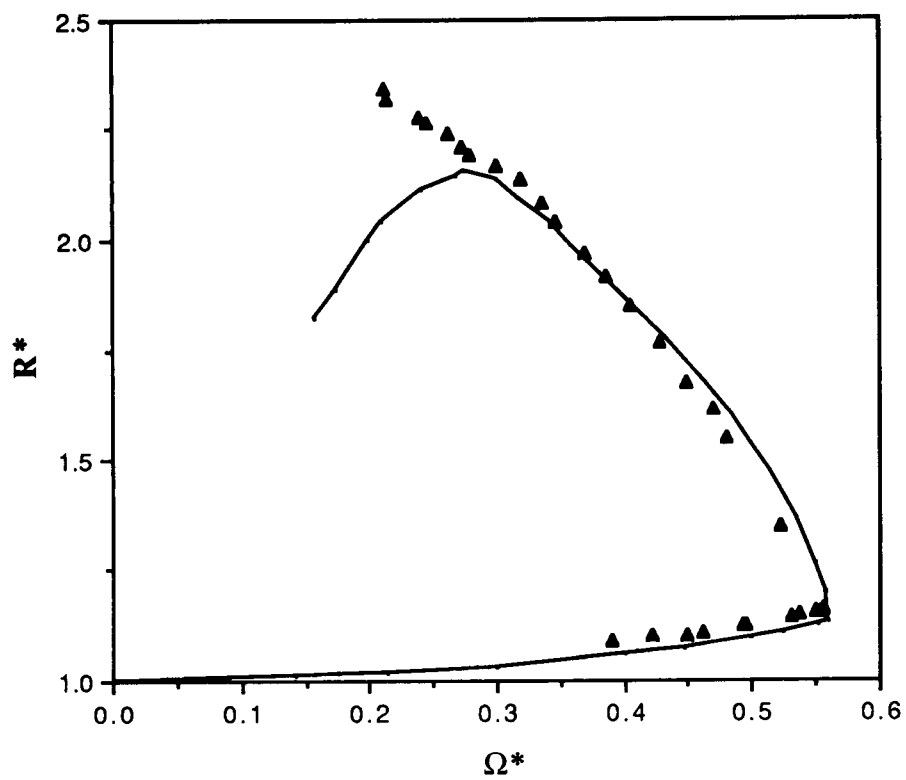


Figure 6 Bifurcation of the silicone oil drop of 2.9 cc to fission.

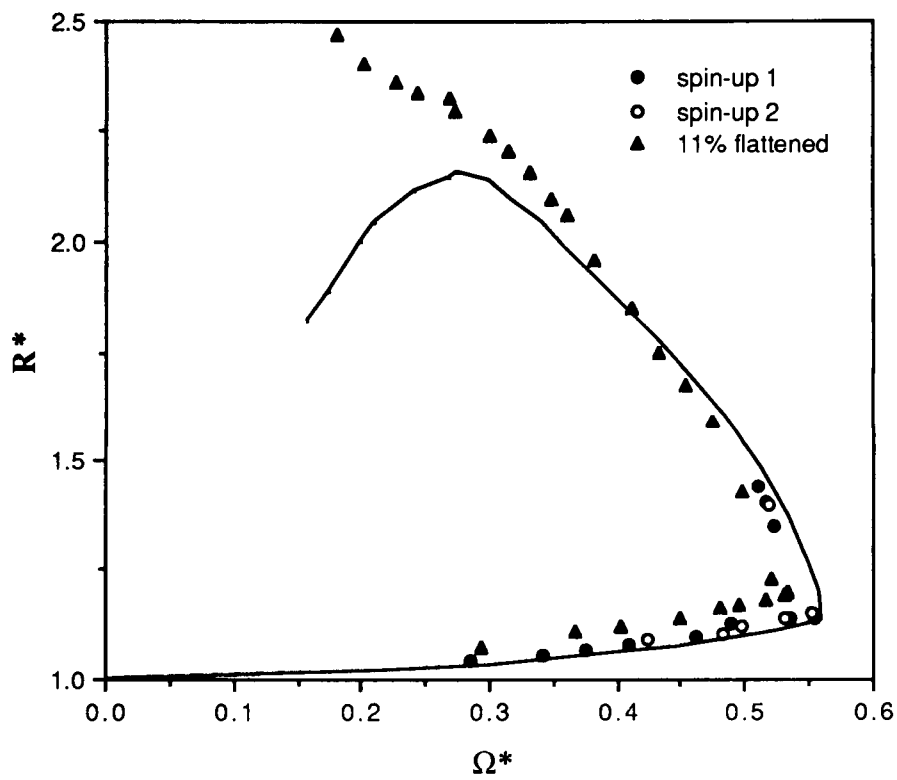


Figure 7 Bifurcation of the silicone oil drop of 2.8 cc (the data points leading to fission was obtained when the drop was flattened with the z-drive by 11%).

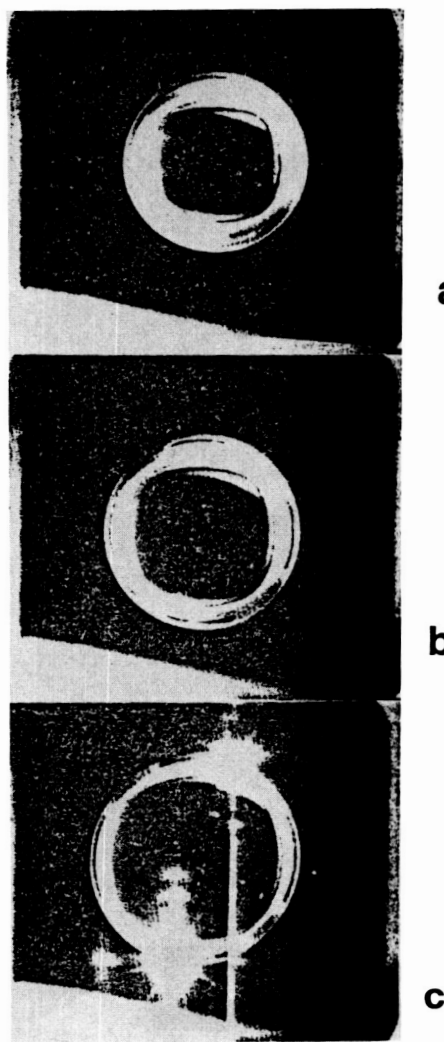


Figure 8 Photographs of the top view of a typical drop being spun up from rest, going through bifurcation to fission: a, b, c = axisymmetric shapes.



Figure 8 (continued) Photographs of the top view of a typical drop being spun up from rest, going through bifurcation to fission: d, e, f, g = two-lobed shapes.

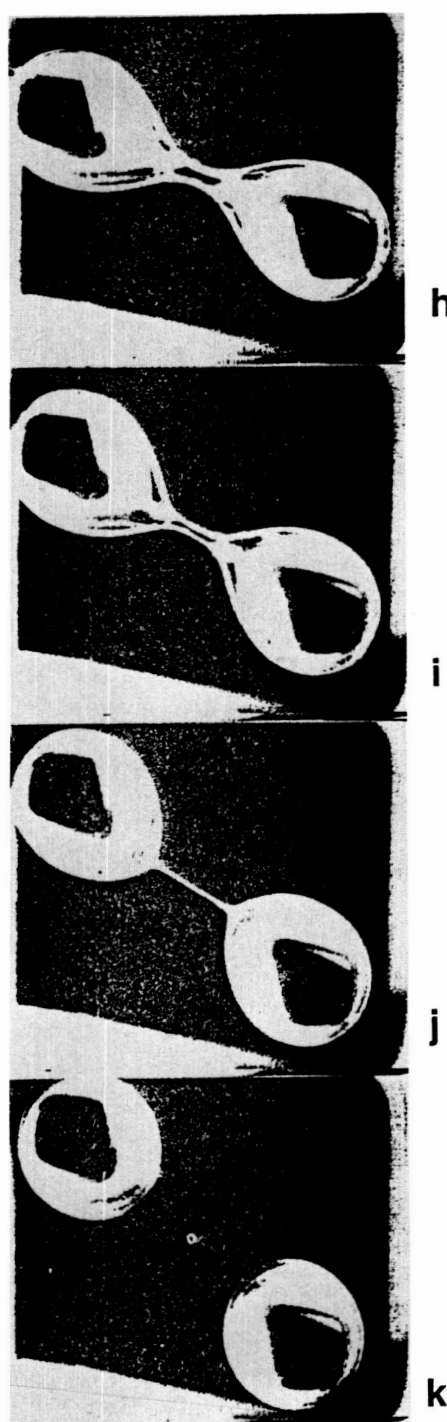


Figure 8 (continued) Photographs of the top view of a typical drop being spun up from rest, going through bifurcation to fission: h, i, j, k = necking and fission.

22P3

1715107806
324085

17025

SURFACE CHARACTERIZATION THROUGH SHAPE OSCILLATIONS OF DROPS IN MICROGRAVITY AND 1-g

Robert E. Apfel, R. Glynn Holt, Yuren Tian, Tao Shi, and Xiaoyu Zheng

Center for Ultrasonics and Sonics
Yale University, New Haven, CT.

P- 21

ABSTRACT

The goal of these experiments is to determine the rheological properties of liquid drops of single or multiple components in the presence or absence of surface active materials by exciting drops into their quadrupole resonance and observing their free decay. The resulting data coupled with appropriate theory should give a better description of the physics of the underlying phenomena, providing a better foundation than earlier empirical results could.

The space environment makes an idealized geometry available (spherical drops) so that theory and experiment can be properly compared, and allows a "clean" environment, by which is meant an environment in which no solid surfaces come in contact with the drops during the test period. Moreover, by considering the oscillations of intentionally deformed drops in microgravity, a baseline is established for interpreting surface characterization experiments done on the ground by ours and other groups.

Experiments performed on the United States Microgravity Laboratory (USML-1) demonstrated that shape oscillation experiments could be performed over a wide parameter range, and with a variety of surfactant materials. Results, however, were compromised by an unexpected, slow drop tumbling, some problems with droplet injection, and the presence of bubbles in the drop samples. Nevertheless, initial data suggests that the space environment will be useful in providing base-line data that can serve to validate theory and permit quantitative materials characterization at 1-g.

INTRODUCTION

A. Research Objectives

The primary goal of this research is to investigate the rheological properties of surfactant-bearing liquid drops. By comparing experimental results in the ideal environment of Spacelab to our theory for perfect spherical-equilibrium drops, the model can be validated. A generic theory which can handle arbitrary acoustic fields and static deformations can then be synthesized in order to have a technique for

studying static and dynamic surface properties for surfactant-bearing drops which can be successfully applied in 1g experiments.

B. Background and Motivation

Consideration of the fluid mechanical oscillations of a pure liquid drop yields unique and well known values for the frequency and damping of single (in the present case, quadrupole) mode shape oscillations about a spherical equilibrium. However, the viscoelastic properties of even dilute surface concentrations of surfactant material affect the motion of the interface, thus coupling the two problems. The decrease in interfacial tension will shift the frequency downwards. Convective transport of the surfactant during oscillations will redistribute the surface concentration of surfactant, resulting in surface tension gradients. If this is not quickly compensated for by diffusive/sorptive transport from the bulk, then the resulting surface stress will give rise to a retarding flow, increasing the effective damping of the mechanical oscillations of the drop. These effects are controlled both by the type and concentration of surfactant, and the relative time scales of the processes involved: diffusion, sorption, and oscillation. Quantifying these changes by inferring interfacial shear and dilatational viscosities from the measurements and theory will allow prediction of the effects of small concentrations of surfactants.

Microgravity affords a unique combination of advantages which facilitate the comparison with existing theory and the development of a testable theory for the 1g case. Drops with an arbitrary equilibrium shape can be produced. This is so because the weight of the drop need not be supported by the external acoustic field. For comparison with the "ideal" theory, low-amplitude, spatially symmetric acoustic fields can be used to observe oscillations of a drop in air about a spherical equilibrium. Nonlinear acoustic effects (which cause distortion and rotation in 1g) are eliminated. Finally, the static deformation (always present in 1g experiments) can be continuously varied, allowing for the validation of models for the pressure/deformation interaction. The eventual coupling of this model with the validated model for surfactant transport in spherical drops will allow for the isolation of the effects of surfactants from the fluid/mechanical effects on the drop dynamics. This will allow researchers to perform relatively inexpensive 1g experiments for surfactant rheology determination, since the microgravity-confirmed model will correct for the fluid-mechanical effects present in high acoustic fields in 1g.

I. THEORY REVIEW

A. Surfactant-bearing drop oscillations

Equations based on the work of Lu et al.¹ have been developed which relate the surface properties (elasticity, surface viscosities, surface concentrations) to the frequency and damping of free quadrupole-mode oscillations for water drops in air with surfactant dissolved in the drops. The equations

for diffusive transport in the bulk plus the equations for sorptive transport from the surface sublayer to the surface are coupled to the velocity field of the oscillation drop to provide a dynamic description of the problem. "Exact" numerical solutions and approximate analytic solutions are restricted to oscillations about a spherical equilibrium. The analytic results² can be described by the following equations, which assume that the sorption time scale << diffusion time scale << oscillation period, and that drops are large (>0.1mm) and viscosities small, comparable to water. [Other limiting cases of transport have been derived but are not included here.]

Transcendental equation for the droplet quadrupole shape oscillation:

The droplet shape is a function of time as $e^{-\alpha\omega t}$

where ω is the Lamb Frequency

α is the nondimensional coefficient

The transcendental equation for the droplet quadrupole shape oscillation is:

$$(\alpha x)^2 + P - 12\beta_s + \left(\frac{x}{\alpha}\right)^2 + Q(\alpha x) \left[\frac{16}{\alpha^2 \chi^2} P \beta_s - (1 + \alpha^{-4})(3P - 4\beta_s) \right] = 0$$

where γ : surface tension

ρ, R, μ : droplet density, radius and (bulk) shear viscosity

β_D, β_S : surface dilatational and shear viscosity numbers

$\beta = -\partial\gamma/\partial 1n(\Gamma^*)$ surface dilatational elasticity

Γ^*, C^* surfactant surface and bulk concentrations

$$P = \frac{\beta \chi^2}{4G} + 2\beta_D$$

$$G = \alpha^2 - \frac{6}{y^2} + \frac{R\kappa C^*_{eq}}{z^2 \Gamma^*_{eq}} \left\{ \frac{\kappa_1}{2 - Q(\alpha z)} - \frac{C^*_{eq} D}{\Gamma^*_{eq} R} \right\}^{-1} \quad (1)$$

$$\chi^2 = \rho R^2 \omega / \mu, \quad y^2 = \omega R^2 / D_S, \quad z^2 = \omega R^2 / D$$

D, D_S surfactant bulk and surface diffusion coefficients

κ, κ_1 surfactant surface and absorption and desorption coefficients

$$Q(\alpha \chi) = \alpha \chi \frac{j_{l+1}(\alpha \chi)}{j_l(\alpha \chi)}, \quad j_l(\alpha \chi) \text{ is Bessel function}$$

Approximate solution:

Assuming

$$\alpha^2 = i(1+\epsilon)$$

$$\epsilon = 0.0 \sim 0.1, \quad \beta = 0.0 \sim 1, \quad \beta_d = 0.0 \sim 10, \quad \beta_s \sim 0$$

For diffusion controlled surface transfer

$$G = 1 - jR^{3/4}/\lambda$$

$$\text{where } i = \sqrt{-1}, \quad j = \sqrt{i}$$

$$\lambda^2 = 8\gamma(\partial\Gamma^*/\partial C^*)^2/D$$

then

$$\epsilon = \frac{\frac{\beta\chi^2}{4G} - 10i - 2\beta_d i + 4\left[\frac{\beta}{G} + \frac{32(1-\beta_d)}{\chi^2}\right](\chi j - 5i)}{2\chi^2 - \left[4(1-3\beta_d) - \frac{3\chi^2\beta}{2G}\right](\chi j - 5i)} \quad (2)$$

In the experiments, droplets with different surfactant concentrations are excited into quadrupole shape oscillations. By measuring their resonance frequencies and free damping constants, ϵ can be determined as a function of the droplet size. When fitting these experimental data with Eq.(2), we can estimate the droplet surface tension, surface elasticity and surface viscosity.

Note

1. Generally speaking, the surface shear viscosity is very small and is negligible.
2. The assumptions of the values of ϵ , β and β_d agree with the experimental results.
3. Langmuir equations, $n = \Gamma^*_{eq}/\Gamma^*_{\infty} = C^*_{eq}/(C^*_{eq} + a)$ and $\gamma - \gamma_0 = -\Gamma^*_{\infty}RT\ln(1-n)$, are used to express the relationships between the surface tension and the surfactant concentration. These equations, which are valid for the surfactant system at low concentrations, are widely used in the literature.

As an example of both exact and approximate solutions, Figure 1 shows the predictions for non-dimensional frequency and damping, plotted vs. surface dilatational elasticity. Similar agreement is found in plots vs. surface dilatational viscosity number. This theory is applied to ground-based experimental results presented in section 3 in order to infer surface properties. (This work will be reported in detail in an article to be submitted to the Journal of Colloid and Interface Science.)

B. Acoustic radiation pressure effects on drop deformation and location; Oscillation frequency shifts.

The importance of understanding the effects of the acoustic field on shape oscillations can be clarified with the aid of Figure 2. When a drop is spherical, the surface tension always serves to restore a deformed drop to its spherical shape. This is true, because work is done to increase the surface area

from the spherical to non-spherical shape. But if a drop is deformed by an acoustic (or any other) field, then a change of this shape toward the more rounded shape actually requires negative work (because the surface area is getting smaller). The restoring force for this motion is not the surface tension, but rather the acoustic field. Therefore, if one oscillates drops about a deformed shape, one must understand in detail the role of any fields that exert a body force on the drop.

The acoustic scattering of a plane acoustic standing wave from a spheroidal drop has been treated theoretically, using the boundary integral technique. The assumptions of small deformations and spherical symmetry have been relaxed in this treatment, allowing the derivation of a self-consistent set of equations to be solved numerically for the unique combination of deformation and scattered acoustic field which solves the problem for known external pressure and drop properties (size, composition). This approach does not rely on small deformations and spherical harmonic expansions to derive the frequency of oscillations about such a deformed equilibrium shape as a function of the drop static deformation. The nonlinear coupling of the acoustic field to the drop during oscillation is explicitly accounted for in the description of the restoring force that returns a drop to its equilibrium state. Details of this procedure will be published by Shi.³

Two basic regimes of behavior are reviewed below.

B1. Small oscillations about a deformed shape

After specification of the velocity potential of zero on the surface, the drop position and shape are followed. Numerical damping is introduced until equilibrium is obtained. Then, the field conditions are perturbed in order to induce small oscillations about the deformed shape. Figure 3 shows an example in which a water drop with aspect ratio of 1.175 and $ka = 0.4$ (where k is the wave number and a is the spherical equilibrium radius) undergoes small oscillations. Both drop size and kinetic energy of the drop are shown as a function of time.

Plots of the results of the frequency of this oscillation vs. aspect ratio for a given ka are given in Section 3, when experimental results are reported. Two cases have been computed: the case of 0g and the case of 1g. By comparing these results with each other and with both ground-based and Spacelab experiments, one should be able to understand the role of the acoustic field in the oscillation dynamics and, therefore, be able to extract surface material properties from 1g experiments.

B2. Large-amplitude oscillations and unstable motions of drops

In this case the ultimate instability of an acoustically stressed drop is examined theoretically. Because the boundary integral method does not depend on small oscillations or spherical harmonic expansions, a completely general result can be obtained. For example, in the case of a water drop of 1.49 mm diameter and a frequency of 21.76 kHz (corresponding to $ka = 0.3$, which is similar to the ka

values of USML tests), it is found that at SPL of 167.2 dB the flattened drop becomes unstable and will break up, as shown in the sequence of Figure 4. These predictions are similar to experimental results reported by Lee et al.⁴

II. EXPERIMENTS

A. Ground-Based (1g)

Ground-based studies of shape deformation and oscillation inform microgravity work in two major ways: First, large numbers of carefully performed experiments with sophisticated diagnostic tools not possible in Spacelab provide invaluable experience in preparation for space-based work. Second, ground-based work will provide one test of new theoretical models for oscillations of a drop about a deformed shape. The ultimate test of the model will come in microgravity tests (as described in section 3.2)

An ultrasonic levitation cell operating at about 28 kHz has permitted a number of experiments with 1-3 mm diameter drops of water and aqueous solutions of surfactants. Experiments have included a) change in static deformation and position of drops as a function of the standing wave field strength (water drops only)⁵ b) determination of free decay frequency and damping constant for water drops and for drops with varying surfactant type and concentration (drops typically have an aspect ratio of 1.1 for these tests)[see ref. 2] and c) frequency of maximum deformation for forced oscillation of drops (water drops only).

A1. Deformation vs. position in an acoustic field, and the determination of surface tension.

Figure 5 shows four frames of the same drop but at four different acoustic field strengths, and thus four different deformations and positions. The white dots around the photographic image represents the theoretical predictions. Tian et al.⁶ have recently proposed a theory which allows one to predict the surface tension of an interface if one can measure the position change in the levitation field as a function of aspect ratio. For instance in Figure 6a there is a plot of the deformation and location of a water drop in an acoustic field of varying strength. In Figure 6b one finds the minimum deviation between theoretical predictions and the experiments of Fig. 6a by adjusting the surface tension coefficient in the theory. In the particular example, it is seen that the minimum deviation occurs for a surface tension of 71 dynes/cm.

A2. Frequency of shape oscillations of deformed water drops

Figure 7 shows 1g experiments of free decay frequency versus aspect ratio for drops with ka ranging from 0.49 to 0.56, along with the theory of Shi who adapts the boundary integral method (as

developed by Baker et al.⁷ and Baker and Lundgren⁸) for the case of an acoustic field. Theoretical results are shown for drops of $ka = 0.4$ and 0.6 . Frequency is normalized to the Lamb frequency (for quadrupole shape oscillations about a spherical shape). This agreement gives one confidence in the ability to apply this model to complex situations.

A3. Interfacial characterization of surfactant laden water drops

In Figure 8 measured free decay frequency and damping constant as a function of drop radius are shown for drops of three surfactant concentrations of N-octyl β -D-glucopyranoside, a nonionic surfactant. (Concentrations are given as fractions of the CMC, critical micelle concentration). The process of extracting interfacial elasticity and viscosity is as follows: The curves are least-squares fitted, as shown by two examples in the figures for frequency and damping constant. Values of the interfacial parameters that are consistent with that fit and the theoretical model can then be plotted, as shown in Figures 9 and 10. Fits have also been performed for two other surfactants (Sodium Dodecyl Sulfate, SDS, an anionic surfactant, and Dodecyltrimethyl-ammonium bromide, a cationic surfactant). These results will be reported in reference 2.

B. Spacelab (USML-1) Results

Microgravity results allow one to extract materials properties from the data and accepted theory for small shape oscillations of spherical drops. Even more importantly, once one knows the properties from the microgravity experiments, one can then see if one can retrieve the same results using oscillations about a deformed shape and a modified but untested theoretical model for this case. If the model is successful, then the microgravity results will have informed the ground-based studies, and interfacial characterization based on oscillations of deformed drops can confidently continue in ground-based research.

The Drop Physics Module flown on USML-1 was designed for acoustical control and manipulation of drops. In order to obtain data from shape oscillations, both the X and Z views of the Module were recorded on video tape for all events, and for some oscillations a split screen X and Z view were filmed at speeds up to 120 frames per second. The quadrupole oscillation should appear in its classical oblate-prolate form in the X-view, and as a circle of increasing or decreasing size in the Z-view. However, in most sequences there was also a bothersome rotation (at about one rotation per second) about an arbitrary axis (often close to the Y-axis). Since the shape oscillations were of the order of 2-4 Hertz, the tumbling rotation represented a severe challenge in the data analysis.

In Figure 11 data from the X-view of a water drop of 2.0 cm diameter is fit with a decaying sinusoidal curve. From this fitted curve one obtains both frequency and damping constant.

In one USML-1 experiment a drop of 2.0 cm diameter was oscillated about several different deformed shapes. For an acoustic frequency of 1125 Hz, $ka = 0.21$. The cine record of these experiments is plotted in Figure 12, along with Shi's predictions for the case of 0g (and $ka = 0.2, 0.4$, and 0.6). The trend and absolute magnitudes appear to be in reasonable agreement with theoretical predictions for $ka = 0.2$, but the errors in the measurement and data analysis are too significant to have confidence in extracting interfacial properties.

CONCLUSIONS

Ground-based and microgravity experiments and new theoretical models both for the shape oscillations of drops in acoustic fields of arbitrary magnitude and for the transport behavior of surfactants in drops make possible both a more complete understanding of drop dynamics (including the conditions for instability) and the ability to extract surface properties from shape oscillations data.

Although initial microgravity data was compromised by instrument performance, the data that was obtained validated the overall approach for studying drop dynamics and measuring materials properties. Future work will be directed at solving instrumentation problems and continuing ground-based theoretical and experimental research in preparation for future microgravity tests.

ACKNOWLEDGMENTS

The authors acknowledge the significant contributions of the Drop Physics Module team at the Jet Propulsion Laboratory (JPL) and at Loral Inc., and the talented efforts of the Payload Team of the USML-1 mission. This work is supported through a grant from NASA managed by JPL through contract 958722.

REFERENCES

1. Hui-Lan Lu and R. E. Apfel, *Shape oscillations of drops in the presence of surfactants*, J. Fluid Mech. 222, 351-368 (1991).
2. Y. Tian, to be submitted to J. Coll. and Interface Sci.
3. T. Shi, to be submitted to J. Fluid Mech.
4. C. P. Lee, A. V. Anilkumar, and T. G. Wang, *Static shape and stability of an acoustically levitated liquid drop*, Phys. of Fluids A, 3, 2497-2515 (1991).
5. Yuren Tian, R. Glynn Holt, Robert E. Apfel, *Deformation and location of an acoustically levitated liquid drop*, J. Acoust. Soc. Am. 93, 3096-3104 (1993).
6. to be published
7. G. R. Baker, D. I. Meiron, and S. A. Orszag, *Boundary integral methods for axisymmetric and three-dimensional Rayleigh-Taylor instability problem*, Physica 12D, 19-31 (1984).
8. T. S. Lundgren and N. N. Mansour, *Oscillations of drops in zero gravity with weak viscous effects*, J. Fluid Mech. 194, 479-510 (1988).

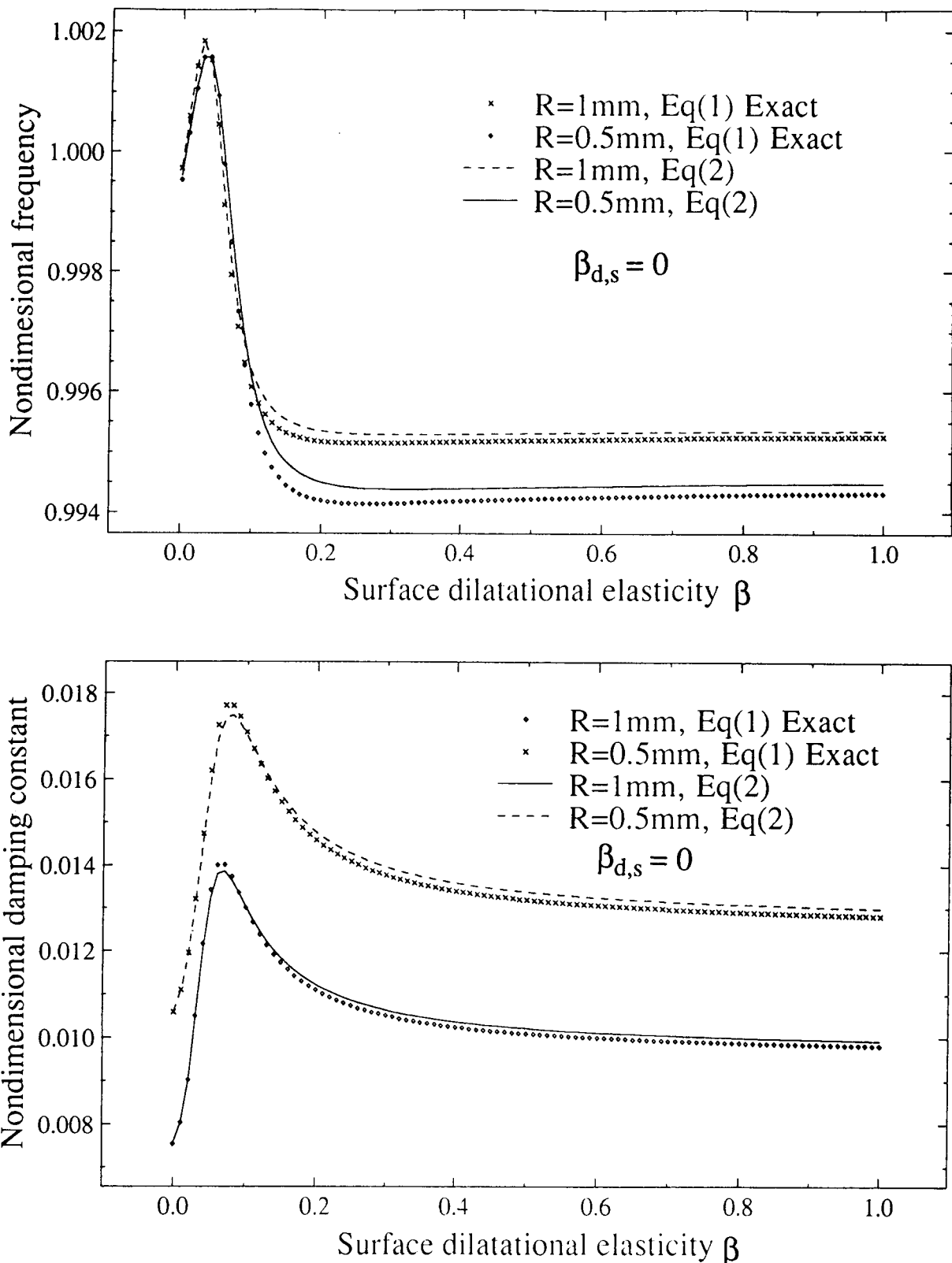
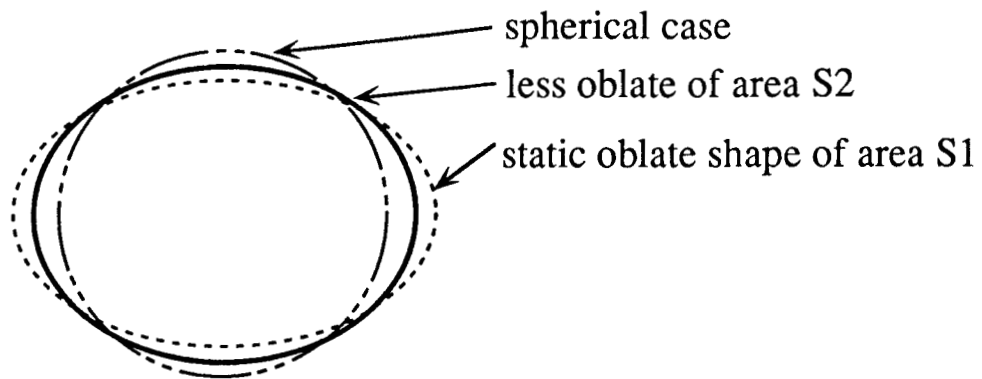


Figure 1a and b. Variations of the non-dimensional resonance frequency, Im (a), and the damping constant, Re (a), versus droplet surface dilatational elasticity. Here the surface dilatational and shear viscosities are zero.

Oscillations about deformed equilibrium

Effect on frequency



Drop	Restoring force
spherical equilibrium (low acoustic field)	\rightarrow prolate } - γ oblate }
oblate (S1) equilibrium (high acoustic field)	more prolate ($F_{rad} - \gamma$) more oblate ($\gamma - F_{rad}$)

∴ Oscillations nonlinearly coupled to acoustic field:

$$E_p \cong \gamma \Delta S + W_{rad}$$

Figure 2. Schematic showing shape oscillations about a deformed drop, and the relevant restoring forces.

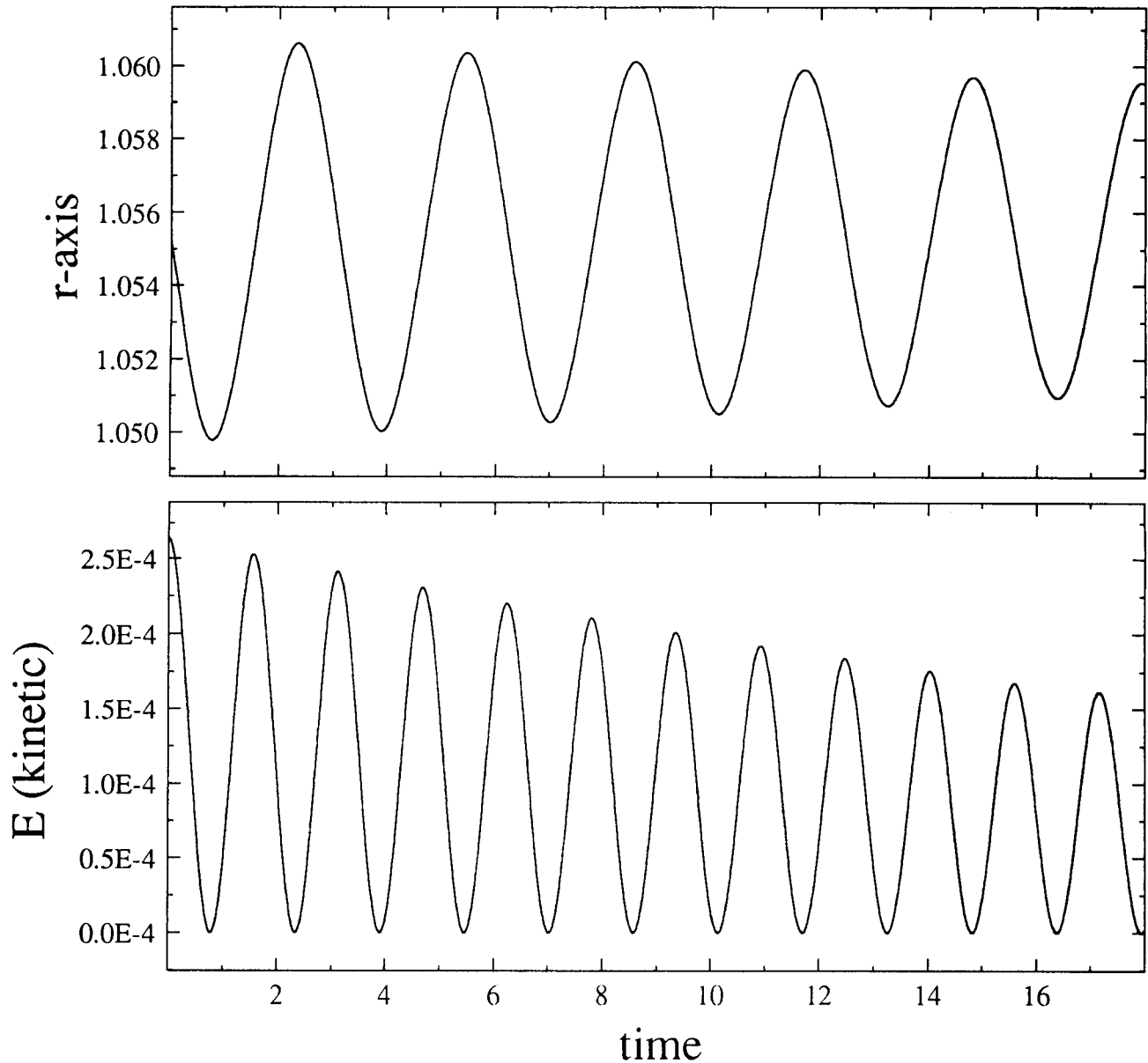


Figure 3. Predicted decay of acoustically deformed drop (aspect ratio 1.175; $ka = 0.4$) as seen through the r coordinate (lateral dimension) and the drop kinetic energy.

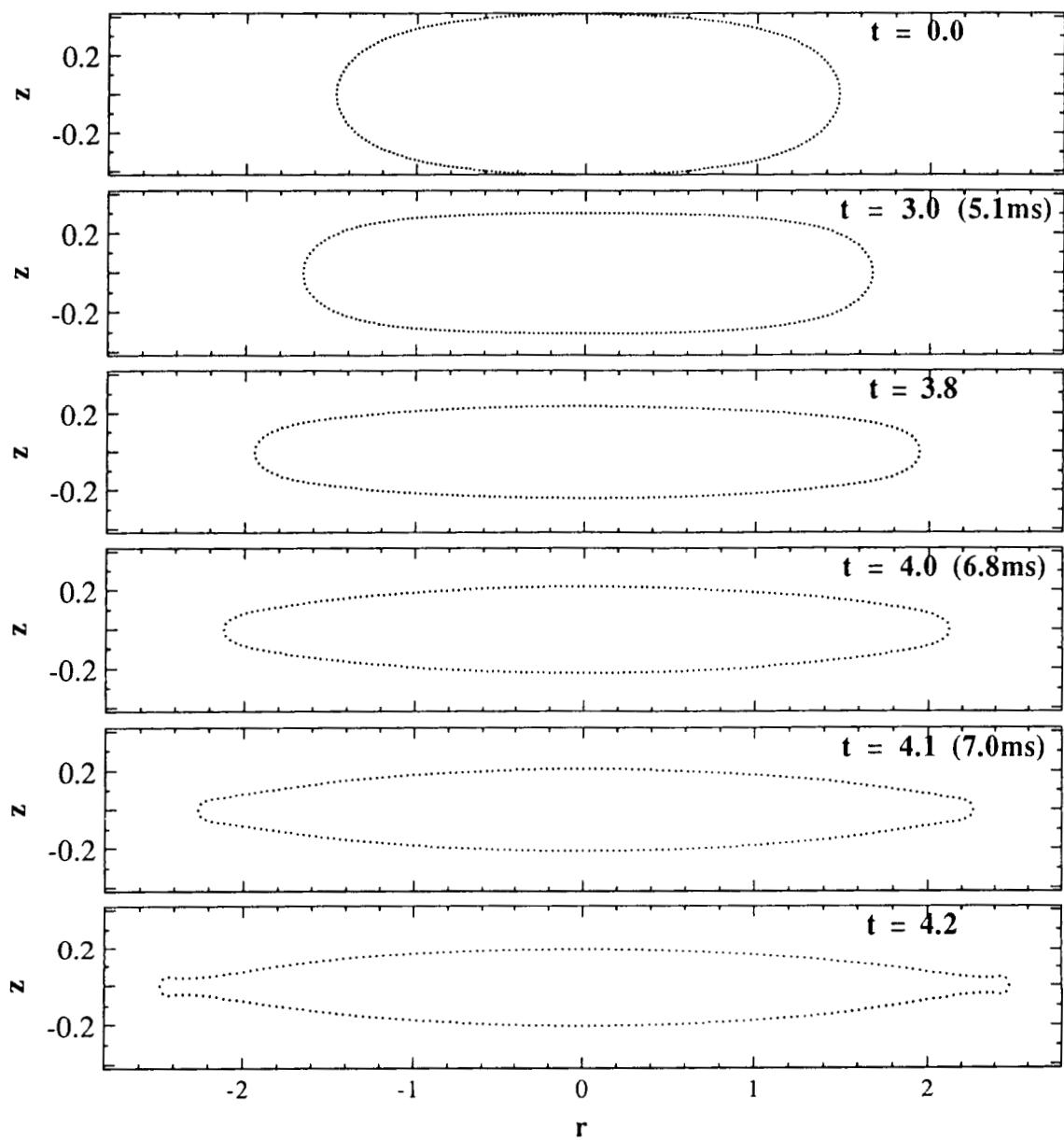


Figure 4 Sequence showing evolution of drop shape instability over a period of approximately 8 ms, for conditions described in text.

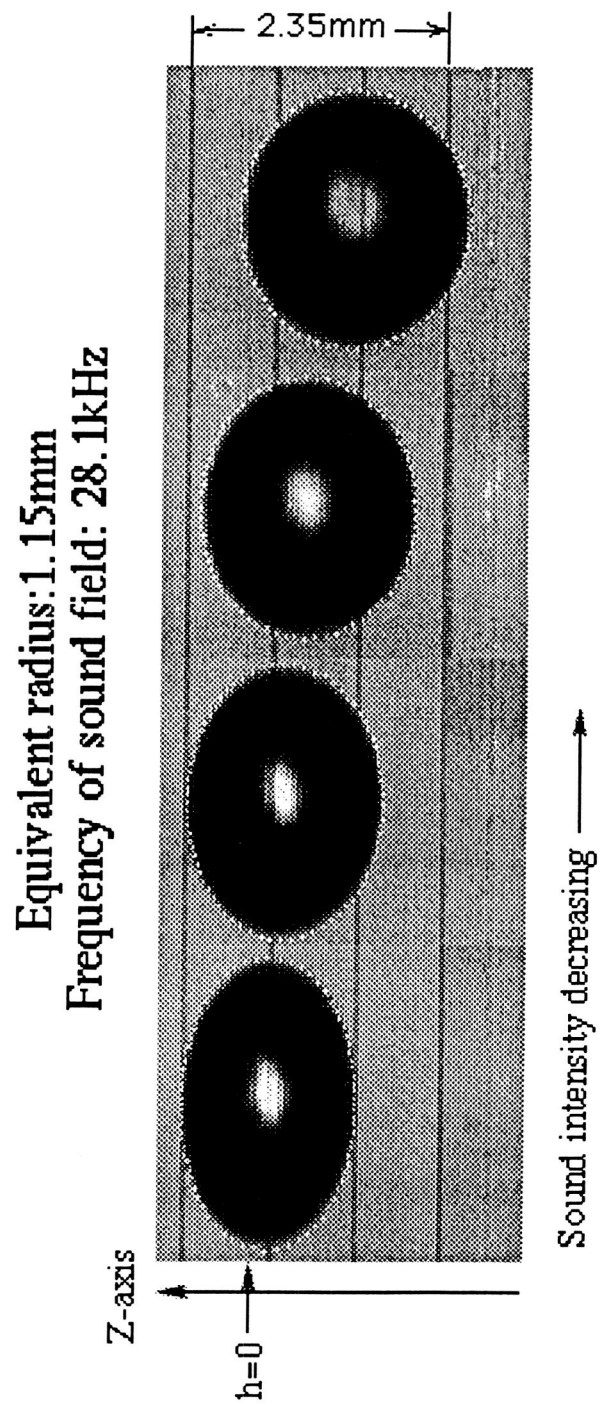
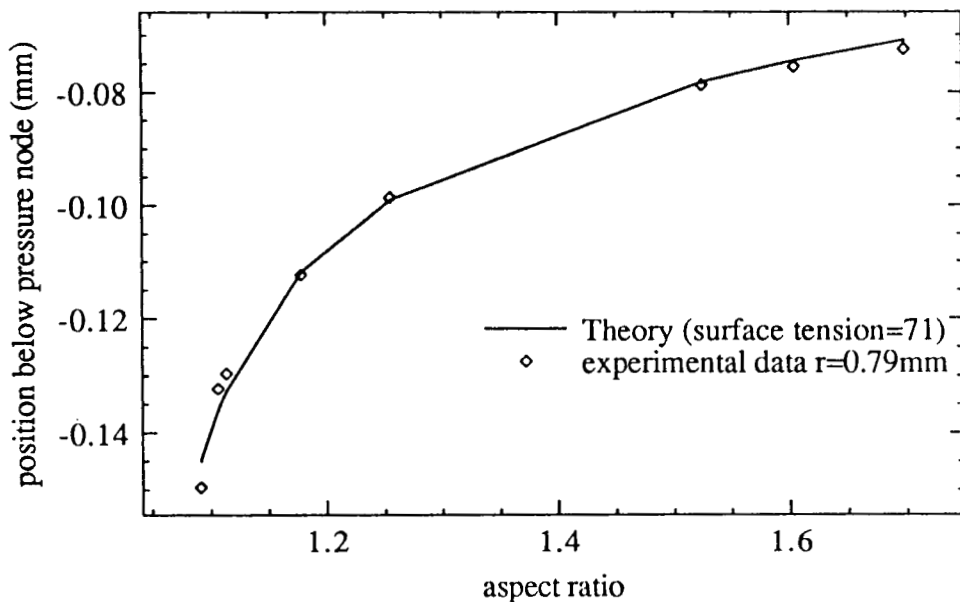


Figure 5 Experimental drop deformation and location, as affected by acoustic field. The white dots around the images are theoretical predictions. (From reference 5)

Deformation vs Location (Water drop)



Deviation vs surface tension

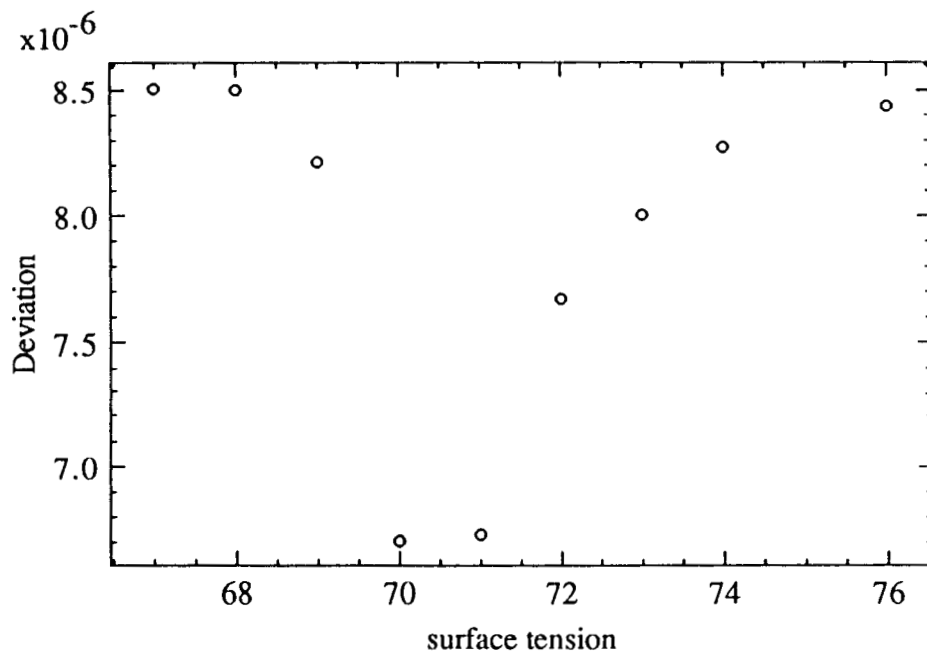


Figure 6a Experimental data of a water droplet deformations versus its locations. These data are fit with the theoretical model by using surface tension as a fitting parameter. (b) gives the standard deviation of these fittings. It shows that the best selection of the surface tension for this drop is about 71 dyn/cm.

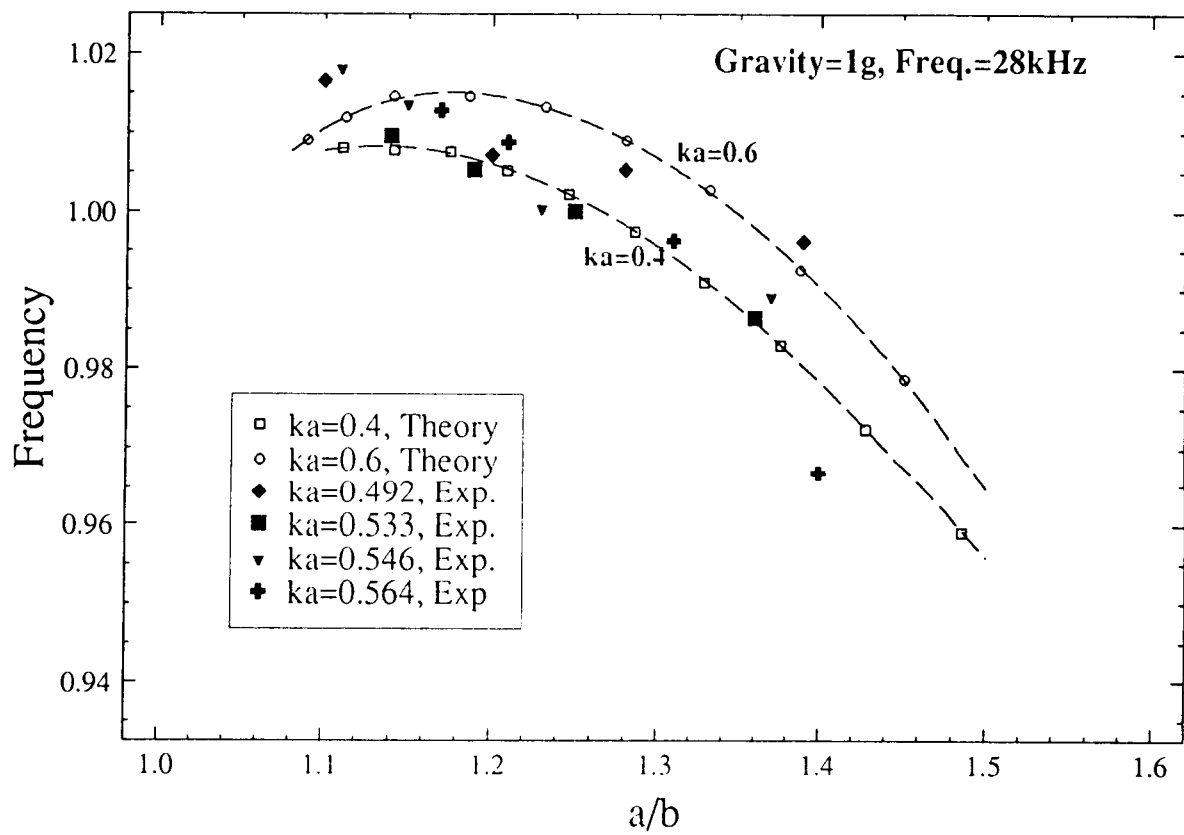
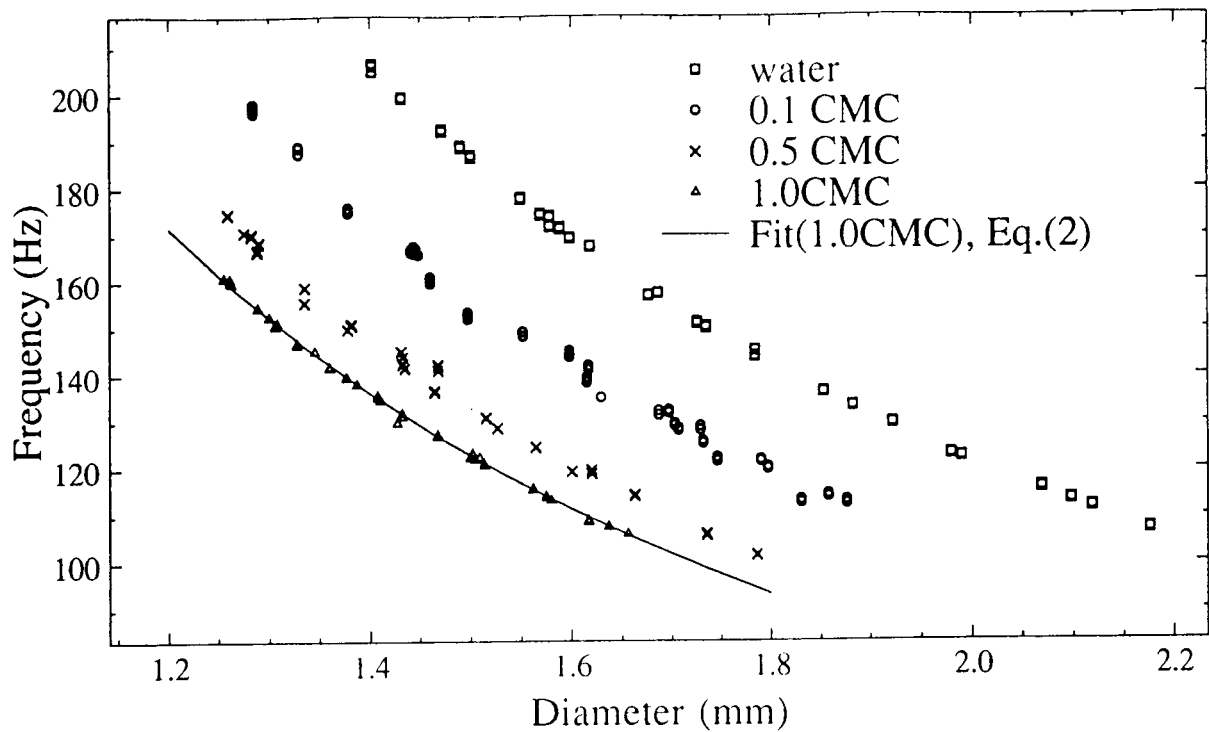


Figure 7 Experimental (ultrasonic) and theoretical results for the change in shape oscillation frequency with aspect ratio for the 1g case.

N-octyl β -D-Glucopyranoside (CMC=25mM)



N-octyl β -D-Glucopyranoside (CMC=25mM)

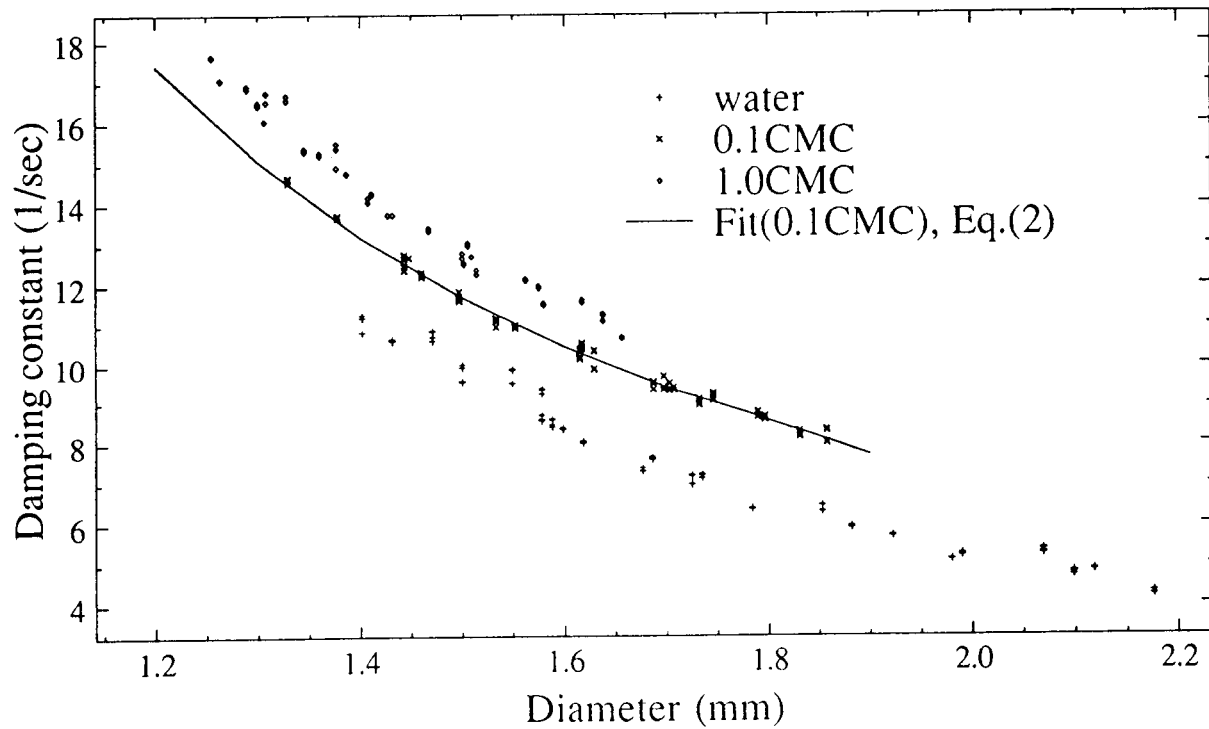


Figure 8 Measured free shape oscillation frequency and damping constant vs. drop diameter for water drops containing varying amounts of N-octyl β -D-glucopyranoside, a nonionic surfactant. Measurements were at 1g.

N-octyl β -D-Glucopyranoside (CMC=25mM)

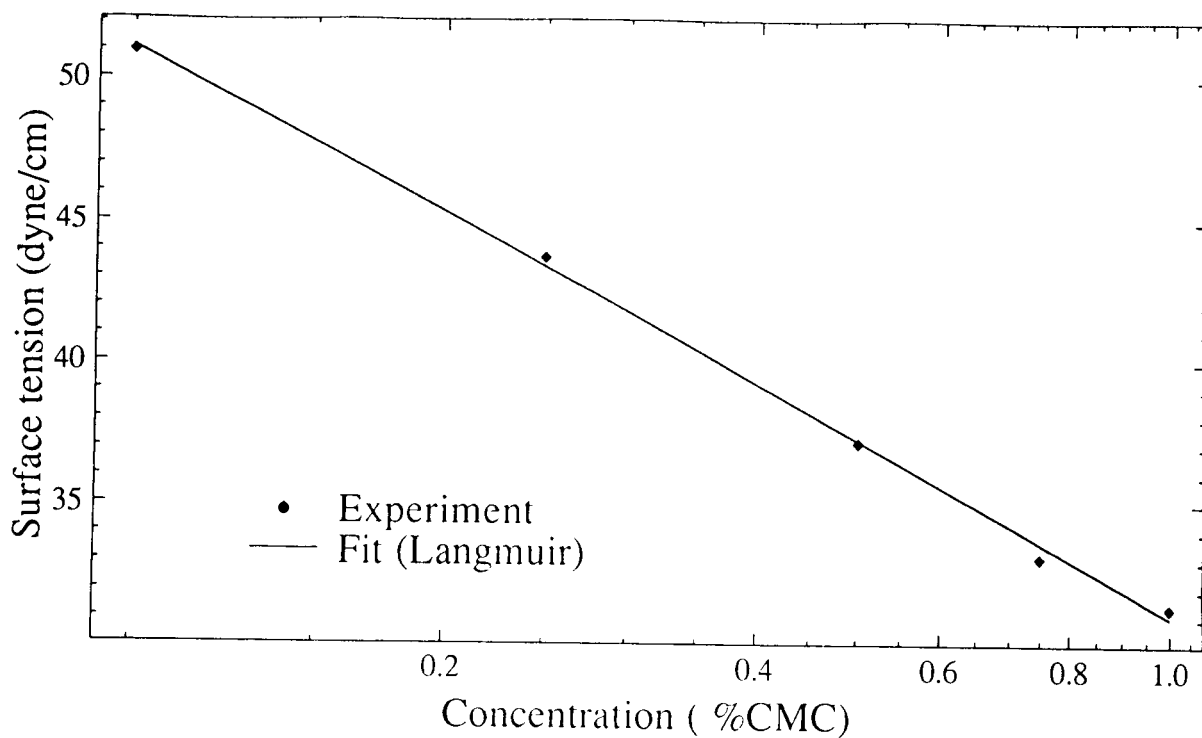


Figure 9 Surface tension vs surfactant concentration, based on theoretical model and experimental results as shown in figure 8.

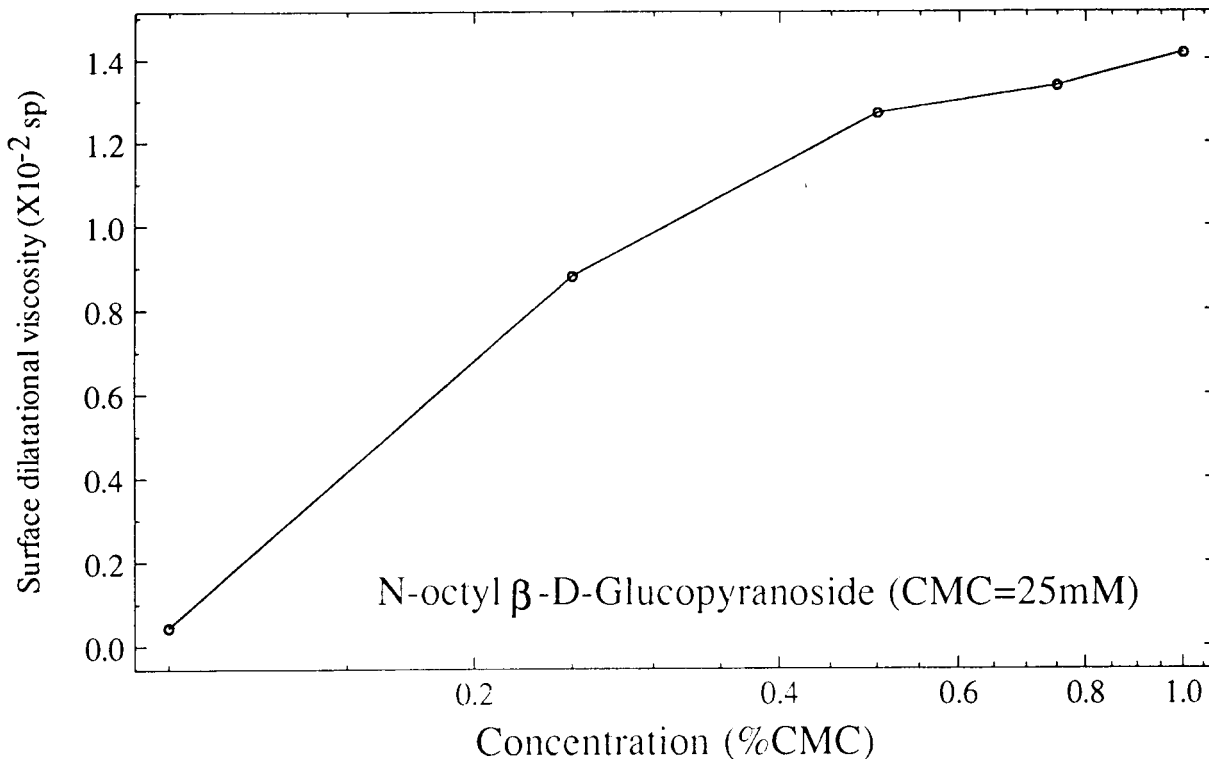


Figure 10 Surface dilatational viscosity vs. surfactant concentration, based on theoretical model and experimental results as shown in figure 8.

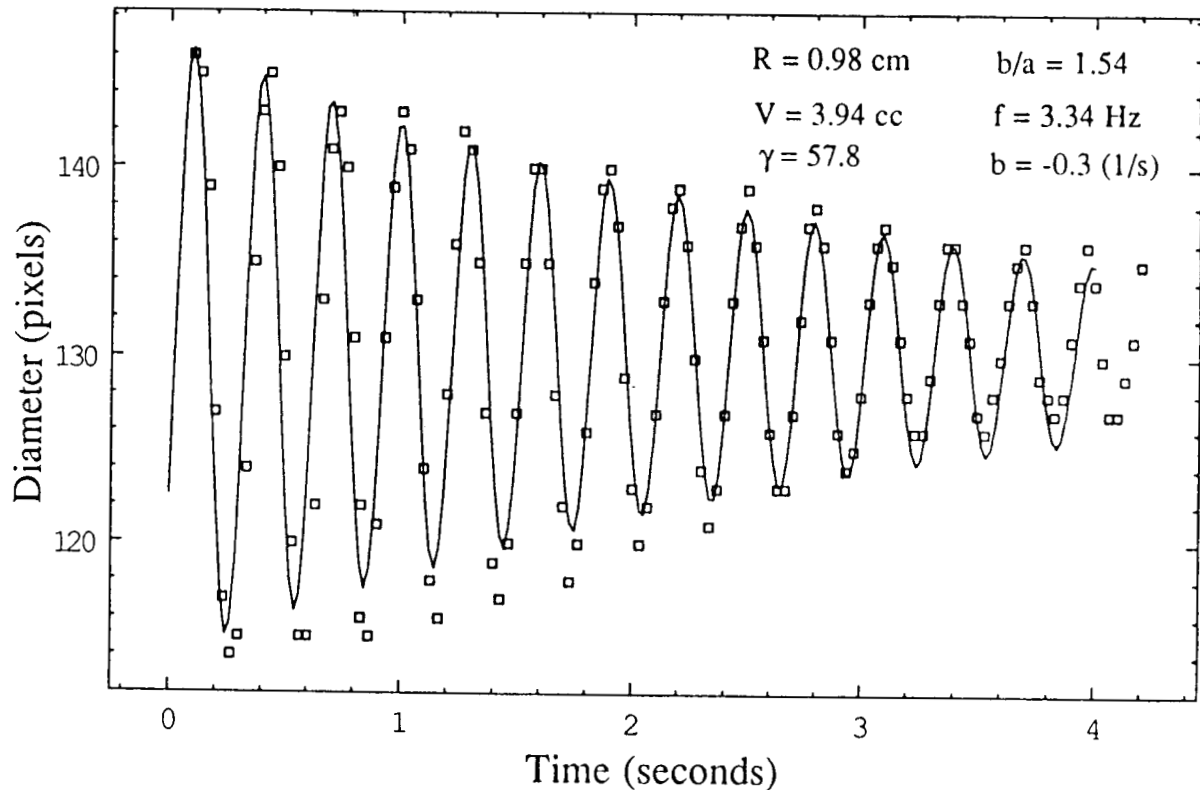


Figure 11 Microgravity data from video tape records for shape oscillations of a water drop.

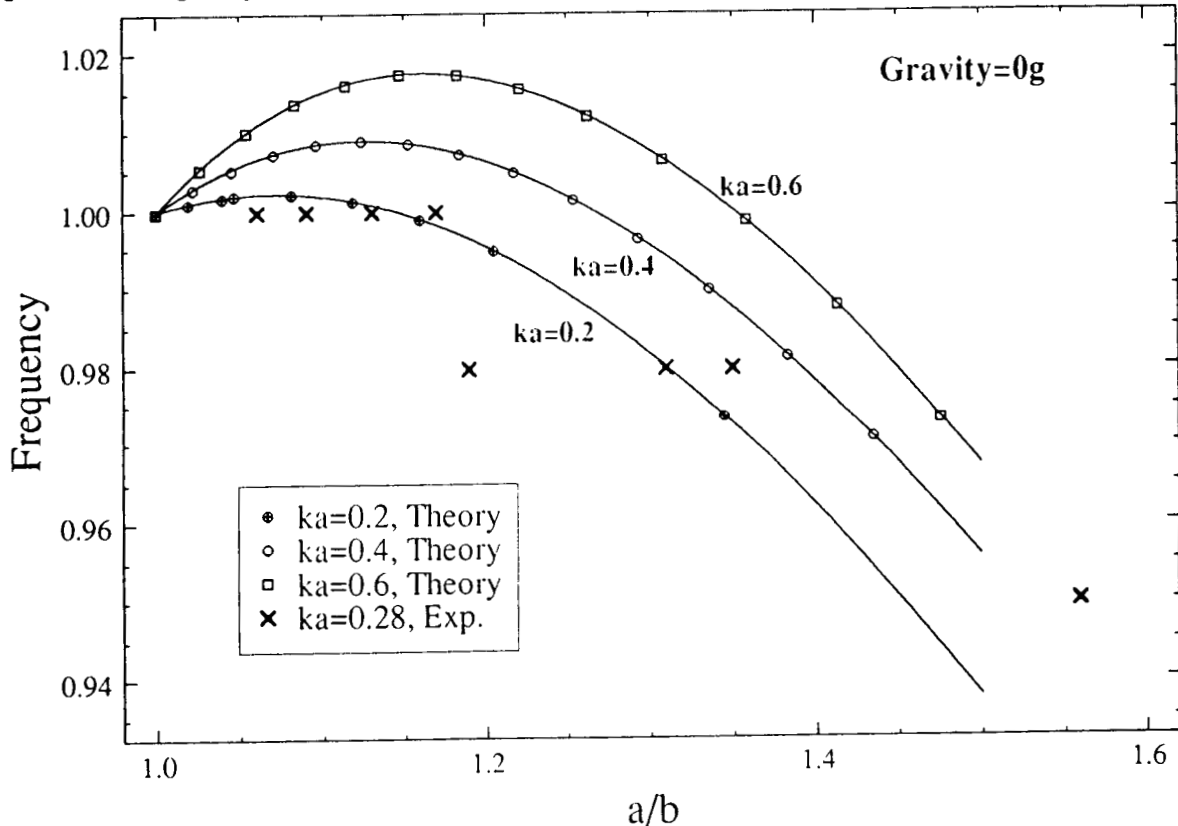


Figure 12 Spacelab experimental results from USML-1, based on data analysis of film, and theoretical predictions at 0g.

Discussion

Question: *In your slides, you had interaction between the bulk motion and the surface motion, however, you never included bulk viscosity in these. Can you explain that ?*

Answer: That is definitely in the equations.

Question: *But not in the slide ?*

Answer: I hate to disagree with you. This term is the viscosity in both fluids. There is an analysis presented in the written paper that will give those parameters and how they are interrelated. This is based on the work done by Lou that is recorded in the Journal of Fluid Mechanics for oil and water which we have changed, reduced, and simplified for the case of just a water drop surfactant in air, which makes the analysis much easier to deconvolve.

Comment : *Do I gather this correctly from your observations, that the drop dynamics with the usual Kelvin equilibrium equation does seem then to lead to satisfactory results in your opinion for all the observations ? Or are there some additional changes (involved) to that boundary condition, either to the dynamics of that absorption or whatever ? I gathered from your talk that you seemed quite satisfied.*

Answer: The Kelvin equation will do all right for the static case. But for the dynamic case, of course, you have to include these additional terms. We have a long way to go to be able to answer questions like you are asking.

Comment: *The reason I asked the question is that, I was very impressed with the damping data that you showed.*

Question: *However, the extraction of the properties from the damping data implicitly assumes that the Kelvin boundary condition is fine and then you get the result out, which is in accord with that assumption. I am wondering, that since the Kelvin equation is strictly an equilibrium statement, whether you are comfortable with proceeding from that point and extracting surface properties ?*

Answer: One thing we have to do, is we have to compare some of our results with some of the best data done by other methods. That's going to help us focus in on this question about whether the parameters we measure are unique or real material properties and that is an excellent question.

Question: *On your coalescence experiment, that looked far from random; Is that because of the acoustic field ?*

Answer: Yes. You saw when the drops get closer together there is actually a secondary force that pulls them to themselves, because they are both oscillating in the sound field and get about 1 diameter away. So that process is not random it's totally controlled by the acoustic field.

Question: Could you comment on the error analysis on the second set of data ?

Answer: Our error bars were quite large in this high aspect ratio because we are getting this tumbling rotation going on at the same time. I mean we have to do these experiments again. There is absolutely no question about the quality of the data is greatly compromised by tumble rotation and also with bubbles in the drops.

Comment: So it is not due to your release mechanism. The reason I am asking is because you have different aspect ratios, so there has to be some variation in frequency despite all other factors.

Answer: I think the error bars are large and it is not an uniform error bar. Part of the thing is just how you do the data analysis, how you get the frequencies from these plots. You do the Fourier transform of this thing. You try to get the frequencies but the data analysis is not adequate at this stage. I think, I wouldn't want to say that this is showing any real physical trend, I think it is more problem with the data quality.

14PG

1995107807

N95-14221

324086

14-21

326

MEASUREMENT OF INTERFACIAL TENSION OF IMMISCIBLE LIQUID PAIRS IN MICROGRAVITY

P-14

Michael C. Weinberg*, George F. Neilson*, Carl Baertlein*, R. Shankar Subramanian+ and
Eugene H. Trinh#

*Materials Science and Engineering Department, University of Arizona, Tucson, AZ.

+Chemical Engineering Department, Clarkson University, Potsdam, NY.

#Jet Propulsion Laboratory, Pasadena, CA.

ABSTRACT

A discussion is given of a containerless microgravity experiment aimed at measuring the interfacial tension of immiscible liquid pairs using a compound drop rotation method. The reasons for the failure to execute such experiments in microgravity are described. Also, the results of post-flight analyses used to confirm our arguments are presented.

INTRODUCTION

The primary objective of this flight experiment was the measurement of the liquid-liquid interfacial tension between immiscible liquid pairs. A secondary goal was the detection and measurement of certain instability points associated with a rotating, compound drop.

The surface tensions were to be measured by a contactless, drop rotation method. A triple-axis acoustic positioning chamber was to be utilized for both maintaining the position and inducing controlled rotation of compound liquid drops. The shape distortions of the inner and outer droplets caused by the induced rotation were to be analyzed quantitatively through the analysis of cine film and video records. From accurate measurements of the major and minor axes of the inner droplet (and correction for optical distortion due to the lens effect from the outer liquid), the liquid-liquid interfacial tensions were to be determined using the theory developed by Bauer and Siekmann (1). This theory was developed to predict the equilibrium shapes of a liquid sphere which contains a concentrically positioned gas bubble or immiscible liquid droplet of lower density. The equilibrium shapes which are formed at a given rotation rate are functions of the densities and volumes of each phase, the interfacial tension between the phases, and the surface tension of the outer phase. Thus, knowledge of the pertinent droplet volumes and densities and liquid-air surface tension of the outer droplets, used in conjunction with the measured values of the lengths of the minor and major axes of the prolate spheroid shaped inner droplet (produced by rotation), allows for the determination of the liquid-liquid interfacial tension.

Several nearly immiscible organic liquid pairs were selected for the flight experiment, and the interfacial tension determinations were to have been performed at room temperature. Since several simpler techniques are available for making such measurements on Earth (2-5), one might question the motivation for this flight experiment. In response, however, one should note that the use of conventional methods for measurement of liquid-liquid surface tension at high temperatures are fraught with difficulties (6) and in some instances not possible. Thus, the use of a contactless, low-gravity technique for making such measurements is highly desirable. The low gravity requirement stems from the fact that there can be significant density differences between the droplets, and this feature precludes the execution of such experiments in a 1-g levitator.

Hence, the room-temperature liquid-liquid flight experiment was viewed as a logical prelude to a more difficult high temperature glass experiment which would have been conducted on a future flight. The interfacial tension data which were to have been generated from the microgravity study were to have been compared with values obtained from ground-based measurements (7) employing methods which are standard for measuring liquid-liquid interfacial tensions at room temperature and under 1-g conditions. Thus, the flight experiment was to have demonstrated the feasibility of the method.

The reason that the measurement of the liquid-liquid interfacial tension between immiscible solutions at high temperature is important relates to the problem of liquid-liquid phase separation in glass forming systems. There have been theories developed to predict the kinetics of the different types and various stages of phase separation processes. An initial nucleation process, intermediate growth processes, and a final coarsening process can be distinguished. There have been many experimental investigations conducted to test these various theoretical mechanisms. However, there have been only a few attempts to quantitatively compare theory and experiment. For the simpler binary glass compositions which should be most amenable to theoretical treatment, a major stumbling block has been the unavailability of sufficiently accurate values of some of the needed thermodynamic parameters, in particular, those for the interfacial tensions between co-existing phases. The accurate determination of the interfacial tension for the separating phase in a single simple glass system should allow, for the first time, a critical test of the essential correctness of some of these important kinetic theories.

In summary, the specific goals of the flight experiment were: (1) to determine the liquid-liquid interfacial tension between immiscible liquid pairs via the rotation of a compound droplet, (2) to determine the rotation rates at which bifurcation of compound droplets occur, and (3) to ascertain if "burst through" (i.e. penetration of inner droplet through the outer) could be evoked under appropriate conditions.

I. BACKGROUND

Three sets of partially immiscible organic liquid pairs were chosen for employment on USML-1. These were (1) ethylhexyl acetate (EHA) / 1,2-propanediol (P); (2) 2-octanol (O) / formamide (F); and (3) 1-nonal (N) / formamide. The first liquid given for each of these sets is the liquid of lower density, which becomes the inner droplet of the compound drop. In addition, the denser liquids contained trace concentrations of 55 μm cross-section aluminum particles, which were introduced to allow accurate determination of the angular velocities of the compound drops. Four experimental runs were planned using the EHA/P pair in the first and fourth runs, the O/F pair in the second run, and the N/F pair in the third run.

The above liquid pairs were selected from more than one hundred totally or partially immiscible organic liquid pairs which were considered based upon the following criteria:

1. Density differences between pair liquids should be as large as possible.
2. Interfacial tensions should be as small as possible (and less than 5 dynes/cm).
3. All of the flight liquids must be non-explosive, of low combustibility, and of low toxicity.
4. All liquids must have relatively low vapor pressures, and the denser liquids should have very low vapor pressures to avoid appreciable evaporation in the DPM chamber.
5. The refractive index differences between inner and outer liquids should be sufficiently large as to allow their interfaces to be readily optically visible.

The five liquids and their respective pairs listed above were found to be acceptable according to these requirements. The interfacial tensions of these pairs, which were measured in our laboratory, ranged from 1.5 dynes/cm for the EHA/P pair to 3.4 dynes/cm for the N/F pair. Also, the density of each liquid when saturated with its pair liquid was determined in our laboratory by two independent methods, and the density differences found to be satisfactory. Information concerning the other parameters was obtained from the literature for the pure components. These data are summarized in Table 1.

The saturated liquids for the flight samples were prepared by the following procedure. Three 250 ml separatory funnels (one for each liquid pair) were cleaned by washing with distilled water followed by washing with spectroscopic grade acetone. The contents from bottles (100 ml each) of octanol, nonanol and propanediol were then poured, respectively, into the three funnels. To each of the first two sep funnels 100 ml of formamide was added, and to the third sep funnel 100 ml of ethylhexyl acetate. Then each sep funnel was closed with its glass stopper and shaken vigorously for about one minute until the liquid pair contained within formed a single homogeneous emulsion. The sep funnels were placed upright in ring stands and the liquids allowed to re-separate (a process which required less than one minute for the O/F pair and nearly 30 minutes for the EHA/P pair). The emulsifying and re-separating procedure was repeated an additional five times over a two day period. After the final agitation, the

heavy and light liquid fractions were allowed to segregate over a two day period. The room temperature during this time was 25-26 °C. The heavier bottom fractions were drained through the bottom glass stopcocks of the sep funnels into Erlenmeyer bottles (having screw-on lined plastic caps). These heavier liquids were drained to about 1 cm from the horizontal interface layer which indicated the separation of the heavy and light fractions. About 10 ml of the middle fraction about the interface (which contained both heavy and light liquids) was drained off from each sep funnel. Finally, the remainders of the lighter upper liquids were drained into bottles. All bottles were appropriately labeled, with each bottle containing about 95 ml of saturated liquid. Each bottle was visibly inspected and its contents noted to be clear and single phase. About 25 mg of 55 µm aluminum powder was then weighed out and introduced into each of the three bottles containing the formamide and propanediol. Each bottle was then capped and sealed. The manufacturer label information concerning the chemicals and aluminum powder used is shown in Table 2.

II. FLIGHT RESULTS

The procedure which was specified for the execution of the flight experiments is described below. Each compound drop was to have been prepared in the DPM chamber as follows: A precise measured volume of the liquid pair member of greater density containing the dispersed aluminum tracer particles (with a density of about 1.1 g/cm³) was to have been deployed first. Next a precisely measured volume of the less dense liquid was to have been injected into the denser drop. For each drop rotation experiment, an incremental increasing acoustic torque was to have been applied to produce equilibrium drop angular velocities from a minimum of about 2 radians/sec to a maximum of from about 8 to 12 radians/sec, depending upon the characteristics of the particular sample. The particular rotation rates were chosen to produce axial ratios of the distorted inner drop of about 1.1, 1.2, and 1.3, after the shape had equilibrated at a given constant velocity.

After a drop shape and rotation rate had equilibrated, high speed filming was to have been conducted. Filming at frame rates of 100-400 frames/sec for 3 sec per measurement or 12 sec per sample was required. For the short time periods indicated above, two orthogonal high resolution cine or video pictures of the sample were to have been taken, with one of the cameras having its axis coinciding with the rotation axis of the drop. Single frame fields of view were required to be 2.7 x 2.7 cm with a linear resolution of 20 µm. Also, combinations of lens aperture/film rate/lighting to obtain sharpest focus of entire compound drops and view of inner droplets were to have been tested pre-flight under simulated Spacelab conditions to verify the adequacy of the resolution in the film data, and to set the employment conditions for these parameters for the Spacelab experiments. Finally, a dedicated real-time video downlink between the experiment operator and the PI team was requested to be available during the

critical times of the experiment, such as during the creation and deployment of the compound drops and at each step just prior to recording the high speed film data.

In the first flight experiment the P and EHA immiscible pairs were to have been used. After a long delay, due to experiment set-up time and incorrect specification of injector tips, the outer droplet was deployed successfully. However, there was great difficulty in injecting the inner droplet, and the first several attempts failed. Eventually the inner drop was deployed, but with several unwanted consequences. In addition to the major inner droplet, several satellite droplets formed and a very large air bubble was introduced between the two fluids. The air bubble obscured the visibility of the inner droplet. Also, the lighting arrangement was so poor that the liquid-liquid interface was not detectable. Shortly after the formation of the compound drop, the time allotted for this experiment expired. Therefore, it is unlikely that any useful results will be obtained from this experiment although the video tapes are being analyzed currently.

The second flight experiment was an even greater disaster. The saturated octanol and nonanol solutions were observed to contain colored droplets. Since we couldn't explain their origin, NASA would not permit us to deploy these flight samples.

III. POST FLIGHT ANALYSIS (PFA)

A. PFA Goals

The goals of the post flight analysis are: (1) to attempt to find causes for the problems encountered with the flight experiment fluids, and (2) to analyze the flight data for the first experiment. In order to pursue the first objective the sensitivity of the equilibrium compositions to temperature changes has been studied. In addition, potential contamination of the flight samples by water and/or a colored dye solution has been investigated. The analysis of the flight data is being performed at Clarkson University.

B. Temperature Effects

Since the equilibrium concentrations are functions of temperature, we measured the octanol-formamide and nonanol formamide binodals in order to gauge the sensitivity of the saturated formamide, octanol, and nonanol solutions to temperature excursions.

The experiment was conducted using a system consisting of a viewing cell partially submerged in an isothermal temperature bath (see Fig.(1)). Specifics of the bath varied with the experimental temperature range. A 16 liter transparent acrylic tank filled with water was used to collect all data below 90°C. To obtain data between 90°C and 150°C a 15 liter cylindrical glass tank filled with an ethylene glycol/water mixture was used. For temperatures above 150°C the heating bath consisted of a 2 liter

pyrex dish with mineral oil. The isothermal heater/circulator was capable of attaining a maximum temperature of 150°C, and thus for those points above 150°C a simple stirring hot plate was used to heat the oil bath. Regardless of the bath arrangement used, the heating solutions were stirred continually and the temperature was monitored with thermometers at several locations in the bath to ensure a constant and uniform temperature

The liquids used were used as received from the manufacturer (Aldrich) with no further purification. A complete list of liquids and properties can be found in Tables 2 and 1, respectively. These solutions were placed in a 25 ml cylindrical viewing cell with a magnetic stir bar spinning at approximately 700 rpm and partially submerged in the bath. Care was taken to keep the total solution volume between 5 and 10 ml so the stir bar was capable of stirring through the entire volume of liquid and not just the bottom fraction. The viewing cell was sealed with a septum at all times while in the heating bath to prevent moisture from entering. A small gauge needle was placed through the septum to prevent the pressure from building up at higher temperatures.

Data points were obtained by heating a solution of predetermined composition until it cleared and there was no visual evidence of a second phase. The clear solution was then cooled slightly until it clouded or a second phase appeared. This procedure was repeated three times or until a consistent clearing temperature was observed. These temperatures were recorded and used as data to construct the binodal curves. The composition was then altered by adding a small known amount of one of the liquids and the heating/cooling procedure was repeated for that composition. At temperatures above 150 °C new liquids were used for each repeated measurement since there was some concern about reaction and/or decomposition of the solutions.

The results of these measurements are shown in Figs. (2) and (3), which are the binodal curves for the octanol-formamide and nonanol-formamide pairs, respectively. These two curves are nearly identical, both exhibiting steep slopes on the formamide rich side and much smaller slopes on the formamide poor side. This feature indicates that at room temperature the saturated octanol and nonanol solutions should be much more sensitive to temperature deviations than the saturated formamide solutions.

This result explains why the saturated octanol and nonanol solutions showed a much greater tendency to phase separate than the saturated formamide flight samples. In particular, a simple calculation employing the lever rule shows that 3.2 ml and 3.8 ml of liquid will phase separate when 100 ml of saturated nonanol and octanol solutions are cooled from room temperature to 0°C. Since we were not informed of the thermal history experienced by our flight samples, we are unable to compute the anticipated degree of phase separation. However, we can conclude that it is highly probable that the

small extent of phase separation experienced by several of our flight samples was due to unwanted temperature excursions.

C. Water

As was mentioned, the saturated octanol and nonanol in the returned flight syringes were both contaminated with several or more ml of bluish-green foreign droplets. A further objective of the first PFA goal was to determine the chemical identity of these colored droplets and to ascertain how they might have gotten there. Since water is largely insoluble in either octanol or nonanol, we sought to determine if they might have been contaminated by the green-colored aqueous dye solution used in other of the DPM experiments.

However, IR analysis of small droplets extracted from the foreign colored liquids in the octanol and nonanol showed them to be mostly or almost entirely formamide and not mostly water. Since the saturated octanol and nonanol solutions contain about 24 mol % formamide each, and since formamide is completely soluble in water, the following experiments were conducted to determine if water might somehow have been introduced into the syringes and caused the formation of the colored formamide drops.

- 1) The solubility of water in pure octanol and nonanol was measured and determined to be about 5 wt % in each.
- 2) The effect of adding 1% and 10% water to pure formamide and to formamide saturated with octanol and nonanol was observed, and the IR spectra of these solutions obtained. It was noted that these additions of water caused no visual change to the formamide liquids and no new liquid phase to form. However, the most intense IR band of formamide at 3350 cm^{-1} was found to broaden somewhat with the addition of water (due to the overlap of the fundamental OH stretch band in this same region).
- 3) The effects of adding several drops of water to saturated solutions of O/F and N/F were observed. In these experiments the solutions + water were shaken and then allowed to stand for a total of four days. Immiscible droplets settled from each solution. The N/F droplet increased in size with time, but the O/F droplet appeared to remain a constant size. The immiscible droplets were extracted and their IR spectra were obtained. The IR spectrum from the (O/F + water) droplet was found to be essentially identical to the F/O + 1% water spectrum. The IR spectrum of the (N/F + water) droplet was also found to be very similar to the F/N + 1% water spectrum, but even more similar to the spectrum of pure F/N.

The IR spectra of the foreign colored droplets in the O/F and N/F flight syringes were compared with the spectra of the prepared solutions described above. As was mentioned earlier, it is clear from

these comparisons that the colored syringe droplets are mostly formamide. However, it is inconclusive as to whether or not the colored droplet in the octanol also contain water, due to the similarity of the spectra. The spectrum of the droplet from the nonanol syringe is most similar to that of pure formamide without added water.

D. Contamination

The returned flight syringes showed three separate signs of contamination: (1) the octanol in the syringe was yellow instead of being colorless as sent, (2) the octanol syringe contained blue-green droplets of a second immiscible liquid, and the nonanol syringe contained a blue foreign drop, and (3) most of the syringes contained varying amounts of blue flakes around their metal tips. A further goal was to investigate the source of this contamination.

The blue flakes in the tips of the octanol and nonanol syringes were extracted for experimentation. They were found to be completely insoluble in pure octanol, nonanol and formamide. They also appeared to be completely insoluble in water, acetone and alcohol. It was thus not possible to obtain their IR absorption spectrum. It was conjectured that the flakes might be the remnants of some lubricant (possibly silicone grease) that was employed. At any rate, they were apparently not related to the green dye, since they were not water soluble.

The dried McCormick green food color dissolved readily in pure formamide and in the F/O and F/N solutions to form greenish solutions. The IR spectra of these colored solutions were all identical to that of pure formamide. Thus, it was not possible to determine the source of the color of the droplets in the octanol and nonanol syringes by the use of IR spectroscopy.

The dried McCormick green dye would only partially dissolve in the N/F solution to form a blue solution. The dye would not dissolve at all nor color the O/F solution. Hence, this dye does not appear to be the source of the yellow color of the octanol in the returned flight syringe.

CONCLUSIONS

Our tentative conclusions regarding the flight experiment are as follows:

- (1) The small degree of phase separation exhibited by several of the flight samples was probably due to temperature variation experienced by these fluids prior to flight, although
- (2) Small quantities of water (less than 1%) will cause perceptible phase separation in the octanol and nonanol solutions.
- (3) Several of the flight samples were contaminated either during loading into the syringes or some time thereafter.

(4) Although we have not excluded the possibility that the food dye was the source of the colored droplets, this possibility seems unlikely since the dye did not dissolve in the saturated octanol solution.

REFERENCES

1. H.F. Bauer and J. Siekmann, ZAMP 22 (1971) 532
2. M.J. Jaycock and G.D. Parfitt, "Chemistry and Interfaces" (Ellis Horwood, Chichester, 1986)
3. D.S. Donahue and F.E. Bartell, J. Phys. Chem. 56 (1952) 480
4. H.M. Princen, I.Y.Z. Zia, and S.G. Mason, J. Colloid Interface Sci. 23 (1967) 99
5. G. Smedley and D. Coles, *ibid* 138 (1990) 42
6. M.C. Weinberg and R.S. Subramanian, J. Non-Cryst. solids 129 (1991) 206
7. A. Yasumori, G.F. Neilson, and M.C. Weinberg, J. Colloid Interface Sci. 155 (1993) 85

Table 1
PROPERTIES OF LIQUID PAIRS

Property	Pair 1 EHA/P	Pair 2 O/F	Pair 3 N/F
interfacial tension* (dyne/cm)	1.5	3.3	3.4
surface tension* (dyne/cm)	<u>25.3</u> 28.0	<u>25.1</u> 29.4	<u>27.0</u> 29.1
density* (g/cm ³)	<u>0.8774</u> 1.0376	<u>0.8422</u> 1.1171	<u>0.8490</u> 1.1279
refractive index** (nD ²⁰)	<u>1.4204</u> 1.4331	<u>1.4203</u> 1.4475	<u>1.4338</u> 1.4475
viscosity** (cm ² /sec)	<u>0.017</u> 0.541	<u>0.095</u> 0.034	<u>0.135</u> 0.034
boiling point** (deg C)	<u>198.6</u> 188.2	<u>179</u> 210.5	<u>215</u> 210.5
flash point** (deg C)	<u>82</u> 107	<u>71</u> 154	<u>75</u> 154
vapor pressure** (mm at 25°C)	<u><0.1</u> 0.08	<u>0.158</u> 0.08	<u>0.024</u> 0.08

*mutually saturated liquids

**pure liquids

Table 2

CHEMICAL INFORMATION SHEET

Formamide
Sigma Chemical Co.
Lot #11H 1015
Toxic

2-Octanol, 98%
Aldrich Chemical Company
Lot #04720LX
Severe eye irritant

2-Ethylhexyl Acetate
Kodak Eastman Fine Chemicals
Lot #8091531240
Causes skin and eye irritation

Propylene Glycol
(1,2-Propanediol)
Sigma Chemical Co.
Lot #51H 0752
Harmful by inhalation
and if swallowed

1-Nonanol, 99%
Aldrich Chemical Company
Lot #05631MV
Toxic

Aluminum Powder
Grade: 5240
Alcan-Toyo America, Inc.
Lot #S071051
Sieved: 53-75 micron range

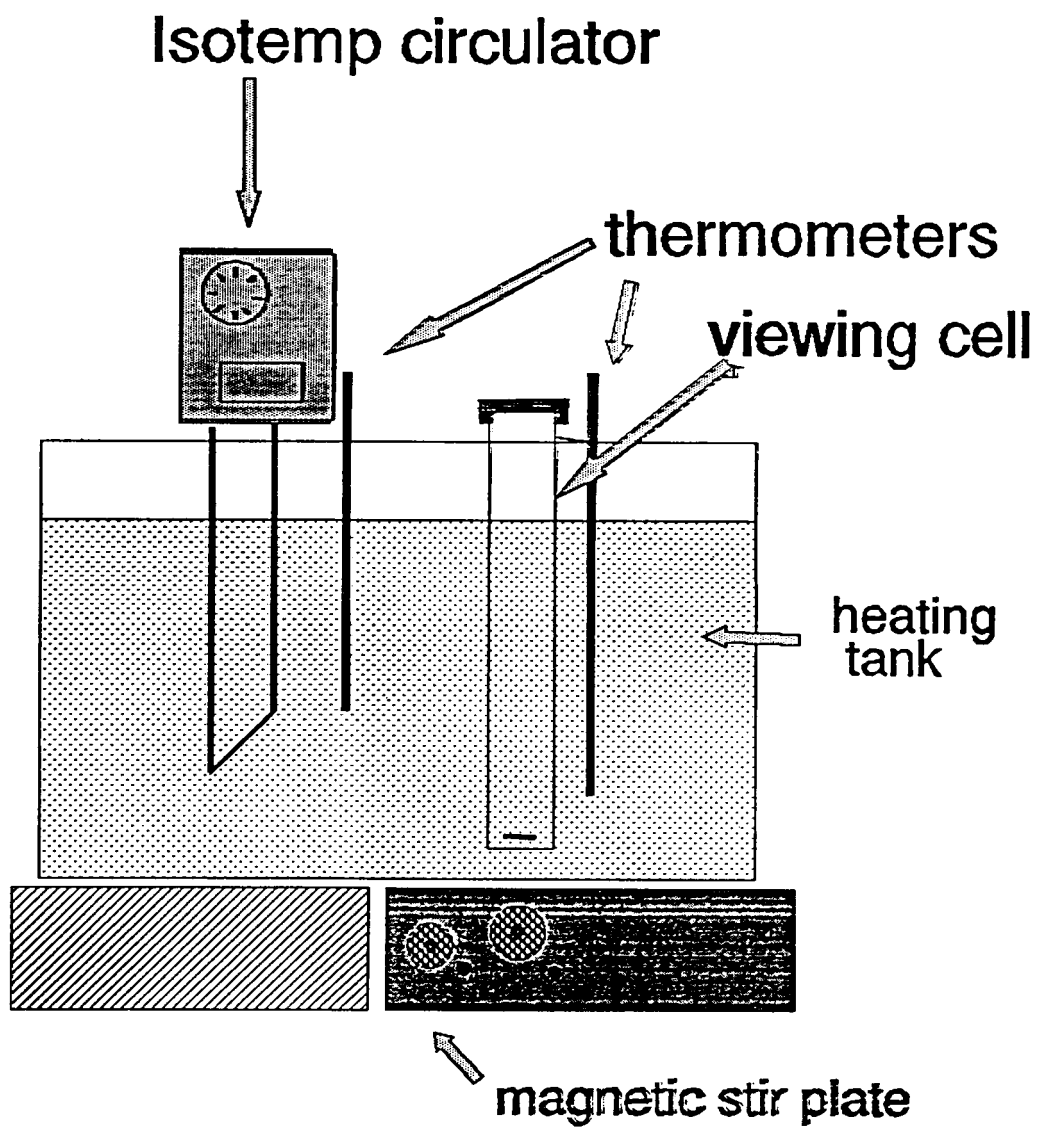


Figure 1 Schematic of experimental arrangement for measuring binodal curves.

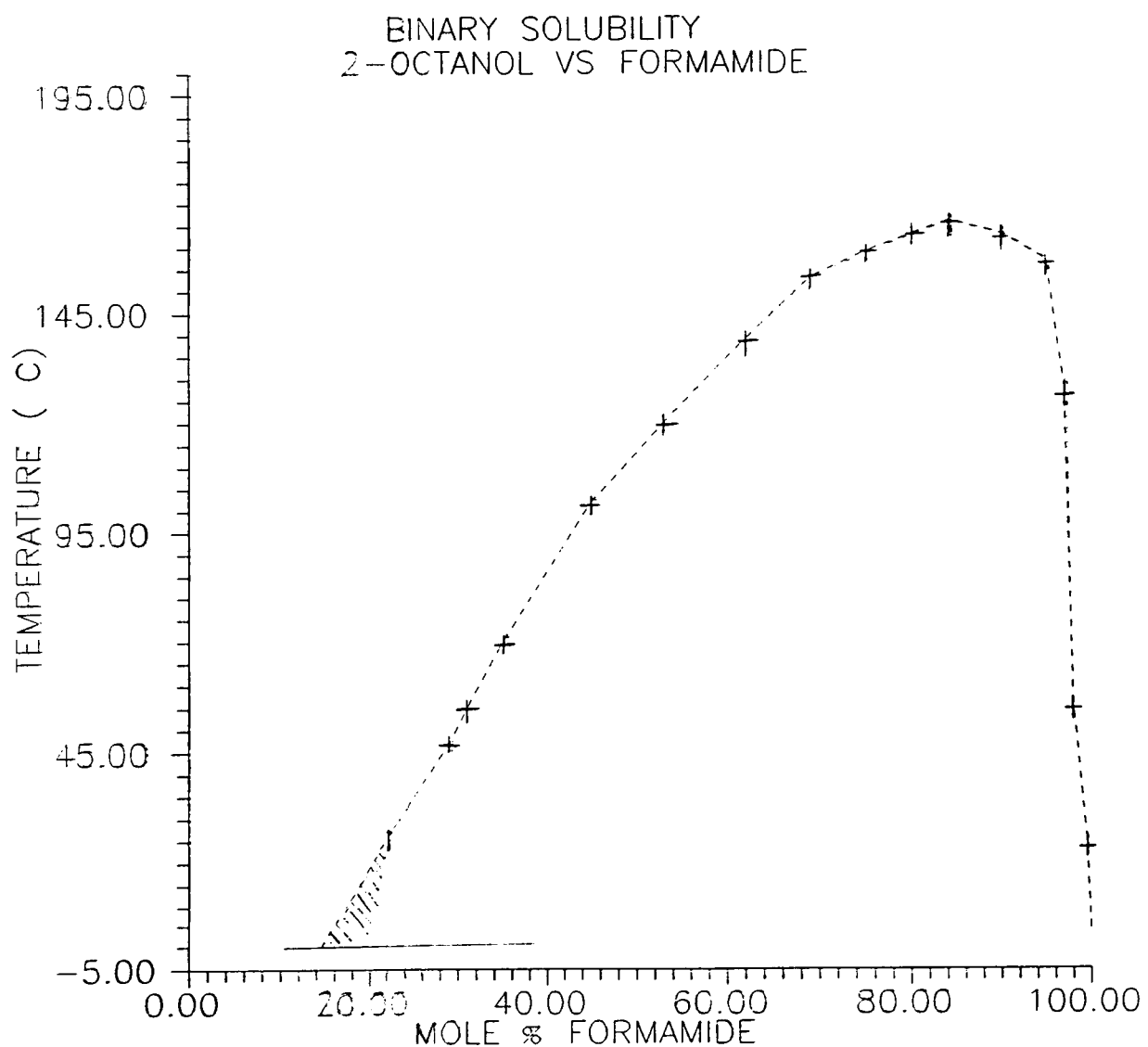


Figure 2 Temperature at which two liquid phases are at equilibrium vs. composition for the octanol-formamide system.

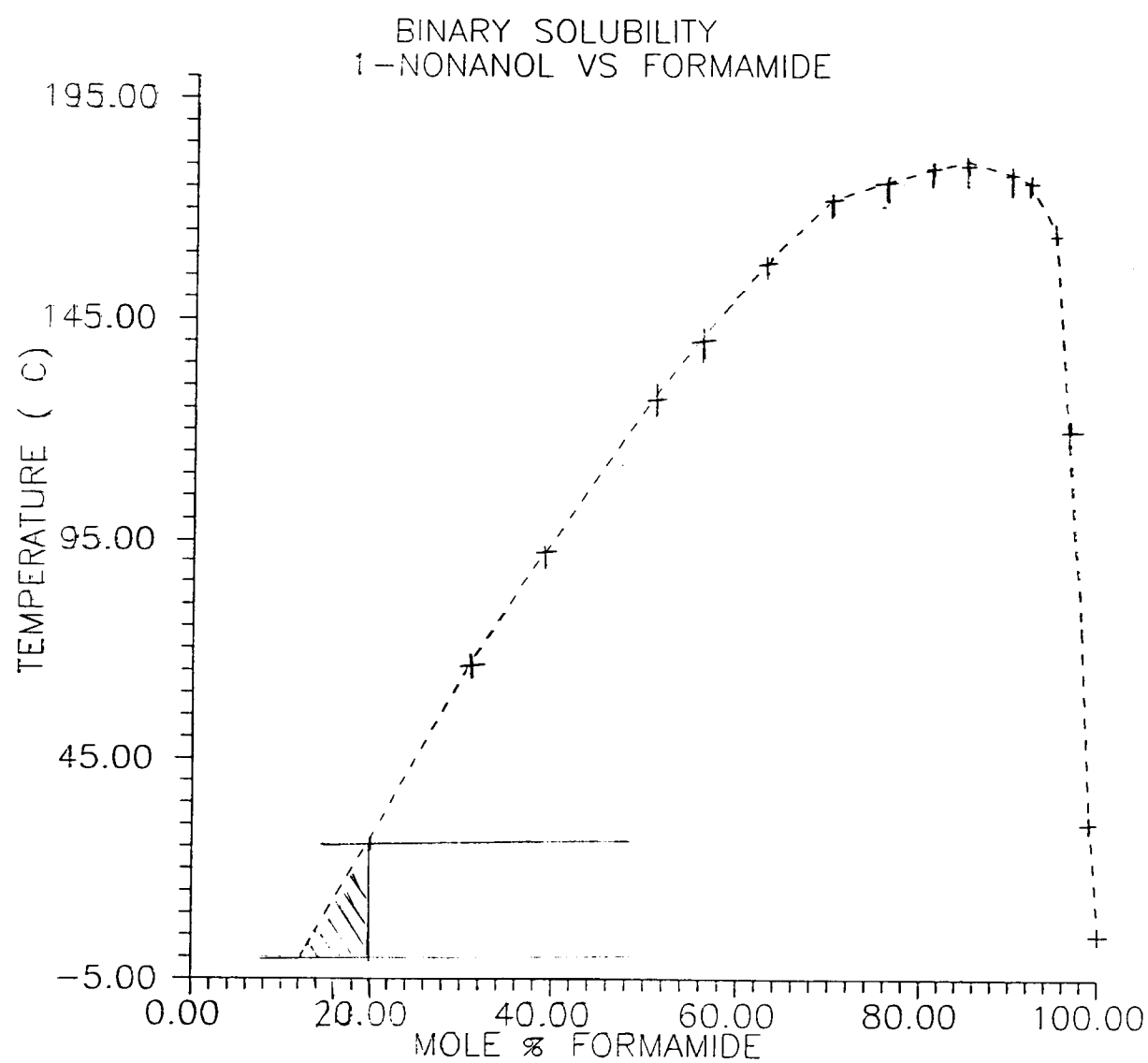


Figure 3 Temperature at which two liquid phases are at equilibrium vs. composition for the nonanol-formamide system.

1995/07/08 N95-14222

8pg

324087

2/5-51

17027

EXTENDED DURATION ORBITER MEDICAL PROJECT

MICROBIAL AIR SAMPLER - STS-50/USML-1

P- 7

Duane L. Pierson*, and Sheila W. Boettcher⁺

*NASA JSC, Houston, Texas

⁺KRUG Life Sciences, Houston, Texas

ABSTRACT

The Microbial Air Sampler was used on Mission Days 1, 7 and 13 in the Spacelab during STS-50/USML-1. Microbial air samples were collected using two types of media strips containing agar (Rose Bengal for yeast and molds, TSA for bacteria.) The bacterial level found on Day 1 was lower than experienced on previous Spacelab missions. A high level of fungi was present on Day 1, however subsequent samples on Day 7 and 13 did not indicate fungal growth. Bacterial growth was also minimized in this microgravity environment as the mission progressed. No pathogenic microorganisms were isolated, and the health risk from airborne microbes was minimal throughout the mission.

NOMENCLATURE

Aspergillus	Type of fungal growth
Bacillus	Type of bacterial growth
CFU/25 cm ²	Colony Forming Units in a 25 x 25 cm area - surface
CFU/m ³	Colony Forming Units in 1 cubic meter - air
Corynebacterium	Type of bacterial growth
EDOMP	Extended Duration Orbiter Medical Project
MAS	Microbial Air Sampler
Micrococcus	Type of bacterial growth
Orbiter	Flight deck and middeck area
Penicillium	Type of fungal growth
Rose Bengal	Agar material used to measure fungal growth
Staphylococcus	Type of bacterial growth
TSA	Trypticase Soy Agar for measuring bacterial growth. TSA has an inhibitor that keeps fungi from growing on this sample.

INTRODUCTION

Acceptable air quality must be maintained in the closed spacecraft environment to ensure that crew health and performance are not compromised (1). Microorganisms in the air can contribute to the degradation of air quality, and at increased levels can cause allergies and/or infections (2). The risk of increased airborne microbial load becomes greater with extended mission durations (1). Periodic sampling of the air to determine microbial levels provides an assessment of the air quality and the efficiency of the spacecraft air handling system (3).

The Microbial Air Sampler (MAS) is a commercially available, portable, hand-held instrument for estimating the number of microbial colony forming units in the air. The MAS facilitates periodic assessment of airborne microbial levels and provides necessary information on the effectiveness of air handling systems. This device is used in hospitals, pharmaceutical and cosmetic manufacturing operations, and in the food industry (4, 5).

Characterization of the airborne microbial load on previous Shuttle flights (STS-40 and STS-45) has not indicated a health risk to the crew (6, 7). With the mission duration increasing and number of crew living in a closed environment, the opportunity for microbial propagation increases (1). The data obtained previously has been insufficient to establish a baseline for microbial load which can be extrapolated to longer duration missions.

The levels and types of airborne bacteria and fungi are listed in the Table 3. For reference purposes, the pre and postflight surface sample results are included in Table 1 and the preflight air sample results in Table 2.

I. RESULTS

Day 1 samples exhibited a higher level (375 colony forming units per m^3 of air) of fungi than has been observed previously, however no fungi were recovered from day 7 and 13 samples. The bacterial level found on day 1 was lower than experienced on previous Spacelab missions. The increased fungal growth may have inhibited the growth of bacteria.

II. DISCUSSION

The low relative humidity (30-50%) in the Spacelab tends to reduce fungal propagation. The fungi present during the day 1 sampling period probably resulted from growth in the Spacelab prior to being activated, as relative humidity levels may have been substantially higher. This hypothesis is further supported by the elimination of fungi during the subsequent sampling periods. The bacterial levels were 162 and 50 colony forming units per m^3 on days 7 and 13, respectively. Unlike some previous missions, the bacterial levels did not increase as the mission progressed.

CONCLUSIONS

The data collected do not indicate an increase in airborne microbial load of the Spacelab during the mission, however the occupancy of this module by the crew is relatively low. Microbial levels in the Orbiter tend to be higher than those in the Spacelab, but no Orbiter samples were taken on this mission. It is recommended that both Orbiter and Spacelab samples be collected on future Spacelab missions for comparative analysis.

ACKNOWLEDGMENTS

The EDOMP team members would like to thank the USML-1 crew for their participation in this investigation.

REFERENCES

1. "Microbiology on Space Station Freedom," NASA Conference Publication 3108.
2. Burge, H. A. and M. Hodgson. 1988. "Health Risks of Indoor Pollutants." ASHRAE Journal. 30:34-38.
3. Pellikka, M., M. J. Jantunen, P. Kalliokoski, and E. Pitkänen. 1986. Ventilation and Bioaerosols," *In* H. D. Goodfellow (ed.), Ventilation '85. Elsevier Science Publishers B. V., Amsterdam, The Netherlands.
4. Casewell, M. W., N. Desai, and E. J. Lease. 1986. "The use of the Reuter Centrifugal air sampler for the estimation of bacterial air counts in different hospital locations." J. Hosp. Inf. 7:250-260.
5. Kang, Y., and J. F. Frank. 1989. "Evaluation of air samplers for recovery of biological aerosols in dairy processing plants." J. Food Prot. 52:655-659.
6. STS-40 Microbiology Mission Report (Memorandum SD4/91-312)
7. STS-45 Microbiology Mission Report (Memorandum SD4/92-186)

Table 1. STS-50 Spacelab Surface Samples

SAMPLE SITE	L-32	L+0	
MICROORGANISMS	QUANTITATION (CFU/25 cm ²)	MICROORGANISMS	QUANTITATION (CFU/25 cm ²)
Air Vent - Right Forward	No bacteria isolated	0	Staphylococcus species
	No fungi isolated	0	Bacillus species
Air Vent - Left Forward	Staphylococcus species	1.5 x 10 ¹	Staphylococcus species
	Micrococcus species		Corynebacterium species
Air Vent - Right Aft	No fungi isolated	0	No fungi isolated
	No bacteria isolated	0	Staphylococcus species
Air Vent - Left Aft	No fungi isolated	0	Micrococcus species
	No bacteria isolated	0	Penicillium species
	No fungi isolated	0	Aspergillus species
	No bacteria isolated	0	Staphylococcus species
			No fungi isolated

Table 1. STS-50 Spacelab Surface Samples (continued)

SAMPLE SITE	L-32 MICROORGANISMS	QUANTITATION (CFU/25 cm ²)	MICROORGANISMS	QUANTITATION (CFU/25 cm ²)
Work Bench Rail	<i>Bacillus</i> species	7.5×10^1	No bacteria isolated	0
	No fungi isolated	0	No fungi isolated	
Work Bench Utility Box	No bacteria isolated	0	<i>Staphylococcus</i> species	<10
	No fungi isolated	0	No fungi isolated	0

TABLE 2. QUANTITATION OF MICROORGANISMS ISOLATED FROM STS-50 ORBITER AIR

AREA	CFU/M ³ OF AIR		
	L-19	L-2	
	BACTERIA	FUNGI	BACTERIA
MIDDECK	162	0	0
FLIGHT DECK	275	0	75

Table 3. STS-50: Results of in-flight air sampling

SAMPLE AREA	DAY 1			
	** TIME	MICROORGANISM	QUANTITATION	
Spacelab Midmodule R5 - L5	9:45	<i>Staphylococcus</i> species	12	
	9:52	<i>Penicillium</i> species	375	
			Bacteria Mean = 194 CFU/m ³	
DAY 7				
Spacelab R6 - R7	1:25	<i>Staphylococcus</i> species	162	
		<i>Micrococcus</i> species No fungi isolated	0	
			Bacteria Mean = 81 CFU/m ³	
DAY 13				
Spacelab Midmodule R5 - L5	3:41	<i>Staphylococcus</i> species <i>Bacillus</i> species	50	
		No fungi isolated	0	
			Bacteria Mean = 25 CFU/m ³	

*CFU / m³

** Mission - elapsed time

803

1995707-19

NASA

N95-14223

324089

10/12/83

P-7

EXTENDED DURATION ORBITER MEDICAL PROJECT**VARIABILITY OF BLOOD PRESSURE AND HEART RATE - STS-50/USML-1**Janice M. Fritsch-Yelle*, John B. Charles* and Sheila W. Boettcher⁺

*NASA JSC, Houston, Texas

+KRUG Life Sciences, Houston, Texas

ABSTRACT

Decreases in arterial baroreflex function after space flight may be related to changes in blood pressure and heart rate patterns during flight. Ambulatory blood pressure and heart rate was measured for 24-hours, in 14 astronauts on two occasions before flight, 2-3 occasions in flight, and two days after landing on Shuttle missions lasting 4 to 14 days. Blood pressure and heart rate were recorded every 20 minutes during awake periods and every 30 minutes during sleep. In pre-and postflight studies, the 24-hour ambulatory measurements were followed by studies of carotid baroreceptor-cardiac reflex responses. Carotid baroreceptors were stimulated using a sequence of neck pressure and suction from +40 to -65 mmHg.

Carotid baroreceptor-cardiac reflex responses were reduced postflight. The variability of blood pressure and heart rate are both reduced in flight. None of the changes in blood pressure and heart rate patterns in-flight related to postflight reductions in baroreflex parameters.

NOMENCLATURE

ABPM	Automatic Blood Pressure Monitor
Carotid Baroreceptors	Blood pressure sensors located in the neck region used to regulate blood pressure and heart rate.
Diastolic Blood Pressure	Amount of pressure in the arteries during the (mmHg) relaxation phase of the heart cycle.
Systolic Blood Pressure	Amount of pressure in the arteries during the (mmHg) contraction phase of the heart cycle.
Barocuff	Inflatable cuff applied to the neck. Pressure in the cuff can be increased and decreased according to the protocol.
Valsalva Maneuver	Forced exhalation against the mouthpiece preventing exhaled air from escaping.

INTRODUCTION

Postflight alterations in cardiovascular responses to exercise and standing are initiated during flight, however, they are not known to impair cardiovascular performance in space (2). Functional problems become apparent on landing day, when most crew members have reduced exercise capacity and orthostatic tolerance (1). The cause of the orthostatic intolerance may be partly related with loss of plasma volume during weightlessness (5). Blood pressure variations in flight may also contribute to the orthostatic intolerance on landing. Data received from crew members on shorter flight durations (4-5 days) demonstrated significant reductions in vagal control of the sinus node that may contribute in part to orthostatic intolerance (3).

This investigation measured the cardiovascular responses (heart rate and blood pressure) of 14 astronauts on Shuttle flights lasting 4-14 days. Blood pressure and heart rate were recorded every 20 minutes during wake periods and every 30 minutes during sleep. Data sessions included preflight, in-flight, and postflight. The pre and postflight activity involved 24-hour ambulatory monitoring followed by studies of carotid baroreceptor-cardiac reflex responses. Baroreflex testing occurred six times postflight for crew members on missions greater than 10 days. Carotid baroreceptors were stimulated using a sequence of neck pressure and suction from +40 to -65 mmHg.

The data from the two subjects from USML-1 will be analyzed with the other 12 subjects to maintain the privacy of their medical data.

I. RESULTS

Daily means and standard deviations of arterial pressure and heart rate were averaged. Carotid distending pressures (systolic - neck pressure) were plotted against R-R intervals. Calculated variables were minimum, maximum, and range of R-R interval responses, maximum slope, and operational point. Maximum slopes were identified with linear regression analyses applied to each set of three consecutive data pairs on the stimulus-response relation. Operational points were defined as [(R-R intervals at 0 mmHg neck pressure minus minimum R-R interval)/R-R interval range] x 100%.

Variability of blood pressure and heart rate were both reduced in flight. Carotid baroreceptor-cardiac reflex responses were reduced postflight. Preflight slope was 4.9 ± 0.3 msec/mmHg, range was 250 ± 22 msec, and operational point was $40.0 \pm 3.8\%$. On landing day, slope was 3.9 ± 0.4 , range was 180 ± 17 msec, and operational point was $27.8 \pm 4.2\%$ ($p < 0.05$ from preflight). Three days after landing the slope was 4.8 ± 0.6 , range was 230 ± 22 , and operational point was $35.2 \pm 2.5\%$. No values three days after landing were different from

preflight. None of the changes in blood pressure and heart rate patterns in flight related to postflight reductions in baroreflex parameters.

II. DISCUSSION

A series of measurements to assess autonomic control of the cardiovascular system on 14 astronauts were performed before and after Shuttle missions lasting 4-14 days. Resting vagal control of R-R intervals as estimated by power spectral analyses was not altered after space flight. The balance between sympathetic and vagal R-R interval control shifted toward greater sympathetic influences on landing day, and for several days after landing. Abnormalities of carotid baroreceptor-cardiac reflexes found after shorter duration missions (4-5 days) were also found after longer missions, but were not greater. In fact, reduction of baroreceptor slope was less after the longer flights. Reductions of range of the R-R interval response were similar after the short and long missions. Systolic and diastolic pressure reductions during, and increases after Valsalva straining were greater on landing day than preflight. In four astronauts, preflight and in-flight "square wave" blood pressure responses changed to sinusoidal patterns on landing day (Figure 4). Several astronauts had orthostatic intolerance both before leaving the Shuttle and later during the stand tests in the clinic. Postflight reductions in standing arterial pressures and postflight reductions in baroreflex operational points were significantly correlated.

The four subjects mentioned above routinely exercised (running 20 to 25 miles per week). It has been suggested that these subjects had expanded plasma volume before flight as a result of their normal daily intense aerobic exercise regimens (4), and the change to a sinusoidal response on landing day is at least partially due to loss of blood volume during flight. Recent studies by the investigator have demonstrated that normal responders become square-wave responders when blood volume is increased by intravenous saline. These same subjects develop exaggerated sinusoidal responses after dehydration. Postural changes reducing central blood volume could also contribute to this phenomena (6).

Twenty-five percent of the 14 crew members experienced severe orthostatic symptoms while in the Shuttle after wheels stop and/or during the stand test later in the clinic. Systolic pressures decreased dramatically with standing on landing day after the longer missions (10 - 14 days) unlike the non-significant changes seen after shorter flights. Changes in diastolic pressures were similar to the short flights.

CONCLUSIONS

While the variability of blood pressure and heart rate are both reduced in flight, those reductions did not relate to changes in baroreflex function after landing for crew members. While this study was useful in systematically documenting for the first time changes in blood pressure and heart during space flight, the original hypothesis of long duration flights reducing the variability was not proven. Blood pressure and heart rate exhibited diurnal variation in flight, however this variation was reduced from preflight data.

ACKNOWLEDGMENTS

The EDOMP team would like to thank the crew members of USML-1 who participated in this study, with the discomforts of 24-hour monitoring and neck suction. We appreciate your dedication to collecting this scientific data and your contribution to the future of long duration space flights. We also thank the personnel of Marshall Space Flight Center whose efforts on this investigation have contributed to the future of long duration space flights.

REFERENCES

1. Bungo, M. W., and P.C. Johnson, Jr. Cardiovascular examinations and observations of deconditioning during the space shuttle orbital flight test program. *Aviation Space Environmental Medicine* 54: 1001-1004, 1983.
2. Dietlein, L. F. Skylab: A Beginning. *In:* Biomedical Results from Skylab, edited by R. S. Johnston and L. F. Dietlein. Washington, DC; NASA, 1977, p. 408-418.
3. Fritsch, Janice M. , Charles, J.B., Bennett, B.S., Jones, M.M., and Eckberg, D.L., Short-duration spaceflight impairs human carotid baroreceptor-cardiac reflex responses. *Journal of Applied Physiology* 73(2): 664-671, 1992.
4. Green, H. G., J.R. Sutton, G. Coates, M. Ali, and S. Jones. Response of red cell and plasma volume to prolonged training in humans. *Journal of Applied Physiology* 70: 1810 - 1815, 1991.
5. Johnson, P. C., T. B. Driscoll, and A.D. Leblanc. Blood volume changes. *In:* Biomedical Results from Skylab, edited by R. S. Johnston and L. F. Dietlein. Washington, DC; NASA, 1977, p. 235-241.
6. Ten Harkel, A.D., J.J. Van Lieshout, E.J. Van Lieshout, and W. Wieling. Assessment of cardiovascular reflexes: influence of posture and period of preceding rest. *Journal of Applied Physiology* 68: 147-153, 1990.

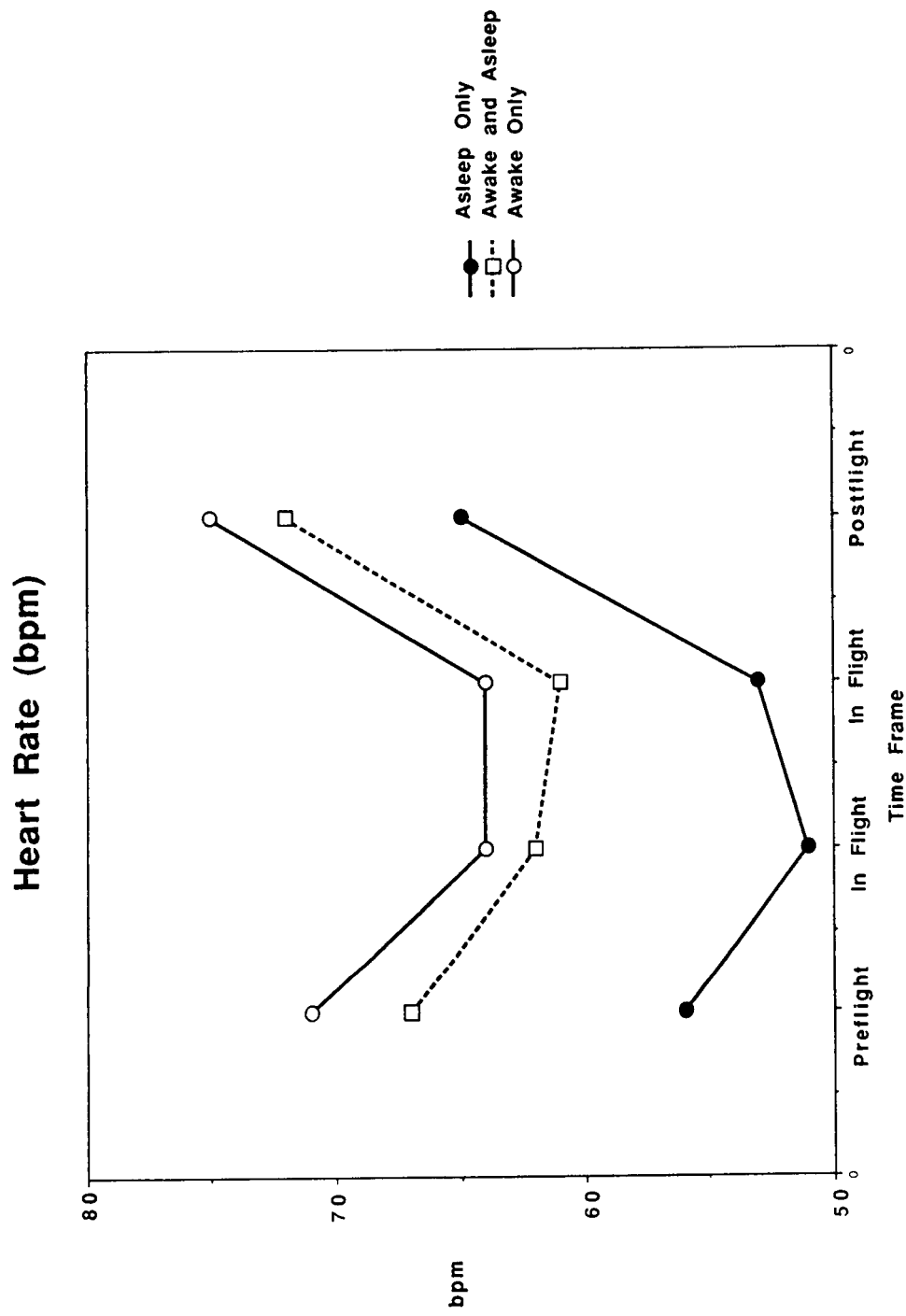


Figure 1 Heart rate variability in 14 astronauts on Shuttle flights of 4–14 days duration.

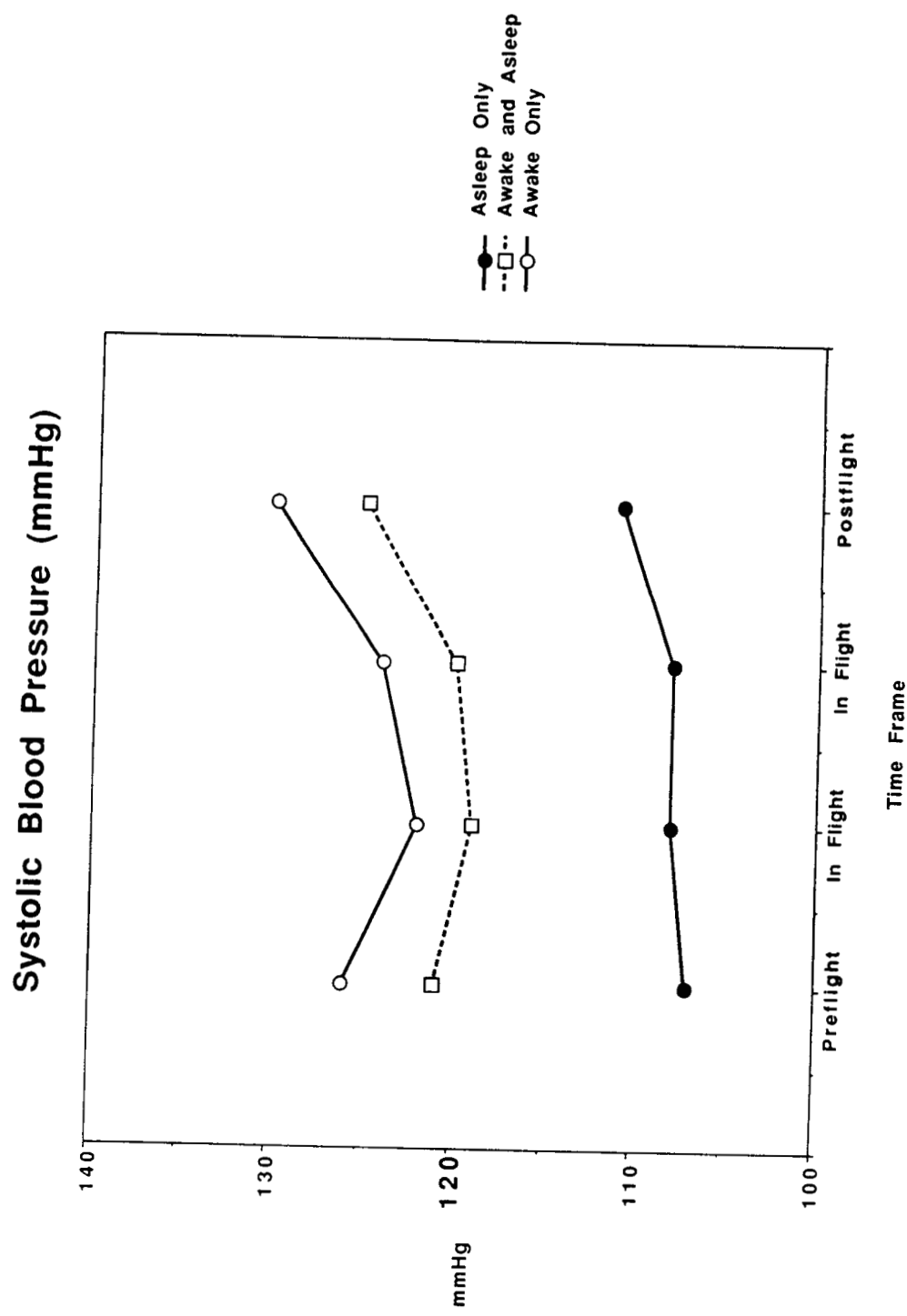


Figure 2 Systolic blood pressure variability in 14 astronauts on Shuttle flights of 4–14 days duration.

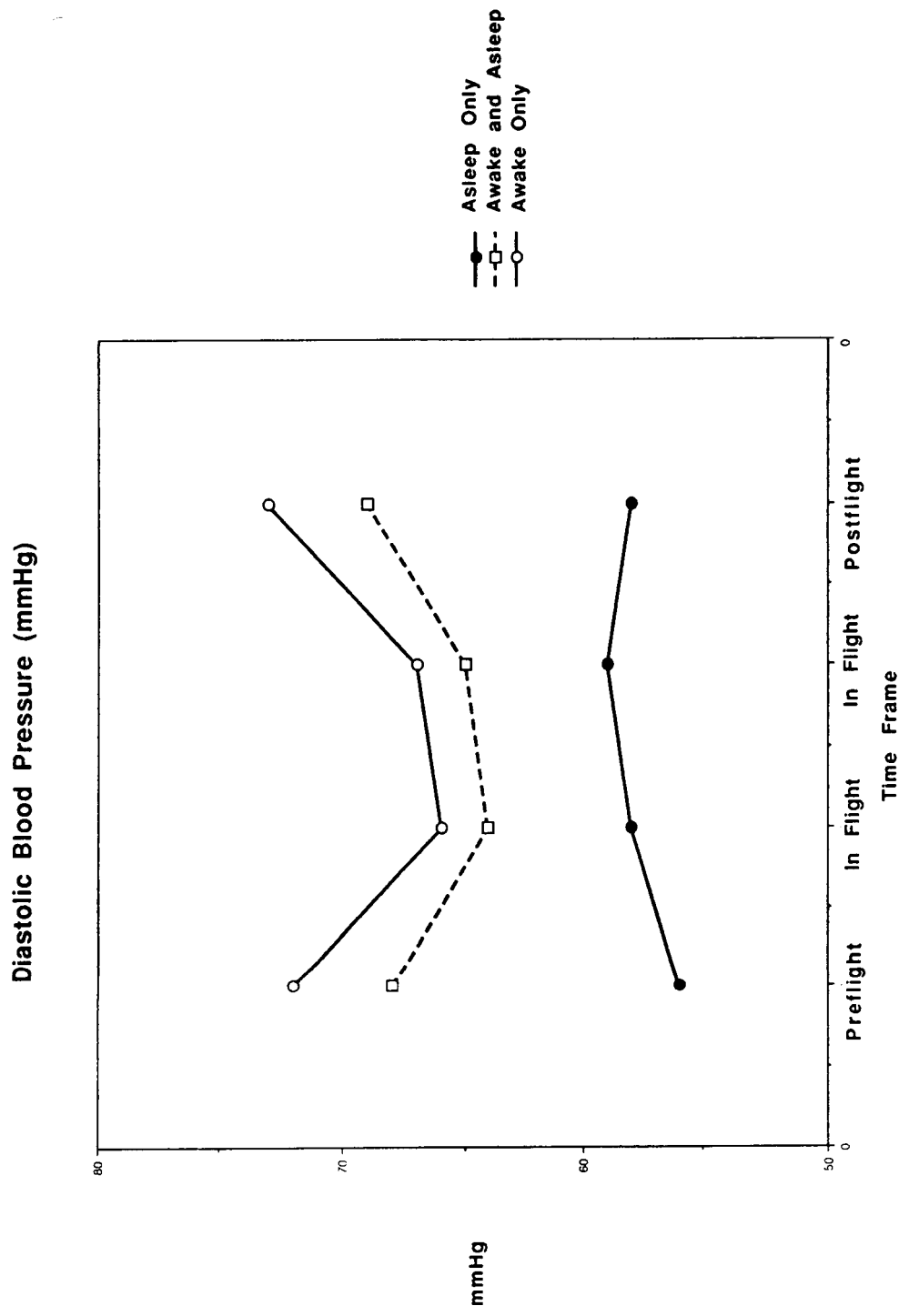


Figure 3 Diastolic blood pressure variability in 14 astronauts on Shuttle flights of 4–14 days duration.

18PG

199570790

NASA

N95-14224

324090

17029

P. 17

EXTENDED DURATION ORBITER MEDICAL PROJECT
COUNTERMEASURE TO REDUCE POST SPACE FLIGHT
ORTHOSTATIC INTOLERANCE (LBNP) - STS-50/USML-1

John B. Charles* and Sheila W. Boettcher⁺

*NASA JSC, Houston, Texas

⁺KRUG Life Sciences, Houston, Texas

ABSTRACT

During the STS-50/USML-1 mission and 5 other Shuttle flights, decompression of the legs and lower abdomen ("lower body negative pressure," LBNP) was used (1) to apply a standardized stress to the cardiovascular system, to document the loss of orthostatic function during an extended period in weightlessness, and (2) to test its efficacy as a treatment which may be used to protect astronauts from gravitationally-induced fainting during and after reentry on Space Shuttle flights.

The loss of orthostatic tolerance (as determined by LBNP) occurred even earlier than indicated by similar testing on Skylab (1973-1974). The treatment was shown to be effective in reversing some of the effects of extended weightlessness on the cardiovascular system for at least one day after treatment.

NOMENCLATURE

ABPM	Automatic Blood Pressure Monitor
AERIS	"American Echocardiograph Research Imaging System", a modified commercial cardiac ultrasound device
BP	Blood pressure, the result of the ejection of blood from the heart into the elastic arteries, especially the aorta
Bradycardia	Slow heart rate
CO	Cardiac output, the volume of blood ejected during one minute
Diastolic	During the relaxation phase of the heart beat
Dysrhythmia	Abnormal heart beat

Joint "L+1" Science Review for USML-1 and USMP-1 with the Microgravity Measurement Group, September 22-24, 1993, Huntsville, Alabama, USA.

391

ECG	Electrocardiogram, also known as EKG
JSC	Johnson Space Center, Houston, Texas
LBNP	"Lower body negative pressure", the decompression of the legs and lower abdomen to allow blood pooling mimicking that in the upright posture
MSFC	Marshall Space Flight Center, Huntsville, Alabama
Orthostatic	Relating to the upright posture on Earth's surface
Plethysmograph	A device for measuring the volume of a limb
SV	Left ventricular stroke volume, the volume of blood ejected with each heart beat
Systolic	During the contraction phase of the heart beat
Tachycardia	Rapid heart rate
TPR	Total peripheral resistance, the result of the constriction of the small arteries throughout the circulatory system

INTRODUCTION

A candidate countermeasure against orthostatic intolerance after space flight was evaluated for its efficacy and operational practicality. This countermeasure, lower body negative pressure (LBNP) combined with salt, and fluid ingestion, is intended as a single-application, end-of-mission treatment to pre-adapt the cardiovascular system to exposure to orthostatic stress during and after Space Shuttle reentry, landing and cabin egress. The countermeasure evaluation involved 12 crew members as in-flight participants on six Shuttle flights of 9-14 days duration.

Exposure to weightlessness, even for short periods, induces significant changes in the cardiovascular system which are proposed to be secondary to headward fluid shifts, subsequent plasma volume contraction, and ensuing adaptations in cardioregulatory function (1). The resulting cardiovascular state is inappropriate for orthostasis on Earth as manifested by the clinical findings of tachycardia, decreased exercise capacity and orthostatic intolerance (demonstrated by symptoms of dizziness) and presyncope or syncope (loss of consciousness) on return to Earth.

These findings prompted operational concerns for Space Shuttle crew members, due to their upright posture during Shuttle reentry and landing maneuvers and to the high degree of pilot involvement in the Shuttle landing process (2). These concerns have become especially pertinent as

Shuttle flight durations are extended, presumably predisposing the astronauts to an even greater risk of orthostatic intolerance during this critical mission phase (2).

Development of appropriate countermeasures to this cardiovascular change has been a priority of NASA's in-house directed medical research. One candidate countermeasure under investigation since the 1960s (6) involves lower body decompression (LBNP). This technique, which typically decompresses the legs and abdomen by up to 50 mm Hg, provides a cardiovascular stress similar to standing upright (orthostasis) by allowing blood to pool in the legs and abdomen (14). Brief decompression is used as a gravity-independent test of orthostatic capacity; longer decompression, either alone or in combination with salt and water ingestion, has been used as a countermeasure to restore orthostatic tolerance in bedrested subjects and astronauts. LBNP has been used in both of these capacities during Russian and U.S. manned space flights.

The first in-flight assessment of orthostatic tolerance was performed on the Soviet Union's Salyut 1 space station in 1971 (4). Two of the three crewmen were tested once in flight, on day 13 of their 24-day flight, using a prototype of the now-standard "Chibis" pneumatic vacuum suit. Two years later, the Skylab program allowed U.S. investigators to determine the time course of the development of orthostatic dysfunction in weightlessness (11, 12, 13). During all three Skylab missions (28, 59, and 84-day durations), crew members' heart rate (HR) and blood pressure (BP) responses to the standardized graded stress provided by the onboard LBNP device were recorded at approximately 3-4 day intervals. During the initial in-flight tests, which were performed on the 4th, 5th, and 6th days of flight, HR responses to the stress were already exaggerated compared to preflight tests. Resting HR plateaued after about 10 days of weightlessness; stressed HR plateaued after 20 days of weightlessness. BP was generally maintained throughout those LBNP studies that did not end in presyncope or bradycardia. The greater increase in HR during flight than before flight could reflect compensation for a reduction in blood volume early in flight. Calf volume increases with LBNP were greater during flight than before flight, probably because greater volumes of blood were required to fill the relatively empty leg veins during flight.

LBNP testing of cardiovascular function has been performed during all but one of the missions to the Russian Salyut and Mir space stations. In agreement with the U.S. Skylab data, testing of the crews of the 49-day and 17-day missions to Salyut 5 indicated that individual responses to in-flight LBNP tests were predictive of postflight responses to orthostatic stress (5).

The development of LBNP-based countermeasures proceeded independently in Russia and the U.S. Soviet researchers developed an LBNP countermeasure for use on long duration space missions (7). Since the mid-1970s, a routine multi-week course of LBNP treatments has gradually been developed for use by the crews of the Salyut and Mir space stations in preparation for landing.

This now typically includes brief, step-wise decompressions over 20-30 minutes at 4 day intervals beginning 3-4 weeks before landing, and culminates with 1-hour sessions of graded decompressions on the last two full days in flight. Extra salt is taken with meals on those days.

In the U. S., a variety of LBNP protocols were developed which were effective in preventing or reversing orthostatic intolerance during bedrest but which were also prohibitively long (several days) at the end of the bedrest (6). The breakthrough came in 1977 when Hyatt and West (9) demonstrated that a single application of only 4 hours of LBNP, when combined with the ingestion of one liter of a bouillon solution, restored plasma volume and orthostatic tolerance to pre-bedrest levels for at least 18 hours, even after seven days of bedrest. This result was confirmed in six subjects after two weeks of bedrest (10). The effective treatment period could not be reduced below 4 hours using the same protocol (one liter of isotonic solution and 30 mm Hg decompression).

These investigations formed the basis for the combined treatment countermeasure for orthostatic intolerance that has been tested during Shuttle flights.

I. METHODS

A collapsible LBNP device developed for use on-board the Space Shuttle was used for all in-flight decompressions (Figure (1)). A modified ambulatory blood pressure monitor measured HR and BP and provided analog electrocardiogram and BP signals for telemetry to MSFC and JSC. Cardiac ultrasound measurements of left ventricular end-diastolic volume) were performed in-flight on 4 Shuttle flights (STS-32, 43, 47, and 50). Ultrasound Doppler measurements of aortic blood flow (for calculation of stroke volume, cardiac output and total peripheral resistance) were performed for the first time in-flight on STS-50 (USML-1) using the AERIS device. In-flight leg volume measurements using the stocking plethysmograph were performed on STS-47 and STS-50 only.

On the USML-1 mission, LBNP was performed in-flight as tests ("ramps") of cardiovascular response, a treatment ("soak") and follow-up ramp tests to determine the effectiveness of the treatment after 24-hours and 48-hours. This time frame was selected to simulate a nominal landing 24-hours after the soak and a 1- day delay in landing (48-hours after the soak). The in-flight ramp and soak protocol are outlined in Figures (2) and (3) respectively.

The ramp tests consisted of 10 minutes of baseline data collection at 0 mm Hg of LBNP device decompression, 5 minutes of data collection at each step of decompression (10, 20, 30, 40 and 50 mm Hg), and 5 minutes of recovery data collection after recompression to ambient pressure. The soak treatment began with a step-wise decompression to 50 mm Hg followed by about 3.5 hours of LBNP at 30 mm Hg below ambient pressure. The total time of decompression of at least

30 mm Hg was 4 hours. One liter of water or artificially sweetened fruit drink and 8 grams of salt (NaCl in 1 gram tablets) were ingested during the first hour at 30 mm Hg decompression. The treatment was evaluated by comparing HR and BP responses to test decompressions on days before and after treatment.

Test termination criteria for LBNP testing included: achieving a HR equal to the maximum HR seen in preflight LBNP testing; one-minute decreases in HR of 15 beats/minute, in systolic BP of 25 mm Hg, and /or in diastolic BP of 15 mm Hg; a variety of clinically significant cardiac dysrhythmias; loss of signal at levels of decompression greater than 30 mm Hg;; and subject request at any time. Some tests were terminated on STS-50 for the maximum HR criterion; this represented a normal physiological response to space flight, and did not imply an increased risk to any subject.

II. RESULTS

The typical HR and BP response to LBNP is shown in Figure 4. Twenty four hours after the combined countermeasure of salt and water ingestion during LBNP at 30 mm Hg below ambient pressure, the HR response to 40-50 mm Hg lower body decompression was not statistically different from the preflight value. However, two days after the combined countermeasure, the HR response to decompression was not statistically different from the last pre-treatment ramp test. Thus, the cardiovascular effect of the soak treatment was present in crew members for at least one day after treatment.

Neither systolic nor diastolic BP responded significantly to the submaximal levels of LBNP tested in-flight.

Leg volume showed no greater increase after the 4-hour soak than after the 25-minute ramp tests.

Cardiac ultrasound measurements documented the expected decrease in left ventricular end-diastolic volume and stroke volume at rest and under LBNP stress. Cardiac output was maintained by an increase in HR. BP was maintained at preflight levels throughout in-flight testing by an appropriate increase in total peripheral resistance. Measurements of SV, CO and TPR responses to the soak treatment were not possible after the AERIS failed on flight day 9.

III. DISCUSSION

The loss of orthostatic tolerance (as reflected by heart rate response to 40-50 mm Hg decompression) occurs even earlier in flight than indicated by the Skylab data. The cardiovascular adaptations to weightlessness are thus shown to be rapid, implying that even short Shuttle flights

invoke nearly the full cardiovascular risk of orthostatic intolerance heretofore expected only on long flights.

The candidate treatment has been shown to be effective in restoring HR response to LBNP stress to its preflight value for at least one day after treatment, but not for two days. Thus, any operational application of this treatment must be planned for the day before landing; last-minute delays in landing, such as occurred on STS-50, will require re-treatment for maximum crewmember safety.

The capability for simulating the effects of orthostatic stress on the cardiovascular system during Space Shuttle flights has been developed and demonstrated. This capability can be used for basic and applied research as well as for the application of countermeasures.

ACKNOWLEDGMENTS

The EDOMP team would like to thank the crew members of USML-1 who participated in this study. LBNP required a substantial commitment on their part, with a certainty of inconvenience if not outright discomfort. We also thank the personnel of Marshall Space Flight Center whose efforts on this investigation have contributed to the future of long duration space flights.

REFERENCES

1. Blomqvist, C. G., and H. L. Stone. Cardiovascular adjustments to gravitational stress. In: *Handbook of Physiology*, Volume III. Edited by: Shepherd, J. T., and F. M. Abboud, Bethesda, MD: American Physiological Society, pp. 1025-1063, 1983.
2. Bungo, M. W., J. B. Charles, and P. C. Johnson, Jr. Cardiovascular deconditioning during space flight and the use of saline as a countermeasure to orthostatic intolerance. *Aviation Space Environmental Medicine* 56: 985-990, 1985.
3. Charles, J. B., and C. M. Lathers. Cardiovascular adaptation to space flight. *Journal of Clinical Pharmacology* 31: 1010-1023, 1991.
4. Degtyarev, V. A. and V. M. Khayutin. Condition of the human cardiovascular system in true and simulated weightlessness. NASA Technical Translation, 1971.
5. Degtyarev, V. A., V. G. Doroshev, Z. A. Kirillova, N.A. Lapshina, S. I. Ponomarev, and O. B. Kulikov. Hemodynamics and phase structure of the cardiac cycle in members of the first crew of Salyut-5 at rest. *Kosm. Biol. Aviakosm. Med.* (English Translation) 14(4): 11-16, 1980.
6. Fortney, S. M. Development of lower body negative pressure as a countermeasure for orthostatic intolerance. *Journal of Clinical Pharmacology* 31: 888-892, 1991.
7. Grigoriev, A. I. Correction of changes in fluid-electrolyte metabolism in manned space flights. *Aviation Space Environmental Medicine* 54(4): 318-323, 1983.

8. Hoffler, G. W. Cardiovascular studies of U. S. space crews: an overview and perspective. In: *Cardiovascular Flow Dynamics and Measurements*. Edited by: Hwang, N. H. C., and N. A. Normann, Baltimore, MD: University Park Press, 1977.
9. Hyatt, K. H., and D.A. West. Reversal of bedrest-induced orthostatic intolerance by lower body negative pressure and saline. *Aviation Space Environmental Medicine* 48: 120-124, 1977.
10. Johnson, P.C., Jr. Fluid volume changes induced by space flight. *Acta Astronautica* 6: 1335-1341, 1979.
11. Johnston, R. L., G. W. Hoffler, A. E. Nicogossian, and S. A. Bergman. Skylab experiment M-092: results of the first manned mission. *Acta Astronautica* 2: 265-296, 1975.
12. Johnston, R. L., A. E. Nicogossian, S. A. Bergman, and G. W. Hoffler. Lower body negative pressure: the second manned Skylab mission. *Aviation Space Environmental Medicine* 47(4): 347-353, 1976.
13. Johnston, R. L., G. W. Hoffler, A. E. Nicogossian, S. A. Bergman, and M. M. Jackson. Lower body negative pressure: third manned Skylab mission. In: *Biomedical Results From Skylab* (NASA SP-377). Edited by Johnston, R. S. and L. F. Dietlein, Washington, DC, U. S. Government Printing Office, pp. 284-312, 1977.
14. Wolthius, R. A., S. A. Bergman, and A. E. Nicogossian. Physiological effects of locally-applied reduced pressure in man. *Physiology Review* 54: 566-595, 1974.

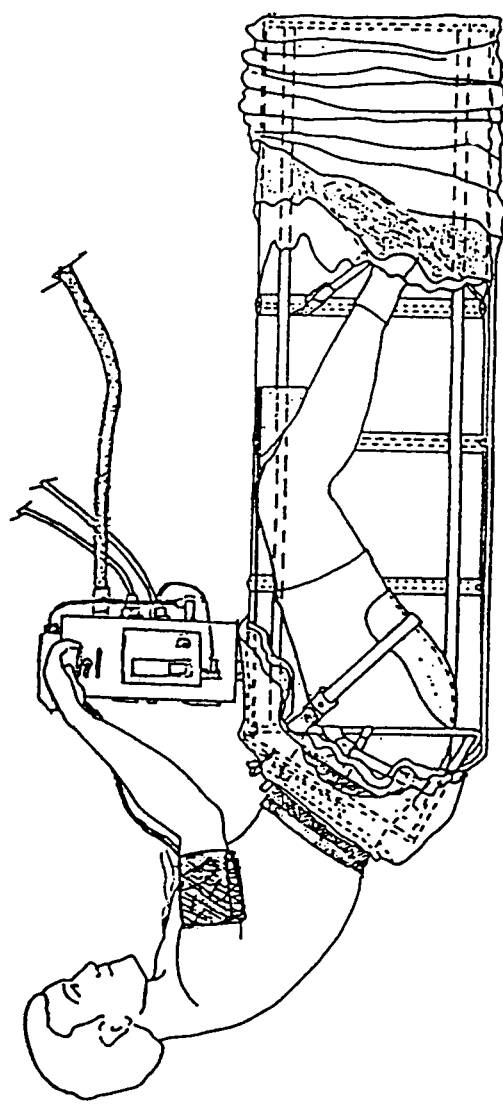


Figure 1 In-flight LBNP hardware configuration.

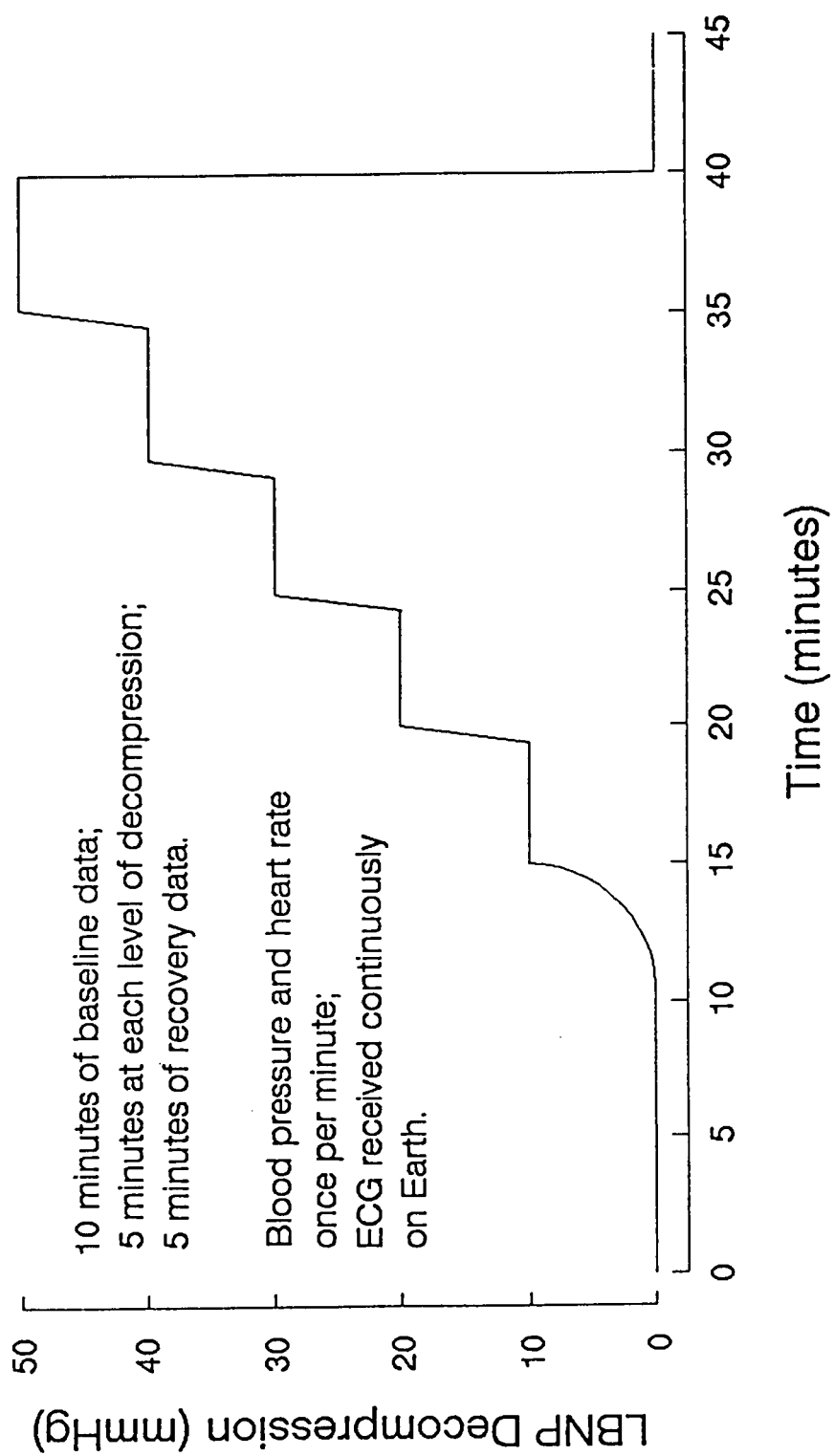


Figure 2 LBNP ramp protocol

**Combined Countermeasure (LBNP + Saline)
Basic Treatment Protocol**

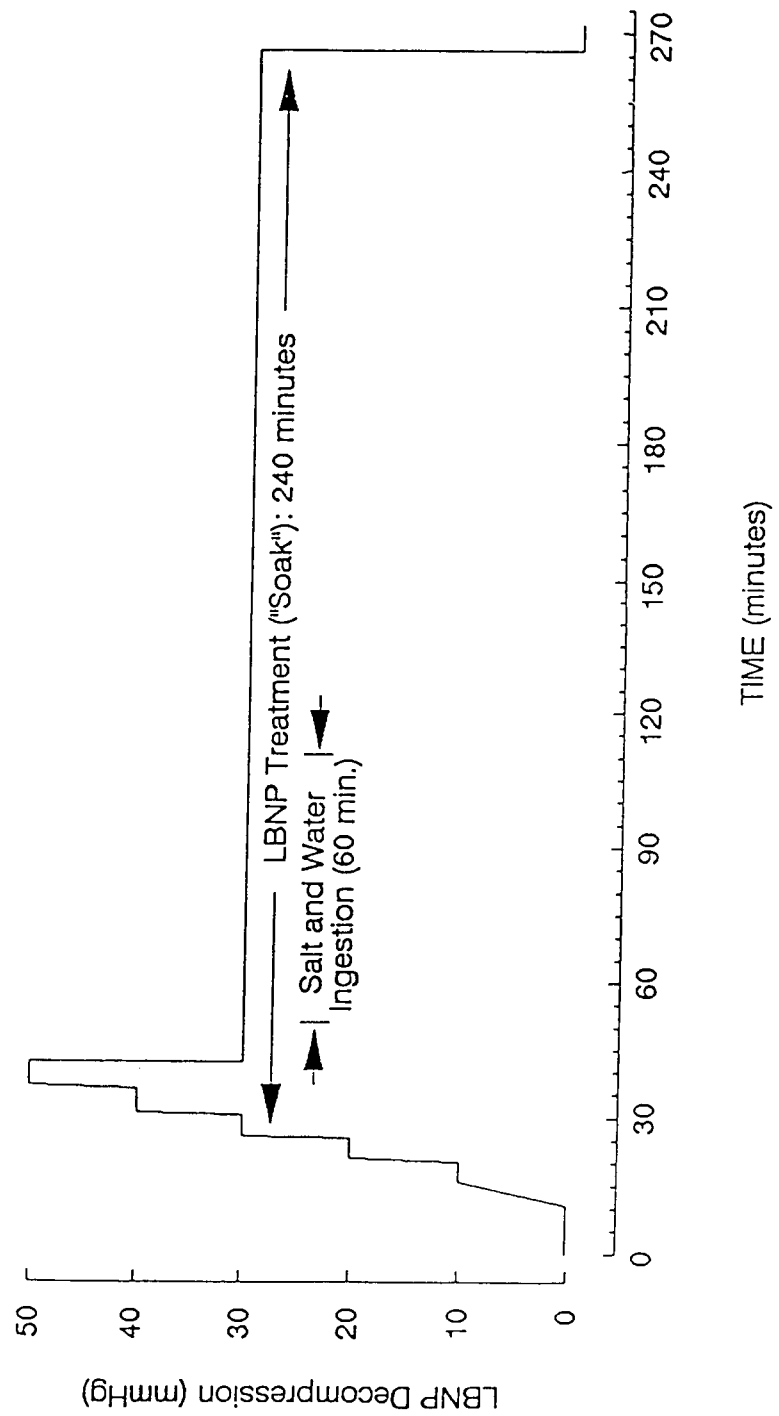


Figure 3 LBNP soak protocol.

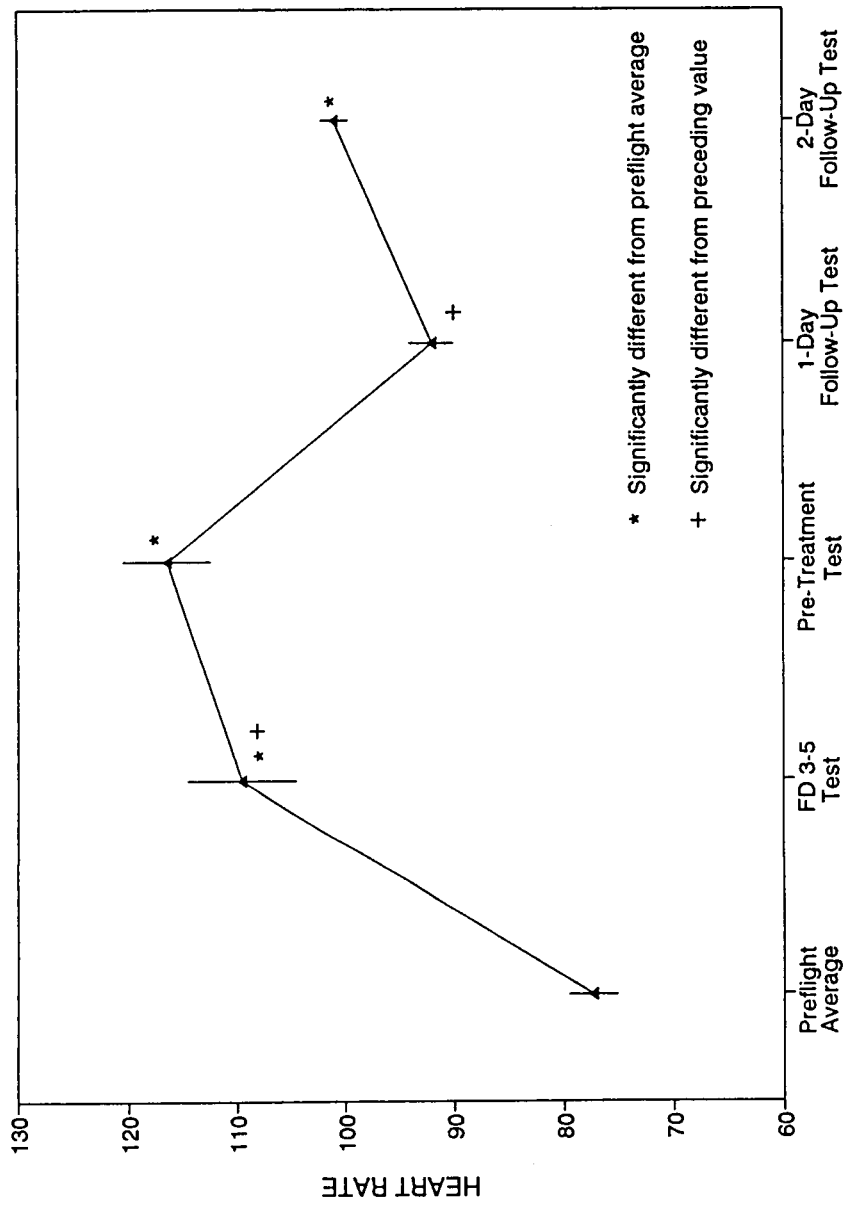


Figure 4 Heart rate during maximum level of the LBNP ramp test before and after soak treatment for 4 astronauts.

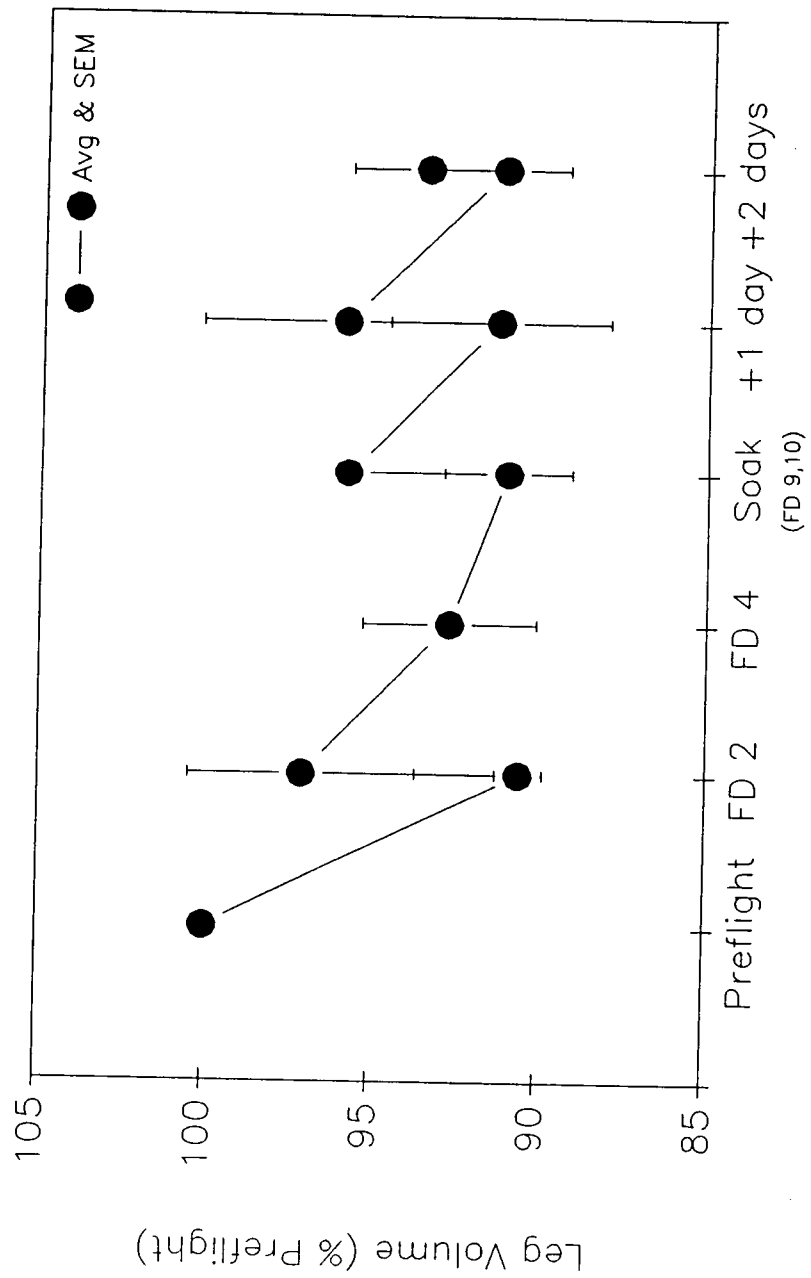


Figure 5 Leg volume responses to in-flight LBNP on STS-50/USML-1; n = 2.

Discussion

Questions: *What causes the blood volume loss you talked about ?*

Answers: The blood volume loss is believed to be caused by the fact that the normal hydrostatic pressure gradient which I am feeling at this moment disappears in 0 g. The blood volume which is normally sequestered in the legs or at least pools in the veins in the legs, then has no reason to pool in the veins in the legs. Those normal physiological mechanisms that squeeze it back up, act unopposed, squeezing the blood back up to the thorax and the upper part of the body, the head. In fact, if you look at photographs of the astronauts in flight, you see sometimes fairly puffy faces and some of the neck veins and head veins stand out. You will also see what some people call the bird legs of space flight which is when the legs on the flight get very small. Those mechanisms act unopposed and squeeze the fluid to the upper part of the body and it just so happens the reflexes which control blood volume are in the upper part of the body. So as far as the sensors that are built in the cardiovascular system are concerned, it is not fluid volume shifted, it is too much fluid volume and so they act through a complex series of mechanisms to reduce the blood volume in the body to an appropriate state. I should stress that all the data we have indicates the appropriate adaptation of normal, healthy people to space flight, and this is fine as long as they stay in space flight. If they are brash, as in to try to land and come to 1-g, then it is not an appropriate adaptation to life at 1-g post flight.

Question: *So the ratio of the red cells to water in the blood goes up ?*

Answer: It goes up briefly in flight, by briefly I mean a few weeks. As you excrete the watery portion of the blood you leave behind the red cells and the fraction increases and so the ratio increases. The body seems to have sensors for this as well, and seems to decrease the production of red cells to bring the ratio back down to normal. That is the adaptation, that is the anemia that you will sometimes hear about in space flight.

Question: *If the baro receptors are being fooled because you have a shift, because you have a shift in your fluid, why is it that the longer you stay in space the thought is, the worse off you will be in terms of this hypertension effect ?*

Answer: Well in fact, we physiologists and medical researchers have made some fairly naive assumptions about the effect of prolonged space flight. My current thinking is the stress in the cardiovascular system changes fairly quickly in orbit, within hours to days within reaching orbit. I think the cardiovascular stresses, especially the change stimulation of the baro receptors in the body occurs quickly in flight, and probably doesn't increase too much beyond the first few days to weeks in flight. It

think the evidence from Skylab, the Shuttle, the Salyut and Mir flights, all experiments from pre and post flight show that the effect of a 4 or 5 day flight probably is not going to differ dramatically from a 14 day flight. What that means and it sounds good, it sounds like we are flying 4 and 5 day flights routinely with no problem so there is no problem flying longer missions, but I am here to tell you that is not the case. We have problems out there with shorter flights that need to be paid attention to.

Question: *Is it possible that as they sit in an environment where there is not much fluctuation, they somehow lose the ability to monitor the situation and so when you return to Earth, they don't work as well?*

Answer: That is our hypothesis. That was the hypothesis of the experiment that was done on the blue shift with the blood pressure variability. I still believe in the hypothesis, I just don't think we have the right technology to demonstrate that.

Question: *There are other counter measures, some we used on our flight (USML-1). Has there now been enough data accumulated to start to compare them and see which one is more effective ?*

Answer: The other counter measures that were used on your flight included an intense bout of exercise. I believe one or two people on your crew did it the day before landing, the idea there being, to follow up on bed rest study which may show that an intense bout of maximal exercise has the effect of restoring the plasma volume as we discussed here a few moments ago, and thereby hopefully increasing other static tolerance. Another counter measure was the application of a synthetic version of a normally occurring hormone. The hormone is called aldosterone which forces the body to retain salt and thereby retain water. That was used in a couple of individuals as well. Both of these investigations have occurred on other flights and the results are equivocal from those investigations. I do not have a high level of confidence in the hormone as an effective counter measure based on the data we have. Because they are attractive in terms of taking a pill versus 4 hours of LBNP, we continue to investigate, making sure we are making the right measurements in bed rest and in space flight, to demonstrate that it does or does not work effectively.

Question: *Could you comment on the amount of variability in cardio-vascular changes among different crew members in flight ?*

Answer: There is a depressing amount of variation among individuals. There are some people who fly 10 and 14 day missions, who are immune, who have no difficulty at all and there are some folks that fly 4 day missions who are in fairly sorry states after landing. I can qualify that with two episodes. One of the treatments for orthostatic intolerance and for a general physiological depressed state is to reinfuse some

fluid volumes. You have all seen the bags of saline that physicians will put through a vein and restore some blood volume. That has occurred on two incidences that I know of on shuttle flights. One after a 10 day flight and one after a four day flight. Based on just that little evidence alone, there is not an appreciable agreement in the cardiovascular or the static effects of 4 to 10 day flights and, like I say, it is not good news for the long flights, but it is bad news for the short flights.

Question: *Is there any correlation between the amount of changes in an individual and the tendency to sea sickness ?*

Answer: Well by the term sea sickness we relate that to space motion sickness and I don't think there is a good correlation. I am told there is not a good correlation between any kind of motion sickness on the ground and motion sickness in flight, but there is no doubt that there is motion sickness. And there is an incidence, depending on how you quantify it, of 25-50% plus of motion sickness in flight. We have shown that the folks that have the most trouble standing up post flight are also the folks that were the sickest on flight. There was a strong correlation between being sick in flight and having this apparently unrelated cardiovascular problem on landing day. Now what that tells me is two things. If you are sick in flight, either you are not eating or drinking and keeping yourself well hydrated and well nourished and you are putting yourself at physiological risk or maybe it is folks that are sick in flight are doomed to be sick in flight and are doomed to have cardiovascular problems post flight because a lot of the reflexes are common in both syndromes. We cannot differentiate between those, but we do encourage crew members to eat, hydrate and nourish themselves properly and to get as much rest as we, the investigators, will allow them to have. I have to wear two different hats because as a physiologist who is doing research, I have to say rest is for the wimpy and let's get on with some more LBNP studies, but as someone who is charged with providing the astronauts well being there is no doubt that properly eating and resting are vital to continued safe function and flight.

Question: *How do you choose the pressure levels selected during LBNP and are you likely to change them ?*

Answer: I am not likely to change them. We have modified them a little bit. The pressure levels that you are thinking of 0, 10, 20, 30, 40, 50 mm-mercury decompressions are based actually on a long history of LBNP work preceding in fact Skylab. The investigators that did the work on Skylab established the -50 millimeters mercury as being a physiological analog to standing upright. So it seemed like a logical thing to investigate, if you are interested in the ability of astronauts to stand upright post-flight. It has become enshrined in literature. So if I want to maintain comparability between Skylab data and my

data in the literature base, I need to maintain comparability to those levels of decompression. But briefly -50 roughly approximates standing upright at 1-g.

Question: Could you comment on the soaking parameters.

Answer: The soaking is done with the -30 mm of mercury pressure because nobody wants to stand upright for 4 hours or longer. It was decided to pick a level that was tolerable for 4 hours but still a significant stress to exercise the cardiovascular system.

Question: Is there any reason that we can't do the soaks during crew sleep period ?

Answer: That is an excellent question. At first brush I am reluctant to do that because part of our monitoring of crew assurance and crew health is that the crew members don't faint during LBNP crew testing. And if someone is asleep you can't tell if they have fainted or not because they are unconscious. That would possibly eliminate a first line of protection in a very conservative medical monitoring situation. However, if we choose the appropriate level of LBNP, for example, say 15 millimeters of mercury for 8 hours instead of 30 millimeters of mercury for 4 hours, we might be able to circumvent with the appropriate medical monitoring equipment for heart rate and blood pressure that I showed you on the first view graph, there may be ways to go around that. I am not saying that 15 mm x 8 hours is equivalent to 30 mm x 4 hours. The only treatment that has been tried and is effective is 30 mm for 4 hours. A lot of investigators spent a lot of time back in the 60's and 70's looking at other combinations and that was the one that worked, really worked, with the addition of salt and water. So one of the tasks as we move in to the Space Station era and as we move further into the Space Shuttle era, is to try to optimize these kind of measures. If we can optimize it, by applying it during the sleep period, we will do so enthusiastically, but that has not been shown yet.

Question: Are the baro receptors localized or distributed in the body ?

Answer: The baro receptors are essentially nerve endings which wrap around the blood vessels. So if this is my artery, the baro receptors sort of wrap around and as your artery expands each time your heart beats those receptors stretch and with the influx of sodium across the membrane trigger additional activity along that nerve's fibers that is interpreted at the brain as whatever is supposed to be occurring at that location. The baro receptors are located preferentially in the carotid sinuses and the aortic arch. The aorta is the large artery that comes off the heart and carries blood throughout the body. In the arch of the aorta there are some baro receptors. Those are the two major areas of baro receptors. Baro meaning pressure, receptors meaning receptors or sensors. Those are the two areas that we are interested in the cardiovascular business. Now how those signals change at the sensor level, how the

mediation of those signals back to the brain and the brain stem changes and how the activity from the brain affects the effective organ changes, those questions all remain to be answered in space flight. They are going to be fairly invasive and fairly complex questions to answer, so we are trying to move in the other direction by applying essentially a black box as a cure to a very complex problem and sort of a stop gap solution to a problem.

38pg

1115 11/11

324091

17030
P. 37

PROTEIN CRYSTAL GROWTH RESULTS FROM THE UNITED STATES
MICROGRAVITY LABORATORY - 1 MISSION

*DeLucas, L. J., Moore, K. M., van der Woerd, M., Bray, T. L., Smith, C., Carson, M., Narayana, S. V. L., Rosenblum, W. M., Carter, D., Clark, Jr., A. D., Nanni, R. G., Ding, J., Jacobo-Molina, A., Kamer, G., Hughes, S. H., Arnold, E., Einspahr, H. M., Clancy, L. L., Rao, G. S. J., Cook, P. F., Harris, B. G., Munson, S. H., Finzel, B. C., McPherson, A., Weber, P. C., Lewandowski, F. A., Navia, M. A., Wilson, K. P., Thomson, J. A., Meade, C. J., Bishop, S. P., Dunbar, B. J., Trinh, E., Prahl, J., Sacco, Jr., A., and Bugg, C. E.

* Deputy Director
Center for Macromolecular Crystallography
University of Alabama at Birmingham
Birmingham, Alabama

ABSTRACT

Protein crystal growth experiments have been performed by this laboratory on 18 space shuttle missions since April, 1985. In addition, a number of microgravity experiments have also been performed and reported by other investigators, (1 - 7). These space shuttle missions have been used to grow crystals of a variety of proteins using vapor diffusion, liquid diffusion, and temperature-induced crystallization techniques. The United States Microgravity Laboratory - 1 mission (USML-1, June 25 - July 9, 1992) was a Spacelab mission dedicated to experiments involved in materials processing. New protein crystal growth hardware was developed to allow in orbit examination of initial crystal growth results, the knowledge from which was used on subsequent days to prepare new crystal growth experiments. In addition, new seeding hardware and techniques were tested as well as techniques that would prepare crystals for analysis by x-ray diffraction, a capability projected for the planned Space Station. Hardware that was specifically developed for the USML-1 mission will be discussed along with the experimental results from this mission.

INTRODUCTION

The study of protein crystal growth in microgravity has generated considerable interest in recent years. Through the support of the National Aeronautics and Space Administration (NASA), we have coordinated a program designed to study protein crystal growth processes in general, and have evaluated the affects of a microgravity environment on these processes. A large co-investigator group, consisting of researchers and/or engineers from universities, NASA, and aerospace or pharmaceutical companies, participated in the hardware development and scientific experiments. Since April, 1985,

experiments have been performed on eighteen U. S. Space Shuttle missions with a variety of crystal growth hardware and crystallization techniques. In a number of cases, results from these experiments indicate that proteins grown in microgravity may be larger, display more uniform morphologies, and yield diffraction data to significantly higher resolutions than the best crystals of these proteins grown on Earth.(8 - 11) This paper will discuss the hardware specifically developed for the USML-1 mission and the results obtained for the proteins flown on this mission.

I. HARDWARE DEVELOPMENT

A. Vapor Diffusion Apparatus

A vapor diffusion apparatus (VDA) (9, 12, 13) was used for protein crystallization experiments on thirteen different space shuttle missions. This hardware incorporates a vapor diffusion technique that is closely related to the widely used hanging drop method of protein crystal growth on Earth. (14) This method was chosen for several reasons: 1. most protein crystallography laboratories have extensive experience with this method and a large percentage of the protein crystals described in recent publications have been obtained by this technique; 2. this technique is particularly amenable to crystallization experiments involving small quantities of protein; 3. in a microgravity environment, relatively large, stable droplets of protein solution can be formed with minimal surface contacts, thereby decreasing possible nucleation sites and minimizing wall effects that generally accompany crystallization experiments on Earth. The hardware was developed from a simple piece of equipment that was easily modified and improved throughout the series of shuttle missions. (9, 12, 13)

Although microgravity experiments with the VDA clearly demonstrate the beneficial effects of this environment for protein crystal growth, only about 20% of the proteins examined were found to exhibit better morphologies or better quality data than their Earth-grown counterparts. Approximately 40% of the space experiments failed to produce crystals, and the remaining 40% yielded crystals that were either too small for x-ray analysis or produced data no better than that obtained from the best Earth-grown crystals. It is important to note that results from a single space experiment, in which each protein is typically allotted five crystallization chambers, are being compared to the best crystals ever produced for that particular protein by any method on Earth. Investigators have no opportunity to optimize crystal growth conditions in microgravity. This may account for some occasions in which unsatisfactory results were obtained in microgravity.

B. USML-1 Glovebox Vapor Diffusion Hardware:

To allow crewmen to optimize microgravity crystal growth conditions, new hardware was developed and flown on the USML-1 mission in June, 1992. A glovebox was available in the Spacelab

module for this mission, providing sufficient containment that liquids (i. e. proteins, buffers, etc.) could be manipulated by methods similar to those employed on Earth. The hardware developed for this mission incorporated several new capabilities: 1. optimization of crystal growth experiments; 2. in-orbit seeding with small crystals produced in microgravity; 3. investigation of crystal-mounting techniques for future shuttle missions and for the planned Space Station; 4. use of video transmission of experimental results to facilitate scientific input from the ground regarding new experiments to be prepared in orbit.

Figure 1 shows the design of the vapor diffusion apparatus. Each chamber (constructed from clear polysulfone material) consists of a rectangular upper and lower half sealed by a neoprene gasket. The upper half contains the protein solutions to be used for three separate vapor diffusion experiments while the opposing half contains depressions which hold their respective reservoir solutions.

The protein and reservoir solutions are prepared on the shuttle using Hamilton syringes in conjunction with a dispensing device that allows microliter quantities to be extruded accurately and rapidly (figure 2). The solutions used to prepare these experiments are contained in vials/bottles with rubber septa so that they can be accessed via the Hamilton syringes (figure 2). Solutions are dispensed into the polysulfone chambers and mixed by withdrawing and re-extruding them from the syringes and/or by gentle stirring with the end of the syringe needle.

After all three crystallization experiments have been prepared, the crystallization chambers are placed together and sealed by tightening a thumbscrew. The experiments can be deactivated (the vapor diffusion process terminated) by a 180° rotation of the upper half of the experimental chamber. Eight chambers (24 vapor-diffusion experiments) are stored in a holder which fits into a lexan containment tube, thereby providing a second level of containment for the fluids. Thirty two of these containment tubes (768 experiments) can be placed into a tray which slides into the refrigerator/incubator module (R/IM) so that a precise temperature can be maintained throughout the crystallization process (figure 3).

In addition, a commercial micro-manipulator (x-y-z translation stage) was adapted to hold a manostat syringe on which capillaries could be attached for crystal mounting (figure 4). The translation stage is attached to a magnetic base that can be affixed to the metal floor of the USML-1 glovebox. Each vapor diffusion experiment could be observed by placing the experiment chamber in a specially constructed x-y-z translation stage with fiber optic back lighting (figure 4). This stage was subsequently used to prepare and observe experiments via a Zeiss binocular microscope with a special adapter that allowed 35 mm photography and/or real time video transmission of the crystals to scientists on Earth.

C. Experimental

The VDA performed flawlessly on this mission. However, it was clear from the photographic sessions taken on day 6 that very little mixing had occurred for the more viscous solutions (i. e. high

molecular weight polyethylene glycols) used to crystallize various proteins. A sharp demarcation (due to a refractive index change) could be seen between the protein and precipitating agent solution indicating that very little mixing had occurred. It was clear from this observation that a new enhanced mixing syringe is necessary for the more viscous solutions used in these experiments.

There were 2 major problems encountered when the glovebox hardware was tested. Commercial Hamilton syringes were used to withdraw liquid (protein, buffer or precipitating agent) for preparation of the experiment in the vapor diffusion chambers. Unfortunately, several of the crystallization solutions produced hundreds of small bubbles when withdrawn into the syringe. The bubbles had to be eliminated by manual centrifugation of the syringe by the crewman, since they would affect accuracy while dispensing solutions. This procedure caused the bubbles to coalesce on one end of the syringe thereby allowing the solution to be precisely dispensed for these experiments. A second problem encountered was difficulty in positioning the protein droplet in the center of the experimental chamber. Once the droplet was extruded from the syringe, it was stirred to ensure adequate mixing of solutions. The stirring action caused droplets to slide along the polysulfone material, often merging with the chamber walls, and spreading into a thin layer, which adversely affected the vapor equilibration profile. Even when droplets were properly positioned, on subsequent days it was noticed that several droplets had repositioned themselves along the chamber wall, which again adversely affected the vapor diffusion profile for these delicate experiments. These two problems are currently being addressed by:

1. the design of a new improved syringe that should minimize bubble formation;
2. the design of new experimental vapor diffusion chambers with multiple pinning edges to contain droplets of varying sizes.

After the mission, the experimental chambers were returned to UAB so that the crystals could be analyzed. Laboratory co-investigators found it very difficult to retrieve some of the crystals, as droplets had moved to the corners of the crystallization chamber in almost every case. It is believed that this was due to the orientation of the hardware during the re-entry high-g profile. As a result, the new experimental chambers are being designed so that their orientation will minimize the adverse effects of higher g-loads experienced by the shuttle on re-entry.

D. X-Ray Analysis

Because evaluation of diffraction resolutions from photographs is highly subjective, and is often dependent on crystal orientations, we have depended primarily on three-dimensional intensity data sets for comparison of space- and Earth-grown crystals.

Intensity data sets from crystals were analyzed in a variety of different ways. The largest Bragg angles at which usable data could be measured were assembled, and the percentage of data above background levels through the data collection range was evaluated. Plots were made of average $I / \sigma(I)$

values, where I is intensity, versus diffraction resolution and of percentages of data above various cutoff levels as functions of resolution. Data sets from space- and Earth-grown crystals were compared by using Wilson plots (15). The Wilson plot can be used to estimate the overall B values for a crystal, the B value being a parameter that reflects the internal order within a crystal. Relative Wilson plots, also known as difference Wilson plots (15), are useful for assessing changes in the internal order of protein crystals. These plots of $\ln(\sum F_a^2 / \sum F_b^2)$, where F is the crystallographic structure factor for crystals of type a and b, versus $4 \sin^2 \theta / \lambda^2$ (resolution) are routinely used to characterize and compensate for the disordering effects resulting from the diffusion of heavy-atom derivatives into protein crystals. The slopes of these plots are directly related to the difference in overall B values for two different crystals, a (space-grown) and b (Earth-grown).

II. RESULTS AND DISCUSSION

A total of 33 proteins (table 1) were selected for crystallization experiments on USML-1. It should be noted that for all previous protein crystal growth experiments performed on Space Shuttle missions, proteins are chosen by a selection committee. This committee typically chooses 30% of those proteins submitted by co-investigators involved in this project. The proteins that are not selected generally fall into one of two main categories: 1. crystallization time is too long for that particular shuttle flight; 2. the protein is very flexible, not stable, not pure, or insufficient ground-based data is available. For the USML-1 mission, it was clear that several proteins selected to fly would fall into one of these two categories. On any other shuttle mission, these proteins would not have been accepted by the committee, but since this mission was unprecedented in that a protein crystallographer would actually accompany and be able to perform these experiments on the shuttle, it was decided that every protein submitted would be flown if possible. Since several of the proteins clearly needed growth periods longer than would be available on this 13 day mission, those proteins were given a lower priority which resulted in typically only one or two vapor diffusion experiments being set up. The experiments were performed on 9 proteins in a 4° C incubator and 10 proteins in a 22° C incubator using the VDA flown on several previous missions. Activation occurred on the first day of the mission and deactivation one day prior to re-entry, thereby allowing thirteen days for crystal growth in microgravity. In addition, 24 proteins (some of which were the same as those in the VDA's housed in the 22° C incubator) were crystallized throughout the mission using the glovebox hardware described in the previous section. Once these experiments were prepared, they were transported back to the middeck and housed in a third incubator set at 22° C. On subsequent days, the glovebox crystallization experiments were observed using a binocular zoom microscope (8x to 64x magnification). Fourteen of the twenty-four proteins prepared in the glovebox required between seven and fourteen days to crystallize in experiments previously

prepared on Earth. As expected, these proteins took at least as long and typically longer to crystallize in microgravity and, as a result, by day thirteen, most of these proteins had recently nucleated and, therefore, failed to grow to an adequate size for diffraction experiments. However, of the remaining ten proteins crystallized in the glovebox, several produced high quality diffraction size crystals, some of which were the largest crystals ever grown. Proteins grown in the glovebox that produced diffraction size crystals included canavalin, malic enzyme, reverse transcriptase, lysozyme, horse serum albumin, factor D, mouse monoclonal antibody, and human α -thrombin.

Four proteins that were crystallized with the glovebox hardware had flown on one or more previous shuttle missions using the VDA hardware. VDA results for these proteins did not produce crystals; this may be due to inadequate mixing of the protein and viscous polyethylene glycol precipitant solutions. With the glovebox hardware, the experimenter could mix the protein and precipitant solutions thoroughly by stirring or by withdrawing and re-extruding the solution from a Hamilton syringe. As a result, all four proteins produced crystals, and crystals of two of the proteins, malic enzyme and factor D, produced high quality x-ray diffraction data.

Malic enzyme, (M.W. = 260 kilodaltons) is an NAD-dependent enzyme isolated from a parasitic nematode. It is being studied to exploit structural differences from the human form of this enzyme to aid in the development of an antiparasitic drug. Malic enzyme was flown on two previous shuttle missions using the VDA with no crystals found at the conclusion of the flights. This lack of success was attributed to inadequate mixing of the viscous precipitating agent (polyethylene glycol 4000). On the USML-1 mission with the glovebox crystallization hardware, the viscous solutions were mixed by excessive stirring of the solutions using the syringe needle tip and, as a result, many small crystals were observed within 5 days. Based on observations made through a binocular microscope in orbit, new conditions were chosen (i.e. lower polyethylene glycol concentrations) that ultimately produced the best crystals (figure 5). Earth-grown crystals of malic enzyme diffract weakly to 3.2 Å resolution. With crystals obtained in microgravity, the ultimate resolution limit achieved was 2.6 Å.

Figure 6a shows the comparison of diffraction intensity data for a space-grown crystal and some of the best Earth-grown crystals. It should be noted that the Earth-grown crystal was 5 times the volume of the space-grown crystal used for this comparison. Nonetheless, the space-grown crystal of malic enzyme produced data with increased signal to noise ratio at all resolution ranges, with an appreciable enhancement in the highest resolution range at which measurable data were obtained. The space-grown crystal, although only 1/5 the volume of the Earth-grown crystal, yielded \approx 25% more data. Figure 6b shows a comparison of the data collected from similar resolution bins for the Earth and space crystals. In addition, a relative Wilson plot comparing the space-grown crystal to the best Earth-grown crystal revealed better internal order for the space-grown crystal (figure 6c).

Based on glovebox results obtained for malic enzyme and other proteins that used viscous precipitating agents, it was clear that the VDA results for these proteins were adversely affected due to the lack of adequate mixing of the protein and precipitating solutions. As a result, a syringe that provided enhanced mixing was designed and flown on a subsequent flight (Spacehab 1, STS-57) with dramatic results. For this experiment, 10 of the original syringes were loaded with malic enzyme and its precipitating agent at varying concentrations and an additional 10 new syringes were loaded with identical conditions. After the 9 day Space Shuttle flight, the original syringes contained only clear solution while 8 of the 10 syringes designed to provide enhanced mixing yielded small well-formed crystals of malic enzyme. These crystals were subjected to a detailed x-ray analysis and compared with control crystals grown with the same batch of protein. The space crystals typically measured 0.17 mm^3 while the Earth-grown control crystals measured 0.5 mm^3 . In spite of the significant increase in volume for the Earth control crystals, the space-grown crystals produced significantly better data. (figure 7) In addition, an analysis of the decay due to x-ray radiation for several of the space and Earth crystals was conducted. (figure 8) The space-grown crystals displayed much longer lifetimes when subjected to radiation than did their Earth-grown counterparts. Although other investigators have noted similar results for other proteins, this represents the first detailed analysis indicating the enhanced stability of space-grown crystals.

Bovine brain prolyl-isomerase, (M. W. = 12 kilodaltons) is the target for a new class of drugs designed to prevent transplant rejection. When crystallized on Earth, this enzyme often forms clusters that twin and are of variable diffraction quality. The crystallization solutions used for this shuttle mission were identical to those used on Earth, yet the space-grown crystals (figure 9) were substantially larger (approaching $3.0\text{ mm} \times 1.0\text{ mm}$ thick as opposed to $0.6\text{ mm} \times 0.2\text{ mm}$ for Earth-grown crystals) and exhibit no clustering, twinning, or large variations in diffraction quality.

The space-grown crystals were even large enough that one might consider neutron-diffraction experiments. The space-grown crystals also had sharper edges and were clearer than their Earth-grown counterparts. Unfortunately, the space-grown crystals suffered some degradation (founding of edges and facets) before they could be examined at the co-investigators x-ray laboratory. (The cause of this degradation is not known). This degradation may have affected the diffraction quality of the space-grown crystals. In spite of this, a complete data set to 2.3 \AA resolution was collected on the best crystal. When these data are compared to those from the best Earth-grown crystals, one can see that diffraction from the space-grown crystal is superior to 2.5 \AA resolution (figure 10).

Factor D (M. W. = 24 kilodaltons) is an essential enzyme for the initiation of the alternative pathway of the complement system. Two crystalline forms, triclinic (space group P1) and monoclinic (space group P21) can be produced using identical crystallization conditions. The monoclinic form was

used to determine the three-dimensional structure. However, these crystals are extremely difficult to grow on a reproducible basis. In fact, using several different batches of protein over a ten month period (including the batch used for the USML-1 microgravity experiments), it was not possible to produce monoclinic crystals. On USML-1, one monoclinic crystal was produced using the glovebox hardware. This crystal was the longest crystal ever grown of factor D (although it was only 1/3 as thick as the best Earth-grown crystal) and produced diffraction data comparable in intensity to the best Earth-grown crystal, but with a slight improvement in resolution (0.1 Å). The relative Wilson plot revealed a significant difference in B values for data in the higher resolution range, indicating better internal order for the space-grown crystal. Using the monoclinic space crystals combined with previously grown Earth crystals, the three-dimensional structure of factor D (figure 11) was recently determined and is in press with the Journal of Molecular Biology. This represents the first structure of a complement protein ever determined at atomic resolution.

Canavalin (M. W. = 11 kilodaltons) is the major storage protein of leguminous plants and an important source of dietary protein for humans and domestic animals. This protein has been crystallized on several shuttle flights using the VDA hardware. For USML-1, large crystals of recombinant canavalin were grown both in the VDA and glovebox hardware. However, canavalin crystals are extremely unstable and as a result, several exhibited severe degradation by the time the crystals were harvested after the shuttle flight. One VDA experiment produced crystals that, although somewhat degraded, were suitable for x-ray data collection. From this experiment, three large rhombohedral crystals were obtained for data collection on an SDMS area detector system. Comparison of average $I / \sigma(I)$ versus resolution for the two space crystals with the best Earth-grown crystals demonstrated a marginal improvement for those crystals grown in space. However, Relative Wilson statistics were not conclusive, indicating that the data produced from microgravity-grown crystals were quite similar to those produced by equivalent crystals grown in the laboratory. Although the average $I / \sigma(I)$ ratio was not improved, an extension of the resolution to higher limits was observed for the space-grown crystal near the high resolution data range (figure 12). This indicates that if the crystal had not experienced the significant decay, it is likely that it would have produced superior data to that of its Earth-grown counterparts. On previous missions, native space-grown canavalin crystals showed more dramatic improvements in diffraction quality (figure 13).

Human α -thrombin (M. W. = 36.5 kilodaltons) is a serine protease involved in the final step of the coagulation cascade cleaving soluble fibrinogen to produce insoluble fibrin. For the USML-1 mission, experiments on α -thrombin yielded several large single crystals and some clusters of smaller crystals. One α -thrombin crystal grown on this space shuttle flight measured 1.0 mm x 0.5 mm x 0.45 mm which is a larger size than typically observed in the lab. The crystal was rectangular in shape with a hollow

area along one edge indicating possible rapid and incomplete crystal growth. The other crystals were perfect in habit, a phenomenon rarely observed for crystals grown on Earth.

Large crystals of HIV-1 reverse transcriptase complexed to a monoclonal antibody Fab fragment and to a 19/18 base-paired double stranded DNA helical fragment (M. W. = 180 kilodaltons) were grown in the 4° C R/IM. Reverse Transcriptase is an enzyme responsible for copying the nucleic acid genome of the AIDS virus from RNA to DNA. Both space-grown and Earth-grown crystals were examined by x-ray oscillation photography at the F1 station of the Cornell High Energy Synchrotron Source (CHESS) with an x-ray wavelength of 0.91 Å. Exposure times for both the space crystals and the Earth-grown crystals were 6 to 8 seconds with an oscillation range of 0.7°. Fuji storage-phosphor imaging plates were the x-ray detection medium with a crystal-to-detector distance of 340 mm. The crystals were large enough (typically 0.8 mm) to permit translation within the beam so that photographs could be taken from multiple positions of the crystals. A total of 101 exposures from 23 space-grown crystals were obtained, from which 88 exposures from 22 crystals proved satisfactory and therefore were included in the final space-crystal data set. For the ground control crystals, 27 exposures were collected from 5 crystals, with 22 of these exposures included in the final control data set. Plots of intensities greater than various s cutoffs versus resolution as well as average $I / \sigma (I)$ versus resolution indicate that there is very little difference between the space and ground crystals. However, a relative Wilson plot indicated that the space-grown crystals had a significantly lower B value than the ground control crystals, particularly at the high resolution end of the plot (figure 14).

This is an indication that the space-grown crystals are better ordered (beyond 4 Å) than are the Earth-grown crystals. Differences in the post-refined unit cell parameters were less than one-half of one percent. The post-refined vertical and horizontal mosaic spread parameters were similar (0.23° to 0.29°) for all crystals.

Other proteins that produced diffraction-sized crystals showed diffraction data either equal in quality or of poorer quality than the best crystals of these proteins produced on Earth. In all of these cases, the crystals grown in space were significantly smaller than the Earth-grown crystals.

CONCLUSION

The USML-1 glovebox hardware was extremely successful in that it demonstrated the usefulness of altering crystallization conditions based on previous results in an attempt to improve the quality of crystals that are grown in space. By comparing results from the glovebox with those for the same protein in the VDA, it was realized that the success rate of these experiments had been adversely affected due to the viscous nature of the crystallizing solutions. The VDA apparatus did not adequately mix these solutions and, therefore, either a clear solution or precipitated protein resulted at the end of the

microgravity experiment. By carefully mixing the solutions using the glovebox hardware, high quality crystals of four proteins were produced that had not yielded successful results using the VDA apparatus.

A micro-manipulator was used to withdraw small seed crystals grown on previous days with the glovebox hardware. This procedure proved to be straightforward and quite useful, although the seed crystals that were injected into new growth solutions never reached a large enough size to be useful for diffraction experiments. In several cases, however, investigators commented that the crystals obtained were of extremely high quality, although small. As a result, these crystals were used as seed crystals for Earth-based crystallization experiments performed after the mission. It was clear during the seeding operation that mounting protein crystals in x-ray capillaries in microgravity is actually easier to successfully complete than it is on Earth. Since the crystals are typically suspended within the middle of the protein drop, the most difficult aspect of this procedure (withdrawing the crystal into the capillary) was easily accomplished in microgravity. The end of the capillary was positioned directly over the crystal, and subsequently withdrawn into the capillary.

It was clear that high magnification microscopy with video transmission will be extremely useful on future missions. This capability will allow crewmen to display results to scientists stationed on the ground so that they can aid in the decision making process thereby optimizing the chance of producing high quality crystals.

In conjunction with co-investigators from universities and pharmaceutical companies and with scientists and engineers from the Marshall Space Flight Center, this laboratory has conducted protein crystal growth experiments utilizing vapor diffusion and/or temperature-induced crystallization on 18 different space shuttle missions. These initial experiments have demonstrated that the microgravity environment present on the space shuttle is beneficial for protein crystal growth experiments. From these few space experiments there are several examples where crystals were grown that were larger, displayed more uniform morphologies, and/or yielded diffraction data to significantly higher resolutions than the best crystals of these proteins grown on Earth by any method. Table 2 summarizes the positive results obtained from these space shuttle missions. Resolution enhancements have ranged from 0.1 Å to as much as 2.0 Å for the space-grown crystals. It should be noted that in several cases where significant resolution enhancements occurred, the space-grown crystals were much smaller in volume than the Earth crystals with which they were being compared. This strongly indicates that the space-grown crystals are more highly ordered at the atomic level. However, in those cases where space-grown crystals were larger, increases in size as much as an order of magnitude were observed which, in some cases, resulted in x-ray diffraction resolution enhancements in excess of 0.5 Å. The success rate in the VDA is approximately 20%, which is quite remarkable since each protein included in the space experiments is crystallized with only a few experiments, usually about 5 experimental chambers are

allotted to each investigator per flight. These space results are then compared with the best crystals ever produced on the ground using any crystallization method (usually hundreds of crystallization conditions were tested on the ground to optimize the crystal growth conditions).

Temperature-induced crystallization (16 - 20) is often the method of choice when large quantities of protein are available and large batches of crystals are required. It is particularly suited for a microgravity environment because temperature-induced convective flow is minimized, thereby providing a more quiescent environment for both the nucleation and subsequent crystal growth stages. This method provides the experimenter with the ability to influence the number, size and quality of protein crystals by precisely controlling the rate of temperature change and, therefore, the protein saturation levels throughout the experiment. Temperature-induced crystallization was performed on 4 separate shuttle flights with high success. Crystals from all 4 shuttle flights were significantly (2 times to as much as 10 times) larger than the best of their Earth-grown counterparts. In addition, x-ray diffraction data for the space-grown crystals showed significant improvements.

These initial experiments have been instrumental in allowing our co-investigator group to better understand the possible benefits of the microgravity environment. Results from the VDA have led to the development of a second generation of hardware to perform vapor diffusion experiments. This hardware provides a number of advantages over the existing hardware including: 1. thorough mixing of the protein and precipitant samples in orbit; 2. real time video monitoring capabilities; and, 3. precise control over equilibration rates. The new enhanced mixing syringe flown on STS-57 conclusively demonstrated that viscous solutions can be completely mixed in microgravity, thereby improving the success rate for these experiments. The combination of dynamic control combined with sensitive optical analysis capabilities will enhance our understanding of the basic mechanisms involved in macromolecular crystal growth processes as well as increasing the overall success of these experiments. We anticipate completing the fabrication of the flight unit by 1996. During this three year period, extensive testing of a laboratory "breadboard" unit will be conducted. This system should improve crystallization results on Earth and provide valuable information regarding the basic mechanisms involved in protein crystal growth processes.

REFERENCES

1. Hilgenfeld, R., Liesum, A., Storm, R., and Plaas-Link, A., "Crystallization of Two Bacterial Enzymes on an Unmanned Space Mission", *Journal of Crystal Growth*, 122: 330 - 336 (1992)
2. Snyder, R. S., Fuhrmann, K., and Walter, H. U., "Protein Crystallization Facilities for Microgravity Experiments", *Journal of Crystal Growth*, 110: 333 - 338 (1991)
3. Asano, K., Fujita, S., Senda, T., and Mitsui, Y., "Crystal Growth of Ribonuclease S Under Microgravity", *Journal of Crystal Growth*, 122: 323 - 329 (1992)
4. Little, W. and John, C., "Protein Single Crystal Growth Under Microgravity", *Science*, 225: 203 - 205 (1984)
5. Day, J., and McPherson, A., "Macromolecular Crystal Growth Experiments on International Microgravity Laboratory - 1", *Protein Science*, 1: 1254 - 1268 (1992)
6. McPherson, A., Greenwood, A., and Day, J. "The Effect of Microgravity on Protein Crystal Growth", *Advances in Space Research* 11: 343 - 356 (1991)
7. Erdmann, V. A., Lippmann, C., Betzel, C., Dauter, Z., Wilson, K., Hilgenfeld, R., Hoven, J., Liesum, A., Saenger, W., Muller-Fahrnow, A., Hinrichs, W., Duvel, M., Schulz, G., Muller, C. W., Wittmann, H. G., Yonath, A., Weber, G., Stegen, K., and Plaas-Link, A., "Crystallization of Protein Under Microgravity", *FEBS Letters*, 259: 194 - 198 (1989)
8. DeLucas, L.J., Smith, C. D., Smith, W. H., Kumar, S. V., Senadhi, S. E., Ealick, S.E., Carter, D. C., Snyder, R. S., Weber, P. C., Salemme, R., Ohlendorf, D. H., Navia, M. A., McKeefer, B. M., Nagabhushan, T. L., Nelson, G. and Bugg, C. E., "Protein Crystal Growth in Microgravity", *Science*, 246: 651 - 654 (1989)
9. DeLucas, L. J., Smith, C. D., Ealick, S. E., Carter, D. C., Twigg, P., He, X.-M., Snyder, R. S., Weber, P. C., Schloss, J. V., Einspahr, H. M., Clancy, L. L., McPherson, A., Koszelak, S., Vandonselaar, M. M., Prasad, L., Quail, J. W., Delbaere, L. T. J., and Bugg, C. E., Proceedings of the Committee on Space Research (COSPAR) XXVIII Plenary Meeting, The Hague, The Netherlands, "Protein Crystal Growth Aboard the U. S. Space Shuttle Flights STS-31 and STS-32", *Advances in Space Research*, Vol. 12, No. 1: 393 - 400 (1992)
10. DeLucas, L. J., Moore, K. M., Narayana, S. V. L., Bray, T. L., Rosenblum, W. M., Einspahr, H. M., Clancy, L. L., Rao, G. S. J., Harris, B. G., Munson, S. H., Finzel, B. C., and Bugg, C. E., "Protein Crystal Growth Results from the United States Microgravity Laboratory - 1 Mission", *Journal of Physics D: Applied Physics* 26: B100 - B103 (1993)
11. DeLucas, L. J., Long, M. M., Moore, K. M., Smith, C., Carson, M., Narayana, S. V. L., Carter, D., Clark, Jr., A. D., Nanni, R. G., Ding, J., Jacobo-Molina, A., Kamer, G., Hughes, S. H., Arnold, E., Einspahr, H. M. Clancy, L. L., Rao, G. S. J., Cook, P. F., Harris, B. G., Munson, S. H., Finzel, B. C., McPherson, A., Weber, P. C., Lewandowski, F., Nagabhushan, T. L., Trotta, P. P., Reichert, P., Navia, M. A., Wilson, K. P., Thompson, J. A., Meade, C., Bishop, S. P., Dunbar, B. J., Trinh, E., Prahl, J., Sacco, Jr., A., and Bugg, C. E. "Recent Results and New Hardware Developments for Protein Crystal Growth in Microgravity", *Journal of Crystal Growth*, submitted (1993)

12. DeLucas, L. J., Suddath, F. L., Snyder R., Naumann, R., Broom, M. B., Pusey, M., Yost, V., Herren, B., Carter, D., Nelson, B., Meehan, E. J., McPherson, A., and Bugg, C. E. "Preliminary Investigations of Protein Crystal Growth Using the Space Shuttle", *Journal of Crystal Growth* 76: 681 - 693 (1986)
13. DeLucas, L. J., and Bugg, C. E., "Protein Crystal Growth Procedure for the U. S. Space Shuttle", *METHODS: A Companion to Methods in Enzymology*, Vol. 1, #1: 105 - 109 (1990)
14. McPherson, A., *Methods in Enzymology*, vol. 114, pp 112 - 119, *Diffraction Methods*, eds., Hirs, C.H.W., Timasheff, S. N., and Wyckoff, H. W., Academic Press, Orlando, Florida (1985)
15. Blundell, T.L., and Johnson, L.J., *Protein Crystallography*, pp 333 - 336, Academic Press, New York (1976)
16. Baker, E. N. and Dodson, G., "X-ray Diffraction Data on Some Crystalline Varieties of Insulin", *Journal of Molecular Biology* 54: 605 - 609 (1970)
17. Longley, W., "Crystalline Structure of Bovine Liver Catalase: A Combined Study by X-ray Diffraction and Electron Microscopy", *Journal of Molecular Biology*, 30: 323 - 329 (1967)
18. Jakoby, W. B., "A Technique for the Crystallization of Proteins", *Analytical Biochemistry*, 26: 295 - 298 (1968)
19. Jakoby, W. B., "Crystallization as a Purification Technique", *Methods in Enzymology*, 11: 248 - 252 (1971)
20. Hanson, A. W., "X-ray Studies on Single Crystals of Escherichia Coli Alkaline Phosphatase", *Journal of Biological Chemistry*, 245: 4975 - 4976 (1970)

Table 1

HIV Reverse Transcriptase Complex	Bacterial Luciferase
Human a-Thrombin	Porcine Aldehyde Reductase
HIV-1 Protease	Human Transferrin
Fab against gp41 of HIV-1	Factor D
Malic Enzyme	DD-Ligase from <u>E. coli</u>
Human Serum Albumin	DD-Ligase from <u>S. tymp.</u>
Recomb. Human Serum Albumin	B-Lactamase
Mouse Monoclonal Antibody	2 domain CD4 (1-183)
Aridicin Aglycone	Recomb. Ricin-A chain
Horse Serum Albumin	Flavodoxin
Interleukin-4	Lac Operator DNA
Interferon a-2b	Urease
Lac Repressor	Bovine Proline Isomerase Complex
Lysozyme	DNA Dodecamer: CGTTTTAAAACG
Canavalin	DNA Dodecamer: CGAAAATTTCG
Human Proline Isomerase	Green Fluorescent Protein
Thermolysin	

Table 2

BENEFICIAL MICROGRAVITY EFFECTS

Flight/Date	Protein	Crystals	Phylogeny	Intensity	Motion	10%		Resolution Improvement	
						New	Increase in Dif. Less	Thermal	0.0 to 0.3 to 0.5A
STS-26/09-88	Inocitrate Lyase	X	X	X	X	X	X	X	X
STS-26/09-88	Elastase	X	X	X	X	X	X	X	X
STS-26/09-88	g-Interferon	X	X	X	X	X	X	X	X
STS-29/08-89	g-Interferon	X	X	X	X	X	X	X	X
STS-31/04-90	Lathyrus ochrus lectin I	X	X	X	X	X	X	X	X
STS-31/04-90	Jel-42 fab fragment			X					
STS-31/04-90	Human serum albumin	X	X	X	X	X	X	X	X
STS-32/01-90	Canavalin			X	X	X	X	X	X
STS-32/01-90	Human serum albumin			X	X	X	X	X	X
STS-37/04-91	Insulin	X	X	X	X	X	X	X	X
STS-43/08-91	Insulin	X	X	X	X	X	X	X	X
STS-49/05-92	Insulin	X	X	X	X	X	X	X	X
STS-42/01-92	Human serum albumin	X	X	X	X	X	X	X	X
STS-42/01-92	Bacterial Luciferase	X	X	X	X	X	X	X	X
STS-42/01-92	2 domain CD4	X	X	X	X	X	X	X	X
STS-42/01-92	Lyozyme			X					
STS-42/01-92	Fab YST9-1 from brucella			X		X	X	X	X
STS-42/01-92	Sat. tobacco mosaic virus	X	X	X	X	X	X	X	X
STS-50/06-92	Malic enzyme			X	X	X	X	X	X
STS-50/06-92	Factor D			X	X	X	X	X	X
STS-50/06-92	Canavalin	X	X	X	X	X	X	X	X
STS-50/06-92	HIV RT antibody								
STS-50/06-92	Human a-thrombin	X	X	X	X	X	X	X	X
STS-50/06-92	Human proline isomerase	X	X	X	X	X	X	X	X
STS-50/06-92	a-interferon	X	X	X	X	X	X	X	X
STS-50/06-92	DD-ligase (<i>E. coli</i>)			X					
STS-52/10-92	a-interferon	X	X	X	X	X	X	X	X
STS-47/09-92	EGF receptor								
STS-57/06-93	Malic Enzyme			X	X	X	X	X	X
STS-57/06-93	Lyozyme			X	X	X	X	X	X
STS-57/06-93	Human Insulin			?	?	?	?	?	?
STS-51/09/93	a-interferon	X	X	X	X	X	X	X	X

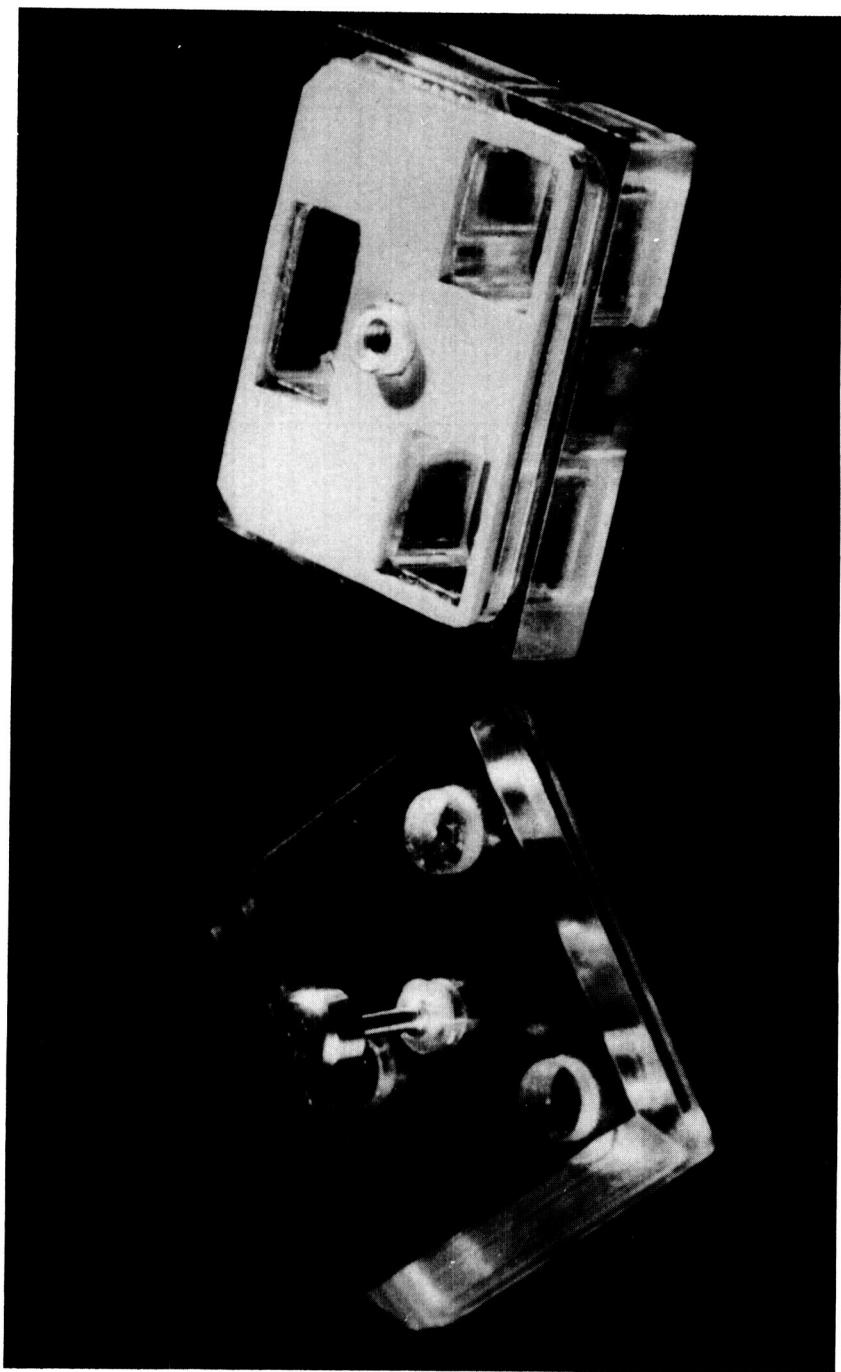


Figure 1 Vapor diffusion experiment chamber - The chamber consists of two polysulfone halves, one containing protein and one containing reservoir solution. The two sections are positioned with respective opposing chambers aligned for activation of the experiment. The experiments are deactivated by rotating the upper half 180°, thereby sealing all chambers on a neoprene gasket.

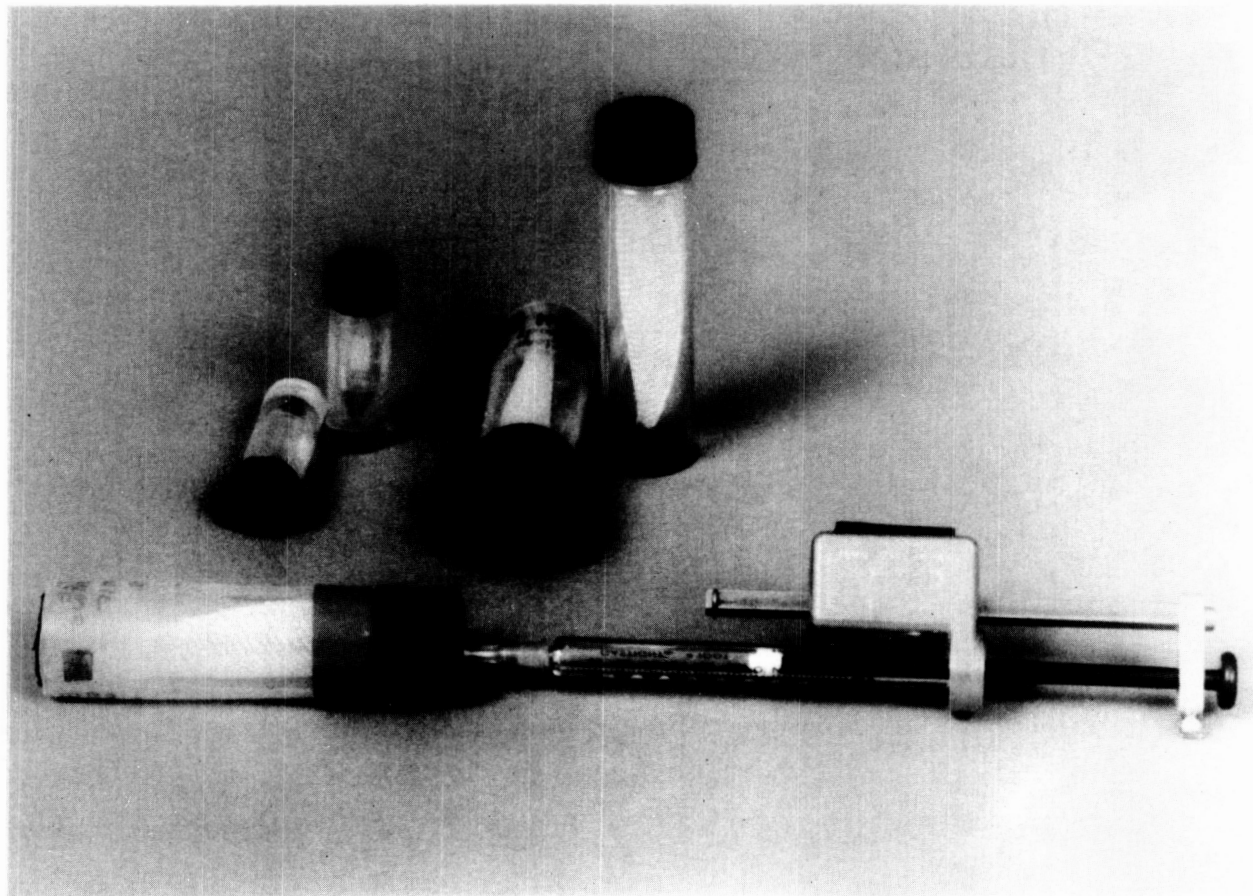


Figure 2 Bottles and dispensing syringe (one syringe is shown with needle puncturing septum of bottle) -
Two bottle and syringe sizes are used:
Bottles: 20 ml volume (for buffer & precipitating solutions)
1 ml volume (for protein solution)
Syringes: 1 ml syringe (for preparation of reservoir solutions)
25 μ l syringe (for preparation of protein droplet)

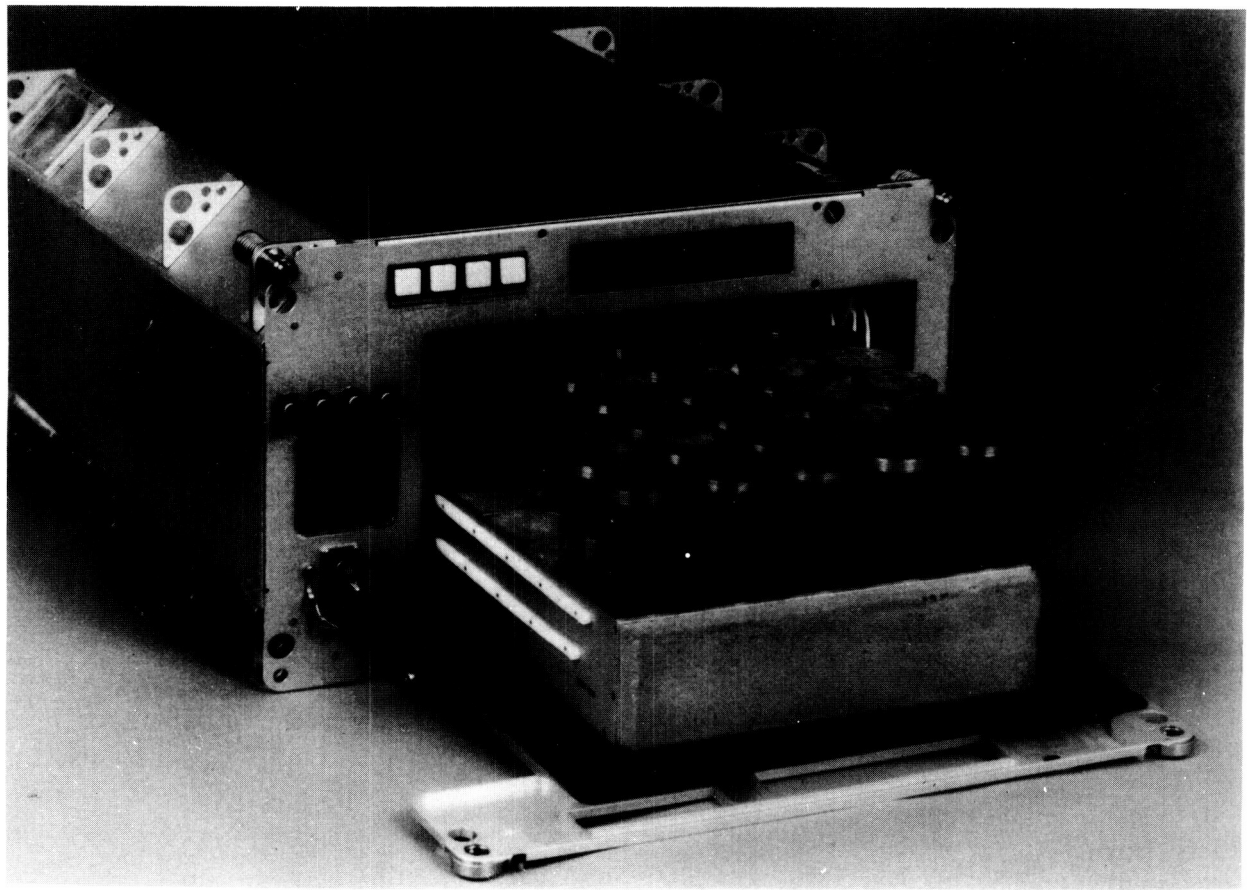


Figure 3 Refrigerator/Incubator module with containment tubes - The tubes are stored in a tray that slides out of the incubator to provide easy access.

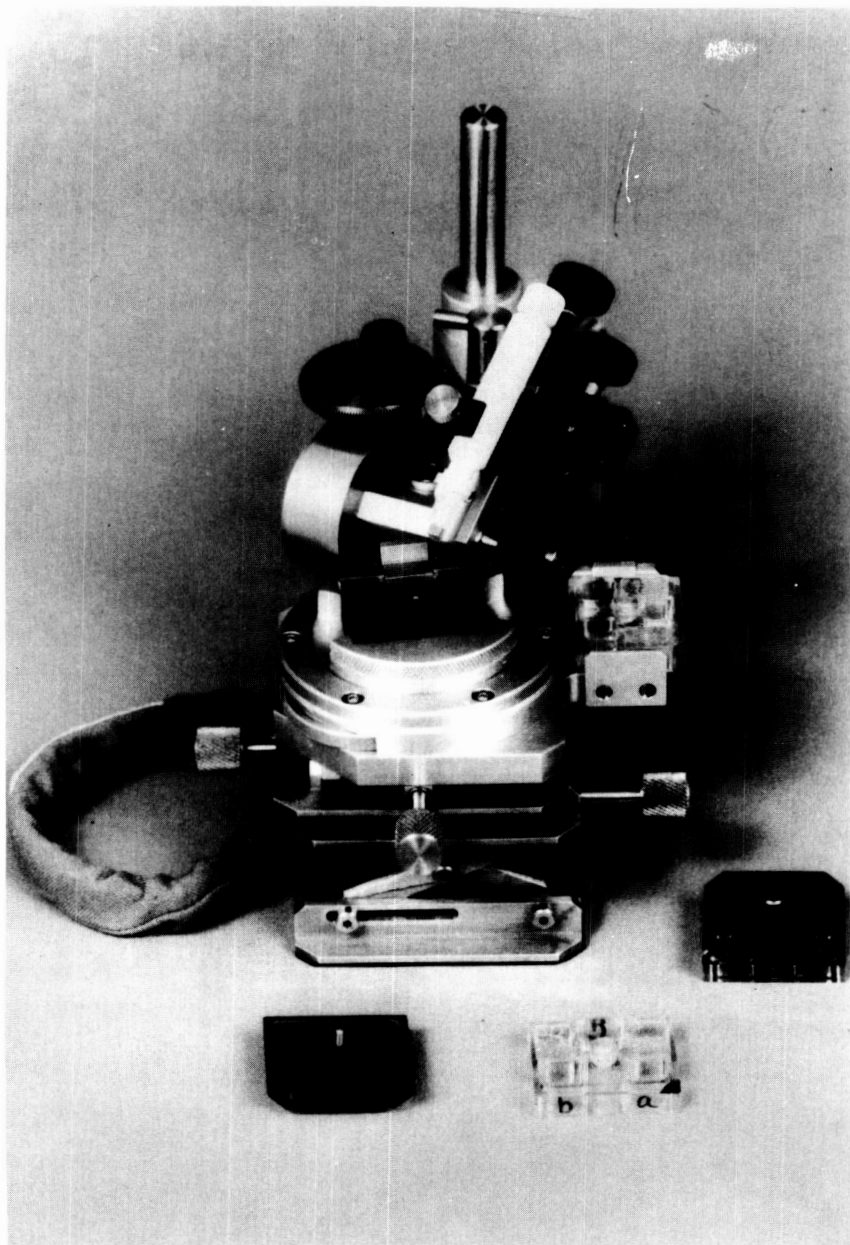


Figure 4 x-y-z translation stage with micromanipulator - A fiber optic bundle provides backlighting for experiment preparation and crystal observation.

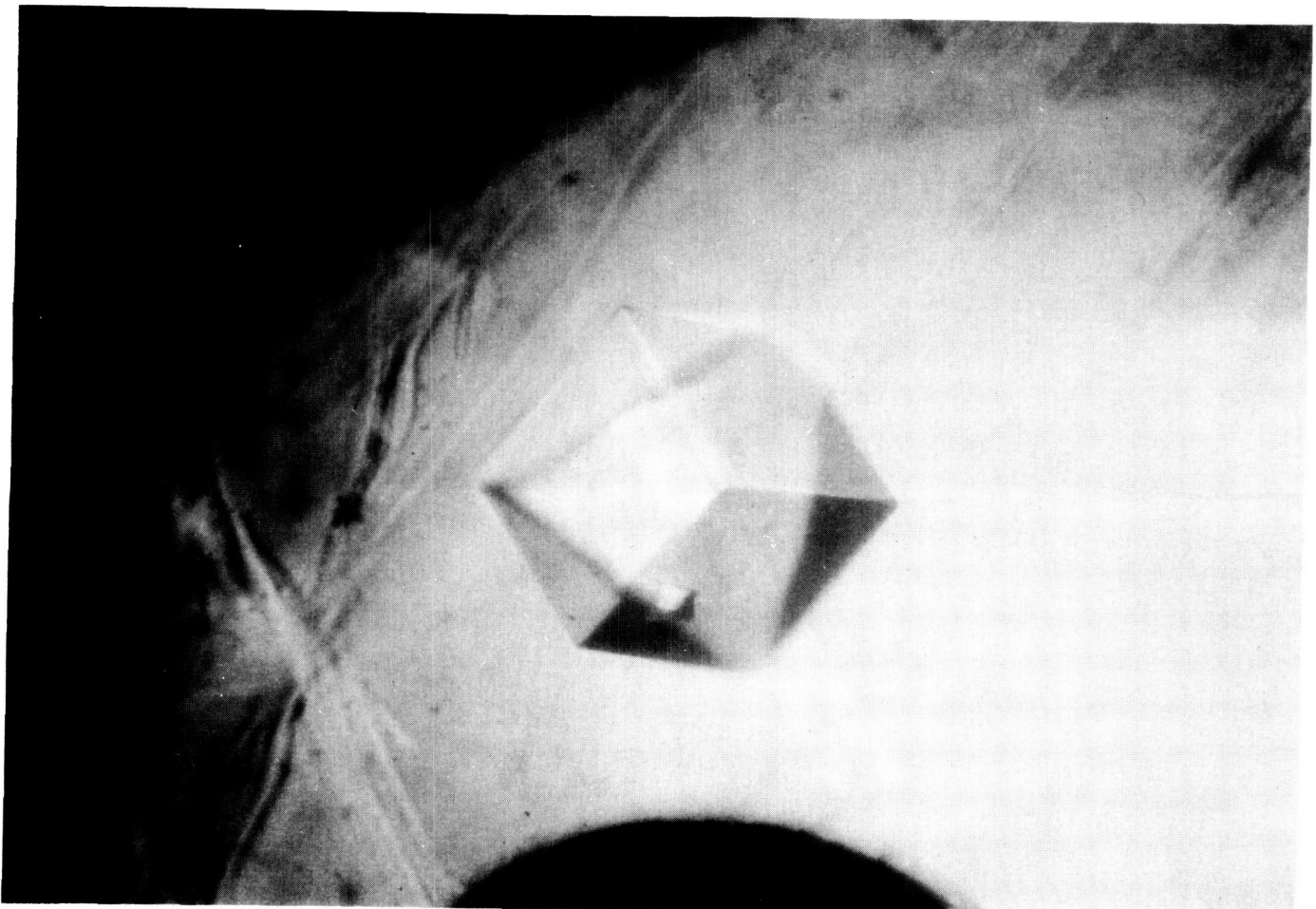


Figure 5 Crystal of malic enzyme grown in space. This space-grown crystal, although only 1/5 the volume of the best earth-grown crystal, produced a significant enhancement in the quality and resolution limit of the diffraction data (see figures 6a and 6c).

MALIC ENZYME AREA DETECTOR DATA

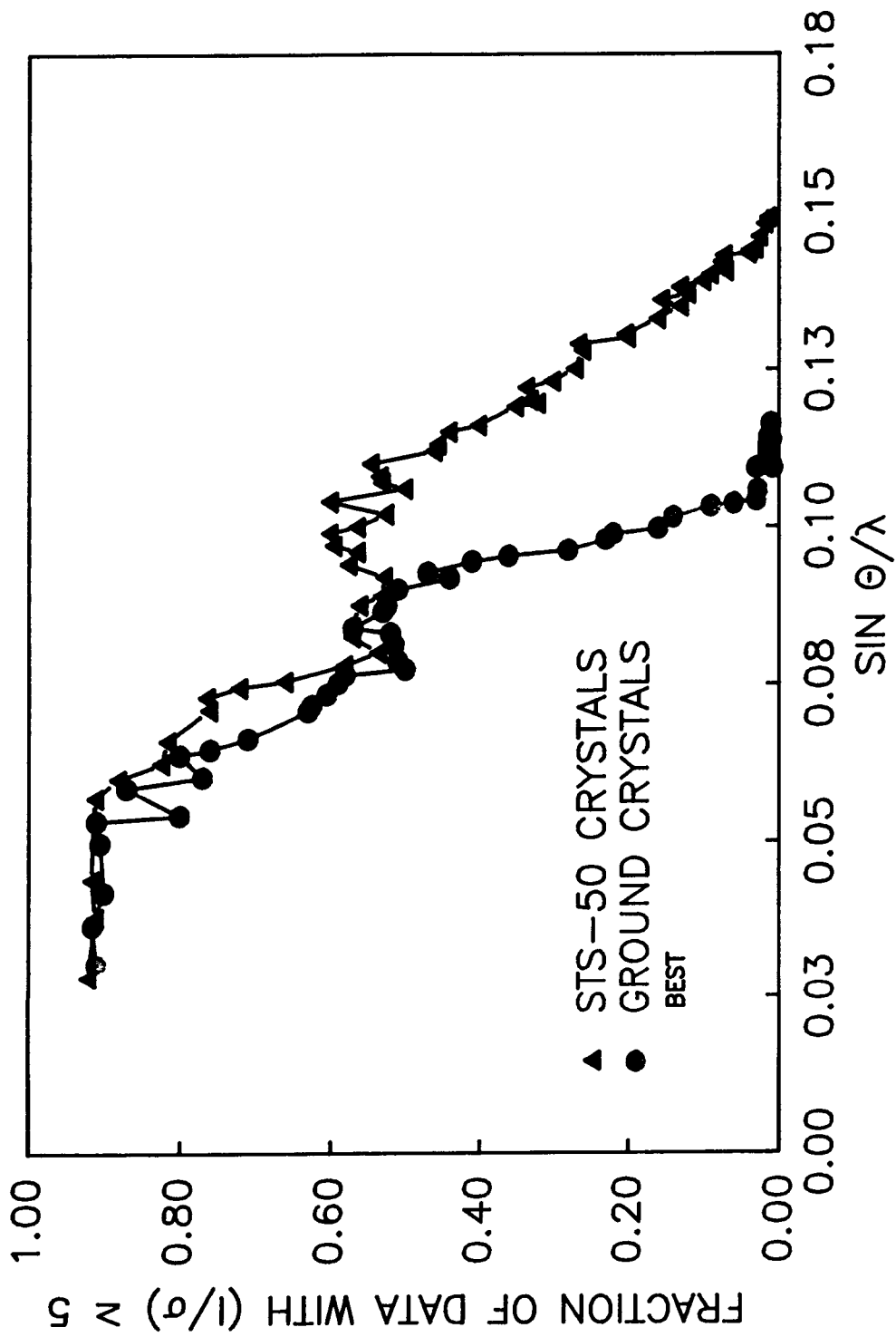


Figure 6a Comparison of diffraction intensity data for space-grown (\blacktriangle) and Earth-grown (\bullet) crystals of malic enzyme. The y-axis shows the fraction of data with $I/\sigma(I) \geq 5$.

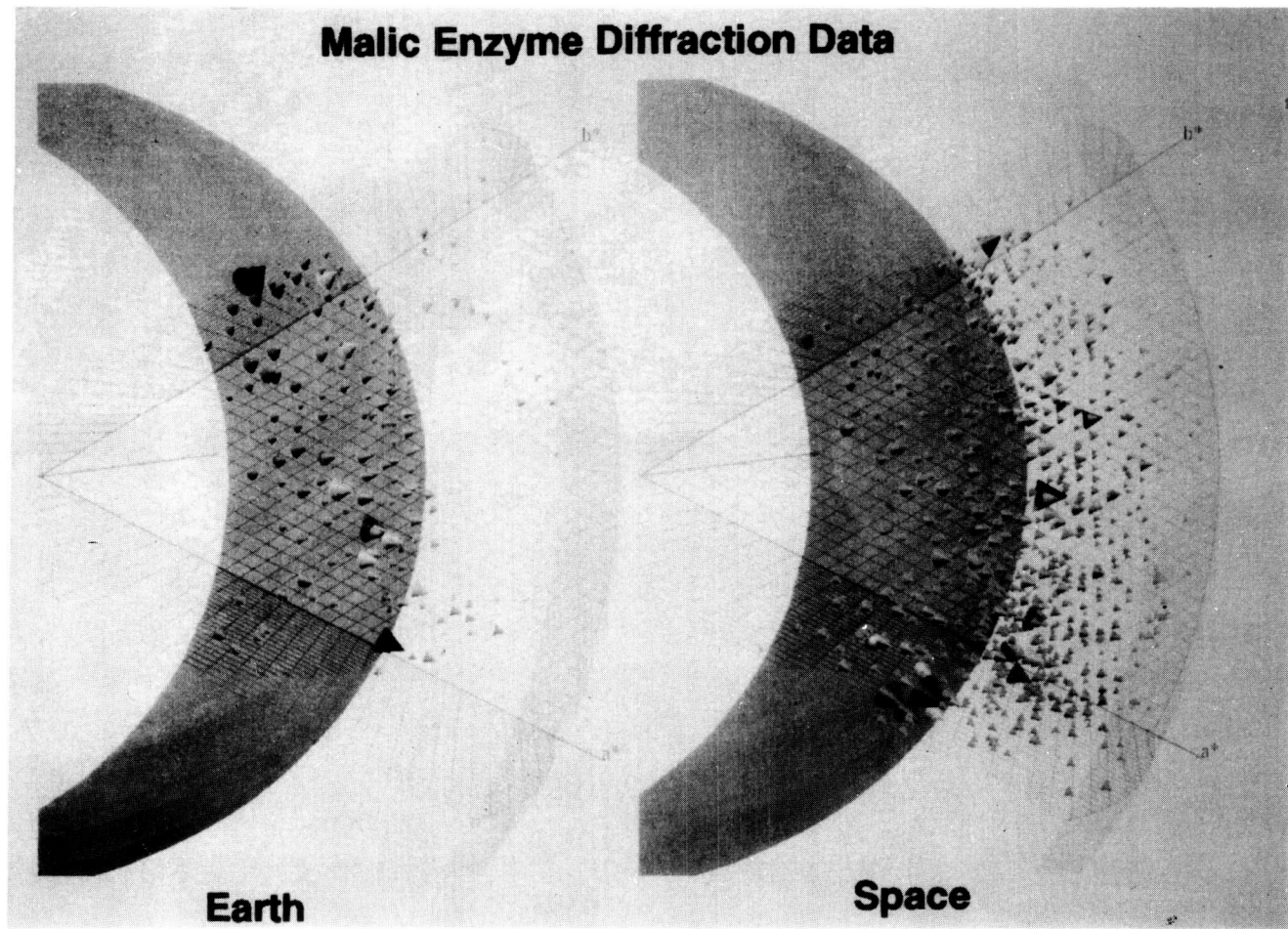


Figure 6b Comparison of diffraction data for the best earth-grown versus best space-grown crystal (obtained on USML-1) of malic enzyme. The size of the earth-grown crystal was 0.04 mm^3 and of the space-grown crystals 0.008 mm^3 . The space crystals yielded 25% more data, most of which occurred at the high resolution range.

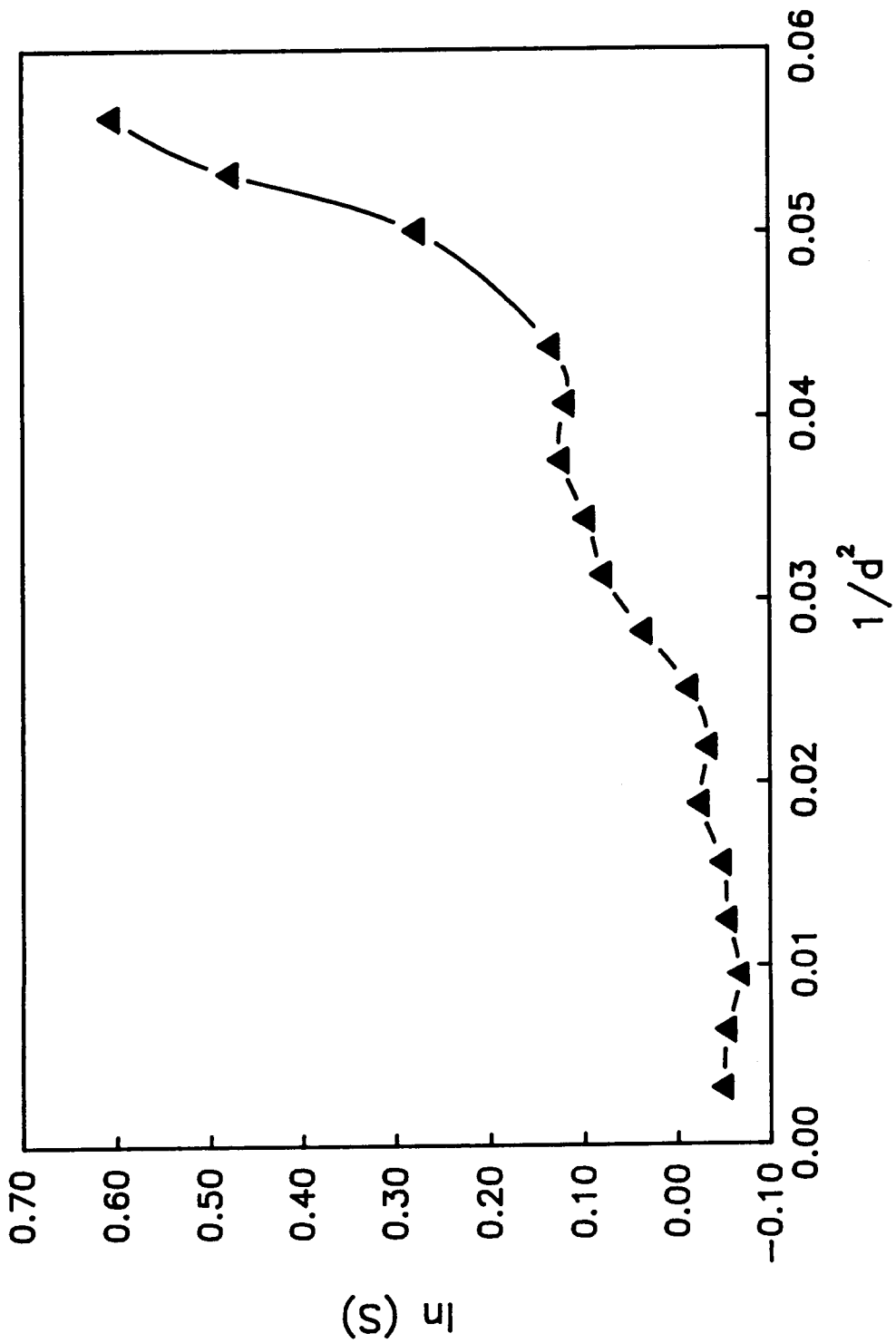


Figure 6c Relative Wilson plot comparing space-grown and Earth-grown crystals of malic enzyme. $s = \Sigma F_a^2 / \Sigma F_b^2$, where a = space-grown and b = Earth-grown crystal.

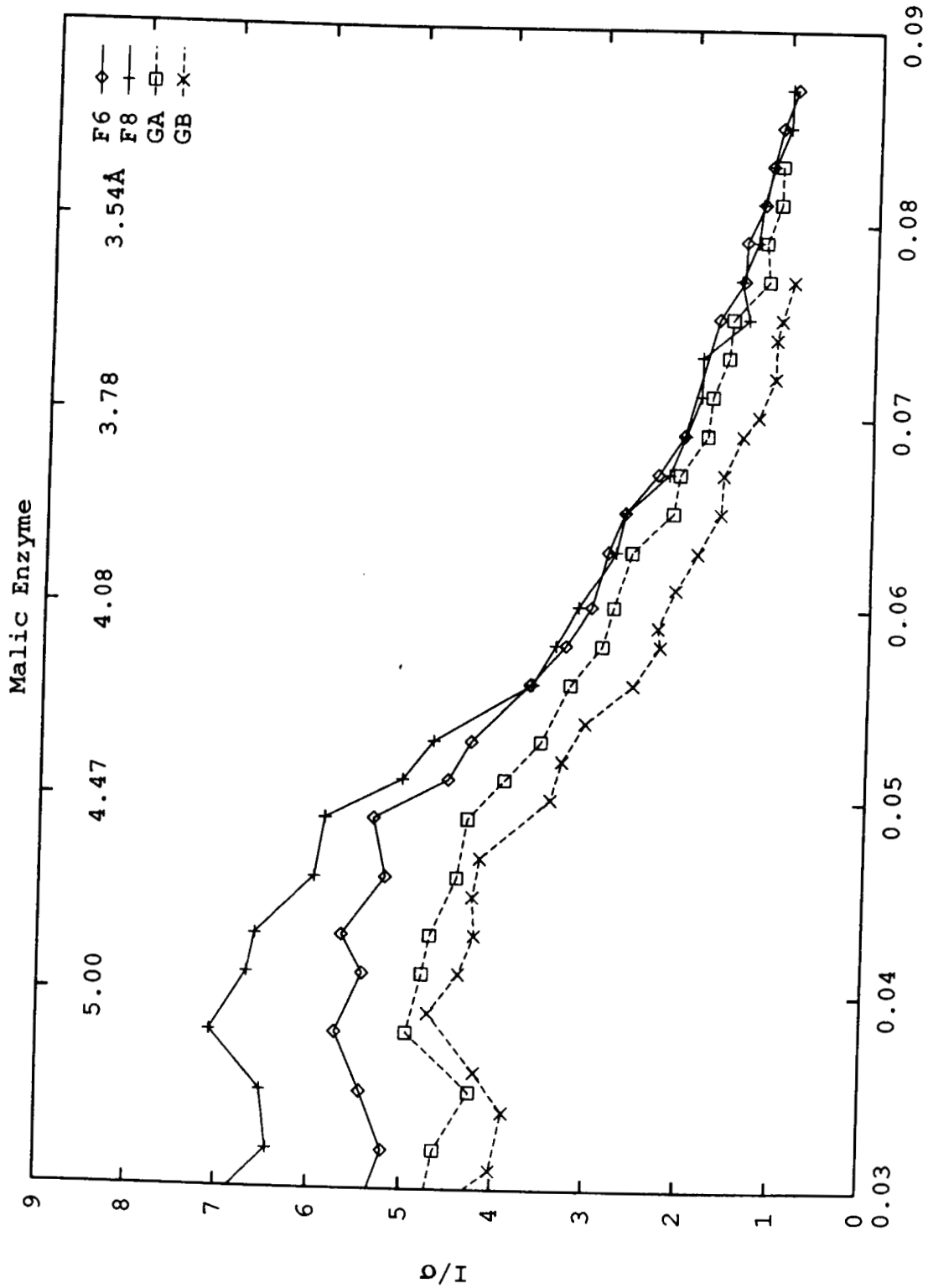


Figure 7 Comparison of diffraction intensity data for 2 space-grown crystals and 2 Earth-grown crystals of malic enzyme using the new enhanced mixing syringe for the VDA. The y-axis shows the ratio of I/σ .

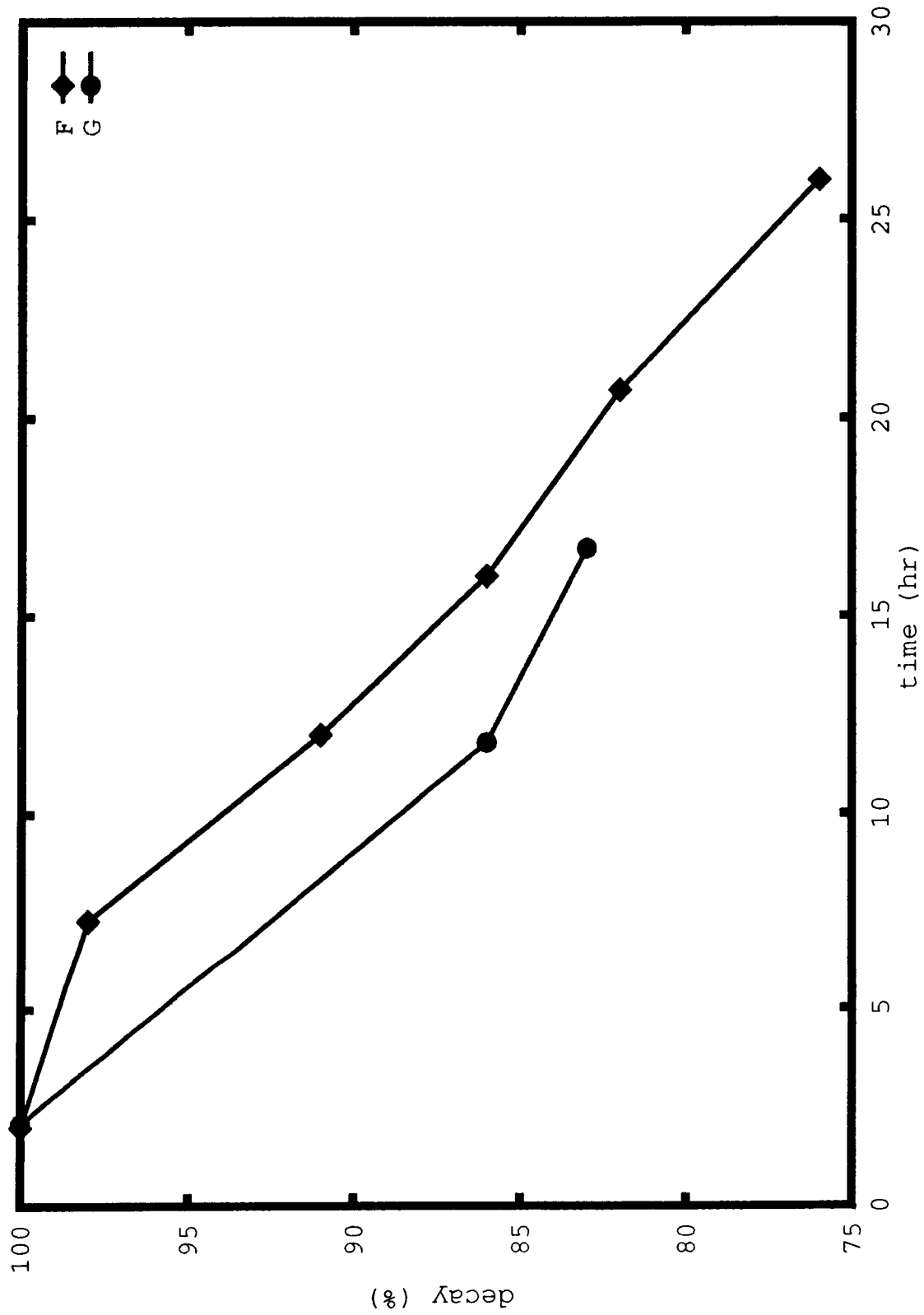


Figure 8 Comparison of percent decay, due to radiation damage for a malic enzyme flight crystal (\blacklozenge) versus ground crystals (\bullet) from the Spacehab I (STS-57) protein crystal growth experiment.



Figure 9 Space-grown crystals of bovine prolyl-isomerase from the USML-1 mission.

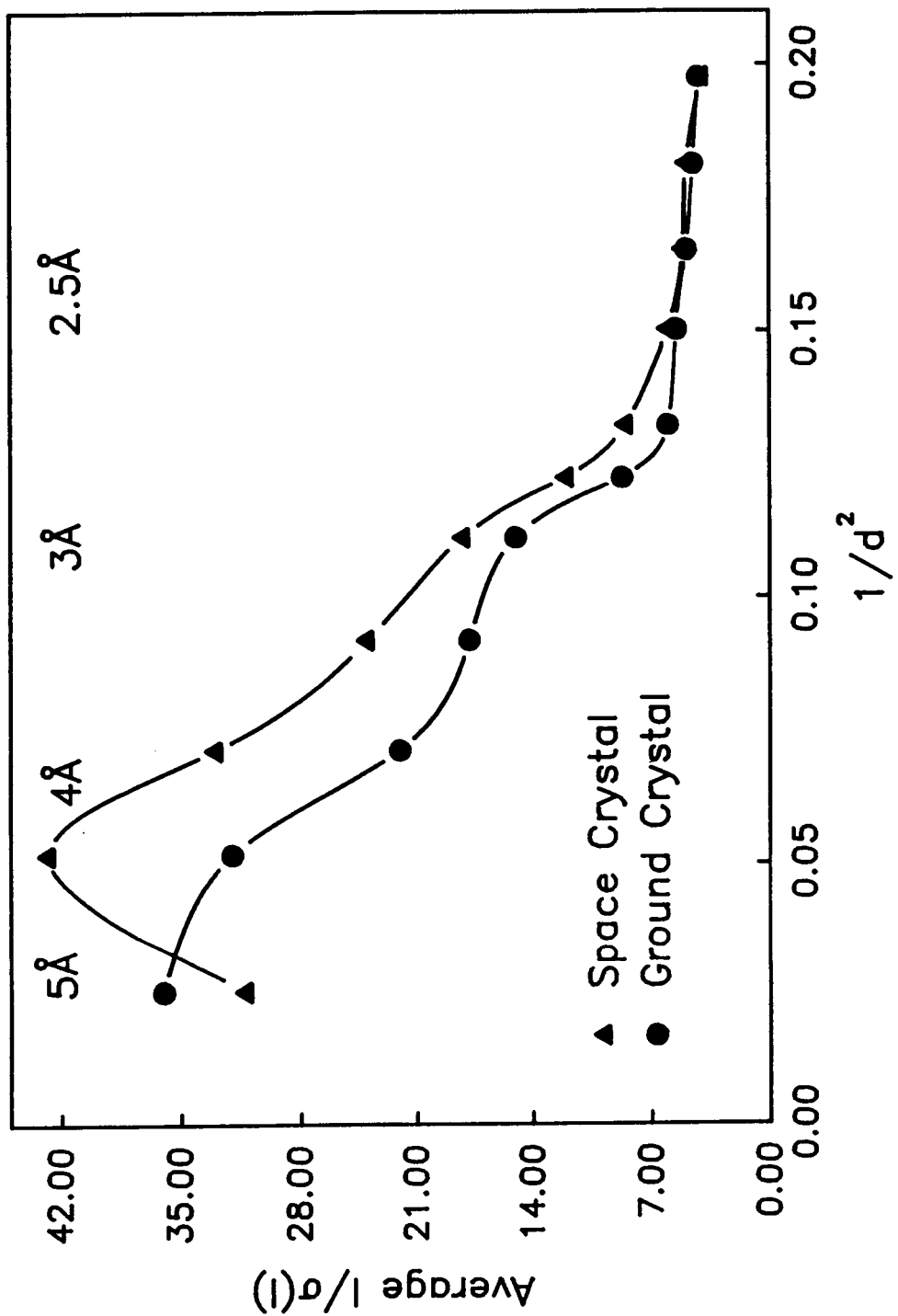


Figure 10 Comparison of diffraction intensity data for space-grown and Earth-grown crystals of polyisomerase.
The y-axis shows the percentage of data with $I/\sigma(I) \geq 5$.

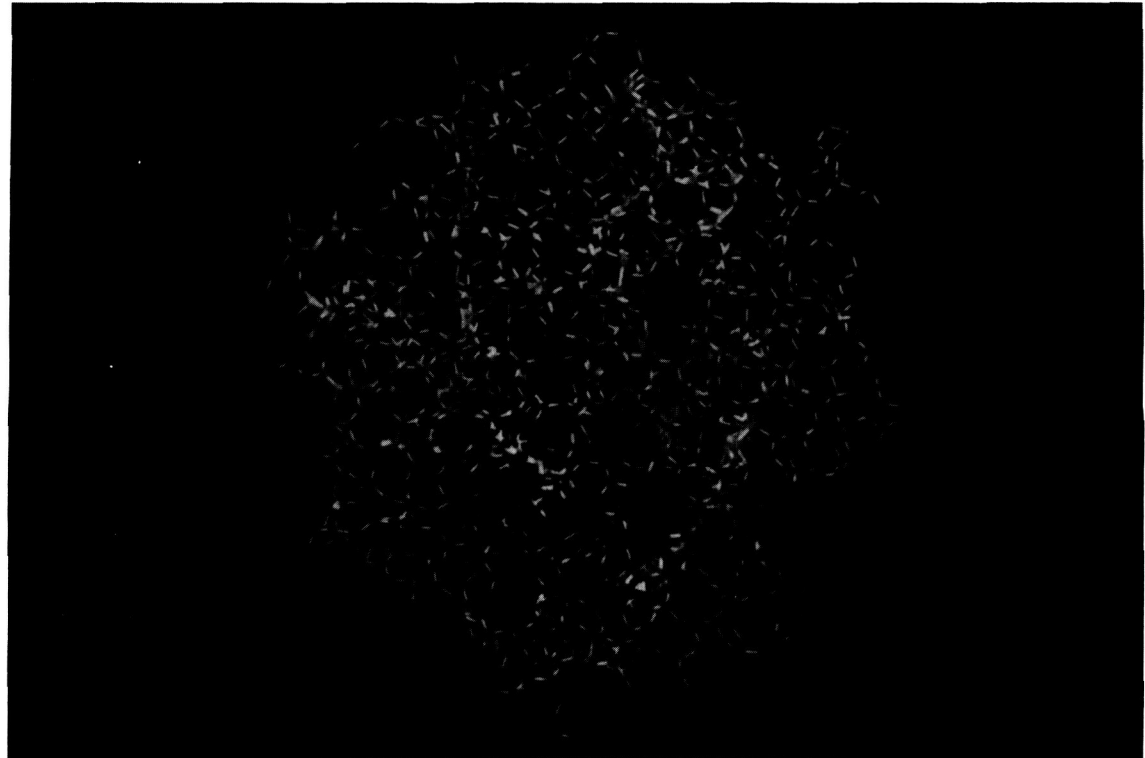


Figure 11 Three-dimensional structure of Factor D determined using a combination of earth-grown and space-grown (from USML-1) crystals.

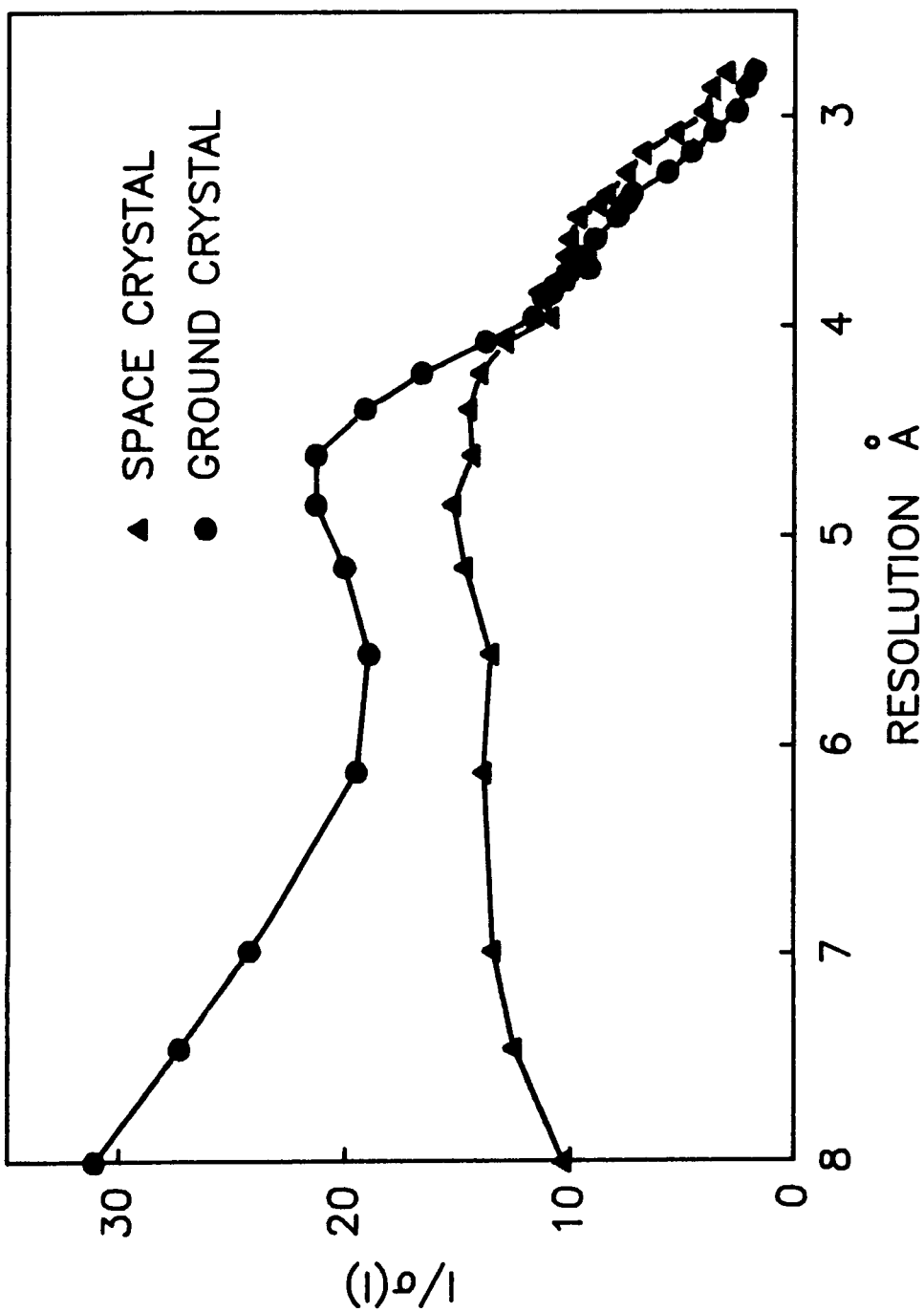


Figure 12 Comparison of diffraction intensity for space-grown (from USML-1) and Earth-grown crystals of canavalin. The y-axis shows the average I .

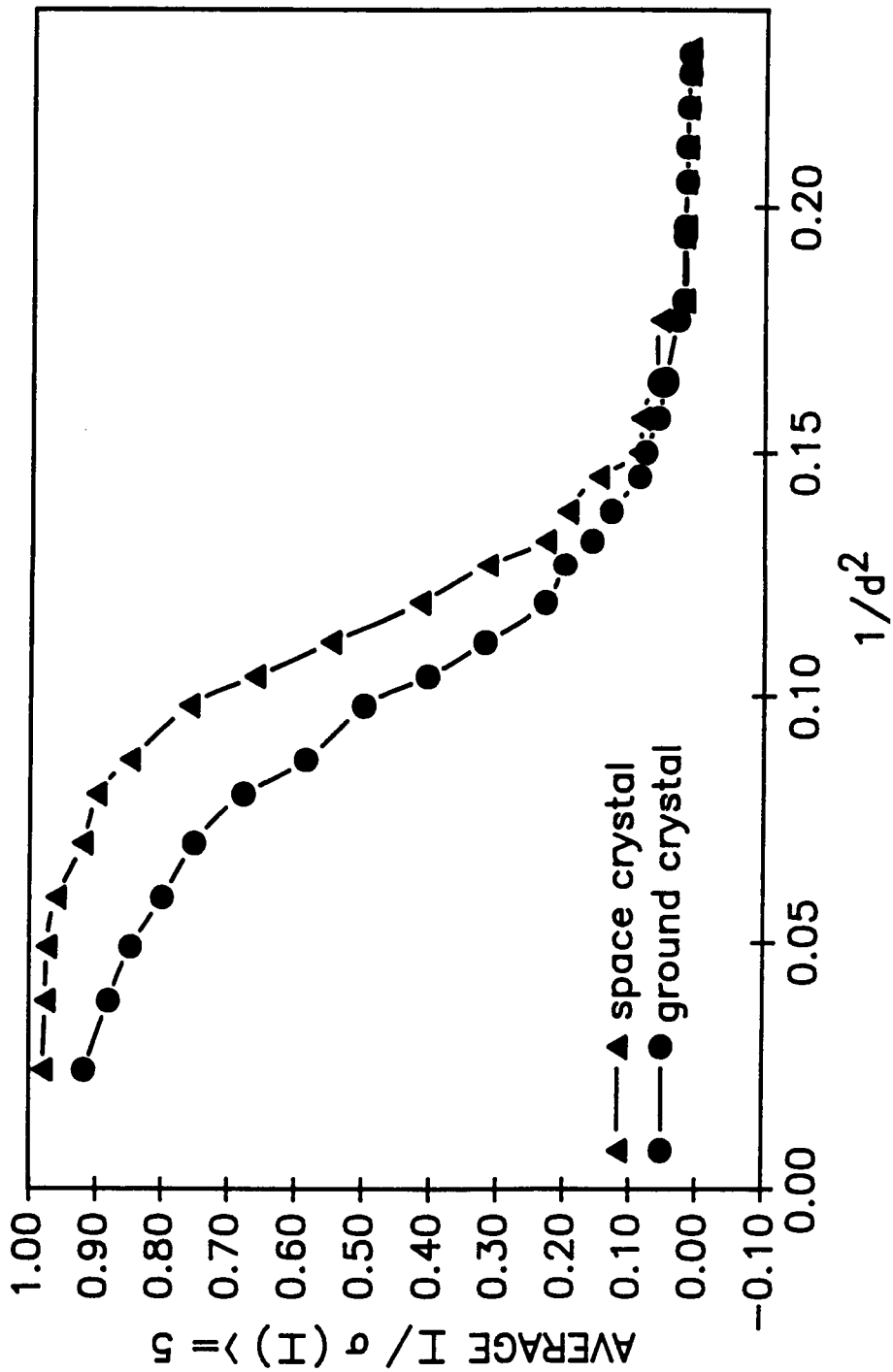


Figure 13 Typical data obtained for canavalin crystals obtained from previous space shuttle missions.

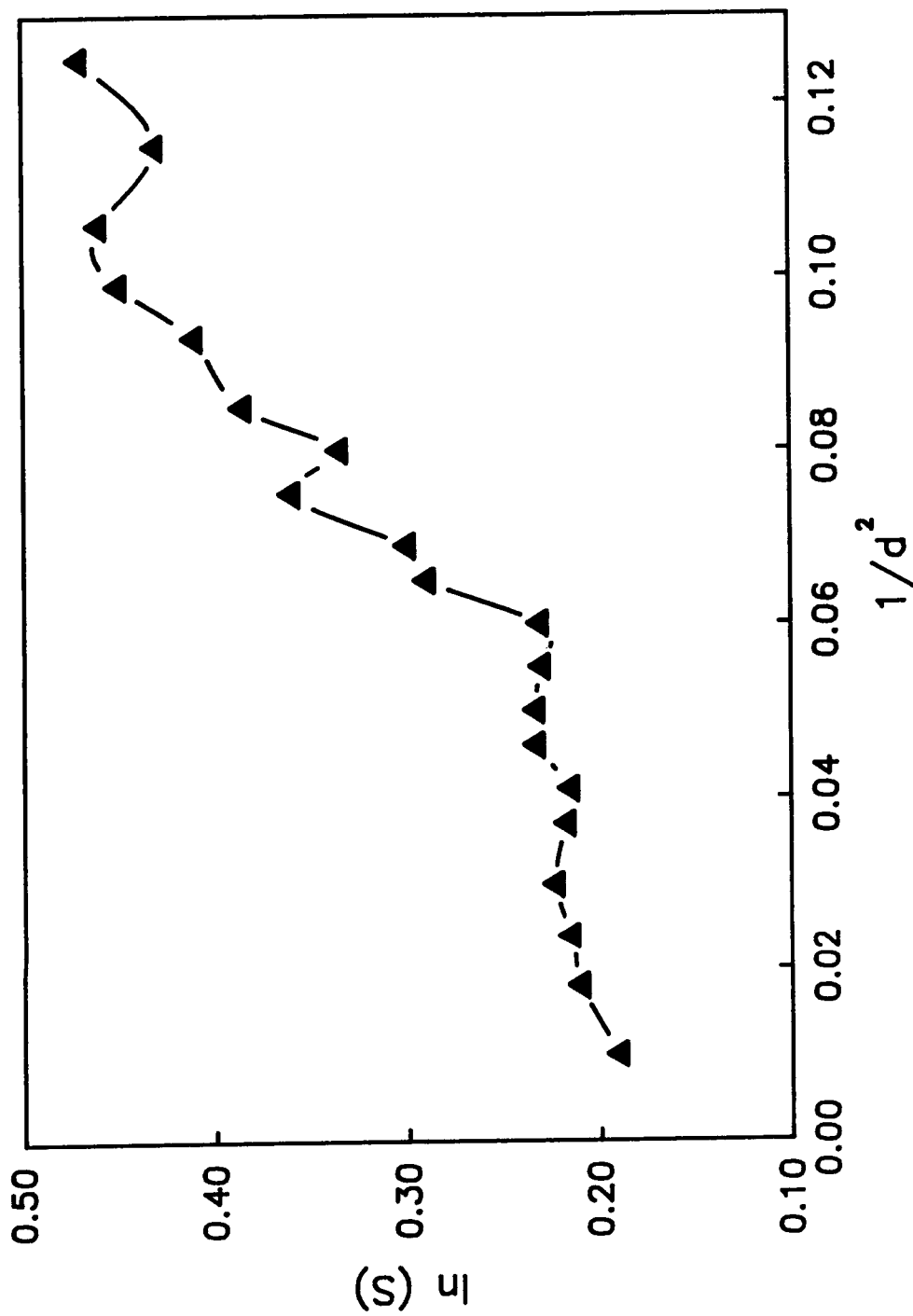


Figure 14 Relative Wilson plot comparing space-grown and Earth-grown crystals of HIV-1 reverse transcriptase complexed to a monoclonal antibody and 19/18 base-paired DNA fragment. $s = \Sigma Fa^2 / \Sigma Fb^2$, where a = space-grown and b = Earth-grown crystal.

Discussion

Question: *You mentioned about flow affecting crystal growth, what about the Brownian motion ?*

Answer: Well it is certainly more gentle than the convective flow due to buoyancy, and we measured those for a protein crystal. For example with lysozyme, the flow is moving up, I believe, at 1 micron per second. It was something like that. It was a lot faster than you are ever going to get just from Brownian motion. I don't know what amount of motion will harm a crystal and what won't. Those crystals that floated through the bottle benefited from that motion. They grew much larger than the ones that were attached. Possibly a controlled flow is what we need to look at in microgravity and also to optimize the length of a shuttle mission to get a crystal that is large enough that we can use.

Question: *Were you concerned at all about activities occurring on the shuttle during the growth, jitter effects and things like that? Did you ever get a chance or are you planning to look at that in a particular way?*

Answer: I don't know what vibrations will do to protein crystals as they grow. Unlike the semi-conductor crystals these are in all different orientations because they are free in solutions. But we have no data on what levels of vibrations may harm protein crystals, so I am not planning to look at that. We have enough things we are worried about, in terms of trying to understand the kinetics of the growth, etc. I think that is the first thing we need to hit. But I know and most protein crystallographers know that vibrations hurt protein crystals. We have a cold room where we grow crystals and the compressor is in another part of the building because if we attached it to the cold room, that vibration gives you a shower of little crystals. So vibration hurts but I don't know at what levels and where you draw the line.

Question: *Is it isolated at all or do you get all the vibrations ?*

Answer: The buildings are not but we have incubators that are on isolation tables in my lab. All of the incubators are isolated.

Comment: Computational fluid dynamic modeling has shown that vibrations in the 1-10 Hz range are the most detrimental for PCG as far as flow is concerned. It tends to wiggle the flow right next to the crystal and it does not take long for the flow to sweep past the crystal because the crystal is so small. This tends to disrupt any profiles, diffusion or otherwise next to the crystal. What it means for attachment kinetics is a whole new ball game and needs to be further researched. But we think that it is a good isolation candidate since frequencies in the 1-10 Hz range can be isolated by not only active but also by passive means.

Answer: On STS-57 we took two of the Malic enzyme crystals grown in this syringe and did something very interesting. What we did in the analysis is to take reflections down along all three principle axes and monitor those over and over as you expose those crystals to the x-ray radiation. We did that with two from space and two from ground and you are looking at the percent decay. The blue curve is the ground data and the top one, the space data from these two smaller space crystals. They (space crystals) last longer in the x-ray beam, and that is a dramatic improvement. This is the first time we have really done this kind of analysis. A lot of data was collected over three days to do this. Other investigators have said this needs to be done, but have never done this kind of experiment. They just collected the data but they didn't keep collecting the swath of data over and over. We did that on this mission. Of course if it does not decay as fast, that should mean it is better ordered once again.

Question: *Is it true in general, that space crystals are smaller than Earth grown crystals ?*

Answer: I think it is definitely due to the fact that it takes too long for these protein molecules to diffuse to the crystal. There are some cases where they are much larger even in the VDA. Unlike small molecule crystal growth, when a protein growth nucleates the supersaturation level is anywhere from two times the normal concentration in solubility to up to 150, 200, 300 times supersaturation. Depending on the supersaturation level, it is conceivable that you can get a pretty big crystal in space. I think that is why it has happened in some cases. Generally, the crystals that come back from space are much smaller than Earth crystals and most of this data that I showed you is from space crystals that are much smaller. In fact if you look at that table, about 70% of those space crystals that were superior resolution were much smaller than the Earth crystals.

It is a double edged sword, because the longer you stay in orbit, the protein degrades and those crystals that have grown will begin to degrade. What you need is to grow a crystal and when it reaches an optimum size, smaller than a capillary, collect data on it in space and we plan to do that on space station.

Question: *Was the crystal data for the transcriptase space grown crystal better than ground data ?*

Answer: They were very comparable. The only thing that was better was that the Wilson plot indicated less thermal motion which does indicate its better order. But the data in the diffraction plot is so close that I am not going to go out on a limb and say that the space data was better.

Question: *In light of your last comment, is the data still useful ?*

Answer: Oh yes. You can use it to help complete the structure. It is as good as any data set that they have put on the ground. Certainly. Probably a tiny bit better.

Discussion from the Glovebox Session

Question: You said in space whenever you were using your syringe, if you went too fast it would develop bubbles. Did that ever happen when you were doing tests on the KC-135 ?

Answer: We did but I never saw anything like I saw up in flight. The amount of bubbles I saw up there depended on the solution we were using. The first day, I think Carl Meade did human serum albumin and he had some problems with bubbles and the next day I had to do the same one but his was clone material and mine was real material. I am not sure which way it was but we used the same precipitate agent. I had bubbles, so I repeated his and got lots of bubbles but I found with other solutions it was not near as bad. There was a marked difference, depending on the solution, on how bad it was. And I never noticed from the KC, that bubbles were going to be as bad a problem as they were. Yes. We did get some on the KC-135 flights.

Question: You mentioned that the ability to do certain mental processes that would be normal (on Earth) you found perhaps a little more difficult. We were always wondering and maybe you can comment on this. You are running an operation that is very tightly timed, literally almost by the minute, and you are running behind as you said early on. How do you sort of mix that requirement with the fact that you have to think about what you are doing, and that, to me, sounds like something they have looked into, but you have experienced it ?

Answer: I felt a world of pressure on me. These proteins are really expensive. Some of the companies gave me protein for this flight that was worth over \$100,000. To make mistakes that are obvious on the ground when you can later look at it is different. I felt a lot of pressure. I was real nervous because I was way behind and I did not do the Glovebox experiment as carefully as I should have. I think I was extruding, sometimes a drop, and I would think, was that a bubble that just came out? On the ground I would have just sucked it back up; but I said, "I just got to keep going". So my accuracy was not what it should have been. So, what I tried to do was to pick the ones that were most valuable. We had a priority list and I tried to give them my attention; but, to be honest with you, the last 12 proteins on that priority list, I didn't set up a lot with them. I did them a lot faster knowing that they were not as valuable, and I knew that they didn't have as much chance for success. In fact, some had very little chance especially at the end. My haste, and not doing a careful experiment, I think, showed in some cases but it is hard to tell where. But I know sometimes when I dispensed liquids it could not be exactly right, but I could not go back and do it again.

Question: Did you put this down in your lessons learned list ?

Answer: Oh, I have. For USML-2, For USML-2, I am proposing 5 proteins, 30 hours for that. So the poor crewmen can relax and do it right.

Question: *Did you have any of the same proteins in the glovebox as in the middeck experiment ?*

Answer: Yes, I had about 4 or 6 that were duplicated across there. Reverse transcriptase was one and they were about equal in quality, Glovebox and the other one. It is hard for me to tell you because they merged them. The PI merged all those because he had to collect 22 crystals on a synchrotron. So all that data got put together. Malic enzyme had flown on two other missions in the VDA's with no crystals. It is mainly because of the viscous solution used. So it just flew in the Glovebox. There were a few others like that where they had viscous solutions and we got crystals in the Glovebox, not always big ones, and didn't get it in the VDA. Just like in every other mission, when we have polyethylene glycol, we typically got, and USML was no exception, just a clear solution or a massive precipitate. If you got something that does not mix and the precipitate is sitting here in the protein, right at that interface you have a high concentration and it will usually tend to make it just precipitate out. That happened on USML in the VDA.

Question: *I was just going to mention that the other day you said you only got three hours of sleep at night on the flight. That may have as much to do with the much lower mental capacity as anything else ?*

Answer: I think with me it was a lot of things. I didn't take sleeping pills. It wasn't three hours every night. Some nights I would get up and then go back to sleep a little later but I didn't get a lot of sleep. But my shoulder hurt the last 5 days. Ellen was wrapping my shoulder and that kept me up. It was just a lot of things but I didn't get a lot of sleep and maybe that affected my mental capacity. I think I would have done that crystal mounting procedure if I wasn't in pain. I would have gone and done it because I know it was important to test that. At that point, I said I had done enough and I am just going to put those things away.

Question: *You were mentioning that you felt almost immediately a reduction of mental capacity ?*

Answer: Well the first two days I guess everybody really feels it but then it gets a lot better and you feel sharp but looking back now I just don't think I was ever what I would be down here. Carl, you probably don't agree with me. We had talked about this a little bit. What do other payload specialists say?

Carl Meade: No. I don't know, but I am surprised, and everybody else is surprised, actually. I think this is an explainable phenomenon. Quite honestly I do not understand why this is a new find.

DeLucas: Well, it is not a new find, but I think people here don't realize it. I did not realize that it could have this kind of effect. It is the increased inner cranial pressure. I think anybody in the medical community will tell you, especially within the first two days.

Carl Meade: Within the first two days, yes. But once everybody gets to their equilibrium position I think the decreased mental capacity is certainly a function of the environment. I think that most people get up to 100%. At least I speak for myself. I think that I am up to 100%. Where that absolutely may be, who knows ? But, you say you are not, but, thinking back on it, I think that is sort of a predictable position. You are in a different environment. If you gave me a bunch of training manuals and then stuck me in your lab for two weeks and said, "quick, go produce something, and, by the way, we are watching the clock !", I would be fumbling around and falling down.

Question: *I was just wondering, did you get any diffraction data from Canavalin or did all the crystals disintegrate?*

Answer: Oh, yes we did. From the VDA, it was very good. From the Glovebox, however, the big one had degraded very significantly. I showed the curve; it actually went above the ground stuff at high resolution; but, at low resolution the signal/noise ratio was much worse than the ground crystals which were smaller and so that just got hurt tremendously.

Question: *So that data was not any better than ground data ?*

Answer: No. I would say that is worse.

Question: *You have a tremendous amount of surfactants in your solutions and because of that, when you did have a cavity form, there was a chemical component stabilizing it and, so, I assume if you tried to put a little more pressure on that cavity and tried to collapse it, it did not work. Is that the case? I mean you form a vapor cavity if your external pressure is above the vapor pressure then you collapse the bubble ?*

Answer: Are you talking about the bubbles in the syringe? I had a lot of little bubbles and I could get them all to the end of the needle and just push the air out. That was no problem.

Comment: *Since chemical diffusion is very slow and the bubble is chemically stabilized, you are stuck with physically removing the bubble as opposed to collapsing it.*

Answer: Well, I never tried to collapse it. I tried to get it out of the end of the syringe. The only thing that I said that if it is at the other end, just like it would on Earth, you are going to compress that air and again you won't dispense accurate amounts.

Question: *Could you comment on the effect of dissolved gases in your solutions ?*

Answer: It is true that in many cases the liquids have dissolved gases in them and most investigators worked hard to prepare their liquids by taking the dissolved gas out. That means putting them under vacuum and heating them, and so forth, and then placing them into containers without any air. STDCE put their fluid in bags. We have flown on several flights all the proteins. We degassed everything. Not only did we degas, it but we vibrated it while we degassed it to get as much air out as we could and it has never made any difference in the bubbles generated by the syringes, i.e., the big syringes that we have in the VDA. I think as the liquid moves, it grabs the surface and cavitates and the faster you move it across there you are just trapping air. Degassing is important to do, but we never saw a difference. Some of our investigators degas now, and some don't, just because we haven't been able to tell a difference. I think, it is so bad because of the syringes' mechanism itself.

26 P^o

1995107812

324092

.. w,
11031
P. 26

THE GROWTH OF ZEOLITES A, X AND MORDENITE IN SPACE

A. Sacco, Jr., N. Bac, E. N. Coker, A. G. Dixon, J. Warzywoda, and R. W. Thompson

Department of Chemical Engineering
 Worcester Polytechnic Institute
 Worcester, Massachusetts.

ABSTRACT

Zeolites are a class of crystalline aluminosilicate materials that form the backbone of the chemical process industry worldwide. They are used primarily as adsorbents and catalysts and support to a significant extent the positive balance of trade realized by the chemical industry in the United States (around \$19 billion in 1991).¹ The magnitude of their effects can be appreciated when one realizes that since their introduction as "cracking catalysts" in the early 1960's, they have saved the equivalent to 60 percent of the total oil production from Alaska's North Slope.¹ Thus the performance of zeolite catalysts can have a profound effect on the US economy. It is estimated that a 1 percent increase in yield of the gasoline fraction per barrel of oil would represent a savings of 22 million barrels of crude oil per year, representing a reduction of \$400 million in the United States' balance of payments.² Thus any activity which results in improvement in zeolite catalyst performance is of significant scientific and industrial interest. In addition, due to their "stability," uniformity, and, within limits, their "engineerable" structures, zeolites are being tested as potential adsorbents to purify gases and liquids at the parts-per-billion levels needed in today's electronic, biomedical, and biotechnology industries and for the environment. Other exotic applications, such as host materials for quantum-confined semiconductor atomic arrays, are also being investigated. Because of the importance of this class of material, extensive efforts have been made to characterize their structures and to understand their nucleation and growth mechanisms, so as to be able to custom-make zeolites for a desired application. To date, both the nucleation mechanics and chemistry (such as what are the "key" nutrients) are, as yet, still unknown for many, if not all, systems. The problem is compounded because there is usually a "gel" phase present that is assumed to control the degree of supersaturation, and this gel undergoes a continuous "polymerization" type reaction during nucleation and growth.

Generally, for structure characterization and diffusion studies, which are useful in evaluating zeolites for improving yield in petroleum refining as well as for many of the proposed new

applications (e.g., catalytic membranes, molecular electronics, chemical sensors) large zeolites (>100 to 1000X normal size) with minimum lattice defects are desired. Presently, the lack of understanding of zeolite nucleation and growth precludes the custom design of zeolites for these or other uses. It was hypothesized that the microgravity levels achieved in an orbiting spacecraft could help to isolate the possible effects of natural convection (which affects defect formation) and minimize sedimentation, which occurs since zeolites are twice as dense as the solution from which they are formed. This was expected to promote larger crystals by allowing growing crystals a longer residence time in a high-concentration nutrient field. Thus it was hypothesized that the microgravity environment of Earth orbit would allow the growth of large, more defect-free zeolite crystals in high yield.

I. CRYSTALLIZATION IN SPACE

The environment of low-Earth orbit makes it a potentially interesting environment for crystal growth from the melt and from solution. Typically the gravity levels in a manned spacecraft are 10^{-5} to $10^{-6}g$ residual accelerations and 10^{-4} to $10^{-3}g$ impulsive accelerations.³ These substantially reduced levels dramatically reduce gravity-driven convection. In addition, in the case of solution crystal growth, crystals will stay essentially suspended in the nutrient pool under a diffusion-limited growth condition. The "folklore" of crystal growth would then predict more uniform (fewer defects), and larger crystals will be produced in this environment. To date, the results have been interesting but inconclusive.^{4,5}

II. BACKGROUND: GAS1-PRELIMINARY RESULTS

The Get Away Special (GAS) program allows low-cost access to space. The "can" itself is 2 cubic feet, must weigh under 200 pounds, has its own power, and all systems must be activated by a single switch. WPI was given a GAS can by the Mitre Corporation and designed and built a number of experiments that flew on STS-40 in June of 1992.⁶ One of those experiments was the growth of zeolite A. Details of the furnace used and the control and archiving equipment are given elsewhere.⁷ Basically it consisted of two 10 ml chambers that housed two premixed zeolite A solutions that were heated to 96°C under their own autogenous pressure. Triethanolamine (TEA) was added to control the initial nucleation and to slow the growth of those crystals already formed.^{8,9} Research had shown that the "gel" formed from this formulation appeared to be "stabilized" for 21 to 30 days at ambient conditions (i.e., if heated within this time, a uniform population of crystals having a cubic morphology were formed).

As a result of flight delays, the premixed zeolite solutions were not launched into space for

110 days after they were initially mixed. After approximately one day on orbit, the furnace was activated and performed perfectly, maintaining the 96°C reaction temperature for 72 hours, after which the solutions convectively cooled. Typical results are illustrated in Figures 1 and 2. Figure 1 presents two micrographs representing crystals from a ground (terrestrial) control sample (also premixed and held at ambient conditions for 110 days) and the crystal from one of the reaction chambers activated (heated) in orbit. The heat-up profiles and cool-down profiles for the control samples were essentially identical to those produced during flight. As illustrated, the crystals are virtually identical in size (25-35 μ) and appear in both cases to be intergrown. Figure 2 confirms these results, showing two populations with identical nucleation and growth histories.

Prior ground-based studies had shown that if these solutions were heated immediately on mixing or after only 21 days, they formed a uniform population of well-formed cubes (typical of zeolite A) with little or no intergrowths. In order to try to understand the discrepancies, an investigation was performed on premixed mixed solutions at room temperature and after heating to 80°C using both small-angle neutron diffraction and small-angle X-ray diffraction. Preliminary results indicated that similar solutions without TEA (solutions with TEA were difficult to analyze due to the low number of scattering centers) began to form prenuclei at room temperature immediately after mixing.¹⁰ Thus it can be hypothesized that prenucleation occurred during the 110 delay period and that this phase of the nucleation event was complete prior to flight and furnace activation. The crystal morphology observed can be rationalized if one postulates that these precursor nuclei settle and interact to produce the intergrowths seen in both the flight samples and the control. This would be consistent with the observation that well-formed crystals are produced when the solutions were processed prior to 21 days and with the NIST results that suggest "nucleation" proceeds immediately on mixing and can explain the intergrowths observed in both the flight and ground-control systems, which are likely to be the prenuclei growing together. These conclusions led to an extensive development program to create a crystallization vessel (autoclave) which would allow the precursor solutions to be loaded 48 to 72 hours prior to launch and held unmixed until activation on orbit. In addition, in order to ensure that the solutions were uniformly mixed, different nozzle designs and mixing protocols were developed (glovebox experiment) to test on orbit.

III. USML-1 THE GROWTH OF ZEOLITES A, X AND MORDENITE

Three different zeolites were chosen to be crystallized in space: zeolite A, zeolite X, and mordenite. Due to the furnace configuration,¹¹ multiple A and X solutions were flown, but only one mordenite formulation was processed. Two of each formulation were processed in orbit to provide reproducibility. The zeolite solution formulations were chosen to test the hypothesis that

larger, more defect-free crystals could be made in orbit. However, no attempt was made to determine the best solution to maximize growth or to minimize defect formation.

A. Zeolite Flight Facilities

The Zeolite Crystal Growth (ZCG) furnace was designed to process 19 autoclave units, each unit consisting of two separate autoclaves, each of which houses two 10 ml sample chambers.¹¹ The furnace is cylindrical in shape and configured in three concentric zones. The central zone was used to process mordenite (experiment temperature 175°C) and could achieve a temperature of 200 °C with a negligible radial temperature gradient and less than a 1°C axial gradient across the sample chambers. The middle zone could process six autoclave units at temperatures of 105°C to 150°C with the same precision as the central zone. Zeolite X was processed within this middle zone, and these samples were processed at 105°C. The outer zone (used to process zeolite A at 96°C) consisted of 12 furnace tubes, and each could be controlled to the same axial and radial precision in the temperature range 90°C to 110°C. The entire unit (furnace module and control system) was at steady state in under 8 hours and used 200 watts of power during heat-up and 91 watts during steady-state operation. The furnace was controlled with its own independent CPU. All furnace tubes and all control and heating subsystems were at least single-fault tolerant. A Ground Control Experimental Laboratory (GCEL) was built to process the terrestrial control experiments. It was identical in every way to the flight unit except the GCEL had no redundant CPU. In addition to the furnace and control system, four different autoclave nozzle designs were tested on orbit, and several operational protocols were utilized.

B. Zeolite Glovebox Experiment (GBX-ZCG)

It is well known that zeolite precursor solutions (e.g., aluminum solutions and silicate solutions) must be well mixed (homogenous) in order to maximize product purity. In addition, for those solutions which form a viscous "gel," if the solution is excessively sheared, the product purity may also be affected. Nuclear Magnetic Resonance Imaging (NMRI) studies were performed in order to test (evaluate) many proposed nozzle designs and mixing protocols.^{12,13} The suggested mixing protocols, which were nozzle and solution dependent, were further tested on low-gravity aircraft. These combined tests formed the basis for the nozzles and activation procedures for the on-orbit observation protocol used to establish how best to mix the zeolite solutions to be processed in the ZCG facility. The results from the glovebox experiment illustrated that real-time observation of the mixing process is necessary to ensure gel uniformity without excessive shear.

Also bubble formation, inherent in the mixing process, was minimized through real-time observation, analysis, and the resulting crew-initiated corrective actions. This on-orbit intervention helped to minimize impurity phases formed and guaranteed that few, if any, nuclei were formed by excess surface area as the result of bubbles or foaming.

IV. RESULTS AND DISCUSSION

The samples flown on STS-50 and the control solutions were all from a common batch prepared for each zeolite formulation. Eighty-eight autoclaves were loaded, representing five zeolite A formulations, five zeolite X formulations, and one mordenite formulation. Forty-four autoclaves were randomly selected for flight, and the remaining autoclaves were used as controls. These forty-four autoclaves represented nineteen duplicate experiments and six spares. Two autoclaves in the control group and in the flight group represented a zeolite A formulation where no nucleation control agent (Triethanolamine, TEA) was present; this represented an on-orbit control to test the hypothesis that to grow large zeolites in space the nucleation event must be controlled. How each autoclave was activated and what, if any, actions were necessary to minimize bubble formation (based on GBX-ZCG) were recorded on video and evaluated real-time prior to activation of the flight and control autoclaves. Also the heat-up and eventually the cool-down thermal profiles were downloaded during the flight and were duplicated in the GCEL control experiment.

In order to quantitatively determine if, and how, low gravity affected the crystallization of these zeolite formulations, the following analysis procedure was performed on all samples. The crystals from the flight and control samples were observed and photographed using optical and scanning electron microscopy, and a particle-size distribution (PSD) was developed for each. Following this documentation, control and flight samples were sent to the University of Connecticut to measure their surface area (BET), lattice parameters (XRD), X-ray photoelectron spectra (XPS), and the associated surface Si/Al ratio. The samples sent to the University of Connecticut were not identified as to which were flight and which were terrestrial controls. This was done to eliminate any unintentional bias.

A. Zeolite A

Figure 3 compares the flight and terrestrial control for zeolite A where no nucleation control agent was used. This experiment was performed to test the hypothesis that if the nucleation event was not controlled, then the resulting burst of nuclei would drop the degree of supersaturation below the point where growth would be possible or of an acceptable rate. As the micrographs illustrate, there is no substantial difference in either size or morphology. In all cases (four

autoclaves: two processed in space and two processed as terrestrial controls), the size is between one and three micrometers, and the growth of the [110] planes in both samples is evident. The PSD presented in Figure 4 confirms the visual observations. The tail at three to four micrometers on the terrestrial PSD represents precipitate Al(OH)_3 . At this time, no explanation can be given for this precipitate. No Al(OH)_3 was found in any of the other flight or control samples. The results represented by Figures 3 and 4 suggest that the hypothesis that in order to grow large crystals from solution in space, the nucleation event must be controlled appears to be correct. X-ray data of these samples indicate that with the exception of the Al(OH)_3 , the samples are essentially pure zeolite A.

Figures 5, 6 and 7 are typical of the results observed when nucleation control was present. The micrographs in Figure 5 represent a typical flight and control sample. As illustrated, the flight crystals are 10 to 25 percent larger in linear dimension, do not show the characteristic [110] plane observed on the control sample, and, in general, appear to have fewer intergrowths. Figure 6 illustrates the PSD's for these flight and control samples. As was suggested by Figure 5, the entire population is shifted to higher average sizes (approximately 10 to 25 percent). The micrographs in Figure 7 represent a comparison for a different zeolite A formulation between crystals made in space, their terrestrial control (both crystallizations were performed with a nucleation control agent), and commercial crystals (no nucleation control). The largest crystals produced in orbit were 10 to 40 percent larger in linear dimension than the largest crystals found in the control and 35 to 40 times as large as those produced commercially. Also as illustrated by the high magnification insert, the morphology of the crystals formed under nucleation control approaches the cubic morphology of an ideal zeolite A crystal. Tables 1 and 2 and Figure 8 represent comparisons of the binding energies, associated spectra, and the resulting Si/Al ratio between flight and control samples for a typical zeolite A experiment. As illustrated in Table 1, the binding levels for the Si KLL and Al KLL transitions for both flight and terrestrial are consistent with literature values. The shape of the peaks and their relative location is illustrated in Figure 8. The arrow shows a satellite peak that represents the mounting medium and is not representative of the samples. Table 2 presents the resulting Si/Al ratios for these samples. As indicated, the crystals produced in space typically gave the same or higher Si/Al ratios than did their control samples. As illustrated in Table 2, flight sample A1 gave the theoretical Si/Al ratio of 1.00. To the authors' knowledge, this is the only time this has been reported. Examples of XRD data are presented in Table 3. As illustrated, the lattice parameters and, thus, the unit cell volumes for the flight samples were frequently less than for the terrestrial controls. This is consistent with fewer lattice defects in the structure. Finally, CO_2 adsorption studies were performed on the flight and terrestrial controls. All samples, both terrestrial

and flight, displayed Type I adsorption isotherms. In general, but not in every case, the flight samples were smaller in surface area. Once again, this is consistent with a crystal structure that has fewer lattice defects.

B. Zeolite X

Figure 9 illustrates typical results from the zeolite X formulations. As shown, the larger crystals of zeolite X were as much as 50 percent longer in linear dimension than their controls. The PSD for this formulation is depicted in Figure 10. As indicated, the terrestrial controls typically had two different populations. The micrographs in Figure 9 suggest this is likely to be an impurity phase: zeolite P. This is an indication of possible poor mixing. The PSD for the flight sample could not be fully characterized due to size restriction in celloscope available to do the analysis. Another formulation used for zeolite X produced the crystals shown in Figure 11. Again, as was most often the case, the crystals grown in space were larger. It is interesting to note that the PSD from this formulation indicates a nonuniform shift in size; a population of larger crystals was produced in space relative to the terrestrial control population (Figure 12). The initial characteristics of the flight-grown crystals relative to their terrestrial controls were similar to the zeolite A samples. Table 4 lists the Si/Al ratio based on XPS. Here, as in the zeolite A case, the Si/Al ratios of the flight samples are greater on average than their controls. Since zeolite X has a range of Si/Al ratio, no conclusions are possible on the defect content from these data alone. The XRD pattern again resulted in significantly smaller lattice parameters and a smaller cell volume for the flight samples versus the ground controls (Table 5). BET analysis, using N₂ as an adsorbent, shows once again these materials produced a Type I adsorption isotherm, characteristic of materials with a high level of microporosity (Figure 13). In Figure 13, the data are presented in pairs: X1 and X2 represent one control and flight pair, while X3 and X4 represent another. As presented, the even-numbered samples (flight) are significantly different from their controls (odd). The surface areas that have resulted from these isotherms are listed in Table 6. In a similar manner to the zeolite A samples, the zeolite X samples that were prepared in flight had smaller surface areas than their terrestrial counterparts. In the cases illustrated here, these differences in surface areas were between 15 percent and 30 percent. The XRD and BET data taken together with the XPS results suggest, once again, that the larger crystals grown in orbit have fewer lattice defects.

C. Mordenite

Analysis continues on the Mordenite samples. To date, the following has been observed: The physical state of the flight samples was powder-like, while what is normally observed is a

compressed mass of individual crystals. The crystals are not unsimilar in morphology and appear on average to be similar in size. At present, the characterization work on the mordenite has not been completed.

CONCLUSIONS

The results from USML-1 were consistent with the hypothesis that larger, more defect-free zeolite crystals can be grown in high yield in space. The size increase for zeolite A and zeolite X varied between 10 to 50 percent for the formulations flown. Mordenite crystals did not increase in size, on average, when processed in space. Characterization of the flight samples versus their controls indicates that the lattice defect concentration is reduced when these crystals are produced in space.

ACKNOWLEDGMENT

Thanks are extended to NASA through the Battelle and Clarkson University CCDS for funding, to Teledyne Brown Engineering for the furnace fabrication, to Intek, Inc., for the design and building of the control system, and to the crew of USML-1 for the great job they did in orbit. In addition, thanks are given to Mr. Jack Ferraro and the graduate students of Worcester Polytechnic Institute who worked on this project. Lisa McCauley of Battelle deserves special thanks for her support.

REFERENCES

1. *CRITICAL TECHNOLOGIES: THE ROLE OF CHEMISTRY AND CHEMICAL ENGINEERING*, Committee on Critical Technologies, Board on Chemical Sciences, Commission on Physical Science, Mathematics, and Applications, and the National Research Council, National Academy Press, Washington, D.C., 1992.
2. *CATALYSIS LOOKS TO THE FUTURE*, Study of the National Research Council, National Academy Press, Washington, D.C., 1992.
3. C. R. Baugher, G. L. Martin, and R. DeLombard, *Review of the Shuttle Vibration Environment*, AIAA Paper 93-0832, AIAA 31st Aerospace Sciences Meeting, Reno, NV, January 1993.
4. W. Schmidt, *The Growth of Zeolite Crystals in a Microgravity Environment: Results of the CASIMIR-1 MISSION*, Final Report, INTOSPACE GmbH, Hannover, Germany, 1992.
5. T. Sano, F. Mizukami, M. Kawamura, H. Takaya, T. Mouri, W. Inaoka, Y. Toida, M. Watanabe, and K. Toyoda, *Crystallization of ZSM-5 Zeolite Under Microgravity*, *Zeolites*, 12, 801, 1992.
6. W. W. Durgin, J. F. Looft, A. Sacco, Jr., R. W. Thompson, A. G. Dixon, D. Roberti, R. Labonte, and L. Moschini, *Space Payload Design Flight Experience G-408*, *Shuttle Small Payloads*

Symposium, NASA Conference Publication 3171, 1992.

7. A. Sacco, Jr., R. W. Thompson, and A. G. Dixon, *Microgravity Processing of Zeolites in Space*, 18th International SAMPE Tech Conf., Vol. 19, 330, 1986.
8. M. Morris, A. Sacco, Jr., A. G. Dixon, R. W. Thompson, *The Role of an Aluminumtertiary Alkanolamine Chelate in the Synthesis of Large Crystal Zeolite NaA*, *Zeolites* 11, 178, 1991.
9. M. Morris, A. G. Dixon, A. Sacco, Jr., and R. W. Thompson, *Investigations of the Relative Effectiveness of Some Tertiary Alkanolamines in the Synthesis of Large-crystal Zeolite NaA*, *Zeolites*, 13, 113, 1993.
10. E. N. Coker, A. G. Dixon, K. E. Hamilton, A. Sacco, Jr., R. W. Thompson, and J. Warzywoda, *Annual Report* (October 1, 1990, through September 30, 1991); and *Quarterly Report* (May 1, 1992, through July 31, 1992), Clarkson University CCDS.
11. M. R. Fiske and R. A. Olsen, *The Development of a Furnace for the Growth of Zeolites in Microgravity and Related Materials Processing Applications*, AIAA Paper 92-0785, 30th Aerospace Sciences Meeting, Reno, NV, January, 1992.
12. E. N. Coker, P. S. Hees, C. H. Sotak, A. G. Dixon, R. W. Thompson, and A. Sacco, Jr., *Zeolite Synthesis in Unstirred Batch Reactors I. NMR Imaging of Non-Uniform Pre-Mixing*, Submitted Microporous Materials, 1994.
13. E. N. Coker, A. G. Dixon, R. W. Thompson, and A. Sacco, Jr., *Zeolite Synthesis in Unstirred Batch Reactors II. Effect of Non-Uniform Pre-Mixing on the Crystallization on Zeolites A and X*, Submitted Microporous Materials, 1994.

Table 1: XPS Binding Energies for typical Zeolite A Flight and Control Samples

Zeolite A Binding Energies

Sample	Si KLL*	Al KLL*
A1(F)	1711.46	1460.23
A2(T)	1711.56	1460.45
A3(F)	1711.53	1460.37
A4(T)	1711.49	1460.38

* - in eV, X-ray Excited Auger Transitions.

Table 2: Si/Al Ratios by XPS for typical Zeolite A Flight and Control Samples

Zeolite A Si/Al Ratios

Sample	Si/Al
A1(F)	1.0
A2(T)	0.97
A3(F)	0.96
A4(T)	0.96

Atomic %.

Table 3: XRD Data comparing Flight (A1, A3) and Control (A2, A4) Samples

Zeolite A

Sample	a*	EDS	Volume**
A1(F)	24.639	0.0110	14,958
A2(T)	24.672	0.0254	15,018
A3(F)	24.130	0.291	14,049
A4(T)	24.575	0.065	14,842

* - in Å.

** - in Å³.

JCPDS Zeolite A = 24.64 Å.

Table 4: Si/Al Ratios by XPS for typical Zeolite X Flight and Control Samples

Zeolite X Si/Al Ratios

Sample	Si/Al
X1(T)	1.24
X2(F)	1.30
X3(T)	1.31
X4(F)	1.38

Atomic %.

Table 5: XRD Data comparing Flight (X2, X4) and Control (X1, X3) Samples

Zeolite X

Sample	a*	EDS	Volume**
X1(T)	24.992	0.0387	15,609
X2(F)	24.900	0.00718	15,439
X3(T)	24.985	0.170	15,597
X4(F)	24.470	0.132	15,652

* - in Å.

** - in Å³.

JCPDS Zeolite X = 24.99 Å.

Table 6: BET Surface Areas comparing Flight and Control Samples

Zeolite X

Sample	SA (m ² /g)
X1(T)	870
X2(F)	735
X3(T)	685
X4(F)	460

T = Terrestrial.

F = Flight.

Type I Adsorption Isotherms.

N₂ Adsorption.

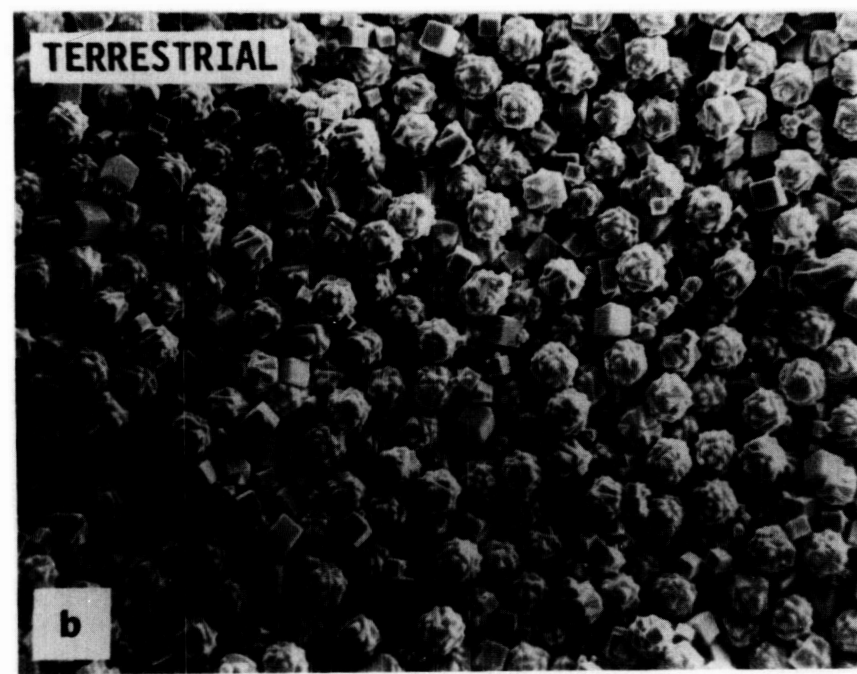
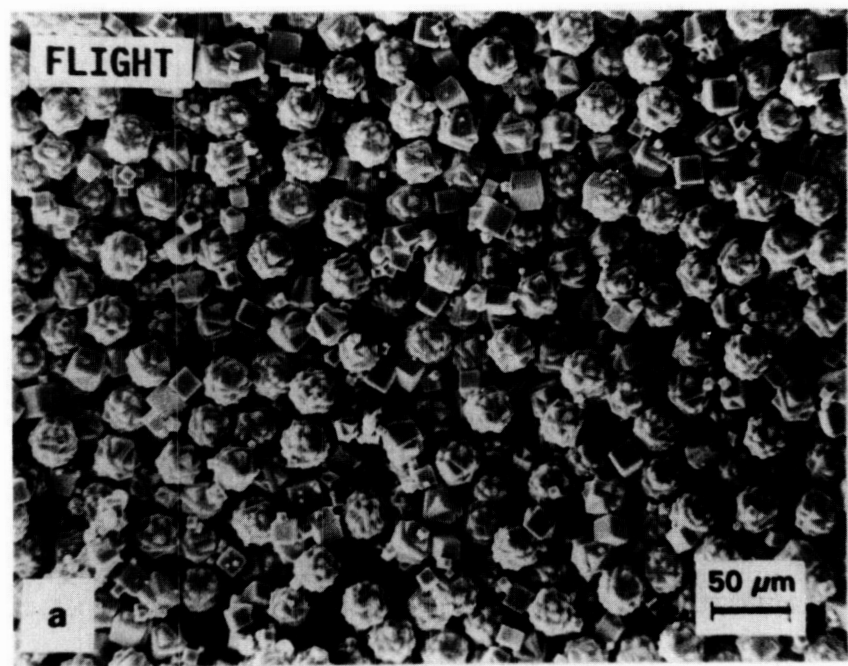


Figure 1 GAS-1: Zeolite A from STS-40 (Premixed 110 days before launch).

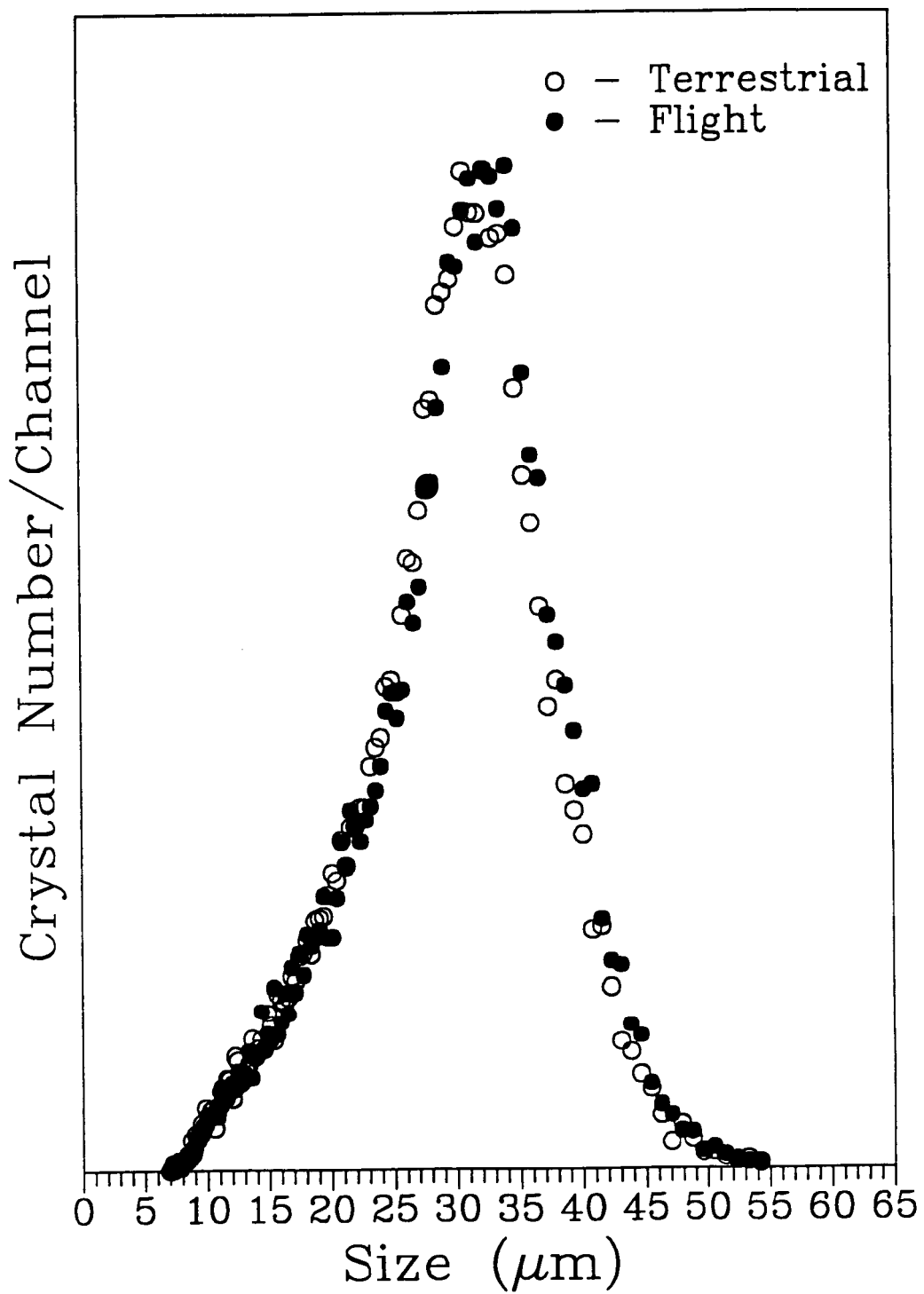


Figure 2 PSD's of Zeolite A (GAS-1).

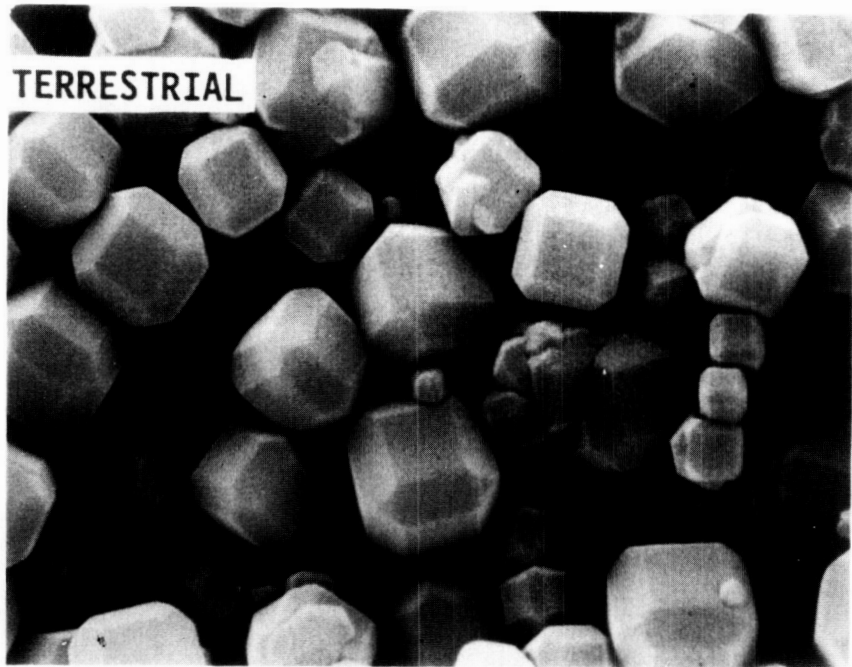
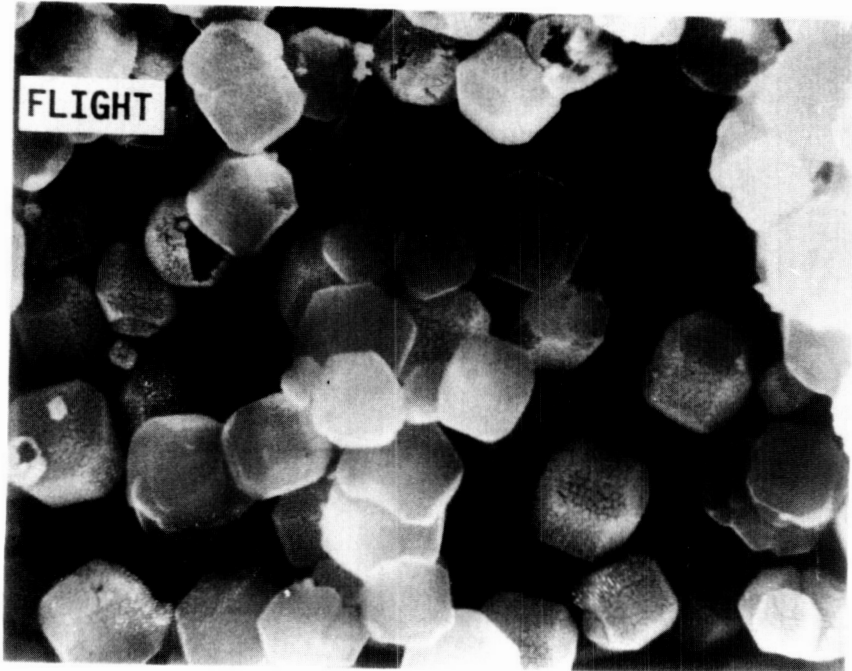


Figure 3 Zeolite A USML-1 (No Nucleation Control).

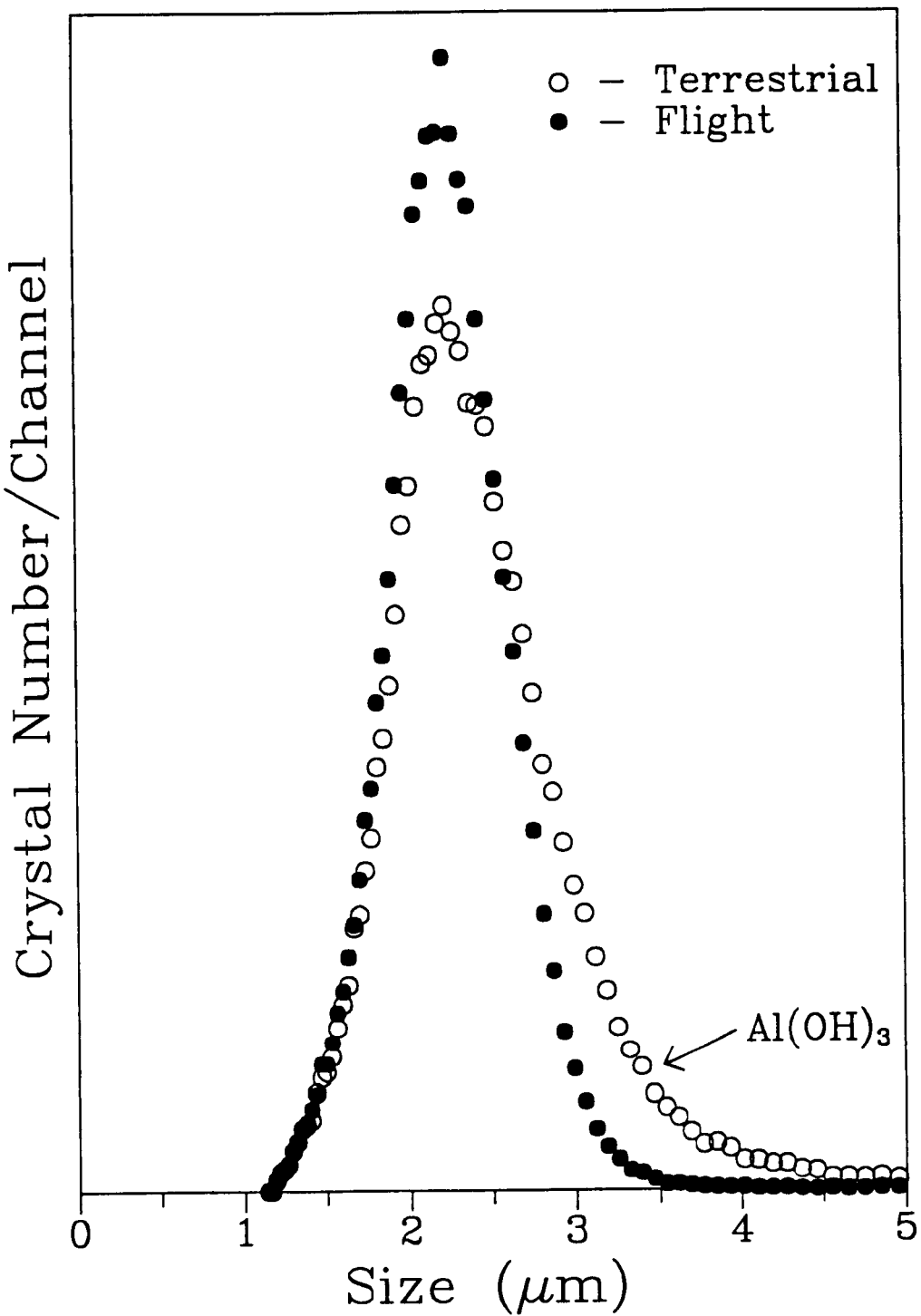


Figure 4 PSD's of Zeolite A USML-1 (No Nucleation Control).

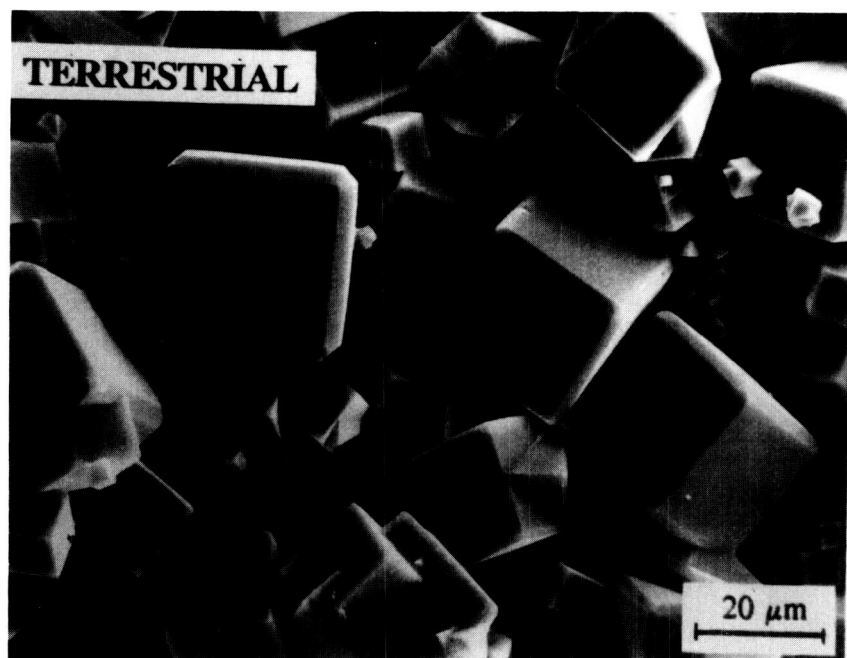
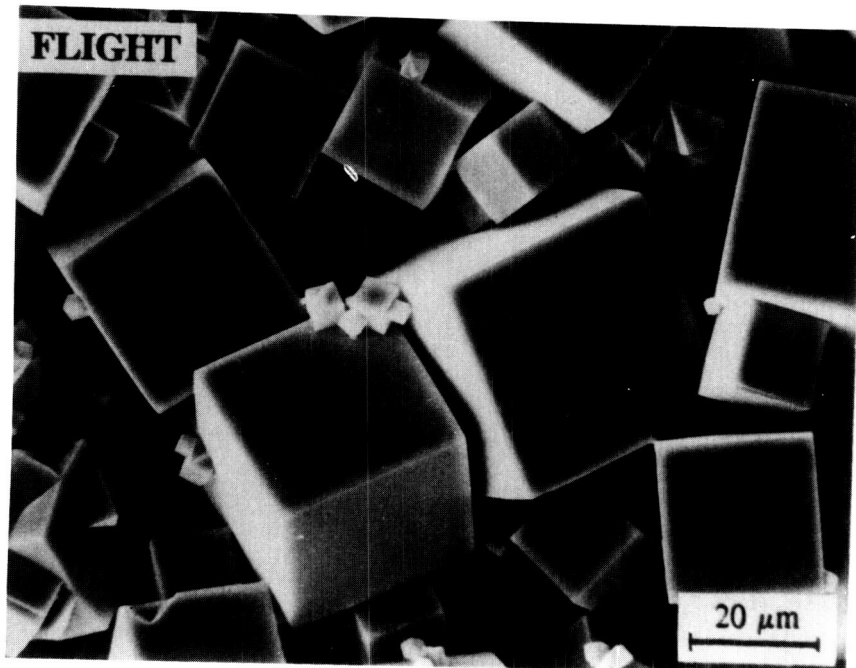


Figure 5 Zeolite A USML-1 with Nucleation Control (5.5 TEA, Piston, 5 Activations).

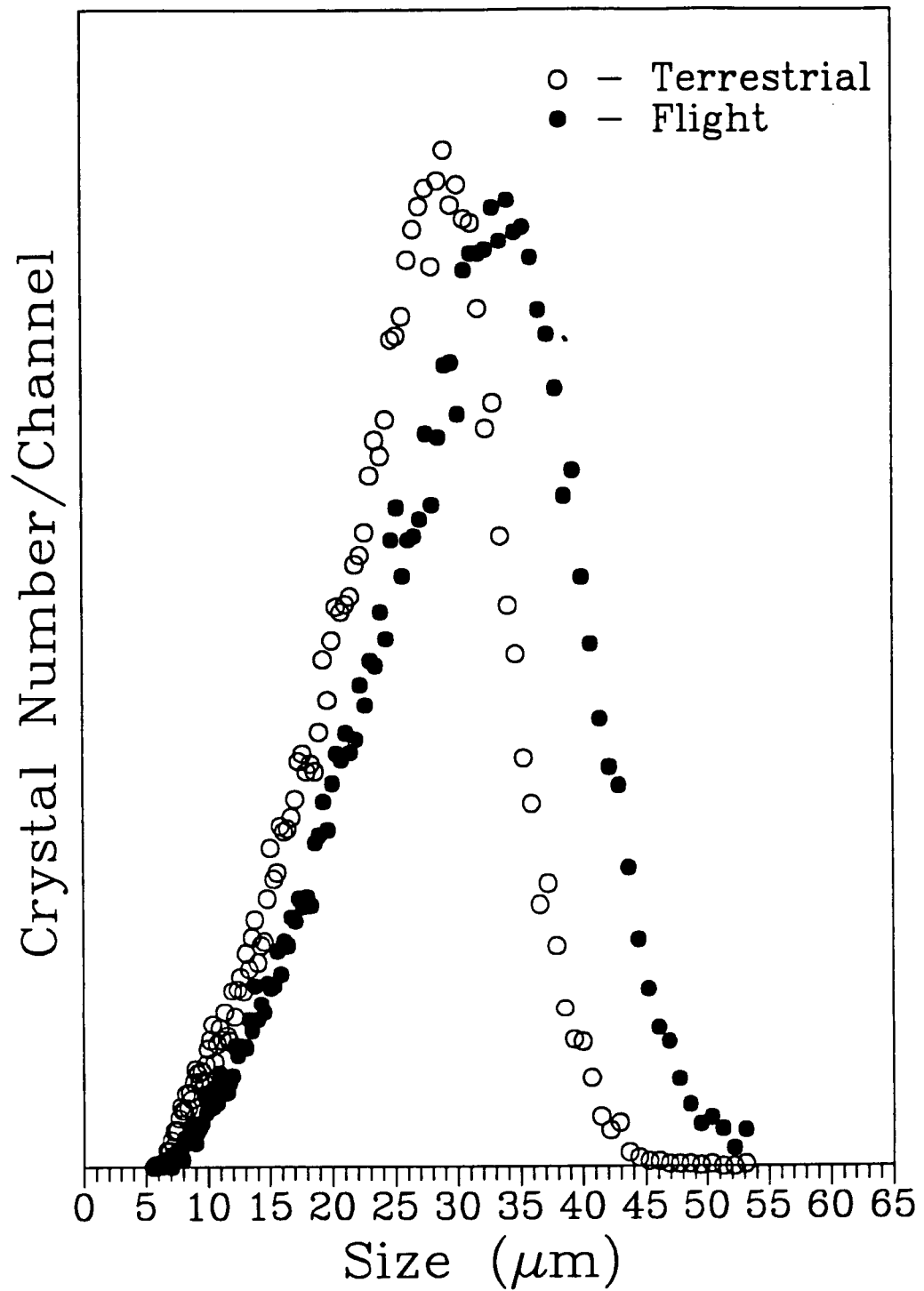


Figure 6 PSD's of Zeolite A with Nucleation Control (5.5 TEA, Piston, 5 Activations).

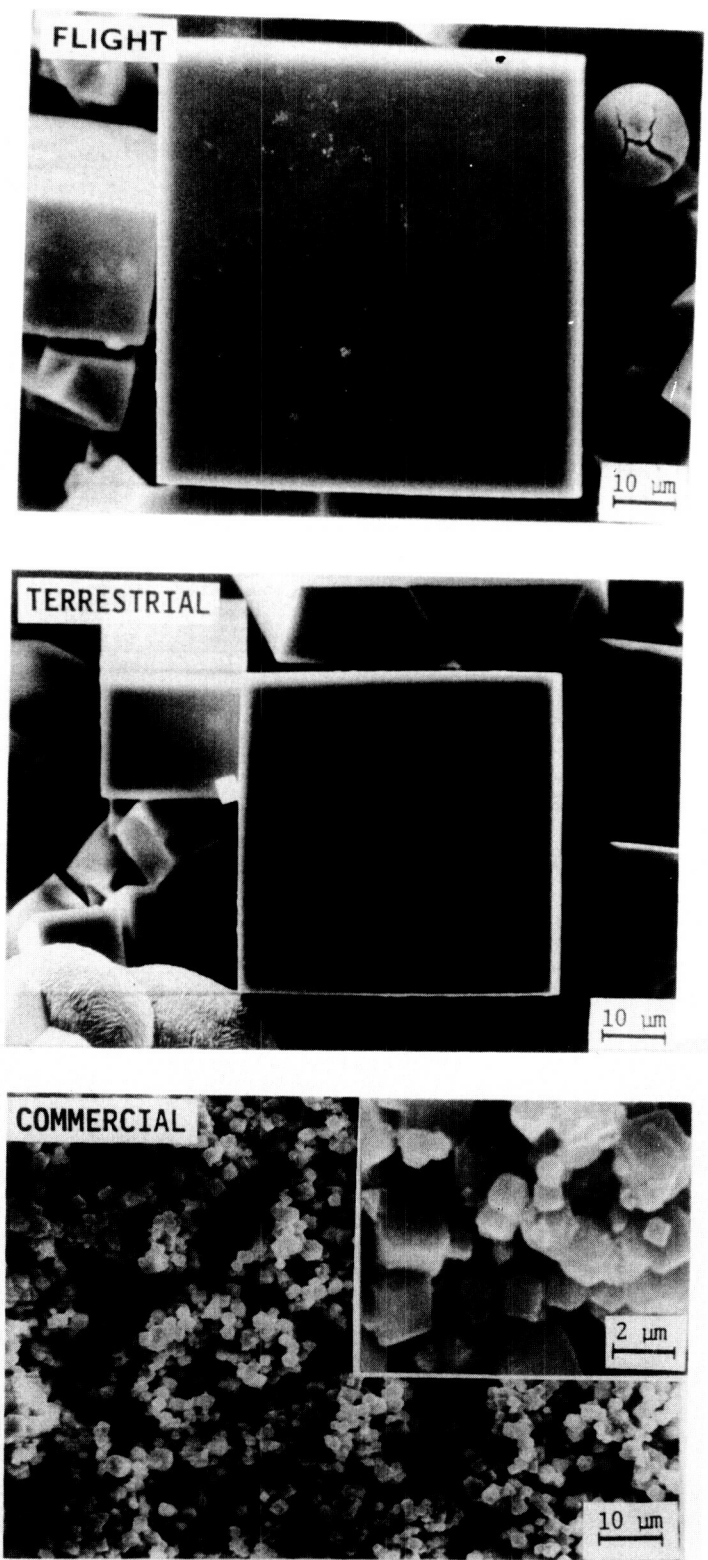


Figure 7 Comparison between Flight, Terrestrial (Control) and Commercial Zeolite A.

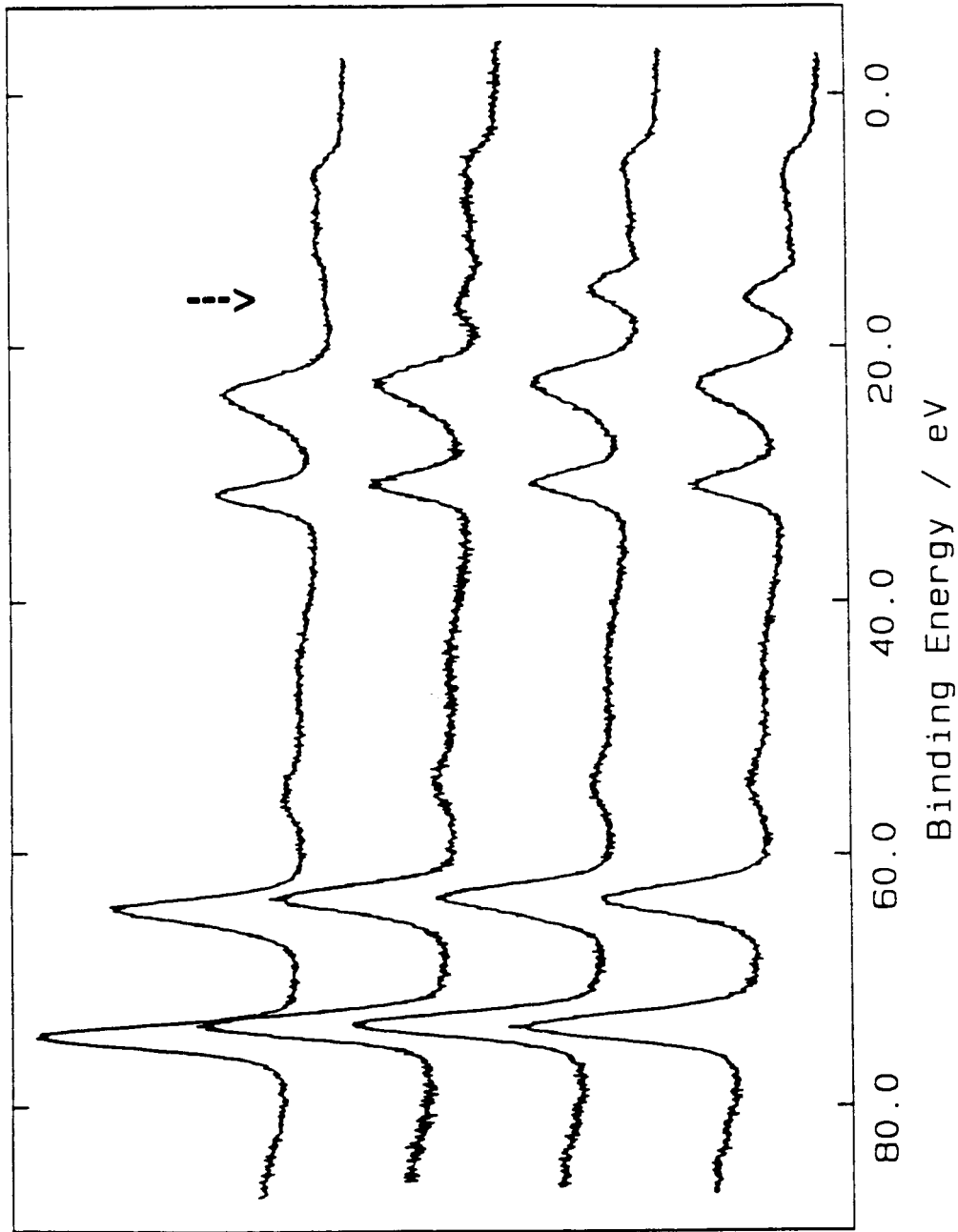


Figure 8 XPS's Valence Band Spectra for two Flight (A1, A3)/Control (A2, A4) pairs.

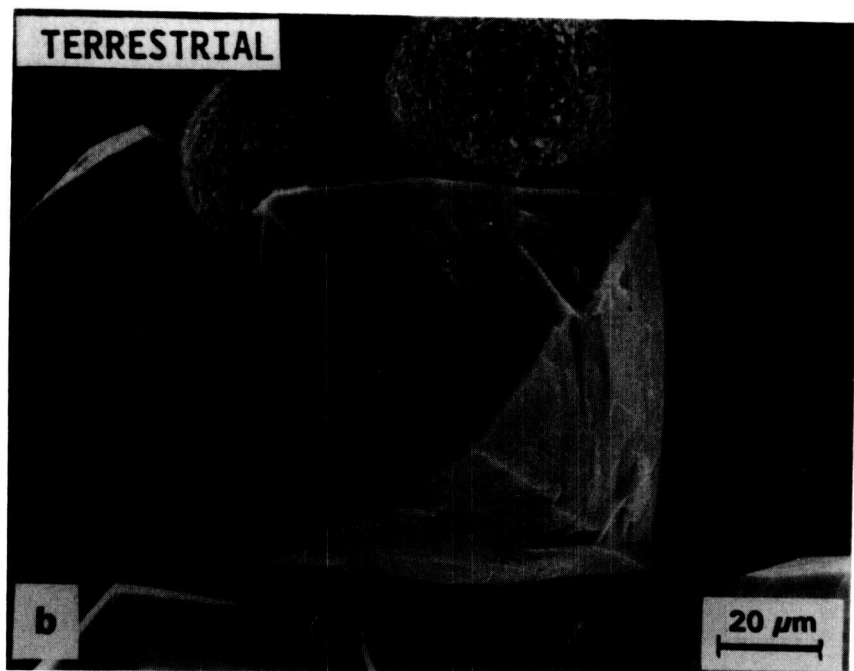
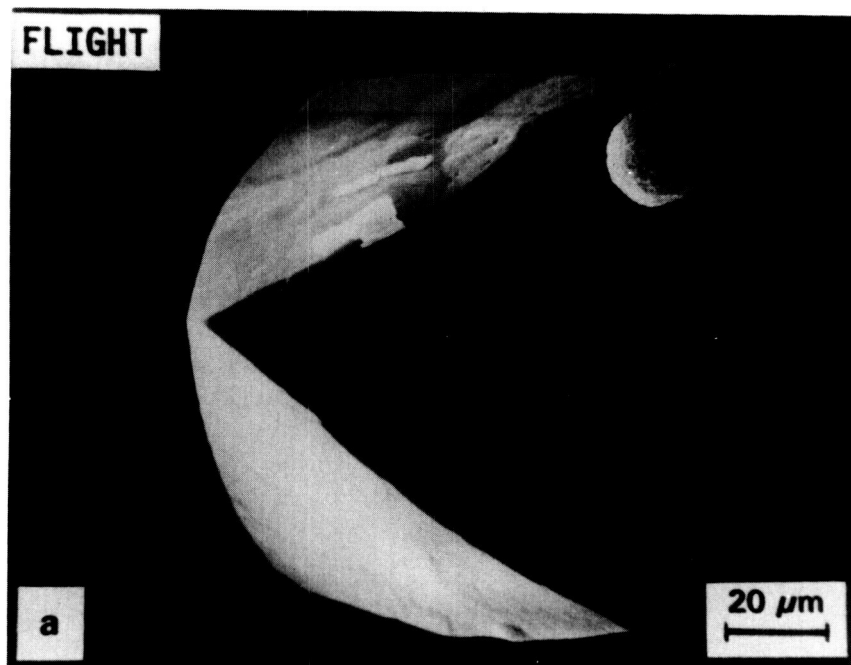


Figure 9 Zeolite X USML-1 with Nucleation Control (2.0 TEA, Sacco Flapper, 3 Activations, Silicic Acid).

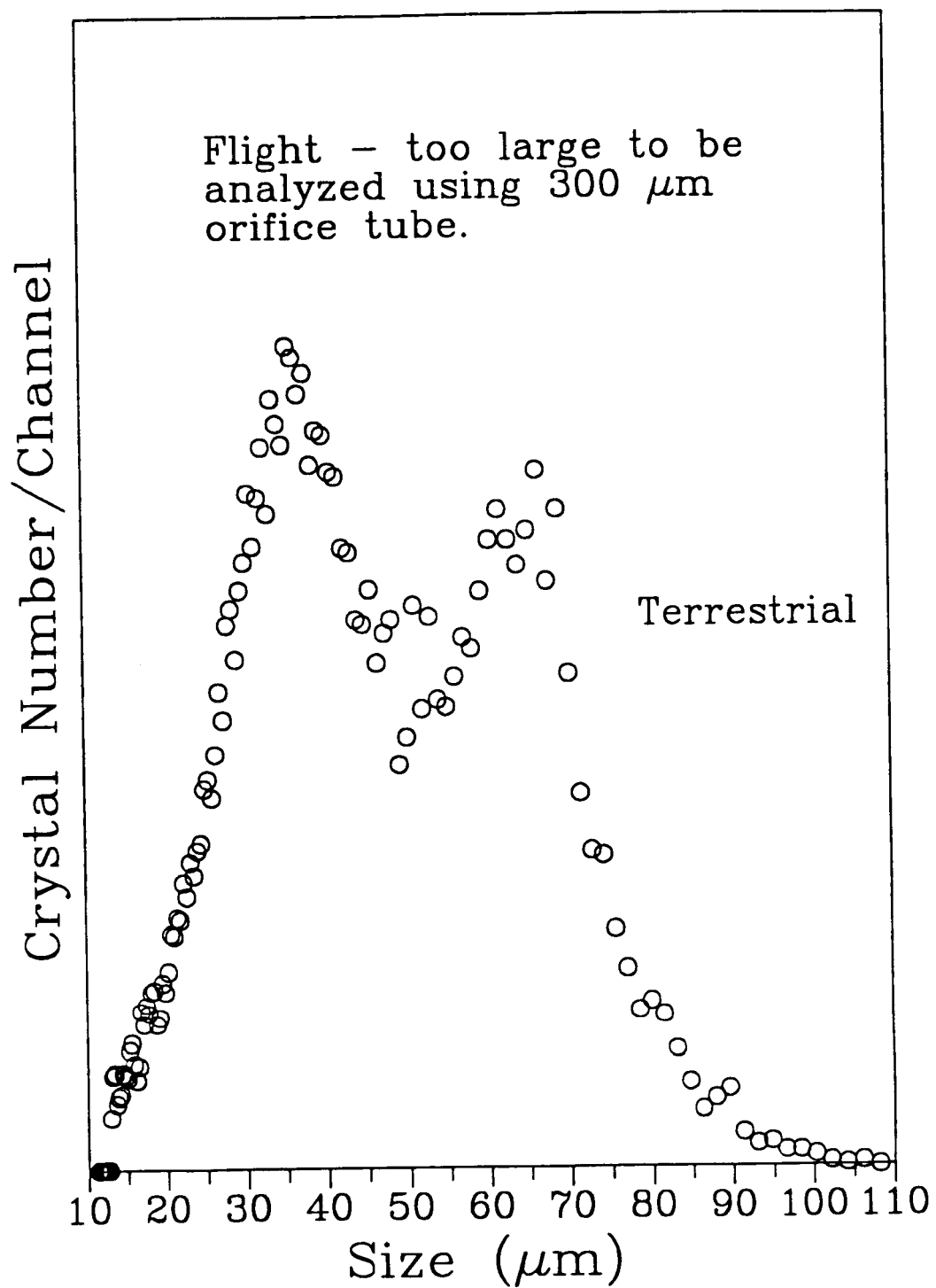


Figure 10PSD for Terrestrial Control showing Two separate Populations.

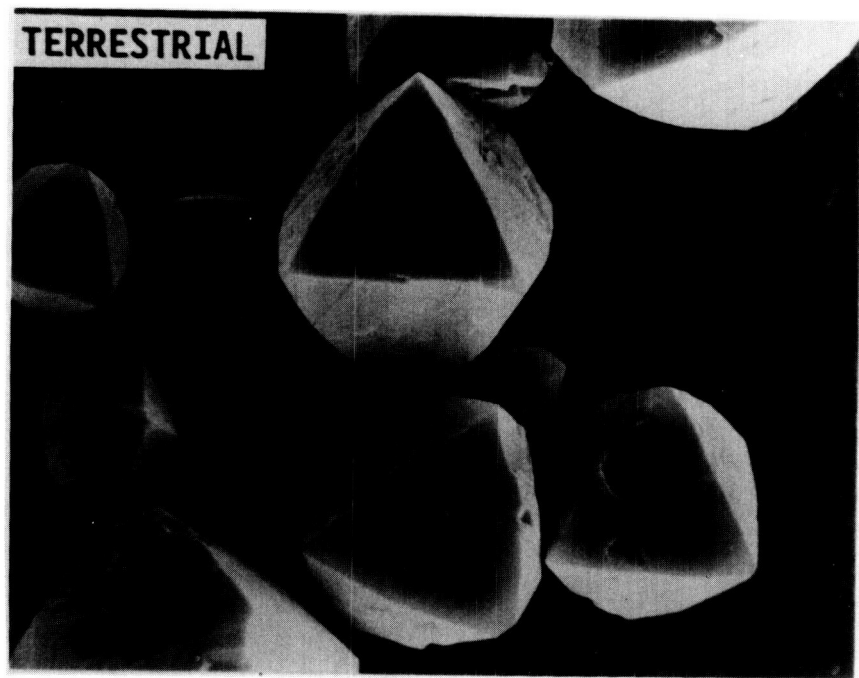
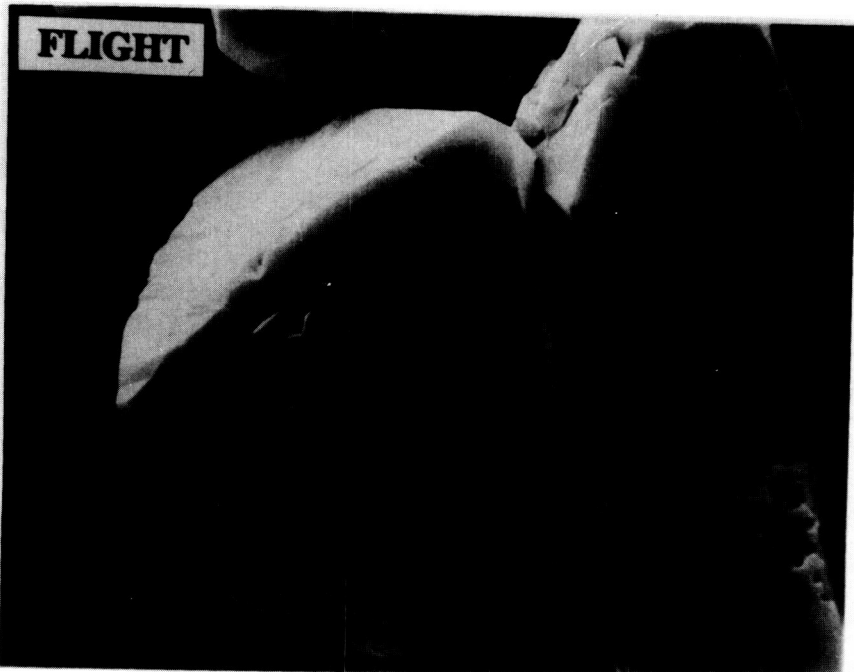


Figure 11 Zeolite X USML-1 with Nucleation Control (2.0 TEA, Sacco Flapper, 3 Activations, Sodium Metasilicate Anhydrous).

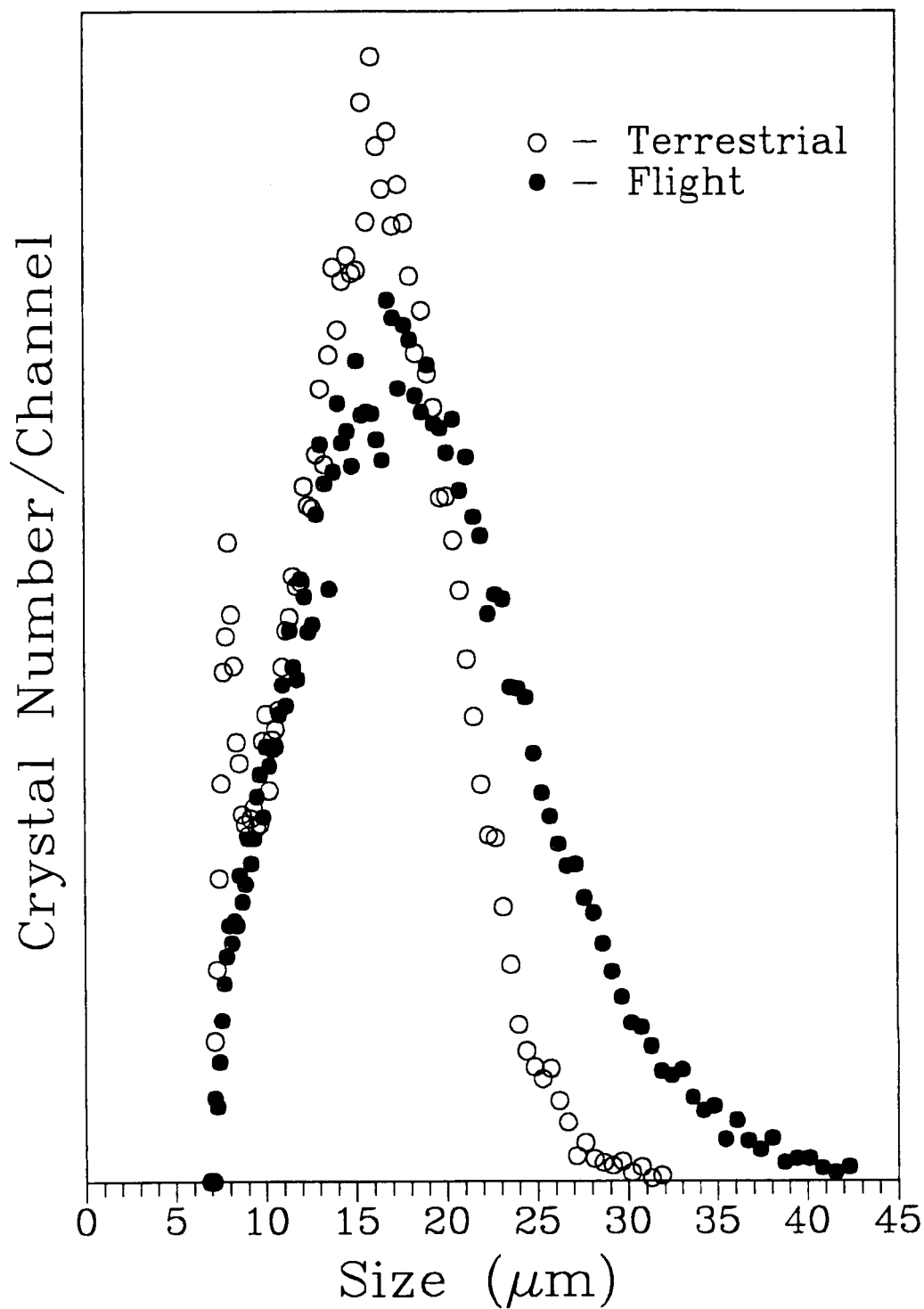


Figure 12 PSD's of Zeolite X USML-1 with Nucleation Control (2.0 TEA, Sacco Flapper, 3 Activations, Sodium Metasilicate Anhydrous).

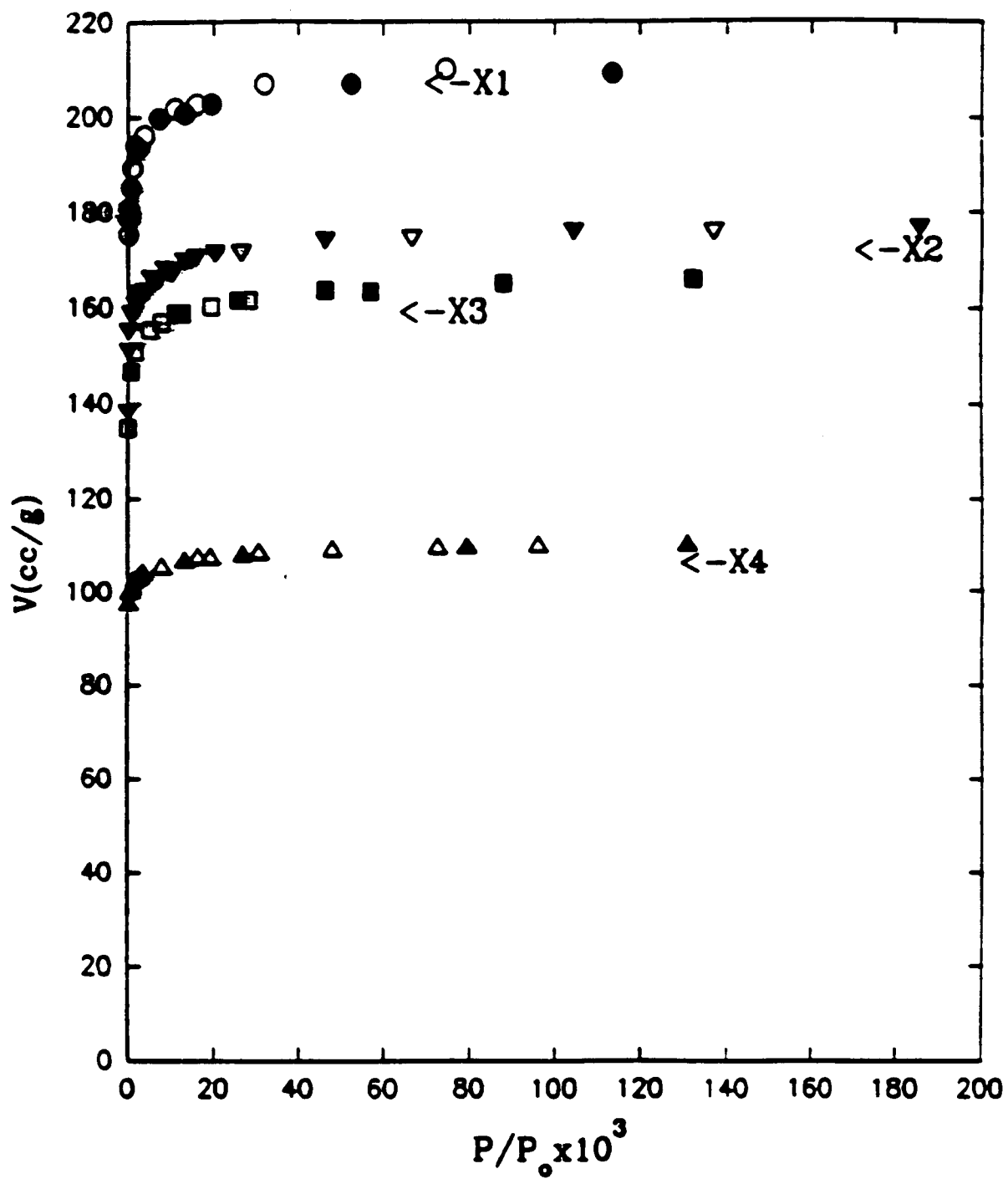


Figure 13 Nitrogen Sorption at 78 K - Isotherms of Pairs Flight (X₂, X₄), Control (X₁, X₃).

Discussion

Question: *What was the reason you said that the crystals would grow larger in space ?*

Answer: If I keep diffusion control for a week or 10 days, they get bigger. Our intention was, based on what had been shown in the literature, we knew that you could grow very large crystals. No one has ever been able to do it synthetically, but nature has done it a number of times. When you look at that data it turns out that they are in salt beds suspended, and the nutrient pool goes by them. So the idea was to suspend it in orbit and try to control the growth parameters, the nucleation parameters. We were hoping we would achieve what nature did but we were not going to wait a billion years or a half billion years, we hope.

Question: *Could you just outline the advantage of larger and more perfectly grown Zeolite crystals ?*

Answer: Yes. Well the advantages are threefold maybe fourfold. One of the obvious advantages is for structural information. Any of you that have done any X-ray work know that is difficult to do; x-ray single crystal work on Zeolite particles of 2 microns. You can't do that. You need about a half a millimeter, or so, to get decent data and with one exception, that is one Zeolite type, I don't know of any that come up to a half a millimeter or millimeter in size. So, structural information, and in particular, in terms of the cation locations which are very important for catalyst activations as well as ion exchange, is difficult to get. A secondary reason is whenever you construct reactions with multiple reactions going on, which is what we do in a chemical process industry all the time, you need to know diffusional rates and those are all estimated for these crystals because they can't do single crystal diffusional studies. What they do is they look at packed beds with crystals that they have been palletized and put in a binder and then they back out with a series of adjustable constants because you have not only particle diffusion as well as a series of other things. People want them for diffusion studies and those are what I call the short term benefits. The other area is they are now experimenting with using them as hosts for semi-conductor materials to bridge the gap between molecular semiconductors and bulk semiconductors. That seems to be going pretty well. They are very interested in defect free crystals for obvious reasons, and in that case, special lattice defects need to be eliminated. The other things they had great hopes for and still do, is if we can grow them big enough that we could use a ceramic binder we could make semi-permeable membranes with them. Zeolites are now used as the main catalytic staple for the chemical process industry. What we are hoping could happen is if we can combine the separation train with a highly selective catalyst that means there is an enormous cost savings. Generally half the cost of production of a commodity chemical is because of the separation train. So if you can get a catalyst that doesn't give you a, b, c, d, and e but just b which is what you can do with a Zeolite membrane, and by

adjusting the diffusional distances and taking advantage of those reaction rates simultaneously, you will have a tremendous advantage.

Question: *Can you affect activation energy by such improvements ?*

Answer: You don't really affect activation energies. What you are going to do is adjust. Certain reactions need a certain amount of time to occur by adjusting the diffusion length or diffusion path. You can selectively get certain reactions to occur and others not to occur. For example, coking in the chemical process industry occurs because the product you are interested in is in contact with an active site for a long period of time. Too long a period of time.

N95-14227

20 Pgs

447405/813
324093

-20 -

COMMERCIAL INVESTIGATION RESULTS FOR THE
GENERIC BIOPROCESSING APPARATUS

17032
P. 35

flown on

UNITED STATES MICROGRAVITY LABORATORY - 1

L. S. Stodieck, M. C. Robinson and M. W. Luttges

BioServe Space Technologies
University of Colorado
Boulder, Colorado.

INTRODUCTION

The GBA payload was developed by BioServe to support the commercial flight development needs of our specialized consortia comprised of business, academic and government entities. The consortia have commitments to explore commercial opportunities in bioprocessing, biomedical models and closed agricultural systems. In addition, some members of BioServe have interests in the development and/or qualification of enabling flight hardware used in life sciences space flight testing. Some business and academic entities have interests in more than one of these consortia. To aid in payload development, flight, and analysis, each consortium member contributes resources ranging from proprietary expertise and materials, to hardware and cash. Professionals from business, academia and government often interact with each other via graduate research assistants who do much of the "hands-on" payload preparation and subsequent data analyses.

The GBA supported research, testing, and development activities for each different BioServe consortium. It produced an environment in which professionals from diverse backgrounds came together with a single focus. And, it provided a truly novel learning environment for a youthful new cadre of space professionals committed to the exploration of commercial opportunities presented by space.

Since the GBA supported a large number of different experiments, this paper will briefly describe the payload characteristics and the essential operations of the payload. Then a summary of the experiments will be presented. Finally, a few of the experiments will be described in detail highlighting some novel effects of space flight on life science systems. Portions of the reported work have or will appear in appropriate archival journals as cited in the bibliography. In several instances, data collected from USML-1 has been supplemented with related data collected on more recent STS missions.

I. PAYLOAD

The GBA was designed as a generic research tool which supports a wide variety of life sciences research. Using simple hardware, experiments can be supported in biochemistry, biophysics, microbiology, cellular biology, developmental biology and physiology. In any given mission, as many as 30 different experiments might be performed using in excess of 400 individual samples.

The GBA was designed from the beginning to support numerous bioprocessing investigations. To accomplish this goal, the hardware was designed based on relatively simple but common laboratory equipment. Similarly, procedures were written based on typical methods applied in a biology lab. This "generic" approach has led to a multiple use instrument that could support a new compliment of experiments with each flight (Luttges, 1992). The hardware has also been intentionally designed to ease the process of changing instrument configuration for subsequent flights so that specialized investigations can be accommodated.

Based on existing operational procedures, the experiments supported by the GBA can be subdivided into molecular, cellular and developmental categories. Molecular experiments are focused on biochemical or biophysical reactions that occur in a bulk fluid. Cellular experiments are those focused on living cultured cells whether they be microorganisms such as bacteria or algae or cells derived from mammalian tissues. Developmental experiments are those focused on whole intact organisms such as germinated seedlings, brine shrimp or miniature wasps.

Assembly of synthetic materials from collagen molecules is an example of molecular processing. Such materials, if formed under the right conditions to yield appropriate structures, could be used as artificial skin, blood vessels, cornea and other biomedical implants. In nominal gravity, formation of collagen materials is disturbed by convective mixing and sedimentation. Collagen materials formed under such conditions do not exhibit the strength and resilience of naturally produced materials. Reduced gravity provides a unique environment to assess the contribution of convective flows and sedimentation on collagen material characteristics. Space may provide conditions under which to manufacture improved biomedical implant materials.

Other molecular experiments include the assembly of liposomes and virus capsids, two different types of microscopic spherical structures that could be used to encapsulate pharmaceuticals. Both of these structures have the potential to be used as targeted drug delivery systems. Preliminary flight experiments have shown that these structures are produced with much greater efficiency in microgravity.

Protein crystals can also be grown using the GBA hardware. If grown to a large enough size and high quality, protein crystals can be analyzed to provide information on the structure of the specific protein. Such information could be used to understand the function of important proteins and design

drugs to inhibit or enhance the function depending on the desired result. The modified Fluid Processing Apparatus used to support protein crystal growth provides additional methods through which to achieve space flight crystal growth.

The GBA can also be used to study the effects of microgravity on cellular systems. For example, microorganism physiology can be studied. These experiments will help to lay the foundation for developing effective ecological waste treatment and water recovery systems for use in space and may lead to a greater understanding of gravitational effects at the cellular level. Such experiments may also shed insight into the alterations in bacteria and other microorganisms that might create health problems for crew members exposed to long duration space flight such as required for a Mars mission. At the same time these evaluations can determine whether space provides a new set of opportunities for achieving emerging novel biotechnological goals such as electroporation and cell fusion.

Experiments have been supported using immune cells such as lymphocytes and macrophages. Previous work has shown significant alterations to immune function in reduced gravity. Experiments can be done at the cellular level to better characterize the mechanism underlying the observed alterations. In addition, such information may shed greater insight into immune diseases that occur on Earth. Space flight immunological alterations may provide the basis for new immunological models in which to test therapies and to evaluate novel diagnostics.

In developing space flight biomedical models, cultured bone cells can be studied to learn more about the mechanism underlying bone mass loss observed in astronauts exposed to long duration space flight. Such information may lead to effective countermeasures that could be of tremendous benefit to crew health. Such countermeasures may also be effective in the treatment of osteoporosis and other bone diseases here on Earth.

The GBA also supports experiments on small organisms. For example, experiments are being done to evaluate seed germination and development in space. This work lays the foundation for developing the technology necessary to grow higher plants in space. It may provide knowledge for use in the closed agricultural industry where greenhouse crops will be more common in the fresh vegetable and flower markets as well as the plant-based pharmaceutical markets.

Other experiments focus on the development of small organisms during exposure to reduced gravity. In the brine shrimp, for example, starting from a cyst, this organism shows significant development during a typical space flight mission. Even though the brine shrimp is a simple organism compared with humans, such experiments may provide fundamental information on the importance of gravity in development and aging processes. Currently being used as a model for toxicological assessments in terrestrial laboratories, the brine shrimp can be used for toxicological assessments in flight, as well. Of similar importance are studies of miniature wasps. Again, these small organisms are

easily maintained in space, they are rapid to mature and they provide a test bed for chronic toxicological examinations. These organisms are also useful in assessing genetic materials inserted by a variety of parasitic mites.

II. Hardware Description

The GBA consists of three different hardware elements including the Generic Bioprocessing Apparatus (GBA), the Refrigerator/Incubator Module (R/IM) and a stowage locker. Each experimental sample is contained in multi-chambered device called a Fluids Processing Apparatus (FPA) (Fig. 1). FPAs were housed in sets of 12 (Fig. 2) in both the R/IM (Fig. 3) and the stowage locker.

FPAs are processed inside the GBA (Fig. 4). The GBA contains a temperature controlled Incubation Module that can hold twelve FPAs in individual incubator cylinders. Temperature is controlled from ambient up to 60°C through sensor feedback and heater control. Three independent electronic controls are used to virtually eliminate the possibility of overheating samples. Touch temperature indicators on the GBA front panel inform the crew if the FPAs are below 45°C and can be safely handled.

Optical sensors and light emitting diodes have been built into the incubation cylinders. The sensors generate signals based on turbidimetric properties of the samples contained in the FPAs. Such measurements relate to reaction kinetics, cell growth or organism behavior depending on the specific experiment. A Data Acquisition and Control Processor (DACP) controls data collection and storage. Each set of twelve FPAs can be treated in a different manner depending on the applicable crew procedure and specific software routine written for the DACP. The DACP is operated using a keypad and display located on the GBA front panel.

The crew can communicate with the DACP through a standard RS-232 interface. Using the Payload and General Support Computer (PGSC), software routines are uploaded into the DACP and data can be downloaded from the DACP. Downloaded data files were copied onto floppy disk for analysis following the mission and were downlinked to ground personnel for evaluation during the mission.

The GBA occupies the space of one middeck locker and attaches to a single payload mounting panel. The outer shell containment module is the only safety critical structure and encloses all other components. The GBA uses a maximum of 110 Watts of 28 volt D.C. electrical power.

The R/IM also occupies the space of a middeck locker and requires 90 Watts of 28 volt power (Fig. 3). The R/IM housed 8 sets of FPAs.

A vent port for cooling is located on the left side of the R/IM and must remain unobstructed for proper temperature control. The R/IM with contents was installed in the middeck approximately 24 hours before launch. This late access was necessary due to the relatively short viability of the biological samples. Power was maintained to the R/IM during both ascent and descent of the Shuttle.

Additional sets of samples were stowed in an ambient locker. Generally, these samples were not as temperature critical. These sets were also late loaded at approximately 24 hours prior to flight.

The Fluids Processing Apparatus consists of a glass barrel and four sliding seals that separate three chambers (Fig. 1). Generally, an experiment consisted of some type of process precursor, initiation and termination fluids contained in the three chambers. Up to 8 mls of fluid can be distributed amongst the FPA chambers. An outer Lexan sheath provides a second level of containment. For hazardous fluids, a third level of containment was in the form of a clear flexible bag.

Operation of the FPA is simple (Fig. 5). By pushing the plunger, the rubber seals and fluids can be moved forward in the glass barrel. As the column moves forward, one of the seals reaches a bypass formed into the glass barrel wall. Continued activation of the plunger transfers the fluid in chamber B via the bypass into chamber A. Following processing in the GBA for a specified period of time, the plunger can again be pushed to transfer fluid from chamber C into chamber A. This was typically done to terminate an experiment using an appropriate fixative or process inhibitor.

III. Payload Operations

Any of four different sample processing procedures were applied to a set of FPAs. These procedures were optimized to different classes of experiments as discussed above. These procedures are summarized as follows.

A. Sample Processing - Molecular. A set of FPAs is removed from stowage, activated by mixing the A and B chambers and inserted into the Incubator Module of the GBA. Temperature is maintained at the desired setpoint and turbidity measurements are obtained at regular intervals from a few seconds to a few minutes. Following incubation times up to 24 hours, the FPAs are removed from the GBA, terminated and returned to stowage.

The DACP data file is then downloaded to the PGSC for backup or downlinked to ground personnel. Additional sets of FPAs were processed sequentially using this procedure.

B. Sample Processing - Cellular. Similar to molecular processing, a set of FPAs is removed from stowage, activated and placed in the GBA. Under this procedure, however, samples are monitored only briefly and then removed from the GBA and stowed. Activation and monitoring is repeated for additional FPA sets processed under this procedure.

At approximately daily intervals throughout the mission, the cellular FPA sets are returned to the GBA and monitored. Depending on programmed information or on turbidimetric values, the DACP will inform the crew which, if any, FPAs are to be terminated on a given day. In this manner, individual FPAs in a set were terminated at different times on orbit.

Data files were downloaded to the PGSC on a periodic basis throughout the mission. This procedure was designed for cellular growth experiments where the expected growth occurs over a period of days.

C. Sample Processing - Developmental. Under this procedure, two FPAs from each developmental set are removed from stowage and activated. At periodic intervals during the mission, sequential pairs of FPAs are activated. By the end of the mission, all FPAs in the set have been activated but at different time points. Thus, an experimental time course is obtained for the biological system under study.

This procedure was designed to study developmental changes in whole organisms such as germinated seeds. The samples in each pair of FPAs were at different stages of development. After all FPAs had been activated, the crew recorded video images of the specimens and then terminated the FPAs.

D. Sample Processing - Undisturbed. Under this procedure, a set of FPAs is removed from stowage, activated and returned to stowage. Towards the end of the mission, the FPA set is removed from stowage, terminated and again returned to stowage.

This procedure was optimized for molecular reactions that require long reaction times and minimal disturbances. Protein crystal growth was an example of this type of experiment.

IV. Configuration and Operations on USML-1

The maiden flight of the Generic Bioprocessing Apparatus (GBA) took place June 25-July 8, 1992 aboard Space Shuttle Columbia as part of the first United States Microgravity Laboratory (USML-1). The record setting 14 day mission provided opportunities for a variety of investigations in biomaterials, biotechnology and life sciences. During the mission, more than 20 separate investigations were performed using 132 Fluids Processing Apparatuses (FPAs) (Table 1). An additional investigation was performed in the Glovebox facility using the Directed Polymerization Apparatus (DPA).

Some of the FPAs (36 total) were prepared for flight approximately 4 months prior to launch. These samples were stowed in the Spacelab Module under ambient temperature conditions. The remaining FPAs (96 total) were prepared, stowed in a Refrigerator/Incubator Module (R/IM) set at 22°C and turned over for integration into Columbia's middeck approximately 24 hours before launch. Preparation of late-access samples was done as planned without significant difficulty.

Following launch, payload operations were supported around the clock by BioServe personnel at the Payload Operations and Control Center (POCC) in Huntsville. Information and data obtained at the POCC were disseminated from there to appropriate investigators located around the country. Using such information, these investigators were able to make recommendations for changes in crew operations or timelines that might improve the science return from their investigations.

From both an operations and science return perspective, excellent payload success was achieved. All of the FPAs were activated and terminated according to the schedules laid out by the investigators and mission support personnel. Some anomalies did occur during the operation of a few of the FPAs. However, only two FPAs failed such that no data were obtained. The remaining 130 FPAs (98.5%) were operated successfully to yield data and samples for analysis.

During the mission, many of the FPAs were transferred from stowage to the GBA for on-orbit collection of optical density data. For many investigations, these data provided an indication of the rate at which a process occurred. Such rates were compared with the rates obtained from ground controls. Data collected in the GBA was transferred by the crew to the Shuttle Payload General Support Computer (laptop) and downlinked to the ground using the Orbiter data modem capability. Once received in the POCC, data was reviewed to determine experiment progress and success as well as to make decisions of when a certain reaction should be terminated.

Within three hours following landing at Kennedy Space Center, the R/IM containing the samples was removed from the Orbiter and transported to Hangar L for deintegration. Samples were photographed, packaged and shipped to each of the investigators. Since nearly all of the samples were preserved on-orbit prior to reentry, no specific processing or analysis was performed at Hangar L. For a few samples, high resolution photographs were obtained using microscopes with camera attachments. Approximately 40 hours after landing, the samples stowed in the Spacelab module were removed and transported to Hangar L. Again, FPAs were photographed, packaged and shipped to appropriate labs for analysis.

Results from some of the GBA investigations are presented in the remainder of this report.

V. Effects of Space flight on Tumor Necrosis Factor-alpha-Induced Cell Lysis

Dr. Keith Chapes

Tumor necrosis factor-alpha (TNF) is an important regulatory and immunological hormone. For example, TNF is involved in the direct rupture of virus-infected cells such as with pox-, adeno- and herpes simplex infected cells. Rupture of virus-infected cells involves the binding of TNF to a receptor on the surface of the cell. Subsequently, several biochemical second messenger systems are activated which ultimately induce rupture of the infected cell.

Previous investigations have suggested that clinorotation and reduced gravity can affect cellular and biochemical processes in the immune system. The present experiment was designed to determine whether TNF-mediated cell toxicity is different in microgravity than in a 1 x G environment (Chapes et al, 1992). This information should aid in learning more about the functional activity of TNF and about the signaling/receptor processes of space flight cells.

Space flight has been shown to affect the human immune system. Knowledge from this investigation should provide a better understanding of immunological changes in space flight and may lead to countermeasures that could be employed by astronauts and by people on Earth with compromised immune function. New models of TNF function are essential in expanding the medical potential of all tumorigenic pharmaceuticals.

A. Methods:

A common mammalian cell line (LM929) was used for this investigation. Cells were attached to Cytodex beads suspended in cell medium and loaded into the A chamber of six FPAs. Medium containing TNF was loaded into the B chamber of half of the FPAs. Medium alone was loaded into the remaining FPAs. Chamber B also contained ^3H -thymidine to measure cell proliferation. Fixative was loaded into the C chamber. FPAs were shipped to KSC for final integration into the payload.

Cells were exposed to TNF approximately 14 hours following launch by mixing the contents of the A and B chambers. The cells were fixed 29 hours later.

Following sample return, the number of cells remaining on the beads was determined. The amount of radioactive thymidine incorporation exhibited by the cells was also quantified.

B. Results:

Results clearly showed that TNF inhibited the incorporation of labeled thymidine into the LM929 cells by 22-59% in the simultaneous ground controls, as expected (Fig. 6). In contrast, essentially no inhibition was observed in the space flight cells. In addition, LM929 cells that were not exposed to TNF incorporated more labeled thymidine than equivalent ground controls.

C. Conclusions:

The incorporation of thymidine by the LM929 cells demonstrate that the cells were healthy at the time the experiment was conducted. The near total loss of inhibition by TNF during space flight was surprising. Two possible conclusions can be drawn from the data. Space flight inhibited the toxic activity of TNF or the samples were subjected to circumstances that did not allow for TNF-mediated toxicity. Additional flight experiments have been completed which confirm the results from USML-1 and show that inhibition of TNF toxicity is related to protein kinase C (Chapes et al, 1993).

VI. Viral Protein Assembly in Microgravity

Dr. Richard Consigli

The effects of convection-driven flows, sedimentation, buoyancy and other fluid phenomena are greatly reduced in microgravity. Thus, microgravity affords the opportunity to investigate molecular self-assembly processes in the absence of these disruptive forces.

This investigation focuses on the self-assembly of polyomavirus major capsid protein (VP1) (Fig. 7). From the BIMDA payload on STS-37 it has been shown that formation of virus capsomeres in space flight is more homogeneous and more efficient compared with ground control formation of these capsomeres (Chang et al, 1993) (Fig. 8). This investigation was to extend the results by focusing on the assembly of complete virus capsids, the outer protein shell of virus particles, beginning with the capsomere subunits.

Virus capsids have significant potential for use in targeted drug delivery. Under the right conditions, virus capsids can be formed to encapsulate a pharmaceutical or gene vector. These special capsids might then serve as carriers to deliver a drug to a specific tissue. As the virus capsids "infect" the tissue, the contents would be introduced directly into the interior of the cells. Thus, virus capsids may find application for the treatment of many diseases including cancer and genetic disorders.

A. Methods:

In one FPA, formed capsomeres were loaded into wells of a special low-volume insert in chamber A. Additional insert wells were loaded with a combination of formed capsids and capsomeres. A buffered solution containing calcium, designed to induce capsid formation, was loaded in chamber B. Two FPAs were used to study the effects of pH (5.0 and 7.0) on the capsid formation process.

The two FPAs were activated 12 hours after launch. Capsid formation was allowed to proceed through the full mission duration. Following sample return, the VP1 products were prepared for transmission electron microscopy. The number of capsomere and capsid units were determined and compared with equivalent samples processed on the ground.

B. Results:

Results from ground controls demonstrated that numerous capsids could be formed in the FPA hardware starting from either capsomer or combination capsomere/capsid samples. In sharp contrast, capsids were not observed in space flown samples. In fact, no capsids could be identified even from flight samples that initially contained capsid structures. Further, capsomeres exposed to extended reduced gravity were amorphous and swollen compared with ground samples.

C. Conclusions:

The results from this investigation are consistent with observations made following STS-37 (Chang et al, 1993). But, it appears that microgravity significantly interferes with virus capsid formation. The specific mechanism is unknown but may relate to effects of gravity on VP1 folding or availability of calcium, an essential component of capsid formation. Further investigation has been undertaken to understand these intriguing results.

VII. Brine Shrimp Development in Space

Dr. Brian Spooner

The brine shrimp is well suited to study the effects of space flight on embryonic and larval development. Shrimp development can be arrested in the cyst stage until activation with salt water. Then, significant development can occur during the typical Shuttle mission durations. This investigation is an extension from proof-of-concept experiments performed using the BIMDA payload flown on STS-37 and STS-43 (Spooner et al, 1993).

Brine shrimp are a major aquaculture food source, are used agriculturally as a quality protein source for livestock and can serve as a human food source. They may serve as a major component to a ecological life support system since they can graze on algae and provide animal protein to higher organisms. Before employed in this manner, however, the effects of microgravity on their development and growth must be understood. Such knowledge may also have application to the development and aging process of other animals, including humans. As noted above, the brine shrimp is currently a model for drug toxicological assessments; a use that can be extended to space flight evaluations.

A. Methods:

Dehydrated brine shrimp cysts along with a dried food source were loaded in the A chamber of eleven FPAs. Sufficient air space was provided as an oxygen source for the shrimp. Salt water was loaded into the B chambers and fixative into the C chambers.

Brine shrimp development was initiated at approximately 15 hours and 1 day 12 hours into the mission. Fixation was done at different time points in the mission. Thus, brine shrimp were obtained after embryonic, at larval and at pre-adult stages of development. Simultaneous ground controls were run for direct comparison with flight specimens.

Video recordings were obtained on-orbit using the Spacelab camcorder to provide data on shrimp swimming behavior.

Following sample return, brine shrimp were analyzed using light, phase-contrast, differential interference, fluorescence, transmission electron and scanning electron microscopy.

B. Results:

Data from one of the flight FPAs was lost as a result of fixative being introduced during activation. From the remaining flight FPAs, 87 fixed brine shrimp were obtained. The hatch rate for the cysts was approximately 40% which was expected based on ground data and previous flight results. Larval morphology determined from scanning and transmission electron micrographs were not found to differ between flight and ground organisms. The major effect of microgravity was found to be an accelerated rate of development (Fig. 9). As early as 2.25 days after initiation of growth, space flight brine shrimp development was accelerated by one full stage (Spooner et al, 1993).

C. Conclusions:

Based on the preliminary results, it is clear that brine shrimp development during space flight occurs and can be assessed using the FPA hardware. Remarkably, space flight was found to significantly increase the rate of brine shrimp development without altering the organism size or morphology. Additional flight and ground research is being directed at understanding the mechanism for the accelerated development.

VIII. Seed Germination and Early Plant Morphology in Microgravity

Dr. Marvin Luttges

Microgravity provides a unique research environment for the study of gravitational effects on plants otherwise not possible on Earth. In addition, plants would play a central role in future bioregenerative life support systems. Such life support systems will be needed if long-term space exploration is to be undertaken in a cost effective manner. Before higher plants can be routinely grown in reduced gravity, gravitational effects on plant growth and performance must be understood. This investigation (see also: Hoehn, 1993; Hoehn et al, 1992) uses a 'whole plant' approach and focuses on characterizing the effects of microgravity on seed germination and early plant morphology of two legumes, alfalfa (*Medicago sativa*) and white clover (*Trifolium repens*). The experiments were a continuation of studies performed during STS-37 and STS-43 experiments (Abrahamson et al, 1991).

Leguminous plants are capable of obtaining required nitrogen from the air through a symbiotic relation with rhizobia bacteria. Legumes therefore do not require synthetic nitrogen fertilizer and may be particularly useful in the development of larger bioregenerative life support systems. Further, knowledge gained from the study of legumes may lead to the development of methods to transform other plant species, such as wheat, to be less reliant on fertilizer. The use of space flight to help produce new plant materials can be extended to those plants currently used as sources of pharmaceuticals, such as taxol and vinca alkaloids.

A. Methods:

A total of 24 FPAs (12 alfalfa, 12 clover) were used for the seed germination experiment aboard STS-50. Each FPA was loaded with either seven alfalfa and nine clover seeds. The seeds were inserted four millimeter deep into an inert, fibrous plug (14 mm diameter, 20 mm long). The seeds were oriented such that the emerging root would grow deeper into the substratum and the shoot would eventually emerge into the air space above the substratum. Seed germination was initiated at different times on orbit by manually injecting 2.5 ml of distilled water from chamber B into chamber A. Based on the activation times, a profile of plant growth in microgravity for day 2, 3, 4, 5, 7, and 10 was established (two individual FPAs for each species and each time step). After activation, the FPAs were stowed near

a fluorescent lamp in the Spacelab module to provide minimal light levels of approximately $15 \mu\text{mol m}^{-2} \text{s}^{-1}$ during the growth period. On flight day 12, all samples were visually inspected and video images documented plant growth up to that time. All 24 samples were fixed by injecting 1 ml of glutaraldehyde fixative from chamber C into chamber A, thus terminating growth and preserving cellular arrangements in their microgravity state for subsequent analyses. Identical experiments were conducted on ground, closely duplicating environmental conditions in the Spacelab module.

Following sample return, seedlings and non-germinated seeds were evaluated for germination rates, growth orientation, overall plant geometry and mass. Light microscopy analysis of roots and shoot evaluated cell size and organization as well as possible infections by nitrogen-fixing bacteria.

B. Results:

Germination: Some FPAs supported little germination due to the lack of water wicking into the growth substrate. All other flight FPAs showed similar germination rates when space flight samples were compared to ground samples (Alfalfa: 96% flight and 86% ground; Clover: 94% flight and 90% ground; corrected for the five non-viable FPAs). Successful plant development, defined as the growth of a root and shoot with leaves, was lower than the germination rates, but again comparable between flight and ground (Alfalfa: 63% flight, 44% ground; Clover: 60% flight, 68% ground). The low rates when compared to open field tests (approximately 85%) indicate a possibility of water logging, especially for the microgravity samples where water distribution is not controlled by gravity and moisture around the seeds is assumed to be higher than for ground samples (Shah et al, 1993).

Orientation: Despite the attempt to orient seeds within the growth substratum, several roots emerged from the substratum and grew into the air space above. Analysis showed that either the seeds were not oriented appropriately (or had turned during insertion and/or launch) or that the emerging roots had responded to different resistance within the substratum and curved out of the medium. Flight samples showed an increase in directional changes while most ground samples had grown parallel to the gravity vector with only minimal deviations. The deviation from a straight, vertical growth direction of ground experiments was also seen in response to different substratum densities and resistance to the growing plant.

Mass and Plant Morphology: Growth curves for both alfalfa and clover are similar for flight and ground (Fig. 10). No significant differences can be found between the plants that successfully germinated and developed into a seedling (mass, total length, root length, shoot length). Most seeds had developed the hypocotyl hook characteristic for dicotyledons. Older plants that had emerged above the substratum (day 5, 7 and 10) and that were exposed to light had successfully straightened the hook and started to de-etiolate. Clover showed more de-etiolation (dark green leaves, hooks straightened) than alfalfa (some

greening, fewer hooks straightened). Relatively more clover plants had straightened the hypocotyl hook than alfalfa plants under the given low light conditions.

Growth Curves: Due to the relatively large number of samples (84 alfalfa, 108 clover), growth curves could be calculated with good accuracy. Growth slowed down after day 5, indicating a depletion of oxygen and build-up of toxic levels of metabolic byproducts in the hermetically sealed FPA. An improved FPA design now removes metabolic byproducts and enlarges the available oxygen volume for growing plants. Comparison with follow-on studies aboard STS-54 and STS-57 (dark-grown seedlings) showed reduced plant lengths on STS-50 even under the low light conditions. The reduction of growth was readily attributed to a decrease in hypocotyl length in lighted samples where there were similar root lengths for dark and low-light grown samples. Microscopic examination of leaf structure showed that the space flight materials exhibited advanced differentiation compared to matched ground controls.

C. Conclusion:

Despite the constraints of the FPA (hermetically sealed, no gas exchange, low light), the FPA has been successful in supporting large numbers of developing seedlings in a microgravity environment. Direct effects of gravity on gross plant morphology could not be observed. Flight and ground samples show similar mass and geometry (Fig. 10). Differences at the microscopic level were in evidence. Some minor changes in germination rates between flight and ground samples are most likely a response to changes in moisture distribution in the microgravity environment (secondary gravity effect). During the STS-57 mission, a new growth substratum was evaluated to avoid possible water logging while still providing uniform and sufficient moisture to the seeds. Photomorphological expressions were similar for flight and ground samples. However, the light intensities were most likely too low for a more successful phototropic orientation of all emerging seedlings. Prediction of the direction of root-shoot emergence and appropriate seed orientation was only successful in approximately 60% of all seeds because of directional changes imposed by the non-uniform fibrous growth substratum. In the new substratum tested during STS-57, more than 95% of all seeds were oriented successfully, enabling better postflight analyses.

Together with plant morphology data on lettuce seedlings from STS-57, three major plants of importance to bioregenerative life support systems have been characterized in a microgravity environment. With these data, an important step in the design of higher plant bioregenerative life support systems for space has been achieved. Related Rosy Periwinkle germination and morphological studies indicating that plants with pharmacological significance can also be supported. And, plant primary tissue culture experiments have also been supported in the FPAs.

IX. Effects of Gravity on the Growth and Development of *E. coli*

Dr. Louis Stodieck

The effects of gravity at the cellular level are neither well characterized nor understood. Because the bacterium *E. coli* has been extensively studied in general microbiology and is part of the normal human flora, it provides a good model for studying the effects of gravity on single cells. The average mass of an *E. coli* cell is such that the sedimentation rate due to gravity is on the same order of magnitude as randomly occurring Brownian motion (P. Todd, 1989). This implies that, by mass, *E. coli* is at the theoretical limit of being influenced by gravity in a fluid environment. Knowledge gained from empirical studies will be needed for developing bioregenerative life support systems and for understanding changes occurring in the human-microbe relationship during space flight which have potential health related consequences (Pierson et al, 1993). In addition, since *E. coli* is typically the workhorse of cloning and genetic engineering, it may be possible to exploit the microgravity environment to produce novel pharmaceutical or agricultural processes.

Previous space flight experiments using *E. coli* have reported alterations in genetic composition, immunological properties, morphology and viability, and in particular, general increases in population growth rate have been noted. At least one study has generated contradictory results, however. The *E. coli* study on USML-1 was evolved from initial experiments flown as part of the BIMDA payload on STS-37 and STS-43 and has since been continued on STS-54 and STS-57 (Klaus et al., 1993).

A. Methods:

Stock cultures of *E. coli* (ATCC 4157) were grown in a minimal growth medium supplemented with either glucose or ribose. Flight and ground FPAs were loaded from common stock solutions. Growth was initiated approximately 12 hours after launch by adding a concentrated sugar source to the *E. coli* cultures which were initially maintained in the minimal medium without sugar to minimize metabolic activity. Growth was terminated at 1, 2, and 3 days after initiation using ethanol. One FPA was kept viable for the full mission. On-orbit growth rate was sampled daily using the optical density capability of the GBA. Temperature controlled, matched ground FPAs were processed simultaneously. Growth rates and protein composition were compared between flight and ground samples.

B. Results:

E. coli cell population densities achieved after 1, 2, 3, and 14 days of growth were consistently higher in the space flight samples than in corresponding ground controls (Fig. 11). Combining these results with comparable data from the four other missions shows the increase in growth in space to be statistically significant ($p < 0.05$) for a total of 38 samples (19 flight, 19 ground), with cell counts averaging 88% higher. Cultures originally grown in one sugar source (glucose or ribose) and subsequently introduced to the alternate sugar exhibited increases in growth of up to 257% over ground

controls, and were consistently higher than for non-switched samples. Gel electrophoresis analysis from the USML-1 samples indicated an apparent difference in expressed structural proteins between flight and ground *E. coli* samples.

C. Conclusion:

The increased growth rates observed are consistent with most previous investigations and were shown to be statistically significant. The additional increase observed when the bacteria were introduced to an alternate sugar source suggests the metabolic adaptation process was enhanced in space. The electrophoresis data indicating a change at the transcription or translation levels will be further investigated.

X. Fibrin Assembly in Microgravity and Magnetic Fields

Dr. Konrad Pollmann

Fibrinogen is acted upon by the enzyme thrombin to form fibrin monomers. These monomers assemble into protofibrils which then aggregate to form a network of fibrin fibers. In addition to stopping bleeding, fibrin clots play a crucial role in infection, vascular disease, inflammation, wound healing and tumor growth and are of ongoing interest in medical research. Early medical applications of fibrin films and foams as wound-covering membranes and operative blood sponges were replaced by silicone-based materials but might attract renewed interest in the future. Current applications include fibrin spray glue to stop diffusion bleeding and to cover suture lines and to mend ruptured membranes. Strong fibrin fibers are envisioned as excellent suture material.

Microgravity may serve as a unique environment to form novel materials based on fibrin fibers and is the focus of this investigation (Pollmann et al, 1993). Magnetic fields were used to induce orientation of the aggregating fibers as a means of producing stronger materials. By demonstrating the utility of microgravity in forming such materials, the biomedical applications for fibrin might be extended.

A. Methods:

Fibrin clot formation in microgravity was initiated by mixing a thrombin solution in chamber B with fibrinogen in chamber A approximately 16 hours following launch. Four out of 10 FPAs contained small but powerful rare Earth magnets providing magnetic fields of up to 0.7 tesla. One sample contained a geometric dummy to assess the influence of the magnet shapes on the gel structure. Rates of assembly were monitored by transmissivity measurements in the GBA processor. Upon experiment completion, approximately 20 hours following initiation, glutaraldehyde fixative was added to the samples. After landing, the samples were retrieved and returned to our lab for analysis.

B. Results:

Initial analysis of the transmissivity curves indicated that one of the fibrinogen samples had partially precipitated from solution prior to experiment activation (Pollmann et al, 1993). The other curves revealed clear solutions at sample initiation and showed good repeatability for all the flight samples. Within experimental error, fibrin assembly kinetics seem to be similar in micro- and nominal gravity. Scanning electron micrographs revealed significantly greater homogeneity of the arrangement of fibrin fibers in space flight samples (Fig. 12). In contrast, ground samples were found to have numerous cavities and regions of dense fiber networks. Flight fibers were measured to be only about 50% of the diameter of ground produced fibers (Fig. 13). However, this difference may have been caused by slight differences in the temperature conditions experienced by the flight and ground samples during fiber aggregation.

C. Conclusions:

The absence of gravity driven sedimentation and the long clotting times chosen for the experiment should have enhanced the diffusional freedom of the protofibrils and are expected to affect various microscopic clot properties. Current analyses are expected to reveal these affects.

TABLE 1 - GBA INVESTIGATIONS FLOWN ON USML-1

Commercial Opportunity		Experiment/Product Development	Samples
Biomedical	Immune Disorders	Lymphocyte Induction Process	6
	Immune Disorders	T-Cell Induction Test Model	3
	Immune Disorders	Macrophage Induction Process	6
	Pharmaceuticals	Virus Capsid Product	2
	Pharmaceuticals	Liposome Products	3
	Drug Testing	Regeneration Test Model	6
	CELSS and Drug Testing	Brine Shrimp Test System	11
	Cancer	Inhibitor Protein Test Model	10
	Cellular Disorders	Gap Junction Processes	2
	Seed Storage	Seed Germination Products	24
Closed Agriculture	Pharmaceuticals	Seed Plant Products	6
	Tissue Regulation	Seedling Processes	10
	Drug Testing	Miniature Wasp Test System	3
	Crop Products	Rootlet Infection Processes	4
	Biotechnology	Bacterial Products and Processes	7
	Biotechnology	Bacterial Products and Processes	7
	Microbial Control	Pentaiodide Product Testing	5
	Drug Development	Protein Crystal Morphology Products	3
	Drug Development	Osmotic Dewatering Testing	2
	Data Mass Storage	Bacteriorhodopsin Biomatrix Products	2
Biomaterials	Synthetic Implants	Fibrin Clot Materials	10
	Synthetic Implants	Collagen Materials	DPA

REFERENCES

- Abrahamson, K.S.; Lise, J.T., Derby, J.A., Simske, S.J., Luttges, M.W. (1991): *Effects of 6 Day Weightlessness on Leguminous Sprouts*, Presented at 7th Annual Meeting, American Society for Gravitational and Space Biology, Louisville, Kentucky. October 17-20, 1991.
- Chang, D., Paulsen, A., Johnson, T.C. and Consigli, R.A., *Virus Protein Assembly in Microgravity*, 1993, Adv. Space Res., 13(7)7251-7257.
- Chapes, S.K., Morrison, D.R., Guikema, J.A., Lewis, M.L. and Spooner, B.S., *Cytokine secretion by immune cells in space*, 1992, J. Leuk. Biol., 52:104-110.
- Hoehn, A. (1993): *Effects of Gravity and Light on Plant Development and Performance in Reduced and Normal Gravity*, Doctoral Thesis (in progress), University of Colorado, Aerospace Engineering Sciences. December 1993.
- Hoehn, A.; Abrahamson, K.; Gomez, S.; Voorhees, M.; Luttges, M.W.; Stodieck, L. (1992): *Seed Germination and Early Plant Development Aboard STS-50 / USML-1*, Presented at 8th Annual Meeting, American Society for Gravitational and Space Biology, Tucson, Arizona. October 1992.
- Klaus, D., Stodieck, L.S. and Luttges, M.W., *Growth and adaptation to an alternate sugar source of E. Coli exposed to space flight*, 1993, in preparation for J. Gen. Microbiology.
- Luttges, M.W., *Recognizing and optimizing flight opportunities with hardware and life sciences limitations*, 1992, Trans. Kansas Acad. of Sci., 95:76-86.
- Pierson, D.L., Bassinger, V.J., Molina, T.C., Gunter, E.G., Groves, T.O., Cioletti, L.J., and Mishra, S.K., *Preflight and Postflight Microbiological Results from 25 Space Shuttle Crews*, 1993, (SAE 932139) SAE Technical Paper Series.
- Pollmann, K.W., Stodieck, L.S. and Luttges, M.W., *Fibrin Assembly Aboard the Space Shuttle Using Generic Space flight Devices*, 1993, in preparation for J. Biomed. Materials Res.
- Spooner, B.S., Metcalf, J., DeBell, L., Paulsen, A., Noren, W. and Guikema, J.A., *Development of the Brine Shrimp Artemia is Accelerated During Space flight*, 1993, in preparation.
- Shah, S.; Faller, W.E.; Hoehn, A.; Birdsong, M.; Luttges, M.W. (1993): "Characterization of Fluid Distribution Through a Porous Substrate Under Dynamic G Conditions". Biomedical Sciences Instrumentation, Vol. 29, paper #93-050, pp. 401-408.
- Todd, P., *Gravity-dependent Phenomena at the Scale of the Single Cell*, 1989, ASGSB Bulletin, 2:95-113.
- Woods, K.M. and Chapes, S.K., *Abrogation of TNF-Mediated Cytotoxicity by Space Flight Involves Protein Kinase C*, 1993, submitted Exp. Cell Res.

FLUIDS PROCESSING APPARATUS (FPA)

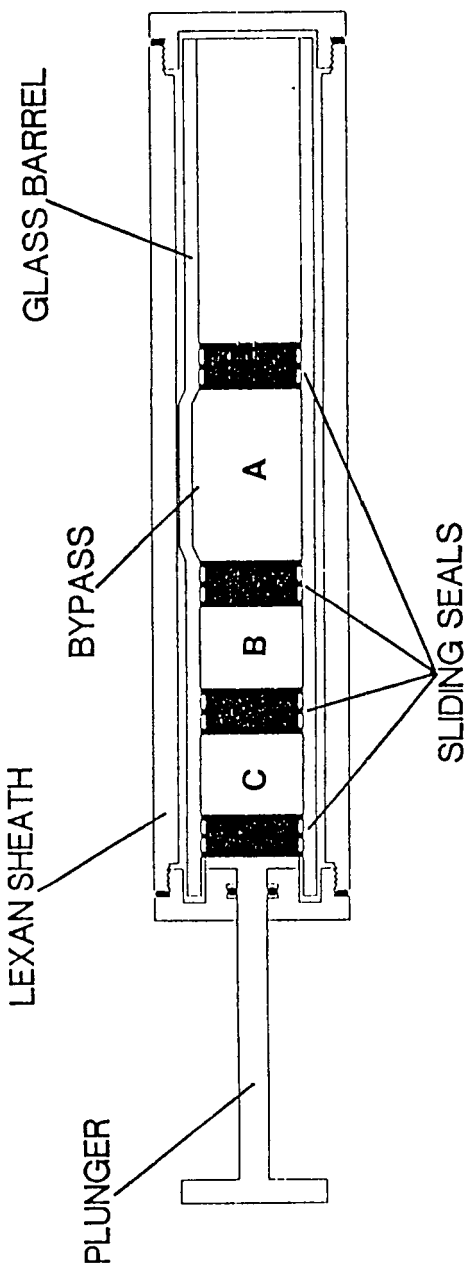


Figure 1 The FPA is a self-contained "test tube" which can hold up to three fluids (liquids or gases) of approximately 7 mls total volume. Once on orbit, the fluids can be sequentially mixed to initiate and terminate a sample process, respectively. As shown, the FPA has two levels of containment, 1) the inner glass barrel and septa and 2) the outer polycarbonate sheath with endcaps and O-rings.

FPA INSTALLATION IN TEFLON CARRIER

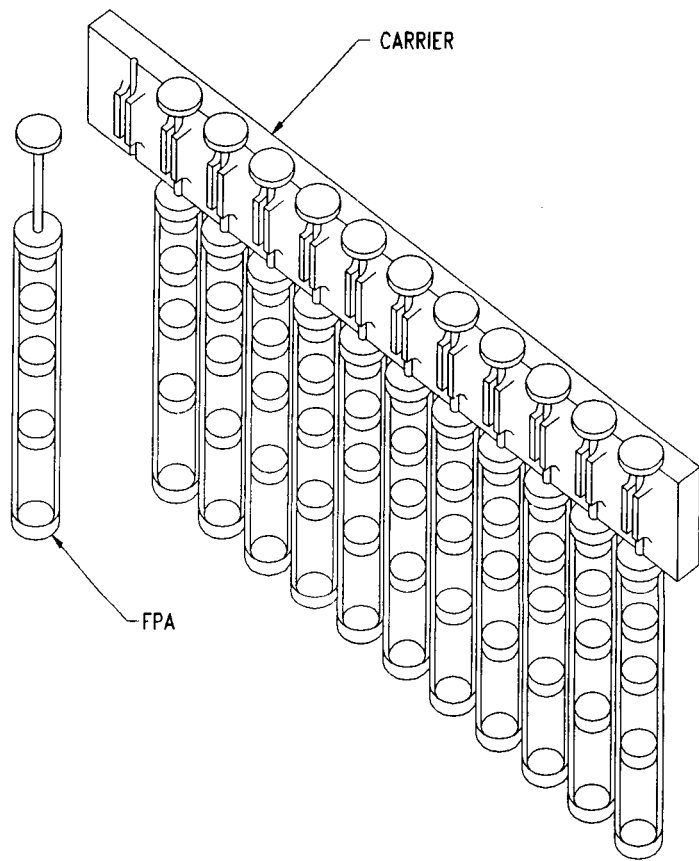


Figure 2 For USML-1, FPAs were processed in sets of 12. A rack carrier was used to hold the FPAs and the whole assembly placed in a plastic bag for stowage. A total of 11 sets of 12 (132) were flown.

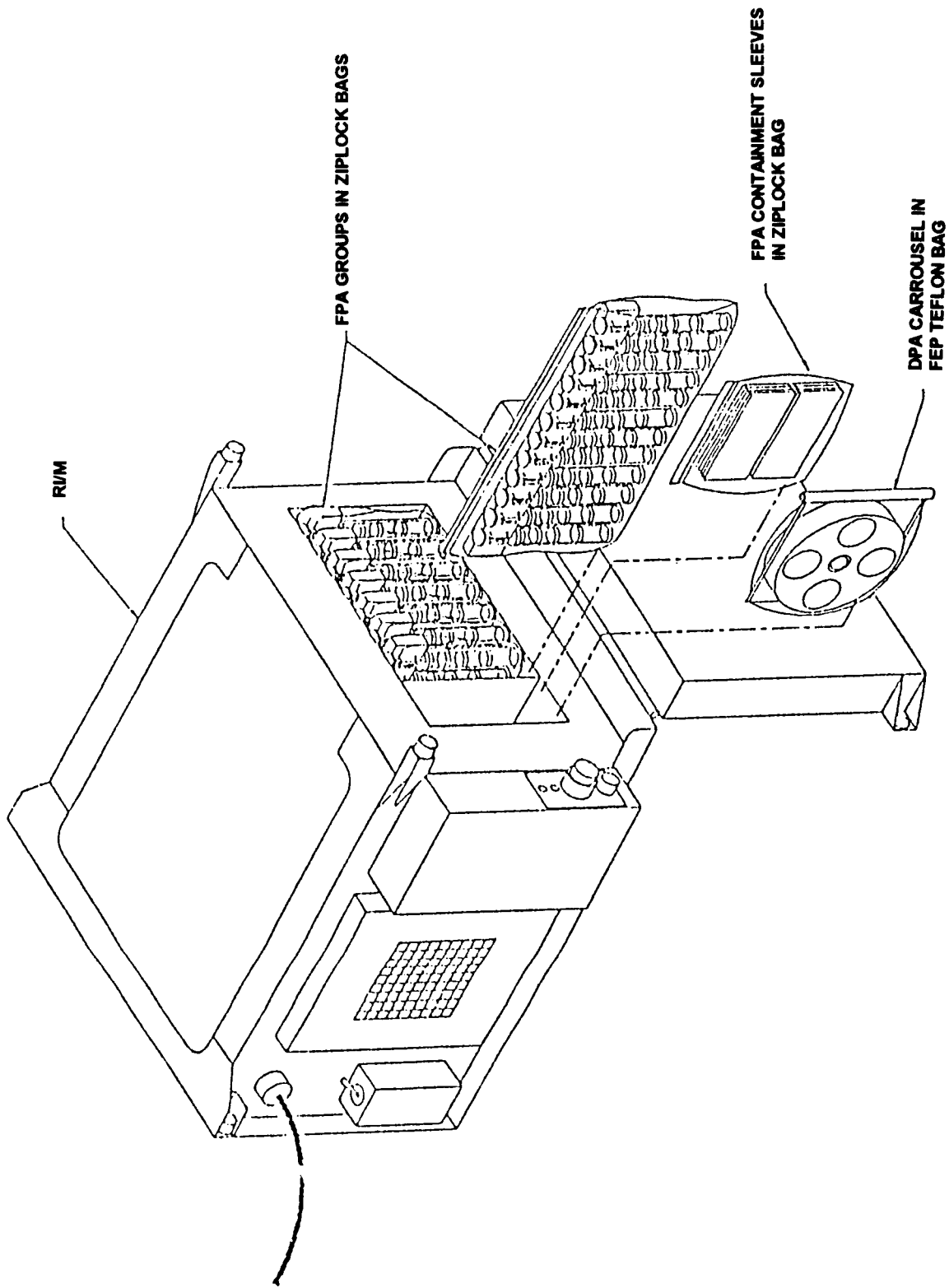


Figure 3 A NASA supplied Refrigerator/Incubator Module (R/IM) was installed in the Orbiter middeck for temperature controlled sample storage. The R/IM held 8 sets of FPAs at a constant temperature of 22 °C.

GENERIC BIOPROCESSING APPARATUS

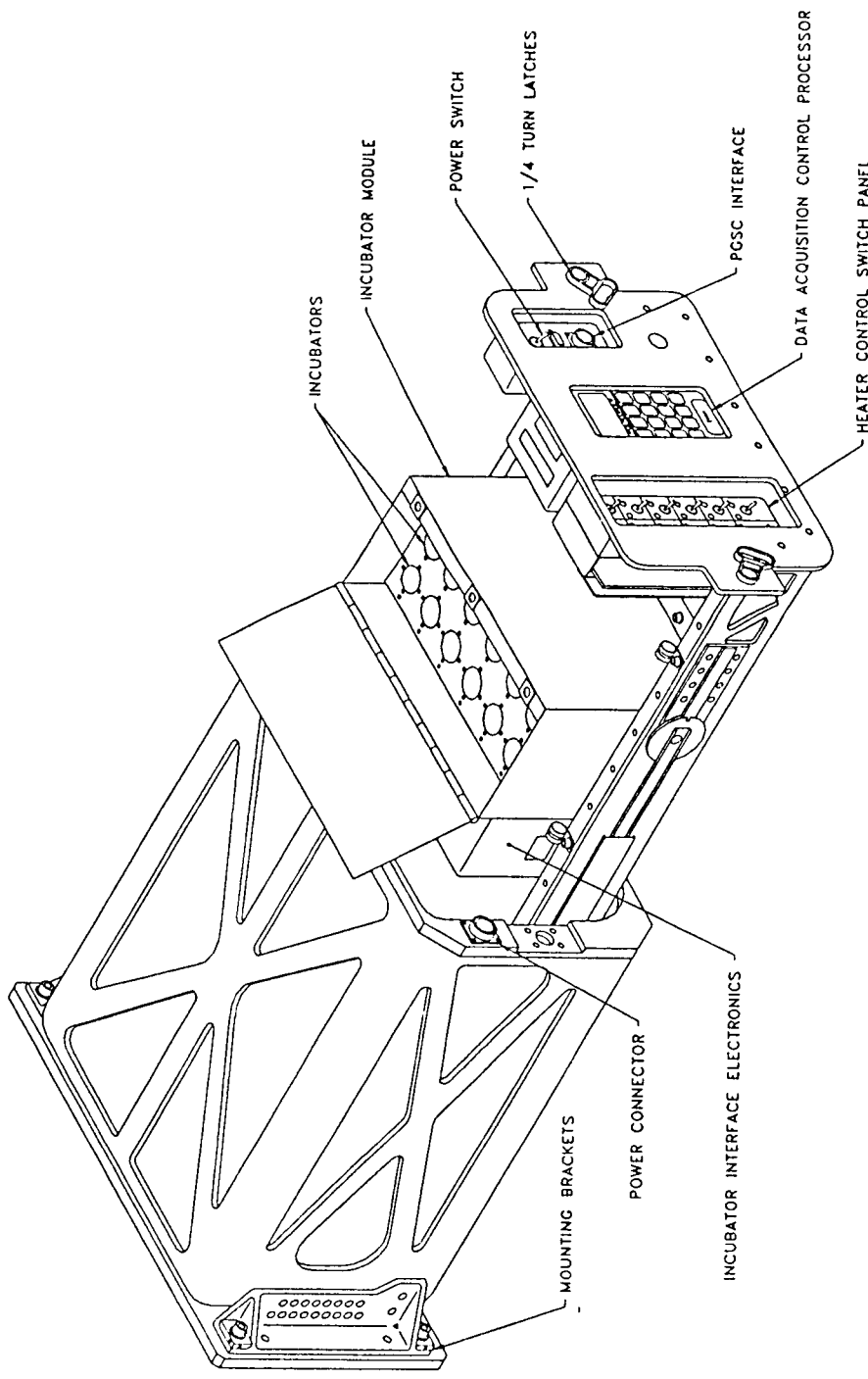


Figure 4 The GBA module was developed to provide spectroscopic measurements from 12 FPAs simultaneously. Temperature controlled incubator tubes were instrumented with LED illumination sources (565 nm) and optical sensors which fed signals to a datalogger (Omnidata Polycorder 700). Data collected on orbit could be transferred to the Payload General Support Computer for backup and downlink to ground personnel.

FLUID PROCESSING APPARATUS

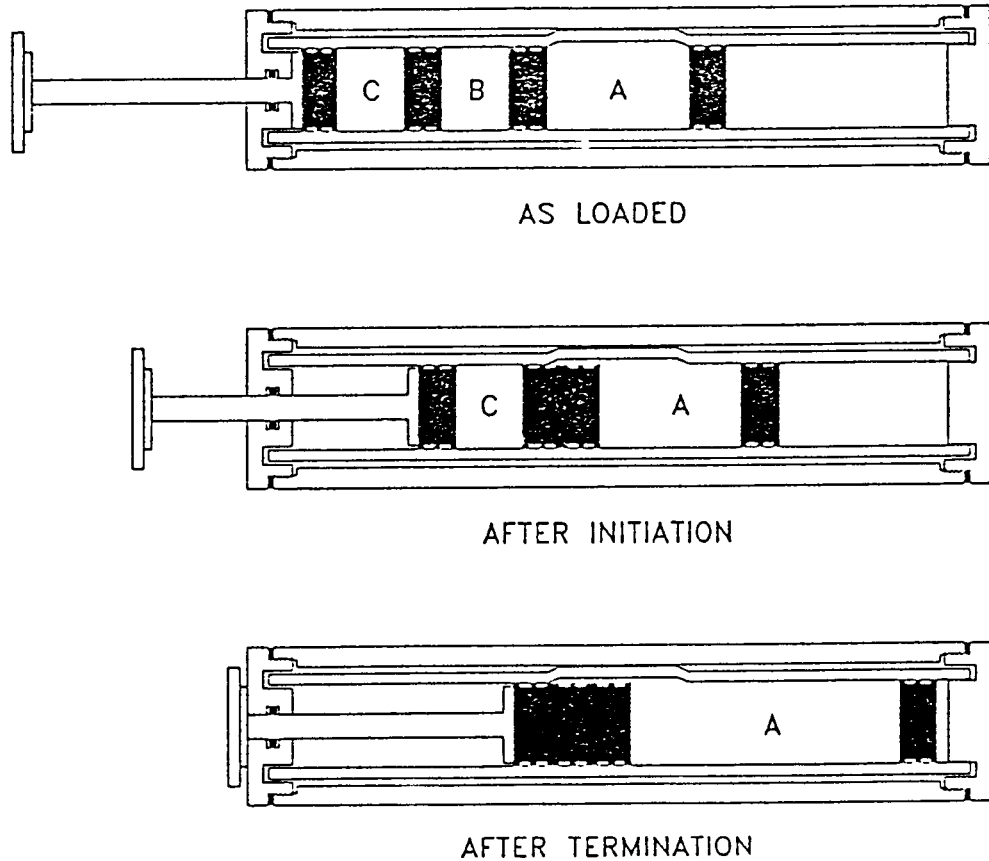


Figure 5 A sample process is typically initiated on orbit by depressing the plunger to transfer the fluid from the B chamber into the A chamber. Similarly, termination can be accomplished by further depression of the plunger to transfer the contents of the C chamber into the combined A/B chamber. An FPA can also be configured such that either the initiation step, termination step or both are omitted for additional flexibility.

TNF-Mediated Cytotoxicity of LM Cells During Spaceflight

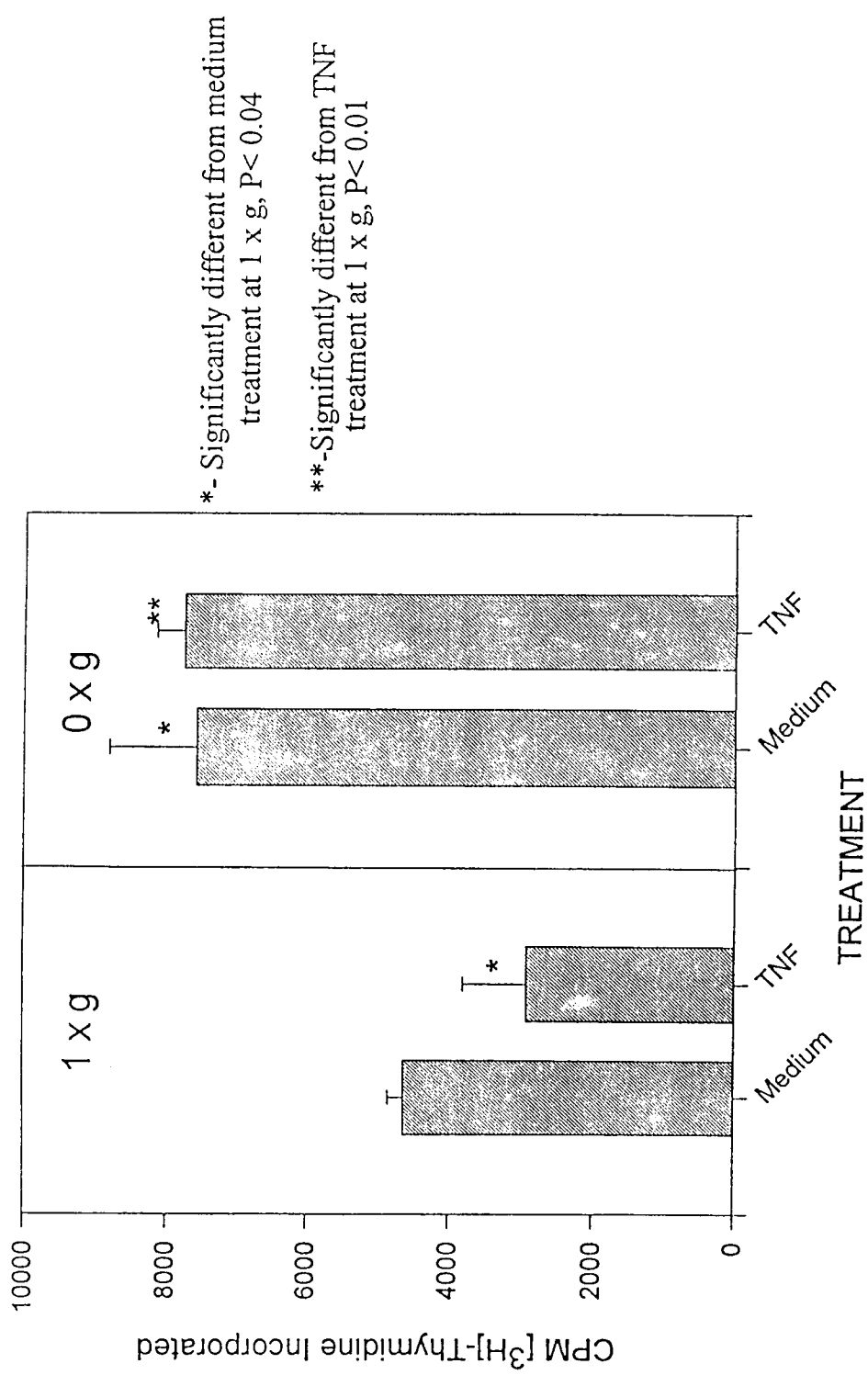


Figure 6 LM929 cells were incubated with [3 H]-thymidine in the presence or absence of TNF. As shown, TNF significantly decreases the amount of thymidine uptake in 1xg as expected. In contrast, TNF activity is inhibited in microgravity. Also of interest, thymidine uptake was increased in microgravity exposed cells. (From Chapes et al., 1993.)

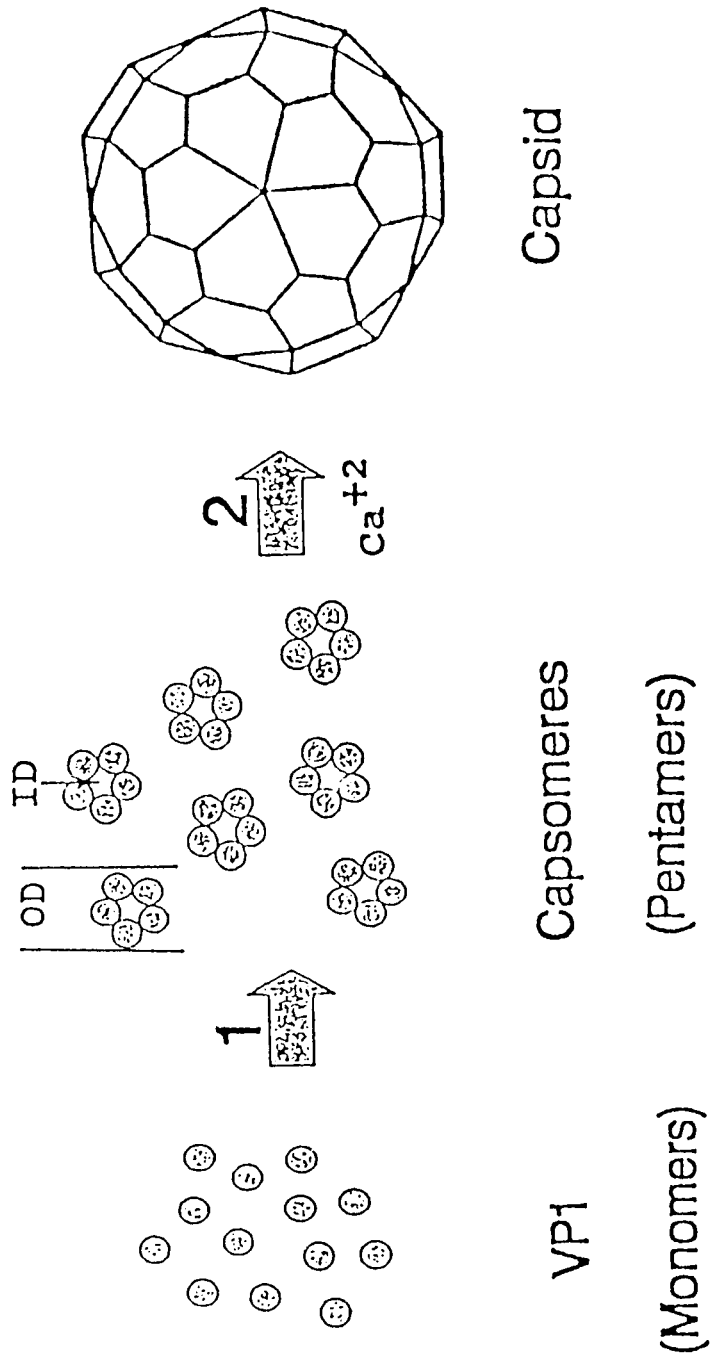
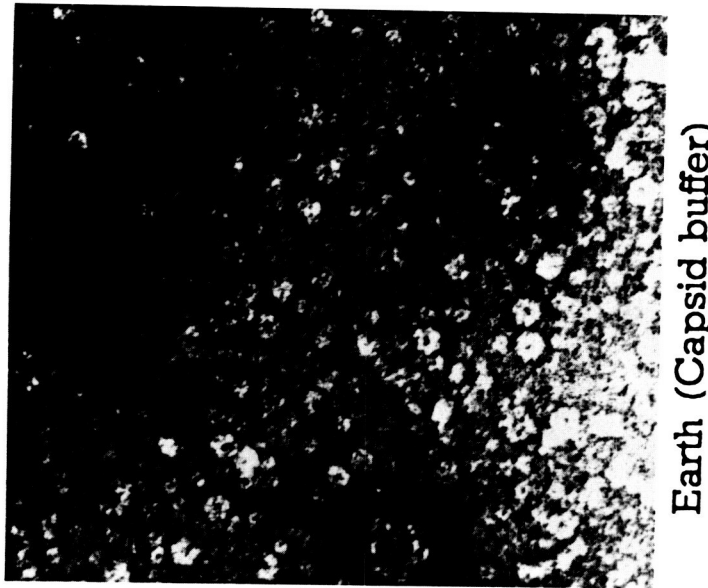


Figure 7 Recombinant, purified virus capsid protein, VP1, will self-assemble into intact virus capsids. The assembly process occurs in two steps, 1) VP1 assembles into smaller capsomeres (approx. 10 nm diameter) and 2) the capsomeres assemble, in the presence of Ca^{+2} , to form capsids (approx. 42 nm diameter). (From Chang et al, 1993.)

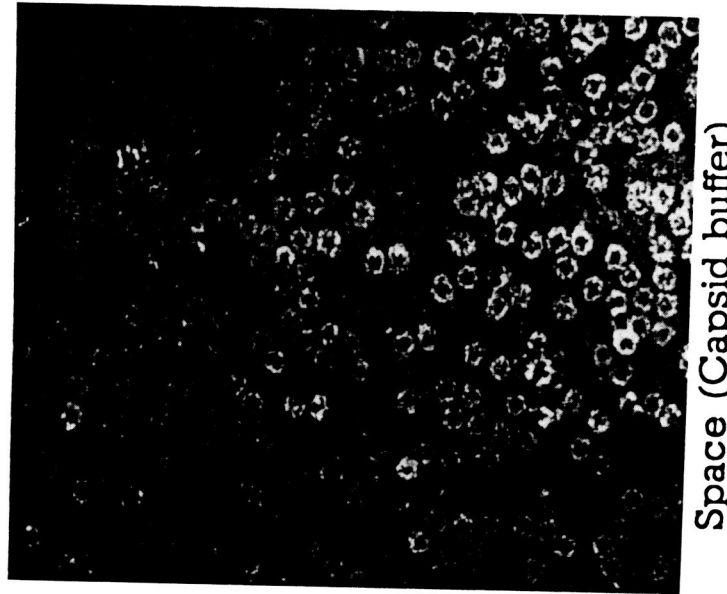
GROUND

FLIGHT



Earth (Capsid buffer)

A



Space (Capsid buffer)

B

Figure 8 Transmission electron micrographs of ground (A) and flight (B) samples of assembly products from capsid protein VP1 from mission STS-37. Three major differences between the micrographs are apparent, 1) flight capsomeres are present with much greater homogeneity and yield, 2) flight capsomeres are swollen compared with ground controls, and 3) capsid structures are absent from flight samples. (From Chang et al, 1993.) An investigation on USML-1 was done to confirm the results and begin to determine the mechanism underlying the profound differences.

Percent of Hatched Shrimp Completing Larval Development to Specific Instar Stages

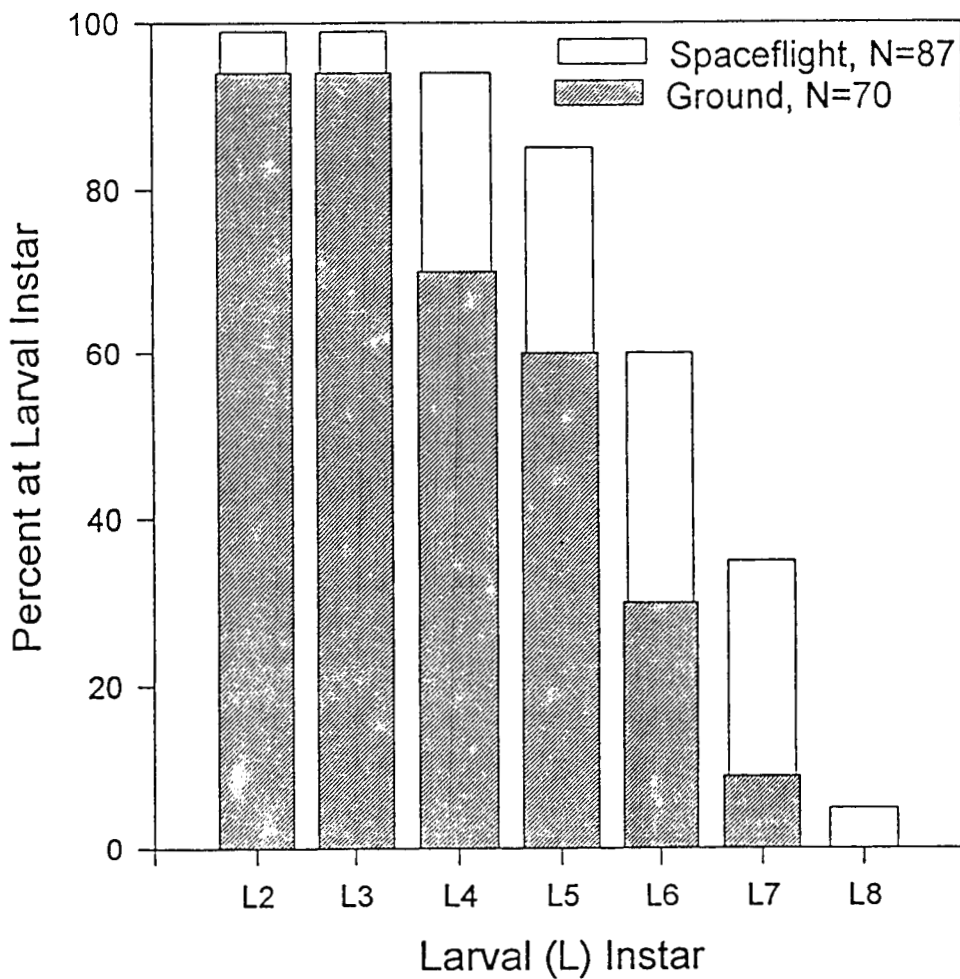


Figure 9 Brine shrimp were hatched on orbit and allowed to develop for 7-10 days. Based on microscopic analysis, the number of shrimp that reached each instar (moultling stage) were determined. Compared with ground controls, significantly more brine shrimp developed to later instar stages suggesting that development occurs more rapidly in microgravity. (From Spooner et al, 1993).

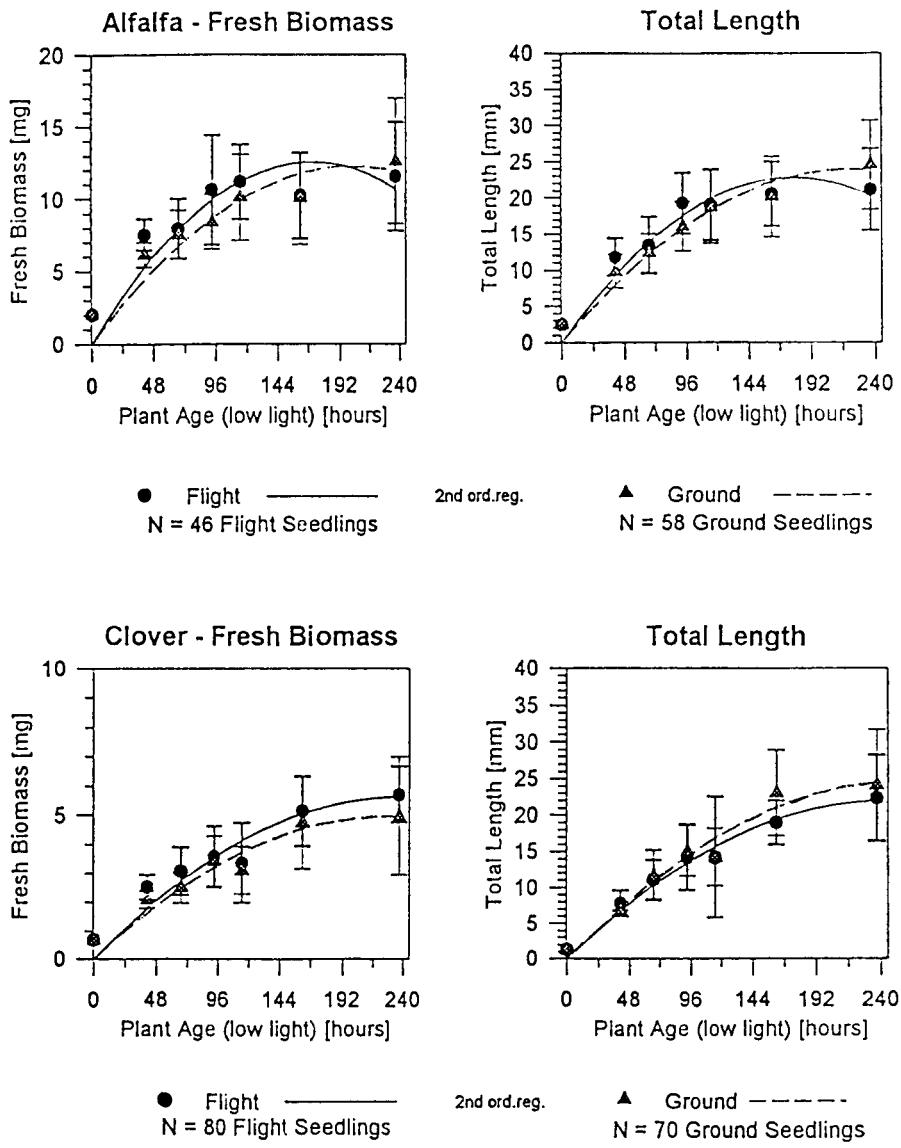


Figure 10 Clover and alfalfa seeds were germinated and grown for periods from 2-10 days on orbit on USML-1 and more recently on STS-54 and STS-57. Growth curves are plotted for the two species for both mass and length. No differences in mass or length of flight versus ground sprouts were observed. However, flight sprouts were found to have significantly greater mass and length committed to the root compared to shoot. (Data not shown.) (From Hoehn, 1993).

STS-50 E. coli Population Growth

Space Flight vs. Ground Control

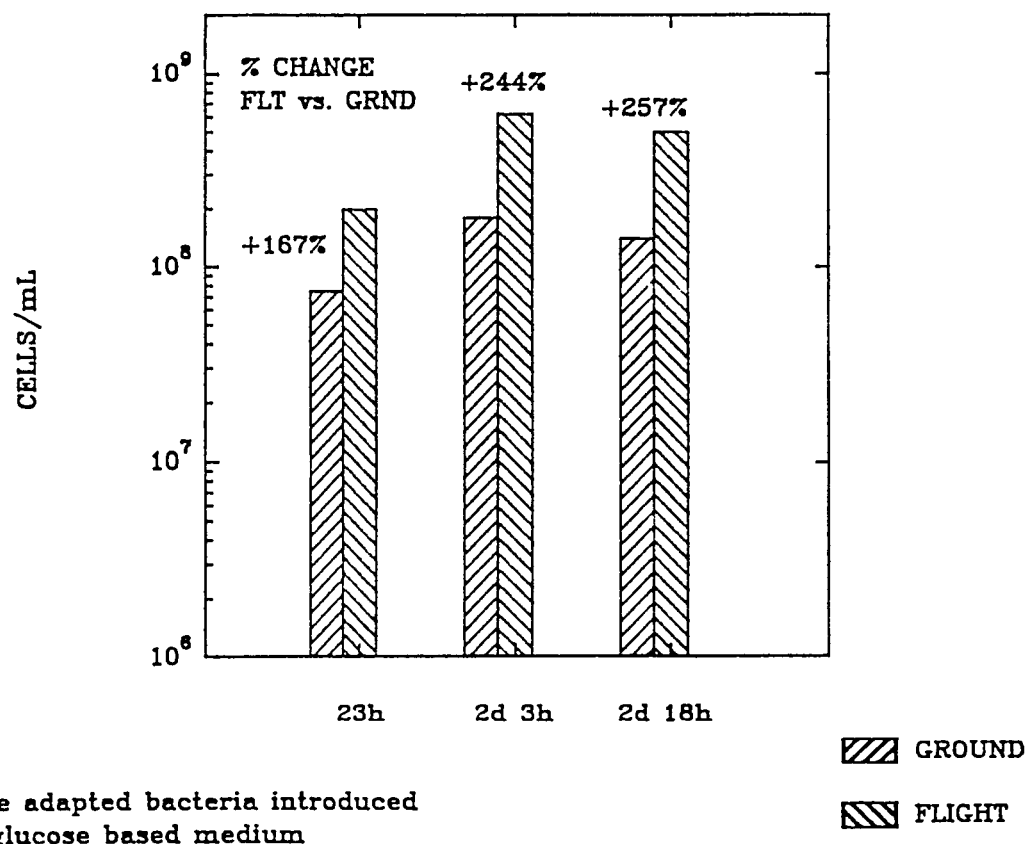


Figure 11 Comparison of *E. coli* samples grown in space vs. matched ground controls. Bacteria from a common ribose-based starting stock were subsequently introduced into a glucose-based medium and allowed to grow for 1 to 3 days to evaluate metabolic adaptation. As shown, cultures grew to significantly higher cell densities during space flight.

GROUND

FLIGHT

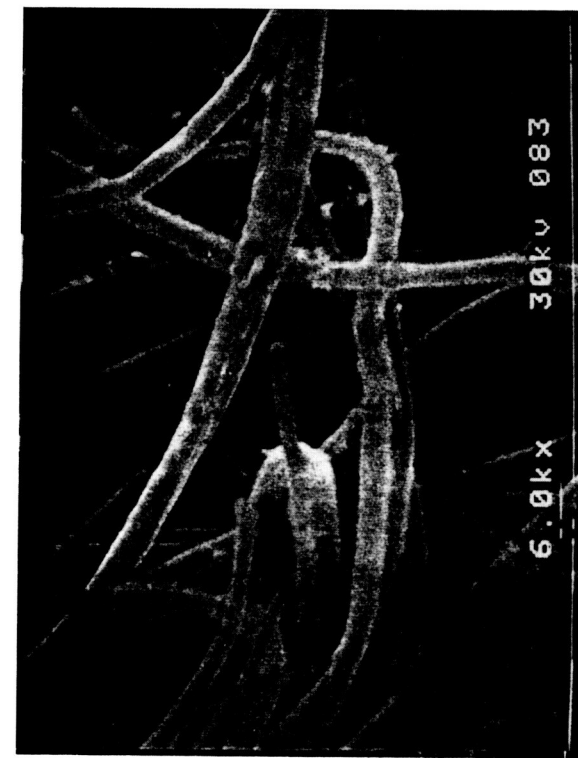
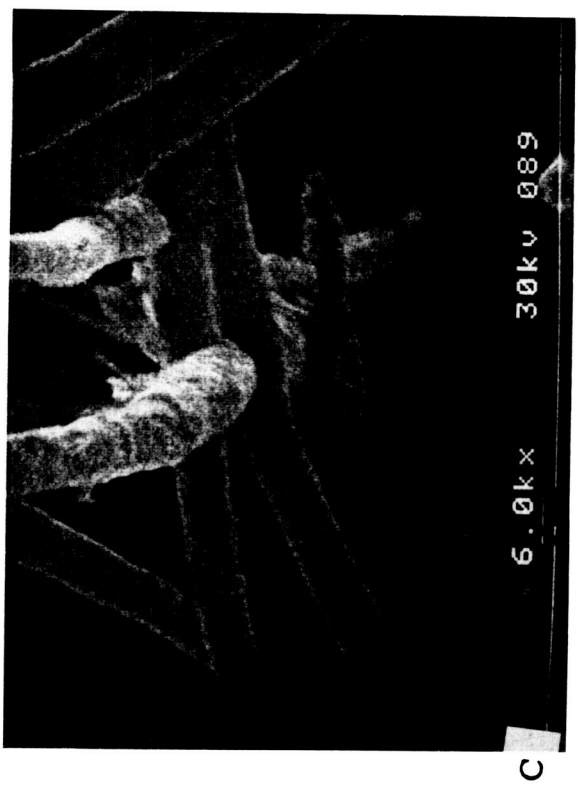


Figure 12 Fibrin materials assembled on orbit (B,D) and ground (A,C) were prepared for scanning electron microscopy at 100x (upper) and 6000x (lower) magnifications. Fibrin formed in space was found to be much more homogeneous than equivalent ground controls. Further, fibers from flight samples exhibited significantly smaller diameters. (From Pollmann et al, 1993.)

FIBER DIAMETERS OF GROUND AND FLIGHT SAMPLES (Low NaCl)

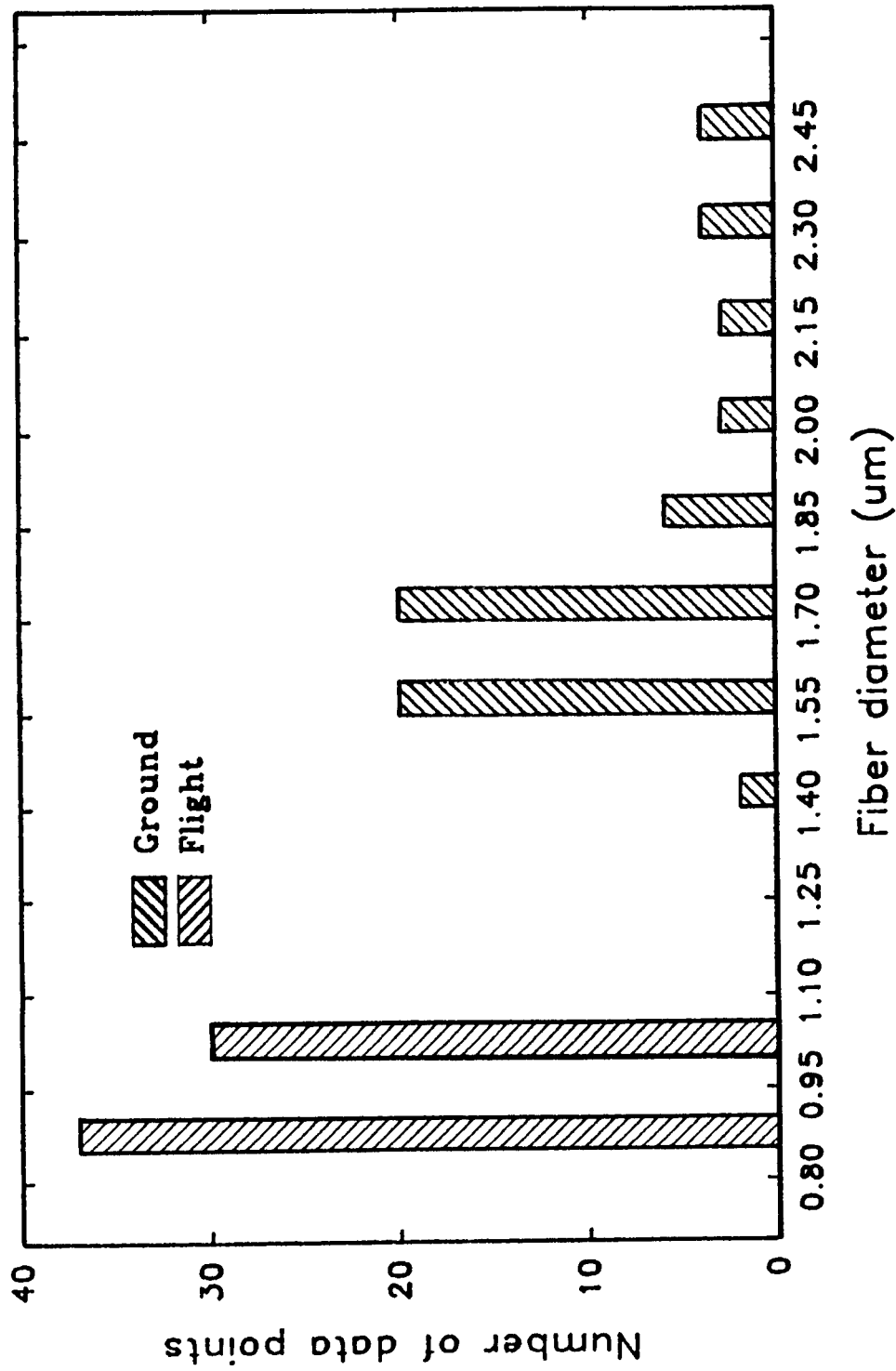


Figure 13 Fibrin fiber diameters were measured from high magnification scanning electron micrographs (6000x) and plotted as a size distribution for both flight and ground samples. Flight samples exhibited significantly smaller diameters of more homogeneous distribution. (From Pollmann et al., 1993.)

Discussion

(Speaker: M. W. Luttges, University of Colorado)

Question: *Does your data indicate a quicker maturity level (for organisms) in space ?*

Answer: Would you believe I really did not know that until I put this talk together. I think you are right. It may be just for what we have selected. I just told my colleagues just give me some of your data, I will probably screw it up but I want to give a summary of what we have been up to. And only when I started going through it did I recognize that they had that one thing in common, there are other things that happen, but they have that one thing in common that they do seem to mature much more quickly.

Question: *Has anybody else observed that effect ?*

Answer: I don't think anybody has had this data before, actually. Especially across such a wide range of materials.

Question: *How many different species were involved in the flight experiment ?*

Answer: Well we have got brine shrimp, we've got the miniature wasps, we've got 4 kinds of plants, we've got the bacterial system, and we've got some of the actual cell differentiations. If you think about it, the mouse L cells, the epithelial cells, also showed enhancing, and I really haven't gone back to the PI's and said, "okay, never mind the other stuff you are doing, give me information on just this one thing". I haven't done that, quite honestly. I'll do that but it looks pretty exciting.

Question: *On the collagen experiment could you say a little bit about combing capabilities of the flight specimens compared to ground and also the diameter of the material ?*

Answer: The diameter of the collagen fibers as you may or may not know depends on the concentration of the starting material that you have and it also depends on the ionic concentration. I sort of briefly touched on that because, basically, we could fill the whole front of the room with those interactions because it is not only that, but it is the thermal reaction. There is not a nice linear relationship between any of those variables. Okay, that having been said, the range of diameters can be as low as 0.06 of a micron all the way up to several microns (in some conditions), very large fibers, and this is without combing. I don't think anyone has reported this, and it has only occurred in space flight. Now with combing, that is something that actually would not work to be quite honest. You take these magnetosomes from the bacteria and then what we are really trying to do is organize the collagen during the polymerization process. We have used Couette flows to try to align all the fibers parallel to one

another so that cross-linking would give rise to really strong material. But something is wrong with the Couette flow because if you think about it unless you stop the rotation of the fluid against itself or against the plate or however you do it, at the right time, it is going to end up shearing the very material you are trying to produce, unless you happen to have a happy circumstance where you can shut it off at the right time. So we have tried variations on that type of thing and you always run into this trait. So we got interested for other reasons in the magnetozomes, in a size scale point of view. We just take the collagen, let it form and at the same time start from a homogeneous distribution of magnetozomes in the solution and just pull them down with just a small magnet. And we have done magnetic effects on collagen before trying to see whether 0.5, 0.8 tesla would give rise to some organization. We have got some results (ground based) on that. Quite to our amazement, because we have not done as much ground based work as we should have, all the flight samples that came back showed a very nice organized combing. The ground samples that we ran seemed to have enough counteractive flow that it disrupted some of the collagen that we got. It was one of those cases, like being little bit lightning struck, when it actually worked like it was supposed to without adequate planning.

Question: *This is about the e-coli samples that grew faster in the space environment. There are many strains of e-coli some of which have a tendency to flocculate. Could you comment on that ?*

Answer: These don't flocculate. They are selected on the basis of size with Paul Todd, based on some of the work that he had done, and he does a whole bunch of biophysical calculations. He thinks physics is important. But they are right from a size point of view, the size that makes sedimentation about on the same order of magnitude as Brownian motion; they don't go very far, at least in the nonflagellated ones. The flagellated ones are different. I don't remember their little identities in terms of all their little numbers. We do some work with Coors on yeast. They are very interested in what products you get with sedimenting yeast as opposed to non-sedimenting flocculating yeast. There, you are talking about gargantuan cells that really do sediment. They are interested in that from an obvious point of view. But this has long been the case, for 2000 years, or so, the people have had a difficult time looking at flocculation and sedimentation in terms of what that meant to a life cycle of different organisms. I know what you are sort of getting at, and it is an interesting question. We selected these bacteria just to get around those issues.

Question: *Essentially, you spend about as much energy in space flight as you do on the ground. It is hard for me to believe that, but do you have any thoughts on that ?*

Answer: I have never understood those kinds of things. I don't know where people come up with those kinds of things. I guess you could put people in a little baggy, and then do metabolic studies to test such concepts.

Question: *Assuming the data is right, and I think it is because somebody did something called a heavy water study, another subject I know nothing about, but if John Charles or somebody is here, maybe he could talk about that. But let's assume that the data is good would you have any theories on why that might be?*

Answer: This is a trap isn't it. I think that for every advantage there is that you could imagine, from a basic passive physics point of view, there are disadvantages in terms of what the organism has to do to make up for it; for example, it was talked about earlier, there is a cephalic fluid shift in space. Well that seems good for now. Maybe the heart does not have to work as hard. That is fine, except that the normal consequence of moving around in a normal gravitational environment, is that, passively, your muscles take the blood that has sedimented, if you will, in the lower extremities and push it up through muscle activity through one-way valves. That is a pretty efficient thing to do, as opposed to using a pressure head from the heart to deliver all the way down from the arteries to the capillary beds, where you have no pressure head hardly anymore, and now you have to use other kinds of mechanisms. It is just an example for everything you get for free you probably have to make up for that in some way. You can go down a whole bunch of things I think in terms of global levels, systemic levels, and even molecular levels that show that, that is really the case. I guess I don't find that terribly surprising. We are also doing some stuff on immune systems on STS-60 on rats. This has got to be one of the most intense studies done on animals. So you have almost everything but the squeak being analyzed by a variety of people, all experts in the area, so we will be able to correlate muscular skeletal things to metabolize things at a cellular level to hormonal changes to cardiovascular things, and that will be pretty interesting. I could probably better answer your question after that.

Question: *Do you have a proposed mechanism for the human necrosis factor difference between ground base and flight ?*

Answer: I don't. Dr. Chase has actually gone further and shown that it was the protein kinase-C. The question is why is there this ineffectiveness of the protein kinase-C ? His speculation right now, as near as I can tell, is that there may well be some buoyancy effects in the membrane of cells themselves that are different from a terrestrial cell as opposed to a space flight cell. In other words, in terms of how much of the molecule is really inserted (and that is sort of what he is looking at) and he has got one of his colleagues that is doing fluorescent labeling of different parts of the molecule to stick into the

membrane to different extents, they are going to be able to fly these different markers and see whether or not there is any believable information there in terms of how buoyant the lipid environment is.

Question: *Are you doing any macrogravity studies? In a centrifuge? Isn't that a less expensive approach?*

Answer: No. We are not doing that right now. We are proposing to do that with animals on the centrifuge out at Ames in the future.

18 pg

1995107814
324094

N95-14228

17033

p. 15

THE ASTROCULTURE™-1 EXPERIMENT ON THE USML-1 MISSION

T. W. Tibbitts, R. J. Bula, and R. C. Morrow

Wisconsin Center for Space Automation and Robotics
University of Wisconsin-Madison
Madison, WI.

ABSTRACT

Permanent human presence in space will require a life support system that minimizes the need for resupply of consumables from Earth resources. Plants that convert radiant energy to chemical energy via photosynthesis are a key component of a bioregenerative life support system. Providing the proper root environment for plants in reduced gravity is an essential aspect of the development of facilities for growing plants in a space environment. The ASTROCULTURE™-1 experiment, included in the USML-1 mission, successfully demonstrated the ability of the Wisconsin Center for Space Automation and Robotics porous tube water delivery system to control water movement through a rooting matrix in a microgravity environment.

INTRODUCTION

Permanent human presence in space will require a life support system that minimizes the need for resupply of consumables from Earth resources¹. A closed loop life support system based on the integration of biological and physiochemical processes offers the potential of being a safe and reliable way of meeting human life support requirements. Plants that convert radiant energy to chemical energy via photosynthesis are a key component of a bioregenerative life support system (Fig 1).

In the process of photosynthesis, plants absorb carbon dioxide, and release oxygen while conserving the carbon in a reduced form that serves as a food source. In addition, plants can be a means of providing purified water since the water transpired (evaporated) by the leaves is essentially of potable water quality. The plant root water and nutrient source can be from the hygiene or human waste water streams. Thus, plants can serve to effectively close the food, air, and water loops of a life support system. Also, such space-based plant growing facilities are a prerequisite for the conduct of meaningful plant science research in space.

Providing the proper root environment for plants is an essential aspect of the development of a facility for growing plants in space since fluid behavior is considerably different in a microgravity environment. Of particular concern is the problem of supplying adequate water to plant roots and

Joint "L+1" Science Review for USML-1 and USMP-1 with the Microgravity Measurement Group, September 22-24, 1993, Huntsville, Alabama, USA.

avoiding oxygen depletion in the root zone because capillary pores remain filled with water. The objective of the ASTROCULTURE™-1 (ASC-1) experiment included in the USML-1 mission was to validate during a long duration exposure to a space environment the performance of a concept developed by the Wisconsin Center for Space Automation and Robotics (WCSAR) for providing water to plants. These data would allow us to more clearly understand the physics of the concept as well as to verify the performance of the components used in the flight hardware.

I. DESCRIPTION OF THE WATER DELIVERY CONCEPT

The WCSAR porous tube water delivery concept is based on the use of an inert matrix material within which are imbedded porous tubes (Fig. 2). Water (nutrient solution) is circulated through the cavity of the porous tubes under a low level of negative pressure. The water moves through the pores of the porous tube into the matrix material via capillary action and forms a water film over the matrix particles. The larger pores of the rooting matrix remain filled with gases (air) while the smaller pores are filled with water. This results in a non-saturated environment that is desirable for effective root functioning. The degree to which the matrix is maintained in a non-saturated condition is dependent on the particle size of the matrix material and the level of negative pressure imposed on the water within the porous tube. Since the water is held by the negative pressure in the tube and by capillary forces in the root zone, the liquid cannot escape from the root chamber into the atmosphere of the microgravity environment.

II. DESCRIPTION OF THE ASTROCULTURE™-1 FLIGHT HARDWARE

The ASC-1 flight hardware was sized to be contained in a middeck locker of the Orbiter (Fig. 3). A front view of the flight unit before it was inserted into the foam liner and into the middeck locker is shown in Fig. 4. A side view diagram of the flight hardware with the various components identified is shown in Fig. 5.

The main units of the hardware included; (1) a covered cavity (manifold) containing inert material that serves as the matrix, (2) porous stainless steel tubes imbedded in the matrix material, (3) a fluid loop (identified as the "supply" loop) consisting of a reservoir, pumps, and appropriate valves for controlling the pressure and flow of the water through the porous tubes, (4) an identical fluid loop identified as the "recovery" loop, and (5) a microprocessor for control and data acquisition function.

The ASC-1 experimental configuration included a manifold containing two rooting chambers. Each rooting chamber contained two porous stainless steel tubes placed side by side. The porous tubes in chamber 1 had a pore size of 30 μm and the tubes in chamber 2 had a pore size of 13 μm , as determined with the method defined in ASTM standard E 128-89². The rooting matrix material used was

a crushed calcined clay (arcillite). The material was sieved to obtain a particle size range of 0.60 to 1.0 mm. The test solution was distilled water. The flow rate through the 6.8 mm ID porous tubes was approximately 230 ml per minute. Figure 6 shows a schematic diagram of the "supply" and "recovery" fluid loops contained in the ASC-1 flight experiment.

Since the primary objectives of the ASC-1 experiment were to provide data to substantiate the physics and mechanical aspects of the concept, no plants were included. Rather, one of the fluid loops (the "recovery" loop) functioned analogous to a plant root system by extracting water from the matrix. Plants will be added in subsequent flight experiments as the various subsystems required to support plant growth are added to the ASC-1 hardware.

III. EXPERIMENTAL PROCEDURE

A pressure differential was established between the "supply" and "recovery" fluid loops, to obtain water movement through the porous wall of the "supply" tube, through the matrix, and into the "recovery" fluid loop. The amount of water transferred was determined by measuring volume changes in the bellows reservoirs. The experimental treatment sequence consisted of two different "supply" pressures used in combination with three different "recovery" pressures. Table 1 shows a listing of the treatment pressure combinations used in the ASC-1 flight experiment. The treatments were programmed into the microprocessor contained in the ASC-1 unit which was capable of operating the ASC-1 unit in a fully automated mode following manual activation.

Before launch, the root chambers were filled with water and the reservoirs were left empty. Upon activation of the ASC-1 unit on orbit, each root chamber was conditioned for a period of 120 minutes to transfer the water not retained by capillary forces in the matrix to the reservoirs. After this initial conditioning, the sequence of experimental pressure combinations were started. The entire treatment sequence had an elapsed time of 28 hours. A second experimental treatment sequence was repeated after a 20 hour quiescent period. The two experimental sequence runs provide a means of estimating the repeatability of the observed data.

IV. EXPERIMENTAL RESULTS AND DISCUSSION

The ASC-1 flight unit was activated on the 5th day of the USML-1 mission by Captain Bowersox and operated for 28 hours (Fig. 7). At the end of this time, the unit was deactivated for 20 hours. The unit was reactivated on the 7th day of the mission for another 28 hour run. The crew periodically (~ every 6 hours during the 28 hour run) voiced down values that were displayed by the on-board payload general support computer. This allowed for real-time tracking of the progress of the experiment.

As an indication of the water delivery function, the amount of water transferred between the "supply" and "recovery" fluid loops during each treatment was computed for the two flight runs and two post-flight ground runs. An example of the volume changes in the "supply" and "recovery" reservoirs during a typical treatment run is shown in Fig. 8. The rate at which water was transferred between the two fluid loops, generally, was constant after 30 minutes of the treatment run. However, in some cases during space flight, the rate of transfer did not reach equilibrium until after 60 minutes of the treatment run. Therefore, for both the space and ground tests, calculation of transfer rates for all treatments were based on reservoir volume changes during the last half of the treatment period when fluid transfer reached a near constant rate.

The data shown in Fig. 9 are values taken from the last hour time period of each treatment when the fluid transfer rates had reached near equilibrium. Values for the two treatment runs in microgravity and for the two post-flight runs were averaged because data from the two runs were remarkably similar. Water transfer values for the "supply" and "recovery" fluid loops indicate that water transfer rates between these fluid loops was greater in microgravity than at 1 g. This suggests that hydrostatic pressures in the fluid loops at 1 g affected the fluid transfer rates in the 1 g environment. In the microgravity environment, such as on the Space Shuttle, hydrostatic pressures are virtually eliminated and consequently are not a factor affecting the transfer rates. Therefore, capillary forces and pressure differentials become the dominant components affecting transfer rates in microgravity. However, the fact that not all treatments show higher transfer rates in microgravity than at 1 g cannot be explained and warrants further evaluation.

Treatments with a "supply" pressure of -10 cm of water showed a significant increase in transfer rates in microgravity compared with values noted at 1 g. Whereas, data from treatments with a "supply" pressure of -5 cm water, with one treatment exception, indicated only a small increase in transfer rates in microgravity compared to data obtained at 1 g. In the 1 g environment, the water film thickness around the matrix particles and hydrostatic pressures likely reduced the transfer rates observed in the ground tests at the -10 cm "supply" pressure.

Porous tubes with a larger diameter pore size appeared to transfer more fluid than tubes with a smaller diameter pore size when the "supply" pressure was -5 cm of water. When the "supply" pressure was -10 cm of water, the transfer rates for the smaller diameter pore size tubes were at least equal to, if not slightly higher than for the larger diameter pore size tubes. These data indicate that when many of the large pores in the matrix are filled with water, as was the case when the "supply" pressure was at -5 cm of water, pore size of the tubes had little effect on the rate at which the "supply" fluid loop can replace the water extracted from the matrix by the "recovery" loop. At the more negative "supply" pressure, the

smaller diameter size pores likely maintain a better capillary interface between the porous tube and the matrix than is the case if the tube has a larger diameter size pore.

Increasing the differential pressure between the "supply" and the "recovery" fluid loops when the "supply" loop was at -10 cm of water had a hindering effect on the transfer rates during the ground runs, but not during the runs made in microgravity. In contrast, when the "supply" pressure was at -5 cm of water, increasing the negative pressure of the "recovery" fluid loop resulted in an increase in transfer rates both in microgravity and during 1 g conditions. It appears that as the thickness of the water layer around the matrix particles becomes thinner and only the small pores in the matrix are filled with water, the transfer rates become more sensitive to hydrostatic pressures if they are present. Thus, at an equal differential of negative pressure in the two fluid loops, a more negative pressure in the "supply" fluid loop (-10 cm of water) reduced the water transfer rate compared to the less negative pressure in the "supply" fluid loop (-5 cm of water). This effect is likely dependent on the particle size range of the rooting matrix used in such evaluations. The effect that matrix particle size has on transfer rates will be investigated in a subsequent ASC flight experiment.

V. SUMMARY

Although some differences were noted in specific aspects of the performance of the water and nutrient delivery system when operated in a microgravity environment compared to operation in a 1 g environment, these differences do not appear to have any significant effect on the use of this system for providing water and nutrients to plants in either environment. It has already been determined that this water and nutrient delivery system can support high rates of plant growth in a 1 g environment and should function equally well to support high plant growth rates in a microgravity or in reduced gravity environment³.

It would be interesting to more clearly define the relationships of matrix particle size, fluid loop pressure, and porous tube pore size with water transfer rates and how these system characteristics relate to plant growth rates when using this concept for providing water and nutrients. Such information when combined with data from the ASC-1 flight experiment conducted during the USML-1 mission and planned subsequent ASC flight experiments will provide the knowledge needed to design the optimal configuration for the water and nutrient delivery system for the plant component of a bioregenerative life support system and for plant growing units for conducting plant research in a space environment.

REFERENCES

1. Stafford, T. P., et al., 1991. Report of the synthesis group on America's space exploration initiative, p. 100. U.S. Government Printing Office Washington, DC.
2. ASTM. 1989. Standard test method for maximum pore diameter and permeability of rigid porous filters for laboratory us. Designation: E 128-189.
3. Morrow, R. C., R.J. Bula, T.W. Tibbitts, and W.R. Dinauer. 1992. A matrix-based porous tube water and nutrient delivery system. SAE Technical Paper Series, Paper #921390, 22nd International Conference on Environmental Systems, Seattle, WA, July 13-16, 1992.

Table 1

**Treatment Protocol Used in the ASTROCULTURE-1 Flight Experiment
and Associated Ground Tests.**

CHAMBER 1 Porous tube size - 30 μm

Fluid Loop Pressure (cm w,c*)

Treatment #	Supply	Recovery	ΔP
C1	- 10	- 10	0
1	- 10	- 10	0
2	- 10	- 15	-5
3	- 10	- 20	-10
4	- 5	- 5	0
5	- 5	- 10	-5
6	- 5	- 15	-10

CHAMBER 2 Porous tube size - 13 μm

Fluid Loop Pressure (cm w,c*)

Treatment #	Supply	Recovery	ΔP
C2	- 10	- 10	0
7	- 10	- 10	0
8	- 10	- 15	-5
9	- 10	- 20	-10
10	- 5	- 5	0
11	- 5	- 10	-5
12	- 5	- 15	-10

*cm water column

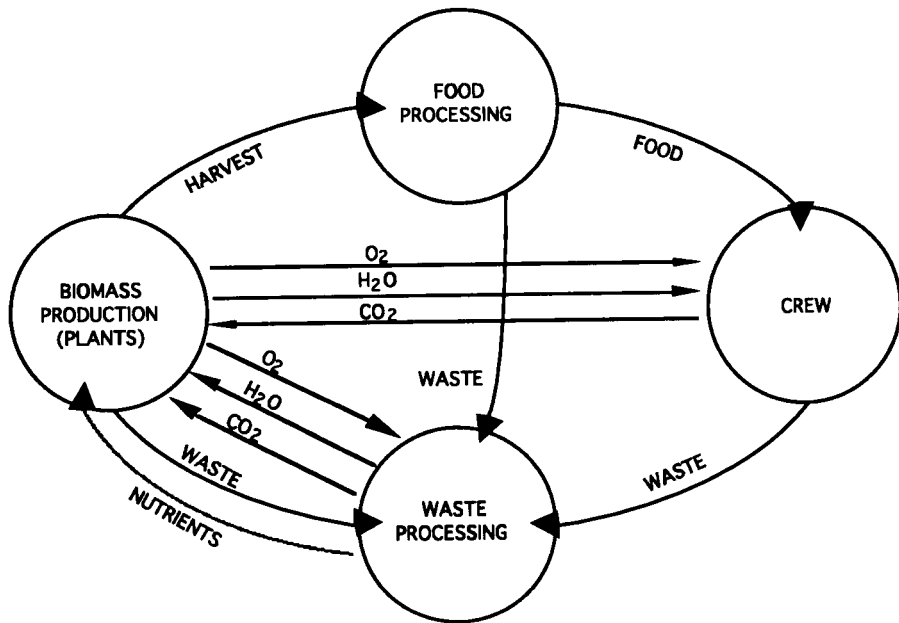


Figure 1 Diagram of a bioregenerative life support system.

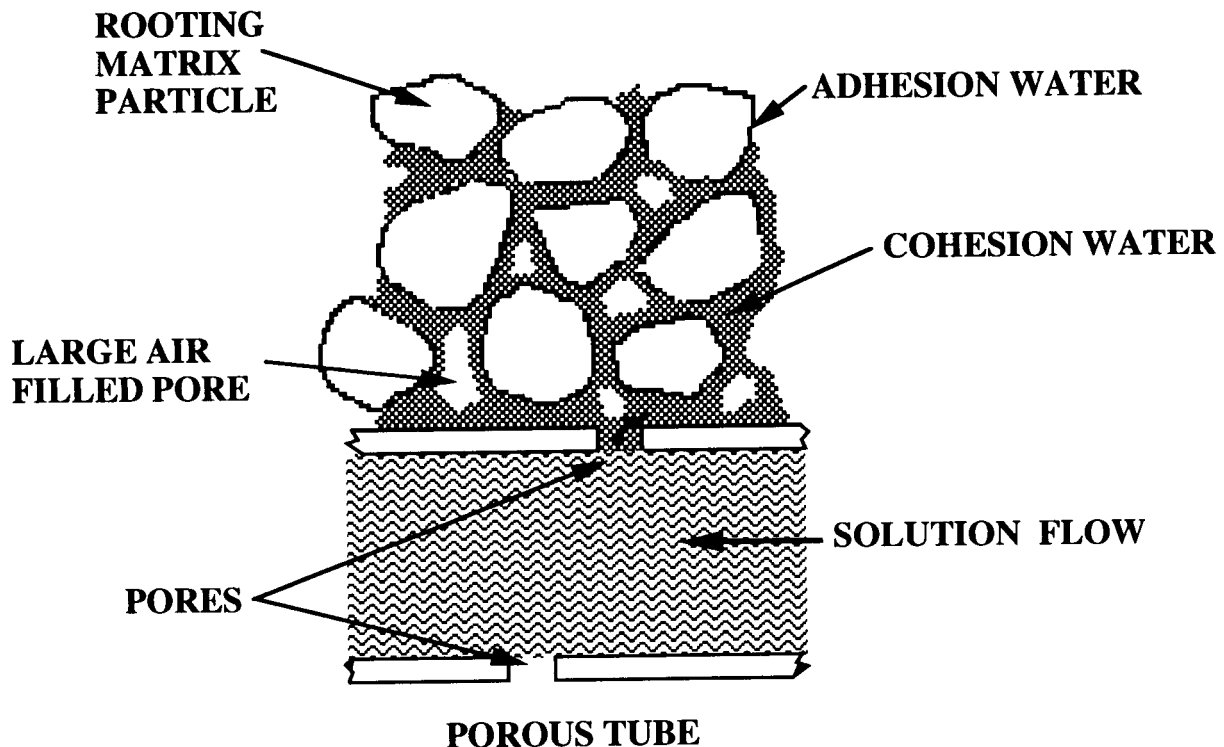


Figure 2 Diagram illustrating the concept of the water delivery system evaluated in the ASTROCULTURE-1 flight experiment.

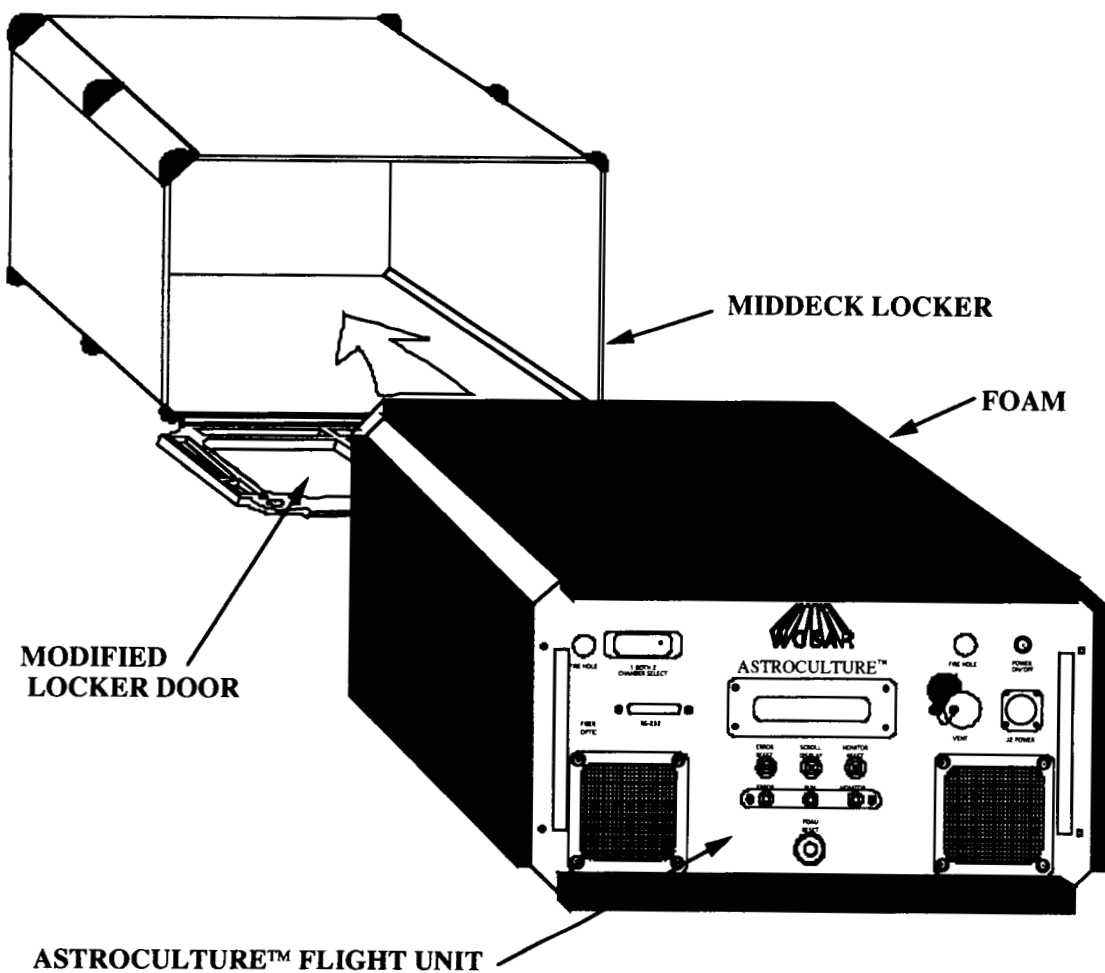


Figure 3 Diagram showing the integration of the ASTROCULTURE-1 flight unit into a middeck locker of the Space Shuttle.

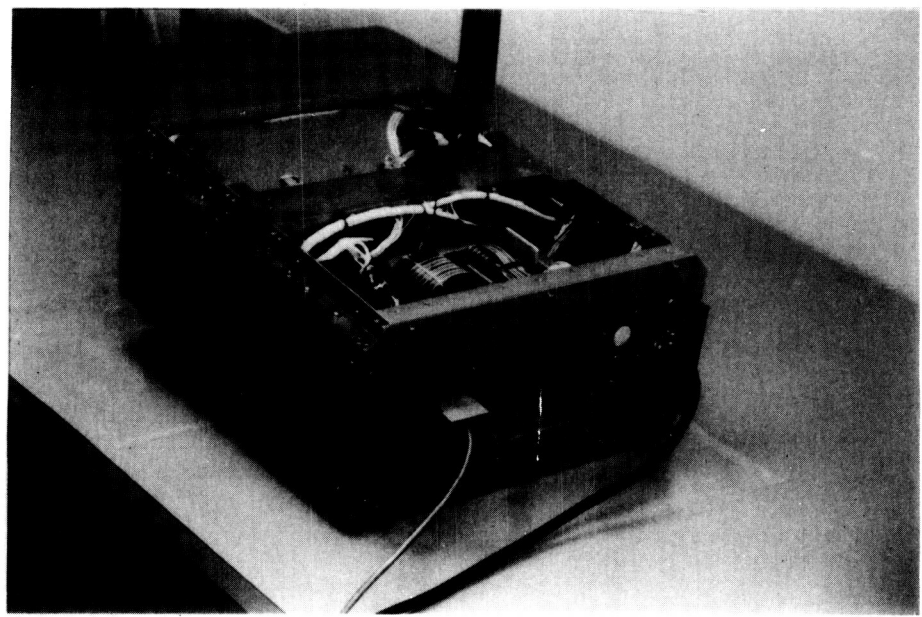


Figure 4 Front view of the ASTROCULTURE-1 flight unit before being inserted into a middeck locker.

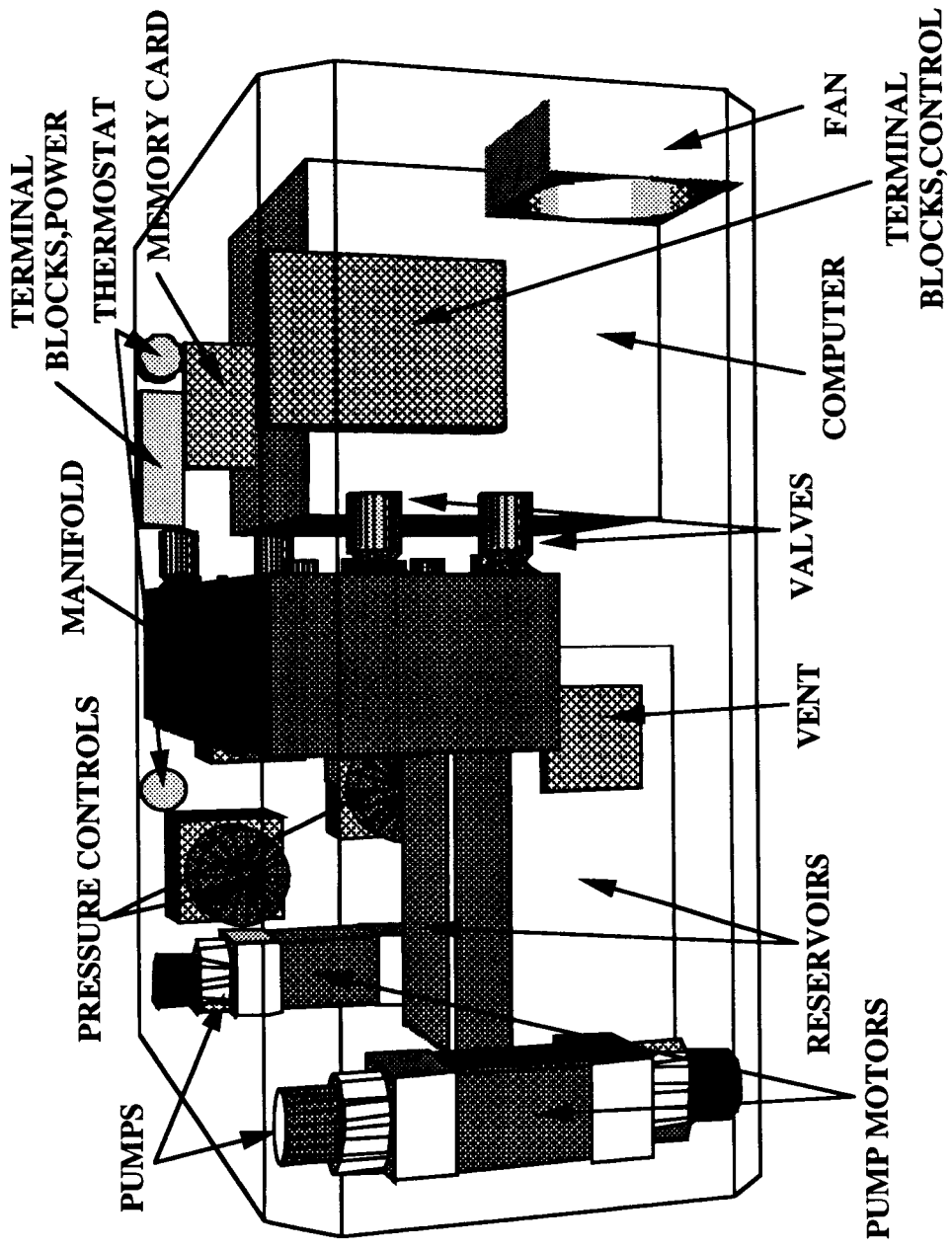


Figure 5 Side view diagram of the ASTROCULTURE-1 flight unit showing the layout of the various components.

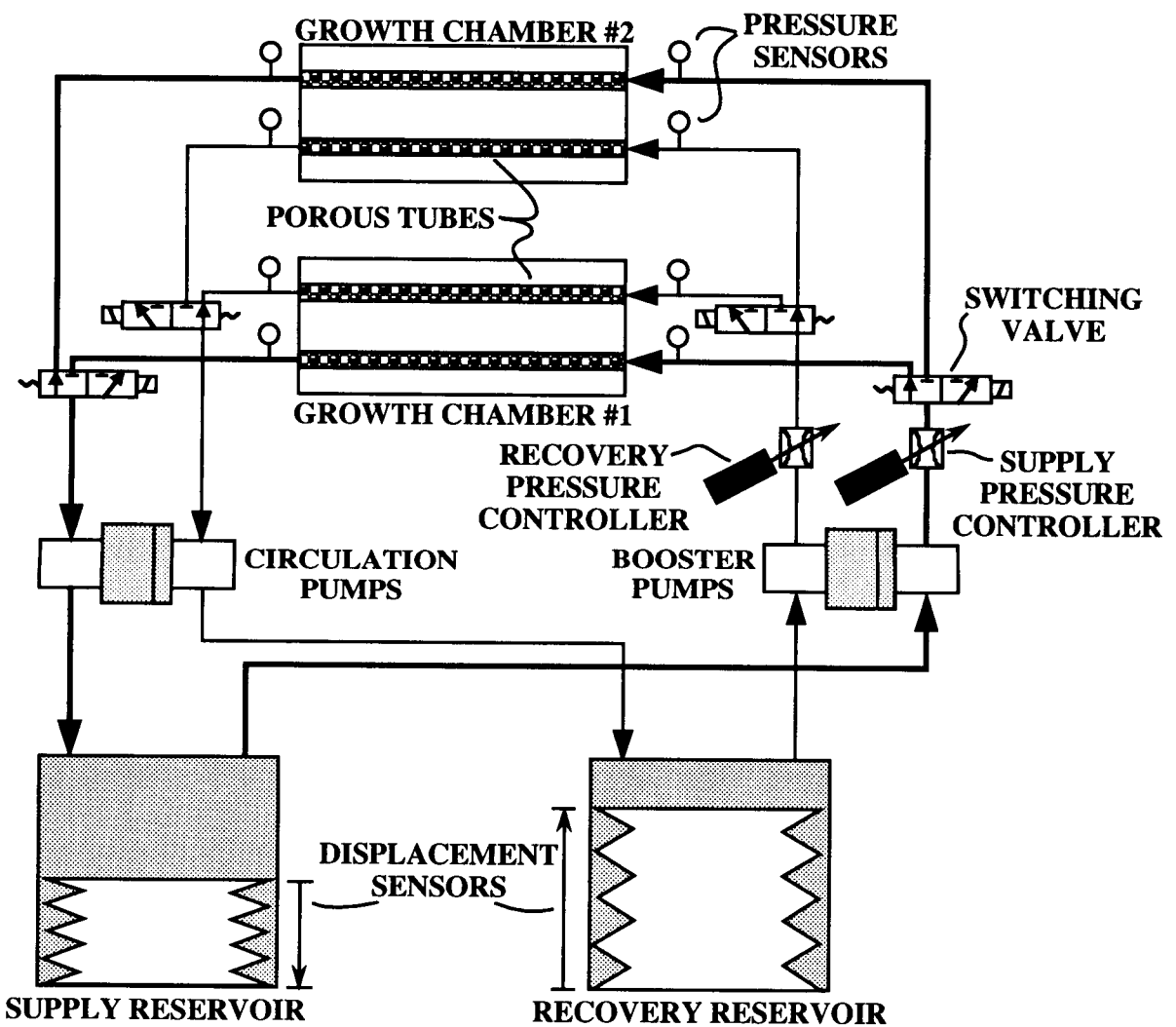


Figure 6 Diagram of the "supply" and "recovery" fluid loops in the ASTROCULTURE-1 flight experiment.



Figure 7 Pilot Ken Bowersox shown activating the ASTROCULTURE-1 flight experiment aboard Space Shuttle Columbia during the USML-1 mission.

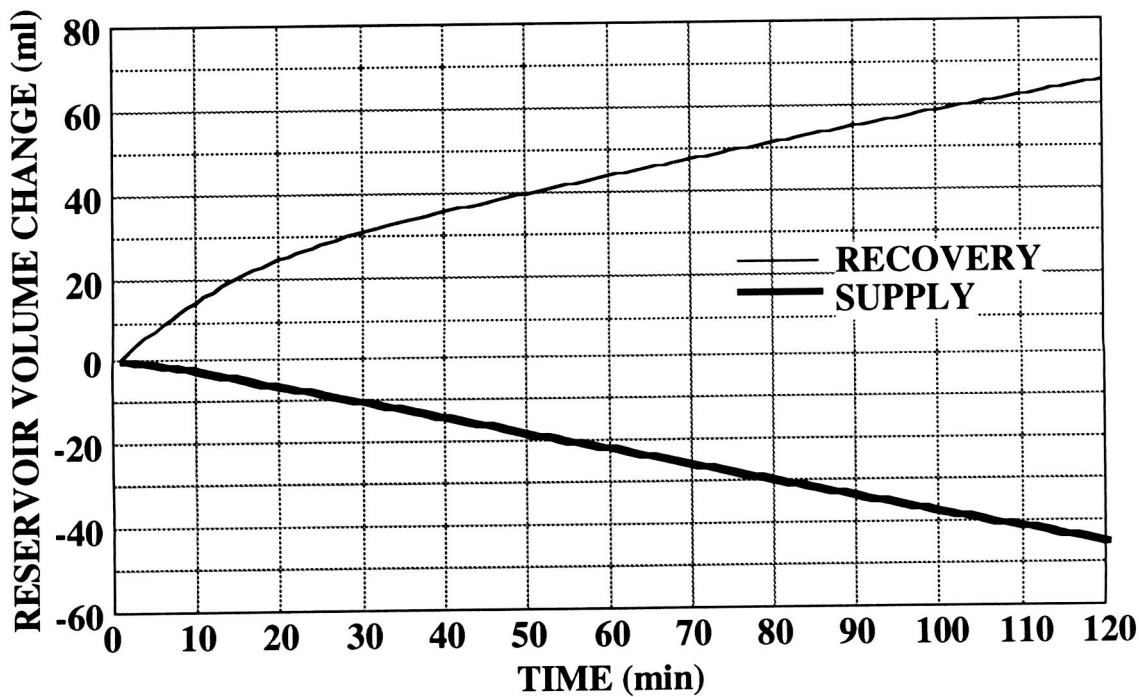


Figure 8 Example of typical "supply" and "recovery" reservoir volume changes observed during a 2 hour treatment period.

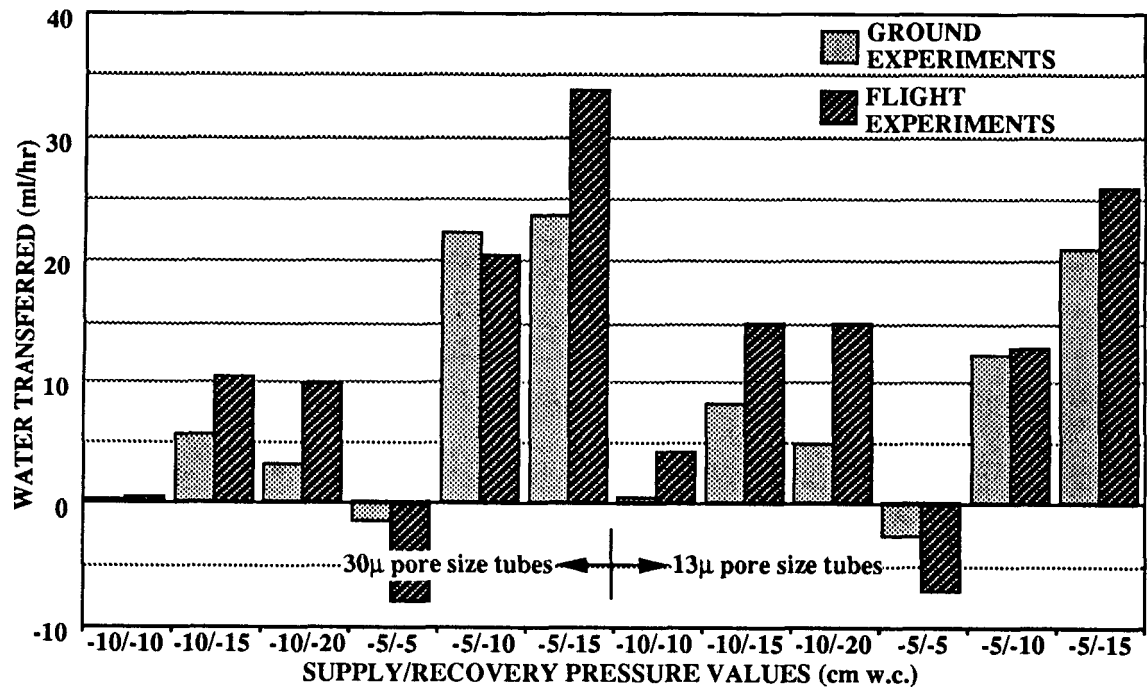


Figure 9 Graphic representation of the amount of volume increase in the "recovery" reservoir of the ASTROCULTURE flight unit during the last 60 minutes of the flight and ground treatment runs. Data are averages of two flight and two post-flight ground runs.

Discussion

Question: Characterizing these tubes that simulated roots through their porosity, you are just describing them with core diameter that you used on these stainless steel tubes. There has got to be more to the characterization of the porosity of those tubes than just the holes that are in them. What about the density of those pores or their distribution and could you say a little bit more about that?

Answer: Bob, do you know about the size of the particles that are used in this. I didn't know that we know the size of the particles of the tubes. Stainless steel is ground up and then we reconstituted it by putting some resin where they have been pressurized. But in no way are we trying to simulate a root with that. We are only simulating a root with it being something that is taking up water and pulling it up.

Question: I fully understand what the simulation concept is. The only problem is that you have a sintered structure; that is how those stainless steel tubes are made, from stainless steel powder and they are sintered into a structure. Somebody does metallography on it and tells you the model has 10 micron pores or 2 micron pores and so on. But the structure of that thing has what is called a permeability. The permeability establishes a relationship between the pressure difference in and out of that tube and the flux per area of the tube. Unless that permeability figure is known, it has to be calibrated because every sintered structure is different. Some of the differences you may be seeing are strictly of permeability effect which will only loosely correlate with the mean core diameter?

Answer: We basically calibrated our porosity by air entry. We have a porosity of about 50 %, I don't know if that is the kind of figure you are looking for.

Question: I am looking for permeability. This is different from porosity.

Answer: We know we checked this statement saying 50% porosity. We were very concerned with what we call an air entry value: how much negative pressure we could pull on those tubes before air would enter. We were in the range with the big pores of 25 cm water tension and then they start pulling air in.

REPORT DOCUMENTATION PAGE

Form Approved
OMB No. 0704-0188

Public reporting burden for this collection of information is estimated to average 1 hour per response, including the time for reviewing instructions, searching existing data sources, gathering and maintaining the data needed, and completing and reviewing the collection of information. Send comments regarding this burden estimate or any other aspect of this collection of information, including suggestions for reducing this burden, to Washington Headquarters Services, Directorate for Information Operations and Reports, 1215 Jefferson Davis Highway, Suite 1204, Arlington, VA 22202-4302, and to the Office of Management and Budget, Paperwork Reduction Project (0704-0188), Washington, DC 20503.

1. AGENCY USE ONLY (Leave blank)	2. REPORT DATE	3. REPORT TYPE AND DATES COVERED		
	May 1994	Conference Publication		
4. TITLE AND SUBTITLE		5. FUNDING NUMBERS		
Joint Launch + One Year Science Review of USML-1 and USMP-1 with the Microgravity Measurement Group				
6. AUTHOR(S)				
N. Ramachandran*, D.O. Frazier, S.L. Lehoczky and C.R. Baugher, Editors				
7. PERFORMING ORGANIZATION NAME(S) AND ADDRESS(ES)		8. PERFORMING ORGANIZATION REPORT NUMBER		
George C. Marshall Space Flight Center Marshall Space Flight Center, Alabama 35812		M-750		
9. SPONSORING/MONITORING AGENCY NAME(S) AND ADDRESS(ES)		10. SPONSORING/MONITORING AGENCY REPORT NUMBER		
National Aeronautics and Space Administration Washington, DC 20546		NASA CP - 3272 Volume I		
11. SUPPLEMENTARY NOTES				
*Universities Space Research Association, Huntsville, Alabama Proceedings of papers presented at a 3-day meeting held in Huntsville, Alabama, September 22-24, 1993, and implemented by Universities Space Research Association under contract to NASA MSFC.				
12a. DISTRIBUTION/AVAILABILITY STATEMENT		12b. DISTRIBUTION CODE		
Unclassified --- Unlimited				
Subject Category: 88				
13. ABSTRACT (Maximum 200 words)				
On September 22-24, 1993, investigators from the First United States Microgravity Laboratory (USML-1) and the First United States Microgravity Payload (USMP-1) Missions met with the Microgravity Measurement Group (MGMG) in Huntsville, Alabama, to discuss science results and the microgravity environments from the respective missions. USML-1 was launched June 1992, and USMP-1 was launched October 1992. This document summarizes from the various investigations, the comprehensive results and highlights, and also serves as a combined mission report for the two missions. USML-1 was the first totally U.S.-sponsored mission dedicated to microgravity research and included 31 investigations in fluid dynamics, crystal growth, combustion, biotechnology, and technology demonstrations supported by 11 facilities. The papers in these proceedings attest to the wealth of information gleaned from the highly successful mission. On the USMP-1 mission, both the MEPHISTO and the Lambda Point experiments exceeded by over 100% their planned science objectives. The mission also marked the first time that acceleration data were down-linked and analyzed in real-time. The meeting, which concentrated on flight results, brought low-gravity investigators, accelerometer designers, and acceleration data analysis experts together. This format facilitated a tremendous amount of information exchange between these varied groups. Several of the experimenters showed results, some for the very first time, of the effects of residual accelerations on their experiment. The proceedings which are published in two volumes also contain transcriptions of the discussion periods following talks and also submittals from a simultaneous poster session.				
14. SUBJECT TERMS		15. NUMBER OF PAGES		
Microgravity, Materials Processing, Bioprocessing, Fluid Physics, Human Physiology, Crystal Growth of Proteins and Semiconductors, G-Jitter, Acceleration Measurements, USML-1, USMP-1		533		
16. PRICE CODE				
		A23		
17. SECURITY CLASSIFICATION OF REPORT		18. SECURITY CLASSIFICATION OF THIS PAGE	19. SECURITY CLASSIFICATION OF ABSTRACT	20. LIMITATION OF ABSTRACT
Unclassified		Unclassified	Unclassified	Unlimited

